frontiers | Research Topics

Computational and experimental approaches on soft tissues biomechanics and mechanobiology

Edited by
Lei Fan, Ge He, Lei Wang and Yih-Kuen Jan

Published in
Frontiers in Bioengineering and Biotechnology

ISSN 1664-8714
ISBN 978-2-8325-6460-8
DOI 10.3389/978-2-8325-6460-8

About Frontiers

Frontiers is more than just an open access publisher of scholarly articles: it is a pioneering approach to the world of academia, radically improving the way scholarly research is managed. The grand vision of Frontiers is a world where all people have an equal opportunity to seek, share and generate knowledge. Frontiers provides immediate and permanent online open access to all its publications, but this alone is not enough to realize our grand goals.

Frontiers journal series

The Frontiers journal series is a multi-tier and interdisciplinary set of open-access, online journals, promising a paradigm shift from the current review, selection and dissemination processes in academic publishing. All Frontiers journals are driven by researchers for researchers; therefore, they constitute a service to the scholarly community. At the same time, the *Frontiers journal series* operates on a revolutionary invention, the tiered publishing system, initially addressing specific communities of scholars, and gradually climbing up to broader public understanding, thus serving the interests of the lay society, too.

Dedication to quality

Each Frontiers article is a landmark of the highest quality, thanks to genuinely collaborative interactions between authors and review editors, who include some of the world's best academicians. Research must be certified by peers before entering a stream of knowledge that may eventually reach the public - and shape society; therefore, Frontiers only applies the most rigorous and unbiased reviews. Frontiers revolutionizes research publishing by freely delivering the most outstanding research, evaluated with no bias from both the academic and social point of view. By applying the most advanced information technologies, Frontiers is catapulting scholarly publishing into a new generation.

What are Frontiers Research Topics?

Frontiers Research Topics are very popular trademarks of the *Frontiers journals series*: they are collections of at least ten articles, all centered on a particular subject. With their unique mix of varied contributions from Original Research to Review Articles, Frontiers Research Topics unify the most influential researchers, the latest key findings and historical advances in a hot research area.

Find out more on how to host your own Frontiers Research Topic or contribute to one as an author by contacting the Frontiers editorial office: frontiersin.org/about/contact

Computational and experimental approaches on soft tissues biomechanics and mechanobiology

Topic editors

Lei Fan — Marquette University, United States

Ge He — Lawrence Technological University, United States

Lei Wang — Capital Normal University, China

Yih-Kuen Jan — University of Illinois at Urbana-Champaign, United States

Citation

Fan, L., He, G., Wang, L., Jan, Y.-K., eds. (2025). *Computational and experimental approaches on soft tissues biomechanics and mechanobiology*.

Lausanne: Frontiers Media SA. doi: 10.3389/978-2-8325-6460-8

Table of contents

frontiers | Frontiers in Bioengineering and Biotechnology

TYPE Original Research
PUBLISHED 21 December 2023
DOI 10.3389/fbioe.2023.1330301

OPEN ACCESS

EDITED BY
Ge He,
University of Wisconsin–Milwaukee,
United States

REVIEWED BY
Zugui Wu,
The Third Affiliated Hospital of Yunnan University of Chinese Medicine, China
Žiga Kozinc,
University of Primorska, Slovenia

*CORRESPONDENCE
Tobias Götschi,
tobias.goetschi@hest.ethz.ch

†These authors have contributed equally to this work and share last authorship

RECEIVED 30 October 2023
ACCEPTED 08 December 2023
PUBLISHED 21 December 2023

CITATION
Götschi T, Snedeker JG, Fitze DP, Sarto F, Spörri J and Franchi MV (2023), Three-dimensional mapping of ultrasound-derived skeletal muscle shear wave velocity.
Front. Bioeng. Biotechnol. 11:1330301.
doi: 10.3389/fbioe.2023.1330301

Three-dimensional mapping of ultrasound-derived skeletal muscle shear wave velocity

Tobias Götschi[1,2,3]*, Jess G. Snedeker[1,2], Daniel P. Fitze[3,4], Fabio Sarto[5], Jörg Spörri[3,4†] and Martino V. Franchi[3,5†]

[1]Orthopaedic Biomechanics Laboratory, Department of Orthopaedics, Balgrist University Hospital, Zurich, Switzerland, [2]Institute for Biomechanics, ETH Zurich, Zurich, Switzerland, [3]Department of Orthopaedics, Sports Medical Research Group, Balgrist University Hospital, University of Zurich, Zurich, Switzerland, [4]Department of Orthopaedics, University Centre for Prevention and Sports Medicine, Balgrist University Hospital, University of Zurich, Zurich, Switzerland, [5]Department of Biomedical Sciences, Institute of Physiology, University of Padua, Padua, Italy

Introduction: The mechanical properties of skeletal muscle are indicative of its capacity to perform physical work, state of disease, or risk of injury. Ultrasound shear wave elastography conducts a quantitative analysis of a tissue's shear stiffness, but current implementations only provide two-dimensional measurements with limited spatial extent. We propose and assess a framework to overcome this inherent limitation by acquiring numerous and contiguous measurements while tracking the probe position to create a volumetric scan of the muscle. This volume reconstruction is then mapped into a parameterized representation in reference to geometric and anatomical properties of the muscle. Such an approach allows to quantify regional differences in muscle stiffness to be identified across the entire muscle volume assessed, which could be linked to functional implications.

Methods: We performed shear wave elastography measurements on the vastus lateralis (VL) and the biceps femoris long head (BFlh) muscle of 16 healthy volunteers. We assessed test-retest reliability, explored the potential of the proposed framework in aggregating measurements of multiple subjects, and studied the acute effects of muscular contraction on the regional shear wave velocity post-measured at rest.

Results: The proposed approach yielded moderate to good reliability (ICC between 0.578 and 0.801). Aggregation of multiple subject measurements revealed considerable but consistent regional variations in shear wave velocity. As a result of muscle contraction, the shear wave velocity was elevated in various regions of the muscle; showing pre-to-post regional differences for the radial assessement of VL and longitudinally for BFlh. Post-contraction shear wave velocity was associated with maximum eccentric hamstring strength produced during six Nordic hamstring exercise repetitions.

Discussion and Conclusion: The presented approach provides reliable, spatially resolved representations of skeletal muscle shear wave velocity and is capable of detecting changes in three-dimensional shear wave velocity patterns, such as those induced by muscle contraction. The observed systematic inter-subject variations in shear wave velocity throughout skeletal muscle additionally underline the necessity of accurate spatial referencing of measurements. Short

high-effort exercise bouts increase muscle shear wave velocity. Further studies should investigate the potential of shear wave elastography in predicting the muscle's capacity to perform work.

KEYWORDS

shear wave elastography, muscle, biomechanics, ultrasound, stiffness, elasticity

Introduction

The mechanical properties of muscles are of relevance in the context of clinical examination and various scientific endeavors. During voluntary contraction, a muscle's stiffness can be related to muscle functional properties, as it is directly related to the tension it produces (Ettema and Huijing, 1994; Morgan, 1977), while localized alterations of stiffness may underlie deleterious conditions, including dysfunctional innervation, muscle contractures and fibrosis (Kawai et al., 2018; Alfuraih et al., 2019). Assessing the change in passive muscle stiffness over the corresponding joint's range of motion yields an estimate for passive tension (Johns and Wright, 1962; Gennisson et al., 2010; Miyamoto et al., 2018; Wang et al., 2019), which in turn may be pivotal in understanding certain injury mechanisms or may help explain conditions of idiopathic musculoskeletal pain or dysfunction (Vandervoort, 1999). Muscle stiffness at rest depends on its structure and composition as well as the nature of any preceding stimuli (Siracusa et al., 2019). Moreover, the extracellular matrix (ECM), the intramuscular connective tissue network of skeletal muscle, is considered a key element contributing to whole muscle stiffness (Kjær, 2004; Fouré et al., 2011). For instance, repeated high-effort muscular contraction generates ECM creep, potentially disturbing the finely tuned interplay between the contractile and noncontractile elements, which may in part account for peripheral fatigue (Siracusa et al., 2019; Lacourpaille et al., 2017).

Whereas manual palpation provides a simple and useful means to assess muscle stiffness (Kvåle et al., 2003), more sophisticated approaches are needed to quantify this muscle feature. Shear wave elastography (SWE) has arisen as one method of choice because it yields quantitative estimates of tissue mechanical properties. Localized displacement induces shear motion propagating through the tissue, the velocity of which is in part dependent on tissue stiffness, with increasing stiffness yielding increasing shear wave velocity (SWV) (Nightingale, 2011). In principle, any soft tissue imaging modality with sufficient spatial and temporal resolution can be used to observe shear wave propagation, but ultrasound (US) has specific appeal due to its low cost and large availability. Moreover, the US transducer can induce the required tissue micromotion by transmitting properly timed compressive waves that superimpose into localized shear displacement.

US SWE has been successfully used on skeletal muscle to estimate active and passive mechanical tension (Hug et al., 2015; Zimmer et al., 2022), to detect disease (Alfuraih et al., 2019; Boulard et al., 2021; Tisha et al., 2018) or exercise-induced damage (Siracusa et al., 2019; Lacourpaille et al., 2017; Chalchat et al., 2020; Lacourpaille et al., 2014) and other stimuli (Sions et al., 2012). The most commonly used US SWE systems work with one-dimensional piezo array transducers, which consequently yield quasi-two-dimensional (2D) measurements of tissue stiffness. 2D arrays of piezo elements for three-dimensional (3D) SWE exist, but their volume of view is limited (Dong et al., 2022).

For the assessment of large structures such as skeletal muscle, 2D US SWE hence carries a significant limitation in that a single measurement only samples a minute portion of the volume of interest. However, the rate of measurement of state-of-the-art US devices is sufficiently high (~2 Hz) that even large skeletal muscles can be sampled in their entirety at a relatively high spatial resolution within a few minutes. Provided that each measurement is annotated with its respective position and the movement of the structure of interest during the scan is negligible or accounted for, the set of acquired measurements can be projected into 3D space to yield a volumetric SWV representation of the structure (Götschi et al., 2021). To enable intra- and inter-individual comparisons of the local SWV, the retrieved volume can be mapped into an abstracted representation of the muscle of study in reference to selected geometrical and anatomical features. A similar approach has already been shown to be technically feasible, reproducible and clinically significant in previous studies for tendons (Götschi et al., 2021; Götschi et al., 2022a; Götschi et al., 2022b). However, it is not clear *a priori* whether this is directly transferable to muscle tissue, particularly given the much larger volumes of interest.

In the current proof-of-concept study, we propose and assess a framework for spatially resolved, three-dimensional anatomically referenced skeletal muscle US SWE measurements. Specifically, we aimed to (1) determine the test-retest reliability of the proposed approach, (2) explore its potential in aggregating measurements of multiple subjects, and (3) assess its capability of detecting changes in the three-dimensional shear wave velocity patterns, such as those induced by muscle contraction.

Materials and methods

Study design and study population

In the current study, we performed SWE measurements on the right vastus lateralis (VL) muscle and the left biceps femoris long head (BFlh) muscle of 16 adult participants who reported being free of any lower extremity musculoskeletal injuries/complaints. (eight females; age: 27.3 ± 2.8 years; height: 174.4 ± 9.2 cm; weight: 67.3 ± 9.2 kg; BMI: 22.1 ± 2.4 kg m^{-2}).

For both muscles, first, two US SWE measurements were performed to determine the reliability of the method; then, a maximum effort task was performed specifically targeting both muscles, consisting of one isometric knee extension for VL and six repetitions of Nordic Hamstring Exercise (NHE) for BFlh muscle, immediately followed by a third US SWE measurement. Additionally, the BFlh muscle was scanned again 5 minutes after the initial post-contraction measurement. The maximum eccentric

hamstring strength (MEHS) performed during the NHE was used to quantify the physical performance during the BFlh contraction exercise and explore any potential associations with the muscle's SWV. The study involving humans was approved by the Cantonal Ethics Committee Zurich, Switzerland (KEK-ZH-NR: 2017-01395). All participants were informed in writing about the measurement procedures and provided written consent.

Shear wave elastography measurement

Participants laid on a physiotherapy bed at least 5 minutes prior to the first acquisition to allow body fluid stabilization and minimize potential confounding factors related to preceding physical activity. For both muscles, the portion between 0% and 70% of the femur length (where 0 was regarded as the mid-patellar point) was measured. The proximal measurement border was determined based on the distance between the patella center and the greater trochanter and marked with a permanent ink pen (Franchi et al., 2020a). For the VL measurements, the participants laid supine on the examination table. For the BFlh measurements, the participants laid prone on the examination table with their feet just outside the table frame. The initial measurements of both muscles were repeated once by the same operator between which the participants lied onto their back and then re-established the measurement position. Immediately after the respective muscle contraction tasks described below, we performed another SWE measurement. The BFlh was scanned 5 min after the first post-contraction measurement once more to track acute changes in SWV over a short period of time.

Maximum effort excercise

The maximum effort exercise for the VL muscle consisted of a 15-s isometric contraction of the knee extensors. The participants sat on the examination table with the knees flexed 90° and the right ankle fixated by a brace. For the BFlh contraction exercise, the participants performed 6 maximum eccentric knee flexion manoeuvres on a hamstring exercise board (NordBord, Vald Performance, Newstead, Australia). The participants were positioned with their knees on a padded board, without shoes, with the ankles secured by braces just above the l ateral malleoli. They were advised to maintain alignment of their shoulders, hips, and knees while crossing their arms in front of their body. They were then instructed to slowly advance forward and exert maximum resistance against the movement using both legs (Kiers et al., 2021). During exercise execution, we recorded the maximum force achieved by the participant during each repetition using the force sensors integrated into the exercise board (Opar et al., 2013). The six recorded maximum force values were aggregated by extracting the median, which was then normalized by the participant's body weight to derive the normalized MEHS.

Shear wave elastography acquisition

The data acquisition procedure has been technically validated and described in detail previously (Götschi et al., 2021). Briefly, measurements of shear wave group velocity were acquired as provided by the ultrasound device (Aixplorer Ultimate, SuperSonic Imagine, Aix-en-Provence, France) using a linear 5 cm transducer (SuperLinear SL18-5). These measurements were transmitted on the fly to the measurement computer via ethernet and the MATLAB interface provided by the manufacturer. The transducer pose was tracked throughout the scan with an optical tracking system and optical markers attached to the transducer. We acquired both brightness-mode (B-mode) and SWV measurements in parallel. The B-mode images were reconstructed analogously to the SWV measurements, provided the basis for anatomical orientation and were segmented manually to mask the respective SWV volume. During scanning, the transducer was oriented parallel to the muscle fibres, and was carefully kept constantly in plane throughout the whole ROI by an expert operator (MVF). Adequate orientation can be ensured by observing and maximizing the striped appearance of the intramuscular structure in relation to transducer rotation (about its long axis). The region of interest was scanned in multiple consecutive swipes with the starting location randomized (distal/proximal). SWV measurements were acquired at 2 Hz.

Parameterization of the shear wave velocity map

To conduct meaningful spatially resolved comparisons and aggregations between different SWE acquisitions, each measurement was transformed into a standardized form. This was achieved by mapping the gridded SWV volume into a geometrically and anatomically referenced representation. Each VL measurement was first aligned along its distal-proximal axis (using principal component analysis). Slices orthogonal to the distal-proximal axis were then retrieved (eight and six for the VL and the BFlh, respectively), and each slice was mapped into a polar coordinate system with its origin given by the circle segment that best fit the respective segmentation mask (least squares). All shear wave velocity estimates within a slice were aggregated into discrete cells of uniform relative radial and azimuthal extent. BFlh measurements were processed analogously with the sole difference that the slice-specific polar coordinate system's origin was given by the geometric mean of the respective segmentation mask. Figure 1 visualizes the parameterization procedure for the VL (top row) and the BFlh (bottom row).

Statistical analysis

Descriptive statistics are presented as the mean and standard deviation. Test-retest reliability was quantified in terms of the intraclass correlation coefficient (ICC(2,1)) (Shrout and Fleiss, 1979) based on a two-way random effects model assessing the absolute agreement of a single-measure approach and the related standard error of measurement (Sem) (de Vet et al., 2006). ICC values were classified as poor (≤0.2), fair (0.21–0.4), moderate (0.41–0.6), good (0.61–0.8), and very good (>0.8) (Ashby, 1991).

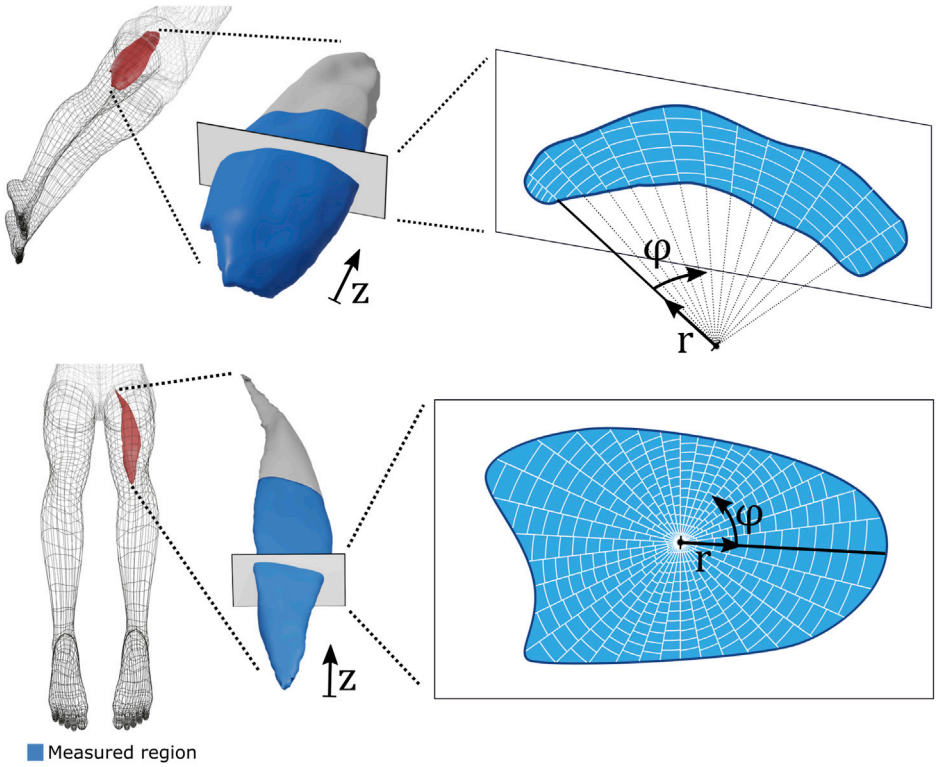

FIGURE 1
Spatial parameterization of volumetric shear wave velocity (SWV) maps. Top row: Vastus lateralis SWV volumes were discretized into longitudinal slices (along z), and each slice was subdivided into angular (φ) and radial (r) partitions in reference to the centre of a best-fit circle (Taubin, 1991). Bottom row: Biceps femoris long head SWV volumes were handled analogously with the sole difference that the origin of the polar coordinate system was placed at the geometric mean of the respective cross-sectional slice.

TABLE 1 Test-retest reliability of whole-muscle SWV measurements. ICC: Intra class correlation coefficient. CI: Confidence interval. SEm: Standard error of measurement.

Structure	ICC (95% CI)	SEm [m/s]
Vastus lateralis	0.941 (0.843, 0.979)	0.044
Biceps femoris long head	0.885 (0.709, 0.958)	0.058

We reported both the reliability of whole-muscle measurements and the reliability of measuring a distinct region of the muscle. The latter measurement was evaluated in both the context of assessing attributes within a subject-muscle (inter-regional) or across subjects (inter-subject). Whole muscle reliability metrics were reported with their estimates and the associated 95% confidence intervals. Analysis of regional reliability requires aggregation of different metrics; hence, we reported median and interquartile range. We conducted paired-sampled t-tests to evaluate the effect of muscular contraction on muscle SWV across both global and regional measurements stratified along one of three dimensions. To explore associations between normalized MEHS and BFlh SWV, we applied Spearman rank correlation tests at both the global and regional levels. The analysis was conducted with MATLAB (2022b, The MathWorks, Inc., Natick, MA, USA). Statistical significance was set at $\alpha = 0.05$.

Results

Global muscle assessment

Whole-muscle measurements were highly reliable in both assessed structures (Table 1).

The VL resting SWV was lower than the BFlh SWV ($p = 0.025$). Immediately following muscular contraction, SWV was elevated in both structures (VL: $p = 0.026$, BFlh: $p = 0.002$), and BFlh SWV remained elevated at the third measurement 5 min after the contraction ($p = 0.038$) (Figure 2).

Whereas normalized MEHS was non-significantly associated with initial BFlh SWV (Spearman correlation coefficient: $\rho = -0.485$, $p = 0.059$) or absolute change in BFlh SWV ($\rho = -0.076$, $p = 0.780$), it was significantly associated with the immediate post-contraction BFlh SWV ($\rho = -0.588$, $p = 0.019$).

Regional muscle assessment

Regional muscle assessments yielded moderate to very good reliability. Inter-regional assessments yielded higher reliability than inter-subject assessments (Table 2).

Aggregation of multiple subject measurements revealed considerable but consistent regional variations in shear wave velocity. Figure 3 and Figure 4 provide visualizations of the

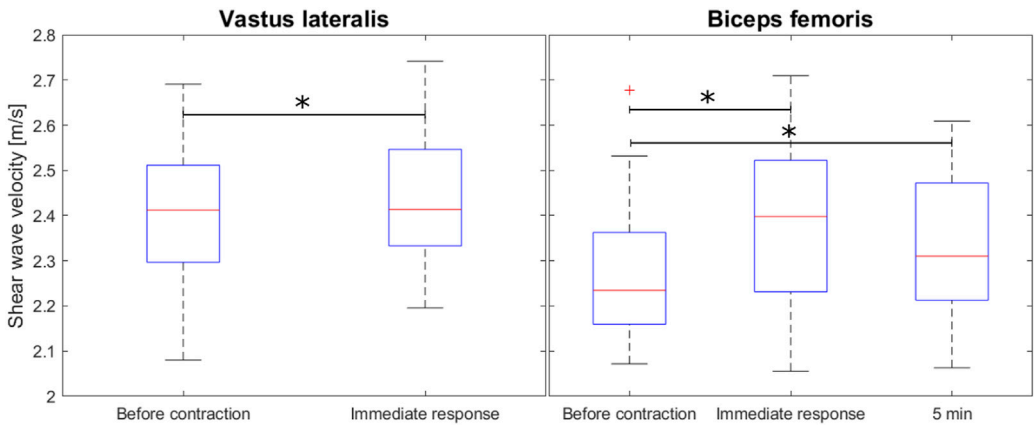

FIGURE 2
Overall shear wave velocity before and after voluntary muscular contraction for the VL (15 s of isometric maximal effort) and after 6 repetions of the Nordic Hamstring Exercise for the BFlh muscle).

TABLE 2 Median test-retest reliability of regional muscle SWV measurements with regards to a repeated assessment of muscle regions within the same subject (Inter-regional) or over multiple subjects (Inter-subject). IQR: Interquartile range. SEm: Standard error of measurement.

Structure	Domain	ICC (IQR)	SEm (IQR) [m/s]
Vastus lateralis	Inter-regional	0.752 (0.673, 0.815)	0.328 (0.289, 0.396)
	Inter-subject	0.600 (0.406, 0.727)	0.273 (0.185, 0.409)
Biceps femoris long head	Inter-regional	0.801 (0.566, 0.843)	0.223 (0.190, 0.252)
	Inter-subject	0.578 (0.419, 0.714)	0.227 (0.170, 0.303)

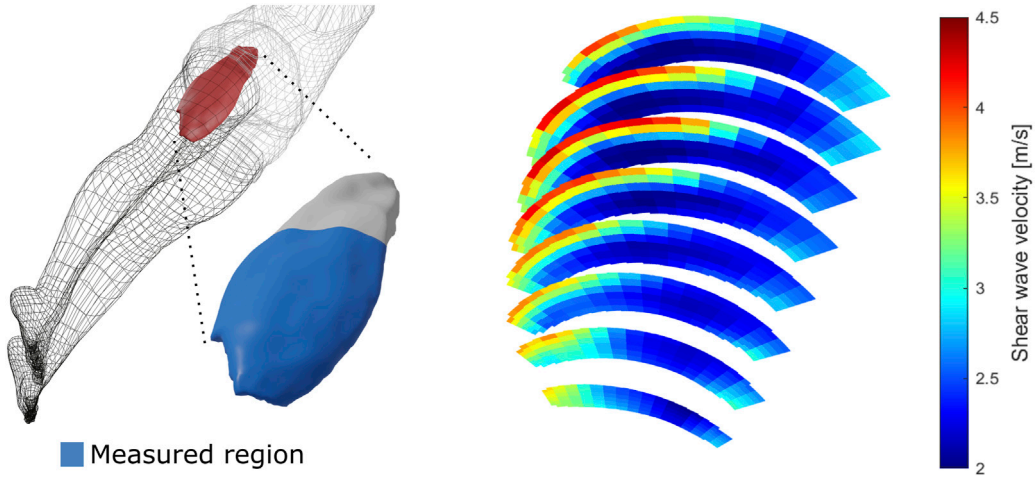

FIGURE 3
Average vastus lateralis regional shear wave velocity at rest. The left side of the figure presents a schematic depiction of the vastus lateralis muscle with the measured region in blue. The right side of the figure shows the three-dimensional measurements of shear wave velocity of the same muscle at rest, averaged over all participant measurements.

parameterized SWV maps of the VL and the BFlh, respectively averaged over the pre-exercise measurements of all subjects.

The VL SWV showed a strong gradient over the radial axis of the muscle, with deep regions displaying lower SWV than superficial regions. Over the angular axis, a U-shaped relationship was evident, with central regions possessing lower SWV compared to the periphery (Figure 5, top row). The BFlh SWV displayed a steady increase from the radial centre to the muscle surface. The distal

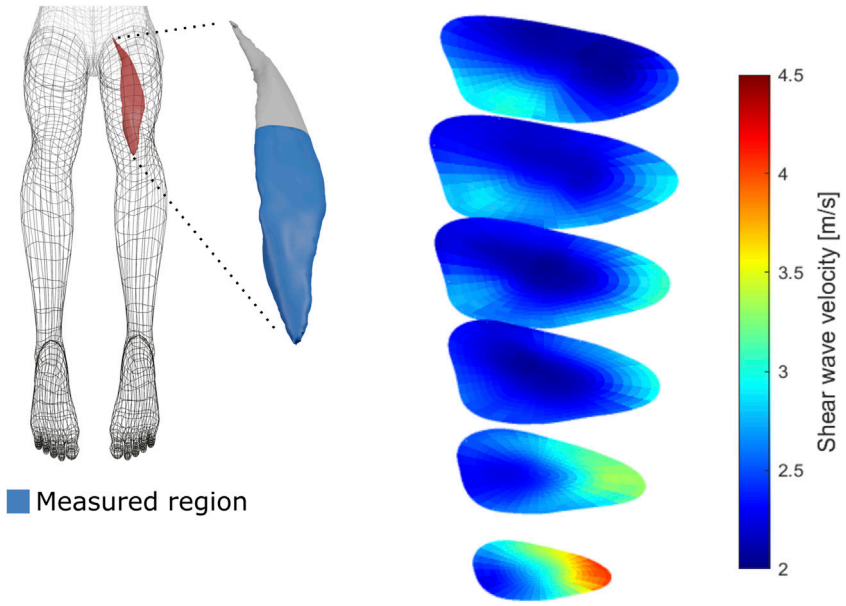

FIGURE 4
Average biceps femoris long head regional shear wave velocity at rest. The left side of the figure presents a schematic depiction of the biceps femoris long head muscle with the measured region in blue. The right side of the figure shows the three-dimensional measurements of shear wave velocity of the same muscle at rest, averaged over all participant measurements.

portion displayed considerably higher SVW than the central and proximal regions (Figure 5, bottom row).

Preceding muscular contraction generally elevated SWV; however, no strong indicator for a region-specific response was evident.

We did, however, find strong regionality in the association between normalized MEHS and BFlh SWV. Specifically, normalized MEHS correlated strongly with the SWV assigned to the central portion (in the radial axis) of the muscle immediately after the exercise bout but not with the one at rest (Figure 6).

Discussion

Test-retest reliability of global and regional muscle assessments

The presented approach revealed reliable results in both muscles assessed. Indeed, global muscle assessment reliability compares favorably with the available literature where reported ICC values for 2D SWV assessments are in the range of 0.800—0.937 (Lacourpaille et al., 2012; Phan et al., 2019; Bravo-Sánchez et al., 2021) and 0.842—0.850 (Lee et al., 2021; Šarabon et al., 2019) for the VL and the BFlh, respectively. VL measurements yielded higher reliability than BFlh measurements possibly because of the more complex architecture of the latter (Pimenta et al., 2018; Franchi et al., 2020b; Brusco et al., 2022), which usually presents a characteristic "s-like shape" fascicle architecture requiring careful alignment of the US transducer during the measurement (Charles et al., 2022). The vastus lateralis muscle, although showing regional architectural differences, is known to present a more "homogeneous" architecture compared to other muscle groups (Blazevich et al., 2006; Franchi et al., 2018; Sarto et al., 2021). Furthermore, the more irregular shape of BFlh complicated its segmentation on the US reconstruction which may have induced additional measurement variability. Global muscle assessments were also more reliable than regional assessments in both muscles. This indicates that many factors modulating muscle shear properties act on the global muscle or subject scale. Spatially resolved measurements suffer from random variability introduced by registration inaccuracies and other noise-generating processes that outweigh systematic regional variation. Many of these inaccuracies are dominant on the between-subject level, and hence, interregional within-subject reliability was superior to inter-subject reliability.

In both muscles, the aggregation of all subject measurements revealed large but consistent variations in SWV, underlining the necessity of accurate spatial referencing of the measurements.

Three-dimensional shear wave velocity variations across different anatomical locations

Our novel approach unveiled, for the first time, distinct regional differences in stiffness within human muscles. Specifically, the deeper regions of the VL displayed lower SWV than superficial regions, while the BFlh exhibited increases from the radial center to the muscle surface. Notably, the VL exhibited a U-shaped relationship over the angular axis, with central regions displaying lower stiffness compared to the periphery (i.e., medial and lateral regions of the VL). Additionally, distal portions of the BFlh showed

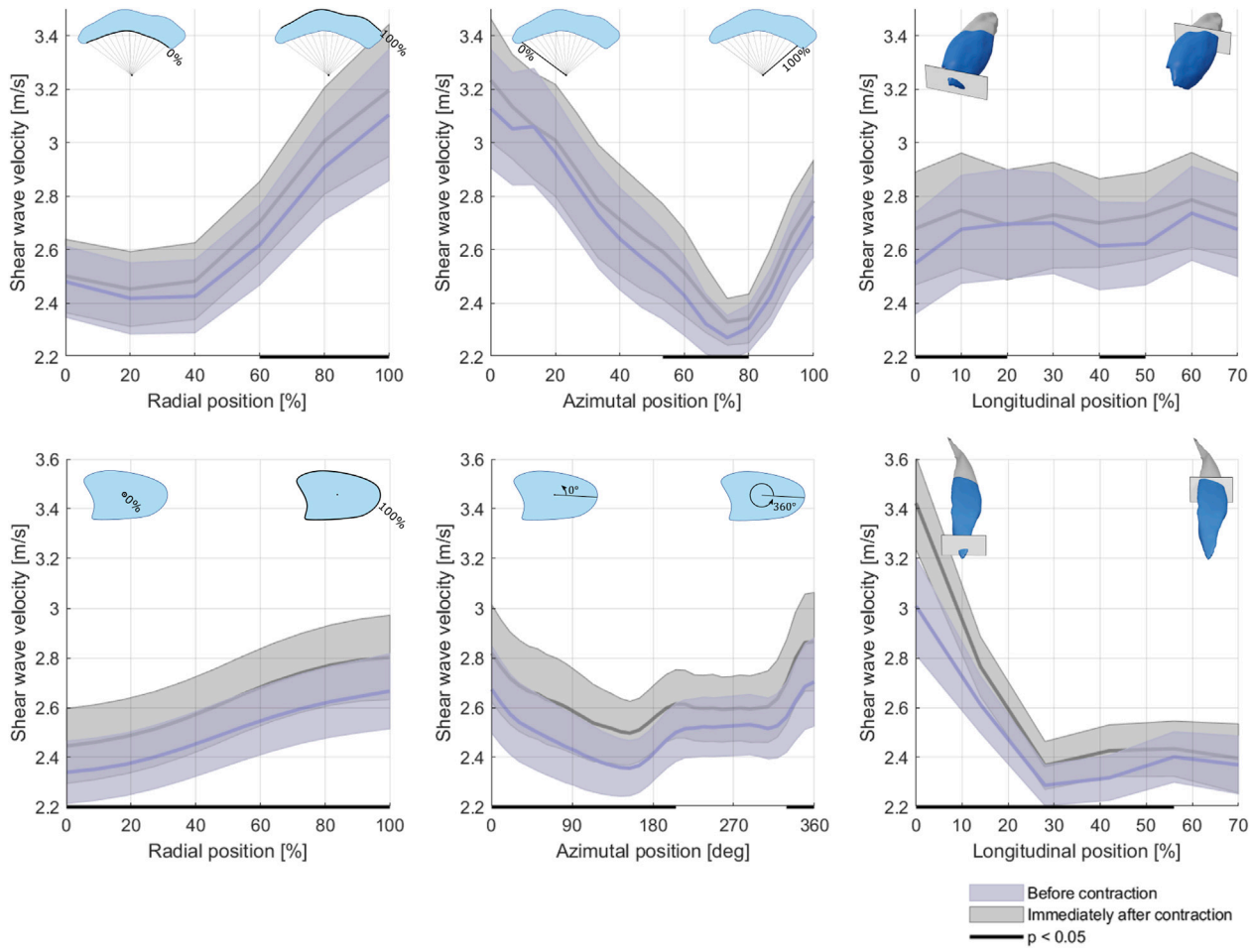

FIGURE 5
Average shear wave velocity over the radial (first column), angular (second column) and longitudinal axes of the vastus lateralis (top row) and biceps femoris long head (bottom row) at rest before and immediately after contraction. Area of uncertainty: Standard error of the mean.

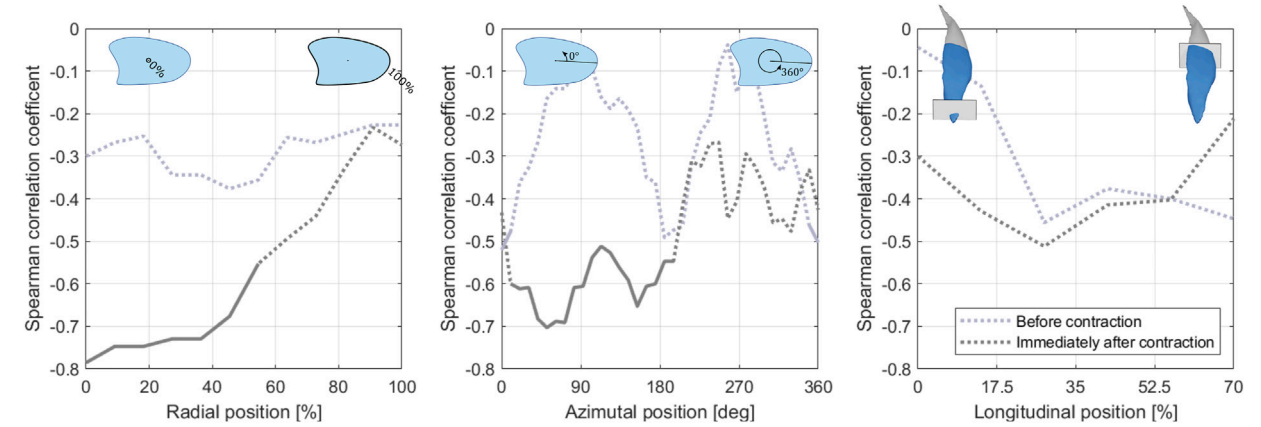

FIGURE 6
Association of the normalized maximum eccentric hamstring strength and the regional (from left to right: radial, angular, longitudinal) biceps femoris long head shear wave velocity before (blue line) and immediately after the exercise bout (grey line). Regions with associations of statistical significance ($p < 0.05$) are delineated with a solid line.

remarkably higher SWV compared to more proximal regions. These location-dependent muscle mechanical properties may significantly contribute to providing new insights into muscle force production and susceptibility to muscle strain injuries in different regions. Several factors could account for these anatomical differences in muscle stiffness observed in different muscle regions. No previous studies have investigated potential regional differences in ECM distribution in humans. However, animal studies have shown that ECM sheaths at the muscle periphery are directly connected to the epimysium, the external layer of dense connective tissue which ensheaths the entire muscle (Sleboda et al., 2020). As the epimysium is known to possess larger collagen fibres, the ECM of external muscle regions may present similar properties, partially explaining the higher SWV at the muscle periphery observed in our study.

In addition, depth-dependent differences in fibre phenotype have been previously documented in seminal cadaver studies (Lexell et al., 1983a; Lexell et al., 1983b), with higher type I fibre percentages reported in deeper compartments of the VL. As resting tension is known to be higher in fast than in slow fibres (Schiaffino and Reggiani, 2011):this may contribute to the lower stiffness observed in deep regions of the VL, although this is just a speculation. Furthermore, the differences in motor unit potential properties observed when comparing different VL depths (Knight and Kamen, 2005; Jones et al., 2021) might suggest a differential muscle innervation profile, which could influence muscle tone. Last, regional differences in intramuscular fat content can also play a role, as it is generally considered inversely associated with muscle stiffness (Pinel et al., 2021). In support of this view, the region where we observed the lower stiffness in BFlh (~40% of femur length) is known to have the highest amount of intramuscular fat in the hamstring muscles (Yoshiko et al., 2017). The determinants of anatomical differences in muscle stiffness warrant further investigation in future studies.

Muscle contraction-induced changes in the three-dimensional shear wave velocity patterns

We observed a spatially uniform increase in SVW in response to both a 15-s isometric contraction exercise for the VL and six eccentric contractions for the BFlh. There are multiple reports in the literature that investigate the 2D shear wave velocity of skeletal muscle at rest in response to physical work. Siracusa et al. had their subjects perform 60 repetitions of 5 s isometric maximum voluntary knee extensions and measured the SWV in one location in the VL (~50% longitudinal, central in the mediolateral axis, in the superficial half of the muscle). SWV was measured every 10 repetitions and showed a significant decrease after the first 10 repetitions followed by further depression, reaching a minimum after 50 repetitions (Siracusa et al., 2019). In accordance with Siracusa et al.'s findings, an isometric trunk extension fatigue protocol depressed the apparent shear modulus of the deep multifidus muscles (Vatovec et al., 2022). Similarly, low-intensity, high-duration loading as generated during a long-distance race elicited a depression in SWV that persisted for at least 72 h (Andonian et al., 2016). Contrary associations were reported by Lacourpaille and others (Lacourpaille et al., 2017), who found increased SWV in elbow flexor and knee extensor muscles 30 min following high-repetition (>60) maximum voluntary eccentric contractions, as well as by Akagi et al., who reported an increase in triceps brachii stiffness immediately after a high effort (80% MVC) resistance training (Akagi et al., 2015). These contrary observations might be consistent insofar, in that muscle fatigue may lower while muscle damage may increase muscle stiffness (Ličen and Kozinc, 2022).

Muscular contraction likely modulates muscle shear properties through various factors. In a previous study, for instance, we found stretching of the tendon to result in an increase in SWV, which may be attributed to transient structural changes, such as collagen fibre relaxation and uncrimping, that occur after an initial load (Götschi et al., 2021; Purslow et al., 1998). Analogous mechanisms may be at play in the extracellular matrix of the muscle, in which collagen is a primary constituent (Csapo et al., 2020). Similarly, elevated perfusion leading to higher muscle blood volume that accompanies contraction may stretch the ECM, thereby increasing its apparent stiffness (Martin et al., 2018; Valic et al., 2005). The increased SWV could also more trivially be a result of involuntary low-level muscular activation following the high-effort contraction, although this mechanism is unlikely to be in effect over 5 minutes. Temperature changes in muscle tissue have been reported to be negatively associated with SWV (Bernabei et al., 2020). Related to its contractile component, preceding muscle activation may alter the myosin configuration caused by perturbations in intramuscular calcium homeostasis, thereby changing muscle shear properties (Colombini et al., 2010; Howell et al., 1993).

The association of maximum eccentric hamstring strength with biceps femoris long head shear wave velocity

The relationship between a muscle's elasticity and its capacity to perform physical work has been studied before (Akkoc et al., 2018; Saito et al., 2019; Yamazaki et al., 2022; Djurić et al., 2023).

Most relevantly, Saito et al. found muscle elasticity (rectus femoris and gastrocnemius, assessed with strain elastography) to be negatively associated with various measures of physical function (Saito et al., 2019). Of note, muscle volume was not indicative of these measures of physical function, which was also not the case in our study (data not shown). In our study, normalized MEHS was negatively associated with post-contraction SWV, although SWV at rest failed to reach statistical significance by a small margin and showed an analogous direction. The change in SWV in response to the exercise bout was, however, not indicative of the exerted force. It therefore appears conceivable that structural or compositional properties of the muscle that positively affect its capacity to produce force, negatively interact with the apparent shear modulus (as assessed by SWE) and that the preceding muscular contraction served as a preconditioning, attenuating confounding factors of the SWV.

Exploiting our novel 3D approach that enables the investigation of regional analysis, we also observed that this relationship predominantly exists in the central (radially) portion of the

muscle, providing further ground for this latter conjecture. Muscular contraction increases the hydrostatic pressure in the muscle caused by muscle fibres being oriented non-parallel to the direction of net force production (Sejersted and Hargens, 1995) and by the Poisson effect, the phenomenon in which a material avoids volume change by expanding in directions perpendicular to the direction of compression, being opposed by the ECM (Wheatley et al., 2018). This tissue pressurization affects interstitial fluid distribution (Sleboda and Roberts, 2020; Fleckenstein et al., 1988) and impedes blood flow (Hill, 1948), and it increases from the periphery to the center of the muscle (Sejersted and Hargens, 1995). Consequently, the central muscle region likely experiences the largest perturbation of fluid distribution during contraction, possibly leading to an equalization of this confounder across participants.

The exact nature of the underlying factors simultaneously affecting eccentric muscle strength and SWV remains to be determined. Loss in muscle strength during aging or due to degeneration has been associated with an increase in connective tissue, in turn increasing muscle elasticity (Wen et al., 2018; Zaid and Goldspink, 1984). On an unexamined avenue, muscle strength is closely related to muscle fibre composition (Frontera et al., 2000), which may in turn influence SWV, potentially caused by a different extent of wave guidance due to the different diameters of the muscle fibre types (Frontera et al., 2008).

Limitations

This study has limitations that should be addressed. Skeletal muscle is anisotropic, and rotations of the measurement plane (relating to the roll axis of the transducer) relative to the muscle fibre direction affect the measured SWV (Gennisson et al., 2010). Theoretically, not only probe orientation but also the load that is applied by the US transducer to the tissue may influence SWV (Gennisson et al., 2010; Eby et al., 2013), but this influence may be negligible at the loads to be expected during US examination (Alfuraih et al., 2018; Rominger et al., 2018). We tested this approach only in VL and BFlh and the reliability observed in this study could differ in other muscle groups. Furthermore, while performing repeated measurements of one subject in quick succession, as was done in this study, primarily provides information on the measurement reliability in terms of the technical aspects of the procedure, it may overlook potential unaccounted within-subject variability introduced by external factors. For instance, inter-day, as opposed to intra-day lower leg US elastography measurement repetitions, accounted for a drop of ~0.15 in ICC in previous studies (Bravo-Sánchez et al., 2021; Taş et al., 2017). Of general note, whereas conversion of SWV into shear modulus is relatively simple in linearly elastic isotropic media, skeletal muscle may critically violate these assumptions, and we therefore decided to report SWV instead (Royer et al., 2011).

Future perspectives

With the proof-of-concept provided here, future studies may apply analogous procedures to investigate research questions both in the realm of medicine, integrative muscle physiology, and sports science. For example, it is known that mechanotransduction is one of the main regulators of muscle growth and adaptations to exercise (Wackerhage et al., 2019). A previous study from our laboratory (Franchi et al., 2014) observed that distinct mechanotransduction proteins show region-specific activation after eccentric exercise only vs. concentric exercise only; notably, such responses were associated with changes in muscle morphology and architecture. As changes in mechanotransductor proteins (i.e., integrins) could be related to an increase in muscle stiffness (Csapo et al., 2020), our novel 3DSWE method could be used in combination with other physiological approaches in an integrative manner, in order to further describe and unravel the basic mechanisms of muscular adaptations to distinct exercise modalities.

One potential application is in the assessment of muscle function and performance. By providing quantitative spatially referenced measurements of muscle elasticity, the method could help evaluate the impact of training interventions, exercise protocols, and performance-enhancing techniques on muscle properties. This information could aid in optimizing training programs, monitoring muscle adaptations, and identifying potential areas of improvement or risk for injury. Additionally, the method can be valuable in understanding the biomechanics of specific sports movements and techniques by assessing the muscle properties involved. This can contribute to the development of evidence-based training strategies and injury prevention protocols tailored to the demands of different sports disciplines (Sarto et al., 2021).

Conclusion

Three-dimensional mapping of skeletal muscle US shear properties as described herein provides reliable measurements and is capable of detecting variations both across anatomical locations and as induced by muscular contraction. A short high-effort exercise bout increases the SWV of skeletal muscle, the underlying mechanisms for which remain to be determined. Our finding that biceps femoris eccentric strength is associated with post-contraction SWV warrants further investigation.

Data availability statement

The original contributions presented in the study are included in the article/Supplementary material, further inquiries can be directed to the corresponding author.

Ethics statement

The study involving humans was approved by the Cantonal Ethics Committee Zurich, Switzerland (KEK-ZH-NR: 2017-01395). The study was conducted in accordance with the local legislation and institutional requirements. The participants provided their written informed consent to participate in this study.

Author contributions

TG: Conceptualization, Data curation, Formal Analysis, Investigation, Methodology, Project administration, Resources, Software, Supervision, Validation, Visualization, Writing–original draft, Writing–review and editing. JGS: Conceptualization, Funding acquisition, Methodology, Project administration, Resources, Supervision, Writing–review and editing. DPF: Conceptualization, Methodology, Writing–review and editing. FS: Conceptualization, Investigation, Writing–review and editing. JS: Conceptualization, Funding acquisition, Investigation, Methodology, Project administration, Resources, Supervision, Writing–original draft, Writing–review and editing. MVF: Conceptualization, Investigation, Methodology, Supervision, Writing–original draft, Writing–review and editing.

Funding

The author(s) declare financial support was received for the research, authorship, and/or publication of this article. This study was generously supported by the Balgrist Foundation.

Acknowledgments

The authors are grateful for Victoria Held's support in volumetric segmentation of the measurements. Imaging was performed with equipment maintained by the Swiss Centre for Musculoskeletal Imaging, SCMI, Balgrist Campus AG, Zürich.

Conflict of interest

The authors declare that the research was conducted in the absence of any commercial or financial relationships that could be construed as a potential conflict of interest.

Publisher's note

All claims expressed in this article are solely those of the authors and do not necessarily represent those of their affiliated organizations, or those of the publisher, the editors and the reviewers. Any product that may be evaluated in this article, or claim that may be made by its manufacturer, is not guaranteed or endorsed by the publisher.

References

Akagi, R., Tanaka, J., Shikiba, T., and Takahashi, H. (2015). Muscle hardness of the triceps brachii before and after a resistance exercise session: a shear wave ultrasound elastography study. *Acta Radiol.* 56 (12), 1487–1493. doi:10.1177/0284185114559765

Akkoc, O., Caliskan, E., and Bayramoglu, Z. (2018). Effects of passive muscle stiffness measured by Shear Wave Elastography, muscle thickness, and body mass index on athletic performance in adolescent female basketball players. *Med. Ultrasonogr.* 20 (2), 170. doi:10.11152/mu-1336

Alfuraih, A. M., O'Connor, P., Hensor, E., Tan, A. L., Emery, P., and Wakefield, R. J. (2018). The effect of unit, depth, and probe load on the reliability of muscle shear wave elastography: variables affecting reliability of SWE. *J. Clin. Ultrasound* 46 (2), 108–115. doi:10.1002/jcu.22534

Alfuraih, A. M., O'Connor, P., Tan, A. L., Hensor, E. M. A., Ladas, A., Emery, P., et al. (2019). Muscle shear wave elastography in idiopathic inflammatory myopathies: a case–control study with MRI correlation. *Skelet. Radiol.* 48 (8), 1209–1219. doi:10.1007/s00256-019-03175-3

Andonian, P., Viallon, M., Le Goff, C., de Bourguignon, C., Tourel, C., Morel, J., et al. (2016). Shear-wave elastography assessments of quadriceps stiffness changes prior to, during and after prolonged exercise: a longitudinal study during an extreme mountain ultra-marathon. *PLoS ONE* 11 (8), e0161855. doi:10.1371/journal.pone.0161855

Ashby, D. (1991). Practical statistics for medical research. Douglas G. Altman, Chapman and Hall, London, 1991. No. of pages: 611. Price: £32.00. *Statistics Med.* 10 (10), 1635–1636. doi:10.1002/sim.4780101015

Bernabei, M., Lee, S. S. M., Perreault, E. J., and Sandercock, T. G. (2020). Shear wave velocity is sensitive to changes in muscle stiffness that occur independently from changes in force. *J. Appl. Physiology* 128 (1), 8–16. doi:10.1152/japplphysiol.00112.2019

Blazevich, A. J., Gill, N. D., and Zhou, S. (2006). Intra- and intermuscular variation in human quadriceps femoris architecture assessed *in vivo*. *J. Anat.* 209 (3), 289–310. doi:10.1111/j.1469-7580.2006.00619.x

Boulard, C., Gautheron, V., and Lapole, T. (2021). Mechanical properties of ankle joint and gastrocnemius muscle in spastic children with unilateral cerebral palsy measured with shear wave elastography. *J. Biomechanics* 124, 110502. doi:10.1016/j.jbiomech.2021.110502

Bravo-Sánchez, A., Abián, P., Sánchez-Infante, J., Esteban-Gacía, P., Jiménez, F., and Abián-Vicén, J. (2021). Objective assessment of regional stiffness in vastus lateralis with different measurement methods: a reliability study. *Sensors* 21 (9), 3213. doi:10.3390/s21093213

Brusco, C. M., Pinto, R. S., and Blazevich, A. J. (2022). Reliability and comparison of sonographic methods for *in vivo* measurement of human biceps femoris long-head architecture. *Med. Sci. Sports Exerc* 54 (12), 2216–2226. doi:10.1249/MSS.0000000000003015

Chalchat, E., Gennisson, J. L., Peñailillo, L., Oger, M., Malgoyre, A., Charlot, K., et al. (2020). Changes in the viscoelastic properties of the vastus lateralis muscle with fatigue. *Front. Physiol.* 11, 307. doi:10.3389/fphys.2020.00307

Charles, J., Kissane, R., Hoehfurtner, T., and Bates, K. T. (2022). From fibre to function: are we accurately representing muscle architecture and performance? *Biol. Rev.* 97 (4), 1640–1676. doi:10.1111/brv.12856

Colombini, B., Nocella, M., Bagni, M. A., Griffiths, P. J., and Cecchi, G. (2010). Is the cross-bridge stiffness proportional to tension during muscle fiber activation? *Biophysical J.* 98 (11), 2582–2590. doi:10.1016/j.bpj.2010.02.014

Csapo, R., Gumpenberger, M., and Wessner, B. (2020). Skeletal muscle extracellular matrix – what do we know about its composition, regulation, and physiological roles? A narrative review. *Front. Physiology* 11, 253. doi:10.3389/fphys.2020.00253

de Vet, H. C. W., Terwee, C. B., Knol, D. L., and Bouter, L. M. (2006). When to use agreement versus reliability measures. *J. Clin. Epidemiol.* 59 (10), 1033–1039. doi:10.1016/j.jclinepi.2005.10.015

Djurić, D., Pleša, J., Van Hooren, B., Kozinc, Ž., and Šarabon, N. (2023). The relationship between elastography-based muscle properties and vertical jump performance, countermovement utilization ratio, and rate of force development. *Eur. J. Appl. Physiol.* 123 (8), 1789–1800. doi:10.1007/s00421-023-05191-7

Dong, Z., Kim, J., Huang, C., Lowerison, M. R., Lok, U. W., Chen, S., et al. (2022). Three-dimensional shear wave elastography using a 2D row column addressing (RCA) array. *BME Front.* 2022, 2022. doi:10.34133/2022/9879632

Eby, S. F., Song, P., Chen, S., Chen, Q., Greenleaf, J. F., and An, K.-N. (2013). Validation of shear wave elastography in skeletal muscle. *J. Biomechanics* 46 (14), 2381–2387. doi:10.1016/j.jbiomech.2013.07.033

Ettema, G. J. C., and Huijing, P. A. (1994). Skeletal muscle stiffness in static and dynamic contractions. *J. Biomechanics* 27 (11), 1361–1368. doi:10.1016/0021-9290(94)90045-0

Fleckenstein, J., Canby, R., Parkey, R., and Peshock, R. (1988). Acute effects of exercise on MR imaging of skeletal muscle in normal volunteers. *Am. J. Roentgenol.* 151 (2), 231–237. doi:10.2214/ajr.151.2.231

Fouré, A., Nordez, A., McNair, P., and Cornu, C. (2011). Effects of plyometric training on both active and passive parts of the plantarflexors series elastic component stiffness of muscle–tendon complex. *Eur. J. Appl. Physiol.* 111 (3), 539–548. doi:10.1007/s00421-010-1667-4

Franchi, M. V., Atherton, P. J., Reeves, N. D., Flück, M., Williams, J., Mitchell, W. K., et al. (2014). Architectural, functional and molecular responses to concentric and eccentric loading in human skeletal muscle. *Acta Physiol. (Oxf)* 210 (3), 642–654. doi:10.1111/apha.12225

Franchi, M. V., Fitze, D. P., Hanimann, J., Sarto, F., and Spörri, J. (2020a). Panoramic ultrasound vs. MRI for the assessment of hamstrings cross-sectional area and volume in a large athletic cohort. *Sci. Rep.* 10 (1), 14144. doi:10.1038/s41598-020-71123-6

Franchi, M. V., Fitze, D. P., Raiteri, B. J., Hahn, D., and Spörri, J. (2020b). Ultrasound-derived biceps femoris long-head fascicle length: extrapolation pitfalls. *Med. Sci. Sports Exerc* 52 (1), 233–243. doi:10.1249/MSS.0000000000002123

Franchi, M. V., Raiteri, B. J., Longo, S., Sinha, S., Narici, M. V., and Csapo, R. (2018). Muscle architecture assessment: strengths, shortcomings and new Frontiers of *in vivo* imaging techniques. *Ultrasound Med. Biol.* 44 (12), 2492–2504. doi:10.1016/j.ultrasmedbio.2018.07.010

Frontera, W. R., Hughes, V. A., Fielding, R. A., Fiatarone, M. A., Evans, W. J., and Roubenoff, R. (2000). Aging of skeletal muscle: a 12-yr longitudinal study. *J. Appl. Physiology* 88 (4), 1321–1326. doi:10.1152/jappl.2000.88.4.1321

Frontera, W. R., Reid, K. F., Phillips, E. M., Krivickas, L. S., Hughes, V. A., Roubenoff, R., et al. (2008). Muscle fiber size and function in elderly humans: a longitudinal study. *J. Appl. Physiology* 105 (2), 637–642. doi:10.1152/japplphysiol.90332.2008

Gennisson, J.-L., Deffieux, T., Macé, E., Montaldo, G., Fink, M., and Tanter, M. (2010). Viscoelastic and anisotropic mechanical properties of *in vivo* muscle tissue assessed by supersonic shear imaging. *Ultrasound Med. Biol.* 36 (5), 789–801. doi:10.1016/j.ultrasmedbio.2010.02.013

Götschi, T., Franchi, M. V., Schulz, N., Fröhlich, S., Frey, W. O., Snedeker, J. G., et al. (2022b). Altered regional 3D shear wave velocity patterns in youth competitive alpine skiers suffering from patellar tendon complaints – a prospective case–control study. *Eur. J. Sport Sci.* 23, 1068–1076. doi:10.1080/17461391.2022.2088404

Götschi, T., Hanimann, J., Schulz, N., Huser, S., Held, V., Frey, W. O., et al. (2022a). Patellar tendon shear wave velocity is higher and has different regional patterns in elite competitive alpine skiers than in healthy controls. *Front. Bioeng. Biotechnol.* 10, 858610. doi:10.3389/fbioe.2022.858610

Götschi, T., Schulz, N., Snedeker, J. G., Hanimann, J., Franchi, M. V., and Spörri, J. (2021). Three-dimensional mapping of shear wave velocity in human tendon: a proof of concept study. *Sensors* 21 (5), 1655. doi:10.3390/s21051655

Hill, A. V. (1948). The pressure developed in muscle during contraction. *J. Physiol.* 107 (4), 518–526. doi:10.1113/jphysiol.1948.sp004296

Howell, J. N., Chleboun, G., and Conatser, R. (1993). Muscle stiffness, strength loss, swelling and soreness following exercise-induced injury in humans. *J. Physiology* 464 (1), 183–196. doi:10.1113/jphysiol.1993.sp019629

Hug, F., Tucker, K., Gennisson, J.-L., Tanter, M., and Nordez, A. (2015). Elastography for muscle biomechanics: toward the estimation of individual muscle force. *Exerc. Sport Sci. Rev.* 43 (3), 125–133. doi:10.1249/JES.0000000000000049

Johns, R. J., and Wright, V. (1962). Relative importance of various tissues in joint stiffness. *J. Appl. Physiology* 17 (5), 824–828. doi:10.1152/jappl.1962.17.5.824

Jones, E. J., Piasecki, J., Ireland, A., Stashuk, D. W., Atherton, P. J., Phillips, B. E., et al. (2021). Lifelong exercise is associated with more homogeneous motor unit potential features across deep and superficial areas of vastus lateralis. *GeroScience* 43 (4), 1555–1565. doi:10.1007/s11357-021-00356-8

Kawai, M., Taniguchi, K., Suzuki, T., and Katayose, M. (2018). Estimation of quadriceps femoris muscle dysfunction in the early period after surgery of the knee joint using shear-wave elastography. *BMJ Open Sport Exerc Med.* 4 (1), e000381. doi:10.1136/bmjsem-2018-000381

Kiers, K., Ellenberger, L., Javet, M., Bruhin, B., Frey, W. O., and Spörri, J. (2021). A cross-sectional observation on maximal eccentric hamstring strength in 7- to 15-year-old competitive alpine skiers. *Biology* 10 (11), 1128. doi:10.3390/biology10111128

Kjær, M. (2004). Role of extracellular matrix in adaptation of tendon and skeletal muscle to mechanical loading. *Physiol. Rev.* 84 (2), 649–698. doi:10.1152/physrev.00031.2003

Knight, C. A., and Kamen, G. (2005). Superficial motor units are larger than deeper motor units in human vastus lateralis muscle. *Muscle and Nerve* 31 (4), 475–480. doi:10.1002/mus.20265

Kvåle, A., Ljunggren, A. E., and Johnsen, T. B. (2003). Palpation of muscle and skin. Is this a reliable and valid procedure in assessment of patients with long-lasting musculoskeletal pain? *Adv. Physiother.* 5 (3), 122–136. doi:10.1080/14038190310016526

Lacourpaille, L., Hug, F., Bouillard, K., Hogrel, J.-Y., and Nordez, A. (2012). Supersonic shear imaging provides a reliable measurement of resting muscle shear elastic modulus. *Physiol. Meas.* 33 (3), N19–N28. doi:10.1088/0967-3334/33/3/N19

Lacourpaille, L., Nordez, A., Hug, F., Couturier, A., Dibie, C., and Guilhem, G. (2014). Time-course effect of exercise-induced muscle damage on localized muscle mechanical properties assessed using elastography. *Acta Physiol.* 211 (1), 135–146. doi:10.1111/apha.12272

Lacourpaille, L., Nordez, A., Hug, F., Doguet, V., Andrade, R., and Guilhem, G. (2017). Early detection of exercise-induced muscle damage using elastography. *Eur. J. Appl. Physiol.* 117 (10), 2047–2056. doi:10.1007/s00421-017-3695-9

Lee, Y., Kim, M., and Lee, H. (2021). The measurement of stiffness for major muscles with shear wave elastography and myoton: a quantitative analysis study. *Diagnostics* 11 (3), 524. doi:10.3390/diagnostics11030524

Lexell, J., Henriksson-Larsén, K., and Sjöström, M. (1983b). Distribution of different fibre types in human skeletal muscles 2. A study of cross-sections of whole m. vastus lateralis. *Acta Physiol. Scand.* 117 (1), 115–122. doi:10.1111/j.1748-1716.1983.tb07185.x

Lexell, J., Henriksson-Larsén, K., Winblad, B., and Sjöström, M. (1983a). Distribution of different fiber types in human skeletal muscles: effects of aging studied in whole muscle cross sections. *Muscle Nerve* 6 (8), 588–595. doi:10.1002/mus.880060809

Ličen, U., and Kozinc, Ž. (2022). Using shear-wave elastography to assess exercise-induced muscle damage: a review. *Sensors* 22, 7574–7619. doi:10.3390/s22197574

Martin, J. A., Brandon, S. C. E., Keuler, E. M., Hermus, J. R., Ehlers, A. C., Segalman, D. J., et al. (2018). Gauging force by tapping tendons. *Nat. Commun.* 9 (1), 1592. doi:10.1038/s41467-018-03797-6

Miyamoto, N., Hirata, K., Miyamoto-Mikami, E., Yasuda, O., and Kanehisa, H. (2018). Associations of passive muscle stiffness, muscle stretch tolerance, and muscle slack angle with range of motion: individual and sex differences. *Sci. Rep.* 8 (1), 8274. doi:10.1038/s41598-018-26574-3

Morgan, D. L. (1977). Separation of active and passive components of short-range stiffness of muscle. *Am. J. Physiology-Cell Physiology* 232 (1), 45–49. doi:10.1152/ajpcell.1977.232.1.C45

Nightingale, K. (2011). Acoustic radiation force impulse (arfi) imaging: a review. *CMIR* 7 (4), 328–339. doi:10.2174/157340511798038657

Opar, D. A., Piatkowski, T., Williams, M. D., and Shield, A. J. (2013). A novel device using the nordic hamstring exercise to assess eccentric knee flexor strength: a reliability and retrospective injury study. *J. Orthop. Sports Phys. Ther.* 43 (9), 636–640. doi:10.2519/jospt.2013.4837

Phan, A., Lee, J., and Gao, J. (2019). Ultrasound shear wave elastography in assessment of skeletal muscle stiffness in senior volunteers. *Clin. Imaging* 58, 22–26. doi:10.1016/j.clinimag.2019.06.006

Pimenta, R., Blazevich, A. J., and Freitas, S. R. (2018). Biceps femoris long-head architecture assessed using different sonographic techniques. *Med. Sci. Sports Exerc* 50 (12), 2584–2594. doi:10.1249/MSS.0000000000001731

Pinel, S., Kelp, N. Y., Bugeja, J. M., Bolsterlee, B., Hug, F., and Dick, T. J. M. (2021). Quantity versus quality: age-related differences in muscle volume, intramuscular fat, and mechanical properties in the triceps surae. *Exp. Gerontol.* 156, 111594. doi:10.1016/j.exger.2021.111594

Purslow, P., Wess, T., and Hukins, D. (1998). Collagen orientation and molecular spacing during creep and stress-relaxation in soft connective tissues. *J. Exp. Biol.* 201, 135–142. doi:10.1242/jeb.201.1.135

Rominger, M., Kälin, P., Mastalerz, M., Martini, K., Klingmüller, V., Sanabria, S., et al. (2018). Influencing factors of 2D shear wave elastography of the muscle – an *ex vivo* animal study. *Ultrasound Int. Open* 04 (02), E54–E60. doi:10.1055/a-0619-6058

Royer, D., Gennisson, J.-L., Deffieux, T., and Tanter, M. (2011). On the elasticity of transverse isotropic soft tissues (L). *J. Acoust. Soc. Am.* 129 (5), 2757–2760. doi:10.1121/1.3559681

Saito, A., Wakasa, M., Kimoto, M., Ishikawa, T., Tsugaruya, M., Kume, Y., et al. (2019). Age-related changes in muscle elasticity and thickness of the lower extremities are associated with physical functions among community-dwelling older women. *Geriatrics Gerontology Int.* 19 (1), 61–65. doi:10.1111/ggi.13567

Šarabon, N., Kozinc, Ž., and Podrekar, N. (2019). Using shear-wave elastography in skeletal muscle: a repeatability and reproducibility study on biceps femoris muscle. *PLoS ONE* 14 (8), e0222008. doi:10.1371/journal.pone.0222008

Sarto, F., Spörri, J., Fitze, D. P., Quinlan, J. I., Narici, M. V., and Franchi, M. V. (2021). Implementing ultrasound imaging for the assessment of muscle and tendon properties in elite sports: practical aspects, methodological considerations and future directions. *Sports Med.* 51, 1151–1170. doi:10.1007/s40279-021-01436-7

Schiaffino, S., and Reggiani, C. (2011). Fiber types in mammalian skeletal muscles. *Physiol. Rev.* 91 (4), 1447–1531. doi:10.1152/physrev.00031.2010

Sejersted, O. M., and Hargens, A. R. (1995). Intramuscular pressures for monitoring different tasks and muscle conditions. *Adv. Exp. Med. Biol.* 384, 339–350. doi:10.1007/978-1-4899-1016-5_27

Shrout, P. E., and Fleiss, J. L. (1979). Intraclass correlations: uses in assessing rater reliability. *Psychol. Bull.* 86 (2), 420–428. doi:10.1037//0033-2909.86.2.420

Sions, J. M., Tyrell, C. M., Knarr, B. A., Jancosko, A., and Binder-Macleod, S. A. (2012). Age- and stroke-related skeletal muscle changes a review for the geriatric clinician. *J. Geriatric Phys. Ther.* 35 (3), 155–161. doi:10.1519/JPT.0b013e318236db92

Siracusa, J., Charlot, K., Malgoyre, A., Conort, S., Tardo-Dino, P. E., Bourrilhon, C., et al. (2019). Resting muscle shear modulus measured with ultrasound shear-wave elastography as an alternative tool to assess muscle fatigue in humans. *Front. Physiol.* 10, 626. doi:10.3389/fphys.2019.00626

Sleboda, D. A., and Roberts, T. J. (2020). Internal fluid pressure influences muscle contractile force. *Proc. Natl. Acad. Sci. U.S.A.* 117 (3), 1772–1778. doi:10.1073/pnas.1914433117

Sleboda, D. A., Stover, K. K., and Roberts, T. J. (2020). Diversity of extracellular matrix morphology in vertebrate skeletal muscle. *J. Morphol.* 281 (2), 160–169. doi:10.1002/jmor.21088

Taş, S., Onur, M. R., Yılmaz, S., Soylu, A. R., and Korkusuz, F. (2017). Shear wave elastography is a reliable and repeatable method for measuring the elastic modulus of the rectus femoris muscle and patellar tendon. *J. Ultrasound Med.* 36 (3), 565–570. doi:10.7863/ultra.16.03032

Taubin, G. (1991). Estimation of planar curves, surfaces, and nonplanar space curves defined by implicit equations with applications to edge and range image segmentation. *IEEE Trans. Pattern Analysis Mach. Intell.* 13 (11), 1115–1138. doi:10.1109/34.103273

Tisha, A. L., Armstrong, A. A., Johnson, A. W., and López-Ortiz, C. (2018). Skeletal muscle adaptations and passive muscle stiffness in cerebral palsy: a literature review and conceptual model. *J. Appl. Biomechanics* 35 (1), 68–79. doi:10.1123/jab.2018-0049

Valic, Z., Buckwalter, J. B., and Clifford, P. S. (2005). Muscle blood flow response to contraction: influence of venous pressure. *J. Appl. Physiology* 98 (1), 72–76. doi:10.1152/japplphysiol.00151.2004

Vandervoort, A. A. (1999). Ankle mobility and postural stability. *Physiother. Theory Pract.* 15 (2), 91–103. doi:10.1080/095939899307793

Vatovec, R., Kozinc, Ž., and Voglar, M. (2022). The effects of isometric fatigue on trunk muscle stiffness: implications for shear-wave elastography measurements. *Sensors* 22 (23), 9476. doi:10.3390/s22239476

Wackerhage, H., Schoenfeld, B. J., Hamilton, D. L., Lehti, M., and Hulmi, J. J. (2019). Stimuli and sensors that initiate skeletal muscle hypertrophy following resistance exercise. *J. Appl. Physiology* 126 (1), 30–43. doi:10.1152/japplphysiol.00685.2018

Wang, A. B., Perreault, E. J., Royston, T. J., and Lee, S. S. M. (2019). Changes in shear wave propagation within skeletal muscle during active and passive force generation. *J. Biomechanics* 94, 115–122. doi:10.1016/j.jbiomech.2019.07.019

Wen, J., Wang, Y., Jiang, W., Luo, Y., Peng, J., Chen, M., et al. (2018). Quantitative evaluation of denervated muscle atrophy with shear wave ultrasound elastography and a comparison with the histopathologic parameters in an animal model. *Ultrasound Med. Biol.* 44 (2), 458–466. doi:10.1016/j.ultrasmedbio.2017.08.1887

Wheatley, B. B., Odegard, G. M., Kaufman, K. R., and Haut Donahue, T. L. (2018). Modeling skeletal muscle stress and intramuscular pressure: a whole muscle active–passive approach. *J. Biomech. Eng.* 140 (8), 0810061–0810068. doi:10.1115/1.4040318

Yamazaki, K., Inoue, K., and Miyamoto, N. (2022). Passive and active muscle elasticity of medial gastrocnemius is related to performance in sprinters. *Eur. J. Appl. Physiol.* 122 (2), 447–457. doi:10.1007/s00421-021-04848-5

Yoshiko, A., Hioki, M., Kanehira, N., Shimaoka, K., Koike, T., Sakakibara, H., et al. (2017). Three-dimensional comparison of intramuscular fat content between young and old adults. *BMC Med. Imaging* 17 (1), 12. doi:10.1186/s12880-017-0185-9

Zaid, N. S. A., and Goldspink, G. (1984). Connective tissue changes and physical properties of developing and ageing skeletal muscle. *J. Anat.* 139 (Pt 4), 677–689.

Zimmer, M., Kleiser, B., Marquetand, J., and Ates, F. (2022). Shear wave elastography characterizes passive and active mechanical properties of biceps brachii muscle *in vivo*. *J. Mech. Behav. Biomed. Mater*. doi:10.2139/ssrn.4101072

frontiers | Frontiers in Bioengineering and Biotechnology

TYPE Original Research
PUBLISHED 21 December 2023
DOI 10.3389/fbioe.2023.1321241

OPEN ACCESS

EDITED BY
Lei Wang,
Capital Normal University, China

REVIEWED BY
Zhan Liu,
Sichuan University, China
Uriel Zapata,
EAFIT University, Colombia

*CORRESPONDENCE
Zexian Xu,
kqxuzx@163.com
Jianjun Yang,
yjjqd@qdu.edu.cn

RECEIVED 13 October 2023
ACCEPTED 11 December 2023
PUBLISHED 21 December 2023

CITATION
Gao Y, Luo D, Yuan M, Yang Y, Xu Z and Yang J (2023), The relationship between the oblique sagittal temporomandibular joint disc position and the volume surface area of the condyle in young TMD adults. *Front. Bioeng. Biotechnol.* 11:1321241. doi: 10.3389/fbioe.2023.1321241

The relationship between the oblique sagittal temporomandibular joint disc position and the volume surface area of the condyle in young TMD adults

Yudong Gao[1,2], Dan Luo[1,2], Mujie Yuan[1,2], Yanhao Yang[1,2], Zexian Xu[1,2,3]* and Jianjun Yang[1,2,3]*

[1]The Affiliated Hospital of Qingdao University, Qingdao, China, [2]School of Stomatology, Qingdao University, Qingdao, China, [3]Dental Digital Medicine and 3D Printing Engineering Laboratory of Qingdao, Qingdao, China

The present study aims to compare the volume surface area of the condyle, the horizontal condylar axial angle and the disc-condyle angle between temporomandibular disorder (TMD) and asymptomatic volunteers, explore and analyze the relationship between the temporomandibular joint (TMJ) disc position in oblique sagittal plane and the volume surface area of the condyle in young adults with TMD symptoms. 84 young adult volunteers were received TMJ examination by Magnetic Resonance Imaging (MRI) and Cone Beam Computed Tomography (CBCT). TMD and asymptomatic volunteers were 42 each. MRI was used to assess the position of TMJ disc in the oblique sagittal plane with the condyle apex method. CBCT data were used for three-dimensional (3D) reconstruction of condyle and the measurements of the horizontal condylar axial angle and the volume surface area of the condyle. The condylar volume surface area of the TMD group was smaller than that of the asymptomatic group ($p < 0.05$), the disc condyle angle was larger than that of the asymptomatic group ($p < 0.05$), and no significant difference was found in the horizontal condylar axial angle ($p > 0.05$). In terms of correlation, the volume surface area of the condyle were negatively correlated with the position of the articular disc in TMD patients ($p < 0.05$). This significant negative correlation suggests that the possibility of disc displacement can be considered when poor condylar morphology is found.

KEYWORDS

temporomandibular joint disc, condyle apex method, the volume of the condyle, the surface area of the condyle, MRI, CBCT

1 Introduction

Mandibular condylar growth center can respond adaptively to stimulation of the surroundings through bone rebuilding. This adaptive response plays an important role in the growth and development period of individual maxillofacial growth stability (Krisjane et al., 2007), while in adulthood, it may cause changes in condylar bone such as flattening, sclerosis, osteophyte formation and erosion, resorption of the condylar head (Seo et al.,

2022), thus changing the size and morphology of the condyle. Some researchers believe that anterior disc displacement alters the microenvironment of the condyle, which may irritate to impair condylar growth and remodeling (Xie et al., 2016; Yasa and akgül, 2018; Liu et al., 2023). In clinical practice, we have also found that condyle morphology changes in some TMD patients, such as the condyle of patients with joint click symptoms may show flattening in oblique sagittal CBCT, the bilateral condyle of patients with mandibular dyskinesia may show inconsistent size, and the condyle osteophyte formation and erosion of patients with pain symptoms. On subsequent MRI examination, we also found that these patients were accompanied by various degrees of changes in the position of the articular disc.

However, most previous studies have used linear or angular indices to assess the morphology of the condyle (Rabelo et al., 2017; de Pontes et al., 2019; Yildizer and Odabaşı, 2023), necessitating an examination of the disc-condyle relationship from the perspective of volume surface area of the condyle. Furthermore, our research group previously proposed that the condyle apex method was more accurate than the condyle center method in measuring the disc-condyle angle, suggesting that the position of the articular disc in asymptomatic young adults should be in the anterosuperior region of the condyle (Luo et al., 2022). This method was continued in this study to assess the angle of the articular disc in an oblique sagittal direction in young volunteers. In addition, as the mandibular condyle is divided into left and right sides, the horizontal condylar axial angle on both sides was also measured.

The aim of this study was to compare the volume surface area of the condyle, the horizontal condylar axial angle and the disc-condyle angle between TMD and asymptomatic volunteers, and to analyze the relationship between the position of articular disc in oblique sagittal plane and the volume surface area of the condyle in young TMD adults.

2 Materials and methods

2.1 Sample selection

Eighty-four students were selected from a university in Qingdao. The inclusion criteria of TMD volunteers were as follows: 1) volunteers were aged over 18; 2) volunteers had TMD symptoms such as joint clicking when opening or closing mouth through the examination of TMD specialists; 3) volunteers underwent MRI and CBCT examinations simultaneously. Exclusion criteria were 1) systemic diseases affecting bones; 2) TMJ surgery history or Congenital odontomaxillofacial deformity; 3) Malocclusion.

The inclusion and exclusion of asymptomatic volunteers was referred to the criteria of Luo (Luo et al., 2022). Inclusion criteria were 1) age >18 years; 2) no signs or symptoms of a TMD, as confirmed by an experienced clinical specialist; 3) the acquisition of CBCT and MRI in the oblique sagittal of the bilateral TMJ in closed-mouth position; 4) Consistent with individual normal occlusion. Exclusion criteria were 1) rheumatoid arthritis in childhood or systemic inflammatory arthritis; 2) any contraindication to CBCT and MRI due to a general condition such a claustrophobia or metal implants.

The study was approved by the Ethics Committee of the Affiliated Hospital of Qingdao University (NO. QYFYWZLL 27452). All volunteers gave written informed consent.

2.2 MRI acquisition and measurement analysis

MRI was used to examine the position of TMJ disc in the oblique sagittal plane with the condylar apex method. Images acquisition were executed by the Siemens Magnetom Prisma 3.0T MRI system (Siemens, Erlangen, Germany), with a 64-channel head coil that captures the global spatial information of the TMJ muscle and soft tissue structures. The volunteers were instructed to assume a supine position, while keeping the articular disc position in the oblique sagittal plane in the closed mouth position. The TMJ OSAG-PDW-FSE sequences were obtained by three-dimensional (3D) volume scanning and parallel acquisition technology, with an excitation time of 3s, repetition time (TR) of 2070 m, echo time (TE) of 28 m, field of view (FOV) of 120 × 120 mm, matrix of 192 × 144, and plane resolution of 0.6 × 0.6. A total of 16 images were taken (left and right TMJ, eight images each). The layer thickness of each one was 2 mm and the layer spacing 10%. Two dental imaging specialists with no prior knowledge of the sample data independently measured the disc condyle angle.

The condyle apex method, simply stated, entails first determining the apex of the condyle and drawing a line perpendicular to the axial plane (The axial plane of MRI is the plane perpendicular to the horizontal ground) through it, and then determining the posterior edge of the articular disc posterior band and connecting it to the apex of the condyle. The angle formed by the two lines can be used to determine where the articular disc is located (Figure 1).

2.3 CBCT acquisition and measurement analysis

CBCT was used to access the condylar bone condition, and i-CAT scanner (Imaging Sciences International 17–19, Hatfield, PA, United States) was adopted with the following parameters: 120KV, 5mA, exposure time of 26.9 s, image matrix size of 640 × 640, voxel size of 0.25 mm, and field of view (FOV) of 16.0 × 11.0 cm. All participants had their CBCT images acquired by a radiologist with the same parameter settings. They were required to sit up straight with their mandibles kept in the intercuspal position, the Frankfurt plane paralleled to the horizontal ground, and the midsagittal plane of the head perpendicular to the horizontal ground. The CBCT image data obtained were saved in a Digital Imaging and Communications in Medicine (DICOM) format.

The CBCT data in DICOM format was then imported into mimics21 (Materialise, Leuven, Belgium) software for 3D reconstruction of condyles (Figure 2). After setting the direction, the shape and size of the craniofacial bone could be observed in the coronal plane, sagittal plane and axial plane. The operator selected the software's gray value range (226–3,071) of the bone for the first mask creation. At this point, the mask of skull and mandibular condyle can been observed.

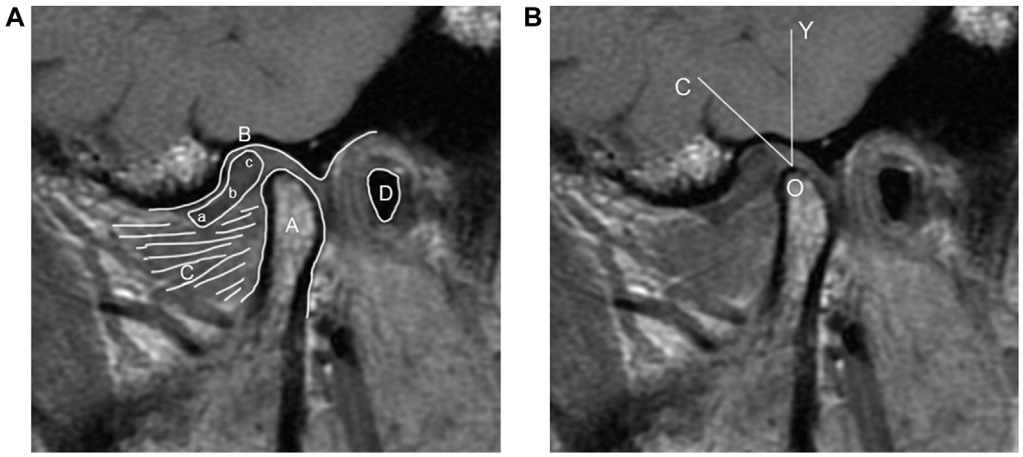

FIGURE 1
(A) MRI diagram of oblique sagittal joint structure. (A) Condyle; (B) glenoid fossa; (C) Lateral pterygoid muscle; (D) External auditory meatus; (a) anterior band; (b) intermediate zone; (c) posterior band. **(B)** Schematic diagram of the condyle apex method (O) the apex of the condyle (O–Y) a line perpendicular to the axial plane (O–C) a line connecting the apex of the condyle and the posterior edge of the articular disc posterior band (∠COY) disc condyle angle.

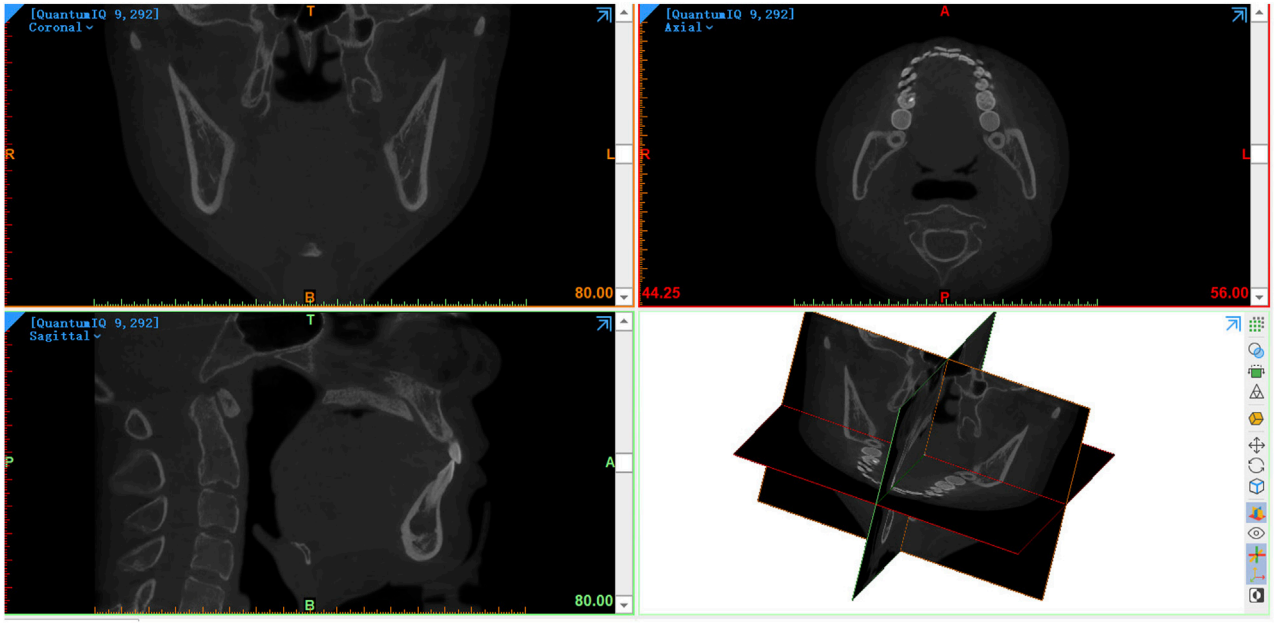

FIGURE 2
The CBCT data in DICOM format was imported into mimics21 software.

The anatomical structure of the condyle was divided according to the method mentioned by Tecco et al. (Tecco et al., 2010). In the axial plane (The axial plane of CBCT is the plane parallel to the horizontal ground), the mask was slid sequentially from top to bottom until the first radiopaque point in the articular fossa was observed, defining this as the upper condylar boundary. When the interface between the condyle and the coracoid process was observed, the upper layer of the condyle mask of this interface was defined as the lower boundary of the condyle. The outer shape of the mask can be clearly observed between the upper and lower boundaries of the condyle, ranging from long ellipse to ellipse and then to water-drop roughly (Figure 3).

The Region Growing tool was used to select a point from the original mask's condylar region for the second mask creation. The mask of the condyle was thus separated from the mask of the majority of the skull. The surface quality of the final condyle mask was therefore improved by viewing the condylar mask layer by layer, filling the internal cavity, and smoothing the irregular

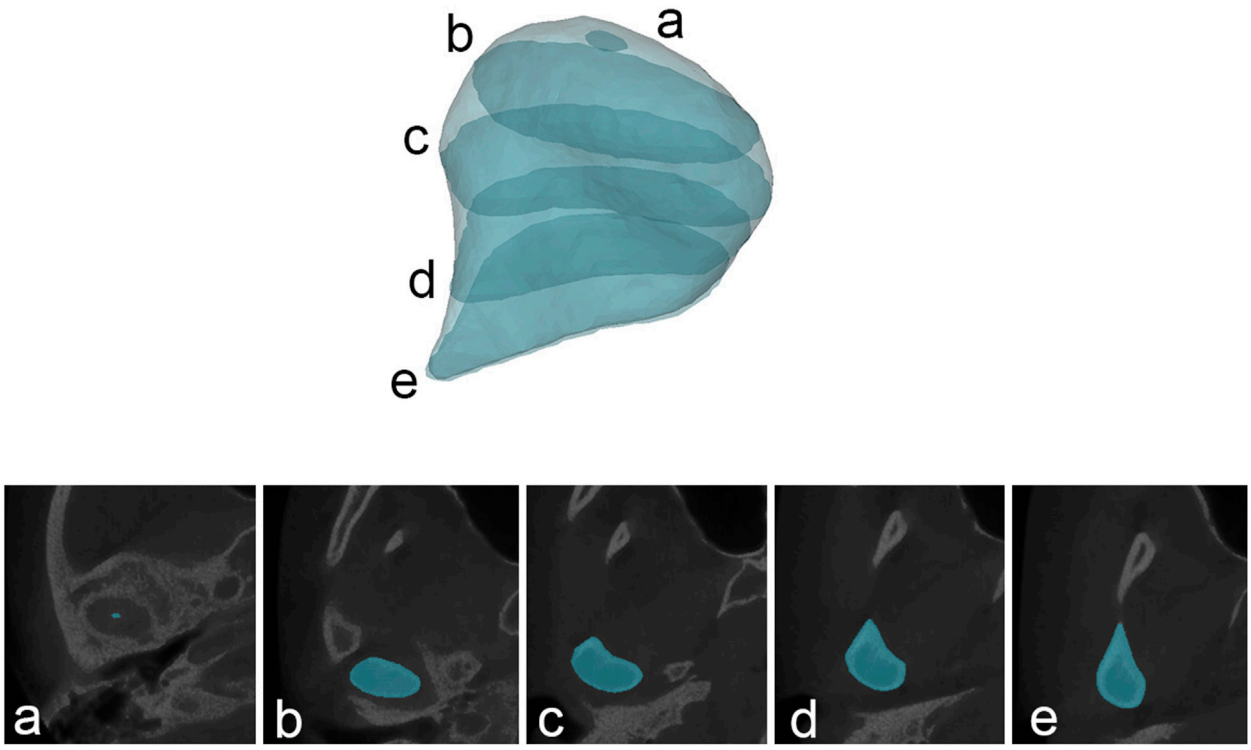

FIGURE 3
The shape of the condylar mask at different levels. **(A)** the upper condylar boundary; **(B)** long ellipse mask; **(C)** elliptic mask; **(D)** water-drop mask; **(E)** the lower boundary of the condyle.

artifacts on the outside. The final step was to calculate part from the condyle mask. Following the completion of the reconstruction of 3D model of condyle (Figure 4), the software automatically calculated the volume and surface area of the condyle.

On the axial plane, the layer with the largest area of the condyle was selected as the measurement plane, and a line connecting the inner and outer poles of the condyle was made. The angle between this line and the perpendicular line of the sagittal axis was measured, that is, the horizontal condylar axis angle (Figure 5).

2.3 Statistical analysis

SPSS 27 software (SPSS; IBM, Chicago, IL) was adopted to conduct statistical analysis, and $p < 0.05$ was considered statistically significant. Shapiro-Wilk testing confirmed normal distribution of all data. Data were expressed in terms of the maximum, minimum, mean, and standard deviation. Paired *t*-test for comparing data from different genders and sides within the same group, and two-sample t-tests was used to compare data between two groups. In terms of analyzing the correlation between the disc condyle angle and the volume surface area of the condyle, pearson test was employed, if the data conformed to the normal distribution; otherwise, the Spearman test was used. To test the magnitude of the measurement error, 20 joints were randomly selected for measurement and then measured again 4 weeks after the first measurement. The reliability of measurement had intraclass correlation coefficients higher than 0.95.

3 Results

A total of 168 joints were analyzed, with 84 each in asymptomatic and TMD volunteers. The age distribution of the two groups were shown in Table 1. Age difference was not statistically significant ($p > 0.05$).

Table 2 have shown the condylar volume of asymptomatic and TMD volunteers. In the asymptomatic group, the condylar volume was significantly larger in males than that in females ($p < 0.05$), however, no significant difference was found between the left and right sides ($p > 0.05$). In the TMD group, the condylar volume was significantly larger in males than that in females ($p < 0.05$), the left condylar volume was significantly larger than the right ($p < 0.05$). Condylar volume was significantly reduced in the TMD group compared to the asymptomatic group, regardless of gender and side ($p < 0.05$).

Table 3 have shown the condylar surface area of asymptomatic and TMD volunteers. In the asymptomatic group, the condylar surface area was significantly larger in males than that in females ($p < 0.05$), however, no significant difference was found between the left and right sides ($p > 0.05$). In the TMD group, the condylar surface area was significantly larger in males than that in females ($p < 0.05$), the left condylar surface area was significantly larger than the right ($p < 0.05$). Condylar surface area was significantly reduced in the

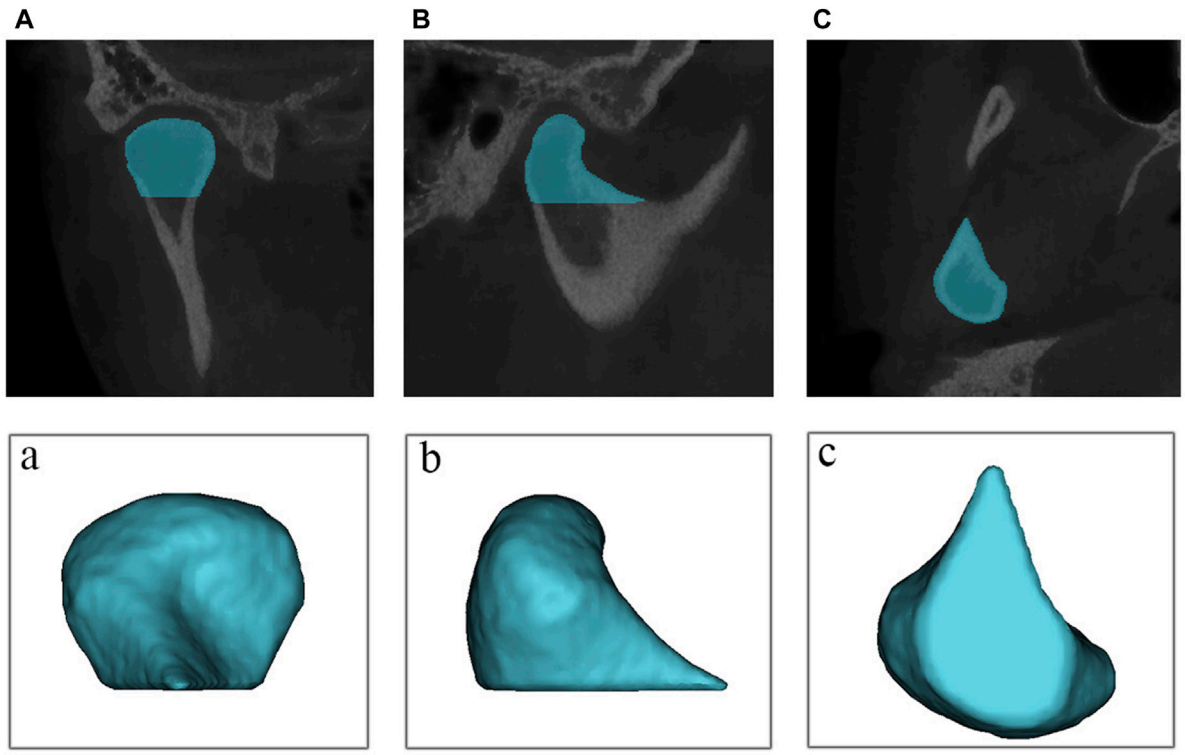

FIGURE 4
The reconstruction of 3D model of condyle. **(A)** coronal view of the mask **(B)** sagittal view of the mask **(C)** overhead view of the mask; (a) coronal view of the model; (b) sagittal view of the model; (c) sagittal view of the model.

TMD group compared to the asymptomatic group, regardless of gender and side ($p < 0.05$).

Table 4 have shown the disc condyle angle of asymptomatic and TMD volunteers. In the asymptomatic group, there were no significant gender and side differences ($p > 0.05$), while in the TMD group, the disc condyle angle in females was significantly larger than that in males ($p < 0.05$), the right disc condyle angle was significantly larger than the left ($p < 0.05$). Compared with the asymptomatic group, the disc condyle angle was significantly larger in the TMD group, regardless of gender and side ($p < 0.05$).

Table 5 have shown the horizontal condylar axial angle of asymptomatic and TMD volunteers. In the asymptomatic group, there were no significant gender and side differences ($p > 0.05$), while in the TMD group, the horizontal condylar axial angle in females was significantly larger than that in males ($p < 0.05$), no significant difference was found between the left and right sides ($p > 0.05$). Compared with the asymptomatic group, the horizontal condylar axial angle was significantly larger in the TMD group, regardless of gender and side ($p < 0.05$).

The disc condyle angle measurement results were displayed in Figure 6. The asymptomatic volunteers have a disc condyle angle of 20°–30° mostly, whereas TMD volunteers have a disc condyle angle of 40°–50°.

Figure 7 have shown the analysis of correlation between condyle volume surface area and the disc condyle angle in TMD volunteers. There was a significant negative correlation between the volume surface area of the condyle and the disc condyle angle, regardless of gender and side ($p < 0.05$).

4 Discussion

TMD is an extremely challenging topic that affects people's quality of life. Symptoms without imaging findings and imaging findings without symptoms may occur simultaneously in the population. Nevertheless, the necessary imaging examination are needed, such as CBCT and MRI. The advantage of CBCT is to show the condylar bone more clearly (Larheim et al., 2015), while the advantage of MRI is to show the soft tissues such as articular discs, muscles and blood vessels (Xiong et al., 2021). The combination of the advantages of the two examinations can be used in the clinical diagnosis and evaluation of TMD.

In this study, both TMD and asymptomatic volunteers underwent MRI and CBCT. Many studies have shown that the incidence of TMD is significantly correlated with changes in TMJ structure (Ahn et al., 2006; Seo et al., 2020), so joint morphological measurement based on these two examinations is clinically significant and may contribute to TMD diagnosis. Studies have confirmed that the progression of condylar osseous changes is strongly correlated with age (Ogura et al., 2012; de Farias et al., 2015), so the research subjects of this study are limited to young adults to reduce the effect of age on condylar bone.

Incesu proposed a method to determine the position of articular disc by measuring 122 TMJs of 61 TMD patients (Incesu et al., 2004). The anterior displacement of the articular disc was divided into 11°–30° (slight), 30°–50° (mild), 51°–80° (moderate), and over 80° (severe). The articular disc positions of 11°–30° were the most

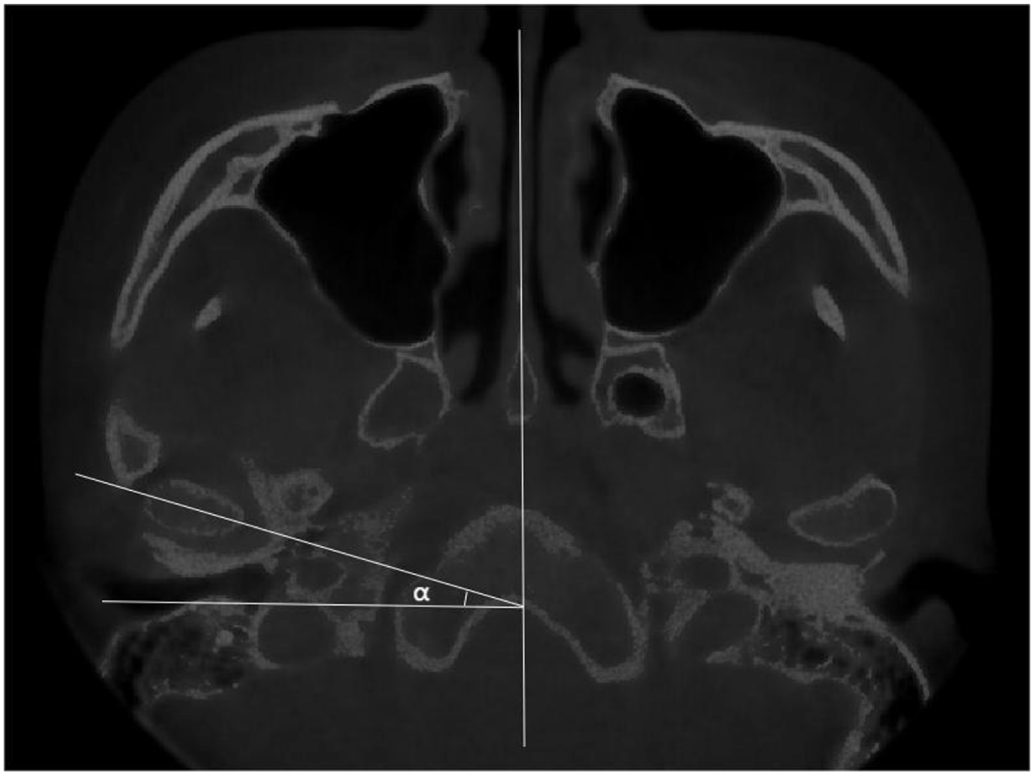

FIGURE 5
The measurements of the horizontal condylar axial angle (α).

TABLE 1 The age distribution of the two groups (years old).

	Asymptomatic volunteers (n = 42)				TMD volunteers (n = 42)				*p*-value
	Min	Max	Mean	SD	Min	Max	Mean	SD	
Age	20	25	23.07	1.31	20	26	23.51	1.56	˃ 0.05
Gender									˃ 0.05
Male	20	25	23.15	1.46	20	26	23.45	1.84	
Female	21	25	23.09	1.19	21	25	23.54	1.29	

SD, standard deviation; n, number of people.

common. In this study, the disc condyle angles were measured by using the condyle apex method, and the distribution frequency of the disc condyle angles was greater in patients with TMD than in asymptomatic volunteers. Asymptomatic volunteers had a disc condyle angle of 20°–30° mostly, whereas TMD volunteers had a disc condyle angle of 40°–50°. This indicates an anterior articular displacement in TMD group compared to asymptomatic volunteers. In addition, here were gender and side differences in the TMD group ($p < 0.05$), but not in the asymptomatic group ($p > 0.05$). This suggests that bilateral articular discs are basically symmetrical in asymptomatic volunteers, as opposed to in the TMD group. In TMD volunteers, the degree of anterior disc displacement was higher in females than in males. This may correspond to the higher clinical incidence of TMD in females (Bagis et al., 2012).

3D visualization of dental imaging seems to be a new direction for future diagnosis. Tecco measured the volume surface area of bilateral condyles in 150 adult Caucasians (Tecco et al., 2010), and found statistically significant differences in condyle volume regardless of gender and side. For the condylar surface area, the difference between the right and the left sides is statistically significant, while those between males and females is not statistically significant. This may be related to racial differences and malocclusion in the study sample. In this study, the volume and surface area of the condyle were measured using CBCT and found to be smaller in TMD volunteers than in asymptomatic group ($p < 0.05$). This suggests that TMD patients may have degenerative remodeling of the condyle, which is consistent with previous findings (Cortés et al., 2011). Gender differences existed in both

TABLE 2 Condylar volume of asymptomatic and TMD volunteers (mm^3).

	Asymptomatic volunteers				TMD volunteers				*p*-value
	Min	Max	Mean	SD	Min	Max	Mean	SD	
Total (n = 84)	1,255.19	30.61.41	2031.09	390.62	1,056.89	2,887.34	1733.03	418.57	˂ 0.05
Gender									˂ 0.05
Male (n = 40)	1,546.94	2,836.89	2,199.17	311.43	1,124.76	2,887.32	1929.68	465.52	
Female (n = 44)	1,255.19	3,061.41	1878.28	395.46	1,056.89	2,120.94	1,551.26	281.97	
p-value	˂ 0.05				˂ 0.05				
Side									˂ 0.05
Left (n = 42)	1,255.19	2,836.89	2049.53	399.01	1,117.67	2,887.32	1826.28	389.43	
Right (n = 42)	1,325.81	3,061.41	2012.64	386.01	1,056.89	2,563.24	1,637.74	429.44	
p-value	˃ 0.05				˂ 0.05				

SD, standard deviation; n, number of joints.

TABLE 3 Condylar surface area of asymptomatic and TMD volunteers (mm^2).

	Asymptomatic volunteers				TMD volunteers				*p*-value
	Min	Max	Mean	SD	Min	Max	Mean	SD	
Total (n = 84)	684.05	1,484.16	979.36	179.52	592.14	1,499.35	858.59	183.51	˂ 0.05
Gender									˂ 0.05
Male (n = 40)	822.94	1,484.16	1,083.69	166.48	655.99	1,499.35	946.85	192.45	
Female (n = 44)	684.05	1,266.52	894.67	134.35	592.14	1,205.64	775.81	136.74	
p-value	˂ 0.05				˂ 0.05				
Side									˂ 0.05
Left (n = 42)	684.05	1,422.68	988.56	174.66	592.14	1,499.35	886.79	183.87	
Right (n = 42)	714.71	1,484.16	970.16	185.91	595.23	1,226.93	830.41	180.92	
p-value	˃ 0.05				˂ 0.05				

SD, standard deviation; n, number of joints.

TABLE 4 The disc condyle angle of asymptomatic and TMD volunteers (°).

	Asymptomatic volunteers				TMD volunteers				*p*-value
	Min	Max	Mean	SD	Min	Max	Mean	SD	
Total (n = 84)	5.2	56.7	24.27	9.29	8.4	103.6	48.86	19.82	˂ 0.05
Gender									˂ 0.05
Male (n = 40)	5.2	38.5	23.51	7.51	8.4	103.6	43.24	19.91	
Female (n = 44)	8.1	56.7	25.21	11.06	12	101.4	53.51	18.96	
p-value	˃ 0.05				˂ 0.05				
Side									˂ 0.05
Left (n = 42)	5.2	56.7	23.87	9.39	8.4	101.4	45.48	19.38	
Right (n = 42)	7.5	45.6	24.66	9.27	10.3	103.6	52.24	19.91	
p-value	˃ 0.05				˂ 0.05				

SD, standard deviation; n, number of joints.

TABLE 5 The horizontal condylar axial angle of asymptomatic and TMD volunteers (°).

	Asymptomatic volunteers				TMD volunteers				*p*-value
	Min	Max	Mean	SD	Min	Max	Mean	SD	
Total (n = 84)	10.1	30.2	19.15	4.48	10.5	33.2	23.01	4.78	< 0.05
Gender									< 0.05
Male (n = 40)	10.1	27.5	18.71	4.36	10.5	31.8	21.31	4.73	
Female (n = 44)	10.2	30.2	19.44	4.76	15.3	33.2	24.52	4.33	
p-value	> 0.05				< 0.05				
Side									< 0.05
Left (n = 42)	10.1	30.2	19.19	4.82	12.9	30.4	23.42	4.53	
Right (n = 42)	10.2	28.2	19.11	4.18	10.5	33.2	22.57	5.03	
p-value	> 0.05				> 0.05				

SD, standard deviation; n, number of joints.

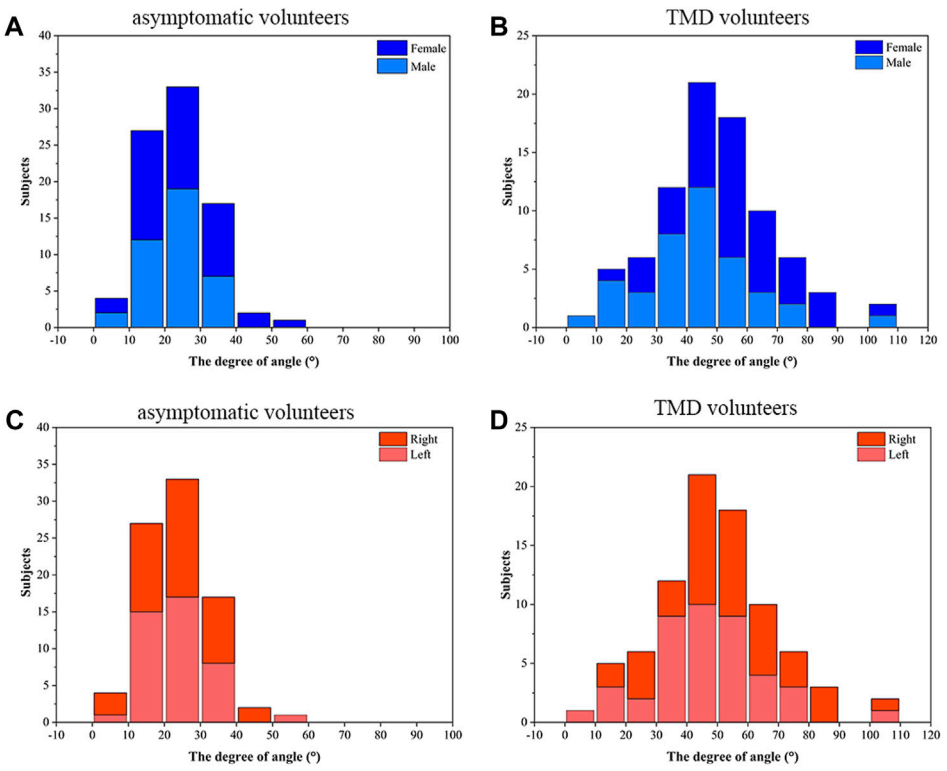

FIGURE 6
The disc condyle angle measurement results. **(A)** The gender distribution of disc condylar angle in asymptomatic volunteers **(B)** The gender distribution of disc condylar angle in TMD volunteers **(C)** The side distribution of disc condylar angle in asymptomatic volunteers **(D)** The side distribution of disc condylar angle in TMD volunteers.

groups ($p < 0.05$), while side differences only existed in the TMD group ($p < 0.05$). This indicates that the volume surface area of the female condyle is smaller than that of the male, regardless of the presence or absence of TMD. In the TMD group, bilateral condylar morphology may not be consistent due to differences in the degree of disc displacement. Due to different imaging methods, research sample and determination of reference lines, the influence of horizontal condylar axis angle on condylar process morphology is still controversial (Alfaleh, 2021). In this study, the horizontal condylar axial angle was significantly larger in the TMD group ($p < 0.05$). This is consistent with the results of Kurita and Lee's study (Kurita et al., 2003; Lee et al., 2017). Although there was no gender difference in the asymptomatic group ($p > 0.05$), the horizontal condylar axis angle in females was larger than that in males, this may

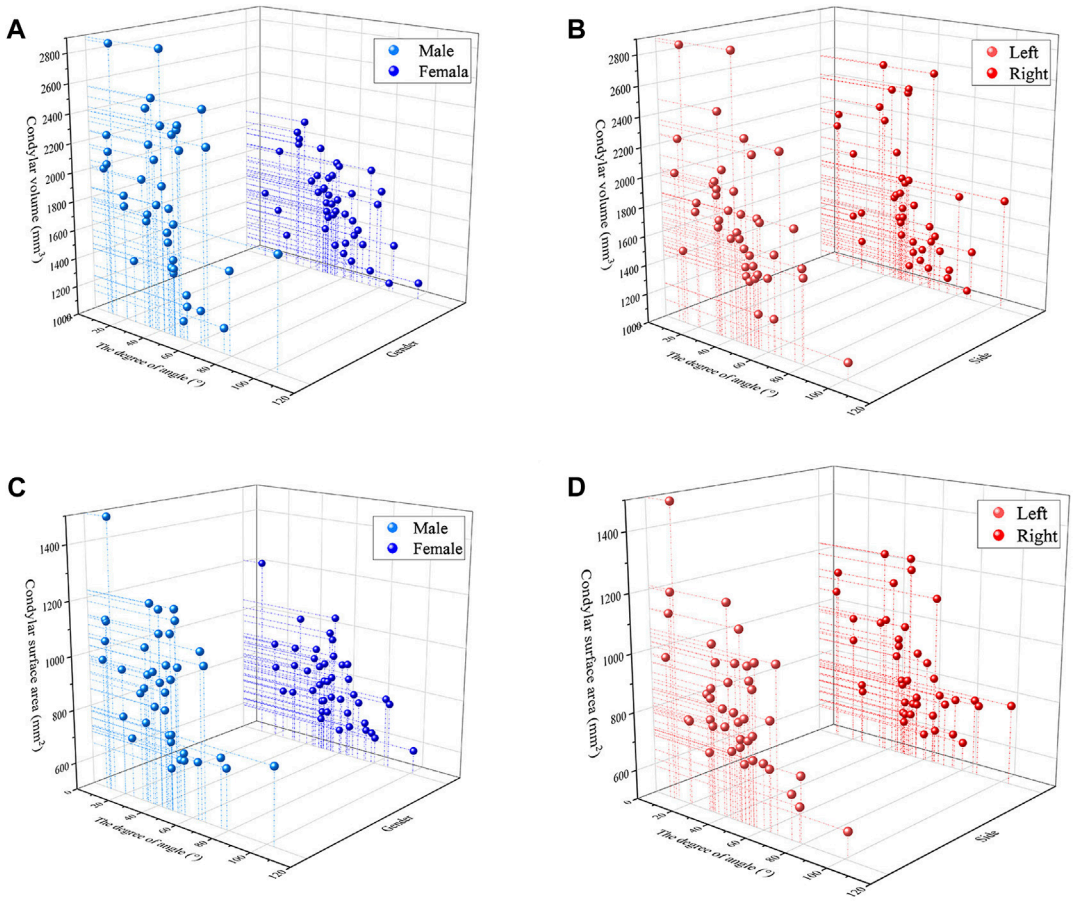

FIGURE 7
The analysis of correlation **(A)** Condylar volume and the disc condyle angle in males and females **(B)** Condylar volume and the disc condyle angle in left and right **(C)** Condylar surface area and the disc condyle angle in males and females **(D)** Condylar surface area and the disc condyle angle in left and right.

explain why females are prone to TMD in terms of anatomical structure. Although no significant side differences were found in both two groups ($p > 0.05$), the left horizontal condylar axis angle was larger than the right in TMD group, this may be related to the occurrence of mandibular dyskinesia in some TMD patients.

In terms of correlation, most previous studies have used linear or angular indices to assess the correlation between condylar morphology and articular disc position. Ahn et al. confirmed that patients with disc displacement without reduction has a lower condylar height than those with disc displacement with reduction or normal disc position (Ahn et al., 2006). Guercio et al. had shown that subjects with disc displacement without reduction had a shorter medio-lateral condylar dimension than those with normal disc position. In the anterior-posterior sizes of the condyle, disc displacement without reduction had smaller dimension than disc displacement with reduction (Guercio Monaco et al., 2022). This suggests that condylar morphology is associated with the change of articular disc position. Animal studies corroborated the findings. Li et al. developed a modified model of anterior articular disk displacement in rabbits, where the contour of the condyle in the joint was reshaped and flattened with increasing tensile force and disc displacement (Li et al., 2014).

In this study, statistical analysis revealed a significant negative correlation between condylar volume surface area and oblique sagittal articular disc position in young TMD volunteers ($p < 0.05$), which is consistent with Chang's research (Chang et al., 2018). The condylar volume of normal disk position, disk displacement with reduction and disk displacement without reduction were compared. The results show that the volume of the condyle decreases as anterior disc displacement increases. One possible explanation for this significant negative correlation is that osteoarthritis is more common in TMD patients with anterior articular disc displacement. As anterior disc displacement advances, bone resorption and remodeling of the condyle occur concurrently, and the trend of bone resorption becomes more obvious (Kurita et al., 2003; Campos et al., 2008).

5 Conclusion

The volume surface area of the condyle in TMD volunteers are inversely proportional to the position of the articular disc. This significant negative correlation suggests that the possibility of disc displacement can be considered when poor condylar morphology is found.

Data availability statement

The original contributions presented in the study are included in the article/Supplementary material, further inquiries can be directed to the corresponding authors.

Ethics statement

The studies involving humans were approved by The Ethics Committee of the Affiliated Hospital of Qingdao University (No. QYFYWZLL 27452)/The Affiliated Hospital of Qingdao University. The studies were conducted in accordance with the local legislation and institutional requirements. The participants provided their written informed consent to participate in this study.

Author contributions

YG: Investigation, Writing–original draft. DL: Data curation, Investigation, Writing–original draft. MY: Methodology, Visualization, Writing–original draft. YY: Data curation, Methodology, Writing–original draft. ZX: Formal Analysis, Writing–review and editing. JY: Resources, Supervision, Writing–review and editing.

Funding

The author(s) declare financial support was received for the research, authorship, and/or publication of this article. This study was approved by the Qingdao science and technology plan projects (2023-2-005-YY).

Conflict of interest

The authors declare that the research was conducted in the absence of any commercial or financial relationships that could be construed as a potential conflict of interest.

Publisher's note

All claims expressed in this article are solely those of the authors and do not necessarily represent those of their affiliated organizations, or those of the publisher, the editors and the reviewers. Any product that may be evaluated in this article, or claim that may be made by its manufacturer, is not guaranteed or endorsed by the publisher.

References

Ahn, S. J., Kim, T. W., Lee, D. Y., and Nahm, D. S. (2006). Evaluation of internal derangement of the temporomandibular joint by panoramic radiographs compared with magnetic resonance imaging. *Am. J. Orthod. Dentofac. Orthop.* 129, 479–485. doi:10.1016/j.ajodo.2005.12.009

Alfaleh, W. (2021). Relationship between horizontal condylar angle and radiographically detectable morphological changes of the condyle in asymptomatic and symptomatic patients with TMD. *Saudi Dent. J.* 33, 1154–1159. doi:10.1016/j.sdentj.2021.02.003

Bagis, B., Ayaz, E. A., Turgut, S., Durkan, R., and Özcan, M. (2012). Gender difference in prevalence of signs and symptoms of temporomandibular joint disorders: a retrospective study on 243 consecutive patients. *Int. J. Med. Sci.* 9, 539–544. doi:10.7150/ijms.4474

Campos, M. I., Campos, P. S., Cangussu, M. C., Guimarães, R. C., and Line, S. R. (2008). Analysis of magnetic resonance imaging characteristics and pain in temporomandibular joints with and without degenerative changes of the condyle. *Int. J. Oral Maxillofac. Surg.* 37, 529–534. doi:10.1016/j.ijom.2008.02.011

Chang, M. S., Choi, J. H., Yang, I. H., An, J. S., Heo, M. S., and Ahn, S. J. (2018). Relationships between temporomandibular joint disk displacements and condylar volume. *Oral Surg. Oral Med. Oral Pathol. Oral Radiol.* 125, 192–198. doi:10.1016/j.oooo.2017.11.001

Cortés, D., Exss, E., Marholz, C., Millas, R., and Moncada, G. (2011). Association between disk position and degenerative bone changes of the temporomandibular joints: an imaging study in subjects with TMD. *Cranio* 29, 117–126. doi:10.1179/crn.2011.020

de Farias, J. F., Melo, S. L., Bento, P. M., Oliveira, L. S., Campos, P. S., and de Melo, D. P. (2015). Correlation between temporomandibular joint morphology and disc displacement by MRI. *Dentomaxillofac Rad.* 44, 20150023. doi:10.1259/dmfr.20150023

de Pontes, M. L. C., Melo, S. L. S., Bento, P. M., Campos, P. S. F., and de Melo, D. P. (2019). Correlation between temporomandibular joint morphometric measurements and gender, disk position, and condylar position. *Oral Med. Oral Pathol. Oral Radiol.* 128, 538–542. doi:10.1016/j.oooo.2019.07.011

Guercio Monaco, E., De Stefano, A. A., Hernandez-Andara, A., and Galluccio, G. (2022). Correlation between condylar size on CT and position of the articular disc on MRI of the temporomandibular joint. *Cranio* 40, 64–71. doi:10.1080/08869634.2019.1692283

Incesu, L., Taşkaya-Yilmaz, N., Oğütcen-Toller, M., and Uzun, E. (2004). Relationship of condylar position to disc position and morphology. *Eur. J. Radiol.* 51, 269–273. doi:10.1016/s0720-048x(03)00218-3

Krisjane, Z., Urtane, I., Krumina, G., Bieza, A., Zepa, K., and Rogovska, I. (2007). Condylar and mandibular morphological criteria in the 2D and 3D MSCT imaging for patients with Class II division 1 subdivision malocclusion. *Stomatologija* 9, 67–71.

Kurita, H., Ohtsuka, A., Kobayashi, H., and Kurashina, K. (2003). Relationship between increased horizontal condylar angle and resorption of the posterosuperior region of the lateral pole of the mandibular condyle in temporomandibular joint internal derangement. *Dentomaxillofac Rad.* 32, 26–29. doi:10.1259/dmfr/23245517

Larheim, T. A., Abrahamsson, A. K., Kristensen, M., and Arvidsson, L. Z. (2015). Temporomandibular joint diagnostics using CBCT. *Dentomaxillofac Rad.* 44, 20140235. doi:10.1259/dmfr.20140235

Lee, P. P., Stanton, A. R., and Hollender, L. G. (2017). Greater mandibular horizontal condylar angle is associated with temporomandibular joint osteoarthritis. *Oral Surg. Oral Med. Oral Pathol. Oral Radiol.* 123, 502–507. doi:10.1016/j.oooo.2016.12.008

Li, H., Cai, X., Wang, S., Yang, C., Song, H., and Huang, L. (2014). Disc positions and condylar changes induced by different stretching forces in the model for anterior disc displacement of temporomandibular joint. *J. Craniofac Surg.* 25, 2112–2116. doi:10.1097/scs.0000000000001065

Liu, S. S., Xu, L. L., Lu, S. J., Mao, M. Y., Liu, L. K., and Cai, B. (2023). Diagnostic performance of magnetic resonance imaging for degenerative temporomandibular joint disease. *J. Oral Rehabil.* 50, 24–30. doi:10.1111/joor.13386

Luo, D., Yang, Z., Qiu, C., Jiang, Y., Zhou, R., and Yang, J. (2022). A magnetic resonance imaging study on the temporomandibular joint disc-condyle relationship in young asymptomatic adults. *Int. J. Oral Max Surg.* 51, 226–233. doi:10.1016/j.ijom.2021.06.010

Ogura, I., Kaneda, T., Mori, S., Sakayanagi, M., and Kato, M. (2012). Magnetic resonance characteristics of temporomandibular joint disc displacement in elderly patients. *Dentomaxillofac Rad.* 41, 122–125. doi:10.1259/dmfr/1286942

Rabelo, K. A., Sousa Melo, S. L., Torres, M. G. G., Peixoto, L. R., Campos, P. S. F., Rebello, I. M. C. R., et al. (2017). Assessment of condyle position, fossa morphology, and disk displacement in symptomatic patients. *Oral Surg. Oral Med. Oral Pathol. Oral Radiol.* 124, 199–207. doi:10.1016/j.oooo.2017.04.007

Seo, B. Y., An, J. S., Chang, M. S., Huh, K. H., and Ahn, S. J. (2020). Changes in condylar dimensions in temporomandibular joints with disk displacement. *Oral Surg. Oral Med. Oral Pathol. Oral Radiol.* 129, 72–79. doi:10.1016/j.oooo.2019.04.010

Seo, Y. S., Park, H. J., Yu, S. K., Jeong, S. R., and Ryu, J. W. (2022). Evaluation of cortical bone formation on mandibular condyle in asymptomatic adolescents and young adults using cone-beam computed tomography. *Life (Basel)* 12, 2032. doi:10.3390/life12122032

Tecco, S., Saccucci, M., Nucera, R., Polimeni, A., Pagnoni, M., Cordasco, G., et al. (2010). Condylar volume and surface in Caucasian young adult subjects. *Bmc Med. Imaging* 10, 28. doi:10.1186/1471-2342-10-28

Xie, Q., Yang, C., He, D., Cai, X., Ma, Z., Shen, Y., et al. (2016). Will unilateral temporomandibular joint anterior disc displacement in teenagers lead to asymmetry of condyle and mandible? A longitudinal study. *J. Cranio Maxill Surg.* 44, 590–596. doi:10.1016/j.jcms.2016.01.019

Xiong, X., Ye, Z., Tang, H., Wei, Y., Nie, L., Wei, X., et al. (2021). MRI of temporomandibular joint disorders: recent advances and future directions. *J. Magn. Reson Imaging* 54, 1039–1052. doi:10.1002/jmri.27338

Yasa, Y., and Akgül, H. M. (2018). Comparative cone-beam computed tomography evaluation of the osseous morphology of the temporomandibular joint in temporomandibular dysfunction patients and asymptomatic individuals. *Oral Radiol.* 34, 31–39. doi:10.1007/s11282-017-0279-7

Yildizer, E., and Odabaşı, O. (2023). Differences in clinical and radiographic features between bilateral and unilateral adult degenerative temporomandibular joint disease: a retrospective cross-sectional study. *Int. Orthod.* 21, 100731. doi:10.1016/j.ortho.2023.100731

frontiers | Frontiers in Bioengineering and Biotechnology

TYPE Original Research
PUBLISHED 07 February 2024
DOI 10.3389/fbioe.2024.1322008

OPEN ACCESS

EDITED BY
Lei Fan,
Marquette University, United States

REVIEWED BY
Mario Fleischer,
Charité University Medicine Berlin, Germany
Romain David,
Natural History Museum, United Kingdom

*CORRESPONDENCE
Xiang Wu,
x_wu@xzhmu.edu.cn
Shen Yu,
yushen@dlut.edu.cn
Lijie Xiao,
lijiexiao@163.com

†These authors have contributed equally to this work and share first authorship

RECEIVED 15 October 2023
ACCEPTED 26 January 2024
PUBLISHED 07 February 2024

CITATION
Zhang J, Zhang S, Li Y, Xiao L, Yu S, Wu X, Shen S and Xu H (2024), Investigation on biomechanical responses in bilateral semicircular canals and nystagmus in vestibulo-ocular reflex experiments under different forward-leaning angles.
Front. Bioeng. Biotechnol. 12:1322008.
doi: 10.3389/fbioe.2024.1322008

Investigation on biomechanical responses in bilateral semicircular canals and nystagmus in vestibulo-ocular reflex experiments under different forward-leaning angles

Jing Zhang[1†], Shili Zhang[2†], Yue Li[1], Lijie Xiao[3]*, Shen Yu[4]*, Xiang Wu[1]*, Shuang Shen[5] and Hang Xu[1]

[1]School of Medical Imaging, Xuzhou Medical University, Xuzhou, China, [2]Department of Otolaryngology, Affiliated Hospital of Xuzhou Medical University, Xuzhou, China, [3]Department of Neurology, General Hospital of Xuzhou Mining Group, Xuzhou, China, [4]State Key Laboratory of Structural Analysis for Industrial Equipment, Dalian University of Technology, Dalian, China, [5]School of Rehabilitation Medicine, Binzhou Medical University, Yantai, China

Different head positions affect the responses of the vestibular semicircular canals (SCCs) to angular movement. Specific head positions can relieve vestibular disorders caused by excessive stimulating SCCs. In this study, we quantitatively explored responses of human SCCs using numerical simulations of fluid-structure interaction and vestibulo-ocular reflex (VOR) experiments under different forward-leaning angles of the head, including 0°, 10°, 20°, 30°, 40°, 50°, and 60°. It was found that the horizontal nystagmus slow-phase velocity and corresponding biomechanical responses of the cupula in horizontal SCC increased with the forward-leaning angles of the head, reached a maximum when the head was tilted 30° forward, and then gradually decreased. However, no obvious vertical or torsional nystagmus was observed in the VOR experiments. In the numerical model of bilateral SCCs, the biomechanical responses of the cupula in the left anterior SCC and the right anterior SCC showed the same trends; they decreased with the forward-leaning angles, reached a minimum at a 40° forward tilt of the head, and then gradually increased. Similarly, the biomechanical responses of the cupula in the left posterior SCC and in the right posterior SCC followed a same trend, decreasing with the forward-leaning angles, reaching a minimum at a 30° forward tilt of the head, and then gradually increasing. Additionally, the biomechanical responses of the cupula in both the anterior and posterior SCCs consistently remained lower than those observed in the horizontal SCCs across all measured head positions. The occurrence of these numerical results was attributed to the consistent maintenance of mutual symmetry in the bilateral SCCs with respect to the mid-sagittal plane containing the axis of rotation. This symmetry affected the distribution of endolymph pressure, resulting in biomechanical responses of the cupula in each pair of symmetrical SCCs exhibiting same tendencies under different

forward-leaning angles of the head. These results provided a reliable numerical basis for future research to relieve vestibular diseases induced by spatial orientation of SCCs.

KEYWORDS

semicircular canals, vestibulo-ocular reflex, biomechanical responses of the cupula, nystagmus, symmetry

1 Introduction

The vestibular semicircular canals (SCCs) in the human inner ear can detect the angular motion of the head (Jaeger et al., 2002; Hullar and Williams, 2006; Zuma e Maia et al., 2020; Yu et al., 2021), which play an important role in maintaining body balance and visual stability. The SCCs are located in the labyrinthine cavity of the temporal bone, which includes the horizontal, anterior, and posterior SCCs. The planes of each canal are approximately orthogonal to each other. When the SCCs experience angular motion, the endolymph fluid interacts with the cupulae because of inertia, the cupulae are deflected, and the bundle of sensory hair cells embedded in the cristae are bent. The cupulae in the vestibular SCCs plays a role in sensing both velocity and acceleration (Boselli et al., 2013; Goyens et al., 2019). Based on the principle of the vestibulo-ocular reflex (VOR) (Squires et al., 2004; Boselli et al., 2014; Rabbitt, 2019; Giannoni et al., 2020; Rey-Martinez et al., 2020), involuntary eye movements called nystagmus are generated. Slow-phase velocity (SPV) is a characteristic of nystagmus, which has a quantitative relationship with maximal cupula displacements and shear strain (Wu et al., 2020).

Most angular movements of the head do not generally occur in a single corresponding SCC plane. The labyrinth usually decomposes the rotational stimulus to the head into components along the direction of the three SCCs. Each SCC undergoes excitation or inhibition, producing and transmitting neural signals to the brain, which eventually causes contraction or relaxation of the corresponding extraocular muscles to induce nystagmus. The type of nystagmus and the magnitude of SPV are determined by the effects of excitation or inhibition generated by different SCCs. Rabbitt (1999) developed a mathematical model of three SCCs in toadfish and found that the volume displacements of the cupulae obey a simple cosine rule when the tilt angles of the SCCs change. Moreover, Wu et al. (2021a) investigated the biomechanical response of human SCCs and nystagmus SPV under different left-leaning head positions. They found that a variation in head positions affected the distribution of endolymphatic fluid pressure in SCCs. In addition, these studies suggested that the cupula response in each pair of SCCs located approximately in the same plane had similar variation trends and approximately complied with the cosine law, providing a quantitative numerical basis for analysing the magnitude and type of nystagmus under different left-leaning head positions.

However, for any rotation axis included in the midsagittal plane of the head, the positions of bilateral SCCs are mutually symmetric. Considering the pressure gradient of the endolymph fluid in the SCCs distributed along the direction of rotation, the transcupular pressure in mutually symmetric SCCs with respect to the mid-sagittal plane containing the axis of rotation may be similar when the head experiences a rotational stimulus. These conditions markedly differ from those observed in left-leaning head positions, where significant effects on the biomechanical response of each SCC to the angular motion of the head and the functional response of the VOR may result from the combined effects of excitation or inhibition generated by each SCC. In this study, we aimed to quantitatively explore the biomechanical responses of the cupulae in each SCC and the volunteers' nystagmus SPV under different forward-leaning angles of the head by numerical simulation of the SCC model in human and VOR experiments. The forward-leaning angles of the head we investigated included the head tilted at 0°, 10°, 20°, 30°, 40°, 50°, and 60° forward (see Figure 1A).

2 Materials and methods

2.1 Model of SCCs

We built a geometrical model of the bilateral SCCs in the inner ear based on the geometrical parameters provided in the literature (Ifediba et al., 2007). However, the method for defining the geometry of the cupula has not been previously described in Ifediba et al. (2007). Thus, we constructed simplified geometries of the cupulae by trimming the ampullae regions in the SCCs. The cupula was simplified to a cylindrical structure with a thickness of approximately 4.03×10^{-4} m (Kassemi et al., 2005; Selva et al., 2009; Goyens et al., 2019), and the connection of the endolymph in

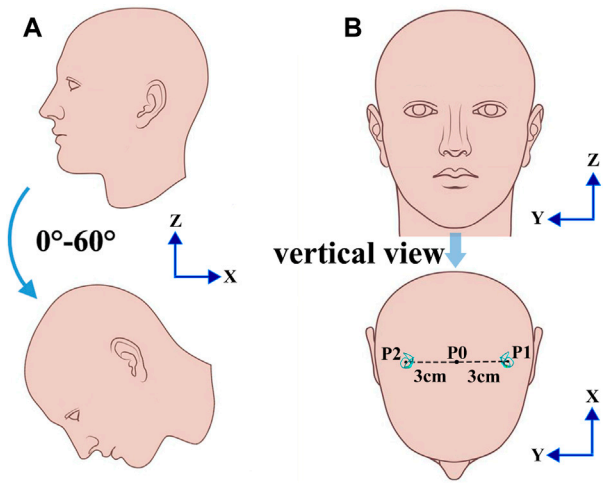

FIGURE 1
Different head positions. **(A)** Different positions of the head tilted 0°, 10°, 20°, 30°, 40°, 50°, and 60° forward. **(B)** The location of SCCs with a normal head position.

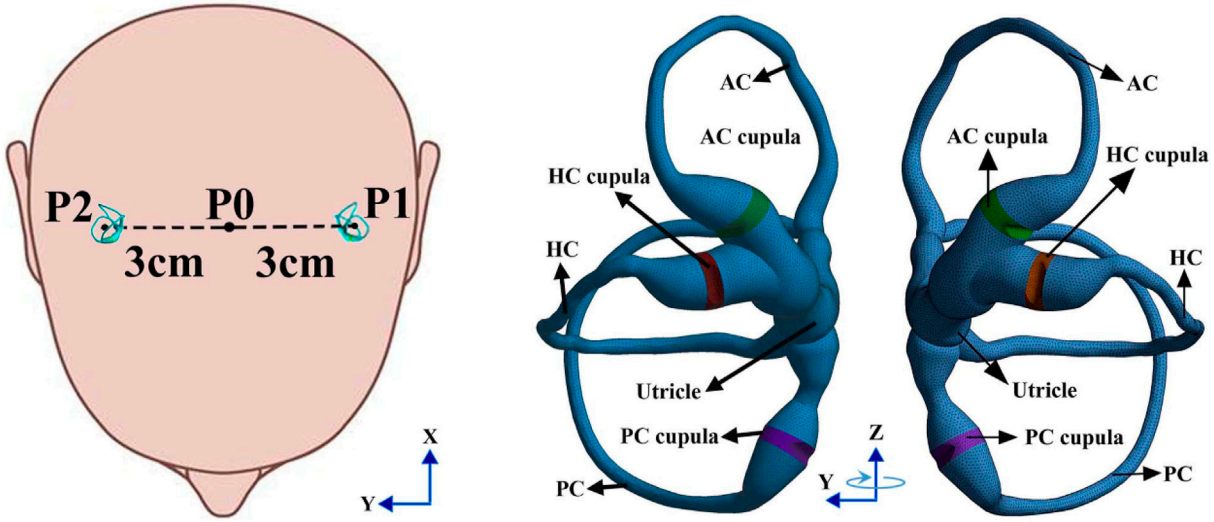

FIGURE 2
Finite element model of the bilateral SCCs in humans: The rotation radius of the bilateral SCCs was 3 cm, and the centre of rotation was P0.

TABLE 1 Physical properties of endolymph and cupula.

Parameters for physical properties	Value
Endolymphatic density (Kg/m^3)	1000 (Steer et al., 1967)
Endolymphatic viscosity (Pa s)	0.001 (Boselli et al., 2013)
Cupular density (Kg/m^3)	1000 (Damiano and Rabbitt, 1996)
Young's modulus of cupula (Pa)	5.4 (Selva et al., 2009)
Poisson ratio of cupula	0.48 (Damiano, 1993)

the ampullae was blocked. The heights of the cupulae in the anterior SCC, horizontal SCC and posterior SCC were approximately 1.35×10^{-3} m, 1.32×10^{-3} m, and 1.29×10^{-3} m, respectively (i.e., the diameters of the ampullae in SCCs). The geometries of the cristae in the ampullae were constructed by trimming cupular solids in Hypermesh 12.0 based on the geometric parameters provided by Selva et al. (2009). The height of the cristae was approximately 2×10^{-4} m which was smaller than that of Selva et al. due to the height of the cupulae in our model being smaller. The fluid region of the endolymph in the unilateral SCCs was meshed with 183 k tetrahedral elements and 39 k nodes. In contrast, the solid region of the cupulae in the unilateral SCCs was meshed with 42 k tetrahedral elements and 9 k nodes. The finite element model of the bilateral SCCs in humans is shown in Figure 2. The physical properties of the endolymph and cupula employed in the numerical model are detailed in Table 1.

In this study, a computational model of bilateral SCCs was constructed using ANSYS Workbench (version 16.0). The specific modeling techniques and parameter configurations were derived from Goyens et al. (2019) (see Supplementary Material). In the Fluent module, we established a fluid dynamics model of the endolymphatic fluid, which is generally considered a Newtonian incompressible fluid (Boselli et al., 2013; Wu et al., 2021b). The rationale for considering the endolymph as an incompressible fluid was detailed in the Supplementary Material. The boundary of the endolymphatic fluid was set to "no slip" walls. In the relative reference frame of the SCCs, the movement of the endolymphatic fluid far from the wall of the SCCs lags behind the movement of the SCCs when they follow the head to undergo angular motion. The behavior of the endolymph can then be defined by the Navier-Stokes equation (Eq. 3·3·I4 on pages 147–148 in Batchelor, 2007; Goyens, 2020):

$$\rho_f \frac{\partial \boldsymbol{v}}{\partial t} + \rho_f (\boldsymbol{v} \cdot \nabla)\boldsymbol{v} = -\nabla P + \mu \nabla^2 \boldsymbol{v} - 2\rho_f \Omega \times (\Omega \times \boldsymbol{r}) - \rho_f \frac{\partial \Omega}{\partial t} \times \boldsymbol{r} \quad (1)$$

where ρ_f is the fluid density, $\boldsymbol{v}$ is the fluid velocity vector relative to the velocity of the moving reference frame, P is the pressure, μ is the dynamic viscosity, $\boldsymbol{\Omega} = (0, 0, \omega)$ is the angular velocity vector of the moving reference frame, and $\boldsymbol{r}$ is the radial coordinates of the fluid element.

In addition, a computational model of the cupulae was established in the transient structural module. In previous studies, the cupula was assumed as either simple elastic structures (Buskrik et al., 1976; Oman et al., 1987) or visco-elastic structures (Rabbitt et al., 1994). However, the mechanical properties of the cupula in the human vestibular system have not been experimentally determined thus far. Based on the research by

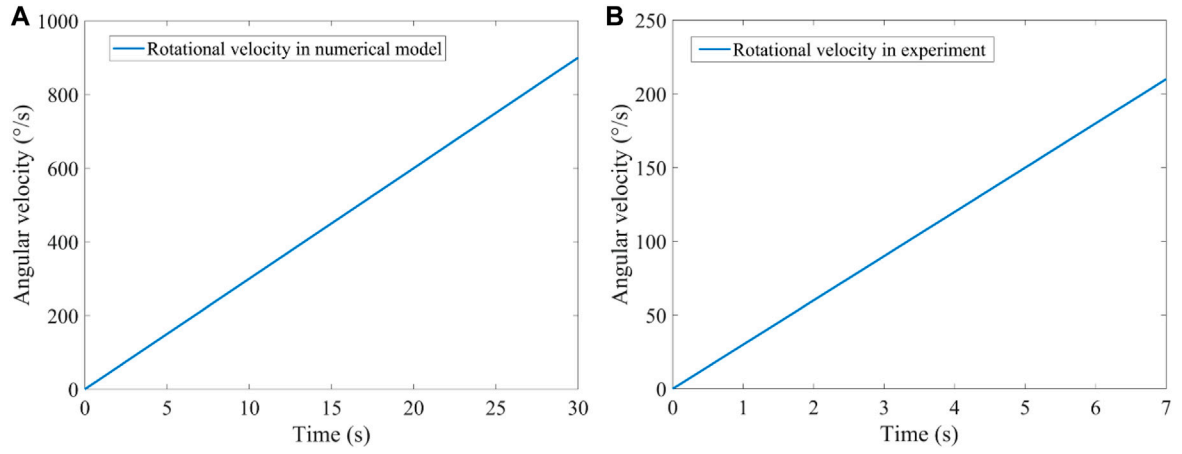

FIGURE 3
Rotational stimulus. **(A)** Rotational velocity loaded in the numerical model. **(B)** Rotational velocity loaded in the VOR experiment.

Selva et al. (2009), we set the elastic modulus of the cupula to 5.4 Pa when constructing the solid structural model in ANSYS Workbench. Besides, other studies also assumed the cupula to be a linear elastic structure (Kassemi et al., 2005; Shen et al., 2016). In our investigation, the maximal cupula deformation induced by the simulated rotational stimulus did not exceed 6 μm, which was very small relative to its dimensions (the thickness of the cupula >400 μm). We considered that the cupula deformation was still in the stage of linear elastic deformation. Considering the factors mentioned above, we assumed the cupula to be a linear elastic isotropic structure. When the SCCs are stimulated by rotational movement, the behaviour of the cupula can be defined by the Navier equation:

$$\rho_s \frac{\partial^2 \boldsymbol{d}}{\partial t^2} = \nabla \cdot \boldsymbol{\sigma_s} + 2\rho_s \Omega \times (\Omega \times \boldsymbol{r}) + \rho_s \frac{\partial \Omega}{\partial t} \times \boldsymbol{r} \tag{2}$$

where ρ_s is the cupular density, $\boldsymbol{d}$ denotes the displacement vector and $\boldsymbol{\sigma_s}$ denotes the stress tensor:

$$\boldsymbol{\sigma_s} = 2\mu\boldsymbol{\varepsilon} + \lambda tr(\boldsymbol{\varepsilon})\mathbf{I} \tag{3}$$

where $\boldsymbol{\varepsilon}$ **is** the strain tensor, tr represents the trace of a matrix, and μ and λ are the Lamé coefficients related to Young's modulus E and Poisson's ratio ν, described by the following equations:

$$\mu = \frac{E}{2(1+\nu)} \tag{4}$$

$$\lambda = \frac{\nu E}{(1+\nu)(1-2\nu)} \tag{5}$$

Eqs 3–5 are cited in Selva et al. (2010).

As shown in Figure 1B, the rotation axis of the bilateral SCCs passes through point P0 along the positive direction of the z-axis when the head is located in different forward-leaning angles of the head. The rotational centre of the bilateral SCCs was P0, and the rotational radii of P0-P1 and P0-P2 were 3 cm. A clockwise angular velocity was applied to the numerical model of the bilateral SCCs. The temporal variation in the magnitude of angular velocity is depicted in Figure 3A. In the system coupling module, the fluid-structure interaction in the SCCs was set. With a maximal number of iterations per time step of 100, the convergence tolerance was set to 0.01. The time step was set as 0.001.

2.2 Rotating chair experiments

2.2.1 Volunteers and equipment

Three people volunteered to participate in the rotating chair experiment and provided written informed consent. They were informed of the experimental procedures and allowed to stop the experiments at any time. All volunteers had normal vestibular function. The experimental research was approved by the Biological and Medical Ethics Committee of Dalian University of Technology (registration number 2020–077). All the experimental procedures were performed in accordance with the principles of the Declaration of Helsinki. Each volunteer was asked to wear an eyepatch and sit on a rotatable chair (Figure 4A). A small infrared camera was fixed to the left side of the eye patch to record the movements of the left eye. The camera recorded the videos at a frame rate of 50 fps. A gyroscope was fixed to the right side of the eyepatch to measure and record the instantaneous velocity of the head. The sampling frequency of the gyroscope was 50 Hz.

The eyepatch was tightly fixed to the volunteer's head to ensure that there was no relative movement between the eyepatch and head. The volunteers wore a seatbelt during the experiment to ensure their safety. They were also required to hold the chair's armrests with their hands and use the headrest and backrest to increase the physical restraint of the head so as to reduce the relative movement of the head during rotation. In addition, auxiliary signs were marked on the armrest of the chair to keep the volunteers seated in the correct position. A gyroscope was used to adjust the head positions of the volunteers.

2.2.2 Experimental procedure

The volunteers sat on a rotatable chair and were asked to fasten their seatbelt. The volunteers wore an eyepatch which was adjusted

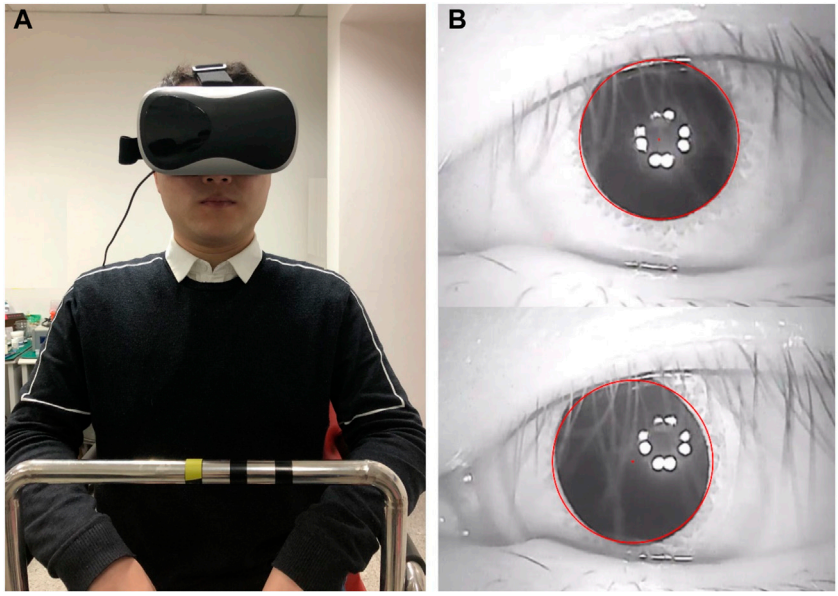

FIGURE 4
Volunteer participating in the VOR experiment. **(A)** A volunteer sitting on a rotatable chair. **(B)** Tracking and locating the pupil.

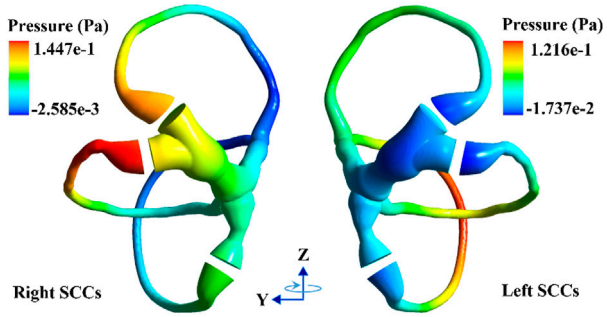

FIGURE 5
The pressure distribution of endolymph with a normal head position.

so that a small infrared camera could record the movements of the left eye. Each volunteer participated in the rotating chair experiment with their head tilted forward at 0°, 10°, 20°, 30°, 40°, 50°, and 60°. The horizontal angular velocity of the chair was clockwise. The temporal variation in the magnitude of angular velocity is illustrated in Figure 3B. All experiments were performed in a dark room to eliminate any interference from eye movement. When the same volunteer participated in multiple experiments, they were required to rest for at least 30 min before commencing the next session.

2.2.3 Nystagmus data processing

The videos of the eye movements recorded during the experiments were processed using MATLAB R2017b software. The pupil centre was then tracked and located using an image processing method (see Figure 4B). To reduce the statistical error, the first and last nystagmus data obtained were removed. We also discarded the nystagmus data from when the volunteers blinked. The SPV of the volunteers was calculated based on a method provided in the study by Wu et al. (2020). Moreover, the average SPV per second was calculated and used as the SPV of the nystagmus per second.

3 Results

3.1 Biomechanical response in the SCCs with a normal head position

When the head experiences angular acceleration, the distribution of the endolymphatic fluid pressure gradient in the SCCs is generated along the rotational direction because of inertia (see Figure 5). Within 0–30 s of accelerated rotation, the transcupular pressure was found to first increase and then gradually stabilise (Figures 6A, B). Meanwhile, the cupulae were deflected by the transcupular pressure in the bilateral SCCs. As shown in Figures 6A–F, the maximal displacement and shear strain of the cupula in each SCC were found to be consistent with the variation trend of the corresponding transcupular pressure. From 0 to 20 s, the maximal displacement and shear strain of the cupulae in the bilateral SCCs were found to increase. During the 20–30 s period, the elastic force of the cupula in each SCC was balanced by the corresponding transcupular pressure, indicating that the maximum displacement and shear strain of the cupulae had reached a stable state. Maximal cupula displacement was found to occur at the centre of the cupula, whereas the maximal cupula shear strain appeared near the centre of the crista surface. When the head rotated at a constant velocity, the endolymphatic pressure difference caused by the angular acceleration disappeared, which would no longer deflect the cupulae. The cupula gradually returned to its resting position under the

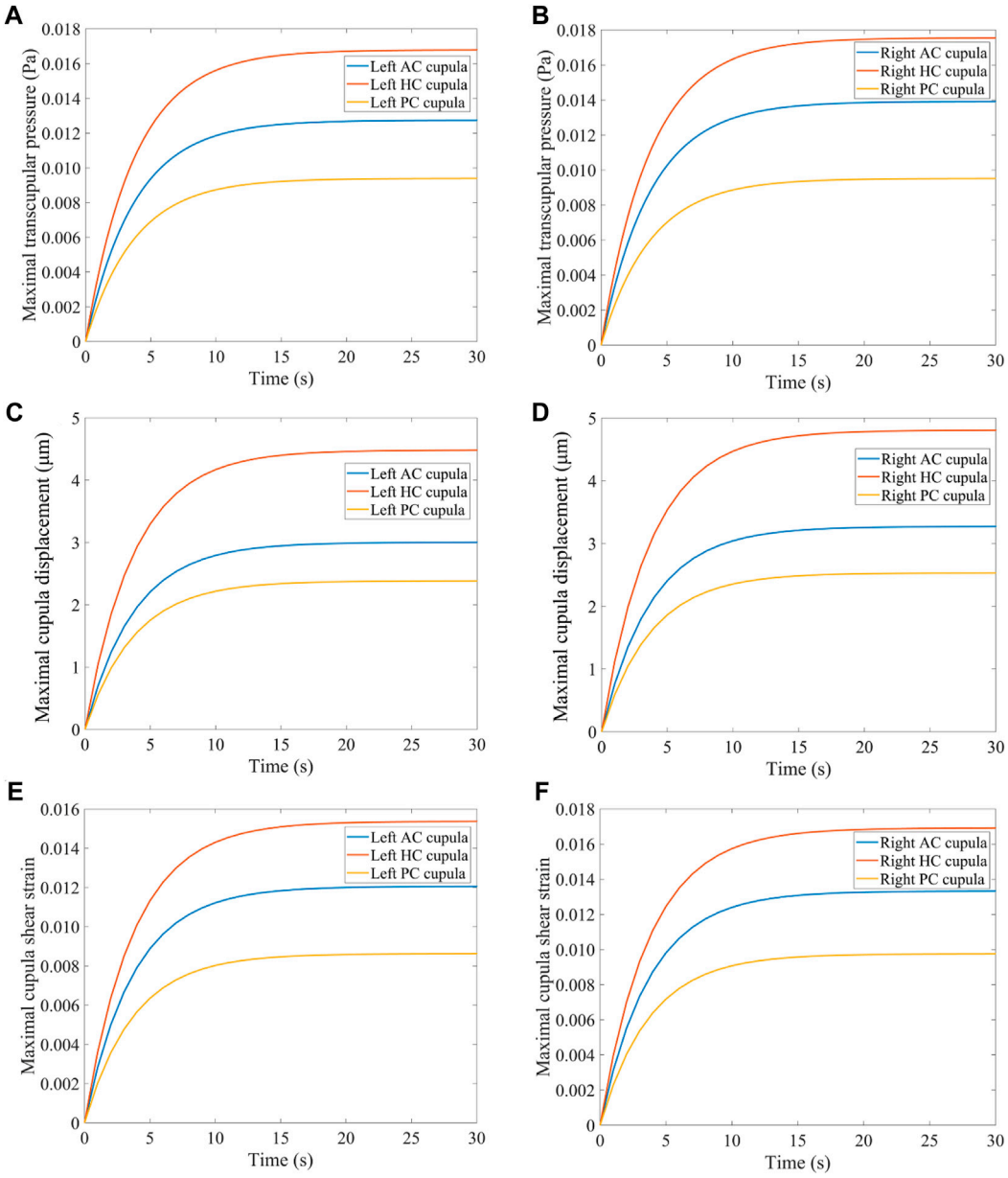

FIGURE 6
Biomechanical responses in the bilateral SCCs. **(A)** Maximal transcupular pressure changes over time in the left SCCs. **(B)** Maximal transcupular pressure changes over time in the right SCCs. **(C)** Maximal cupula displacement changes over time in the left SCCs. **(D)** Maximal cupula displacement changes over time in the right SCCs. **(E)** Maximal cupula shear strain changes over time in the left SCCs. **(F)** Maximal cupula shear strain changes over time in the right SCCs.

combined action of its own elastic restoring force and the viscous resistance of the endolymph. The cupula time constant, measured at 3.7 s in the numerical model of the SCCs (see Supplementary Material), reflected the time course in which cupula displacement increased with the elevation of angular velocity of the head under constant angular acceleration. The cupula time constant, an intrinsic parameter of the endolymph-cupula system in SCCs, is only related to the geometry of the SCCs and the physical properties of the endolymph and cupula. Therefore, the cupula time constant remains the same when the SCCs are rotated under different forward-leaning head positions.

3.2 Biomechanical responses of SCCs under different forward-leaning angles

The changes in cupula displacement and shear strain with different forward-leaning angles are shown in Figure 7. With an increase in the forward-leaning angle, the maximal cupula displacement, and shear strain in the horizontal SCCs gradually increased and reached a maximum when the head was titled approximately 30° forward, after which they gradually decreased. However, when the forward-leaning angle of the head increased, the maximal cupula displacement, and shear strain in the anterior SCCs gradually decreased and reached a minimum when the head was

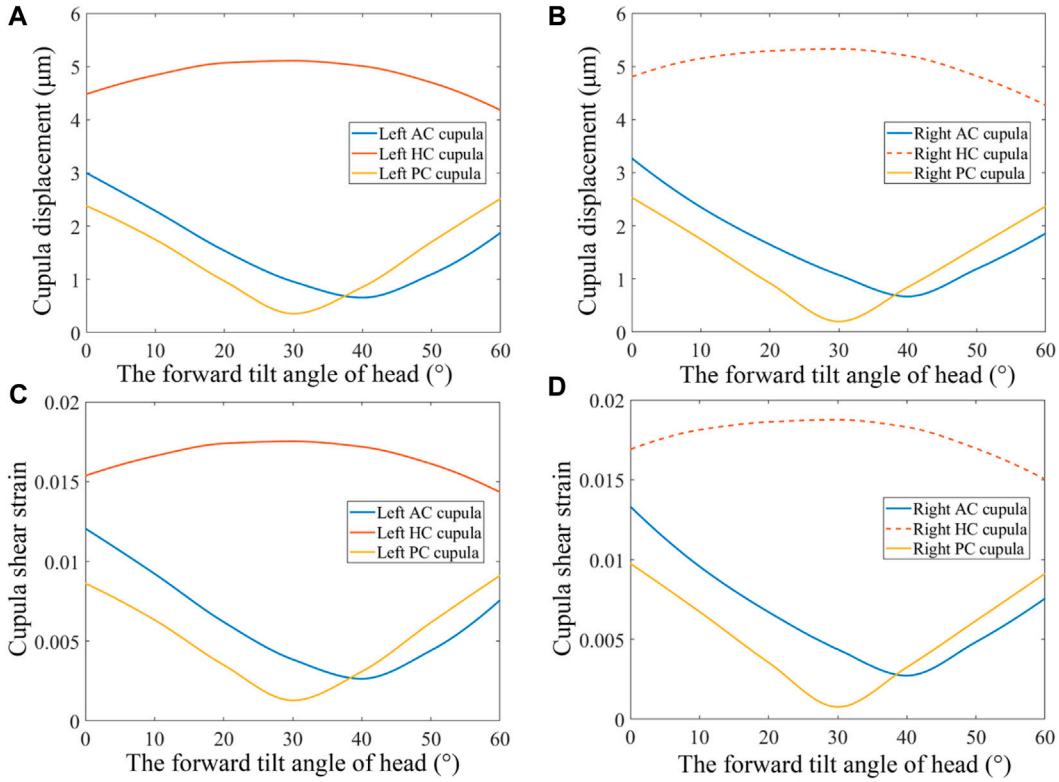

FIGURE 7
Biomechanical responses in the bilateral SCCs under different forward-leaning angles of the head. **(A)** Maximum cupula displacement in the left SCCs under different forward-leaning head positions. **(B)** Maximum cupula displacement in the right SCCs under different forward-leaning head positions. **(C)** Maximum cupula shear strain in the left SCCs under different forward-leaning head positions. **(D)** Maximum cupula shear strain in the right SCCs under different forward-leaning head positions.

tilted approximately 40° forward, after which they gradually increased. For the posterior SCCs, the maximal cupula displacement, and shear strain also decreased gradually with an increase in the forward-leaning angle and reached a minimum when the head was titled forward approximately 30°, after which they gradually increased. Different forward-leaning head positions induced different fluid pressure distribution in the bilateral SCCs (see Figure 8). It is worth mentioning that the endolymphatic fluid pressure on both sides of the cupula in the anterior SCC of the left ear was almost equal leading to the minimum crista shear strain when the head was tilted forward by approximately 40° (see Figure 9A). Due to the negative endolymphatic fluid pressure on both sides of the cupula in the anterior SCC of the left ear, the cupula expanded. In contrast, concerning the anterior SCC of the right ear, the endolymphatic fluid pressures on both sides of the cupula were nearly equal, resulting in the minimum crista shear strain (Figure 9B). The cupula in the anterior SCC of the right ear compressed because of the positive endolymphatic fluid pressure on both sides. Regarding the posterior SCC of the left ear, the endolymphatic fluid pressures on both sides of the cupula were almost equal inducing the minimum crista shear strain (Figure 9C). The cupula in the posterior SCCs of the left ear compressed because the endolymphatic fluid pressure on both sides of the cupula was positive. When the head was tilted forward 40°, the endolymphatic fluid pressure on both sides of the cupula in the posterior SCC of the right ear was almost equal causing the minimum crista shear strain (Figure 9D). Since the endolymphatic fluid pressure on both sides of the cupula in the posterior SCC of the right ear was negative, the cupula in the posterior SCC of the right ear expanded.

3.3 Nystagmus characteristic with a normal head position

When the volunteer's heads were rotated with a horizontal angular acceleration of 30°/s², the horizontal nystagmus was measured with a normal head position. No evidence of vertical or torsional nystagmus was found. Figure 10A shows the horizontal nystagmus trajectory of a volunteer. The trajectory curves with positive slopes were in the slow-phase of nystagmus, while those with negative slopes were in the fast phase of nystagmus. An interrupted part of the trajectory curve indicates that the volunteers blinked. In the fast and slow phases of nystagmus, the absolute value of the slope of the trajectory curve represents the velocity of the eye movements. The SPV of the three volunteers gradually increased from 0 s to 5 s (Figure 10B). When the time was between 5 and 7 s, the SPV of the three volunteers stabilised, indicating that the neural signal transmitted to the brain responsible for triggering the nystagmus SPV had reached saturation. During the constant rotational acceleration of 5–7 s, the average SPV of the three volunteers was 43.7°/s, 38.3°/s, and 27.5°/s, respectively. The nystagmus SPV differed among different

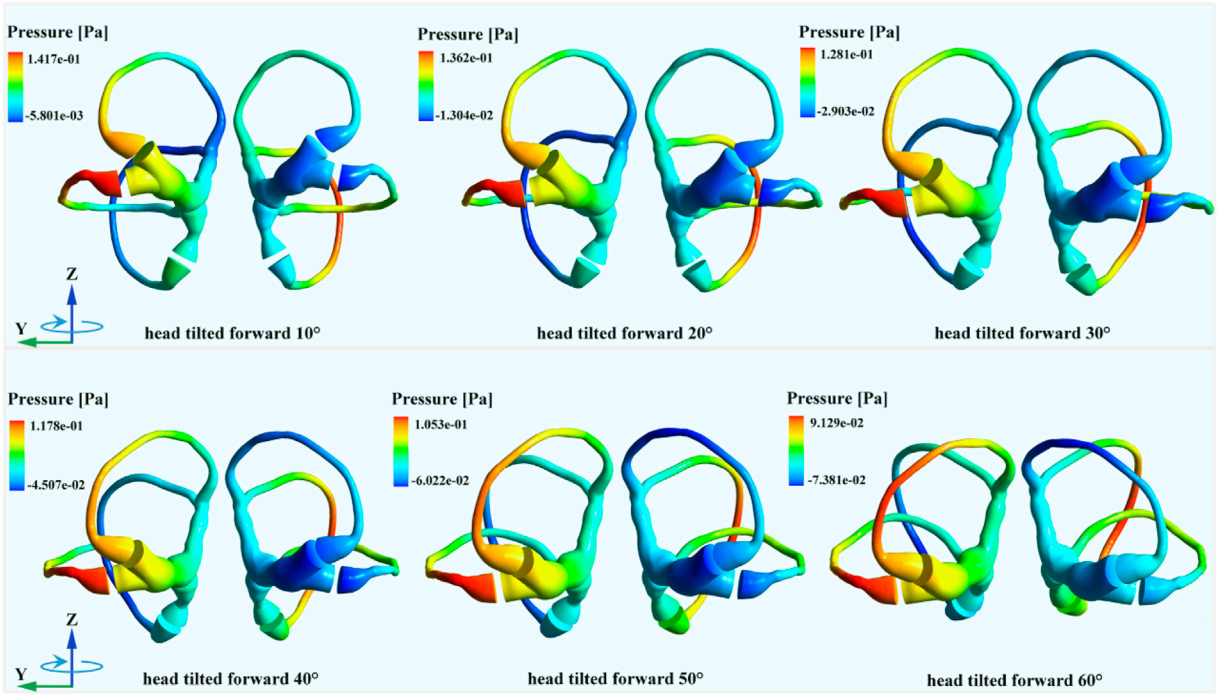

FIGURE 8
The endolymphatic pressure distribution in the bilateral SCCs under different forward-leaning angles of the head (more detailed legends were shown in Supplementary_Material).

volunteers under the stimulation of the same rotational acceleration, which might be caused by individual differences. In addition, no obvious vertical nystagmus or torsional nystagmus was observed in the three volunteers.

3.4 Nystagmus SPV under different forward-leaning angles

The experimental results showed that the three volunteers had horizontal nystagmus under different forward-leaning angles of the head (including the head tilted 0°, 10°, 20°, 30°, 40°, 50°, and 60° forward) but no obvious vertical nystagmus or torsional nystagmus. Considering that the volunteers' nystagmus SPV reached a steady state within 5–7 s, we calculated the average of the volunteers' nystagmus SPV during 5–7 s as stable nystagmus SPV. Figure 10C shows the average nystagmus SPV of the three volunteers under different forward-leaning angles of the head, including 0°, 10°, 20°, 30°, 40°, 50°, and 60°. We found that the horizontal nystagmus SPV of the three volunteers gradually increased with an increase in the forward-leaning angles of the head, reached a maximum when the head was tilted forward approximately 30°, and then gradually decreased.

4 Discussion

When the head experienced angular acceleration, the changes in the forward-leaning angles of the head resulted in different distributions of the endolymphatic fluid pressure gradients in the SCCs, affecting the transcupular pressure and generating different cupula displacement and shear strain. The corresponding vestibular SCCs produced excitation, and the combined action of the excited SCCs induced horizontal nystagmus under different forward-leaning head positions (including the head tilted at 0°, 10°, 20°, 30°, 40°, 50°, and 60°), but no obvious vertical nystagmus or torsional nystagmus.

When the head forward angle was between 0° and 30°, the cupula in the horizontal SCC of the right ear was deflected to the utricle side, and the cupulae in the anterior SCC of the left ear and posterior SCC of the left ear were deflected to the canal side. According to Ewald's law (Ewald, 1892), the horizontal SCC of the right ear, the anterior SCC of the left ear, and the posterior SCC of the left ear were excited. In contrast, the horizontal SCC of the left ear, the anterior SCC of the right ear, and the posterior SCC of the right ear were inhibited. Based on Eggers et al. (2019), the excitation of each SCC influences the extraocular muscles and triggers corresponding eye movements (see Supplementary Material for more detail). Excitation of the horizontal SCC in the right ear would cause the eyeball to move horizontally to the left in the volunteers. Excitation of the anterior SCC in the left ear causes the eyeball to turn up and rotate clockwise, while excitation of the posterior SCC in the left ear causes the eyeball to turn down and rotate clockwise. When the head was tilted forward 0°, the maximum cupula displacement in the horizontal SCC of the right ear was the largest. The horizontal SCC of the right ear was more excited than the other SCCs, resulting in obvious horizontal nystagmus in the volunteers. Compared with the maximal cupula displacement in the horizontal SCC of the right ear, the maximal cupula displacement in the anterior and posterior SCCs of the left ear was smaller. Moreover, the combined excitation of the anterior and posterior SCCs in the left ear would weaken the upward and downward movements of the eyeball. Thus, no obvious vertical

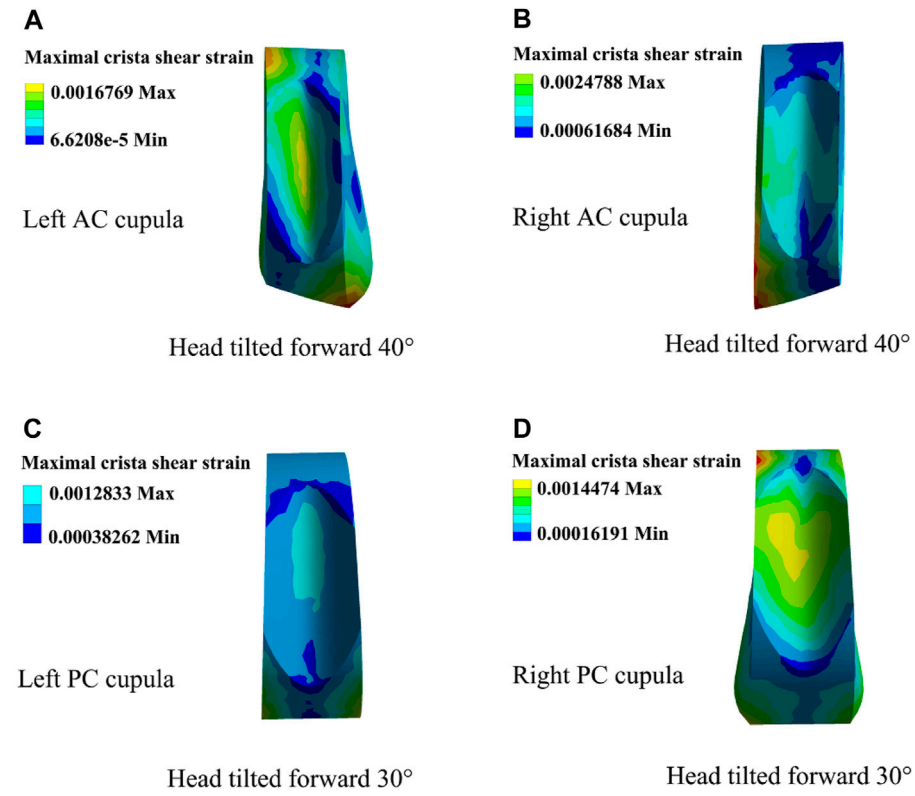

FIGURE 9
Cupula shear strain in the horizontal and anterior SCCs under different forward-leaning angles of the head. **(A)** Left AC cupula shear strain when the head was tilted forward 40°. **(B)** Right AC cupula shear strain when the head was tilted forward 40°. **(C)** Left PC cupula shear strain when the head was tilted forward 30°. **(D)** Right PC cupula shear strain when the head was tilted forward 30°.

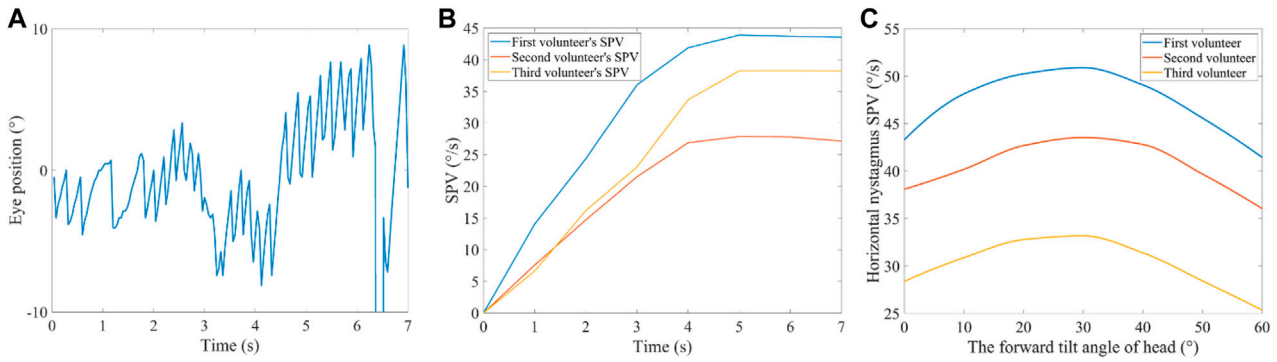

FIGURE 10
Nystagmus in the VOR experiment. **(A)** Horizontal nystagmus of a volunteer with a normal head position. **(B)** Nystagmus SPV in the time domain of the three volunteers with a normal head position. **(C)** Nystagmus SPV of the three volunteers with their heads tilted 0°, 10°, 20°, 30°, 40°, 50°, and 60°, forward.

nystagmus was observed in the volunteers. Although the direction of the rotational eye movement caused by excitation of the anterior and posterior SCCs in the left ear was the same, the maximal cupula displacement in the anterior and posterior SCCs of the left ear was so small that the combined excitation of the anterior and posterior SCCs of the left ear was not sufficient to produce obvious torsional nystagmus in the volunteers. With an increase in the forward-leaning angles of the head, the maximal cupula displacement in the horizontal SCCs gradually increased, while the maximal cupula displacement in the anterior and posterior SCCs of the left ear gradually decreased. When the head was tilted forward 30°, the transcupular pressure in the posterior SCCs was approximately equal, which resulted in no deflection of the cupula. The posterior SCCs were then in a resting state. However, the cupula in the left PC was compressed due to positive fluid pressure on both sides, while the cupula in the right PC was expanded because of the negative fluid pressure on both sides. For the

horizontal SCCs, the cupula displacement reached a maximum that induced maximal SPV in the volunteers.

When the forward-leaning angle of the head was between 30° and 60°, the state of excitation and inhibition in the posterior SCCs changed. The cupula in the posterior SCC of the left ear was deflected to the side of the utricle by the action of transcupular pressure, which induced inhibition. Regarding the posterior SCC of the right ear, the cupula was deflected to the side of the canal by transcupular pressure, which caused excitation. As for the anterior SCCs, they were in a resting state when the head was tilted forward 40°. In addition, the state of excitation and inhibition in the anterior SCCs changed when the forward-leaning angle of the head was between 40° and 60°. The cupula in the anterior SCC of the left ear was deflected to the side of the utricle by transcupular pressure, which induced inhibition. In the anterior SCC of the right ear, the cupula was deflected to the side of the canal by transcupular pressure, which caused excitation. According to a previous report (Eggers et al., 2019), excitation of the anterior SCC in the right ear caused the eyeball to turn up and rotate anticlockwise. Excitation of the posterior SCC in the right ear induced the eyeball to turn down and rotate anticlockwise. When the head was tilted forward between 30° and 60°, the maximal cupula displacement in the horizontal SCC of the right ear decreased as the forward-leaning angle of the head increased, which resulted in a decrease in the horizontal nystagmus SPV in the three volunteers. Regarding the posterior SCC in the right ear, the maximal cupula displacement gradually increased. In contrast, in the anterior SCC in the right ear, the maximal cupula displacement gradually decreased, reached a minimum when the head was tilted 40° forward, and then gradually increased. However, the maximal cupula displacement in the excited anterior SCC of the right ear was still small and partially offset by the maximal cupula displacement in the excited posterior SCC of the right ear. Consequently, the excitation causing the eyeball to move up and down became so weak that there was no significant vertical nystagmus in the volunteers. In addition, there was no obvious torsion nystagmus in the volunteers because the maximal cupula displacement in the excited anterior and posterior SCCs was also very small, which led to the combined effects of the excitation of the anterior and posterior SCCs in the right ear being insufficient to induce torsion nystagmus.

When employing the rotating SCCs as a reference frame, we compared viscous, inertial, and convective terms within the fluid domain under normal head position (see Supplementary Material for details). The maximum magnitudes of inertial and convective terms were comparable in the regions of narrow SCCs, while the convective term could be considered negligible. At the initial moment, there was an increase in inertial forces in the regions of narrow SCCs. As time increased, the inertial force decreased to a negligible level, and the viscous force increased, while the convective forces could be considered negligible in the time domain. This phenomenon might arise due to the deformation of the cupula caused by the pressure gradient, leading to relative flow in the regions of narrow SCCs. These results we obtained were similar to those in the study by Goyens et al. (2019).

Typically, each SCC has a synergistic SCC on the contralateral plane to sense the rotation of the corresponding plane (Shen et al., 2020). For example, the left and right horizontal SCCs constitute a pair of SCCs approximately in the same plane; the left anterior and right posterior SCCs constitute a pair of SCCs approximately in the same plane, and the right anterior and left posterior SCCs constitute a pair of SCCs approximately in the same plane. Previous studies have shown that cupula displacement in each pair of SCCs and results of VOR experiments conforms to the law of cosine and exhibits a similar trend of change under different left-leaning head positions (Blanks et al., 1975; 1985; Estes et al., 1975; Dickman, 1996; Rabbitt, 1999; 2019; Raphan and Cohen, 2002; Della Santina et al., 2007). However, the real geometry of the SCCs in the inner ear of humans is not an ideal ring-shaped structure, and the biomechanical response of the cupula is affected by the geometry of the SCCs and the fluid coupling between the canals (Rabbitt, 1999). The results of the current study suggest that when the rotation axis is located in the mid-sagittal plane, making the bilateral SCCs symmetrical to each other, the biomechanical responses of the cupula in each pair of symmetrical SCCs exhibit approximately the same trends. This is attributed to the horizontal angular acceleration, when decomposed into the direction of each SCC, exerting the same magnitude and direction on each pair of symmetrical SCCs. Consequently, the distribution of endolymphatic pressure gradients along the acting SCCs is very similar. When the bilateral SCCs were asymmetrical with respect to the mid-sagittal plane, the magnitudes of the angular acceleration components were equal. However, the direction differed after decomposing the horizontal angular acceleration on the SCCs in the same plane into the directions of the other SCCs. Therefore, the distribution of the endolymphatic pressure gradient along the acting SCCs was different, which resulted in a significant difference in the biomechanical responses of the cupula in the SCCs located in approximately the same plane. The relative spatial positioning of the geometrical structures of bilateral SCCs, with respect to the mid-sagittal plane where the rotation axis was located, influenced the pressure distribution of the endolymph within the SCCs, subsequently determining the cupula/shear strain. This quantitative investigation into the unique spatial positioning of the SCCs provided in-depth insights into the biomechanical mechanisms of the SCCs and their effects on function. It held important reference value for clinical research aimed at alleviating vestibular diseases caused by spatial orientation.

In this study, the horizontal nystagmus SPV was induced by the cupula displacement/shear strain in the horizontal SCC of the right ear. When the forward-leaning angle of the head increased from 0° to 30°, the maximum cupula displacement in the horizontal SCC of the right ear exhibited an increment of 5 μm, rising from approximately 4.8 μm to about 5.3 μm. The nystagmus SPV showed a significant increase for all three volunteers: the first volunteer's SPV increased by about 8°/s, the second volunteer's SPV increased by approximately 5°/s, and the third volunteer's SPV increased by about 5°/s. The pronounced changes in SPV of nystagmus resulting from subtle cupula displacements were attributed to the presence of numerous sensitive afferent nerves in the crista region (Eatock and Songer, 2011). Consequently, even small displacements of the cupula can trigger significant eye movements. These results have a certain reference value for clinical applications. However, the geometrical morphology of SCCs varies among individuals (Cox and Jeffery, 2010), which quantitatively influences the cupula in response to angular velocity experienced by the head. The current numerical model in this study might not accurately capture the intricate and individualized nature of the vestibular system among volunteers because the construction of geometrical model was based on anatomical parameters from another individual. The vestibular system will exhibit inter-individual variability in terms of anatomical structure

and response magnitude. In fact, noticeable differences in nystagmus SPV among the three volunteers existed under the same angular velocity stimulus due to individual variability. Furthermore, there were variations in the increased nystagmus SPV among the volunteers as the forward-leaning angle increased from 0° to 30°. However, the patterns of biomechanical mechanism in SCCs detecting angular motion exhibited consistent among individuals with normal vestibular function. The geometrical model of SCCs in this study was constructed by the anatomical parameters of a healthy individual. Therefore, the regularities manifested in the numerical results of this study were relevant to these volunteers. However, the quantitative magnitudes of the outcomes may not precisely correspond to responses of their actual SCCs. In summary, the numerical results presented in this study had significant reference value for clinical applications. but were not directly applicable to clinical practice.

5 Conclusion

We quantitatively investigated the responses of human SCCs using the numerical simulation of fluid-structure interaction and VOR experiments under different forward-leaning angles of the head, including 0°, 10°, 20°, 30°, 40°, 50°, and 60°. The horizontal nystagmus SPV and corresponding biomechanical responses of the cupula increased with the forward-leaning angles of the head, reached a maximum when the head was tilted 30° forward, and then gradually decreased. Besides, there was no obvious vertical or torsional nystagmus in the VOR experiments. In the numerical model of bilateral SCCs, the biomechanical responses of the cupula in a pair of anterior SCCs showed the same trends; they decreased with the forward-leaning angles, reached a minimum when the head was tilted 40° forward, and then gradually increased. The biomechanical responses of the cupula in a pair of posterior SCCs also showed the same trend; they decreased with the forward-leaning angles, reached a minimum when the head was tilted 30° forward, and then increased gradually. The reason for these numerical results was that the bilateral SCCs were mutually symmetrical with respect to the mid-sagittal plane containing the axis of rotation. This symmetry resulted in the biomechanical responses of the cupula in each pair of symmetrical SCCs exhibiting the same tendencies under different forward-leaning angles of the head. This quantitative investigation into the unique spatial positioning of the SCCs provided in-depth insights into the biomechanical mechanisms of the SCCs and their effects on function. It provided a reliable numerical basis and played an important role in clinical research for alleviating vestibular diseases caused by spatial orientation.

Data availability statement

The original contributions presented in the study are included in the article/Supplementary Material, further inquiries can be directed to the corresponding authors.

Ethics statement

The studies involving humans were approved by the Biological and Medical Ethics Committee of Dalian University of Technology. The studies were conducted in accordance with the local legislation and institutional requirements. The participants provided their written informed consent to participate in this study.

Author contributions

JZ: Funding acquisition, Software, Writing–original draft, Writing–review and editing. SZ: Investigation, Formal Analysis, Writing–original draft. YL: Formal Analysis, Writing–original draft, Methodology. LX: Investigation, Methodology, Supervision, Writing–review and editing. SY: Conceptualization, Investigation, Methodology, Supervision, Writing–review and editing. XW: Conceptualization, Formal Analysis, Funding acquisition, Investigation, Methodology, Project administration, Software, Validation, Writing–original draft, Writing–review and editing. SS: Data curation, Formal Analysis, Methodology, Validation, Writing–review and editing. HX: Investigation, Supervision, Writing–review and editing.

Funding

The author(s) declare financial support was received for the research, authorship, and/or publication of this article. This study was funded by the Outstanding Talents Start-up Fund Project of Xuzhou Medical University (No. D2021062), Jiangsu Training Program of Innovation and Entrepreneurship for Undergraduates (No. 202210313066Y), and the National Natural Science Foundation of China (Nos 12302404, 12172082, 11572079, and 11772087).

Acknowledgments

The authors would like to thank subjects for volunteering to participate in the experiments and Editage (www.editage.cn) for English language editing.

Conflict of interest

The authors declare that the research was conducted in the absence of any commercial or financial relationships that could be construed as a potential conflict of interest.

Publisher's note

Supplementary material

The Supplementary Material for this article can be found online at: https://www.frontiersin.org/articles/10.3389/fbioe.2024.1322008/full#supplementary-material

References

Batchelor, G. K. (2007). *An introduction to fluid dynamics*. Cambridge: Cambridge University Press.

Blanks, R. H. I., Curthoys, I. S., Bennett, M. L., and Markham, C. H. (1985). Planar relationships of the semicircular canals in rhesus and squirrel monkeys. *Brain. Res.* 340, 315–324. doi:10.1016/0006-8993(85)90928-x

Blanks, R. H. I., Estes, M. S., and Markham, C. H. (1975). Physiologic characteristics of vestibular first-order canal neurons in the cat. II. Response to constant angular acceleration. *J. Neurophysiol.* 38, 1250–1268. doi:10.1152/jn.1975.38.5.1250

Boselli, F., Kleiser, L., Bockisch, C. J., Hegemann, S. C. A., and Obrist, D. (2014). Quantitative analysis of benign paroxysmal positional vertigo fatigue under canalithiasis conditions. *J. Biomech.* 47, 1853–1860. doi:10.1016/j.jbiomech.2014.03.019

Boselli, F., Obrist, D., and Kleiser, L. (2013). Vortical flow in the utricle and the ampulla: a computational study on the fluid dynamics of the vestibular system. *Biomech. Model. Mechanobiol.* 12, 335–348. doi:10.1007/s10237-012-0402-y

Buskrik, W. C., Van Watts, R. G., and Liu, Y. K. (1976). The fluid mechanics of the semicircular canals. *J. Fluid. Mech.* 78, 87–98. doi:10.1017/S0022112076002346

Cox, P. G., and Jeffery, N. (2010). Semicircular canals and agility: the influence of size and shape measures. *J. Anat.* 216, 37–47. doi:10.1111/j.1469-7580.2009.01172.x

Damiano, E. R. (1993). *Continuum models of rotational and caloric stimulation of the vestibular semicircular canal*. PhD Dissertation. Troy, New York, USA: Rensselaer Polytechnic Institute.

Damiano, E. R., and Rabbitt, R. D. (1996). A singular perturbation model of fluid dynamics in the vestibular semicircular canal and ampulla. *J. Fluid Mech.* 307, 333–372. doi:10.1017/S0022112096000146

Della Santina, C. C., Migliaccio, A. A., and Patel, A. H. (2007). A multichannel semicircular canal neural prosthesis using electrical stimulation to restore 3-D vestibular sensation. *IEEE Trans. Biomed. Eng.* 54, 1016–1030. doi:10.1109/TBME.2007.894629

Dickman, J. D. (1996). Spatial orientation of semicircular canals and afferent sensitivity vectors in pigeons. *Exp. Brain. Res.* 111, 8–20. doi:10.1007/BF00229550

Eatock, R. A., and Songer, J. E. (2011). Vestibular hair cells and afferents: two channels for head motion signals. *Ann. Rev. Neurosci.* 34, 501–534. doi:10.1146/annurev-neuro-061010-113710

Eggers, S. D. Z., Bisdorff, A., Brevern, M. V., Zee, D. S., and Newman-Toker, D. E. (2019). Classification of vestibular signs and examination techniques: nystagmus and nystagmus-like movements: consensus document of the committee for the international classification of vestibular disorders of the bárány society. *J. Vestib. Res.* 29, 1–31. doi:10.3233/VES-190658

Estes, M. S., Blanks, R. H. I., and Markham, C. H. (1975). Physiologic characteristics of vestibular first-order neurons in the cat. i. Response plane determination and resting discharge characteristics. *J. Neurophysiol.* 38, 1239–1249. doi:10.1152/jn.1975.38.5.1232

Ewald, J. R. (1892). *Physiologische Untersuchungen ueber das Endorgan des Nervus octavus*. Wiesbaden: JF Bergmann.

Giannoni, B., Marcelli, V., Verdolin, I., Checcucci, C., Pollastri, F., and Pecci, R. (2020). Congruous torsional down beating nystagmus in the third position of the semont's maneuver in patients treated for canalithiasis of posterior semicircular canal benign paroxysmal positional vertigo: its significance and prognostic value. *Front. Neurol.* 11, 949. doi:10.3389/fneur.2020.00949

Goyens, J. (2020). Modelling shows that stimulation of the semicircular canals depends on the rotation centre. *Hear. Res.* 396, 108071. doi:10.1016/j.heares.2020.108071

Goyens, J., Pourquie, M., Poelma, C., and Westerweel, J. (2019). Asymmetric cupula displacement due to endolymph vortex in the human semicircular canal. *Biomech. Model. Mechanobiol.* 18, 1577–1590. doi:10.1007/s10237-019-01160-2

Hullar, T. E., and Williams, C. D. (2006). Geometry of the semicircular canals of the chinchilla (*Chinchilla laniger*). *Hear. Res.* 213, 17–24. doi:10.1016/j.heares.2005.11.009

Ifediba, M. A., Rajguru, S. M., Hullar, T. E., and Rabbitt, R. D. (2007). The role of 3-canal biomechanics in angular motion transduction by the human vestibular labyrinth. *Ann. Biomed. Eng.* 35, 1247–1263. doi:10.1007/s10439-007-9277-y

Jaeger, R., Takagi, A., and Haslwanter, T. (2002). Modeling the relation between head orientations and otolith responses in humans. *Hear. Res.* 173, 29–42. doi:10.1016/S0378-5955(02)00485-9

Kassemi, M., Deserranno, D., and Oas, J. G. (2005). Fluid–structural interactions in the inner ear. *Comput. Struct.* 83, 181–189. doi:10.1016/j.compstruc.2004.08.001

Oman, C. M., Marcus, E. N., and Curthoys, I. S. (1987). The influence of semicircular canal morphology on endolymph flow dynamics:*an anatomically descriptive mathematical model. Acta. Otolaryngol.* 103, 1–13. doi:10.3109/00016488709134691

Rabbitt, R. D. (1999). Directional coding of three-dimensional movements by the vestibular semicircular canals. *Biol. Cybern.* 80, 417–431. doi:10.1007/s004220050536

Rabbitt, R. D. (2019). Semicircular canal biomechanics in health and disease. *J. Neurophysiol.* 121, 732–755. doi:10.1152/jn.00708.2018

Rabbitt, R. D., Boyle, R., and Highstein, S. M. (1994). Sensory transduction of head velocity and acceleration in the toadfish horizontal semicircular canal. *J. Neurophysiol.* 72, 1041–1048. doi:10.1152/jn.1994.72.2.1041

Raphan, T., and Cohen, B. (2002). The vestibulo-ocular reflex in three dimensions. *Exp. Brain. Res.* 145, 1–27. doi:10.1007/s00221-002-1067-z

Rey-Martinez, J., Altuna, X., Cheng, K., Burgess, A. M., and Curthoys, I. S. (2020). Computing endolymph hydrodynamics during head impulse test on normal and hydropic vestibular labyrinth models. *Front. Neurol.* 11, 289. doi:10.3389/fneur.2020.00289

Selva, P., Morlier, J., and Gourinat, Y. (2010). Toward a three-dimensional finite-element model of the human inner ear angular accelerometers sensors. *Int. J. Comput. Vis. Biomech.* 3, 149–156.

Selva, P., Oman, C. M., and Stone, H. A. (2009). Mechanical properties and motion of the cupula of the human semicircular canal. *J. Vestib. Res.* 19, 95–110. doi:10.3233/VES-2009-0359

Shen, S., Sun, X., Yu, S., Liu, Y., Su, Y., Zhao, W., et al. (2016). Numerical simulation of the role of the utriculo-endolymphatic valve in the rotation-sensing capabilities of semicircular canals. *J. Biomech.* 49, 1532–1539. doi:10.1016/j.jbiomech.2016.03.028

Shen, S., Zhao, F., Chen, Z., Yu, S., Cao, T., Ma, P., et al. (2020). Biomechanical analysis of angular motion in association with bilateral semicircular canal function. *Biophys. J.* 118, 729–741. doi:10.1016/j.bpj.2019.12.007

Squires, T. M., Weidman, M. S., Hain, T. C., and Stone, H. A. (2004). A mathematical model for top-shelf vertigo: the role of sedimenting otoconia in bppv. *J. Biomech.* 37, 1137–1146. doi:10.1016/j.jbiomech.2003.12.014

Steer, R. W., Li, Y. T., and Young, L. R. (1967). "Physical properties of the labyrinthine fluids and quantification of the phenomenon of caloric stimulation," in Third symposium on the role of the vestibular organs in space exploration, Pensacola, January 24-26, 409–420.

Wu, X., Yu, S., Liu, W., and Shen, S. (2020). Numerical modeling and verification by nystagmus slow-phase velocity of the function of semicircular canals. *Biomech. Model. Mechanobiol.* 19, 2343–2356. doi:10.1007/s10237-020-01343-2

Wu, X., Yu, S., Shen, S., and Liu, W. (2021a). Quantitative analysis of the biomechanical response of semicircular canals and nystagmus under different head positions. *Hear. Res.* 407, 108282. doi:10.1016/j.heares.2021.108282

Wu, X., Yu, S., Shen, S., and Liu, W. (2021b). Exploring the biomechanical responses of human cupula by numerical analysis of temperature experiments. *Sci. Rep.* 11, 8208. doi:10.1038/S41598-021-87730-W

Yu, S., Wang, J., Shen, S., Tang, Y., Sun, X., Shen, S., et al. (2021). Study of the biomechanical mechanisms of benign paroxysmal positional vertigo. *J. Vestib. Res.* 31, 163–172. doi:10.3233/VES-201547

Zuma e Maia, F., Ramos, B. F., Cal, R., Brock, C. M., Mangabeira Albernaz, P. L., and Strupp, M. (2020). Management of lateral semicircular canal benign paroxysmal positional vertigo. *Front. Neurol.* 11, 1040. doi:10.3389/fneur.2020.01040

frontiers | Frontiers in Bioengineering and Biotechnology

TYPE Original Research
PUBLISHED 07 March 2024
DOI 10.3389/fbioe.2024.1340482

OPEN ACCESS

EDITED BY
Ge He,
University of Wisconsin–Milwaukee,
United States

REVIEWED BY
Rui B. Ruben,
Polytechnic Institute of Leiria, Portugal
Yuanqiao Wu,
Boston University, United States

*CORRESPONDENCE
Yue Chen,
chenyue5523@126.com
Yunkang Yang,
xnykdxff@163.com

†These authors have contributed equally to this work

RECEIVED 18 November 2023
ACCEPTED 26 February 2024
PUBLISHED 07 March 2024

CITATION
Xiang F, Xiao Y, Li D, Ma W, Chen Y and Yang Y (2024), Tension band high-strength suture combined with absorbable cannulated screws for treating transverse patellar fractures: finite element analysis and clinical study.
Front. Bioeng. Biotechnol. 12:1340482.
doi: 10.3389/fbioe.2024.1340482

Tension band high-strength suture combined with absorbable cannulated screws for treating transverse patellar fractures: finite element analysis and clinical study

Feifan Xiang[1,2,3†], Yukun Xiao[2†], Dige Li[2], Wenzhe Ma[1], Yue Chen[3,4,5*] and Yunkang Yang[2*]

[1]The State Key Laboratory of Quality Research in Chinese Medicine, Macau University of Science and Technology, Macau, China, [2]Department of Orthopedic, Affiliated Hospital of Southwest Medical University, Luzhou, China, [3]Department of Nuclear Medicine, Affiliated Hospital of Southwest Medical University, Luzhou, China, [4]Nuclear Medicine and Molecular Imaging Key Laboratory of Sichuan Province, Luzhou, China, [5]Institute of Nuclear Medicine, Southwest Medical University, Luzhou, China

Objective: Few reports exist on the treatment of transverse patellar fractures (TPFs) using absorbable cannulated screws and high-strength sutures, and most screws and sutures lack good biomechanics and clinical trials. Therefore, this study aimed to demonstrate the biomechanical stability and clinical efficacy of tension-band high-strength sutures combined with absorbable cannulated screws (TBSAS) in treating TPFs (AO/OTA 34 C1).

Methods: Finite element models of five internal fixation schemes were established: tension-band wire with K-wire (TBW), TBW with cerclage wire (TBWC), TBW with headless pressure screws (TBWHS), TBW with full-thread screws (TBWFS), and TBSAS. We comprehensively compared the biomechanical characteristics of the TBSAS treatment scheme during knee flexion and extension. Forty-one patients with TPFs in our hospital between January 2020 and August 2022 were retrospectively enrolled and divided into the TBSAS (n = 22) and TBWC (n = 19) groups. Clinical and follow-up outcomes, including operative time, visual analog scale (VAS) pain score, postoperative complications, Bostman score, and final knee range of motion, were compared between both groups.

Results: Finite element analysis (FEA) showed that TBWHS and TBWFS achieved the minimum mean fracture interface relative displacement during knee flexion (45°, 0–500 N bending load) and full extension (0°, 0–500 N axial load). There was no significant difference between TBSAS (0.136 mm) and TBWC (0.146 mm) during knee flexion (500 N); however, TBSAS displacement was smaller (0.075 mm) during full extension (500 N). Furthermore, the stress results for the internal fixation and the patella were generally lower when using TBSAS. Retrospective clinical studies showed that the TBSAS group had a shorter operative time, lower VAS pain score at 1 and 2 months postoperatively, better Bostman knee function score at 3 and 9 months postoperatively, and better final knee joint motion than the TBWC group (all $p < 0.05$). There were five cases (26.3%) of internal fixation stimulation complications in the TBWC group.

Conclusion: TBSAS demonstrated excellent safety and effectiveness in treating TPFs. It is sufficient to meet the needs of TPF fixation and early functional exercise and effectively reduces metal internal fixation-induced complications and secondary surgery-induced trauma.

KEYWORDS

transverse patellar fractures, absorbable cannulated screws, ultrabraid highstrength suture, tension band, finite element analysis, retrospective clinical study

1 Introduction

Patellar fracture is a common intra-articular fracture in clinical practice, with transverse patellar fracture (TPF) being the most common, accounting for approximately 23% of cases (Larsen et al., 2016; Henrichsen et al., 2018). The patella is the largest sesamoid bone in the human body and plays a vital role in transmitting the strength of the quadriceps muscle and in composing a knee extension device (Martin et al., 2019; Jirangkul and Kosiyatrakul, 2021). Patellar fractures cause serious damage to knee extension. Therefore, the treatment goals for patellar fractures are anatomical reduction of the fracture and articular surface and stable fixation, allowing early functional exercise of the knee joint (Ma et al., 2022). Surgical treatment is necessary when the fracture is displaced by > 3 mm or when the joint is inconsistent by > 2 mm (Steinmetz et al., 2020).

There are many surgical options for TPFs, with tension-band wire with K-wire (TBW) being the most widely used (Kruse et al., 2022). The tension band technique converts the patellar surface tension generated by the extensor muscle during knee flexion into the axial compression force of the patellar fracture surface, thereby promoting bone healing and demonstrating good efficacy (Jia et al., 2022). However, owing to the specific anatomic location of the patella, it is associated with a higher overall complication rate (approximately 52%) (Li et al., 2022), including Kirschner needle displacement, tension band breakage, symptomatic hardware, and infection (Lee et al., 2021; Trinchese et al., 2021). The modified regimen of titanium-cannulated screws may have better biomechanical characteristics and stability and can provide a direct compression force between the fracture fragments. Currently, there are mainly headless pressure screws and full-thread screws (Chen et al., 2019). However, clinical complications such as fixation failure (7.5%), postoperative infection (1.5%), and symptomatic implants (23%) remain (Hoshino et al., 2013; Jia et al., 2022). Therefore, another surgery or revision is required to remove the internal fixation, which increases the patient's pain.

In recent years, non-metallic implants have received significant attention and have advanced rapidly, and there are new treatment options for TPFs. Poly lactic-co-glycolic acid (PLGA) is one of the most widely used biodegradable forged composite materials, with good biological activity, biocompatibility, and high mechanical strength (Kobielarz et al., 2020; Rocha et al., 2022). The PLGA absorbable cannulated screw can be directly combined with bone, completely replaced with natural bone, and finally hydrolyzed into alpha-hydroxyl acid, which is fully absorbed in approximately 2 years. Furthermore, steel wire can be replaced with Ultrabraid™ #2 suture (Smith and Nephew, Andover, MA, United States), a nonabsorbable high-strength suture that has strong biomechanical benefits and is widely used in treating tendon and ligament rupture, meniscus injury, and fractures (Liu et al., 2020; Taha et al., 2020). This may provide an effective internal fixation scheme for TPFs. However, there are few reports on the treatment of TPFs using absorbable cannulated screws and high-strength sutures, and most screws and sutures lack good biomechanics and clinical trials (Wright et al., 2009; Sayum Filho et al., 2021). Finite element analysis (FEA) can provide quantitative biomechanical information on orthopedic implants and improve the understanding of the mechanical behavior of implants and bone-implant interactions (Zeng et al., 2020).

Therefore, to further improve the surgical efficacy of TPFs and reduce complications, the present study combined FEA with a retrospective clinical study to evaluate the safety and efficacy of tension-band high-strength sutures combined with absorbable cannulated screws (TBSAS) in treating TPFs.

2 Material and methods

2.1 FEA: establishment of the TPF model

This study was approved by the medical ethics committee of our hospital, and all participants provided informed consent. The patellar image data of a healthy volunteer (age: 41 years, height: 176 cm, weight: 73 kg) were collected using spiral computed tomography (CT) (GE Medical Systems 64-slice spiral CT scanner, layer thickness: 0.5 mm) and saved in Digital Imaging and Communications in Medicine format. The cortical and cancellous bone structures of the patella were extracted using threshold segmentation, region growing, and other commands in Mimics Research 21 (Materialize, Belgium) to build a three-dimensional model of the patella (Figure 1A) (Yuan et al., 2022). Remeshing, wrapping, and smoothing were performed using Geomagic Wrap 2021 (Geomagic, NC, United States) (Mao et al., 2023). Finally, the TPF model (AO/OTA 34C1) was established using SolidWorks 2021 (Dassault, France) (Chang et al., 2023) (Figure 1B).

2.2 Establishment of the internal fixation model

In this study, five types of internal fixation models were selected to fix TPFs to fully compare and discuss the biomechanical effects of TBSAS. Three types of cannulated screws were constructed using the SolidWorks 2021 software (Figure 1C). Fixation was then performed

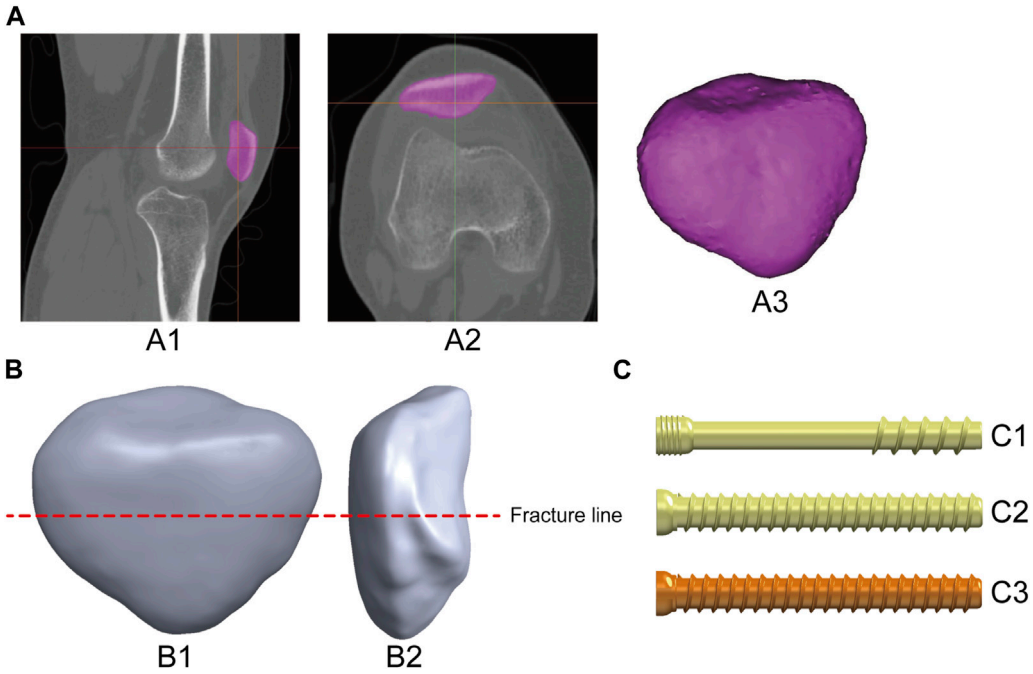

FIGURE 1
Production of the patella and internal fixation model: **(A)** 3D patella model extracted from image data, A1-A2: CT image of the knee joint; A3: 3D patella model. **(B)** Establishing the TPF model, B1-B2: adem position. **(C)** Construct three kinds of cannulated screw internal fixation models, C1: Headless pressure screw (Waston Medical Instrument Co., Ltd., China); C2: Full thread screw (Waston Medical Instrument Co., Ltd., China); C3: Absorbable screw (Bioretec Ltd., Finland).

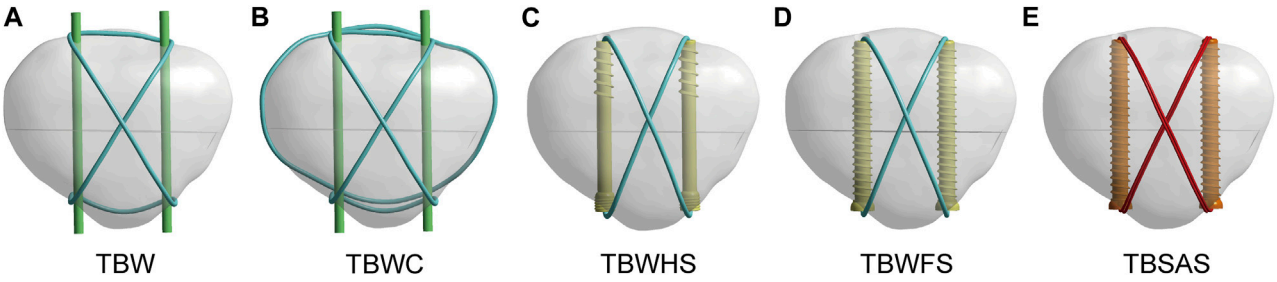

FIGURE 2
TPF internal fixation assembly model: **(A)** Tension band wire with K-wire (TBW). **(B)** TBW with cerclage wire (TBWC). **(C)** TBW with headless pressure screws (TBWHS). **(D)** TBW with full-thread screws (TBWFS). **(E)** Tension band high-strength sutures combined with absorbable cannulated screws (TBSAS). (Blue: steel wire; Green: Kirschner wire; Yellow: titanium screw; Red: sutures; Orange: absorbable screw).

according to the patellar fracture model and the standard surgical protocol (Figure 2). The patients were divided into control groups, including TBW, TBW with cerclage wire (TBWC), TBW with headless pressure screws (TBWHS), and TBW with full-thread screws (TBWFS), and an experimental group, TBSAS. The Kirchner needle and wire diameters were 2 and 1 mm, respectively. Screws with a diameter of 4.5 mm and a length of 40 mm were selected, and high-strength sutures with a diameter of 0.58 mm and made of double strands were selected. From the distal to the proximal end of the fractured patella, two Kirschner needles or screws were placed parallel in the middle third of the patella using "Boolean operation," 5 mm from the articular surface (Ling et al., 2019).

2.3 Finite element structural analysis

The physical models were simulated using ANSYS Workbench 2020 R1 (Swanson Analysis, Houston, PA, United States). The models were meshed using quadratic tetrahedral elements (Figure 3A). A convergence analysis was performed to ensure the stability and accuracy of the mesh state (Huang et al., 2023). Different field variables, such as the maximum von Mises stress and displacement, were <5% with no maximum stress point (Supplementary Information S1). The average sizes of the unit mesh of the patella, Kirschner needle, steel wire, screws, and suture were 0.7, 0.5, 0.5, 0.5, and 0.4 mm, respectively. All materials were modeled as homogeneous and linearly isotropic.

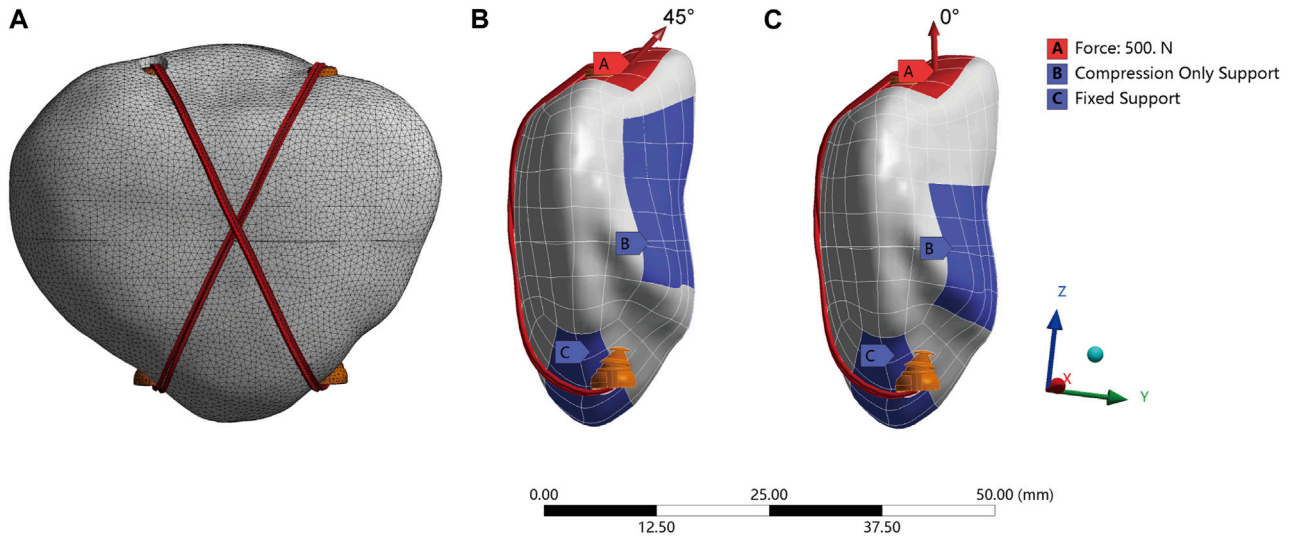

FIGURE 3
The setting of patella model finite element analysis: **(A)** Model mesh rendering. **(B,C)** Boundary and loading conditions of simulated knee flexion (45°bending load) and knee extension (0°axial load).

TABLE 1 Model material parameters.

Material	Young's modulus (MPa)	Poisson's ratio
Cortical bone	10,000	0.3
Cancellous bone	840	0.29
Kirschner wire	200,000	0.3
Screw wire	100,000	0.29
Titanium alloy	110,000	0.3
Absorbable screw	5,500	0.3
Ultrabraid suture	3,000	0.4

The material properties used in this study are as previously described (Bartolin et al., 2021; Du et al., 2022; Xue et al., 2022). The parameters of the various materials are listed in Table 1.

2.4 Boundary and loading conditions

To simulate the actual situation of the contact relationship, all contact types were set within the Coulomb friction law: bone–bone (friction coefficient: μ = 0.45), bone–implant (μ = 0.3), and implant–implant (μ = 0.2) (Chen et al., 2019; Zeng et al., 2020; Xue et al., 2022). Cortical and cancellous bones were used as binding contacts. No prestrain was applied to the screws between the two bone fragments. To simulate the force of the quadriceps muscle during the extension and flexion of the knee joint (Chen et al., 2022), 0° axial load and 45° bending load (0–500 N) were applied on the tip of the patella, and the contact of the patellofemoral joint surface was simulated by setting the "Compression Only Support" boundary condition (Chen et al., 2019). During the analysis, the nodes on the distal surface of the patella were constrained to 0° of freedom, simulating the steady pull of the patellar ligament to prevent rigid-body movement (Figures 3B, C).

2.5 Retrospective clinical study

The clinical and follow-up data of 41 patients with TPF admitted to our hospital between January 2020 and August 2022 were retrospectively analyzed. All participants provided informed consent. The TBSAS and TBWC groups included 22 and 19 patients, respectively (Table 2). The inclusion criteria were as follows: 1) CT or X-ray diagnosis of TPF, 2) acceptance of TBWC or TBSAS, 3) age >18 years, and 4) informed consent and complete clinical data. The exclusion criteria were as follows: 1) other types of patellar fracture; 2) patellar fracture caused by infection, tumor, or metabolic disease; 3) severe structural damage around the patella; and 5) no or <12-month follow-up.

2.6 Surgical procedure

The two groups received treatment for TPFs according to the standard clinical surgical protocol to ensure patellar stability during each operation. All procedures were performed by the same veteran orthopedic trauma surgeon. In the TBSAS group, Kirschner wires and reduction forceps were temporarily fixed after careful reduction of the fracture to ensure a smooth patellar articular surface. Two 4.5 mm absorbable cannulated screws were screwed from the distal to the proximal end. Receding the Kirchner needles, the double-strand Ultrabraid high-strength suture was passed through the absorbable cannulated screws and was bound and fixed using a tension band and "NICE" junction technologies. Furthermore, patellar fixation can be further strengthened using Ultrabraid suture or Ethibond #5 suture cerclage fixation. Passive flexion and extension of the knee joint were performed immediately during the operation to check the stability of

10.3389/fbioe.2024.1340482

TABLE 2 Baseline characteristics of the enrolled patients.

Variables	TBWC (*n* = 19)	TBSAS (*n* = 22)	*p*-value
Age (years) (mean ± SD)	54.63 ± 8.02	52.82 ± 8.92	0.500
Gender			0.752
Male	12 (63%)	12 (55%)	
Female	7 (37%)	10 (45%)	
BMI group, no. (%)			0.308
Normal	8 (42%)	10 (45%)	
Overweight	10 (53%)	12 (45%)	
Obesity	1 (5%)	0	
Fracture side			0.938
Left	8 (42%)	9 (41%)	
Right	11 (58%)	13 (59%)	
Injury mechanism, no. (%)			0.763
Tumble	10 (52%)	14 (64%)	
High fall injury	6 (32%)	5 (23%)	
Car accident	3 (16%)	3 (13%)	
Follow-up (months)	14.47 ± 2.29	14.55 ± 2.54	0.925

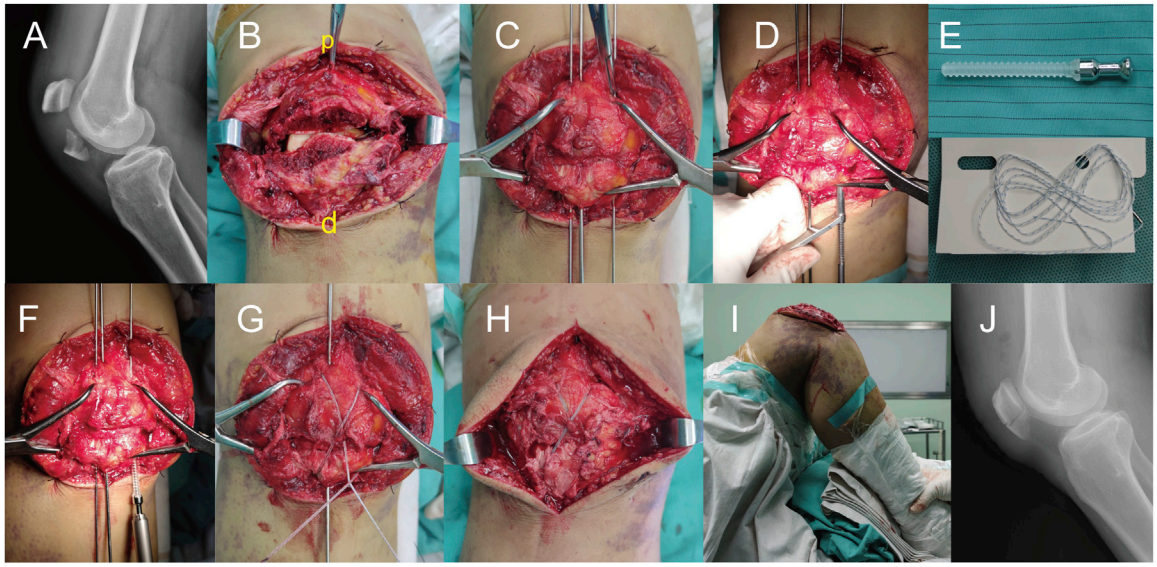

FIGURE 4
Intraoperative treatment of a transverse patellar fracture with TBSAS. **(A)** Preoperative X-ray image; **(B)** Exposed fracture site (p: proximal end of the patella; d: distal end of the patella); **(C)** Reduction fracture; **(D)** Expand the tunnels; **(E)** Absorbable cannulated screw and Ultrabraid high-strength suture; **(F)** Screw in two 4.5 mm absorbable cannulated screws; **(G)** Bound and fix the double-strand high-strength suture; **(H)** Condition after fixation; **(I)** Passive flexion and extension of the knee joint; **(J)** Postoperative X-ray image.

fracture fixation and knee joint movement. The key intraoperative steps are shown in Figure 4.

Notably, strict postoperative management was ensured, including strengthening dressing changes and focusing on wound recovery. Postoperative radiographic examination was performed. Plaster fixation was not required postoperatively, and an adjustable brace could be worn to assist with functional exercises. One day postoperatively, the knee could begin to flex and extend, and semi-weight training could be started gradually. Full weight training could begin 1 month postoperatively, and strenuous exercise should be

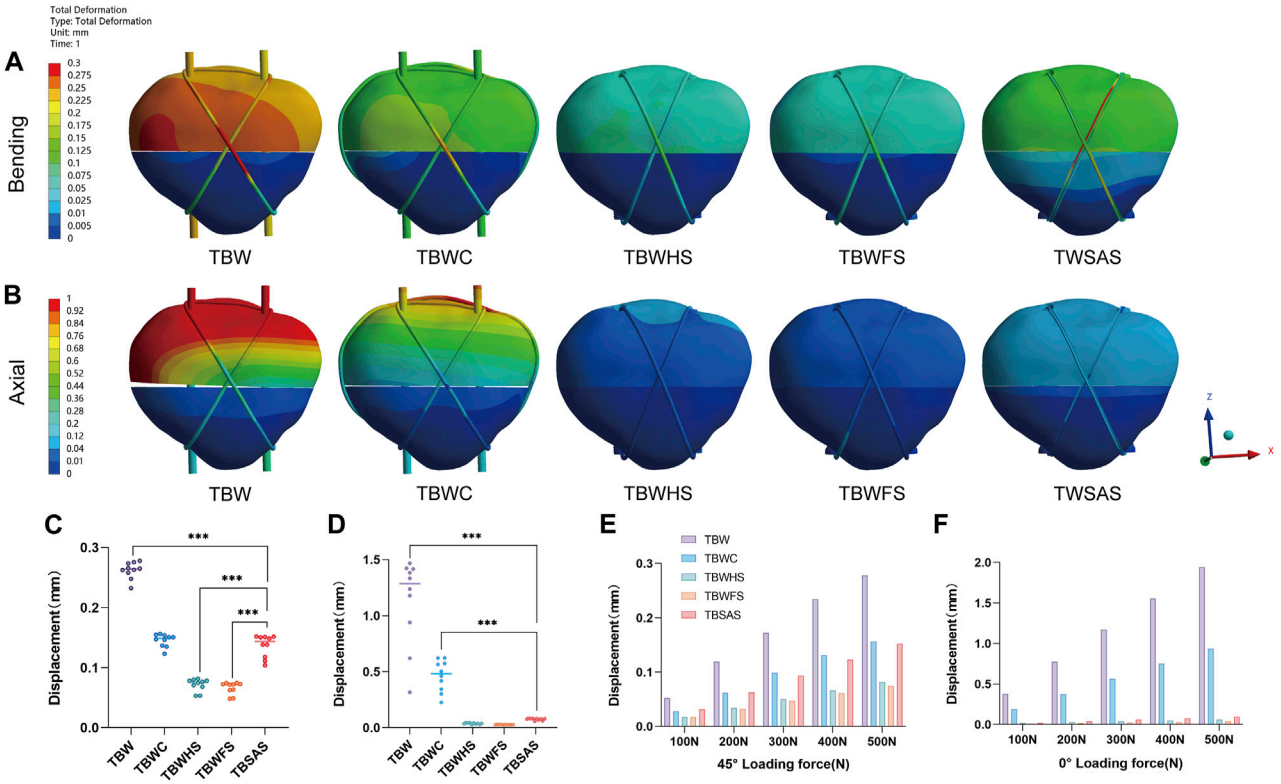

FIGURE 5
Displacements of the five models under bending and axial loads: **(A,B)** Displacement nephograms of the five models under 45° bending load and 0° axial load of 500N; **(C,D)** Statistical graphs of average fracture interface relative displacement of the five models under 45° bending load and 0° axial load of 500N; **(E,F)** Maximum bone displacements of the five models under 45° bending load and 0° axial load (0–500N).

avoided for 3 months (the target motion angle is 90° at 1 month postoperatively).

2.7 Follow-up data collection

The operative times were recorded. Postoperative follow-up was conducted every 4 weeks after discharge. Radiographic review of the affected limb was completed, and knee activity, visual analog scale (VAS) pain score, Bostman knee function score, and patient satisfaction were recorded. Fracture healing was evaluated based on radiographic examination and clinical results, and the patient was instructed to perform functional knee exercises.

2.8 Statistical analysis

Data were analyzed using SPSS software (version 22.0; SPSS Inc., Chicago, IL, United States). Data are presented as mean ± standard deviation. After applying the Kolmogorov–Smirnov normality test, differences between groups were assessed using a one-way analysis of variance or an independent sample *t*-test. Statistical significance was set at $*p < 0.05$, $**p < 0.01$, and $***p < 0.001$.

3 Results

3.1 FEA: displacement of fractures

Under a 45° bending load (0–500 N), the patellar fracture was angled backward. Ten points were uniformly selected at the proximal end of the patellar fracture interface to calculate the average relative displacement of the fracture end (Figure 5). The displacement of the fracture mass in all five models was relatively small. At 500 N, the mean fracture displacements of the two titanium screw groups were smaller than those of the TBSAS group (TBWHS: 0.072; TBWFS: 0.066 mm; TBSAS: 0.136 mm). Notably, no statistically significant difference was observed between TBWC (0.146 mm) and TBSAS. The displacement of the TBW (0.262 mm) was relatively large. However, under a 0° axial load (0–500 N), the patellar articular surface angled forward slightly. The mean fracture interface relative displacement of the patellar articular surface was calculated. In contrast, the interface relative fracture displacement was smaller in all three screw groups at 500 N (TBWHS: 0.037 mm; TBWFS: 0.027 mm; TBSAS: 0.075 mm) than in the TBW (1.132 mm) and TBWC (0.464 mm) groups.

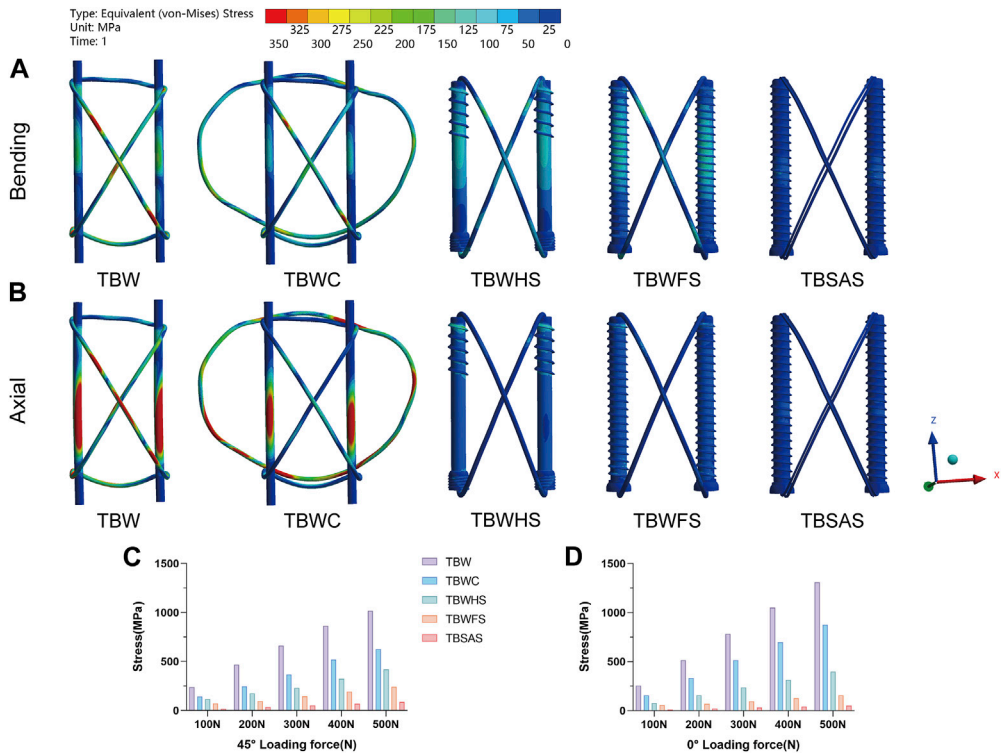

FIGURE 6
Stress distribution on internal fixation of the five models under bending and axial loads: **(A,B)** Stress distribution on internal fixation of the five models under 45° bending load and 0° axial load of 500N; **(C,D)** The maximum stresses on internal fixation of five models under 45° bending load and 0° axial load (0–500N).

3.2 Stress distribution on internal fixation

Under a 45° bending load (0–500 N), stress concentration occurs mainly at the fracture site (Figure 6). At 500 N, the maximum von Mises stress of the five models decreased gradually in the following order: TBW (1,018.1 MPa), TBWC (628.19 MPa), TBWHS (418.8 MPa), TBWFS (242.21 MPa), and TBSAS (88.293 MPa). However, under a 0° axial load (0–500N), the stress concentrations in the three screw groups mainly occurred at the proximal thread of the screws. At 500 N, the maximum stress of the five models gradually decreased in the following order: TBW (1,310.8 MPa), TBWC (876.32 MPa), TBWHS (397.69 MPa), TBWFS (158.18 MPa), and TBSAS (53.201 MPa).

3.3 Stress distribution on the patella

The stress distribution on the patella was mainly concentrated on the part in contact with the internal fixation (Figure 7). The magnitude trend of the patellar stress differed from that of the internal fixation stress, possibly owing to the friction contact of the threads in the three screw groups. Under a 45° bending load (500 N), the maximum von Mises stress from largest to smallest was as follows (Figures 7A, E): TBWHS (203.64 MPa), TBWFS (163.64 MPa), TBW (134.83 MPa), TBSAS (88.224 MPa), and TBWC (66.945 MPa). Under the 0° axial load (500 N), the maximum stress, from largest to smallest, was as follows (Figures 7B, F): TBWHS (181.62 MPa), TBW (165.88 MPa), TBWC (137.39 MPa), TBWFS (117.21 MPa), and TBSAS (73.591 MPa). As for the fracture interface contact stress (Figures 7C, D), all three groups of screws produced good interface compression. However, there was a gradual separation between TBW and TBWC, which was more significant at 0° axial loading.

3.4 Clinical outcomes

All included patients received standard surgical treatment within 48 h of admission and were discharged within 3–5 days postoperatively. Strict follow-up attention and guided functional exercises were ensured. In both groups, the average follow-up period was 14.51 months (range, 12–18 months), the fracture healing rate was 100%, and limb function recovery was satisfactory in most patients. In the TBWC group, the average operative time was 71.21 min, and the average VAS scores were 5.16 and 3.26 at 1 and 2 months postoperatively, respectively. The average Bostman scores were 21.53 and 25.53 at 3 and 9 months postoperatively, respectively, and the average final knee range of motion was 127.5°. In the TBSAS group, the average operative time was 53.95 min, and the average VAS scores were 3.14 and 1.32 at 1 and 2 months postoperatively, respectively. The average Bostman scores were 25.18 and 28.55 at 3 and 9 months postoperatively, respectively, and the average final knee range of motion was 131.5° (Table 3). Regarding postoperative complications, three patients in the TBWC group had postoperative

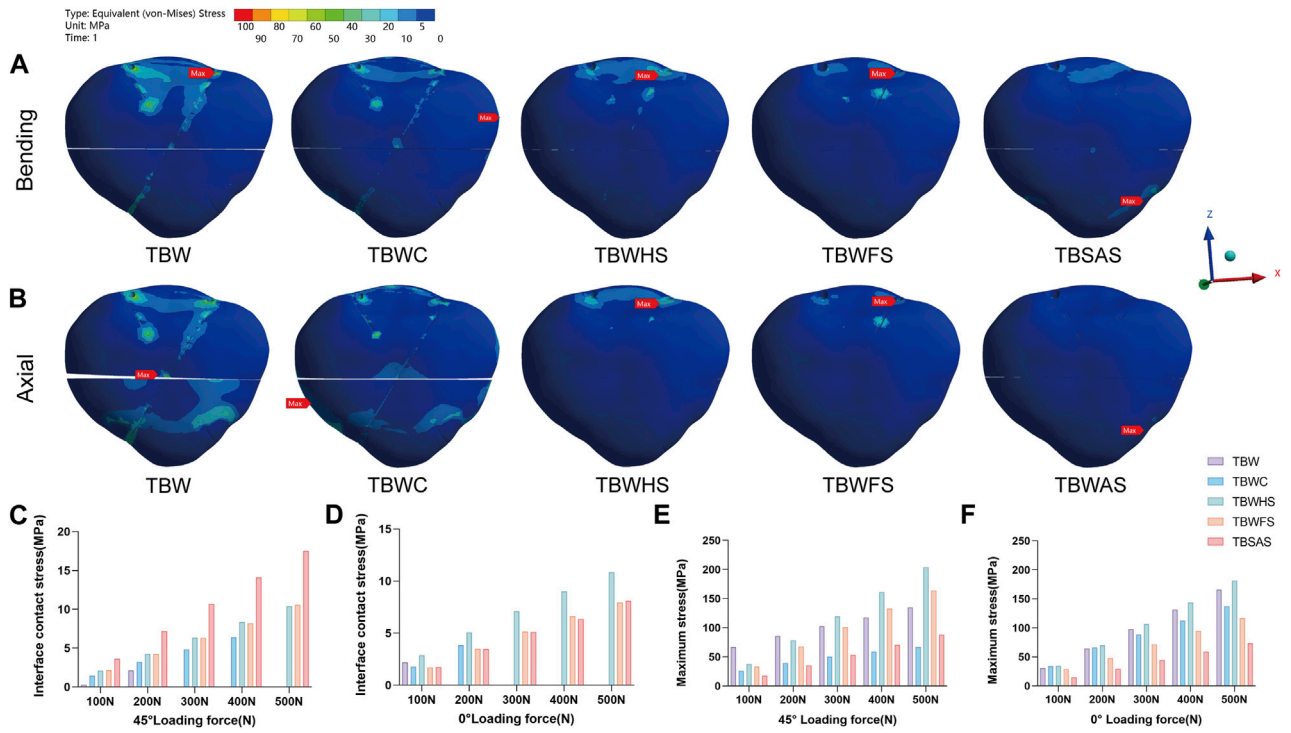

FIGURE 7
Stress distribution on patella of the five models under bending and axial loads: **(A,B)** Stress distribution on patella of the five models under 45° bending load and 0° axial load of 500N; **(C,D)** The maximum fracture interface contact stress of five models under 45° bending load and 0° axial load (0–500N) (y = 0 indicates separation of the fracture interface); **(E,F)** The maximum stresses on patella of five models under 45° bending load and 0° axial load (0–500N).

TABLE 3 Comparison of clinical data between TBWC and TBSAS in treating TPFs (mean ± SD).

Variables	TBWC (*n* = 19)	TBSAS (*n* = 22)	*p*-value
Duration of Surgery (min)	71.21 ± 9.78	53.95 ± 4.82	<0.05
VAS Score 1	5.16 ± 0.96	3.14 ± 0.83	<0.05
VAS Score 2	3.26 ± 1.05	1.32 ± 0.78	<0.05
Bostman Score 3	21.53 ± 2.04	25.18 ± 1.14	<0.05
Bostman Score 9	25.53 ± 1.68	28.55 ± 0.96	<0.05
Final ROM	127.5 ± 4.26	131.5 ± 1.37	<0.05

Note: VAS, Score 1 and VAS Score 2 represent VAS, scores at the one and 2 months postoperatively, respectively; Bostman Score 3 and Bostman Score 9 represent Bostman scores at the third and ninth months postoperatively, respectively. ROM: knee range of motion.

redness and swelling at the incision site, which reduced after symptomatic treatment. Five patients treated with TBWC had persistent subcutaneous soft tissue irritation, which was relieved after removing the metal fixation 12 months postoperatively. A typical example is shown in Figure 8.

4 Discussion

At 500 N, during knee flexion (45° bending load), the maximum fracture displacement of the TBW model was small (0.27823 mm). However, when the knee joint was fully extended (0° axial load), probably owing to the constraint of the tension band, the fracture displacement of the patellar articular surface was larger. The fracture interface gradually separated, and the maximum fracture displacement of the TBW model reached a very dangerous value (1.9426 mm). Fracture space > 3 mm indicates the failure of internal fixation (Patel et al., 2000; Song et al., 2014). TBW also exhibited a higher stress concentration (approximately 1,310.8 MPa). Therefore, the K-wire tension band system alone may not provide sufficient compression in the early stage, especially when performing leg extensions. TBWC effectively reduces the structural stress and displacement and enhances the stability of the system; however, it exhibits similar biomechanical characteristics. Owing to the superficial position of the patella, complications associated with this system, such as

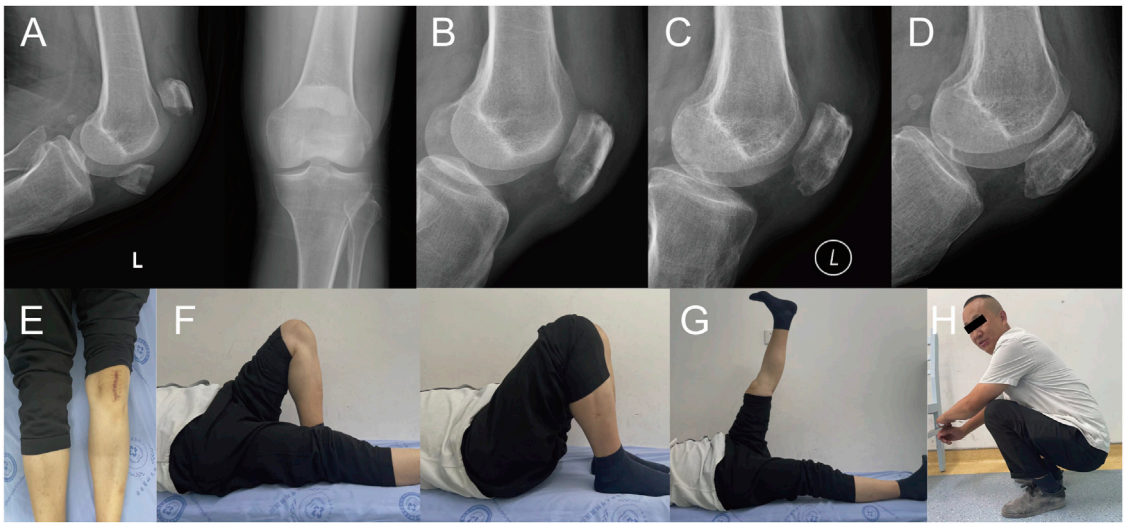

FIGURE 8
A 51-year-old male with a left TPF from a fall. X-rays: **(A)** Before the fracture. **(B)** The first day after surgery. **(C)** Three months after surgery. **(D)** Twelve months after surgery. **(E)** External observation; **(F–H)** Functional reexamination photos 1 year after surgery.

implant irritation, postoperative pain, and delayed wound healing, cannot be ignored.

Therefore, metal-titanium cannulated screws are introduced when fracture conditions permit their use. According to previous reports, metal cannulated screws combined with TBW exhibit very strong rigid fixation strength, providing better stability and reducing the risk of fractures and dislocations (Liu et al., 2022). Lag screws can also produce sustained compression at patellar fracture sites. In the present study, TBWFS and TBWHS had good fixation results and produced continuous compressive stability at the fracture interface. Among them, TBWFS is the most stable, with the smallest fracture displacement during knee flexion and full extension (500 N; 0.074938, and 0.038759 mm, respectively), possibly due to the larger frictional contact area of the full-length thread. This provides a more comprehensive and lasting stability. The tension and compression effects of TBWHS result in a relatively large stress on the screws and patella. In addition, to avoid the high complication rate associated with TBW, some scholars avoid using TBW or replace it with suture treatment (Jia et al., 2022). However, re-surgery is often required to remove the internal fixation, and complications such as stress shielding also exist.

To promote the development of minimally invasive surgical treatments for the patella, we selected TBSAS for TPFs. Notably, several clinical reports have described this fixation regimen. Qi et al. (2011) reported that 12 months after patellar fracture fixation using two absorbable cannulated screws combined with a No. 5 Ethibond braid polyester suture tension band had an average Lysholm score of 95.7, and good clinical results were observed without any postoperative complications. Usami et al. (2021) reported that after patellar fracture fixation using two F-unsintered hydroxyapatite/poly-L-lactide screws and three FiberLoop sutures, there were no complications and a general return to the pre-injury level of work and activities of daily living. Biomechanical studies have also suggested that bioabsorbable implants demonstrate an efficacy comparable to that of metal prostheses in patellar fracture fixation (Adjal et al., 2022; Edoardo et al., 2022), consistent with the FEA results of the present study. At 500N, the maximum fracture displacement of TBWC (0.15633 mm) was similar to that of TBSAS (0.15272 mm) during knee flexion (45° bending load). No statistically significant difference was observed in the mean relative displacement of the fault ends. This further proves the feasibility of our finite element model. However, at full extension of the knee joint (0° axial load), TBSAS showed better data results than TBWC but close results to those of TBWFS and TBWHS. This may be due to the better axial holding capacity of the full-thread friction contact of the rigid screws. Furthermore, because of the material particularity of absorbable cannulated screws and high-strength sutures, the Young's modulus of PLGA is closer to that of bone, and the suture material has better elasticity. Internal fixation and patellar stress results were lower in the TBSAS group. However, previous biomechanical studies have shown that the maximum load delivered by a knee extension device is approximately 316 N (Patel et al., 2000). Therefore, in the biomechanical experiments in the present study (0–500 N), although the stability of TBSAS was lower than that of TBWHS and TBWFS, it may be superior to that of TBW and comparable to or better than that of TBWC. Even under a stress load of 500 N, TBSAS exhibits good structural stability and stress loading, which meets the mechanical requirements of knee flexion and extension device movement, allowing early functional exercise.

Satisfactory results have been obtained in clinical trials. TBSAS is simple and flexible, with a shorter mean operative time than that of TBWC. In the clinical follow-up data, owing to each patient's strict wound management and exercise guidance, no significant postoperative infection, internal fixation failure, revision, or other serious complications occurred in either patient group. However, in the early postoperative period, patients treated with TBSAS showed significantly smaller postoperative pain responses, shorter recovery-remission cycles, and lower VAS scores, which further affected the possibility of early functional exercises among patients. Notably, many patients in the TBSAS group achieved >100° knee flexion at

1 month postoperatively, which was more difficult to achieve in the TBWC group. This is consistent with the results of previous studies (Bai et al., 2021; Du et al., 2022). The Bostman score and final knee motion were slightly lower in the TBWC group than in the TBSAS group. Therefore, TBSAS demonstrated sufficient fixation strength and stability without significant abnormal complications, meeting the need for TPF fixation and early functional exercise. A single operation costs relatively high; however, it reduces metal-related complications and eliminates the pain associated with reoperation. In the present study, more patients were willing to undergo TBSAS treatment.

As a new type of internal fixation material, absorbable screws have unique advantages: 1) histocompatibility, degradability, non-toxicity, and low foreign body reaction; 2) Young's modulus is closer to that of the bone and gradually degrades over a long period, resulting in adaptive stress transfer, promotion of bone growth, and prevention of stress shielding; 3) the fracture end can produce fretting (<0.5 mm) (Wang et al., 2023), which is conducive for fracture healing and reconstruction; and 4) the material begins to expand radially and shrink longitudinally 2 h after implantation, making the fixation firmer, and the initial fixation strength maintenance time can reach 3 months (Zhang et al., 2014). Combining absorbable screws with high-strength sutures using the tension band and "NICE" junction technologies can further strengthen the compression fixation of patellar fractures. The results of the biomechanical and clinical trials in the present study demonstrate their effectiveness and feasibility.

Notably, some researchers have developed simple suturing programs. Jirangkul and Kosiyatrakul (2021) demonstrated the stability and efficacy of Fiber Wire in treating TPFs through prospective clinical trials. Tang et al. (2018) used double 0-0 polydioxone sutures for braided five-pointed star lattice fixation. However, most of these studies were clinical cases, the follow-up duration was short, and plaster fixation was required for 2–3 weeks to ensure stability. Therefore, TBSAS treatment is more commonly recommendable for TPFs. Under the minimally invasive condition of reducing metal internal fixation-induced complications and secondary surgery-induced trauma, greater stability of the rigid fixation can be guaranteed to meet the need for early functional exercise of the knee joint.

Notably, TBSAS may be more appropriate for TPFs (AO/OTA 34 C1) and longitudinal patellar fractures (AO/OTA 34 B1.1/B2.1), whereas TBW and other suitable internal fixation regimens should be considered for complex comminuted patellar fractures.

This study had some limitations. First, biomechanical FEA was used to compare the mechanical trends of various internal fixation schemes. The construction of the models and the applied forces were simplified. Furthermore, the sample size of the clinical study was small, follow-up duration was insufficiently long, and prospective studies were lacking. In the future, we will completely reconstruct the kinematic structural model of the knee joint and incorporate the patellar force into the gait cycle for biomechanical studies. With better clinical patient follow-up, we will conduct in-depth biomechanical studies of screw absorption and fracture healing. We also intend to conduct a multi-center prospective clinical study was conducted to compare the clinical efficacy of several internal fixation schemes for treating TPFs.

5 Conclusion

Our biomechanical and clinical experiments showed that TBSAS is safe and effective for treating TPFs. It is insufficient compared to TBWHS and TBWFS; however, the fixation stability is comparable to that of TBWC, and it is also sufficient to meet the needs of fixation and early functional exercise for TPFs. Furthermore, it can effectively reduce metal internal fixation-induced complications and secondary surgery-induced trauma. Therefore, TBSAS is worthy of clinical application and promotion.

Data availability statement

The raw data supporting the conclusion of this article will be made available by the authors, without undue reservation.

Ethics statement

The studies involving humans were approved by This study was conducted in accordance with the Declaration of Helsinki and its later amendments or comparable ethical standards, and was approved by the Medical Ethics Committee of the Affiliated Hospital of Southwest Medical University (Finite element experiment: No. KY2022269; Retrospective clinical study: No. KY2023042). The studies were conducted in accordance with the local legislation and institutional requirements. The participants provided their written informed consent to participate in this study. Written informed consent was obtained from the individual(s) for the publication of any potentially identifiable images or data included in this article.

Author contributions

FX: Conceptualization, Funding acquisition, Project administration, Resources, Validation, Writing–original draft, Writing–review and editing. YX: Data curation, Formal Analysis, Methodology, Software, Writing–original draft, Writing–review and editing. DL: Data curation, Formal Analysis, Writing–original draft. WM: Project administration, Resources, Supervision, Validation, Writing–review and editing. YC: Project administration, Resources, Supervision, Validation, Writing–review and editing. YY: Conceptualization, Funding acquisition, Methodology, Project administration, Resources, Supervision, Validation, Writing–review and editing.

Funding

The author(s) declare financial support was received for the research, authorship, and/or publication of this article. This study has received funding by the National Natural Science Foundation of China (Grant No. U20A20384), Sichuan Province Science and Technology Plan Joint Innovation Project (Grant No. 2022YFS0628), and Sichuan Medical Association (Shang Antong) Special (Grant No. 2022SAT12).

Conflict of interest

The authors declare that the research was conducted in the absence of any commercial or financial relationships that could be construed as a potential conflict of interest.

Publisher's note

All claims expressed in this article are solely those of the authors and do not necessarily represent those of their affiliated organizations, or those of the publisher, the editors and the reviewers. Any product that may be evaluated in this article, or claim that may be made by its manufacturer, is not guaranteed or endorsed by the publisher.

Supplementary material

The Supplementary Material for this article can be found online at: https://www.frontiersin.org/articles/10.3389/fbioe.2024.1340482/full#supplementary-material

References

Adjal, J., Haugaard, A., Vesterby, L., Ibrahim, H. M., Sert, K., Thomsen, M. G., et al. (2022). Suture tension band fixation vs. metallic tension band wiring for patella fractures – a biomechanical study on 19 human cadaveric patellae. *Injury* 53 (8), 2749–2753. doi:10.1016/j.injury.2022.05.015

Bai, Z.-B., Gao, S.-C., Zhou, H.-B., Zhang, C., and Chen, C. (2021). Comparison of the clinical efficacy of different fixation systems for the treatment of transverse patellar fractures. *Chin. J. Traumatology* 24 (3), 169–173. doi:10.1016/j.cjtee.2021.02.009

Bartolin, P. B., Boixadera, R., and Hudetz, D. (2021). Experimental testing and finite element method analysis of the anterior cruciate ligament primary repair with internal brace augmentation. *Med. Eng. Phys.* 95, 76–83. doi:10.1016/j.medengphy.2021.07.013

Chang, C.-W., Chen, Y.-N., Chang, H.-C., and Li, C.-T. (2023). Biomechanical comparison of different screw-included angles in crossing screw fixation for transverse patellar fracture in level walking: a quasi-dynamic finite element study. *J. Orthop. Surg. Res.* 18 (1), 5. doi:10.1186/s13018-022-03482-x

Chen, C. H., Chen, Y. N., Li, C. T., Chang, C. W., Chang, C. H., and Peng, Y. T. (2019). Roles of the screw types, proximity and anterior band wiring in the surgical fixation of transverse patellar fractures: a finite element investigation. *BMC Musculoskelet. Disord.* 20 (1), 99. doi:10.1186/s12891-019-2474-7

Chen, Y. N., Chang, C. W., Chang, H. C., Yang, T. H., Chang, C. J., Li, C. T., et al. (2022). Triangular configuration with headless compression screws in the fixation of transverse patellar fracture. *Injury* 53 (2), 698–705. doi:10.1016/j.injury.2021.11.048

Du, B., Ma, T., Bai, H., Lu, Y., Xu, Y., Yang, Y., et al. (2022). Efficacy comparison of Kirschner-wire tension band combined with patellar cerclage and anchor-loop plate in treatment of inferior patellar pole fracture. *Front. Bioeng. Biotechnol.* 10, 1010508. doi:10.3389/fbioe.2022.1010508

Edoardo, M., Andrea, D. D., Silvia, C., Fabio, M., Alessandro, C., Adnan, S., et al. (2022). Fixation of patella fractures with metallic implants is associated with a significantly higher risk of complications and re-operations than non-metallic implants: a systematic review and meta-analysis. *Int. Orthop.* 46 (12), 2927–2937. doi:10.1007/s00264-022-05565-0

Henrichsen, J. L., Wilhem, S. K., Siljander, M. P., Kalma, J. J., and Karadsheh, M. S. (2018). Treatment of patella fractures. *Orthopedics* 41 (6), e747–e755. doi:10.3928/01477447-20181010-08

Hoshino, C. M., Tran, W., Tiberi, J. V., Black, M. H., Li, B. H., Gold, S. M., et al. (2013). Complications following tension-band fixation of patellar fractures with cannulated screws compared with kirschner wires. *J. Bone Jt. Surg.* 95 (7), 653–659. doi:10.2106/jbjs.K.01549

Huang, Q., Zhang, C., Bai, H., Wang, Q., Li, Z., Lu, Y., et al. (2023). Biomechanical evaluation of two modified intramedullary fixation system for treating unstable femoral neck fractures: a finite element analysis. *Front. Bioeng. Biotechnol.* 11, 1116976. doi:10.3389/fbioe.2023.1116976

Jia, X., Wu, Y., Rui, Y., Ma, Y., Liu, J., Wang, J., et al. (2022). Percutaneous minimally invasive treatment of transverse patellar fracture using cannulated screws combined with high-strength sutures and Nice knots: a retrospective study. *Ann. Palliat. Med.* 11 (3), 1085–1092. doi:10.21037/apm-22-208

Jirangkul, P., and Kosiyatrakul, A. (2021). Abstaining from symptomatic implants of modified tension band wiring by nonabsorbable suture fixation for transverse patella fractures. *J. Orthop. Surg. Res.* 16 (1), 367. doi:10.1186/s13018-021-02494-3

Kobielarz, M., Tomanik, M., Mroczkowska, K., Szustakiewicz, K., Oryszczak, M., Mazur, A., et al. (2020). Laser-modified PLGA for implants: *in vitro* degradation and mechanical properties. *Acta Bioeng. Biomechanics* 22 (1), 179–197. doi:10.37190/abb-01532-2019-02

Kruse, M., Wolf, O., Mukka, S., and Brüggemann, A. (2022). Epidemiology, classification and treatment of patella fractures: an observational study of 3194 fractures from the Swedish Fracture Register. *Eur. J. Trauma Emerg. Surg.* 48 (6), 4727–4734. doi:10.1007/s00068-022-01993-0

Larsen, P., Court-Brown, C. M., Vedel, J. O., Vistrup, S., and Elsoe, R. (2016). Incidence and epidemiology of patellar fractures. *Orthopedics* 39 (6), e1154–e1158. doi:10.3928/01477447-20160811-01

Lee, K. W., Ma, S. B., Yang, D. S., Oh, S. H., and Park, S. H. (2021). Open reduction and internal fixation using multiple nonabsorbable suture materials in acute patella fracture: comparison of clinical and radiological outcome with tension band wiring. *Knee Surg. Relat. Res.* 33 (1), 34. doi:10.1186/s43019-021-00116-0

Li, Y., Tian, Q., Leng, K., and Guo, M. (2022). The clinical outcomes and complications of combined fixation with cannulated screws and the modified Pyrford technique for the treatment of transverse patellar fractures: a case series study. *BMC Surg.* 22 (1), 336. doi:10.1186/s12893-022-01788-5

Ling, M., Zhan, S., Jiang, D., Hu, H., and Zhang, C. (2019). Where should Kirschner wires be placed when fixing patella fracture with modified tension-band wiring? A finite element analysis. *J. Orthop. Surg. Res.* 14 (1), 14. doi:10.1186/s13018-019-1060-x

Liu, J., Ge, Y., Zhang, G., Zheng, X., Gao, L., Xing, E., et al. (2022). Clinical outcomes of cannulated screws versus ring pin versus K-wire with tension band fixation techniques in the treatment of transverse patellar fractures: a case-control study with minimum 2-year follow-up. *BioMed Res. Int.* 2022, 1–10. doi:10.1155/2022/5610627

Liu, W., Diao, Y., Wang, Z., Guo, L., Yang, W., Luo, Y., et al. (2020). Optimization of the knot configuration for early accelerated rehabilitation after Achilles tendon rupture. *Clin. Biomech.* 80, 105139. doi:10.1016/j.clinbiomech.2020.105139

Ma, X.-Y., Liu, B., Zhou, D.-P., and Xiang, L.-B. (2022). Treatment for transverse patella fractures with minimally invasive techniques (Review). *Exp. Ther. Med.* 23 (3), 192. doi:10.3892/etm.2022.11115

Mao, W., Chang, S. M., Zhang, Y. Q., Li, Y., Du, S. C., Hu, S. J., et al. (2023). Positive medial cortical support versus anatomical reduction for trochanteric hip fractures: finite element analysis and biomechanical testing. *Comput. Methods Programs Biomed.* 234, 107502. doi:10.1016/j.cmpb.2023.107502

Martin, J. M., Applin, D. T., McGrady, L. M., Wang, M., and Schmeling, G. J. (2019). Biomechanical comparison of tension band fixation of patella transverse fracture: headless screws versus headed screws. *J. Orthop. Trauma* 33 (6), e240–e245. doi:10.1097/bot.0000000000001447

Patel, V. R., Parks, B. G., Wang, Y., Ebert, F. R., and Jinnah, R. H., (2000). Fixation of patella fractures with braided polyester suture: a biomechanical study. *Injury* 31 (1), 1–6. doi:10.1016/s0020-1383(99)00190-4

Qi, L., Chang, C., Xin, T., Xing, P. F., Tianfu, Y., Gang, Z., et al. (2011). Double fixation of displaced patella fractures using bioabsorbable cannulated lag screws and braided polyester suture tension bands. *Injury* 42 (10), 1116–1120. doi:10.1016/j.injury.2011.01.025

Rocha, C. V., Goncalves, V., da Silva, M. C., Banobre-Lopez, M., and Gallo, J. (2022). PLGA-based composites for various biomedical applications. *Int. J. Mol. Sci.* 23 (4), 2034. doi:10.3390/ijms23042034

Sayum Filho, J., Lenza, M., Tamaoki, M. J. S., Matsunaga, F. T., and Belloti, J. C. (2021). Interventions for treating fractures of the patella in adults. *Cochrane Database Syst. Rev.* 2021 (2). doi:10.1002/14651858.CD009651.pub3

Song, H. K., Yoo, J. H., Byun, Y. S., and Yang, K. H. (2014). Separate vertical wiring for the fixation of comminuted fractures of the inferior Pole of the patella. *Yonsei Med. J.* 55 (3), 785. doi:10.3349/ymj.2014.55.3.785

Steinmetz, S., Brgger, A., Chauveau, J., Chevalley, F., Borens, O., and Thein, E. (2020). Practical guidelines for the treatment of patellar fractures in adults. *Swiss Med. Wkly.* 150, w20165. doi:10.4414/smw.2020.20165

Taha, M. E., Schneider, K., Clarke, E. C., O'Briain, D. E., Smith, M. M., Cunningham, G., et al. (2020). A biomechanical comparison of different suture materials used for arthroscopic shoulder procedures. *Arthroscopy* 36 (3), 708–713. doi:10.1016/j.arthro.2019.08.048

Tang, X., Liu, Y., Wu, H., Gong, F., Li, Y., Zeng, H., et al. (2018). Five-pointed star lattice sutures for fixation of patella transverse fractures: a clinical study. *Eur. J. Orthop. Surg. Traumatology* 29 (1), 163–168. doi:10.1007/s00590-018-2272-1

Trinchese, G. F., Cipollaro, L., Calabrese, E., and Maffulli, N. (2021). Platelet-rich plasma, mesenchymal stem cell, and non-metallic suture-based fixation technique in a patellar fracture nonunion: a technical note and systematic review. *Clin. Orthop. Surg.* 13 (3), 344. doi:10.4055/cios20175

Usami, T., Takada, N., Sakai, H., Endo, S., Sekiya, I., Ueki, Y., et al. (2021). Treatment of patellar fractures using bioresorbable forged composites of raw particulate unsintered hydroxyapatite/poly-L-lactide cannulated screws and nonabsorbable sutures. *Injury* 52 (6), 1587–1591. doi:10.1016/j.injury.2020.12.015

Wang, F., Liu, Y., Huo, Y., Wang, Z., Zhang, J., Xu, M., et al. (2023). Biomechanical study of internal fixation methods for femoral neck fractures based on Pauwels angle. *Front. Bioeng. Biotechnol.* 11, 1143575. doi:10.3389/fbioe.2023.1143575

Wright, P. B., Kosmopoulos, V., Coté, R. E., Tayag, T. J., and Nana, A. D. (2009). FiberWire® is superior in strength to stainless steel wire for tension band fixation of transverse patellar fractures. *Injury* 40 (11), 1200–1203. doi:10.1016/j.injury.2009.04.011

Xue, H., Zhang, Z., Liu, M., Lin, Z., Endo, Y., Liu, G., et al. (2022). Finite element analysis of different fixation methods of screws on absorbable plate for rib fractures. *Front. Bioeng. Biotechnol.* 10, 960310. doi:10.3389/fbioe.2022.960310

Yuan, D., Wu, Z., Luo, S., Zhou, Y., Teng, J., and Ye, C. (2022). Improve biomechanical stability using intramedullary nails with femoral neck protection in femoral shaft fractures. *Comput. Methods Programs Biomed.* 225, 107078. doi:10.1016/j.cmpb.2022.107078

Zeng, W., Liu, Y., and Hou, X. (2020). Biomechanical evaluation of internal fixation implants for femoral neck fractures: a comparative finite element analysis. *Comput. Methods Programs Biomed.* 196, 105714. doi:10.1016/j.cmpb.2020.105714

Zhang, J., Wang, X., and Yang, L. (2014). Biomechanical study of absorbable screws tension band in the treatment of transverse patella fractures. *J. Pract. Orthop.* 20 (12), 1100–1103. doi:10.13795/j.cnki.sgkz.2014.12.011

frontiers | Frontiers in Bioengineering and Biotechnology

TYPE Original Research
PUBLISHED 26 June 2024
DOI 10.3389/fbioe.2024.1401899

OPEN ACCESS

EDITED BY
Lei Fan,
Marquette University, United States

REVIEWED BY
Qiang Chen,
Southeast University, China
Xijin Hua,
University of Exeter, United Kingdom

*CORRESPONDENCE
Yongtao Lyu,
yongtaolu@dlut.edu.cn

RECEIVED 16 March 2024
ACCEPTED 07 June 2024
PUBLISHED 26 June 2024

CITATION
Jiang J, Huo Y, Peng X, Wu C, Zhu H and Lyu Y (2024), Design of novel triply periodic minimal surface (TPMS) bone scaffold with multi-functional pores: lower stress shielding and higher mass transport capacity.
Front. Bioeng. Biotechnol. 12:1401899.
doi: 10.3389/fbioe.2024.1401899

Design of novel triply periodic minimal surface (TPMS) bone scaffold with multi-functional pores: lower stress shielding and higher mass transport capacity

Jian Jiang[1], Yi Huo[2], Xing Peng[3], Chengwei Wu[2,4], Hanxing Zhu[5] and Yongtao Lyu[2]*

[1]Department of Spinal Surgery, Central Hospital of Dalian University of Technology, Dalian, China, [2]School of Mechanics and Aerospace Engineering, Dalian University of Technology, Dalian, China, [3]Tribology Research Institute, School of Mechanical Engineering, Southwest Jiaotong University, Chengdu, China, [4]State Key Laboratory of Structural Analysis Optimization and CAE Software for Industrial Equipment, Department of Engineering Mechanics, Dalian University of Technology, Dalian, China, [5]School of Engineering, Cardiff University, Cardiff, United Kingdom

Background: The bone repair requires the bone scaffolds to meet various mechanical and biological requirements, which makes the design of bone scaffolds a challenging problem. Novel triply periodic minimal surface (TPMS)-based bone scaffolds were designed in this study to improve the mechanical and biological performances simultaneously.

Methods: The novel bone scaffolds were designed by adding optimization-guided multi-functional pores to the original scaffolds, and finite element (FE) method was used to evaluate the performances of the novel scaffolds. In addition, the novel scaffolds were fabricated by additive manufacturing (AM) and mechanical experiments were performed to evaluate the performances.

Results: The FE results demonstrated the improvement in performance: the elastic modulus reduced from 5.01 GPa (original scaffold) to 2.30 GPa (novel designed scaffold), resulting in lower stress shielding; the permeability increased from 8.58×10^{-9} m^2 (original scaffold) to 5.14×10^{-8} m^2 (novel designed scaffold), resulting in higher mass transport capacity.

Conclusion: In summary, the novel TPMS scaffolds with multi-functional pores simultaneously improve the mechanical and biological performances, making them ideal candidates for bone repair. Furthermore, the novel scaffolds expanded the design domain of TPMS-based bone scaffolds, providing a promising new method for the design of high-performance bone scaffolds.

KEYWORDS

bone scaffold, multi-functional pore, additive manufacturing, mechanical behavior, mass transport capacity

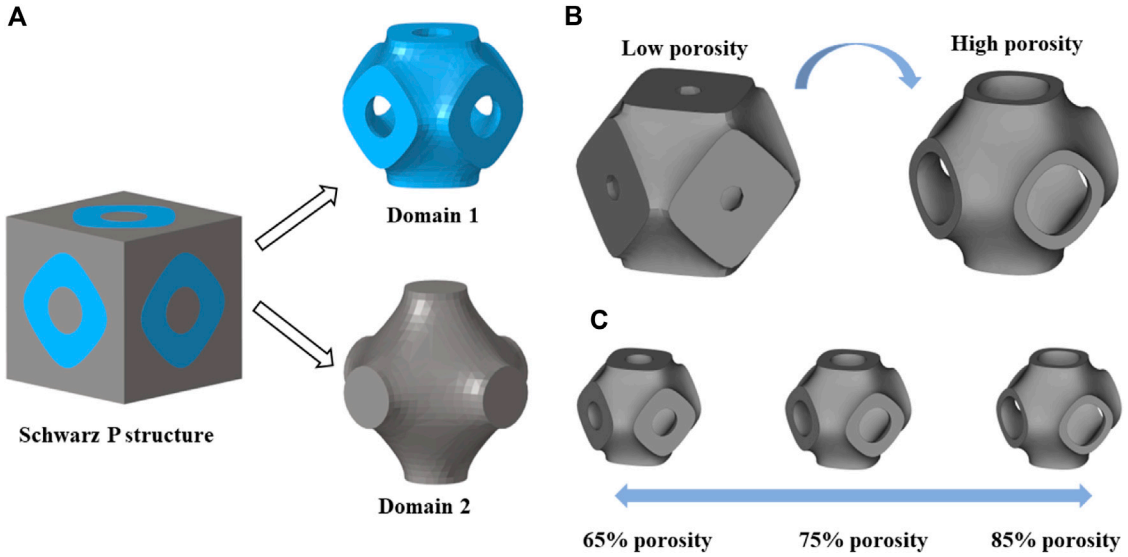

FIGURE 1
(A) Two domains divided by a Schwarz P structure. **(B)** Schwarz P structures with different porosities obtained by changing the constant *c*. **(C)** Three basic Schwarz P structures with different porosities (65%, 75%, and 85%).

1 Introduction

The demand for high performance artificial bone implants is growing due to the rising prevalence of bone diseases and traumas (Kurtz et al., 2007; Campana et al., 2014; Wallace et al., 2017). Porous bone scaffolds are considered ideal for bone repair because their porosity and stiffness can be adjusted to mimic human bone. Additionally, a microscopic porous scaffold can provide a suitable physiological environment for bone ingrowth (Peng et al., 2022). Recently, studies have used triply periodic minimal surface (TPMS) as a porous structure to design bone scaffold (Davoodi et al., 2020; Jiang et al., 2020; Vijayavenkataraman et al., 2020). The advantage of TPMS lies in its ability to easily adjust pore sizes using control equations, allowing the mechanical properties of the scaffolds to closely resemble those of human bone (Maconachie et al., 2019). Moreover, TPMS can provide micropores larger than 300.0 μm to allow for bone growth. Barba et al. (2019) concluded that a 300.0–600.0 μm pore size is best for osseointegration since it facilitates vascularization and cell growth. Consequently, TPMS-based bone scaffolds are being extensively studied and designed to address clinical challenges. On the other hand, additive manufacturing (AM) provides an ideal solution for manufacturing highly complex geometries such as TPMS scaffolds (Askari et al., 2020). AM describes a range of processes used to fabricate components directly from a digital representation of the intended geometry by the layer wise combination of a common source material (Zhai et al., 2014). As a result, TPMS-based bone scaffolds manufactured using AM have become the ideal choice for bone implants.

However, there are two problems with TPMS-based scaffolds that urgently need to be solved—the stress shielding effect caused by the high elastic modulus and the insufficient mass transport capacity caused by the low permeability. A bone scaffold should have an elastic modulus similar to that of the human bone to avoid the stress shielding effect. This effect occurs when the load is predominantly borne by the bone scaffold, leading to loosening at the interface (Barba et al., 2019). Although the elastic modulus of a TPMS scaffold is lower than that of the traditional cubic structure, it is still higher than that of cancellous bone. Sevilla et al. (2007) reported that the elastic modulus of cancellous bone is 1.08 GPa. Wu et al. (2018) investigated the elastic modulus of cancellous bone under different loading directions. The results indicated that the modulus of cancellous bone is 3.47 GPa in the longitudinal direction and 2.57 ± 0.28 GPa in the transverse direction. While there are discrepancies in reported elastic moduli of cancellous bone across studies, it is generally agreed that a bone scaffold's elastic modulus should not exceed 3.00 GPa to align with cancellous bone. However, the modulus of a Schwarz P TPMS scaffold with 70% porosity is 5.60 GPa (Khaleghi et al., 2021), which is greater than that of cancellous bone. Additionally, the permeability of cancellous bone is in the range of 3.66×10^{-8} m^2 to 1.90×10^{-7} m^2 (Rabiatul et al., 2021), but the permeability of a TPMS structure is in the range of 4.31×10^{-10} m^2 to 8.44×10^{-9} m^2 (Santos et al., 2020). Therefore, broadening the limited TPMS design domain to simultaneously improve its mechanical and biological performances to meet the clinical needs is a big challenge in the design of TPMS bone scaffolds.

In recent years, there have been efforts to enhance the performance of TPMS scaffolds through innovative design approaches. The most common design method is structural optimization, which aims to find the best design scheme based on specific goals and constraints. Moreover, the integration of structural optimization with additive manufacturing (AM) presents a realm of creative opportunities for bone scaffold design (Tan et al., 2017). This method has been applied in clinic to fabricate devices such as pelvic protheses (Iqbal et al., 2019), craniofacial prostheses (Sutradhar et al., 2016), and femoral stem protheses (Arabnejad et al., 2017; Sun et al., 2018). Additionally, some studies have designed hybrid TPMS scaffolds and functional graded TPMS scaffolds to improve the performances. For example, Liu et al. (2022) designed a hybrid TPMS structure to increase the permeability to 1.20×10^{-8} m^2. Fan et al. (2021) designed functional graded TPMS scaffolds to control the elastic modulus, but both the graded TPMS

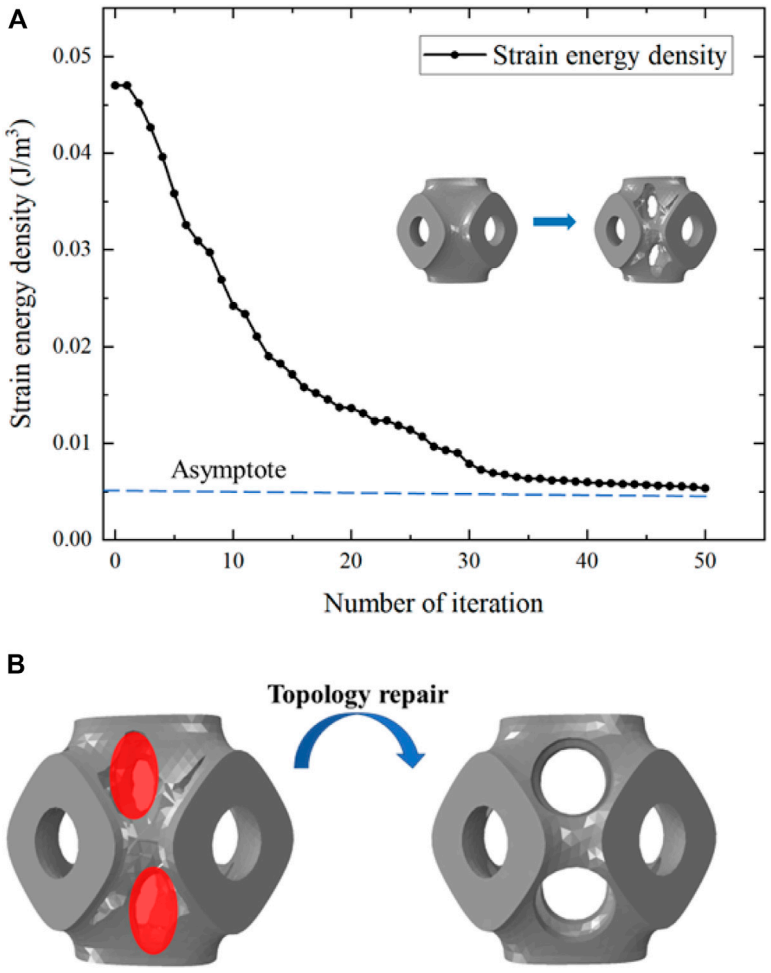

FIGURE 2
(A) Evolution of the strain energy density during the structural design. **(B)** Illustration of the geometric repair process.

scaffolds and the hybrid TPMS scaffolds still have the elastic moduli much higher than that of cancellous bone. In addition, these designed scaffolds have many shortcomings, such as poor controllability and lack of reasonable optimization framework guidance. Take the design of functional graded TPMS bone scaffold as example, before designing a functional graded bone scaffold, scholars cannot predict its performance. In these studies, the scaffolds were designed first, and then the performance improvements of the new scaffolds can be proved only by the research results. Therefore, such design method is very inefficient. In addition, the design method in the current study usually can only consider one optimization objective such as elastic modulus, but the permeability is not evaluated. Besides, whether the designed TPMS bone scaffolds meet the requirements of the manufacturing technique has not been considered and explained. Therefore, novel scaffolds that can be controlled and simultaneously improve the mechanical and biological performances are needed to be designed.

In order to address the problems of poor controllability and limited optimization objectives in the optimal design of TPMS bone scaffolds, we propose a novel design method: introducing a new geometric variable, that is, optimization-guided multi-functional pore. The novel TPMS scaffolds with optimization-guided multi-functional pores were designed to address the problems of high elastic modulus and low permeability in this study. The functions of these pores are: to reduce the elastic modulus, to improve the permeability, and to broaden the design domain. Therefore, we name it “multi-functional pores” to represent these functions. In addition, the position of multi-function pore is not random, but determined under the guidance of optimization theory. After determining the position of the multi-function pore, change its radius to evaluate the effect of different size pores on the performance. The introduction of this multi-functional pore solves many difficulties in the design of TPMS bone scaffolds. First, the multi-functional pore is designed under the optimization framework of reducing the elastic modulus of the bone scaffold, and the elastic modulus of the new designed bone scaffold must be reduced to avoid the stress shielding effect. In the previous design methods, the performance of the new structure cannot be predicted before the design. Therefore, the proposed design method has higher controllability and efficiency. Second, there are few design variables of TPMS structure at present. By introducing the new variable of multi-function pore, the design domain of TPMS structure can be broadened, and the design of high-performance TPMS bone scaffold can be realized. To investigate the performances of the novel designed bone scaffolds, all the scaffolds were fabricated

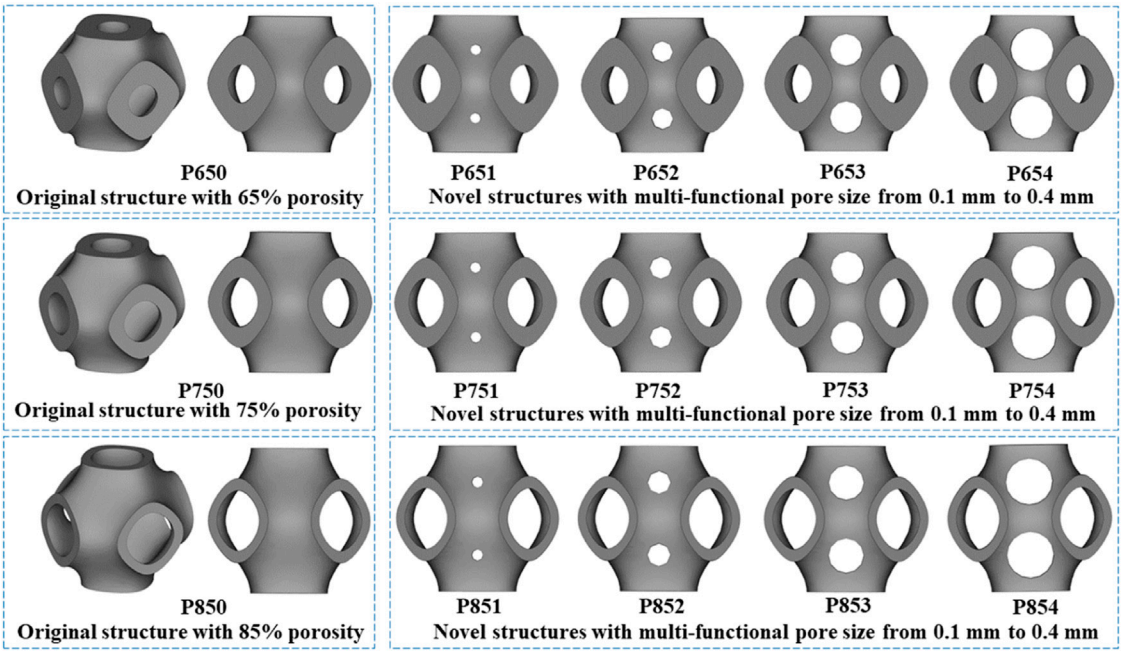

FIGURE 3
Three original scaffolds before optimization (named P650, P750, and P850) and the corresponding optimized novel scaffolds with multi-functional pore sizes from 0.1 mm to 0.4 mm (named P651–P654, P751–P754, and P851–P854).

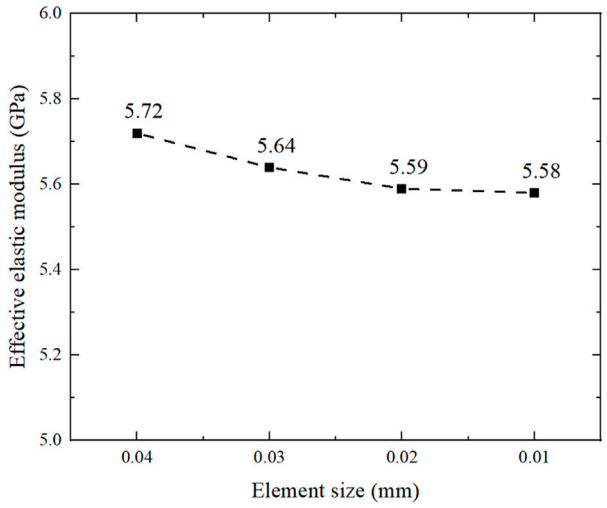

FIGURE 4
Convergence analysis of equivalent elastic modulus with different element sizes.

from Ti6Al4V using selective laser melting (SLM). Experiments and FE simulations were used to evaluate the elastic modulus, permeability, and anisotropy of the structures.

2 Materials and methods

In this section, the method to design the novel TPMS scaffolds with multi-functional pores is first detailed. Then, the experimental and simulation methods for evaluating the elastic modulus and permeability behaviors of the TPMS scaffolds are illustrated. In the end, the anisotropic elastic response of the new scaffold is evaluated using the numerical homogenization method.

2.1 Modelling method of basic TPMS scaffolds

TPMS is a minimal surface that can extend periodically in three directions, and its topological shape is determined by functional expressions. Common TPMS structures include Schwarz P, Gyroid, Diamond, I-WP, etc. (Blanquer et al., 2017). It is worth mentioning that the concept of minimal surface was first proposed by the scientist Schwarz in 1883 (Strömberg, 2021), so Schwarz P is also one of the most classical and widely used types of TPMS structures. Besides, this structure has been shown to have a more stable curvature to promote cell growth (Blanquer et al., 2017). Therefore, this paper chooses Schwarz P as the basis of structural design. The 3D Schwarz P structure was formed by adding the thickness of the minimal surface (Figure 1A). The Schwarz P structure can be characterized by the following mathematical function (Khaleghi et al., 2021):

$$f(x,y,x) = \cos\left(\frac{2\pi}{n}x\right) + \cos\left(\frac{2\pi}{n}y\right) + \cos\left(\frac{2\pi}{n}z\right) - c \quad (1)$$

where f determines the TPMS topology type; x, y, z are the coordinates of a point in the design space; n denotes the length of a unit cell, and the constant c is used to control the two-phase domain, which determines the porosity of the structure (Peng et al.,

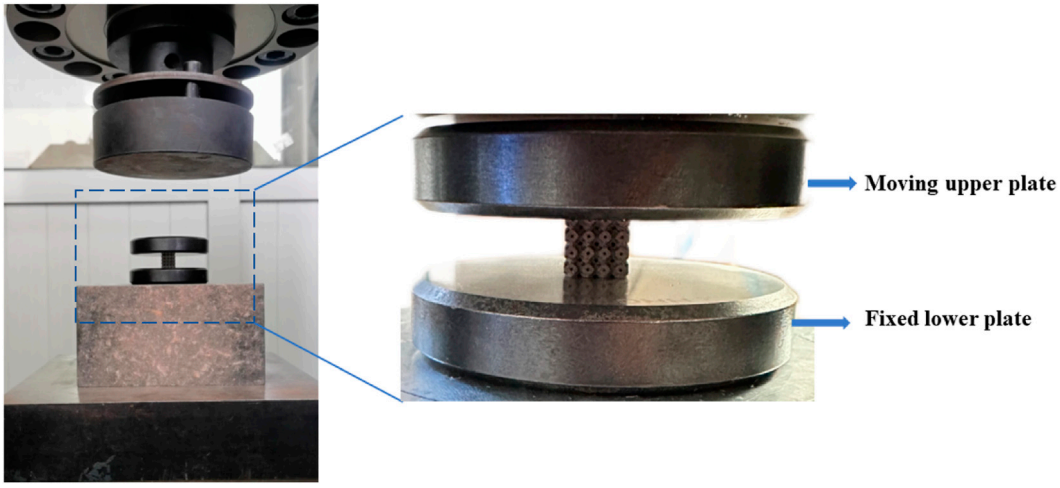

FIGURE 5
Experiment setup for the compression test: equipment and sample.

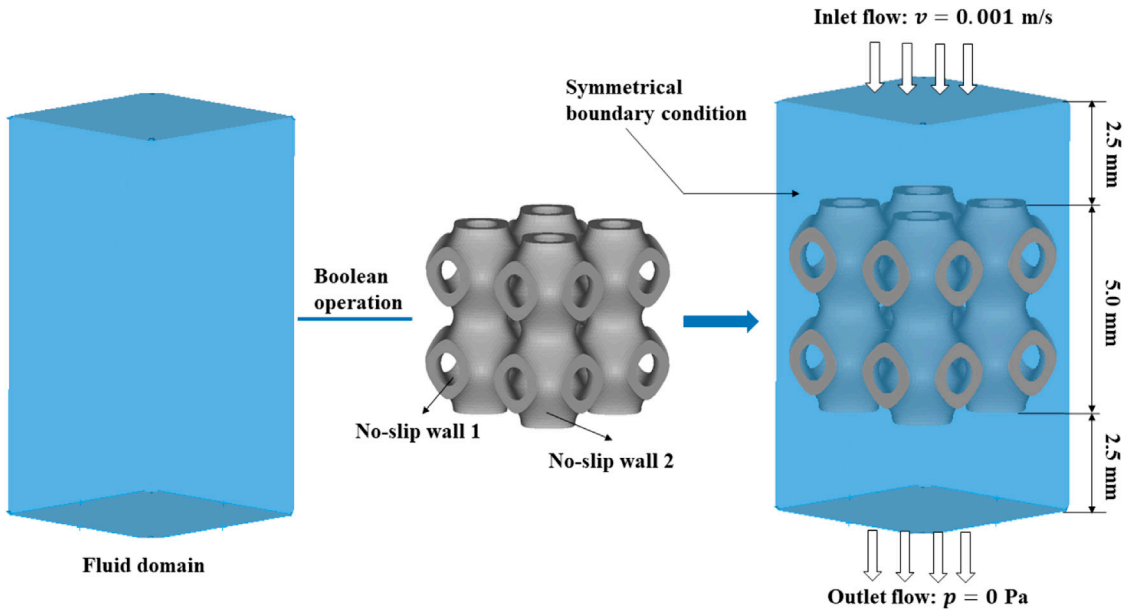

FIGURE 6
The modeling process of the fluid domain and the boundary conditions in CFD analysis.

2023). With the increase of the constant c from −0.5 to 0.5, the porosity of the Schwarz P structure increases (Figure 1B). Previous studies have proved that there is a linear relationship between the constant c in the Eq. 1 and the porosity of TPMS structure (Al-Ketan and Abu Al-Rub, 2019). As for Schwarz P, the porosity can be represented by: 0.2876 c +0.4967. Therefore, when the constant c equal to 0.53, 0.88, and 1.23, the Schwarz P structure with porosity of 65%, 75% and 85% can be obtained (Figure 1C). These structures were visualized using in-house developed MATLAB code (R2020b, MathWorks, Massachusetts, US), and the dimensions of unit cell were set to 2.5 mm × 2.5 mm × 2.5 mm.

2.2 Design of the novel TPMS structures with multi-functional pores

By adjusting the constants in Eq. 1, only structures with different porosities can be obtained, that is, porosity is the only variable when designing the scaffolds. However, the mass transport capacity of the scaffold depends on the pore size and the obstructed area (Ali et al., 2020). Therefore, the multi-functional pores were added to the scaffold to improve the permeability. These multi-functional pores were designed and guided by structural optimization method, which is detailed in this section.

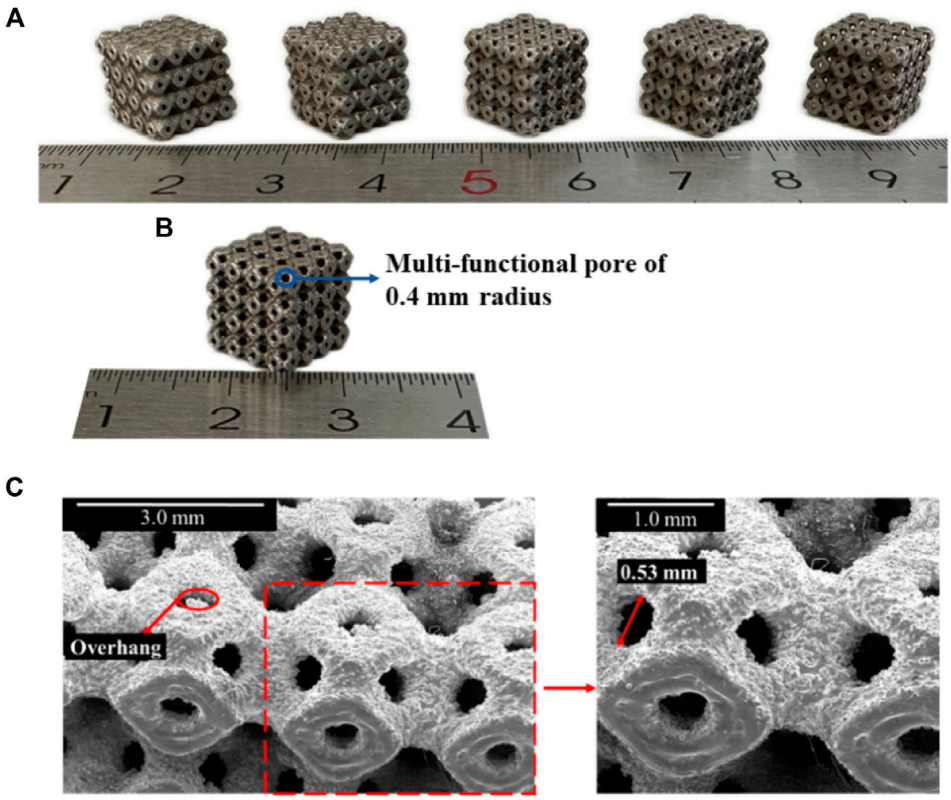

FIGURE 7
(A) SLM-fabricated Ti6Al4V specimens for P650–P654 scaffolds (P650 to P654 from left to right). **(B)** SLM-fabricated Ti6Al4V specimen for P654. **(C)** SEM image showing details of the fabricated sample of P654.

Mechanical parameters, including the elastic modulus and anisotropy, are crucial factors for structural design (Feng et al., 2021), and they can be obtained through the constitutive relation. The constitutive relation of a TPMS structure is given by Eq. 2 (Lee et al., 2017):

$$\{\sigma\} = [C]\{\varepsilon\} \tag{2}$$

where the stress and strain can be expressed in matrix form:

$$\{\sigma\} = \begin{pmatrix} \sigma_{11} \\ \sigma_{22} \\ \sigma_{33} \\ \sigma_{12} \\ \sigma_{13} \\ \sigma_{23} \end{pmatrix} \{\varepsilon\} = \begin{pmatrix} \varepsilon_{11} \\ \varepsilon_{22} \\ \varepsilon_{33} \\ \varepsilon_{12} \\ \varepsilon_{13} \\ \varepsilon_{23} \end{pmatrix} \tag{3}$$

The stiffness matrix can be expressed as Eq. 4:

$$[C] = \begin{bmatrix} C_{11} & C_{12} & C_{13} & C_{14} & C_{15} & C_{16} \\ C_{21} & C_{22} & C_{23} & C_{24} & C_{25} & C_{26} \\ C_{31} & C_{32} & C_{33} & C_{34} & C_{35} & C_{36} \\ C_{41} & C_{42} & C_{43} & C_{44} & C_{45} & C_{46} \\ C_{51} & C_{52} & C_{53} & C_{54} & C_{55} & C_{56} \\ C_{61} & C_{62} & C_{63} & C_{64} & C_{65} & C_{66} \end{bmatrix} \tag{4}$$

Moreover, Schwarz P is a cubic symmetric structure with three independent elastic constants, which means that $C_{11} = C_{22} = C_{33}$; $C_{12} = C_{13} = C_{23}$; $C_{44} = C_{55} = C_{66}$; and all other constants are zero. Thus, the stiffness matrix can be simplified as Eq. 5:

$$[C] = \begin{bmatrix} C_{11} & C_{12} & C_{12} & 0 & 0 & 0 \\ C_{12} & C_{11} & C_{12} & 0 & 0 & 0 \\ C_{12} & C_{12} & C_{11} & 0 & 0 & 0 \\ 0 & 0 & 0 & C_{44} & 0 & 0 \\ 0 & 0 & 0 & 0 & C_{44} & 0 \\ 0 & 0 & 0 & 0 & 0 & C_{44} \end{bmatrix} \tag{5}$$

where C_{11}, C_{12}, and C_{44} are the three independent elastic constants of the Schwarz P structure. Typically, when the two load cases $\{\varepsilon^{(1)}\} = \{1\,0\,0\,0\,0\,0\}$ and $\{\varepsilon^{(2)}\} = \{1\,1\,1\,0\,0\,0\}$ are applied to the Schwarz P structure, the relationship between C_{ij} and σ_{ij} can be determined based on Eqs 2, 3, 5:

$$\begin{cases} c_{11} = \sigma_{11}^{(1)} \\ c_{12} = \sigma_{22}^{(1)} = \sigma_{33}^{(1)} \\ c_{11} + 2c_{12} = \sigma_{11}^{(2)} = \sigma_{22}^{(2)} = \sigma_{33}^{(2)} \end{cases} \tag{6}$$

The energies of two load cases can be defined as shown in Eq. 7 (Ma et al., 2021):

$$\begin{cases} w^{(1)} = \frac{1}{2}\sigma_{11}^{(1)} V \\ w^{(2)} = \frac{1}{2}\left(\sigma_{11}^{(2)} + \sigma_{22}^{(2)} + \sigma_{33}^{(2)}\right) V \end{cases} \tag{7}$$

where V represents the volume of the Schwarz P structure. Based on Eqs 6, 7, the relationship between the energies and elastic constants can be expressed as Eq. 8:

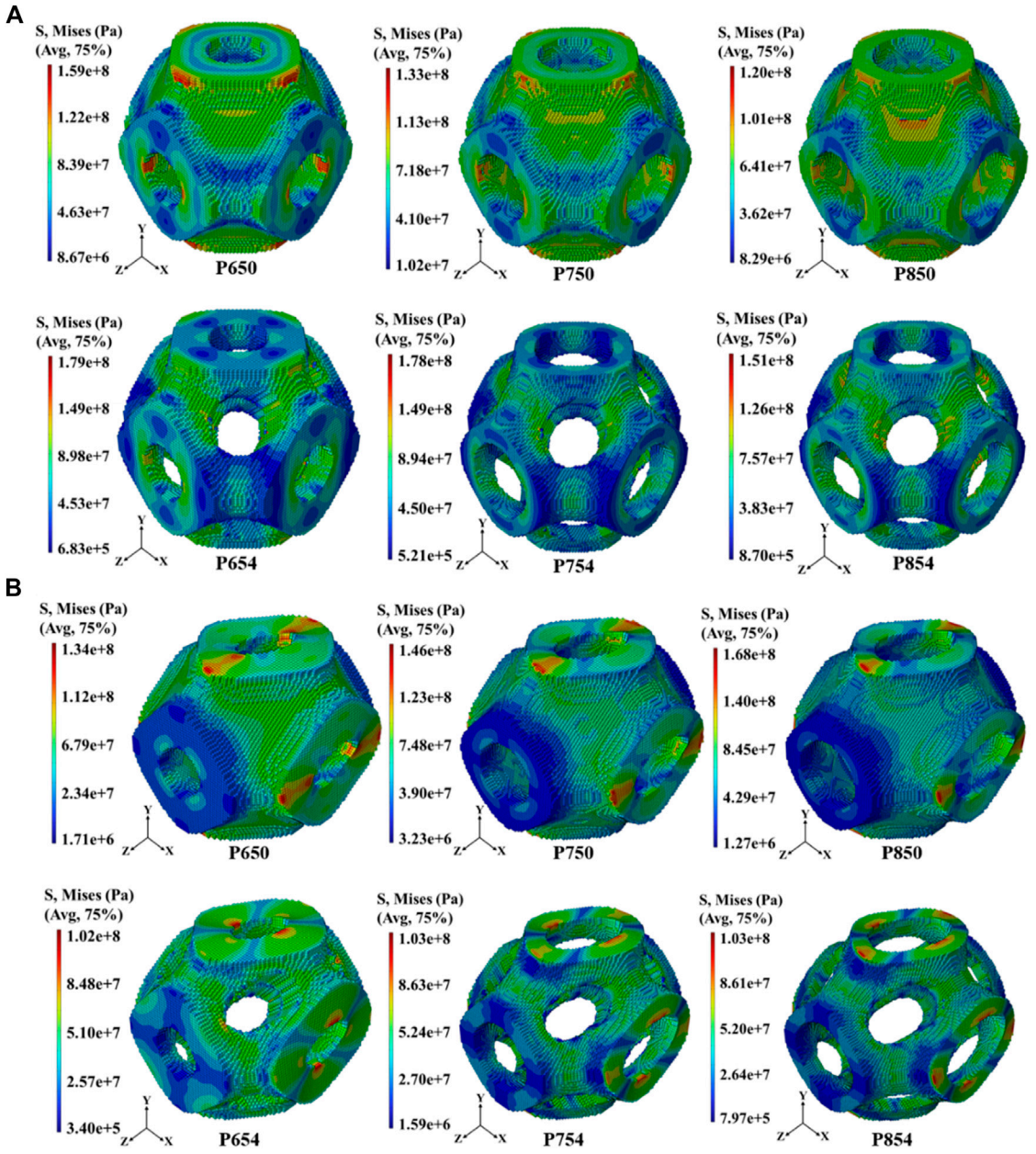

FIGURE 8
(A) Distribution of von Mises stress in the scaffolds before and after structural design at 65%, 75%, and 85% porosities under the uniaxial tensile load condition $\{\varepsilon^{(1)}\}$. **(B)** Distribution of von Mises stress in the scaffolds before and after structural design at 65%, 75%, and 85% porosities under the shearing load condition $\{\varepsilon^{(2)}\}$.

$$\begin{cases} c_{11} = \dfrac{2}{V} w^{(1)} \\ c_{12} = \dfrac{1}{V}\left[\dfrac{1}{3} w^{(2)} - w^{(1)}\right] \end{cases} \tag{8}$$

The elastic modulus of the Schwarz P structure can be obtained as Eq. 9 (Feng et al., 2021):

$$E = \frac{C_{11}^2 + C_{12}C_{11} - 2C_{12}{}^2}{C_{11} + C_{12}} \tag{9}$$

Based on Eqs 8, 9, the elastic modulus of the Schwarz P structure can be expressed as Eq. 10:

$$E = \frac{18w^{(1)}w^{(2)} - 2\left[w^{(2)}\right]^2}{3V\left[3w^{(1)} + w^{(2)}\right]} = \frac{18v_\varepsilon^{(1)}v_\varepsilon^{(2)} - 2\left[v_\varepsilon^{(2)}\right]^2}{3\left[3v_\varepsilon^{(1)} + v_\varepsilon^{(2)}\right]} \tag{10}$$

where $v_\varepsilon = \frac{w}{V}$ represents the strain energy density.

To match the mechanical properties of cancellous bone, it is necessary to reduce the elastic modulus. Thus, the optimization objection is to find the minimum value of Eq. 10, which can be expressed as Eq. 11:

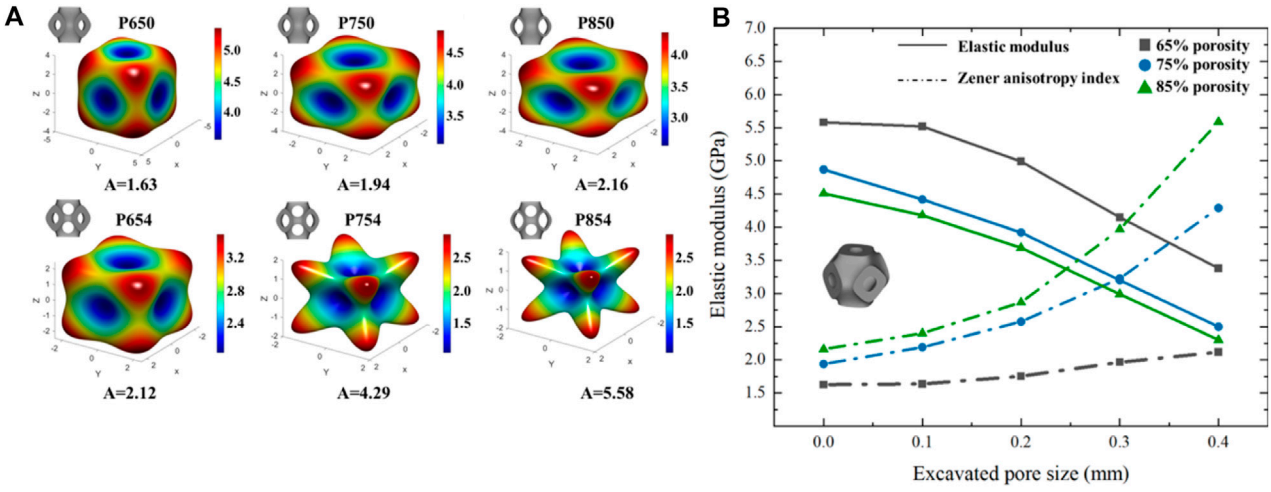

FIGURE 9
(A) Three-dimensional elastic modulus surface for different Schwarz P scaffolds. **(B)** Variation trend of structural elastic modulus and Zener anisotropy index with the increase of multi-functional pore size under different porosities.

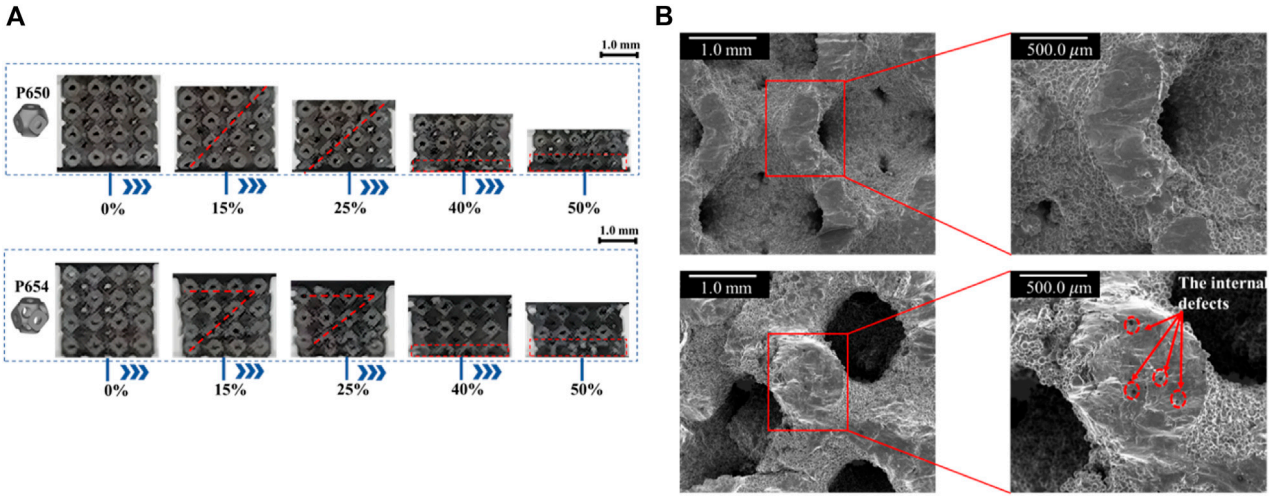

FIGURE 10
(A) Deformation behaviors of P650 and P654. **(B)** SEM views of the compressive fracture surfaces of P650 (upper) and P654 (lower).

$$\begin{cases} \text{find } v_\varepsilon = \left(v_\varepsilon^{(1)}, v_\varepsilon^{(2)}\right) \\ \min f\left(v_\varepsilon\right) = \dfrac{18 v_\varepsilon^{(1)} v_\varepsilon^{(2)} - 2\left[v_\varepsilon^{(2)}\right]^2}{3\left[3 v_\varepsilon^{(1)} + v_\varepsilon^{(2)}\right]} \\ \text{subject to } 0.5V_0 \le V \le 0.8V_0 \end{cases} \tag{11}$$

where V represents the volume of the Schwarz P scaffold after optimization, V_0 represent the original volume before optimization. Since the objection is to reduce the elastic modulus, the volume of the scaffold after optimization should be smaller than the original volume. On the other hand, in order to ensure that the optimized bone scaffold has enough volume to complete the function of mechanical support, the optimized volume should not be too small. Therefore, we set the constrain $0.5V_0 \le V \le 0.8V_0$. In the "Topology Optimization" part of ABAQUS (v2020, Dassault Systems SIMULIA Ltd., Providence, RI), we set the objection as to find the minimum value of Eq. 10; the constrain as $0.5V_0 \le V \le 0.8V_0$. It is worth noting that although the volume size is not directly related to the design variables, the volume constraint in the "Topology Optimization" part of ABAQUS is very important to achieve the optimization goal. Therefore, we summarize it into a unified optimization framework, which is Eq. 11. Moreover, the range of elastic modulus of human cancellous bone is 1.0–3.0 GPa. If the elastic modulus is lower than 1.0 GPa, the strength will not satisfy the requirement. Therefore, instead of directly calculating the minimum value of $f\left(v_\varepsilon\right)$, we find that calculate the minimum values of $v_\varepsilon^{(1)} + v_\varepsilon^{(2)}$ can make sure the elastic modulus of the structure will not be lower than 1.0 GPa.

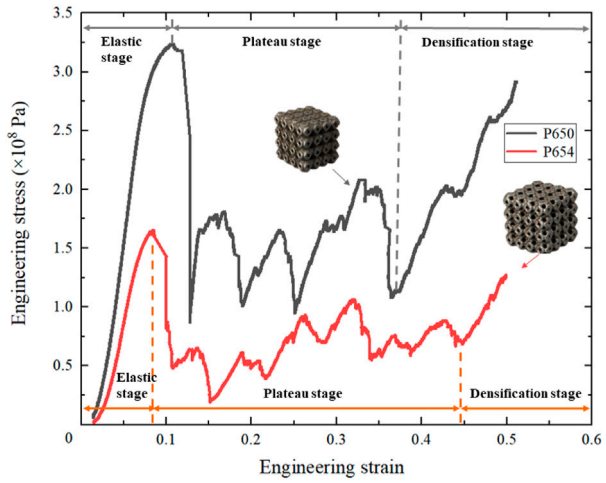

FIGURE 11
Stress–strain curves of the Schwarz P scaffolds: P650 and P654.

The optimization process was carried out using ABAQUS with the following set: find the minimum value of $v_{\varepsilon}^{(1)} + v_{\varepsilon}^{(2)}$ when subject to $0.5V_0 \leq V \leq 0.8V_0$. The solid isotropic material with penalization (SIMP) was set. Figure 2A shows the calculation process of the optimization. To ensure that the obtained scaffolds can be fabricated using SLM, the thickness t should be limited within a certain range: $t \geq 0.2$. Materialise Magics (v24.0, Leuven, Belgium) is an AM-guided software, which can detect the thickness of the structure to ensure that it meets the manufacturing requirements. All the optimized structures in this paper are verified that the wall thickness meets the manufacturing requirements.

The disadvantage of the SIMP method was that the boundary of the structure's topology was not sufficiently clear and the structure was not able to be directly fabricated (Strömberg, 2021). Therefore, topology repair was necessary to ensure the scaffolds can be fabricated. This repair process involved adding multi-functional pores to the scaffolds where material had been removed, determined through ABAQUS calculations (Supplementary Figure 2.2B). To illustrate the structural design process, multi-functional pores with varying radii (0.1 mm, 0.2 mm, 0.3 mm, and 0.4 mm) were added (Figure 3). To maintain the cubic symmetry of the scaffold, eight multi-functional pores were added in each unit cell. P654 is taken as an example to illustrate the naming method for each scaffold: the letter "P" stands for the Schwarz P scaffold, the number "65" stands for the 65% porosity scaffold before the optimization, and "4" stands for the 0.4-mm radius of the multi-functional pores.

2.3 Additive manufacturing of Ti6Al4V Schwarz P structure

A group of Schwarz P structures with 65% porosity (P650–P654) were selected for manufacturing to carry out mechanical tests on them. Besides, in this process, it can also be proved that the designed new TPMS bone scaffold can be manufactured and has practical clinical significance. It is worth noting that all the TPMS bone scaffolds designed at 65% (P650-P654), 75% (P750-P754) and 85% (P850-P854) porosity meet the manufacturing requirements: $t \geq 0.2$ by verifications. The FE calculation results showed that the performance changes of each group of bone scaffolds are similar. Therefore, only a group of bone scaffolds with 65% porosity are selected to cross-verify with the results of FE calculation. The specimens were manufactured from Ti6Al4V powder using the SLM technique (Renishaw AM400, Wotton-under-Edge, United Kingdom). Due to the high melting point of Ti6Al4V materials, in the SLM

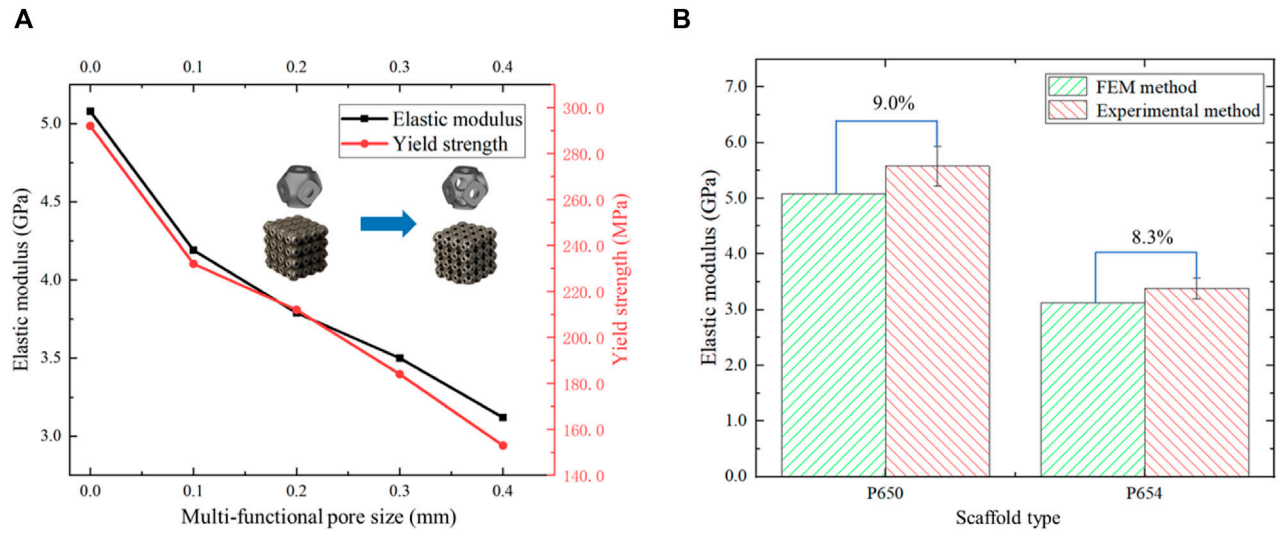

FIGURE 12
(A) Elastic moduli and yield strengths of scaffolds P650 to P654 calculated from experimental data. **(B)** Error in the elastic moduli of scaffolds P650 and P654 calculated by mechanical experiment and FE analysis.

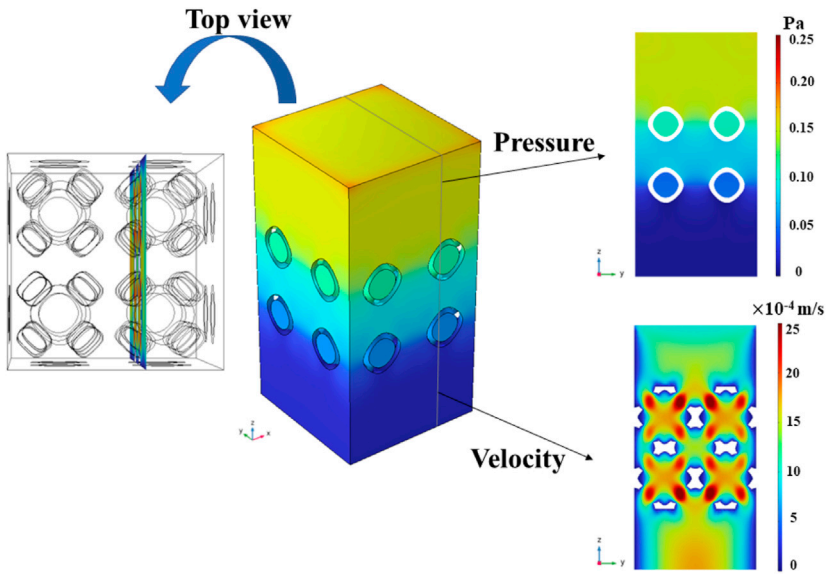

FIGURE 13
Pressure field and local flow velocity for the chosen cross section in the representative CFD model with symmetrical boundary conditions.

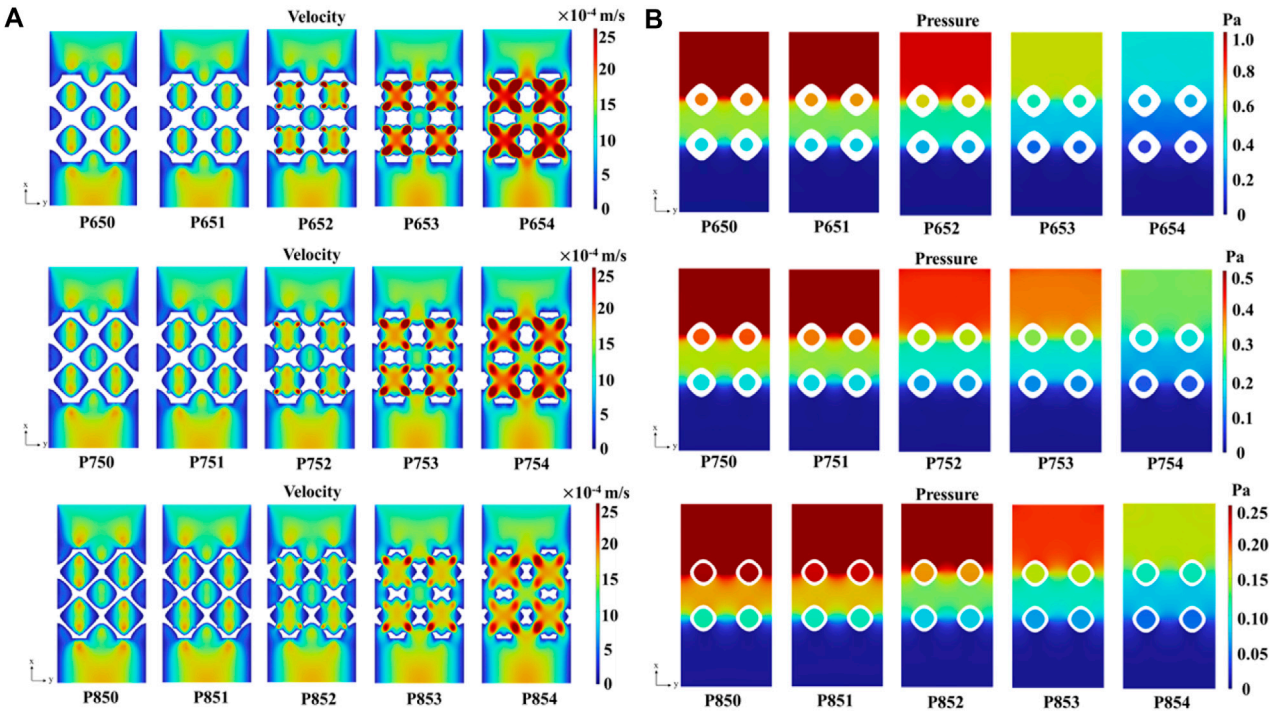

FIGURE 14
(A) Velocity field in the Schwarz P scaffolds with symmetrical boundary conditions. **(B)** Pressure distribution in the Schwarz P scaffolds with the symmetrical boundary conditions.

process (Wauthle et al., 2015; Soro et al., 2019), the input laser power needed to be 280 W, and the scanning speed needed to be 7.3 mm/s. After the printing process, the samples were placed at a temperature of 1200°C for 2 hours, and the white corundum spraying process was carried out.

2.4 Mechanical simulations and analysis

To evaluate the mechanical behavior of the novel scaffolds, both FE simulations and mechanical experiments were performed. Based on the obtained elastic moduli, the Zener anisotropy indexed were

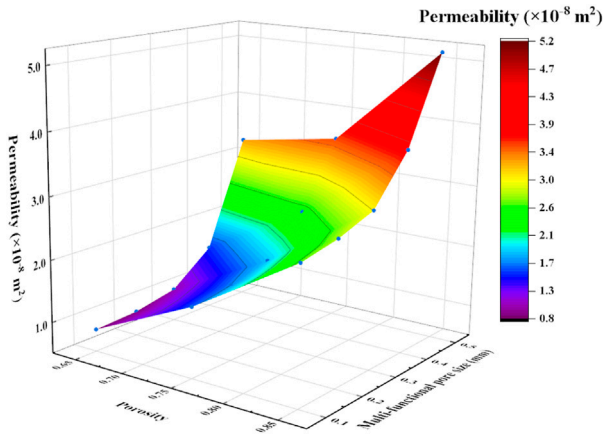

FIGURE 15
Effects of porosity and radius of multi-functional pores on the permeability of Schwarz P scaffolds.

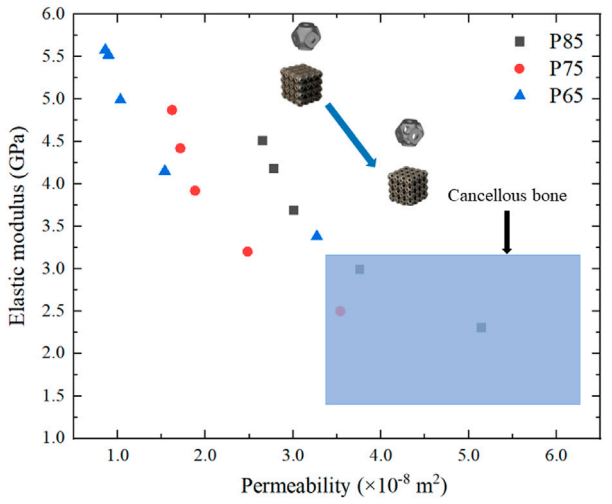

FIGURE 16
Optimization of the elastic modulus and permeability of Schwarz P scaffold and comparison with those of cancellous bone (the blue area is the range of the elastic modulus and permeability of cancellous bone).

calculated. The elastic moduli and Zener anisotropy indexes were used to evaluate the performance of the novel scaffolds.

For the FE simulations, the boundary condition of $\{\varepsilon^{(1)}\}$ was set as follows:

$$\begin{cases} \Delta l_x\big|_{x=l_x} = 0.001 l_x \\ \Delta l_x|_{x=0} = \Delta l_y\big|_{y=0} = \Delta l_y\big|_{y=l_y} = \Delta l_z|_{z=0} = \Delta l_z\big|_{z=l_z} = 0 \end{cases} \tag{12}$$

The boundary condition of $\{\varepsilon^{(2)}\}$ was set as follows:

$$\begin{cases} \Delta l_x\big|_{z=l_x} = 0.0005 l_z, \Delta l_z\big|_{x=l_z} = 0.0005 l_x \\ \Delta l_z|_{x=0} = \Delta l_y\big|_{y=0} = \Delta l_y\big|_{y=l_y} = \Delta l_z\big|_{z=l_z} = \Delta l_x|_{z=0} = 0 \end{cases} \tag{13}$$

According to the derivation in Section 2.2, C_{11} and C_{12} could be obtained when the strain was set to $\{\varepsilon^{(1)}\}$; similarly, C_{44} could be obtained when the strain was set to $\{\varepsilon^{(2)}\}$. It is worth noting that the elastic constants should be averaged, which can be accomplished using Eq. 14:

$$C_{ij} = \bar{\sigma} = \frac{1}{V}\int_V \sigma_{ij} \mathrm{dV} \tag{14}$$

where the sigma-bar of the stress $\bar{\sigma}$ represents the average of the stress values of all points in the entire volume region. Because in the process of FE calculation, the model is divided into many elements and nodes. In order to ensure the accuracy of the calculated stress values, the stress values of all nodes in the FE model are extracted, and the average value of these stress values is $\bar{\sigma}$. The reliability of this data processing method has been confirmed by many previous studies (Feng et al., 2021; Peng et al., 2023).

The scaffolds after topology repair were meshed using C3D8R elements with all element size of 0.01 mm. In order to ensure that the results based on this element size can be converged, the convergence analysis is shown in the Figure 4. The smaller the size of the element is, the greater number of meshes is, and the result tends to converge. Therefore, four different element sizes of 0.04 mm, 0.03 mm, 0.02 mm and 0.01 mm are taken to calculate the effective elastic modulus. According to the results obtained, the elastic modulus is 5.59 GPa when the element size is 0.02 mm and 5.58 GPa when the element size is 0.01 mm. Therefore, it can be considered that the result is convergent when the element size is 0.01 mm. At present, the material of bone scaffold is Ti6Al4V, which is widely used in clinic, that is, elastic modulus is 110.0 GPa and Poisson's ratio is 0.3 (Montazerian et al., 2017). Then, the FE simulations were carried out in ABAQUS with an input elastic modulus of 110.0 GPa and Poisson's ratio of 0.3. Eventually, the elastic moduli were calculated using Eq. 9.

The Zener anisotropy index, which is commonly used to evaluate the anisotropic properties of materials (Chen et al., 2019), is given by Eq. 15:

$$A = \frac{2C_{44}}{C_{11} - C_{12}} \tag{15}$$

After the FE analyses with the boundary conditions in Eq. 12 and Eq. 13, the stiffness matrix C was obtained, and then the Zener anisotropy index was calculated using Eq. 15. Next, the 3D anisotropic elastic responses of the Schwarz P scaffolds were visualized in MATLAB.

Quasi-static uniaxial compression tests were performed using INSTRON 5985 (Instron Company, Massachusetts, United States) and the loading speed was 0.5 mm/min according to the mechanical test standard ISO13314 (Ma et al., 2020). The samples were placed at the center of the lower fixture. The lower plate of the fixture remained fixed, while the upper plate was loaded at 0.5 mm/min, and the force and displacement were recorded using the sensors of the equipment (Figure 5). The stress was calculated by dividing the measured force by the cross-sectional area of the sample, and the strain was calculated by dividing the displacement by the height of the sample in the loading direction. The elastic modulus was calculated from the slope of the linear part of the stress–strain curve, and the yield stress was calculated using the 0.2% offset method. One camera was mounted in front of the samples to record the whole deformation process.

10.3389/fbioe.2024.1401899

2.5 Mass transport simulations and analysis

Mass transport capacity (measured by permeability) is very important for bone scaffolds, because a high mass transport capacity is beneficial for the transmission in the scaffold, which is crucial for the growth of cells. Computational fluid dynamics (CFD) was used to simulate the process of transmission using COMSOL (v6.0, COMSOL Multiphysics, Stockholm, Sweden). The permeabilities of the novel scaffolds with multi-functional pores were calculated to evaluate the mass transport capacity.

All the structures were arrayed to 2 × 2 × 2 unit cells with a dimension of 5.0 mm × 5.0 mm × 5.0 mm. To avoid the boundary effect caused by the inlet and outlet area, a 5.0 mm × 5.0 mm × 2.5 mm virtual fluid domain was built at both the fluid flow inlet and outlet. Thus, a 5.0 mm × 5.0 mm × 10.0 mm parallelepipedal fluid domain was built (Figure 6). A common boundary condition for permeability was set with a flow rate of 0.001 m/s at the inlet and a pressure of 0.0 Pa at the outlet (Zhang et al., 2020; Qureshi et al., 2021). The external surface of the fluid domain and the surface of the Schwarz P scaffold were set as walls under no-slip state.

Darcy's law is given by Eq. 16:

$$R_e = \frac{v\rho D}{\mu} \tag{16}$$

where R_e is the Reynolds number; v is the velocity of the fluid (m/s); ρ is the density of the fluid (kg/m^3); and D is the diameter of the pore (m).

The pressure drop between the inlet and outlet can be obtained from CFD calculation, and the permeability (K) of the structures can be calculated as:

$$K = \frac{v\mu L}{\Delta P}\ v = \frac{Q}{A} \tag{17}$$

where K is the permeability of the structure; v is the velocity of the fluid (m/s); μ is the dynamic viscosity coefficient of the fluid (Pa · S); L is the length of the flow path (m); ΔP is the pressure drop (Pa); Q is the flow rate of scaffold (m^3/s); and A is the cross-section area of the fluid domain (m^2). The fluid properties of water were assumed to be ρ = 1000 kg/m^3, μ = 0.001 Pa · S, and v = 0.001 m/s.

3 Results

In this section, the geometric characteristics of the Schwarz P scaffolds are discussed first, including the difference in size between the designed and the SLM fabricated multi-functional pores. Then, the mechanical properties of all Schwarz P scaffolds under loading cases $\{\varepsilon^{(1)}\}$ and $\{\varepsilon^{(2)}\}$ are investigated using FE analysis in terms of elastic modulus and structural anisotropy. Additionally, the mass transport capacities of all Schwarz P scaffolds are investigated, including the pressure fields, velocity distributions, and structural permeabilities. Finally, the optimization results are presented, offering insights into how the scaffolds perform in comparison to natural cancellous bone and highlighting any improvements achieved through the design and optimization process.

3.1 Morphological characteristics

The SLM-fabricated structures are visualized in Figure 7A, and the sizes of the multi-functional pores are in the increasing order from the original structure to the novel optimized structure (P650–P654). To assess the accuracy of fabrication, the discrepancy between the fabricated specimens and the theoretical designs was examined, with particular focus on the P654 structure (Figure 7B) through a scanning electron microscope (SEM). The designed diameter of the multi-functional pore of P654 was 0.80 mm, and the theoretical observation size of the diameter was calculated to be 0.56 mm with the equation $R_o = R \times \cos 45°$. The actual size of the diameter observed by SEM was 0.53 mm (Figure 7C), so the error between the fabricated and designed sizes was 5.4%. It is worth noting that the multi-functional pores were located on the curved surface, which could not be observed in a tangent plane direction. Therefore, the specimen was placed flat on the SEM observation platform, and the multi-functional pores were observed along a 45° angle.

3.2 Mechanical properties of the novel structures

The overall distribution of the von Mises stress under the tensile load condition $\{\varepsilon^{(1)}\}$ showed a decreasing trend after adding multi-functional pores to P654, P754, and P854. However, the overall distribution of von Mises stress under the shearing load condition $\{\varepsilon^{(2)}\}$ did not change much (Figure 8). With an increase in the radii of the multi-functional pores, the Zener anisotropy indexes of the novel scaffolds demonstrated a rising trend, while the elastic moduli displayed a decreasing trend. For instance, the Zener isotropy index of P650 was 1.63, and that of P654 was 2.12. The elastic moduli of P650, P750, and P850 were 5.58 GPa, 4.87 GPa, and 4.51 GPa, respectively, whereas the elastic moduli of P654, P754, and P854 were 3.38 GPa, 2.50 GPa, and 2.30 GPa, respectively. Notably, the elastic moduli of P754 and P854 fell within the range of 1.0–3.0 GPa, which is characteristic of human cancellous bone (refer to Figure 9B). To investigate the structural anisotropy, the effective stiffness was homogenized and every elastic modulus surface was colored according to the magnitude of the effective stiffness (Figure 9A).

The uniaxial compressive deformation behavior of the novel designed scaffold was basically consistent with that of the original scaffold. Both P650 and P654 scaffolds showed a shear band at the compressive strain of 0.15, which can be attributed to the slip. At the compressive strain of 0.40, the first fracture positions of the P650 and P654 structures were marked in the experimental results. Specifically, at this stage, the P654 structure exhibited a V-shaped shear band, while the P650 structure displayed a single diagonal shear band. Moreover, the fracture characteristics differed between the two structures. The fracture surface of the P650 specimen appeared smooth, whereas that of the P654 specimen was relatively rough, as depicted in Figure 10.

In Figure 11, the deformation behaviors of the P650 and P654 structures can be observed to follow a pattern consisting of three main stages: the elastic stage, plateau stage, and densification stage. Both curves started in the linear elastic stage, dropped sharply

after reaching the peak stress, began a long plateau stage, and finally entered the densification stage from the strain of 0.4. In addition, the strains experienced by both structures at the ultimate compressive strength were found to be approximately the same.

The elastic modulus of the P650 scaffold was 5.58 GPa and that of the P654 structure was 3.38 GPa, showing the same trend as the FE simulation results. In addition, the yield strength of the P650 structure was 292.0 MPa, and that of the P654 structure was 153.0 MPa. The error between the measured elastic modulus and the FE simulation result was 9.0% for the P650 structure and 8.3% for the P654 structure (Figure 12).

3.3 Mass transport capacity of the novel new structures

The pressure field in the entire model was homogenized along the vertical direction, indicating that the same pressure drop could be obtained by selecting any cross section. Since the multi-functional pores facilitated the fluid flow, the chosen cross-section position was strategically placed to intersect the centers of these pores, as illustrated in Figure 13.

With an increase in the radius of the multi-functional pores, the fluid velocity experienced a significant rise, culminating in a maximum velocity 2.8×10^{-3} m/s in the P654 scaffold (Figure 14A). In addition, the pressure drop decreased with the increase of the radius of the multi-functional pore (Figure 14B). According to Darcy's law shown in Eq. 17, the permeability of the scaffold was greatly improved by adding the multi-functional pores.

The permeabilities of the scaffolds increased with the increase of porosity (Figure 15). For example, the permeability of the P650 structure was 8.58×10^{-9} m^2, while that of the P850 structure was 2.65×10^{-8} m^2. The permeability increased approximately three times with the increase of porosity from 65% to 85%. Furthermore, when holding porosity constant, the addition of multi-functional pores led to a significant enhancement in permeability. For example, the permeability of the P650 structure was 8.58×10^{-9} m^2, and that of the P654 structure was 3.23×10^{-8} m^2. The permeability increased approximately four times with the increase of the radius of the multi-functional pore from 0.1 mm to 0.4 mm.

Finally, the elastic moduli and permeabilities of the scaffolds were compared with those of cancellous bone (Figure 16). As a result of the design process, the coordinate points gradually shifted from the upper left corner (higher elastic modulus and lower permeability) of the graph to the lower right corner (lower elastic modulus and higher permeability). The elastic moduli and permeabilities of three structures, P754, P853, and P854, had been optimized to fall within the range observed for cancellous bone.

4 Discussion

Novel TPMS structures were designed and fabricated in this study. The morphological properties, mechanical properties, and mass transport capacities of the structures were investigated using FE simulations and mechanical experiments. In this section, the calculated results of the novel scaffolds are discussed and compared with those of cancellous bone, proving that the novel scaffolds in this study are ideal candidates for clinical applications.

4.1 Morphological characteristics

The error between the fabricated and designed values was 5.4%, indicating that the fabricated scaffolds were of good quality. However, it is necessary to discuss the possible reasons for the error. First, overhang structures were observed (Supplementary Figure 3.1C), which were the defects in the printing process generated by powder attachment. The side attachment was due to the partial melting of the powder around the contour line by laser tracking (Yan et al., 2012) and the bottom attachment was due to the improper thickness of the adjacent layers (Tian et al., 2017). Manufacturing defects such as overhang structures and residual powder are inevitable, and the same phenomena have been observed in other studies (Fan et al., 2021; Qiu et al., 2023). Second, the accuracy of the STL model and the internal structure of the specimen can also affect the manufacturing precision, but these factors are beyond the scope of this study. Although we can eliminate errors as much as possible, due to the limitations of AM technology, errors cannot be completely avoided. The error analysis of AM technology is another complex research field. Therefore, it may be possible to avoid errors by printing multiple times in the future, but in this study, considering the acceptable error of the multi-functional pore (5.4%), it is believed that the fabricated scaffolds meet the requirements of clinical applications.

4.2 Mechanical properties of the novel structures

The FE analysis results revealed that the novel scaffolds designed in this study do not produce stress concentration near the multi-functional pores, which will benefit the long-term service of the scaffolds (Supplementary Figure 3.2). Large stress will inevitably be generated near the multi-functional pores, but such a stress concentration phenomenon is not obvious, and it will not cause the structure to be damaged at the multi-functional pores. It is important to highlight that, in this study, mixed boundary conditions were employed instead of periodic boundary conditions to determine the scaffolds' elastic moduli. This choice not only enhances computational efficiency but has also been validated for its reliable calculation accuracy in previous research (Feng et al., 2021; Baghous et al., 2023; Peng et al., 2023).

The Zener anisotropy indexes (A) of all scaffolds closely resembled those of cancellous bone, affirming the consistent anisotropic behaviors of the designed structures. The index A increased with the increase of the radius of the multi-functional pore and showed the following two trends. First, the larger the radius of the multi-functional pore, the faster the increase of index A (Supplementary Figure 3.3A). For structures with the same porosity of 85%, index A increased by 12.1% with the increase of the radius of the multi-functional pores from 0.1 mm to 0.2 mm. In contrast, the index A increased by 53.8% when the radius of the multi-functional pores increased from 0.2 mm to 0.3 mm. Second, the larger the porosity of the scaffold, the larger the difference between anisotropy

indexes of the original and the novel designed scaffolds. For example, at 65% porosity, index *A* changed by 23% after novel design, whereas at 85% porosity, it changed by 61.4%. The index *A* of human cancellous bone is 1.0–4.0 (Kang et al., 2020). The index of the cancellous bone of the femur measured by CT scanning is 3.5 (Augat et al., 1998), and the index of the spine measured by the compressive testing method is 4.8 (Dendorfer et al., 2008). Thus, there is no unified conclusion on the range of the Zener anisotropy index of cancellous bone. However, the anisotropic behavior of P854 is still obvious, which may affect its mechanical properties. In conclusion, while the Zener anisotropy indexes of the novel scaffolds align with cancellous bone standards, the challenge of managing anisotropy during structural design necessitates further exploration and resolution.

The deformation behavior of the newly designed structure closely mirrored that of the original structure, as illustrated in Supplementary Figure 3.4. Within the strain range of 0–0.1, both structures exhibited stress-strain relationships that were predominantly linear. Notably, at a strain of 0.1, the stresses of P650 and P654 experienced significant drops to 27.4% and 51.3% of their peak stress levels, respectively. This phenomenon was related to the brittle failure of pillars in the Ti6Al4V lattice treated by SLM (Kadkhodapour et al., 2017), and this same phenomenon has been observed in previous studies. For example, Qiu et al. (2023) reported that the stress dropped to 39.4% of the peak stress, and Rezapourian et al. (Rezapourian et al., 2023) reported that the stress dropped to 8.9% of the peak stress. As the stress decreased, both the P650 and P654 structures exhibited a shear band along a diagonal direction of 45°, and P654 produced an additional horizontal shear band (Supplementary Figure 3.4A). The shear band along the diagonal was caused by the diagonal distribution of the maximum local curvature of the Schwarz P structure (Fan et al., 2021). In the plateau stage, the stresses were lower than the ultimate strength and increased in waves. Subsequently, the two structures entered the densification stage, and the stress–strain curve showed an upward trend and reached its initial peak. As the strain increased, the fracture zone of the structure continued to expand, resulting in a state of collapse in the lower layer and a state of yield in the upper layer. The P650 structure displayed smooth and flat fracture characteristics, indicating that the structure's fracture type was primarily due to tensile deformation (Supplementary Figure 3.4B). Furthermore, some internal defects were observed on the fracture cross section of the P654 structure, which may have led to the formation of the horizontal shear band of P654. Similar internal defects have been documented in other studies as well, indicating a potential influence on the mechanical behavior and failure mode of the structure (Fan et al., 2021; Qiu et al., 2023).

The compressive strength and yield strength of the novel scaffolds were compared with those of cancellous bone, indicating that the novel scaffolds had sufficient strength. The compressive strength of cancellous bone is 5.8 MPa and the yield strength of cancellous bone is 4.1 MPa (Syahrom et al., 2011). The P654 structure had compressive strength of 165.0 MPa and yield strength of 153.0 MPa. Therefore, the novel scaffolds met the strength requirements. The error between the FE method and experimental method was 9.0% for the P650 structure and 8.3% for the P654 structure. The error between the two methods evaluated by Jia et al. (2020) fluctuated between 8.0% and 20.0%, so the error in this study was within the acceptable range.

4.3 Mass transport capacity of the novel structures

With the increase of the radius of the multi-functional pore, the velocity of the fluid in the scaffold increased gradually (Supplementary Figure 3.8A). When the radius of the multi-functional pore reached 0.4 mm, the internal structure was completely connected, which significantly improved the permeability of the scaffold. In the past, the method to improve permeability was to increase porosity, but the possible porosity for a certain TPMS scaffold (Maskery et al., 2018) is limited to a certain range. For example, the permeability of P650 was 8.58×10^{-9} m^2, and the permeability of P850 was 2.65×10^{-8} m^2. By increasing the porosity from 65% to 85%, the permeability of the structure was increased approximately 3.1 times. However, the permeability of P654 was 3.27×10^{-8} m^2. Thus, the permeability of the P650 scaffold increased 3.8 times after adding multi-functional pores with a 0.4-mm radius to the scaffold. Therefore, the novel designed scaffolds proposed in this study introduce a new way to control the permeability of TPMS scaffolds.

After adding the multi-functional pores to the scaffolds, the elastic moduli and permeabilities of P754, P853, and P854 fall within the corresponding ranges of cancellous bone (Supplementary Figure 3.10). In addition, with the progress of adding multi-functional pores, the change of permeability was much larger than the change of elastic modulus. From the P650 scaffold to the P654 scaffold, the elastic modulus decreased by 39.0% and the permeability increased by 281.0%. Previous studies have shown that the permeability of a TPMS scaffold is more sensitive to pore size than is the elastic modulus (Sutradhar et al., 2016). The results shown in Supplementary Figure 3.10 also prove that the design method proposed in this study can expand the design domain of TPMS structure. To be specific, since the TPMS structure is controlled by mathematical equation such as Eq. 1, it means that the variable parameters in Eq. 1 is the only variable, which leads to great limitations in the design domain of TPMS structures. To solve this problem, novel TPMS structures such as functional graded TPMS structures are designed in previous studies to broaden the design domain (Fan et al., 2021; Liu et al., 2022). The optimal design method proposed in this study introduced a new variable: multi-functional pore, it can broaden the design domain of TPMS structure, so more different TPMS bone scaffolds can be designed. As shown in Supplementary Figure 3.10, the bone scaffolds that possess elastic modulus and permeability meet the requirements of cancellous bone can be designed by this method, which are new scaffolds cannot be obtained in the previous design domain.

Although promising results were obtained in this study, there are still some limitations that should be resolved in the future. First, the novel design method proposed in this study is only suitable for symmetric structures such as TPMS structures. Because the TPMS structures are symmetrical, its stiffness matrix *C* can be simplified and the optimization framework was based on the simplified stiffness matrix *C*. Second, only the Schwarz P scaffolds were evaluated in this study, and other types of TPMS scaffolds remain to be analyzed. Last but not least, at present, only a group of bone scaffolds with 65% porosity have been manufactured and mechanical experiments have been carried out.

The manufacture of bone scaffolds with more porosity needs to be carried out in the future.

5 Conclusion

To address the problems of high elastic modulus and low permeability in current bone scaffolds, novel TPMS bone scaffolds with optimization-guided multi-functional pores were designed in this study. The performances of the novel TPMS scaffolds were investigated using experimental characterization and numerical simulations. The main conclusions are as follows:

(1) The effective elastic modulus reduced from 5.58 GPa (original scaffold) to 3.38 GPa (novel designed scaffold), resulting in lower stress shielding.
(2) The multi-functional pores greatly improved the mass transport capacities of the TPMS scaffolds by providing new pores on the walls. The permeability increased from $8.58 \times 10^{-9}\,m^2$ (original scaffold) to $5.14 \times 10^{-8}\,m^2$ (novel designed scaffold)
(3) The deformation mode of the novel TPMS bone scaffolds at 65% porosity remained unchanged, which ensured that the new scaffolds can be used as stably as the previous scaffolds. The compressive strength and yield strength of the structure met the clinical requirements, i.e., the scaffolds need to have enough strengths to ensure that they will not break easily.
(4) The novel scaffolds expanded the design domain of TPMS-based bone scaffolds, providing a promising new method for the design of high-performance bone scaffolds.

Data availability statement

The original contributions presented in the study are included in the article/Supplementary Material, further inquiries can be directed to the corresponding author.

Author contributions

JJ: Funding acquisition, Investigation, Writing–review and editing. YH: Methodology, Software, Writing–original draft. XP: Methodology, Writing–original draft. CW: Investigation, Writing–review and editing. HZ: Supervision, Writing–review and editing. YL: Conceptualization, Formal Analysis, Methodology, Writing–review and editing.

Funding

The author(s) declare that financial support was received for the research, authorship, and/or publication of this article. This work was supported by National Natural Science Foundation of China [grant numbers 12211530062 and 12072066], State Key Laboratory of Structural Analysis for Industrial Equipment [grant number GZ22105], Natural Science Foundation of Liaoning Province [grant numbers 2022-MS-443 and 2022-YGJC-21], Dalian Medical Science Research Program Project [grant number 2111005], Dalian University of Technology and Affiliated Central Hospital joint research fund [grant numbers 2022ZXYG45 and DUT23YG217] and the DUT-BSU Joint Institute fund [grant number ICR2303].

Conflict of interest

The authors declare that the research was conducted in the absence of any commercial or financial relationships that could be construed as a potential conflict of interest.

Publisher's note

Supplementary material

The Supplementary Material for this article can be found online at: https://www.frontiersin.org/articles/10.3389/fbioe.2024.1401899/full#supplementary-material

References

Ali, D., Ozalp, M., Blanquer, S., and Onel, S. (2020). Permeability and fluid flow-induced wall shear stress in bone scaffolds with TPMS and lattice architectures: a CFD analysis. *Eur. J. Mechanics-B/Fluids* 79, 376–385. doi:10.1016/j.euromechflu.2019.09.015

Al-Ketan, O., and Abu Al-Rub, R. K. (2019). Multifunctional mechanical metamaterials based on triply periodic minimal surface lattices. *Adv. Eng. Mater.* 21 (10), 1900524. doi:10.1002/adem.201900524

Arabnejad, S., Johnston, B., Tanzer, M., and Pasini, D. (2017). Fully porous 3D printed titanium femoral stem to reduce stress-shielding following total hip arthroplasty. *J. Orthop. Res.* 35 (8), 1774–1783. doi:10.1002/jor.23445

Askari, M., Hutchins, D., Thomas, P., Astolfi, L., Watson, R. L., Abdi, M., et al. (2020). Additive manufacturing of metamaterials: a review. *Addit. Manuf.* 36, 101562. doi:10.1016/j.addma.2020.101562

Augat, P., Link, T., Lang, T., Lin, J. C., Majumdar, S., and Genant, H. K. (1998). Anisotropy of the elastic modulus of trabecular bone specimens from different anatomical locations. *Med. Eng. Phys.* 20 (2), 124–131. doi:10.1016/S1350-4533(98)00001-0

Baghous, N., Barsoum, I., and Al-Rub, R. (2023). Generalized yield surface for sheet-based triply periodic minimal surface lattices. *Int. J. Mech. Sci.* 252, 108370. doi:10.1016/j.ijmecsci.2023.108370

Barba, D., Alabort, E., and Reed, R. (2019). Synthetic bone: design by additive manufacturing. *Acta Biomater.* 97, 637–656. doi:10.1016/j.actbio.2019.07.049

Blanquer, S., Werner, M., Hannula, M., Sharifi, S., Lajoinie, G. P. R., Eglin, D., et al. (2017). Surface curvature in triply-periodic minimal surface architectures as a distinct design parameter in preparing advanced tissue engineering scaffolds. *Biofabrication* 9 (2), 025001. doi:10.1088/1758-5090/aa6553

Campana, V., Milano, G., Pagano, E., Barba, M., Cicione, C., Salonna, G., et al. (2014). Bone substitutes in orthopaedic surgery: from basic science to clinical practice. *J. Mater. Sci. Mater. Med.* 25, 2445–2461. doi:10.1007/s10856-014-5240-2

Chen, Z., Xie, Y., Wu, X., Wang, Z., Li, Q., and Zhou, S. (2019). On hybrid cellular materials based on triply periodic minimal surfaces with extreme mechanical properties. *Mater. Des.* 183, 108109. doi:10.1016/j.matdes.2019.108109

Davoodi, E., Montazerian, H., Khademhosseini, A., and Toyserkani, E. (2020). Sacrificial 3D printing of shrinkable silicone elastomers for enhanced feature resolution in flexible tissue scaffolds. *Acta Biomater.* 117, 261–272. doi:10.1016/j.actbio.2020.10.001

Dendorfer, S., Maier, H., Taylor, D., and Hammer, J. (2008). Anisotropy of the fatigue behaviour of cancellous bone. *J. Biomechanics* 41 (3), 636–641. doi:10.1016/j.jbiomech.2007.09.037

Fan, X., Tang, Q., Feng, Q., Ma, S., Song, J., Jin, M., et al. (2021). Design, mechanical properties and energy absorption capability of graded-thickness triply periodic minimal surface structures fabricated by selective laser melting. *Int. J. Mech. Sci.* 204, 106586. doi:10.1016/j.ijmecsci.2021.106586

Feng, J., Liu, B., Lin, Z., and Fu, J. (2021). Isotropic porous structure design methods based on triply periodic minimal surfaces. *Mater. Des.* 210, 110050. doi:10.1016/j.matdes.2021.110050

Iqbal, T., Wang, L., Li, D., Dong, E., Fan, H., Fu, J., et al. (2019). A general multi-objective topology optimization methodology developed for customized design of pelvic prostheses. *Med. Eng. Phys.* 69, 8–16. doi:10.1016/j.medengphy.2019.06.008

Jia, H., Lei, H., Wang, P., Meng, J., Li, C., Zhou, H., et al. (2020). An experimental and numerical investigation of compressive response of designed Schwarz Primitive triply periodic minimal surface with non-uniform shell thickness. *Extreme Mech. Lett.* 37, 100671. doi:10.1016/j.eml.2020.100671

Jiang, H., Le, B., Bednarcyk, B., Scarpa, F., and Chen, Y. (2020). Bioinspired multilayered cellular composites with enhanced energy absorption and shape recovery. *Addit. Manuf.* 36, 101430. doi:10.1016/j.addma.2020.101430

Kadkhodapour, J., Montazerian, H., Darabi, A. C., Zargarian, A., and Schmauder, S. (2017). The relationships between deformation mechanisms and mechanical properties of additively manufactured porous biomaterials. *J. Mech. Behav. Biomed. Mater.* 70, 28–42. doi:10.1016/j.jmbbm.2016.09.018

Kang, J., Dong, E., Li, D., Dong, S., Zhang, C., and Wang, L. (2020). Anisotropy characteristics of microstructures for bone substitutes and porous implants with application of additive manufacturing in orthopaedic. *Mater. Des.* 191, 108608. doi:10.1016/j.matdes.2020.108608

Khaleghi, S., Dehnavi, F., Baghani, M., Safdari, M., Wang, K., and Baniassadi, M. (2021). On the directional elastic modulus of the TPMS structures and a novel hybridization method to control anisotropy. *Mater. Des.* 210, 110074. doi:10.1016/j.matdes.2021.110074

Kurtz, S., Ong, K., Lau, E., Mowat, F., and Halpern, M. (2007). Projections of primary and revision hip and knee arthroplasty in the United States from 2005 to 2030. *J. Bone Jt. Surg.* 89 (4), 780–785. doi:10.2106/JBJS.F.00222

Lee, D., Khan, K., and Al-Rub, R. (2017). Stiffness and yield strength of architectured foams based on the Schwarz Primitive triply periodic minimal surface. *Int. J. Plasticity* 95, 1–20. doi:10.1016/j.ijplas.2017.03.005

Liu, Z., Gong, H., Gao, J., and Liu, L. (2022). Topological design, mechanical responses and mass transport characteristics of high strength-high permeability TPMS-based scaffolds. *Int. J. Mech. Sci.* 217, 107023. doi:10.1016/j.ijmecsci.2021.107023

Ma, Q., Zhang, L., Ding, J., Qu, S., Fu, J., Zhou, M., et al. (2021). Elastically-isotropic open-cell minimal surface shell lattices with superior stiffness via variable thickness design. *Addit. Manuf.* 47, 102293. doi:10.1016/j.addma.2021.102293

Ma, S., Song, K., Lan, J., and Ma, L. (2020). Biological and mechanical property analysis for designed heterogeneous porous scaffolds based on the refined TPMS. *J. Mech. Behav. Biomed. Mater.* 107, 103727. doi:10.1016/j.jmbbm.2020.103727

Maconachie, T., Leary, M., Lozanovski, B., Zhang, X., Qian, M., Faruque, O., et al. (2019). SLM lattice structures: properties, performance, applications and challenges. *Mater. Des.* 183, 108137. doi:10.1016/j.matdes.2019.108137

Maskery, I., Aremu, A., Parry, L., Wildman, R., Tuck, C., and Ashcroft, I. (2018). Effective design and simulation of surface-based lattice structures featuring volume fraction and cell type grading. *Mater. Des.* 155, 220–232. doi:10.1016/j.matdes.2018.05.058

Montazerian, H., Davoodi, E., Asadi-Eydivand, M., Kadkhodapour, J., and Solati-Hashjin, M. (2017). Porous scaffold internal architecture design based on minimal surfaces: a compromise between permeability and elastic properties. *Mater. Des.* 126, 98–114. doi:10.1016/j.matdes.2017.04.009

Peng, X., Huang, Q., Zhang, G., Li, J., Zhang, X., Lu, Y., et al. (2022). Compensating the anisotropic mechanical properties of electron beam melting-based Gyroid scaffolds using structural design. *Int. J. Mech. Sci.* 226, 107442. doi:10.1016/j.ijmecsci.2022.107442

Peng, X., Huo, Y., Zhang, G., Cheng, L., Lu, Y., Li, J., et al. (2023). Controlled mechanical and mass-transport properties of porous scaffolds through hollow strut. *Int. J. Mech. Sci.* 248, 108202. doi:10.1016/j.ijmecsci.2023.108202

Qiu, N., Zhang, J., Li, C., Shen, Y., and Fang, J. (2023). Mechanical properties of three-dimensional functionally graded TPMS structures. *Int. J. Mech. Sci.* 1, 108118. doi:10.1016/j.ijmecsci.2023.108118

Qureshi, Z., Al-Omari, S., Elnajjar, E., Al-Ketan, O., and Al-Rub, R. A. (2021). Using triply periodic minimal surfaces (TPMS)-based metal foams structures as skeleton for metal-foam-PCM composites for thermal energy storage and energy management applications. *Int. Commun. Heat Mass Transf.* 124, 105265. doi:10.1016/j.icheatmasstransfer.2021.105265

Rabiatul, A., Fatihhi, S., Md, S., Zakaria, Z., Harun, M. N., Kadir, M. R. A., et al. (2021). Fluid–structure interaction (FSI) modeling of bone marrow through trabecular bone structure under compression. *Biomechanics Model. Mechanobiol.* 20, 957–968. doi:10.1007/s10237-021-01423-x

Rezapourian, M., Jasiuk, I., Saarna, M., and Hussainova, I. (2023). Selective laser melted Ti6Al4V split-P TPMS lattices for bone tissue engineering. *Int. J. Mech. Sci.* 251, 108353. doi:10.1016/j.ijmecsci.2023.108353

Santos, J., Pires, T., Gouveia, B., Castro, A. P., and Fernandes, P. R. (2020). On the permeability of TPMS scaffolds. *J. Mech. Behav. Biomed. Mater.* 110, 103932. doi:10.1016/j.jmbbm.2020.103932

Sevilla, P., Aparicio, C., Planell, J. A., and Gil, F. (2007). Comparison of the mechanical properties between tantalum and nickel–titanium foams implant materials for bone ingrowth applications. *J. Alloys Compd.* 439 (1-2), 67–73. doi:10.1016/j.jallcom.2006.08.069

Soro, N., Attar, H., Brodie, E., Veidt, M., Molotnikov, A., and Dargusch, M. S. (2019). Evaluation of the mechanical compatibility of additively manufactured porous Ti–25Ta alloy for load-bearing implant applications. *J. Mech. Behav. Biomed. Mater.* 97, 149–158. doi:10.1016/j.jmbbm.2019.05.019

Strömberg, N. (2021). Optimal grading of TPMS-based lattice structures with transversely isotropic elastic bulk properties. *Eng. Optim.* 53 (11), 1871–1883. doi:10.1080/0305215X.2020.1837790

Sun, C., Wang, L., Kang, J., and Jin, Z. (2018). Biomechanical optimization of elastic modulus distribution in porous femoral stem for artificial hip joints. *J. Bionic Eng.* 15, 693–702. doi:10.1007/s42235-018-0057-1

Sutradhar, A., Park, J., Carrau, D., Nguyen, T. H., Miller, M. J., and Paulino, G. H. (2016). Designing patient-specific 3D printed craniofacial implants using a novel topology optimization method. *Med. Biol. Eng. Comput.* 54, 1123–1135. doi:10.1007/s11517-015-1418-0

Syahrom, A., Abdul, K., Abdullah, J., and Öchsner, A. (2011). Mechanical and microarchitectural analyses of cancellous bone through experiment and computer simulation. *Med. Biol. Eng. Comput.* 49, 1393–1403. doi:10.1007/s11517-011-0833-0

Tan, X., Tan, Y., Chow, C., Tor, S., and Yeong, W. (2017). Metallic powder-bed based 3D printing of cellular scaffolds for orthopaedic implants: a state-of-the-art review on manufacturing, topological design, mechanical properties and biocompatibility. *Mater. Sci. Eng. C* 76, 1328–1343. doi:10.1016/j.msec.2017.02.094

Tian, Y., Tomus, D., Rometsch, P., and Wu, X. (2017). Influences of processing parameters on surface roughness of Hastelloy X produced by selective laser melting. *Addit. Manuf.* 13, 103–112. doi:10.1016/j.addma.2016.10.010

Vijayavenkataraman, S., Kuan, L., and Lu, W. (2020). 3D-printed ceramic triply periodic minimal surface structures for design of functionally graded bone implants. *Mater. Des.* 191, 108602. doi:10.1016/j.matdes.2020.108602

Wallace, I., Worthington, S., Felson, D., Jurmain, R. D., Wren, K. T., Maijanen, H., et al. (2017). Knee osteoarthritis has doubled in prevalence since the mid-20th century. *Proc. Natl. Acad. Sci.* 114 (35), 9332–9336. doi:10.1073/pnas.1703856114

Wauthle, R., Van Der Stok, J., Yavari, S., Van Humbeeck, J., Kruth, J. P., Zadpoor, A. A., et al. (2015). Additively manufactured porous tantalum implants. *Acta Biomater.* 14, 217–225. doi:10.1016/j.actbio.2014.12.003

Wu, D., Isaksson, P., Ferguson, S. J., and Persson, C. (2018). Young's modulus of trabecular bone at the tissue level: a review. *Acta Biomater.* 78, 1–12. doi:10.1016/j.actbio.2018.08.001

Yan, C., Hao, L., Hussein, A., and Raymont, D. (2012). Evaluations of cellular lattice structures manufactured using selective laser melting. *Int. J. Mach. Tools Manuf.* 62, 32–38. doi:10.1016/j.ijmachtools.2012.06.002

Zhai, Y., Lados, D., and Lagoy, J. (2014). Additive manufacturing: making imagination the major limitation. *Jom* 66, 808–816. doi:10.1007/s11837-014-0886-2

Zhang, L., Song, B., Yang, L., and Shi, Y. (2020). Tailored mechanical response and mass transport characteristic of selective laser melted porous metallic biomaterials for bone scaffolds. *Acta Biomater.* 112, 298–315. doi:10.1016/j.actbio.2020.05.038

frontiers | Frontiers in Bioengineering and Biotechnology

TYPE Original Research
PUBLISHED 08 July 2024
DOI 10.3389/fbioe.2024.1387768

OPEN ACCESS

EDITED BY
Ge He,
University of Wisconsin–Milwaukee,
United States

REVIEWED BY
Wenxin Niu,
Tongji University, China
Uriel Zapata,
EAFIT University, Colombia

*CORRESPONDENCE
Yaodong Gu,
guyaodong@hotmail.com

RECEIVED 18 February 2024
ACCEPTED 19 June 2024
PUBLISHED 08 July 2024

CITATION
Zhang L, Zhang Q, Zhong Y, Hortobagyi T and Gu Y (2024), Effect of forefoot transverse arch stiffness on foot biomechanical response--based on finite element method.
Front. Bioeng. Biotechnol. 12:1387768.
doi: 10.3389/fbioe.2024.1387768

Effect of forefoot transverse arch stiffness on foot biomechanical response--based on finite element method

Linjie Zhang[1,2], Qiaolin Zhang[3,4], Yilin Zhong[5], Tibor Hortobagyi[1,2] and Yaodong Gu[1,5]*

[1]Department of Radiology, Ningbo No. 2 Hospital, Ningbo, China, [2]Department of Kinesiology, Hungarian University of Sports Science, Budapest, Hungary, [3]Doctoral School of Safety and Security Sciences, Obuda University, Budapest, Hungary, [4]Faculty of Engineering, University of Szeged, Szeged, Hungary, [5]Faculty of Sport Science, Ningbo University, Ningbo, China

Background: The plantar vault, comprising the transverse and longitudinal arches of the human foot, is essential for impact absorption, elastic energy storage, and propulsion. Recent research underscores the importance of the transverse arch, contributing over 40% to midfoot stiffness. This study aimed to quantify biomechanical responses in the ankle-foot complex by varying the stiffness of the deep metatarsal transverse ligament (DTML).

Methods: Using CT image reconstruction, we constructed a complex three-dimensional finite element model of the foot and ankle joint complex, accounting for geometric complexity and nonlinear characteristics. The focus of our study was to evaluate the effect of different forefoot transverse arch stiffness, that is, different Young's modulus values of DTML (from 135 MPa to 405 MPa), on different biomechanical aspects of the foot and ankle complex. Notably, we analyzed their effects on plantar pressure distribution, metatarsal stress patterns, navicular subsidence, and plantar fascial strain.

Results: Increasing the stiffness of the DTML has significant effects on foot biomechanics. Specifically, higher DTML stiffness leads to elevate von Mises stress in the 1st, 2nd, and 3rd metatarsals, while concurrently reducing plantar pressure by 14.2% when the Young's modulus is doubled. This stiffening also impedes navicular bone subsidence and foot lengthening. Notably, a 100% increase in the Young's modulus of DTML results in a 54.1% decrease in scaphoid subsidence and a 2.5% decrease in foot lengthening, which collectively contribute to a 33.1% enhancement in foot longitudinal stiffness. Additionally, doubling the Young's modulus of DTML can reduce the strain stretch of the plantar fascia by 38.5%.

Conclusion: Preserving DTML integrity sustains the transverse arch, enhancing foot longitudinal stiffness and elastic responsiveness. These findings have implications for treating arch dysfunction and provide insights for shoe developers seeking to enhance propulsion.

KEYWORDS

forefoot transverse arch, foot stiffness, stress distribution, metatarsal stress, finite element model, plantar fascia strain

1 Introduction

In various human physical activities including walking, running, jumping, and other sports, the foot serves as the terminal point of movement. It functions to attenuate the impact forces from ground contact during landing (Chan and Rudins, 1994; Pan et al., 2023), generate propulsive force for the body during push-off (Bramble and Lieberman, 2004; Takahashi et al., 2016; Xu et al., 2024), and optimize energy conversion efficiency (Kuo et al., 2005; Zelik and Kuo, 2010; Khuyagbaatar et al., 2024). To accommodate the multifunctional demands placed upon them, humans have evolved a pair of remarkably flexible feet capable of modulating stiffness to suit various requirements across different athletic endeavors (Bojsen-Møller, 1979; Ker et al., 1987; Kuo et al., 2005; Zelik and Kuo, 2010). The differential stiffness observed in the foot can largely be attributed to the structural composition of the plantar vault, which is formed by the medial longitudinal arch (MLA), lateral longitudinal arch (LLA), and transverse arch (TA). These arches play a significant role in determining the overall stiffness characteristics of the foot (Gwani et al., 2017; Venkadesan et al., 2020).

The MLA has traditionally been a focal point for researchers investigating foot elasticity and mechanical functionality (Morton, 1924b; Elftman and Manter, 1935; Hicks, 1954a; Bojsen-Møller, 1979; Susman, 1983; Williams and McClay, 2000; Heard-Booth, 2017; Holowka and Lieberman, 2018). It is widely recognized as a primary determinant of the foot's elastic response in the sagittal plane and contributes significantly to midfoot stiffness. Working in conjunction with the bow-string configuration established by the plantar fascia (PF) (Morton, 1924a; Ker et al., 1987) and the windlass mechanism facilitated by dorsiflexion of the metatarsophalangeal joint (Hicks, 1954b), the MLA contributes to midfoot lengthening and stiffness. During forefoot loading, ground reaction forces compel passive stretching of the PF (Morton, 1924b; Ker et al., 1987). Similarly, dorsiflexion of the metatarsophalangeal joints during foot propulsion also results in stretching of the PF (Hicks, 1954b). These two mechanisms of stretching the PF serve to impede MLA collapse and are directly correlated with MLA height (Williams and McClay, 2000). Furthermore, a cadaveric investigation revealed a reduction in foot stiffness following transection of the PF, albeit this reduction was limited to less than 25% (Huang et al., 1993). In light of these observations, the hypothesis proposing that MLA height correlates with foot stiffness emerged, leading to the arch height index becoming a widely utilized metric for foot stiffness assessment (Williams and McClay, 2000; Xiang et al., 2024). However, the premise of utilizing MLA height as a proxy for adequate stiffness possesses inherent limitations, as evidenced by several studies. For instance, individuals with MLA collapse can exhibit normal gait patterns (DeSilva et al., 2015). Even in cases where the PF is transversely severed, foot stiffness diminishes by only a fraction, as indicated in previous research (Huang et al., 1993). In a comparative analysis of individuals with normal arches and flat feet, Kido et al. (2013) observed that midfoot deformation under body weight loading was twice as pronounced in patients with flat feet, with the disparity in stiffness between normal arches and flat feet surpassing the contribution of the PF. Moreover, in conditions characterized by low MLA height such as diabetic foot and peripheral neuropathy, the winch mechanism persists but fails to furnish adequate stiffness support (Gelber et al., 2014). Collectively, these findings underscore the inadequacy of solely relying on sagittal plane foot mechanics to elucidate foot stiffness, signaling the need for a deeper understanding of foot biomechanics.

The TA comprises two bony structures exhibiting slight curvature in the vertical direction of the MLA, situated at the tarsometatarsal joint and metatarsophalangeal joint, respectively (Ridola and Palma, 2001). Biomechanical investigations of the TA have been relatively scarce in recent years, with the majority focusing on the forefoot transverse arch (FTA) at the metatarsophalangeal joint (Iaremenko, 1967; Daentzer et al., 1997; Luger et al., 1999; Weishaupt et al., 2002; Kanatli et al., 2003; Masłoń et al., 2017; Nakai et al., 2019). Plantar pressure data appear to contradict the anatomical configuration and function of the FTA during foot loading (Daentzer et al., 1997; Kanatli et al., 2003), as higher plantar pressure is observed beneath the 2nd and 3rd metatarsals compared to other metatarsals. Conversely, Powell et al. (2014) conducted X-ray imaging and measurements of the forefoot under maximal load in 200 randomly selected Danish subjects, affirming the persistent presence of a bony FTA in the forefoot with an average height of 1.4 mm even under maximum load. Recent investigations have underscored the significance of the TA in contributing to midfoot stiffness, thereby addressing the inadequacy of utilizing MLA height as a sole indicator of foot stiffness (Venkadesan et al., 2020). Venkadesan et al. (2020) demonstrated through mechanical simulations that the TA constitutes the primary determinant of foot stiffness, accounting for over 40% of total foot stiffness. This phenomenon stems from the mechanical coupling between sagittal plane bending of the foot and perpendicular stretching of the metatarsal heads, akin to the significant stiffening observed when folding a banknote crosswise. Yawar et al. (2017) conducted experiments involving subjects with FTA wrapped in elastic bandages and employed mathematical models to ascertain that augmenting the lateral stiffness of the FTA resulted in an average increase of 53% in foot stiffness. Furthermore, they posited that the orientation of the adjacent metatarsal joint axis carried more significance than the external curvature in influencing foot biomechanics. Despite the absence of an overt transverse arch in some foot configurations, the geometric features of the tarsal/metatarsal joints and ligament arrangement may lead to misalignment of the preferred bending direction of adjacent metatarsals. This functional bending capability enables the storage of elastic potential energy generated by the stretching of interosseous ligaments. Further exploration is warranted to elucidate the relationship between the TA and foot stiffness. Schmidt et al. (2024) conducted a retrospective analysis of weight-bearing CT images from 32 Progressive collapsing foot deformity and 32 control feet, revealing a greater degree of TA collapse in progressively collapsing clubfeet compared to controls. The most significant collapse was observed between the medial cuneiform and the second metatarsal bones. This observation suggests a potential coupling mechanism between the TA and the MLA, specifically occurring between the medial cuneiform and the second metatarsal. Moreover, the biomechanical responses of different FTA lateral stiffnesses on foot mechanics remain unexplored and merit investigation.

In 1973, Belytschko et al. (1973) pioneered the application of the finite element (FE) method in biomechanical research. This method has gained widespread popularity due to its capacity to conduct iterative mechanical analyses of structures characterized by irregular geometric shapes and intricate material properties within complex boundaries. It stands as one of the foremost methodologies in foot biomechanics research (Yu et al., 2020). Consequently, we aimed to construct a three-dimensional FE model of the foot-ankle complex using CT data obtained from healthy subject. The lateral stiffness of the FTA within the foot-ankle complex was manipulated by adjusting the Young's modulus of the DTML. Comprising a series of four short ligaments spanning the distal ends of adjacent metatarsals, the DTML plays a pivotal role in stabilizing deformations of the foot's transverse arch (Wang et al., 2015). Our objective is to investigate the corresponding impacts of varying FTA lateral stiffness on von Mises stress, strain, and plantar pressure across foot bones and PF tissue under identical loading conditions.

We hypothesized that augmenting the lateral stiffness of the FTA would mitigate forefoot plantar pressure, induce alterations in metatarsal von Mises stress and stress distribution, diminish navicular bone descent, and attenuate PF strain.

2 Materials and methods

2.1 Participant information

This study included one healthy male subject (age: 26 years, height: 186 cm, weight: 75 kg). The subject's feet exhibited no signs of neurological disease, biomechanical abnormalities resulting from acute foot injuries, or previous foot bone surgeries, and there were no hereditary foot deformities observed. Prior to measurements, subjects were provided with comprehensive information regarding the experimental procedures and were required to sign an informed consent form. Ethical approval for this study was obtained from the Human Subjects Ethics Committee of Ningbo University (RAGH20230428), and all laboratory procedures adhered to the principles outlined in the Declaration of Helsinki.

2.2 Model construction

A coronal CT scan, conducted without weight bearing, was performed on the subject's right foot in a neutral position, with a 2 mm interval between slices. The DICOM image was segmented using Mimics16.0 (Materialise, Leuven, Belgium) to generate a three-dimensional model encompassing both bone tissue and capsular soft tissue. Geometric irregularities present on the surfaces of bony components and soft tissues were smoothed using Geomagic Studio 2013 (Geomagic Inc, Research Triangle Park, North Carolina, United States). Subsequently, a PF model was established based on foot anatomy (Tao et al., 2010). Each surface member was individually imported into SolidWorks 2016 (Massachusetts, United States, SolidWorks) to create solid parts. A solid cartilage structure was constructed based on the bone contact surface. Volumetric Boolean operations were performed to subtract all bone and cartilage components, resulting in the encapsulated soft tissue being derived from the total soft tissue. The numerical foot model comprises 28 bone segments, which include the tibia, fibula, talus, calcaneus, cuboid, navicular, 3 cuneiforms, 5 metatarsals, and 14 phalanges (Zhang et al., 2022) (refer to Figure 1A).

2.3 Geometry reconstruction and mesh creation

The mesh was generated utilizing the Ansys Workbench (ANSYS, Inc., United States) grid tool, as illustrated in Figure 1B. Each bone, cartilage component, and surrounding soft tissue was segmented into sub volumes, with tetrahedral elements assigned to each volume. The mesh sizes for the two models were set as follows: 4.5 mm for the encapsulated soft tissue, 3 mm for the bone, and 2.5 mm for the cartilage structure. Local refinement was implemented to accommodate contact areas and fine geometries. The solid part was meshed using tetrahedral elements. Except for the PF, DTML, and metatarsophalangeal joint capsule, other ligaments are non-solid line units that only stretch. Employing a method of gradually reducing mesh size, a mesh sensitivity test was conducted on the full-foot model at a static station. Acceptable mesh generation was determined by evaluating the deviation of peak equivalent von Mises stress synthesized by the first metatarsal bone. Further mesh reduction was undertaken until the von Mises stress deviation remained within 5% of the original value (Chen et al., 2019).

2.4 Material property assignment

With the exception of the encapsulated soft tissue, all materials are modeled as isotropic and linearly elastic (Cheung et al., 2005). Two material constants, Young's modulus (E) and Poisson's ratio (ν), are defined to characterize elasticity. The soft tissue is treated as a nonlinear hyper elastic material. The material properties of the soft tissue are derived from the second-order polynomial strain potential energy measured by *in vivo* ultrasound. A hyperelastic material model is used to define the soft tissue portion of the model, as shown in Eq. 1:

$$U = \sum_{i+j=1}^{2} C_{ij} \left(\bar{I}_1 - 3\right)^i \left(\bar{I}_2 - 3\right)^i + \sum_{i=1}^{2} \frac{1}{D_i} (J_{el} - 1)^{2i} \qquad (1)$$

U is the strain energy per unit reference volume; C_{ij} and D_i are material parameters. J is the volume ratio; I_1 and I_2 are the 1st and 2nd deviator strain invariants. The superelastic material coefficients used for soft tissue are C_{10} = 0.08556, C_{01} = −0.0841, C_{11} = −0.02319, C_{02} = 0.00851, D_1 = 3.65273, D_2 = 0 (Lemmon et al., 1997). Material properties for each component are detailed in Table 1 (Siegler et al., 1988; Gefen, 2002; Cho et al., 2009; Gu et al., 2010; Brilakis et al., 2012; Gu et al., 2012). Cheung et al. (2004) simulated the effect of changing the stiffness of the PF on plantar pressure and the biomechanical interaction between bones and ligaments by changing the Young's modulus of the PF. Therefore, we changed the Young's modulus in the range of 135–405 MPa. Various values of the modulus are assigned to DTML to study the effect of FTA stiffness on load distribution. A Young's modulus of 270 MPa was selected as the reference value to represent normal DTML stiffness (Gu et al., 2012), with the cross-sectional area of the fascia maintained constant across all simulation cases.

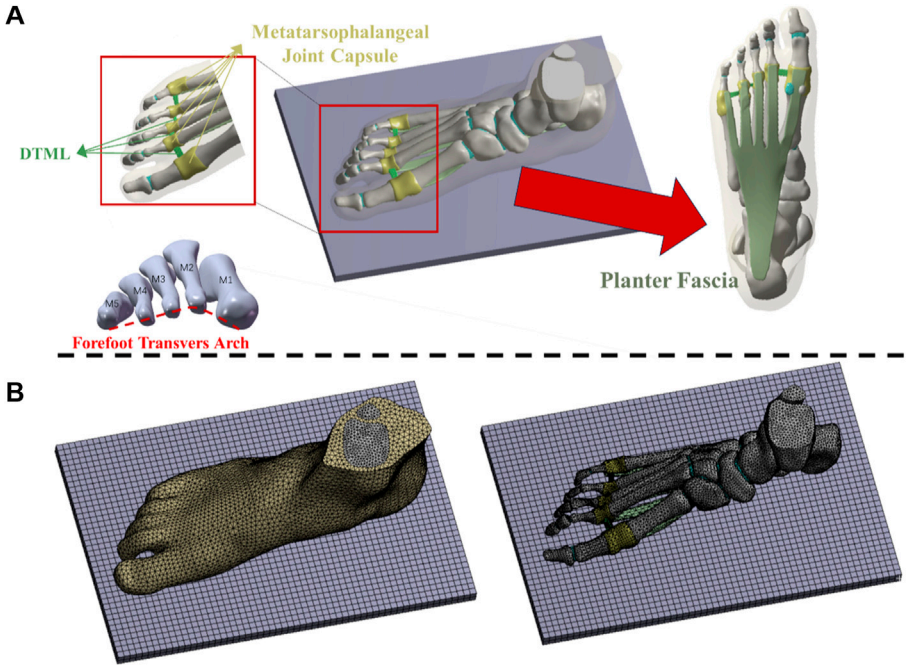

FIGURE 1
(A) Three-dimensional finite element models of soft tissue, bone and ligament structures; **(B)** Mesh model of foot-ankle complex under load.

TABLE 1 Material properties of the components in the finite element model.

Component	Young's modulus E (Mpa)	Poisson's ratio ν	Size	Elements	Nodes	Reference
Bony Structures	7300	0.30	2 mm	253,217	709,301	Gefen (2002)
Soft tissue	—	—	3 mm	203,652	502,541	Cho et al. (2009)
Cartilage	1	0.40	0.5 mm	103,542	312,358	Gu et al. (2010)
Ligament	260	0.40	\	\	\	Siegler et al. (1988)
Planter fascia	350	0.40	1 mm	85,423	214,528	Brilakis et al. (2012)
DTML	270 (135–405)	0.40	1 mm	98,456	245,627	Gu et al. (2012)
Ground plate	17,000	0.10	3 mm	170	1360	Gu et al. (2010)

2.5 Boundary and loading conditions

This study investigated the impact of FTA stiffness on the biomechanics of the foot and ankle complex during running. The AMTI force plate (Advance Mechanical Technology Inc., Watertown, NY, United States) was utilized to capture the force exerted by the subject's right foot from ground contact to lift-off. Ground reaction force was recorded at a frequency of 1,000 Hz, with running speed determined by the subject's self-selected pace. The number of experiments is three, and the interval between each experiment is 3 min. A flexible metal plate, capable of vertical movement only, was employed to simulate the ground (Kasiri-Bidhendi et al., 2015). The upper surface of the soft tissue, distal tibia, and distal fibula were fixed, as depicted in Figure 2. The average value of the second peak vertical ground reaction force of 1074N measured by the force plate is applied to the bottom of the metal plate as the ground reaction force of the FE analyze. Interaction between the foot and the plate was simulated as a contact surface with a friction coefficient of 0.6 (Yu et al., 2008). An equivalent force vector representing the Achilles tendon force was applied to the posterior aspect of the calcaneus. The magnitude of the Achilles tendon force was estimated as half of the reaction force (187.5 N) exerted by one foot when maintaining balance (Cheung et al., 2004).

2.6 Experimental validation

The model's validity was assessed by comparing plantar pressure computed via FE analysis with plantar pressure measurements obtained using an Emed pressure plate (Novel, Munich, Germany), both conducted on the same subject. The subject was instructed to stand stationary on the Emed pressure plate for a duration of 5 s. Data collected during the middle 3 seconds were selected and averaged for analysis. This

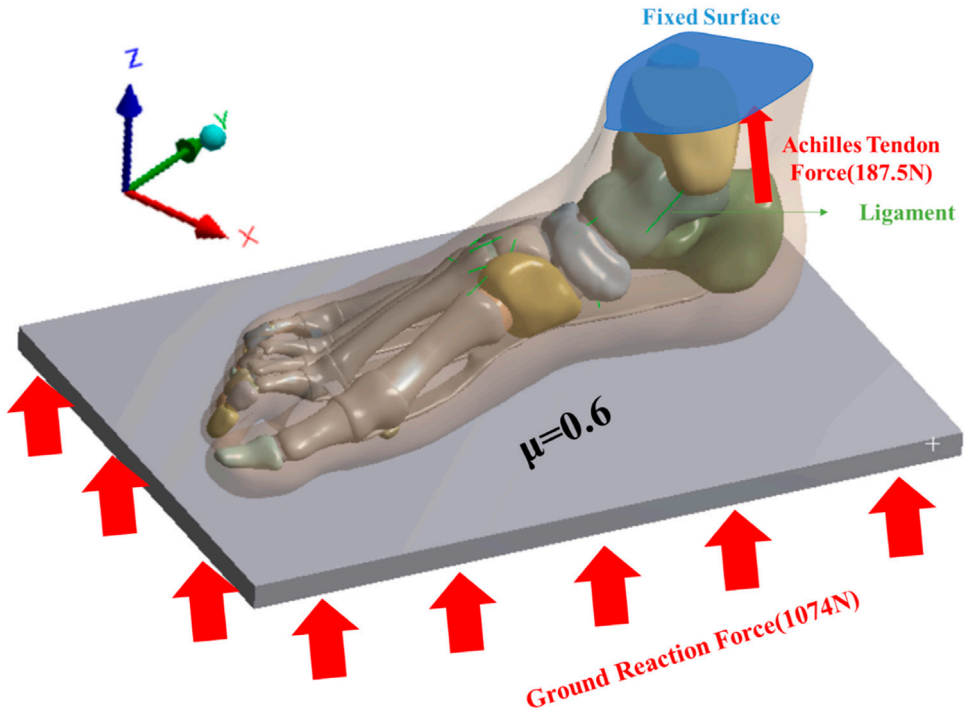

FIGURE 2
Loading and boundary conditions for FE analyses.

procedure ensured a representative assessment of plantar pressure distribution during static stance (El-Sallam et al., 2013).

3 Results

3.1 Model verification

Figure 3 displays the plantar pressure distribution predicted by the Emed pressure plate and FE analysis while the subject maintained balance. The FE model utilized a DTML Young's modulus (E) of 270 MPa as the reference value. Notably, the FE model demonstrates strong agreement with experimentally measured plantar pressure distribution and pressure values. Specifically, the simulated forefoot plantar peak pressure is 0.318 MPa, closely aligning with the measured value of 0.293 MPa, while the simulated and measured hindfoot plantar peak pressures are 0.353 MPa and 0.336 MPa, respectively.

3.2 Plantar pressure

As the Young's modulus of DTML increases, peak plantar pressure decreases, accompanied by pressure redistribution. From DTML Young's modulus E = 135 MPa to E = 405 MPa, forefoot peak plantar pressure initially increases before exhibiting a decreasing trend (Figure 4). Compared to the reference value E = 270 MPa, when the Young's modulus of DTML is reduced by 50%, the peak pressure of the forefoot increases by 4.7% (0.334 MPa), the peak pressure of the midfoot increases by 11.3% (0.267 MPa), and the peak pressure of the rearfoot decreases by 8.8% (0.322 MPa). When the Young's modulus of DTML increases by 100%, the peak pressure of the forefoot and midfoot decreases by 19.2% (0.269 MPa) and 39% (0.163 MPa) respectively, while the peak pressure of the rearfoot increases by 11.4% (0.359 MPa). The overall foot plantar pressure is reduced by 14.2%.

3.3 PF strain

The tensile strain distribution of the PF, as simulated by FE, is depicted in Figure 5. Increasing the Young's modulus of DTML effectively reduces the peak strain across various areas of the PF, particularly evident in the distal and middle segments. A 100% increase in DTML Young's modulus correlates with a 38.5% reduction in the strain stretch of the PF.

3.4 Foot height and length

In the unloaded simulated state, the height of the scaphoid measures 52.5 mm, with a foot length of 273 mm. During running, the scaphoid experiences a 21% reduction, measuring 41.5 mm. When the Young's modulus of DTML decreases to 50% of the reference value E = 270 Mpa, the scaphoid drops to 34 mm. Conversely, under the condition of DTML Young's modulus E = 405 Mpa, the scaphoid measures 44mm, representing an 8.5 mm reduction compared to the unloaded state (Figure 6A). Altering the Young's modulus of DTML by ± 50% from the reference value results in a 0.4% decrease and a 2.1% increase in foot length, respectively (Figure 6B).

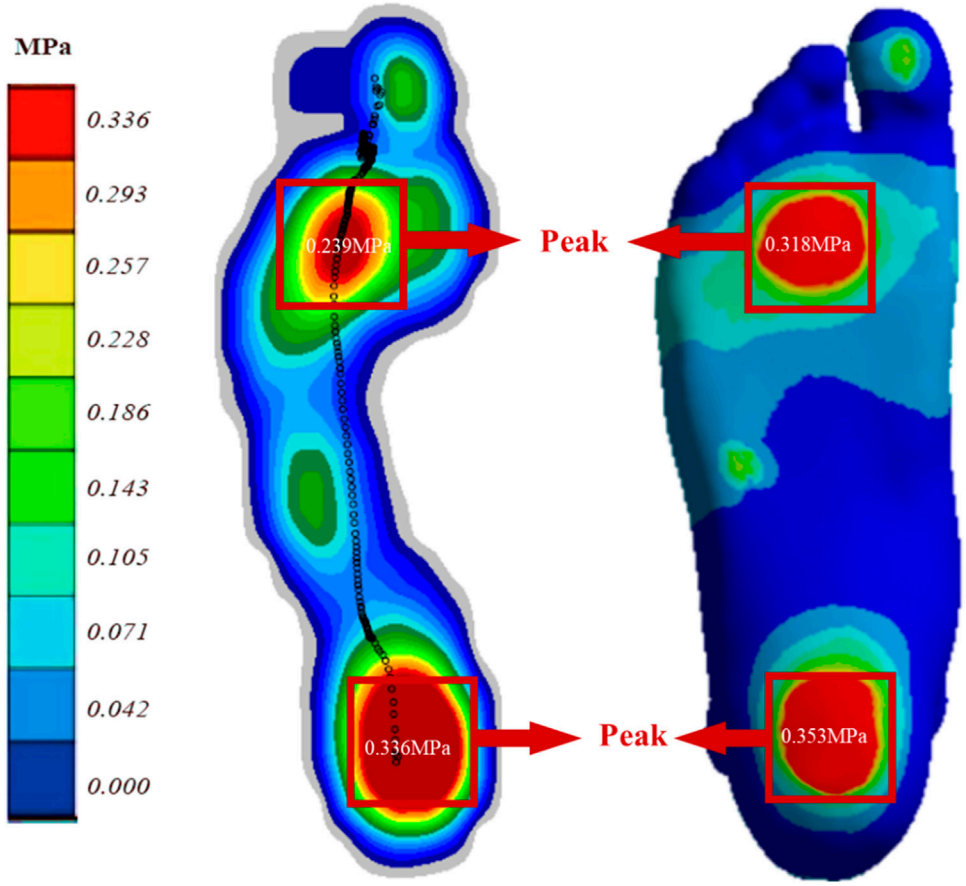

FIGURE 3
Comparison of FE predicted (right) and experimentally measured (left) peak pressure during balanced standing for model validation.

3.5 Metatarsal stress

As the Young's modulus of DTML increases from one-half the reference value, metatarsal von Mises stress generally escalates, except for M5 (Figure 7A). Comparatively, at 1.5 times the Young's modulus reference value, the von Mises stress on the 2nd and 3rd metatarsals increases by 14.7% and 9.3%, respectively. Conversely, the von Mises stress on the 1st and 4th metatarsals decreases by 8.9% and 6.1%, respectively. The von Mises stress on the fifth metatarsal bone diminishes by 8.4% within the 100% change range of DTML Young's modulus. With increasing DTML Young's modulus, the von Mises stress distribution of the metatarsals becomes more concentrated. The von Mises stress on the 1st, 4th, and 5th metatarsals tends to shift towards the 2nd and 3rd metatarsals. Furthermore, the von Mises stress center also shifts vertically, transitioning from the base of the 3rd metatarsal to the posterior aspect of the 2nd (Figure 7B).

4 Discussion

Despite the acknowledged significance of the FTA in contributing to foot stiffness (Yawar et al., 2017; Venkadesan et al., 2020), detailed insights into the precise impact of FTA stiffness on internal foot structures remain limited. To comprehensively investigate the biomechanical response of the FTA within the context of internal foot structures, this study developed a subject-specific three-dimensional FE model of the foot-ankle complex and systematically assessed the quantitative influence of FTA stiffness on plantar load-bearing characteristics and internal foot structural parameters. Experimental findings indicate that progressive increases in FTA stiffness consistently reduce peak plantar pressure, as well as tension and strain levels within the PF, and mitigating scaphoid subsidence. Notably, variations are observed in the effects of FTA stiffness on the von Mises stress distribution across the five metatarsal bones. These nuanced biomechanical responses underscore the complexity of foot mechanics and highlight the need for further investigation to elucidate the precise interplay between FTA stiffness and internal foot structures.

As the Young's modulus of the DTML increased from 50% to 150% of the reference value (E = 270 MPa), a notable decrease of 14.2% in peak plantar pressure was observed. This reduction primarily manifested as a decrease in peak pressure in the midfoot and forefoot regions. However, a rising trend in forefoot peak pressure was observed as the DTML Young's modulus increased from 50% to 75% of the reference value. This phenomenon may be attributed to the increased stiffness of the

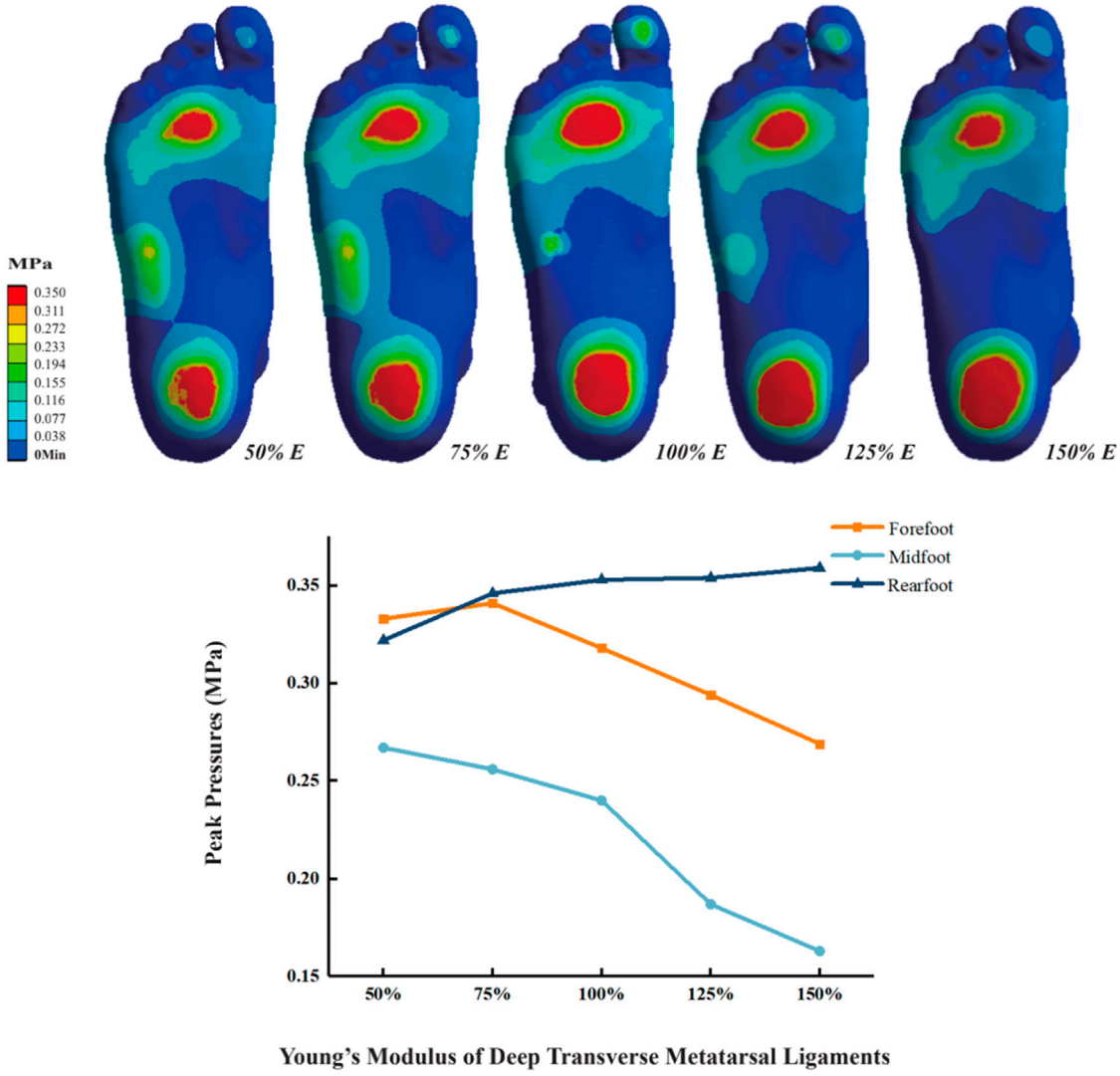

FIGURE 4
Effect of different DTML Young's modulus on plantar peak pressure.

FTA, which impedes midfoot sinking and redistributes pressure towards the front and rear feet. Despite the increase in the Young's modulus of the DTML during this period, it proved insufficient to fully convert all increments of forefoot plantar pressure into elastic potential energy stored within the ligament. With further escalation in the lateral stiffness of DTML, the mechanical coupling between the foot's sagittal plane bending and metatarsal head opening becomes more pronounced. This coupling facilitates the conversion of a greater proportion of ground reaction forces into the elastic force exerted by DTML, consequently reducing peak plantar pressure. Viewed from this perspective, the mechanical interplay between foot dorsiflexion and metatarsal head opening, along with increased FTA lateral stiffness, effectively reduces plantar pressure. Conversely, elevated plantar pressure, particularly in the forefoot, may heighten the risk of injury during movement (Wilzman et al., 2022).

The PF represents a crucial passive stabilizer in maintaining midfoot stiffness. In this study, a three-dimensional model of the PF was constructed to investigate its association with the FTA. Experimental findings revealed that a reduction in the Young's modulus of the DTML resulted in increased peak strain within the PF. The deep PF inserts into the interosseous fascia, deep transverse plantar ligament, metatarsophalangeal joint plantar ligament, periosteum, and fibrous sheath at the base of each proximal phalanx, forming a sheath surrounding the flexor tendons (Davies, 2005). A decrease in the stiffness of the DTML disrupts the stability of the metatarsophalangeal joint, causing the metatarsals to expand along the Le Lie`vre metatarsal parabola. Consequently, the distal end of the PF undergoes increased passive stretching. This abnormal stretching of the distal end of the PF may contribute to forefoot pain associated with FTA dysfunction, such as hallux valgus (Nakai et al., 2019). Additionally, reduced stiffness across the foot, stemming from decreased forefoot lateral stiffness, elevates strain in the mid PF and heel, potentially exacerbating PF strain and predisposing to conditions like plantar fasciitis (Buchbinder, 2004; Irving et al., 2006; Wearing et al., 2006).

10.3389/fbioe.2024.1387768

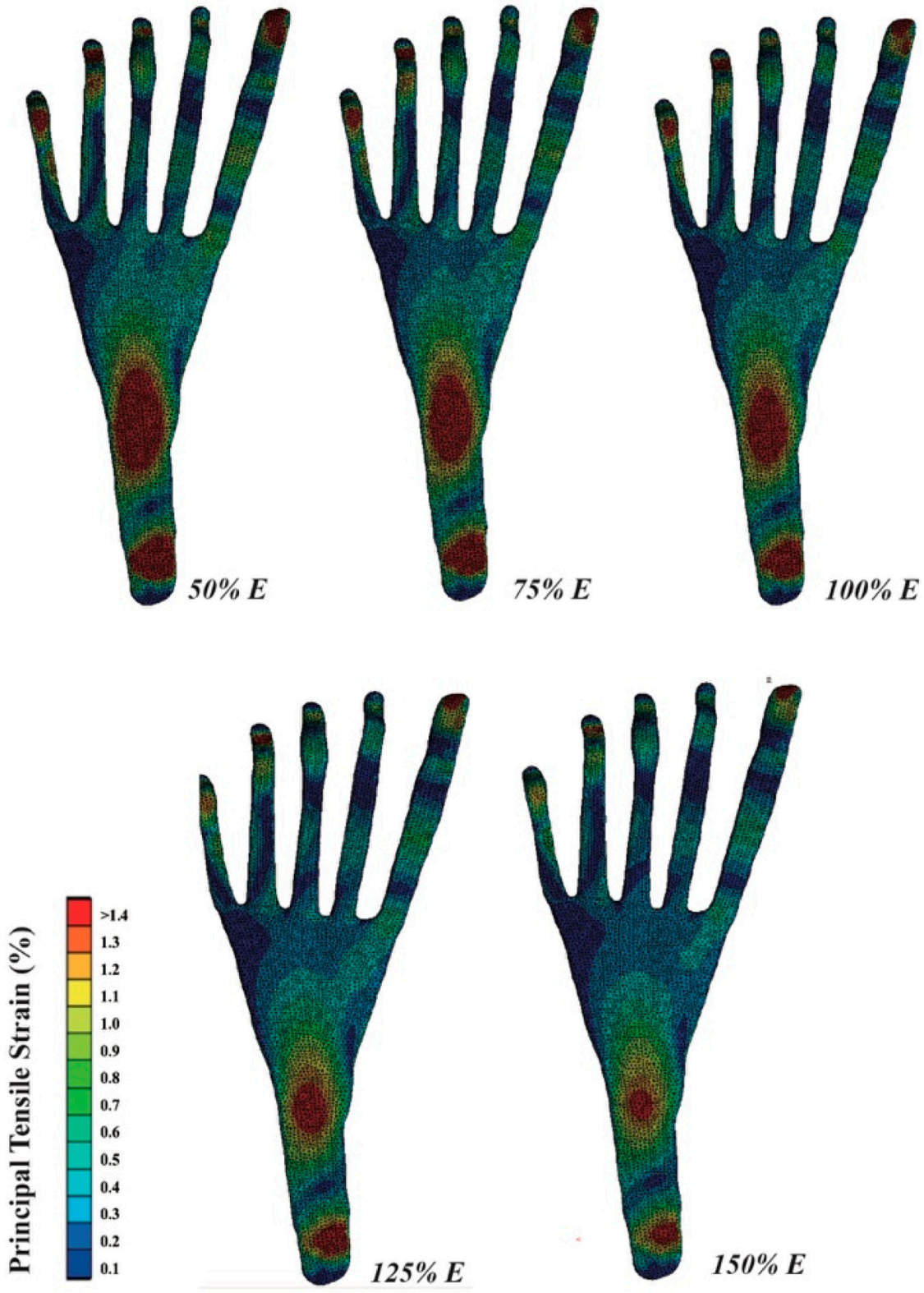

FIGURE 5
Graphic representation of plantar fascia strain distribution.

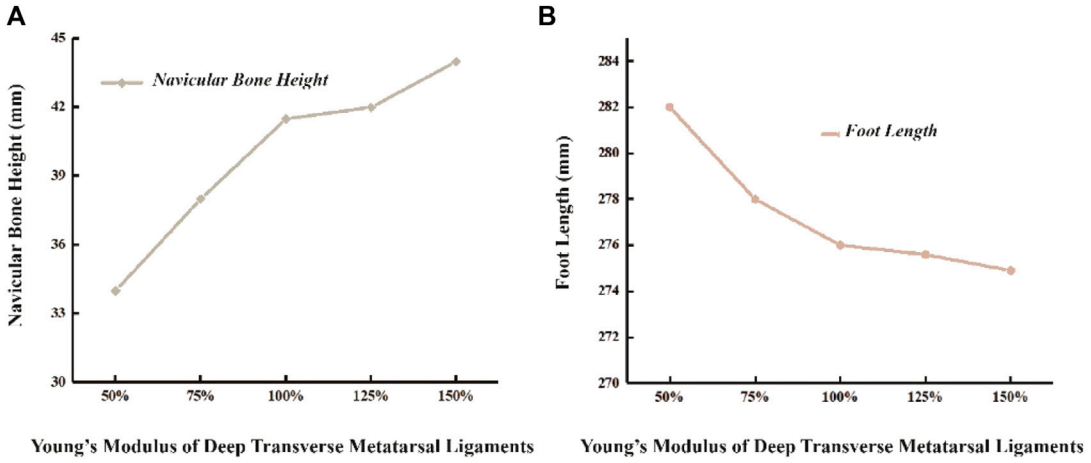

FIGURE 6
Effects of different DTML Young's modulus on changes in **(A)** navicular bone height and **(B)** foot length.

Conversely, augmenting the stiffness of the FTA can effectively alleviate peak strain on the PF, thereby mitigating the risk of PF injury attributable to excessive fatigue.

Research findings indicate that augmenting the Young's modulus of the DTML effectively prevents scaphoid collapse. A 100% increase in the Young's modulus of DTML from half the reference value (E = 270 MPa) results in a 54.1% reduction in scaphoid subsidence and a 33.1% increase in midfoot stiffness. Through a combination of experiments and FE simulations, this study presents, for the first time in a foot model, the crucial role of the FTA in maintaining arch shape and enhancing foot stiffness. Previous studies primarily inferred the contribution of the TA to foot stiffness through mechanical models and mathematical methods, estimating contributions ranging from 40% to 50% (Yawar et al., 2017; Venkadesan et al., 2020). The contribution of the FTA to foot stiffness fundamentally differs from that of the PF. Whether through the bow-string configuration or the windlass mechanism, both aim to increase tension of the PF to resist flattening of the bony arch under gravity. The inherent stiffness of the foot's arch structure, mediated by the joint capsule, key ligaments, and muscles, is augmented more directly by the FTA through alterations in lateral arch curvature, metatarsal bone expansion, and dorsalis curvature coupling. While medial arch support insoles have historically been favored for flat-footed patients and proven effective in symptom relief (Su et al., 2017; Wahmkow et al., 2017; Peng et al., 2021), this method may inadvertently increase pressure on the medial midfoot region, potentially leading to long-term discomfort. Additionally, excessive arch support from foot orthotics can impose undue von Mises stress on the foot-ankle complex's articular cartilage and ligaments (Su et al., 2017). The research suggests that enhancing arch stiffness through adjustments in FTA curvature and lateral expansion may offer a novel therapeutic avenue for treating flat feet, potentially mitigating the need for excessive arch support and minimizing associated risks of discomfort and structural strain in the foot-ankle complex.

As the Young's modulus of the DTML increases, von Mises stress on the first, second, and third metatarsals also increases, with a concentration of von Mises stress towards the center. Despite the reduction in peak forefoot pressure, the second and third metatarsal bones still experience elevated peak von Mises stress levels, which may partly explain why most metatarsal von Mises stress fractures occur in these regions (Sullivan et al., 1984). It is noteworthy that when the DTML Young's modulus reaches 150% of the reference value (E = 270 MPa), peak metatarsal von Mises stress shifts from the base of the third metatarsal to the dorsal side of the second metatarsal. This phenomenon of von Mises stress transfer may be attributed to alterations in the forces acting on the metatarsal bone. With low DTML stiffness, the maintenance of the FTA shape is compromised, leading to shear forces at the base of the metatarsal heads under the influence of gravity and ground reaction forces, thereby concentrating von Mises stress at the base of the third metatarsal bone. As the stiffness of DTML increases, the second metatarsal rises to become the apex of the FTA. Consequently, shear forces diminish, and the dorsal aspect of the metatarsal experiences downward pressure, resulting in a concentrated peak von Mises stress at the proximal end of the second metatarsal. In contrast, the peak von Mises stress on the fourth and fifth metatarsals decreases proportionally as pressure diminishes.

Further experimental research is necessary to ascertain whether alterations in von Mises stress due to DTML stiffness have a discernible impact on the risk of injury. This will help elucidate the biomechanical implications of foot structure and function under varying ligamentous stiffness conditions, contributing to a deeper understanding of foot mechanics and injury prevention strategies.

It is important to acknowledge potential limitations inherent in this study. Firstly, the reliance on data from a single individual for all simulations may raise concerns regarding the generalizability of the results to broader populations. The use of a single subject limits the ability to capture variations in foot biomechanics across different individuals (Wong et al., 2021). Follow-up studies should consider multiple human sample models for study (Zhan et al., 2024). Secondly, while this study examined internal effects through intra-test differences, it did not assess external effects, which may limit the generalizability of the research conclusions (Chen et al., 2020). In terms of materials, except the wrapped soft tissue, all

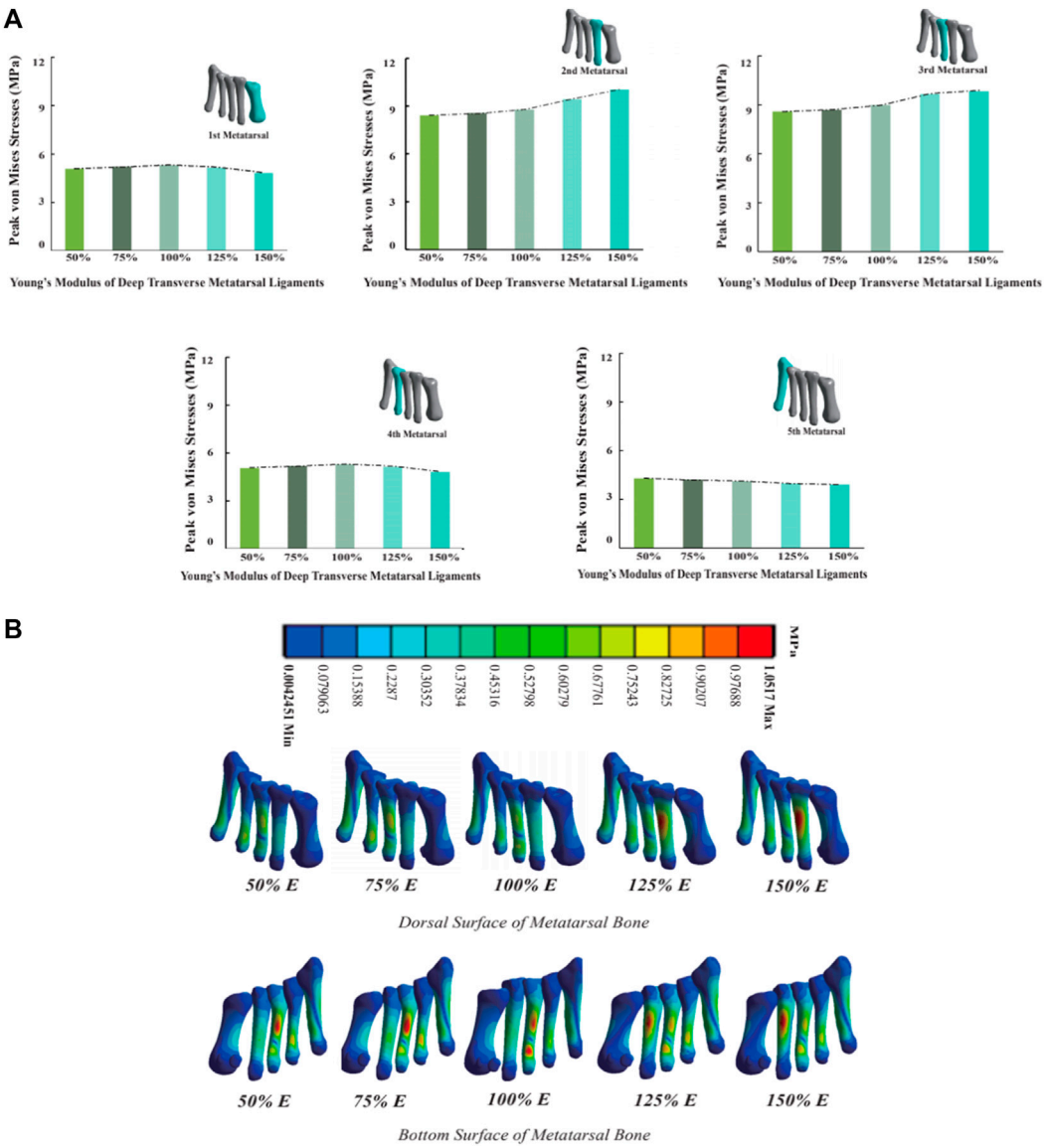

FIGURE 7
(A) Histogram and trend curve of the peak von Mises von Mises stress of the 1st-5th metatarsal bones; **(B)** Peak von Mises stress distribution cloud diagram of the 1st-5th metatarsal bones under the influence of different DTML Young's modulus.

materials are isotropic linear elastic materials. Bone is divided into cortical bone and cancellous bone. If a bone is defined as a linear elastic material, the stress value of the bone will increase, which requires simplifying some secondary tissues and structures of complex organisms, which cannot be completely accurate. In addition, due to the use of the FE method, the results are based on some assumptions, which may be reflected as potential limitations (Malakoutikhah et al., 2022). Therefore, improving the geometric similarity and accuracy of the FE model is an important direction of biomechanical FE analysis.

5 Conclusion

To our knowledge, this study represents the first attempt to investigate the influence of the transverse arch on midfoot stiffness by quantifying its impact on internal load-bearing characteristics of the foot. Through experimental validation, we have confirmed that augmenting the stiffness of the transverse arch effectively enhances the overall stiffness of the midfoot. As a result, we recommend considering methods aimed at preserving the shape and increasing the stiffness of the forefoot transverse arch when addressing symptoms associated with medial longitudinal arch collapse in the foot. Furthermore, preserving the shape and curvature of the TA could serve as a strategy in the design of running shoes to enhance the stiffness of the foot during running.

Data availability statement

The original contributions presented in the study are included in the article/Supplementary Material, further inquiries can be directed to the corresponding author.

Ethics statement

Ethical approval for this study was obtained from the Human Subjects Ethics Committee of Ningbo University (RAGH20230428), and all laboratory procedures adhered to the principles outlined in the Declaration of Helsinki.

Author contributions

LZ: Conceptualization, Formal Analysis, Investigation, Methodology, Project administration, Writing–original draft. QZ: Investigation, Methodology, Writing–original draft. YZ: Data curation, Formal Analysis, Investigation, Writing–original draft. TH: Conceptualization, Project administration, Writing–review and editing. YG: Conceptualization, Funding acquisition, Investigation, Project administration, Supervision, Writing–review and editing.

Funding

The author(s) declare that financial support was received for the research, authorship, and/or publication of this article. This study was sponsored by the Zhejiang Provincial Natural Science Foundation of China for Distinguished Young Scholars (LR22A020002), Zhejiang Provincial Natural Science Foundation (LTGY23H040003), Ningbo key R&D Program (2022Z196), Research Academy of Medicine Combining Sports, Ningbo (No. 2023001), the Project of NINGBO Leading Medical &Health Discipline (Nos 2022-F15 and 2022-F22), Ningbo Natural Science Foundation (20221JCGY010532 and 20221JCGY010607), Public Welfare Science & Technology Project of Ningbo, China (2023s145), and K. C. Wong Magna Fund in Ningbo University, Zhejiang Rehabilitation Medical Association Scientific Research Special Fund (ZKKY2023001).

Conflict of interest

The authors declare that the research was conducted in the absence of any commercial or financial relationships that could be construed as a potential conflict of interest.

The author(s) declared that they were an editorial board member of Frontiers, at the time of submission. This had no impact on the peer review process and the final decision.

Publisher's note

References

Belytschko, T., Andriacchi, T., Schultz, A., and Galante, J. (1973). Analog studies of forces in the human spine: computational techniques. *J. Biomechanics* 6, 361–371. doi:10.1016/0021-9290(73)90096-1

Bojsen-Møller, F. (1979). Calcaneocuboid joint and stability of the longitudinal arch of the foot at high and low gear push off. *J. Anat.* 129, 165–176.

Bramble, D. M., and Lieberman, D. E. (2004). Endurance running and the evolution of Homo. *nature* 432, 345–352. doi:10.1038/nature03052

Brilakis, E., Kaselouris, E., Xypnitos, F., Provatidis, C. G., and Efstathopoulos, N. (2012). Effects of foot posture on fifth metatarsal fracture healing: a finite element study. *J. foot ankle Surg.* 51, 720–728. doi:10.1053/j.jfas.2012.08.006

Buchbinder, R. (2004). Plantar fasciitis. *N. Engl. J. Med.* 350, 2159–2166. doi:10.1056/nejmcp032745

Chan, C. W., and Rudins, A. (1994). Foot biomechanics during walking and running. *Mayo Clin. Proc.* 69 (5), 448–461. doi:10.1016/S0025-6196(12)61642-5

Chen, T. L.-W., Wong, D. W.-C., Peng, Y., and Zhang, M. (2020). Prediction on the plantar fascia strain offload upon Fascia taping and Low-Dye taping during running. *J. Orthop. Transl.* 20, 113–121. doi:10.1016/j.jot.2019.06.006

Chen, T. L.-W., Wong, D. W.-C., Wang, Y., Lin, J., and Zhang, M. (2019). Foot arch deformation and plantar fascia loading during running with rearfoot strike and forefoot strike: a dynamic finite element analysis. *J. Biomechanics* 83, 260–272. doi:10.1016/j.jbiomech.2018.12.007

Cheung, J. T.-M., Zhang, M., and An, K.-N. (2004). Effects of plantar fascia stiffness on the biomechanical responses of the ankle–foot complex. *Clin. Biomech.* 19, 839–846. doi:10.1016/j.clinbiomech.2004.06.002

Cheung, J. T.-M., Zhang, M., Leung, A. K.-L., and Fan, Y.-B. (2005). Three-dimensional finite element analysis of the foot during standing—a material sensitivity study. *J. biomechanics* 38, 1045–1054. doi:10.1016/j.jbiomech.2004.05.035

Cho, J.-R., Park, S.-B., Ryu, S.-H., Kim, S.-H., and Lee, S.-B. (2009). Landing impact analysis of sports shoes using 3-D coupled foot-shoe finite element model. *J. Mech. Sci. Technol.* 23, 2583–2591. doi:10.1007/s12206-009-0801-x

Daentzer, D., Wülker, N., and Zimmermann, U. (1997). Observations concerning the transverse metatarsal arch. *Foot Ankle Surg.* 3, 15–20. doi:10.1046/j.1460-9584.1997.00039.x

Davies, M. (2005) "Muscles and fascia of the foot," in *Gray's anatomy: the anatomical basis of clinical practice*. London: Elsevier, 1509.

Desilva, J., Bonne-Annee, R., Swanson, Z., Gill, C., Sobel, M., Uy, J., et al. (2015). Midtarsal break variation in modern humans: functional causes, skeletal correlates, and paleontological implications. *Am. J. Phys. Anthropol.* 156, 543–552. doi:10.1002/ajpa.22699

Elftman, H., and Manter, J. (1935). The evolution of the human foot, with especial reference to the joints. *J. Anat.* 70, 56–67.

EL-Sallam, A., Bennamoun, M., Sohel, F., Alderson, J., Lyttle, A., and Rossi, M. (2013) "A low cost 3D markerless system for the reconstruction of athletic techniques," in 2013 IEEE workshop on applications of computer vision (WACV). (IEEE), 222–229.

Gefen, A. (2002). Stress analysis of the standing foot following surgical plantar fascia release. *J. biomechanics* 35, 629–637. doi:10.1016/s0021-9290(01)00242-1

Gelber, J. R., Sinacore, D. R., Strube, M. J., Mueller, M. J., Johnson, J. E., Prior, F. W., et al. (2014). Windlass mechanism in individuals with diabetes mellitus, peripheral neuropathy, and low medial longitudinal arch height. *Foot ankle Int.* 35, 816–824. doi:10.1177/1071100714538416

Gu, Y. D., Rong, M., Li, Z.-Y., Lake, M., and Ruan, G. (2012). Finite element analysis of deep transverse metatarsal ligaments mechanical response during landing. *Adv. Mater. Res.* 472, 2558–2561. doi:10.4028/www.scientific.net/amr.472-475.2558

Gu, Y., Ren, X., Li, J., Lake, M., Zhang, Q., and Zeng, Y. (2010). Computer simulation of stress distribution in the metatarsals at different inversion landing angles using the finite element method. *Int. Orthop.* 34, 669–676. doi:10.1007/s00264-009-0856-4

Gwani, A. S., Asari, M. A., and Ismail, Z. M. (2017). How the three arches of the foot intercorrelate. *Folia Morphol.* 76, 682–688. doi:10.5603/fm.a2017.0049

Heard-Booth, A. N. (2017). *Morphological and functional correlates of variation in the human longitudinal arch*.

Hicks, J. (1954a). The mechanics of the foot: II. The plantar aponeurosis and the arch. *J. Anat.* 88, 25–30.

Hicks, J. (1954b). The mechanics of the foot. II. The plantar aponeurosis and the arch. *J. Anat.* 88, 25–30.

Holowka, N. B., and Lieberman, D. E. (2018). Rethinking the evolution of the human foot: insights from experimental research. *J. Exp. Biol.* 221, jeb174425. doi:10.1242/jeb.174425

Huang, C.-K., Kitaoka, H. B., An, K.-N., and Chao, E. Y. (1993). Biomechanical evaluation of longitudinal arch stability. *Foot ankle* 14, 353–357. doi:10.1177/107110079301400609

Iaremenko, D. (1967). Methods of study of the" transverse arch" of the foot. *Ortop. Travmatol. i protezirovanie* 28, 20–24.

Irving, D. B., Cook, J. L., and Menz, H. B. (2006). Factors associated with chronic plantar heel pain: a systematic review. *J. Sci. Med. sport* 9, 11–22. doi:10.1016/j.jsams.2006.02.004

Kanatli, U., Yetkin, H., and Bolukbasi, S. (2003). Evaluation of the transverse metatarsal arch of the foot with gait analysis. *Archives Orthop. trauma Surg.* 123, 148–150. doi:10.1007/s00402-002-0459-7

Kasiri-Bidhendi, S., Fookes, C., Morgan, S., Martin, D. T., and Sridharan, S. (2015) "Combat sports analytics: boxing punch classification using overhead depthimagery," in 2015 IEEE international conference on image processing (ICIP). (IEEE), 4545–4549.

Ker, R., Bennett, M., Bibby, S., Kester, R., and Alexander, R. M. (1987). The spring in the arch of the human foot. *Nature* 325, 147–149. doi:10.1038/325147a0

Khuyagbaatar, B., Tumurbaatar, M., Tsenkherjav, K., Purevsuren, T., Shambaljamts, T., Kim, K., et al. (2024). Kinematic comparison of snatch and clean lifts in weightlifters using wearable inertial measurement unit sensors. *Phys. Activity Health* 8, 1–9. doi:10.5334/paah.306

Kido, M., Ikoma, K., Imai, K., Tokunaga, D., Inoue, N., and Kubo, T. (2013). Load response of the medial longitudinal arch in patients with flatfoot deformity: *in vivo* 3D study. *Clin. Biomech.* 28, 568–573. doi:10.1016/j.clinbiomech.2013.04.004

Kuo, A. D., Donelan, J. M., and Ruina, A. (2005). Energetic consequences of walking like an inverted pendulum: step-to-step transitions. *Exerc. sport Sci. Rev.* 33, 88–97. doi:10.1097/00003677-200504000-00006

Lemmon, D., Shiang, T.Y., Hashmi, A., Ulbrecht, J.S., and Cavanagh, P.R. (1997). The effect of insoles in therapeutic footwear—a finite element approach. *J. biomechanics* 30 (6), 615–620. doi:10.1016/s0021-9290(97)00006-7

Luger, E., Nissan, M., Karpf, A., Steinberg, E., and Dekel, S. (1999). Patterns of weight distribution under the metatarsal heads. *J. Bone & Jt. Surg. Br.* 81, 199–202. doi:10.1302/0301-620x.81b2.0810199

Malakoutikhah, H., DE Cesar Netto, C., Madenci, E., and Latt, L. D. (2022). Evaluation of assumptions in foot and ankle biomechanical models. *Clin. Biomech.* 100, 105807. doi:10.1016/j.clinbiomech.2022.105807

Masłoń, A., Golec, J., Szczygieł, E., Czechowska, D., and Golec, B. (2017). Assessment of the influence of jogging on the shape of female foot arches. *Ann. Agric. Environ. Med.* 24, 596–601. doi:10.5604/12321966.1230672

Morton, D. J. (1924a). Evolution of the longitudinal arch of the human foot. *JBJS* 6, 56–90.

Morton, D. J. (1924b). Mechanism of the normal foot and of flat foot: part i. *JBJS* 6, 368–386.

Nakai, K., Zeidan, H., Suzuki, Y., Kajiwara, Y., Shimoura, K., Tatsumi, M., et al. (2019). Relationship between forefoot structure, including the transverse arch, and forefoot pain in patients with hallux valgus. *J. Phys. Ther. Sci.* 31, 202–205. doi:10.1589/jpts.31.202

Pan, J.W., Ho, M.Y. M., Loh, R.B. C., Iskandar, M.N. S., and Kong, P.W. (2023). Foot morphology and running gait pattern between the left and right limbs in recreational runners. *Phys. Activity Health* 7, 43–52. doi:10.5334/paah.226

Peng, Y., Wong, D. W.-C., Chen, T. L.-W., Wang, Y., Zhang, G., Yan, F., et al. (2021). Influence of arch support heights on the internal foot mechanics of flatfoot during walking: a muscle-driven finite element analysis. *Comput. Biol. Med.* 132, 104355. doi:10.1016/j.compbiomed.2021.104355

Powell, D. W., Williams, D. B., Windsor, B., Butler, R. J., and Zhang, S. (2014). Ankle work and dynamic joint stiffness in high-compared to low-arched athletes during a barefoot running task. *Hum. Mov. Sci.* 34, 147–156. doi:10.1016/j.humov.2014.01.007

Ridola, C., and Palma, A. (2001). Functional anatomy and imaging of the foot. *Italian J. Anat. embryology= Archivio italiano di anatomia ed embriologia* 106, 85–98.

Schmidt, E., Lalevée, M., Kim, K. C., Carvalho, K. A. M., Dibbern, K., Lintz, F., et al. (2024). The role of the transverse arch in progressive collapsing foot deformity. *Foot Ankle Int.* 45, 44–51. doi:10.1177/10711007231205298

Siegler, S., Block, J., and Schneck, C. D. (1988). The mechanical characteristics of the collateral ligaments of the human ankle joint. *Foot ankle* 8, 234–242. doi:10.1177/107110078800800502

Sullivan, D., Warren, R. F., Pavlov, H., and Kelman, G. (1984). Stress fractures in 51 runners. *Clin. Orthop. Relat. Research®* 187, 188–192. doi:10.1097/00003086-198407000-00028

Su, S., Mo, Z., Guo, J., and Fan, Y. (2017). The effect of arch height and material hardness of personalized insole on correction and tissues of flatfoot. *J. Healthc. Eng.* 2017, 1–9. doi:10.1155/2017/8614341

Susman, R. L. (1983). Evolution of the human foot: evidence from Plio-Pleistocene hominids. *Foot ankle* 3, 365–376. doi:10.1177/107110078300300605

Takahashi, K. Z., Gross, M. T., VAN Werkhoven, H., Piazza, S. J., and Sawicki, G. S. (2016). Adding stiffness to the foot modulates soleus force-velocity behaviour during human walking. *Sci. Rep.* 6, 29870. doi:10.1038/srep29870

Tao, K., Ji, W.-T., Wang, D.-M., Wang, C.-T., and Wang, X. (2010). Relative contributions of plantar fascia and ligaments on the arch static stability: a finite element study. *Biomed Tech.* 55 (5), 265-271. doi:10.1515/BMT.2010.041

Venkadesan, M., Yawar, A., Eng, C. M., Dias, M. A., Singh, D. K., Tommasini, S. M., et al. (2020). Stiffness of the human foot and evolution of the transverse arch. *Nature* 579, 97–100. doi:10.1038/s41586-020-2053-y

Wahmkow, G., Cassel, M., Mayer, F., and Baur, H. (2017). Effects of different medial arch support heights on rearfoot kinematics. *PloS one* 12, e0172334. doi:10.1371/journal.pone.0172334

Wang, B., Guss, A., Chalayon, O., Bachus, K. N., Barg, A., and Saltzman, C. L. (2015). Deep transverse metatarsal ligament and static stability of lesser metatarsophalangeal joints: a cadaveric study. *Foot ankle Int.* 36, 573–578. doi:10.1177/1071100714563310

Wearing, S. C., Smeathers, J. E., Urry, S. R., Hennig, E. M., and Hills, A. P. (2006). The pathomechanics of plantar fasciitis. *Sports Med.* 36, 585–611. doi:10.2165/00007256-200636070-00004

Weishaupt, D., Treiber, K., Jacob, H. A., Kundert, H. P., Hodler, J., Marincek, B., et al. (2002). MR imaging of the forefoot under weight-bearing conditions: position-related changes of the neurovascular bundles and the metatarsal heads in asymptomatic volunteers. *J. Magnetic Reson. Imaging* 16, 75–84. doi:10.1002/jmri.10130

Williams, D. S., and Mcclay, I. S. (2000). Measurements used to characterize the foot and the medial longitudinal arch: reliability and validity. *Phys. Ther.* 80, 864–871. doi:10.1093/ptj/80.9.864

Wilzman, A. R., Tenforde, A. S., Troy, K. L., Hunt, K., Fogel, N., Roche, M. D., et al. (2022). Medical and biomechanical risk factors for incident bone stress injury in collegiate runners: can plantar pressure predict injury? *Orthop. J. Sports Med.* 10, 232596712211047. doi:10.1177/23259671221104793

Wong, D. W.-C., Chen, T. L.-W., Peng, Y., Lam, W.-K., Wang, Y., Ni, M., et al. (2021). An instrument for methodological quality assessment of single-subject finite element analysis used in computational orthopaedics. *Med. Nov. Technol. Devices* 11, 100067. doi:10.1016/j.medntd.2021.100067

Xiang, L., Gu, Y., Shim, V.B., Yeung, T., Wang, A., and Ferandez, J. (2024). A hybrid statistical morphometry free-form deformation approach to 3D personalized foot-ankle models. *J. biomechanics* 168, 112120. doi:10.1016/j.jbiomech.2024.112120

Xu, D., Zhou, H., Quan, W., Jiang, X., Liang, M., Li, S., et al. (2024). A new method proposed for realizing human gait pattern recognition: inspirations for the application of sports and clinical gait analysis. *Gait Posture* 107, 293–305. doi:10.1016/j.gaitpost.2023.10.019

Yawar, A., Korpas, L., Lugo-Bolanos, M., Mandre, S., and Venkadesan, M. (2017). Contribution of the transverse arch to foot stiffness in humans. *arXiv*.

Yu, G., Fan, Y., Fan, Y., Li, R., Liu, Y., Antonijevic, D., et al. (2020). The role of footwear in the pathogenesis of hallux valgus: a proof-of-concept finite element analysis in recent humans and homo naledi. *Front. Bioeng. Biotechnol.* 8, 648. doi:10.3389/fbioe.2020.00648

Yu, J., Cheung, J. T.-M., Fan, Y., Zhang, Y., Leung, A. K.-L., and Zhang, M. (2008). Development of a finite element model of female foot for high-heeled shoe design. *Clin. Biomech.* 23, S31–S38. doi:10.1016/j.clinbiomech.2007.09.005

Zelik, K. E., and Kuo, A. D. (2010). Human walking isn't all hard work: evidence of soft tissue contributions to energy dissipation and return. *J. Exp. Biol.* 213, 4257–4264. doi:10.1242/jeb.044297

Zhang, Q., Zhang, Y., Huang, J., Teo, E. C., and Gu, Y. (2022). Effect of displacement degree of distal chevron osteotomy on metatarsal stress: a finite element method. *Biol. (Basel)* 11, 127. doi:10.3390/biology11010127

Zhan, S., Jiang, D., Hu, Q., Wang, M., Feng, C., Jia, W., et al. (2024). Single-plane osteotomy model is inaccurate for evaluating the optimal strategy in treating vertical femoral neck fractures: a finite element analysis. *Comput. Methods Programs Biomed.* 245, 108036. doi:10.1016/j.cmpb.2024.108036

frontiers | Frontiers in Bioengineering and Biotechnology

TYPE Original Research
PUBLISHED 12 July 2024
DOI 10.3389/fbioe.2024.1418047

OPEN ACCESS

EDITED BY
Ge He,
University of Wisconsin–Milwaukee,
United States

REVIEWED BY
Claudio M. Garcia-Herrera,
Universidad de Santiago de Chile, Chile
Bitian Wang,
Shandong University, China

*CORRESPONDENCE
Rong Liu,
rong.liu@polyu.edu.hk

RECEIVED 15 April 2024
ACCEPTED 17 June 2024
PUBLISHED 12 July 2024

CITATION
Shi Y, Ye C and Liu R (2024), Three-dimensional dynamic homogenous modeling: The biomechanical influences of leg tissue stiffness on pressure performance of compression biomedical therapeutic textiles.
Front. Bioeng. Biotechnol. 12:1418047.
doi: 10.3389/fbioe.2024.1418047

Three-dimensional dynamic homogenous modeling: The biomechanical influences of leg tissue stiffness on pressure performance of compression biomedical therapeutic textiles

Yu Shi[1,2], Chongyang Ye[1] and Rong Liu[1,2]*

[1]School of Fashion and Textiles, The Hong Kong Polytechnic University, Hong Kong Special Administrative Region (SAR), Kowloon, Hong Kong SAR, China, [2]Laboratory for Artificial Intelligence in Design, Hong Kong Science Park, Kowloon, Hong Kong SAR, China

Patient compliance and therapeutic precision of compression textiles (CTs) are frequently limited by the inaccurate pressure distributions along biological bodies in physical-based compression therapy. Therefore, the biomechanical influences of physiological tissue material characteristics of lower extremities on compression generations of CTs need to be explored systematically to improve pressure management efficacy. In this study, we developed three-dimensional (3D) homogenous finite element (FE) CT-leg systems to qualitatively compare the pressure diversities along lower limbs with different biomaterial tissue properties under each external compression level. Simultaneously, through the obtained leg circumferential displacement, a contact analysis model was applied to quantitatively explore the impact mechanisms of soft leg indentations on the pressure performance of CTs. Based on the experimental validation study, the proposed FE systems could be efficiently utilized for compression performance prediction (error ratio: 7.45%). Through the biomechanical simulation and theoretical calculations, the tissue stiffness characteristics of applied bodies showed significant correlations ($p < 0.05$) with the body circumferential displacements but no correlations ($p > 0.05$) with pressure delivery differences of CTs. This study facilitates the pressure fit design principle and leg mannequin material selection guidance for the development and experimental assessment of CTs. It also provides effective simulation methods for pressure prediction and property parametric optimization of compression materials.

KEYWORDS

biomechanical analysis, numerical simulation, tissue stiffness characteristics, medical compression textiles, pressure supply

1 Introduction

Functional textile-based compression interventions are generally considered as acceptable and effective therapeutic modalities for venous ulceration, chronic venous insufficiency, and deep vein thrombosis (Liu et al., 2017; Kankariya et al., 2021; Kankariya, 2022). By applying controllable fabric tensions during wearing for an

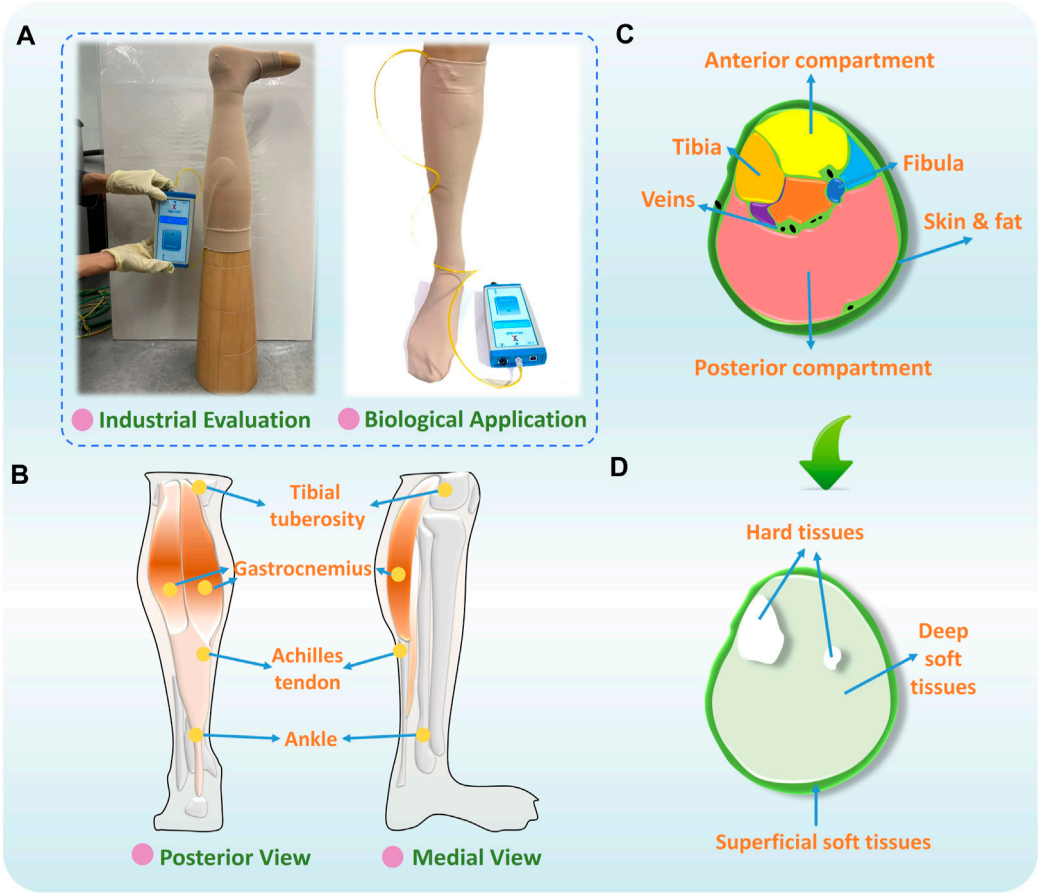

FIGURE 1
(A) Quality evaluation and bio-application of CTs, **(B)** physiological structure, **(C)** sectional segmentation, and **(D)** main compositions of human lower extremity.

extended time, elastic compression textiles (CTs) positively generate external pressure dosages along the required bodies for compression therapy (Barhoumi et al., 2020). The pressure generation/performance of CTs indicate the generated pressure magnitudes between the interfaces of body skin surface and CT fabrics. Through population-based studies, although the prevalence of venous diseases has increased approximately from 8.9% to 16.5% (Gong et al., 2020; Kim et al., 2021), patient compliance is still only 25.6% (Ziaja et al., 2011), which is limited by the inaccurate pressure distributions and discomfort when wearing CTs.

The pressure diversities are the pressure value differences generated by identical CTs among various applied bodies. In the production process, the fabricated commercial CTs are necessarily measured by using standard-sized leg mannequins (i.e., wooden leg models) for quality control estimations (Figure 1A). Therefore, insufficient compression deliveries are frequently generated, which are caused by the cross-sectional shape profile and material property discrepancies between the applied leg models and biological bodies (Li et al., 2020). Due to individual physiological diversity and anatomic structural differences (Liu et al., 2013), including morphological irregularities and heterogeneous tissue characteristics (Ghosh et al., 2008; Liu et al., 2018a), the medical efficiency and user adherence of readymade CTs have been limited by inappropriate pressure generation in practical bio-applications. In compression therapy, the interfacial pressure distributions determine the clinical effectiveness of CT materials (Kankam et al., 2018). Thus, the scientific biomechanical analysis of the impact of lower limb individual diversity on compression delivery could improve the pressure fitness and therapeutic precision of CTs.

For lower extremity morphological variations, research workers (Liu et al., 2018b) have explored the impacting mechanisms of body sectional irregularities on functional compression performances of CTs. They found that the cross-sectional irregular applied leg patterns led to uneven pressure magnitudes caused by the non-constant fabric stretching strains. For lower limb material tissues, based on the leg's physiological structure (Figure 1B) and sectional segmentation (Figure 1C), three components with varying composition have been identified, including the superficial tissues (i.e., adipose tissues, skin, and veins), deep (i.e., muscles, tendons, and veins) soft tissues (STs), and hard tissues (i.e., tibia and fibula) (Figure 1D) (Cieślak et al., 2016). Therefore, except for the rigid support (i.e., bones), to replace traditional rigid mannequin materials and improve the accuracy of experimental pressure estimation, in previous studies, research workers have selected alternative ST materials, such as silicone and flexible

polyurethane foam (Yu et al., 2004; Frauziols et al., 2017; Li et al., 2020). Using these, research workers have developed substitutable leg models for the design and interfacial pressure testing of CTs. Nevertheless, to date, there is a lack of research fundamentally exploring the effects of biomaterial mechanical stiffness of lower limbs on pressure distributions of CTs. The design guidance and leg mannequin selection criteria need to be established for the biodevelopment and pressure assessment of compression functional fabrics.

Based on non-linear mechanical behaviors, the applied strain energy functions of biological STs can be commonly defined by neo-Hookean, Mooney–Rivlin, first-order Ogden, or Fung material models, *etc*. (Heydon, 2011; Parker, 2016). For digitalized property investigations, the ST constitutive parameters were measured by direct identification experiments through ultrasound shear wave elastography (Ranger et al., 2023; Frauziols et al., 2013; Mo et al., 2022; Affagard et al., 2014). Furthermore, the computational finite element (FE) simulations and inverse methodologies were also applied to numerically quantify leg ST biomaterial properties. Among them, the subjects' legs were reconstructed through reverse engineering technologies by employing the magnetic resonance imaging or computed tomography scanning (Avril et al., 2011; Dubuis et al., 2012; Lu et al., 2021). Therefore, through the aforementioned determination approaches and obtained mechanical parameters of STs, the stress and strain distributions, interfacial pressure mapping, and hemodynamic response could be visually simulated through FE biomechanical approaches (Liu et al., 2019; Nemati and Shojaei, 2019; Han et al., 2021). For instance, based on the imaging-based reconstruction of the subjects' lower limbs, Ye and Liu. (2020) constructed FE fluid–solid complex interaction systems to analyze the biomechanical properties of veins and STs under CT external compressions. Dubuis et al. (2012), Avril et al. (2011), and Rohan et al. (2015) also examined the pressure transmissions within the ST by simulated FE models to improve the understanding of working mechanisms of CTs. However, the previously proposed FE models were established for patient-specific mechanical analysis with their individual biomaterial tissue characteristics. Limited studies have investigated the pressure performance diversities caused by lower limb stiffness variations through parametric comparisons.

Based on characterization studies, ST stiffness values possibly vary due not only to the studied anatomical locations and muscle measured states but also to individual characteristics, such as gender (Morse, 2011), aging (Ochi et al., 2010), disease progression, occupation (Hobara et al., 2010), and rehabilitation status (Le et al., 2017). Additionally, research workers (Sangpradit et al., 2011; Marinopoulos et al., 2020) have explored the interactions between the external forces and positive exerting devices among soft bodies with varying material characteristics. Nevertheless, the garment-based pressure diversities caused by the mechanical ST properties of bio-legs still remain controversial. Thus, the qualitative influencing mechanisms on, and quantitative relationships of various biomaterial parameters to, pressure generation diversities of compression fabrics need to be explored systematically, to facilitate the material design, pressure dosage selection, and compression prediction of CTs.

Therefore, the main objective of this study was to systematically investigate the biomechanical influences of tissue stiffness of lower extremities on compression generations of CTs for the improvement of pressure management efficacy. The independent leg stiffness influences on pressure performances of CTs were systematically investigated through FE CT-leg simulation modeling, theoretical analysis, and experimental validation studies. For our main research contribution, the compared results could facilitate the scientific biodesign of pressure dosages for CTs and promote model material selection for pressure experimental evaluations. The constructed 3D homogenous FE CT-leg systems also achieve effective visualized assessment and pressure prediction for user-oriented applications.

2 Materials and methods

To investigate the biomechanical influences of lower limb ST stiffness on pressure performance of CTs, this study adopted FE modeling, theoretical analysis, and experimental validation, respectively. As illustrated in Figure 2, the 3D FE homogenous modeling system was constructed through the reconstructed entity legs established by 3D body scanning and reverse engineering technologies. The acceptability of proposed FE models was examined by 3D printing legs with controlled lower limb morphological shapes and identical material characteristics. Then, the pressure performance diversities between legs with varied tissue stiffness were qualitatively compared through the FE CT-leg systems by inputting varying biomaterial parameters. Simultaneously, the theoretical contact analysis model was constructed to quantitatively explore the impacting mechanisms of tissue stiffness on pressure performances of CTs by inputting leg circumferential deformation data. Finally, the experimental validations were adopted to validate the applicability and accuracy of the outcomes and findings of the present study.

2.1 Subject information

Three subjects (code: S1, S2, and S3) with various genders, ages, and leg shape profiles participated voluntarily for lower extremity modeling constructions and experimental investigations. The basic individual information and body mass index (BMI) of each subject are as follows: i) S1: male, age: 32 years old, height: 1.80 m, BMI: 17.7 kg/m^2; ii) S2: female, age: 50 years old, height: 1.57 m, BMI: 25.6 kg/m^2; and iii) S3: male, age: 61 years old, height: 1.60 m, BMI: 22.2 kg/m^2. The study protocol was approved by the Human Subjects Ethics Sub-committee of The Hong Kong Polytechnic University.

2.2 Preparation and physical-mechanical properties of CTs

In practical clinical treatments, pressure magnitudes exerted by CTs are classified as different compression levels (Figure 3A) through the standard of Germany RAL-GZ 387 (Medical Compression Hosiery Quality Assurance) by varying textile material stiffness. Thus, according to the measurement guidance (Figure 3B) and determined subject body dimensions (Figure 3C), different compression knitted fabrics were designed to achieve the

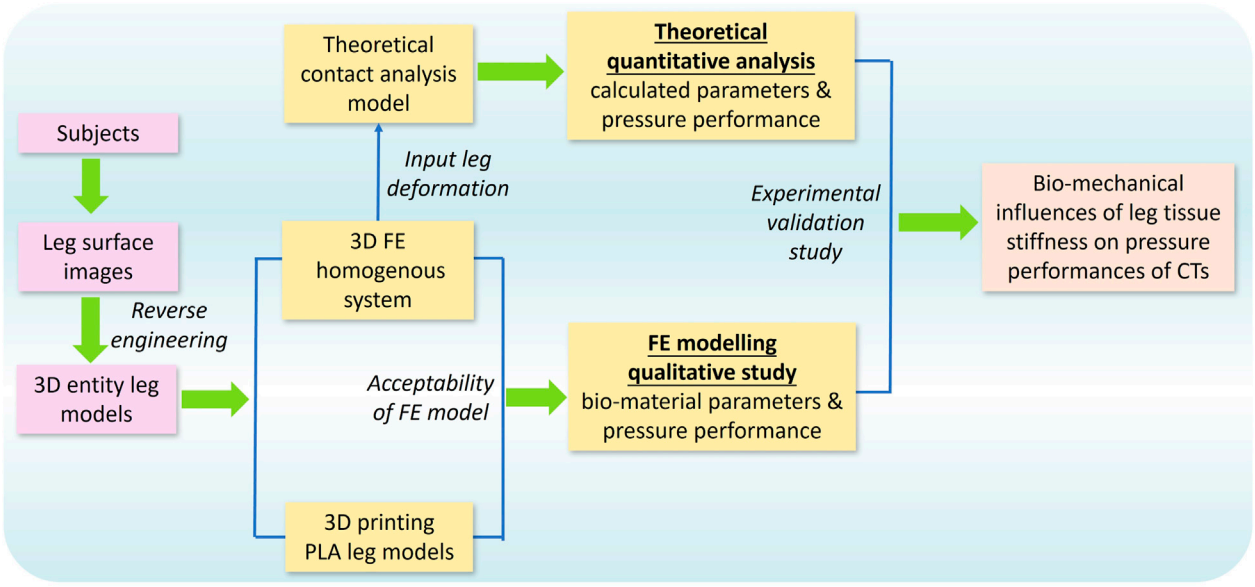

FIGURE 2
Framework of the proposed study.

standardized pressure magnitudes for the light (class: I) and strong (class: III) levels of compression generation. As shown in Figure 3D, Lycra-based elastic yarn materials with various linear densities were adopted as the ground and inlay yarn components according to the designed 1 × 1 laid-in knitted loop pattern. By adjusting the knitting yarn combinations and machinery parameters, tubular CTs with diverse physical and mechanical properties were prepared using the LONATI LA-45 ME 3D seamless knitting machine (Francesco Lonati, Brescia, Italy).

For experimental physical tests, the fabric circumferential radius (R_F), longitudinal lengths (L_F), fabric thickness (h), and mass densities (MD) of CTs were obtained according to the standards of ASTM D3774, ASTM D1777, and ASTM D 3776/D 3776M-09a, respectively. For mechanical tensile behaviors, the elastic Young's modulus along the course (E_F) and wale (E_{Fy}) stretching directions and Poisson's ratio (v_F) were tested by utilizing the Instron 4,411 universal tension tester (Norwood, MA, USA) referred to the ASTM D2256 standard. For stretching tests, to facilitate the appropriate sample size, the knitted samples (width: 50 mm and length: 75 mm) were prepared by the same yarn-machinery settings with the corresponding CT fabrics. The samples were fixed by the two tester clamps and thus were stretched from the initial tension-free state (0%) to the maximum final stretch ratio (100%) at a constant extension velocity of 300 mm/min. Young's moduli values along various loading directions were calculated by $E_{F\text{-}Fy} = F_T/bh\varepsilon$ (where F_T is the fabric tension force, h and b are the fabric thickness and length, respectively, and ε is the fabric extension stretched by the corresponding tension force). Thus, through the measured fabric h and b data, F_T values under the corresponding fabric strain state (ε; 0%–100%) were recorded by the Instron device, and then $E_{F\text{-}Fy}$ could be obtained by the averaged calculated results with different stretching strains. The typical stress–strain curves of CT samples are shown in Figure 3E. Fabric shear modulus (G_F) was obtained using the Kawabata (KES-FB3) pure shear testing assessment system. The applied CTs and corresponding measured fabric properties are listed in Table 1.

2.3 Development of 3D printing rigid leg models

To obtain the lower body surface images for further model reconstruction and 3D printing manufacturing, the handheld professional EinScan-Pro 2X PLUS 3D Scanner (Shining 3D Tech. Co., Ltd. Hangzhou, China) and Solid Edge Shining 3D Edition software were applied with high scan accuracy (scan precision was 0.04 mm) and efficiency (scan speed was 1,500,000 dots/s) (Amornvit and Sanohkan, 2019). Based on the LED light source, participants were requested to stand steadily with torso separation at the instructed boundary pattern markers (Figure 4A). Then, by stably moving and operating the scanner 360° around each subject, the entire lower body surface was produced in cloud points for data acquisition. After body capturing, the initial scanned files were saved in a stereolithography (STL) format and preliminarily processed using the Geomagic Studio 2014 (64 bit) software (Raindrop Geomagic, Research Triangle Park, NC, USA) for the elimination of irrelevant extra scan points, reduction of noises, repair of model holes, and orientation fixation. Then, the 3D entity models were reconstructed by using reverse engineering technology through the SpaceClaim Direct Modeler (SCDM; ANSYS, Pennsylvania, Pittsburgh, USA) and CAD (computer-aided design) systems (Shuxian et al., 2005; Zhan et al., 2011).

After entity model reconstruction, as shown in Figure 4B, rigid leg models were fabricated by the advanced large scale of FDM (fused deposition modeling) Creatbot D600 Pro 3D printer (build volume: 600 mm^3, precision: 0.05 mm). The sustainable filament materials of poly lactic acid (PLA) are commonly utilized as raw materials in bioprinting, biomedical, tissue engineering, and smart textile industries, *etc.* (Tümer and Erbil, 2021; Plesec et al., 2023).

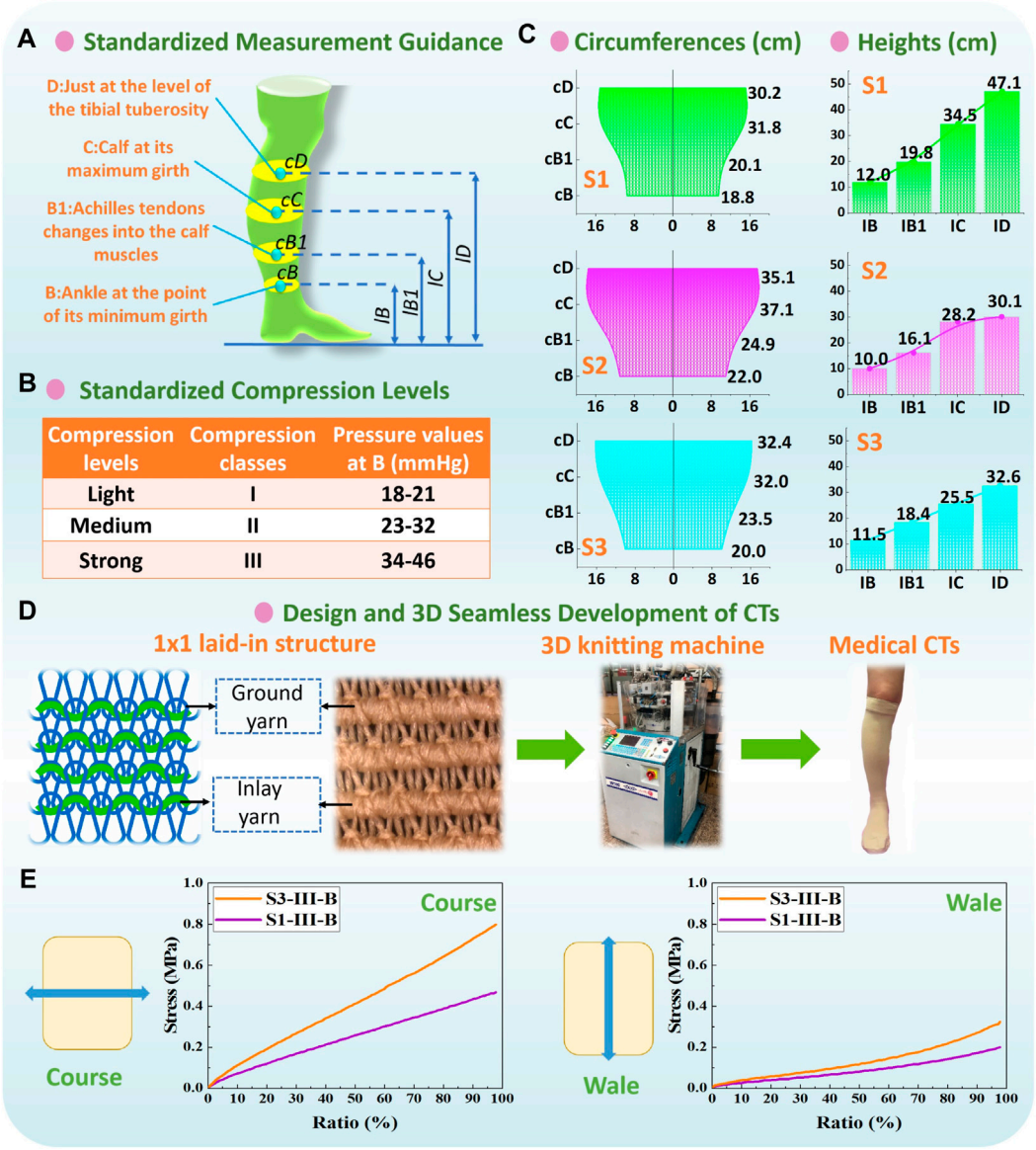

FIGURE 3
(A) Measurement guidance and **(B)** compression classification by Germany RAL-GZ 387 standard. **(C)** Circumferences and heights of each recruited subject legs, and **(D)** applied 1 × 1 laid-in knitting loop pattern and 3D seamless knitting fabrication. **(E)** Typical stress–strain curves of CT samples from stretching tests.

Thus, PLA filaments were applied as the printing materials for replacing the rigid wood lower limb mannequins' *in vitro* compression measurements due to PLA's excellent mechanical properties (tensile strength: 46.8 MPa; compressive strength: 17.9 MPa; Young's modulus: 3.0 GPa) (Gregor et al., 2017). By using 3D printing manufacturing, three PLA-based rigid leg models for each subject with various morphological and geometric characteristics were developed for further pressure estimations.

2.4 Determination of ST stiffness properties

To independently investigate the impact mechanisms of various ST stiffness values on pressure performances of CTs, the ST mechanical properties of human lower extremities (below the knee) were referred from relevant previous literature works measured by various protocols and subject groups (Dubuis et al., 2012; Dubuis et al., 2013; Frauziols et al., 2013; Han et al., 2021). The muscle compositions were determined as the major studied components accounting for the proportion ranging from approximately 85%–94% (Figure 4C) (Ye et al., 2023). Thus, in this study, the digitalized Young's modulus (E_s) range of leg ST (muscle) stiffness was 0.0014–0.0030 MPa and divided into three levels (LS-1: 0.0014 MPa, LS-2: 0.0022 MPa, and LS-3: 0.0030 MPa) for further comparisons in the FE modeling system.

Moreover, to obtain the exact ST stiffness values of studied subjects, the real-time shear wave elastography (SWE) was performed using Aixplorer® MultiWave ultrasound system

TABLE 1 Measured fabric properties of CT knitted samples.

Subject	Class	Leg part	Physical property				Mechanical property			
			R_F (cm)	L_F (cm)	h (mm)	MD (kg/m^3)	E_F (MPa)	E_{Fy} (MPa)	v_F	G_F (MPa)
S1	I	B	2.52	6.0	0.66	479.3	0.35	0.16	0.21	0.14
		B1	2.79	6.5	0.67	468.2	0.33	0.15	0.21	0.14
		C	3.57	7.5	0.68	481.3	0.37	0.21	0.20	0.17
		D	3.50	7.0	0.67	480.6	0.38	0.20	0.20	0.16
	III	B	2.42	6.0	0.62	503.6	0.42	0.14	0.22	0.17
		B1	2.79	6.5	0.64	481.5	0.41	0.17	0.23	0.17
		C	3.25	7.5	0.66	479.3	0.35	0.16	0.21	0.14
		D	3.22	7.0	0.68	468.2	0.33	0.15	0.21	0.14
S2	I	B	2.84	5.5	0.69	484.7	0.38	0.21	0.21	0.14
		B1	3.22	6.0	0.67	468.2	0.37	0.15	0.21	0.15
		C	3.57	6.5	0.67	486.0	0.38	0.21	0.20	0.15
		D	3.50	6.0	0.66	485.4	0.37	0.20	0.19	0.14
	III	B	2.83	5.5	0.62	503.7	0.45	0.19	0.23	0.18
		B1	2.87	6.0	0.67	484.9	0.38	0.22	0.20	0.15
		C	3.22	6.5	0.68	468.2	0.34	0.15	0.20	0.14
		D	3.25	6.0	0.66	480.1	0.33	0.16	0.20	0.14
S3	I	B	2.79	5.5	0.68	468.2	0.33	0.15	0.21	0.14
		B1	3.22	6.0	0.68	484.4	0.38	0.21	0.21	0.15
		C	3.50	7.0	0.67	487.3	0.38	0.21	0.20	0.16
		D	3.57	6.5	0.67	486.3	0.38	0.21	0.21	0.15
	III	B	2.80	5.5	0.64	532.7	0.76	0.27	0.25	0.30
		B1	2.83	6.0	0.62	503.6	0.42	0.18	0.22	0.17
		C	3.25	7.0	0.66	479.3	0.35	0.16	0.21	0.14
		D	3.22	6.5	0.68	468.2	0.33	0.15	0.21	0.14

(Supersonic Imagine, Aix-en-Provence, France), to provide the quantitative color-coded map (rectangular box: 1 cm × 1.5 cm) of lower limb tissue elasticity on an anatomic standard B-Mode image (Figure 4D). To ensure elasticity mapping with the SWE sequence, the parameters were set as the musculoskeletal preset and tissue tuner at 1,540 m/s with the resolution mode enabled. For each subject, the depth setting was fixed at 2 cm to display the entire muscle during examination (Ternifi et al., 2020). For physical testing, two leg regions (at the ankle and calf) with four directions (anterior, posterior, medial, and lateral) were measured using a SuperLinear™ SL10-2 transducer array (element number: 192, bandwidth: 2–10 MHz). Then, E_s for each subject was determined using the calculated average values (listed in Table 2) through Eq. 1.

$$E_S = 3\rho_m v^2, \quad (1)$$

where ρ_m is the muscle density (1,000 kg/m^3) and v is the shear wave velocity range of 0–7.7 m/s (Dubois et al., 2018).

2.5 Construction of 3D FE homogenous CT-leg systems

First, the geometric models of FE-based CTs were constructed according to the specific physical dimensions (R_F and L_F; Table 1) of actual fabrics by adopting ANSYS Workbench Design Modeler software (v19.2, ANSYS, Pennsylvania, Pittsburgh, USA). To ensure the CTs could slide along the leg longitudinal direction, the centers of the cross-sectional leg and CT models were coincident to achieve an alignment by adjusting the model positions. The knitted CTs were commonly assumed as the orthotropic elastic materials (Ye and Liu, 2020), and the inputting fabric property parameters of MD, E_{Fx}, E_{Fy}, v_F, and G_F were based on the experimental material data (Table 1). In the compression analysis, the neo-Hookean model was typically used for mechanical analysis and pressure prediction, and the STs were basically modeled as hyperelastic, incompressible, homogenous,

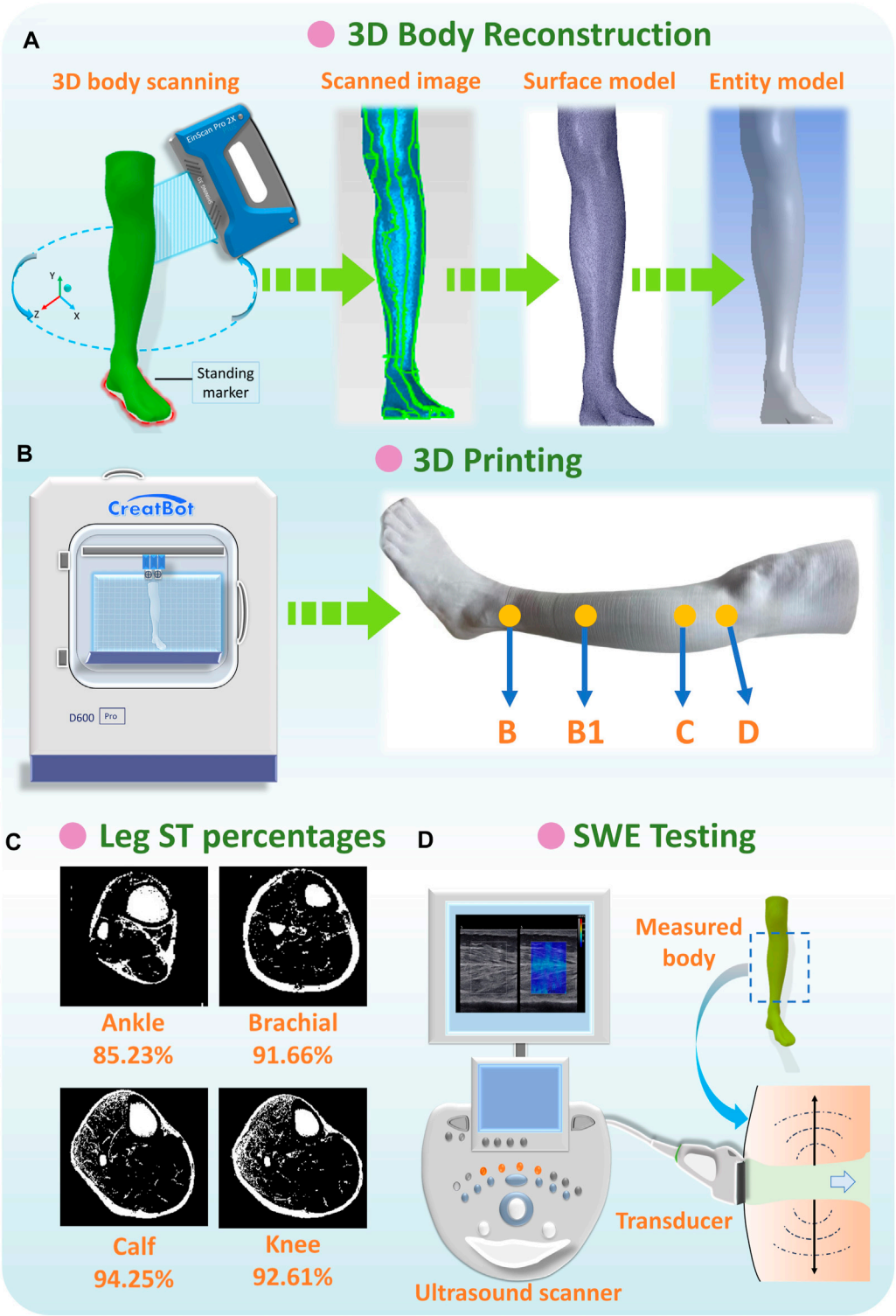

FIGURE 4
(A) Anthropometric data acquisition and reconstruction of lower limbs, **(B)** 3D printing of rigid PLA-based leg models, **(C)** ST percentages of each leg position, and **(D)** SWE testing for lower extremity.

and isotropic materials. Additionally, the constitutive equation is as follows (Eq. 2) (Dubuis et al., 2012; Arnold et al., 2023):

$$A = C_{10}\left(\overline{I_1} - 3\right) + D_1\left(J - 1\right)^2, \quad (2)$$

where A denotes the strain energy density, $\overline{I_1}$ is the first deviatoric strain variant, and J is the Jacobian determinant of the deformation gradient (for the incompressible materials, the J value is 1) (Dubuis et al., 2012; Ye et al., 2023). C_{10} and D_1

TABLE 2 Measured E_S through the SWE testing.

Subject code	Leg position	E_S (MPa)	Mean E_S (MPa)
S1	B	0.001975	0.002040
	C	0.002145	
S2	B	0.002678	0.002976
	C	0.003273	
S3	B	0.003700	0.002750
	C	0.001800	

can be expressed as below under a linear elastic condition, as follows: (Eq. 3)

$$C_{10} = \frac{S}{2}, D_1 = \frac{B}{2}, \tag{3}$$

where S and B are the shear and bulk moduli values, respectively.

Thus, for the lower limbs, the mechanical properties of 3D rigid and bio-soft legs were obtained through Young's modulus of PLA printing material (3 GPa) and biological ST stiffness (S1-0.0034 MPa; S2-0.0050 MPa; S3-0.0046 MPa), respectively. Then, as shown in Figure 5A, to simulate the practical wearing process and

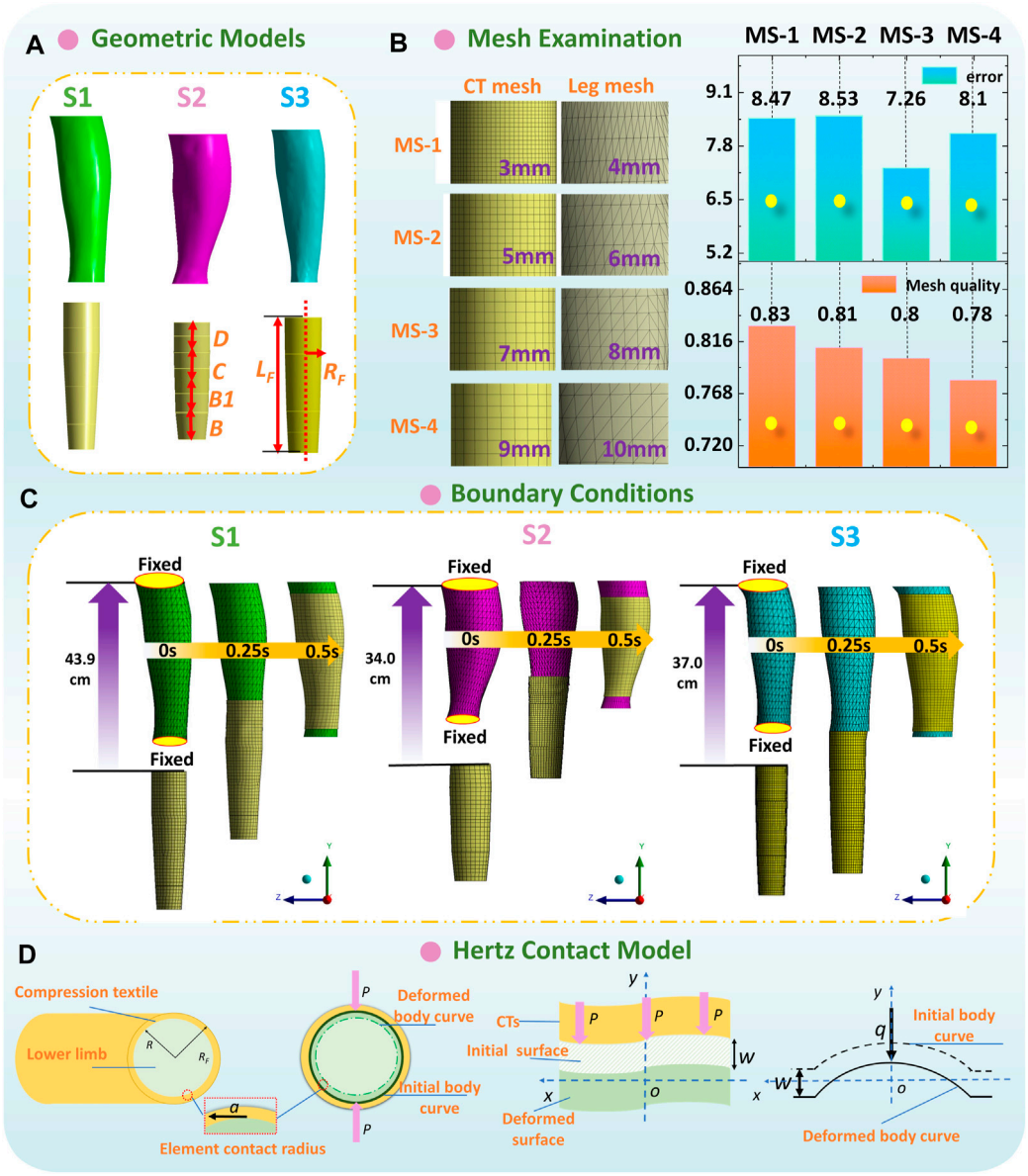

FIGURE 5
(A) Geometric models and **(B)** mesh sensitivity study of 3D FE homogenous modeling. **(C)** Boundary conditions and dynamic wearing process of each FE model. **(D)** Hertz contact model for the CT-leg system.

analyze the interfacial pressure performances of CTs, the constructed leg models (obtained by section 2.2) and applied CTs of each subject were imported into the Ansys LS-DYNA explicit dynamic solver, to solve the non-linear dynamic equilibrium equation based on the center difference method (Rackauskaite et al., 2017; Liu, 2008) (Eq. (4)).

$$M\ddot{u}^n = L^n - Y^n + H^n, \tag{4}$$

where M is the diagonal mass matrix, $\ddot{u}^n$ is the nodal acceleration component, L is the load, Y is the stress component, and H is the damped hourglass, where the damped hourglass was applied to reduce hourglass energy in the explicit dynamic model to achieve the simulation accuracy, and n represents the nth element of a time interval discretization.

Second, as shown in Figure 5B, according to the geometric characteristics of simulated components, CT (shell element) and leg model (solid entity element) were meshed by linear quadrilateral dominant and tetrahedrons elements, respectively. The mesh sensitivity study was performed with various mesh size combinations to examine the mesh independence of proposed FE systems. Through the compared results, 8 mm and 7 mm per element were meshed for CT and leg models, respectively. Thus, the element/node numbers in biomechanical systems for the S1, S2, and S3 subjects were approximately 38500/12300, 60000/14300, and 32000/8000, respectively. The frictional non-linear contact with a coefficient of 0.2 (Huzni et al., 2022) was applied to simulate the interfacial contact conditions.

Third, to promote dynamic wearing and the sliding process, the upper and bottom external surfaces of leg models were fixed to remain stationary and avoid unnecessary movement. Thus, the tubular CTs could slide longitudinally and freely from the distal to the proximal of lower limbs (Figure 5C). The total degrees of freedom (DOF) of built CT-leg models for the S1, S2, and S3 subjects were approximately 34000, 62000, and 45000, respectively. The DOF of each node were six, and conversely, the fixed support condition restricted six DOF. The boundary conditions were applied to the CT geometric models and determined as the longitudinal CT sliding displacements along the y axis. The exactly longitudinal sliding displacements of CTs included the distances between the leg bottom to the upper end of CTs, as well as the leg heights (from the B to D positions; S1-35.1 cm, S2-20.1 cm, and S3-21.1 cm) of each subject. Thus, the total longitudinal displacements for boundary conditions (approximately S1-43.9 cm, S2-34.0 cm, and S3-37.0 cm) were determined by not only the distances between the leg bottom to the upper end of CTs but also the leg heights of each subject. Then, the CTs were freely deformed due to the dimensional diversities between CTs and legs along circumferential directions. Interfacial pressures were generated due to the fabric stretching tensions and produced normal forces. Moreover, the dynamic wearing process was 0.5 s, and we captured the pressure mappings at the 1st seconds, when the CTs were stretched steadily along lower bodies and provided constant tensions. Additionally, the simulated pressure magnitudes along the 3D printing rigid legs and soft legs with multiple ST stiffness values were defined as P_{LM} and P_{LS}, respectively.

2.6 Theoretical contact analysis model

To theoretically analyze the impact mechanisms of tissue stiffness on pressure distributions of CTs, the Hertz contact theory (HzT) was used. The HzT model fundamentally leads the basic understanding of the indentation and mechanical interaction between elastic solids (Chen et al., 2017; Zhang et al., 2019), for investigating the geometrical deformation effects on local elastic deformation properties and pressure performances. For CT-leg systems (Figure 5D), the assumptions of HzT are as follows: i) the fabric–tissue contact area can be divided into FE contacts. Each element contact can be analyzed as two camber concave contacts; ii) the radius of contact circle is relatively smaller than those of the elastic fabric and deformed lower extremity; iii) no displacement changes along fabric thickness direction; and iv) during the wearing process, only the normal pressure is generated and transmitted between the frictionless full contact interface.

Through the initial HzT model, the quantitative relationships among the unit pressure magnitude with the body circumferential displacements, the physical dimensions, and mechanical properties of applied legs and CTs are shown as Eq. 5 (Khot and Borah, 2015).

$$\omega = (k + k_F)\frac{\pi q}{4a}(2a^2 - r^2), \tag{5}$$

where w is the body circumferential displacement (m) and k and k_F are the elastic mismatch factors (Pa^{-1}) of leg and CT fabric, respectively; q is the unit pressure value (Pa); r is the point distance from the contact circle surface to the center of the contact circle (defined as zero due to consumption of the full contact condition); and a is the radius of the contact circle (m).

The elastic mismatch factors are definitively determined by the mechanical properties of CTs and lower limbs. Thus, k and k_F are given by Eq. 6.

$$k = \frac{1 - \nu^2}{\pi E_s},\ k_F = \frac{1 - \nu_F^2}{\pi E_F}, \tag{6}$$

where E_s and ν (where ν is 0.5 (Colombo et al., 2016)) are the tensile elastic Young's modulus (Pa) and Poisson's ratios of applied body (along the transverse direction), respectively.

After deformation, as Eq. 7, Hertz also derived a and q of the contact surface through the determined variables (such as k and R_F) of the two contacting materials.

$$a = \left[\frac{3\pi F(k + k_F)RR_F}{4(R + R_F)}\right]^{1/3},\ q = \frac{3F}{2\pi}\left[\frac{8a^2(R + R_F)}{3F(k + k_F)RR_F}\right]^{2/3}, \tag{7}$$

where F is the applied normal load of external force (N) and R is the radius (m) of the applied leg.

Additionally, through the definition function of interfacial pressure (P, Pa), it can be obtained through the applied normal load and contact area (Eq. 8).

$$P = \frac{F}{2\pi a^2}. \tag{8}$$

Therefore, based on the aforementioned HzT model and FE simulated leg circumferential displacement of w, the pressure ratios

(ΔP) between the rigid leg models and soft legs with various stiffness properties can be compared quantitatively (Eq. 9).

$$\Delta P = \frac{P_{LM}}{P_{LS}} = \frac{w_r}{w_s} \times \frac{(k_s + k_F)}{(k_r + k_F)} = \frac{w_{ratio}}{k_{ratio}}, \quad (9)$$

where w_r and w_s, k_r and k_s are the body circumferential displacements and elastic mismatch factors along the rigid and soft legs, respectively; and w_{ratio} and k_{ratio} are the circumferential displacement and elastic mismatch ratios compared between the rigid and soft legs, respectively.

2.7 Acceptability analysis of FE modelling and experimental validation study

The acceptability of 3D FE homogenous leg models was compared through the simulated P_{LM} and experimentally measured P_{rigid} data obtained along the constructed FE-based and printed PLA leg models with identical mechanical properties (3.0 GPa) and controlled leg morphologies. The pressure prediction errors were compared by the deviation ratio (*DRO*, %; Eq. 10).

$$DRO = \frac{|P_{rigid} - P_{LM}|}{P_{rigid}} \times 100\%. \quad (10)$$

To validate the accuracy and applicability of this study, the pressure performances obtained along the subject-specific FE CT-leg system, user-oriented 3D printing rigid model, and biological leg were compared simultaneously. Additionally, the interfacial compression performance experimental evaluations were measured by utilizing the PicoPress® (Microlab Elettronica, Italy) pressure tester (measurement range: 0–189 mmHg and precision: ±3 mmHg). The pressure sensor probe detected the values over the circular area of the four studied leg positions (B, B1, C, and D).

2.8 Data analysis

Data analysis was performed using the Statistical Package for the Social Sciences (SPSS) software (version 23.0, IBM Corporation, USA). In this study, four (B, B1, C, and D) positions of three legs and two compression levels (class I and class III) were studied in (i) acceptability estimation of the FE CT-leg system, (ii) comparison study, and (iii) experimental validation study. Thus, the processed sample sizes were as follows: (i) simulated group: 24 and tested group: 24; (ii) comparison study: class I-48 and class III-48 in each compared group; and (iii) the experimental validation data were 24 in each compared group. Based on the processed sample size ($n < 50$), the data normal distribution examinations were objectively conducted by the Shapiro–Wilk statistic (Razali and Wah, 2011). Then, the correlations and significant differences between each variable were tested by performing the Pearson correlation analysis and paired t test, respectively (Bolboaca and jantschi, 2006; Tang et al., 2013). The post hoc test of the Bonferroni correction would be applied when significant differences are identified by the paired t tests. The level of significance was set at $\alpha = 0.05$.

3 Results

3.1 Acceptability of 3D FE homogenous CT-leg system

Figures 6A, B show the simulated subject-specific P_{LM} and measured P_{rigid} values supplied by CTs and corresponding calculated *DROs* of each compression level. For instance, for the ankle (B) position of class I CTs, the simulated values for subjects S1, S2, and S3 were 18.02 ± 2.36 mmHg, 21.05 ± 3.87 mmHg, and 19.52 ± 4.46 mmHg, respectively. The corresponding tested pressure values were 19.17 ± 5.15 mmHg, 21.25 ± 2.95 mmHg, and 18.92 ± 2.84 mmHg, respectively. For the knee (D) position of class III CTs, the simulated values for subjects S1, S2, and S3 were 21.77 ± 5.05 mmHg, 19.68 ± 3.01 mmHg, and 23.62 ± 8.31 mmHg, respectively. The corresponding tested pressure values were 20.17 ± 2.68 mmHg, 20.75 ± 5.16 mmHg, and 19.92 ± 2.84 mmHg, respectively. The degressive pressure gradients indicated the pressure distributions generated by CTs were degressively from the distal to the proximal regions (Shi et al., 2024). Through the applied elastic compression fabrics with various physical circumferential dimensions and mechanical tensile properties, the light (class I) and strong (class III) levels with indicated ranges and standardized degressive pressure gradients were generated along the lower extremities. Specifically, the P_{LM} values generated by class I tubular fabrics at the ankle (B) positions of each subject were 18.02 ± 2.36 mmHg, 21.05 ± 3.87 mmHg, and 19.52 ± 4.46 mmHg, respectively. For compression class III, the P_{LM} values were 34.00 ± 8.09 mmHg, 34.50 ± 3.96 mmHg, and 37.39 ± 4.35 mmHg, respectively. According to the comparison tested data of P_{rigid}, the mean *DRO* of constructed FE modeling was approximately 7.45%. Additionally, based on the Shapiro–Wilk statistic results and normal data distribution curves (Figure 6C), the data conformed to the normal distribution. Through the *DRO* values and correlation results, the simulated P_{LM} of class I (Sig. <0.05; $\rho = 0.73$) and class III (Sig. <0.05; $\rho = 0.93$) CTs were compared as the reasonable agreements with the tested evaluation P_{rigid} data, respectively (Huang et al., 2015; Shahzad et al., 2015). These results indicated that the established 3D FE homogenous CT-leg systems could be applied for our further explorations with high acceptability and simulation accuracy.

3.2 FE comparison among various leg tissue stiffness values

To qualitatively investigate the pressure generations along lower bodies with various lower limb tissue characteristics, Figure 7A shows the average compression generations along the simulated rigid (P_{LM}) and soft legs (P_{LS}) with different ST stiffness values supplied by CTs. For the mechanical material, stiffness of the rigid leg model and each tissue group are as follows: leg model: 3.0 GPa, LS-1: 0.0014 MPa, LS-2: 0.0022 MPa, and LS-3: 0.0030 MPa. Through the Shapiro–Wilk statistic tests, the data conformed to the normal distribution. By varying the inputted leg mechanical properties, the exerted interfacial pressure profiles were slightly varied in proposed 3D FE homogenous systems. Furthermore, according to the results of paired t tests (Figure 7B), pressure

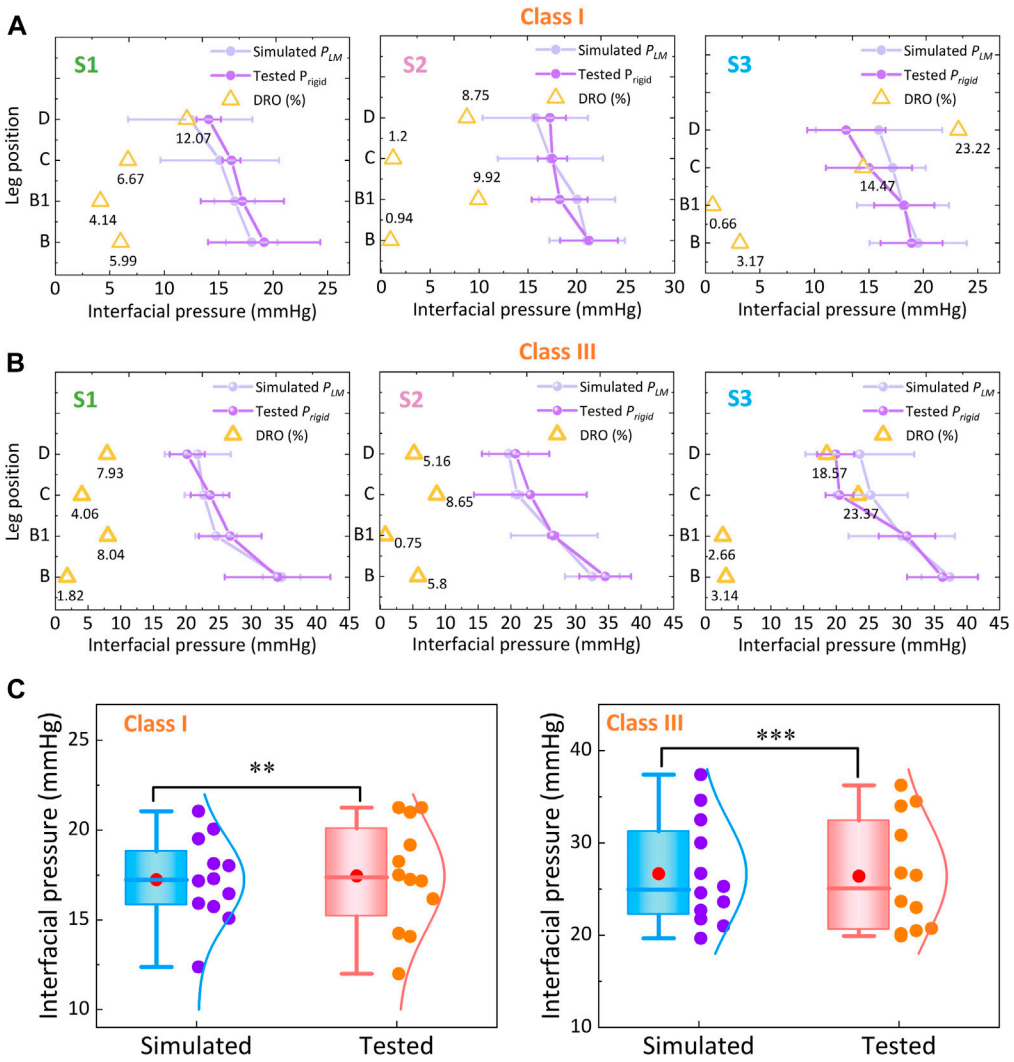

FIGURE 6
Pressure comparisons between the FE simulated and experimental measured values for **(A)** classes I and **(B)** III CTs. **(C)** Data distribution and correlation analysis of FE-based and tested pressure values ('*' represents the *p*-value through the correlation test; **: *Sig.* < 0.01 (correlation); ***: *Sig.* <0.005 (significant correlation)).

performances showed no significant differences among each compared leg tissue stiffness group under the light (Sig. >0.05) and strong (Sig. >0.05) external compression levels. It can be demonstrated that the compression performances of CTs with each pressure delivery level have no correlations with tissue characteristics of soft human bio-bodies as well as the applied rigid leg mannequins.

3.3 Parametric variations through theoretical HzT model

Based on the HzT model, the pressure differences (ΔP) were determined by the relationships of the leg circumferential displacement (w_{ratio}) and tissue elastic factor (k_{ratio}) ratios. Through the constructed homogenous FE systems with various compression generations and ST stiffness properties, the exported leg circumferential displacements and calculated parameters derived by the HzT model are shown in Figure 8A. For the variables of w, it increased with the pressure distribution levels (Sig.<0.05; $\rho = 0.46$), and conversely, decreased with the ST stiffness characteristics (Sig.<0.05; $\rho = -0.53$). For example, Figure 8B shows the compared images plotted by the original bio-body curves, and deformed body curves generated along simulated rigid and soft legs, respectively. The mean w value under the light compression level (class I) and maximum ST tissue magnitude (LS-3) was approximately 3.61 ± 0.26 mm. By contrast, under the class III and minimum ST tissue magnitude (LS-1), the w value was approximately 11.06 ± 1.36 mm. Based on the w variations, the compressed lower limb cross-sectional circumferences varied from 2.27 ± 0.14 cm to 6.95 ± 0.74 cm. Thus, the leg circumferential displacements had correlations with the external pressure levels of CTs and body ST stiffness.

Furthermore, through the calculated parameters of w_{ratio} and k_{ratio}, the pressure diversities of ΔP between the simulated rigid (P_{LM}) and soft (P_{LS}) legs were also obtained quantitatively. ST

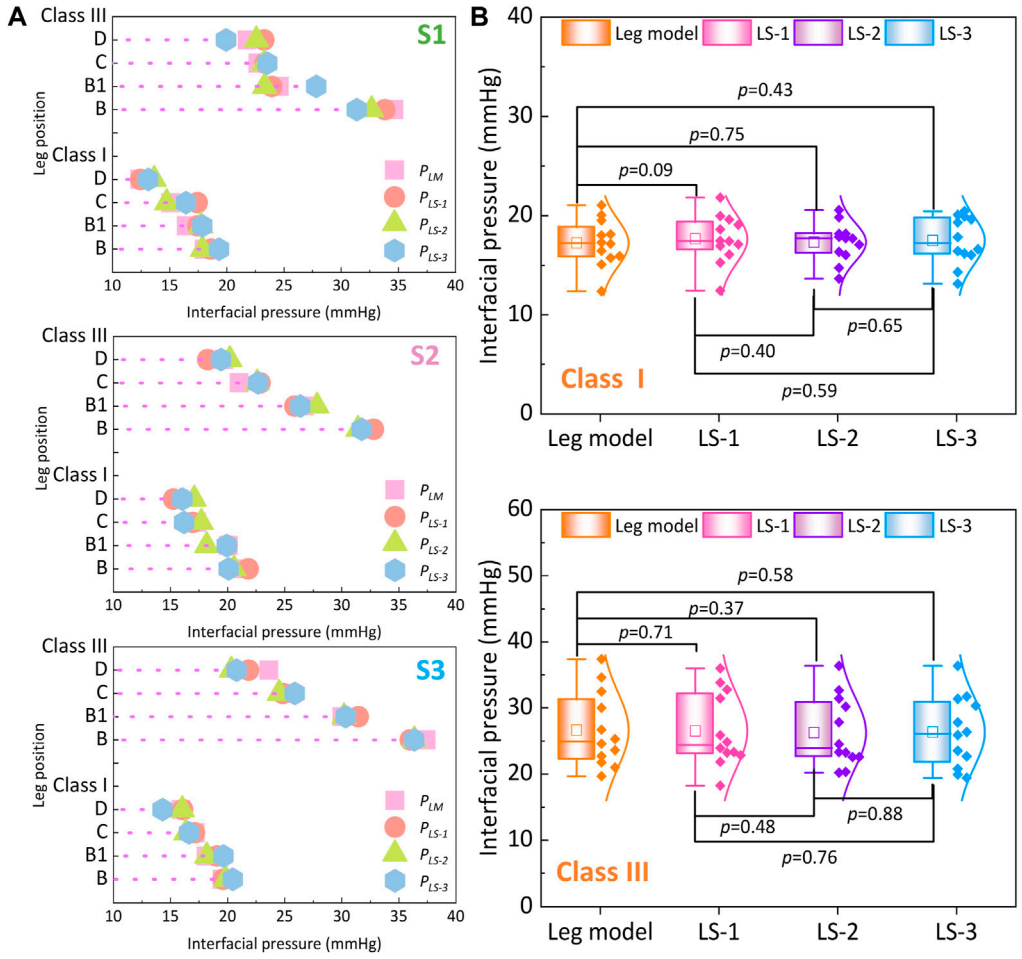

FIGURE 7
(A) Interfacial pressure values generated by different legs with various ST stiffness properties. **(B)** Comparisons of pressure performances generated by class I and class III CTs between each leg stiffness group (the mechanical material stiffness were as follows, leg model: 3.0 GPa, LS-1: 0.0014 MPa, LS-2: 0.0022 MPa, and LS-3: 0.0030 MPa).

stiffness properties showed significant positive correlations with deformed variables of w_{ratio} (Sig.<0.05; ρ = 0.64) and tissue-related defined variables of k_{ratio} (Sig.<0.05; ρ = 0.77), but no correlation with the ΔP (Sig.>0.05; ρ = −0.19). These results indicated that although the external tension forces generated by CTs positively affected the lower body circumferential displacements, the compressed deformed geometric variations caused by diverse tissue stiffness did not lead to proportional changes in pressure performance diversity.

3.4 Experimental validation study

Figures 9–11 represent the subject-specific pressure visualized mappings with class I and class III compression levels delivered by CTs. The inputting leg mechanical properties in FE CT-leg systems were derived from the SWE testing data of each biological body. The standardized pressure gradients and distributions were exerted along each lower extremity and showed individual profile features relating to their morphological characteristics. In addition, the pressure performances along the simulated FE systems (P_{LS}), biological bodies (P_{bio}), and 3D printing models (P_{rigid}) were compared by performing statistical tests. The pressure performances of CTs distributed along biological legs have significant correlations with the values obtained by the simulated FE systems (Sig.<0.05; ρ = 0.97) and experimental measurements along the printing leg mannequins (Sig.<0.05; ρ = 0.96). Therefore, the proposed 3D FE homogenous CT-leg systems could in practice replace the bio-legs for efficiency pressure prediction simulations. In addition, the non-significant correlations between the ST tissue characteristics and pressure diversities are also validated by experimental tests.

4 Discussion

In relevant existing FE CT-leg systems, the lower limbs were reconstructed through medical captured images (i.e., magnetic resonance imaging or computed tomography scanning) and each leg slice was processed individually for composition segmentation and tissue characterization. The mechanical properties of each part of leg were also determined exactly through regional biomaterial

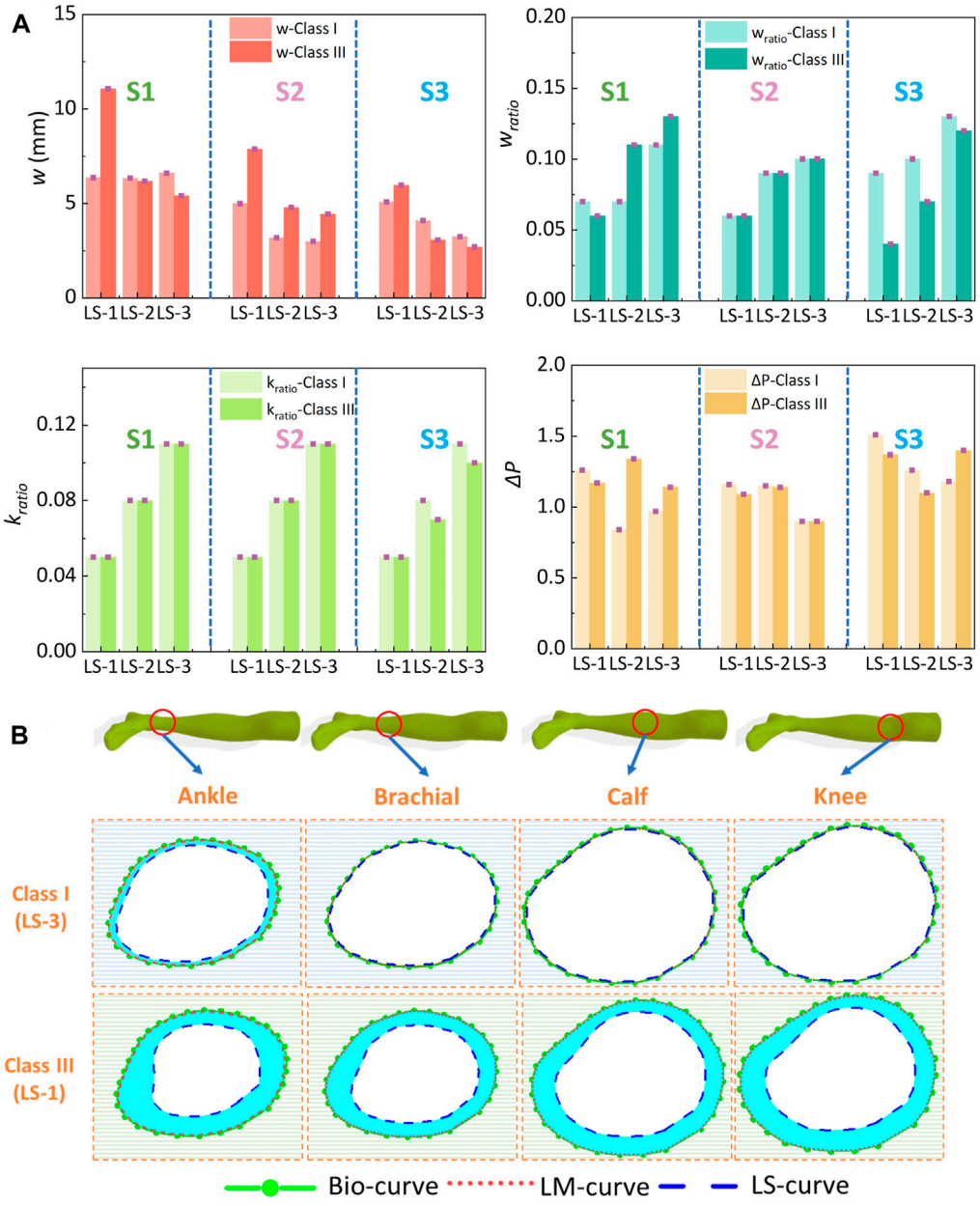

FIGURE 8
(A) Exported leg circumferential curve displacements and calculated parameters through the HzT model of class I and class III CTs. **(B)** Plotted body curves with diverse ST tissue properties and external compressions (from subject S1) (Bio, LM, and LS curves indicated the leg circumferential deformed curves from the subject biological body, 3D rigid PLA model, and simulated soft leg models with ST stiffness values of LS-1 or LS-3).

measurement. After physical data acquisition and mechanical FE modeling construction, their simulated pressure errors were approximately 5.9%–21.4% (Dai et al., 2007; Dubuis et al., 2013; Ye et al., 2023). For our proposed user-oriented FE models, the lower legs were constructed as simplified homogenous models based on 3D body scanning rather than medical operating equipment with complex physiological structural characteristics. The verification results demonstrate that time-saving and effective CT-leg systems with exact scanned morphological profiles and geometric shapes could facilitate the basic interfacial pressure performance visualization and functional assessment for FE compression studies. Based on the relevant literature works (Kankam et al., 2018; Wang et al., 2018), CTs could increase the venous hemodynamics for improving the clinic therapeutic benefits. The accurate pressure prediction could facilitate the medical efficacy and precision of compression therapy in practical use. Thus, the biomaterial characteristics of the studied main muscle compositions could represent leg mechanical properties in compression simulation to achieve efficient pressure prediction and parameter optimization for the development of CTs.

In previous related studies (Korff et al., 2009; Bosnic et al., 2022), ST stiffness varied during the muscle activation states. For instance, muscular contraction and power production could cause around 150% greater increase in stiffness due to the ankle dorsiflexion in the

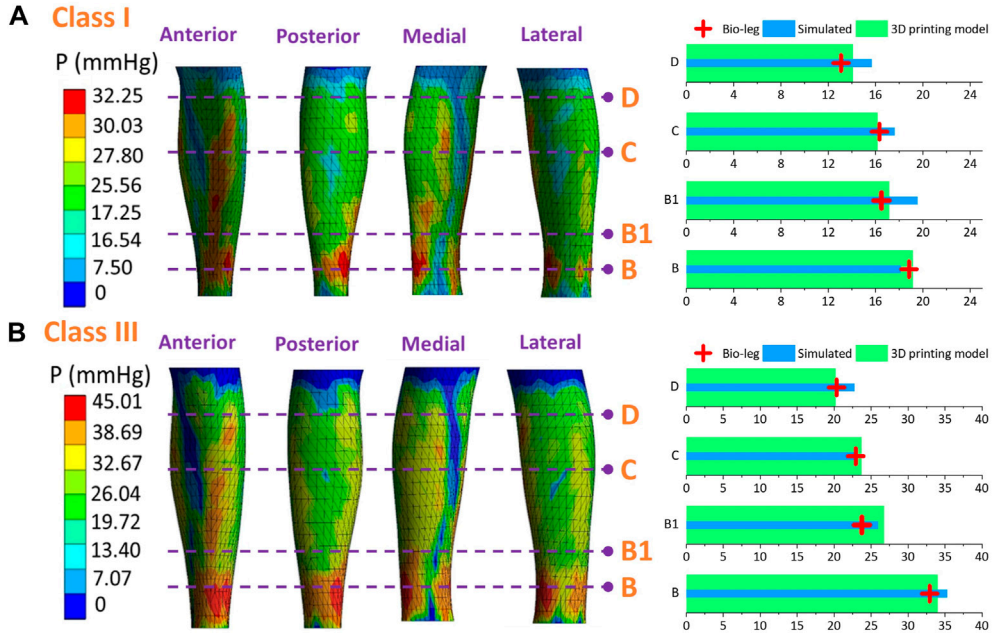

FIGURE 9
Pressure mappings and experimental validation results of compression classes **(A)** I and **(B)** III for subject S1.

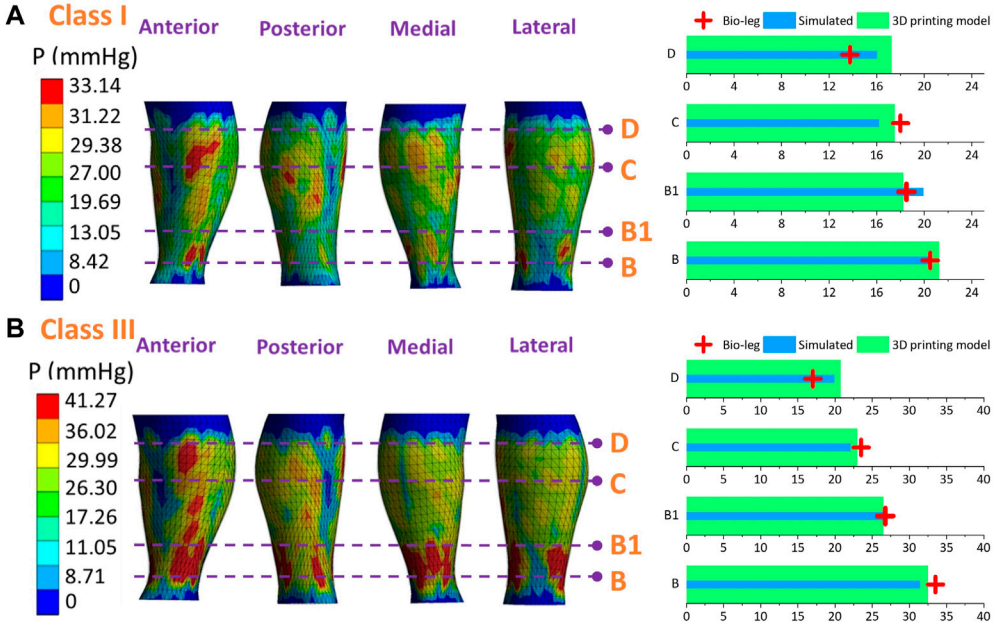

FIGURE 10
Pressure mappings and experimental validation results of compression classes **(A)** I and **(B)** III for subject S2.

moving process. For the patient groups with health conditions, ST stiffness caused by progressive muscular diseases also increased by approximately 120% compared with the control groups (Lin et al., 2021). Based on these ST mechanical variations, the E_S of biological legs could approach maximum 0.0045 MPa in dynamic muscle activities, which is still far smaller than the studied rigid leg model (3.0 GPa). Therefore, the main findings for CTs in our study can be applied not only for different bio-bodies with individual tissue diversities but also in various practical wearing and motion scenarios. Through the obtained pressure mappings of simulated results, the insufficient and peak focal pressures were distributed unevenly along each lower extremity. Thus, the biomechanical

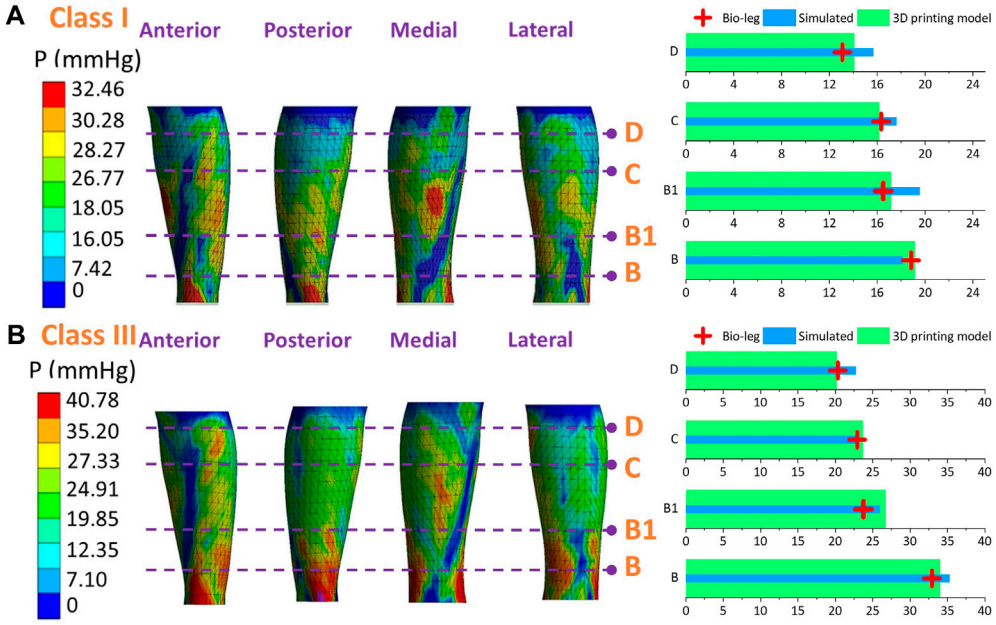

FIGURE 11
Pressure mappings and experimental validation results of compression classes **(A)** I and **(B)** III for subject S3.

system could also provide the design strategy (Fontanella et al., 2021) for user-oriented therapeutic CTs with enhanced medical functions and wearing comforts.

Similarly, based on the HzT model, the pressure differences were determined by the relationships of the leg circumferential displacements and tissue elastic factor ratios. The circumferential displacements were varied caused by the external compression levels. In practical application, through the commercial recommended size selection tables (Reich et al., 2016; Liu et al., 2018a), the circumferential dimension ranges between each size of CTs also commonly span around 2 cm–7 cm for identical compression levels, which are consistent with the previously calculated variations of circumference values (2.27 cm–6.95 cm). For elastic CTs, the pressure performances (P) are mechanically determined by the fabric tensions (T) and body girths (C) through Laplace's law ($P = T/C$) (Aghajani et al., 2011; Shi et al., 2023). Therefore, through the prescribed pressure ranges of 18–46 mmHg and required CT stretched ratios (15%–80%) (Shi et al., 2023), the garment-based transverse tensile stresses (0.05–0.80 MPa) were relatively smaller to generate the adequate deformed indentations along various biological bodies with diverse tissue properties. Therefore, for the design and development of compression textile-based therapeutic stockings, the pressure generations have no correlations not only with body tissue characteristics but also with the leg mannequin material selections in compression experimental estimations. For the limitation of our study, the mechanical properties of CT were simplified as linear elastic materials under the balanced conditions (CT were stretched steadily and provided constant tensions during the wearing states), and the mechanical behavior variations of CT material time-dependent properties caused by the long-term wearing process would be investigated in our future work.

5 Conclusion

This study systematically investigated the biomechanical influences of tissue properties on pressure performances of CTs through FE modeling, theoretical contact modeling, and experimental study. The proposed simplified FE 3D homogenous CT-leg systems effectively and accurately simulated the interfacial pressure performances, and pressure performances of CTs showed no statistically significant differences with the applied lower limbs or leg models with various mechanical tissue properties. The leg circumferential displacements were positively increased by the external fabric tension forces. However, these deformed variations caused by varied biomaterial stiffness could not lead to regular changes in pressure distributions.

Thus, the visualized FE homogenous models provide an efficient biomechanical simulation approach for subject-specific pressure prediction and performance evaluation of CTs. The influencing mechanisms of leg tissue properties on pressure generations of textile-based materials also lead the scientific design principles for the development of CTs with pressure fitness in compression therapy. Therefore, the outcomes of the present study provide not only the biodesign strategy for the pressure management of CTs but also accurate analytical approaches for functional pressure assessments for tailoring rehabilitation equipment and monitoring treatment in compression therapy.

Data availability statement

The original contributions presented in the study are included in the article/Supplementary Material; further inquiries can be directed to the corresponding author.

Ethics statement

The studies involving humans were approved by the Human Subjects Ethics Sub-committee of The Hong Kong Polytechnic University. The studies were conducted in accordance with the local legislation and institutional requirements. The participants provided their written informed consent to participate in this study. Written informed consent was obtained from the individual(s) for the publication of any potentially identifiable images or data included in this article.

Author contributions

YS: Conceptualization, Investigation, Formal analysis, Validation, Methodology, Software, Data analysis, writing–original draft. CY: Conceptualization, Formal analysis, Methodology, Data analysis, Software, Technical support, Validation, writing–review and editing. RL: Supervision, Project administration, Funding acquisition, writing–review and editing.

Funding

The author(s) declare that financial support was received for the research, authorship, and/or publication of this article.

Acknowledgments

The authors would like to thank Laboratory for Artificial Intelligence in Design through project RP1-5, Innovation and Technology Fund (ITF), Hong Kong Special Administrative Region, General Research Fund (GRF) of University Grants Committee through project PolyU252153/18E, and Public Sector Trial Scheme of ITF-The Hong Kong Research Institute of Textiles and Apparel (ITF-HKRITA) through project ITT/010/23TI for supporting this study.

Conflict of interest

The authors declare that the research was conducted in the absence of any commercial or financial relationships that could be construed as a potential conflict of interest.

Publisher's note

All claims expressed in this article are solely those of the authors and do not necessarily represent those of their affiliated organizations, or those of the publisher, the editors, and the reviewers. Any product that may be evaluated in this article, or claim that may be made by its manufacturer, is not guaranteed or endorsed by the publisher.

References

Affagard, J. S., Bensamoun, S. F., and Feissel, P. J. (2014). Development of an inverse approach for the characterization of *in vivo* mechanical properties of the lower limb muscles. *J. Biomech. Eng-t. Asme.* 136, 111012. doi:10.1115/1.4028490

Aghajani, M., Jeddi, A. A., and Tehran, M. A. (2011). Investigating the accuracy of prediction pressure by laplace law in pressure-garment applications. *J. Appl. Polym. Sci.* 121, 2699–2704. doi:10.1002/app.33640

Amornvit, P., and Sanohkan, S. S. (2019). The accuracy of digital face scans obtained from 3D scanners: an *in vitro* study. *Int. J. Environ. Res. Public Health* 16, 5061. doi:10.3390/ijerph16245061

Arnold, N., Scott, J., and Bush, T. R. (2023). A review of the characterizations of soft tissues used in human body modeling: scope, limitations, and the path forward. *J. Tissue. Viability* 32, 286–304. doi:10.1016/j.jtv.2023.02.003

Avril, S., Badel, P., Dubuis, L., Rohan, P. Y., Debayle, J., Couzan, S., et al. (2011). Patient-specific modeling of leg compression in the treatment of venous deficiency. *Patient-specific Model. tomorrow's Med.*, 217–238. doi:10.1007/8415_2011_103

Barhoumi, H., Marzougui, S., and Abdessalem, S. B. (2020). Clothing pressure modeling using the modified laplace's law. *Text. Res. J.* 38, 134–147. doi:10.1177/0887302X19880270

Bolboaca, S. D., and Jäntschi, L. J. (2006). Pearson versus Spearman, Kendall's tau correlation analysis on structure-activity relationships of biologic active compounds. *Leonardo J. Sci.* 5, 179–200.

Bosnic, M., Rasoulian, A., and Brandon, S. C. (2022). Investigating the effects of activation state and location on lower limb tissue stiffness. *J. Biomech.* 135111032, 111032. doi:10.1016/j.jbiomech.2022.111032

Chen, D., Ye, Z., Pan, Z., Zhou, Y., and Zhang, J. (2017). A permeability model for the hydraulic fracture filled with proppant packs under combined effect of compaction and embedment. *J. Pet. Sci. Eng.* 149, 428–435. doi:10.1016/j.petrol.2016.10.045

Cieślak, M., Karaszewska, A., Gromadzińska, E., and Śledzińska, K. (2016). I-SCAN method for the assessment of pressure exerted by textile products. *Fibers. Text. East. Eur.* 6, 121–128. doi:10.5604/12303666.1221746

Colombo, G., Comotti, C., Redaelli, D. F., Regazzoni, D., Rizzi, C., and Vitali, A. (2016). "A method to improve prosthesis leg design based on pressure analysis at the socket-residual limb interface," in International Design Engineering Technical Conferences and Computers and Information in Engineering Conference, USA, August 25–28, 2024. doi:10.1115/DETC2016-60131

Dai, X. Q., Liu, R., Li, Y., Zhang, M., and Kwok, Y. L. (2007). Numerical simulation of skin pressure distribution applied by graduated compression stockings. *Comput. Text.*, 301–309. doi:10.1007/978-3-540-70658-8_20

Dubois, G. J., Bachasson, D., Lacourpaille, L., Benveniste, O., and Hogrel, J. Y. (2018). Local texture anisotropy as an estimate of muscle quality in ultrasound imaging. *Ultrasound. Med. Biol.* 44, 1133–1140. doi:10.1016/j.ultrasmedbio.2017.12.017

Dubuis, L., Avril, S., Debayle, J., and Badel, P. J. (2012). Identification of the material parameters of soft tissues in the compressed leg. *Comput. Method. Biomec.* 15, 3–11. doi:10.1080/10255842.2011.560666

Dubuis, L., Avril, S., Debayle, J., and Badel, P. J. (2012). Patient-specific FE model of the leg under elastic compression. *Int. symposium Comput. methods biomechanics Biomed. Eng.*

Dubuis, L., Rohan, C. Y., Avril, S., Badel, P., and Debayle, J. (2013). Patient-specific computational models: tools for improving the efficiency of medical compression stockings. *Comput. Biomechanics Med. Models, Algorithms Implement.*, 25–37. doi:10.1007/978-1-4614-6351-1_4

Fontanella, C. G., Arduino, A., Toniolo, I., Zampieri, C., Bortolan, L., and Carniel, E. L. (2021). Computational methods for the investigation of ski boots ergonomics. *Sports. Eng.* 24, 15. doi:10.1007/s12283-021-00352-3

Frauziols, F., Badel, P., Navarro, L., Molimard, J., Curt, N., and Avril, S. (2017). Subject-specific computational prediction of the effects of elastic compression in the calf. *Biomechanics Living Organs*, 523–544. doi:10.1016/b978-0-12-804009-6.00024-9

Frauziols, F., Rohan, P. Y., Badel, P., Avril, S., Molimard, J., and Navarro, L. (2013). Patient-specific modelling of the calf muscle under elastic compression using magnetic resonance imaging and ultrasound elastography. *Comput. Methods. Biomech. Biomed. Engin.* 16, 332–333. doi:10.1080/10255842.2013.815955

Ghosh, S., Mukhopadhyay, A., Sikka, M., and Nagla, K. J. (2008). Pressure mapping and performance of the compression bandage/garment for venous leg ulcer treatment. *J. Tissue. Viability.* 17, 82–94. doi:10.1016/j.jtv.2007.09.013

Gong, J. M., Du, J. S., Han, D. M., Wang, X. Y., and Qi, S. L. (2020). Reasons for patient non-compliance with compression stockings as a treatment for varicose veins in the lower limbs: a qualitative study. *PloS. One.* 15, e0231218. doi:10.1371/journal.pone.0231218

Gregor, A., Filová, E., Novák, M., Kronek, J., Chlup, H., Buzgo, M., et al. (2017). Designing of PLA scaffolds for bone tissue replacement fabricated by ordinary commercial 3D printer. *J. Biol. Eng.* 11, 31–21. doi:10.1186/s13036-017-0074-3

Han, Y., He, J., and Lu, Y. J. (2021). Sensitivity of the properties of the graduated compression stocking and soft tissues on the lower limb-stocking interfacial pressure using the orthogonal simulation test. *Med. Eng. Phys.* 95, 84–89. doi:10.1016/j.medengphy.2021.07.011

Heydon, R. (2011). Finite element analysis of knee articular cartilage. *Ryerson Univ.*

Hobara, H., Kimura, K., Omuro, K., Gomi, K., Muraoka, T., Sakamoto, M., et al. (2010). Differences in lower extremity stiffness between endurance-trained athletes and untrained subjects. *J. Sci. Med. Sport.* 13, 106–111. doi:10.1016/j.jsams.2008.08.002

Huang, X., Sun, J., and Li, J. (2015). Finite element simulation and experimental investigation on the residual stress-related monolithic component deformation. *Int. J. Adv. Manuf. Technol.* 77, 1035–1041. doi:10.1007/s00170-014-6533-9

Huzni, S., Oktianda, F., Fonna, S., Rahiem, F., and Angriani, L. J. (2022). The use of frictional and bonded contact models in finite element analysis for internal fixation of tibia fracture. *Frat. Integrità. Strutt.* 16, 130–139. doi:10.3221/igf-esis.61.09

Kankam, H. K., Lim, C. S., Fiorentino, F., Davies, A. H., and Gohel, M. S. (2018). A summation analysis of compliance and complications of compression hosiery for patients with chronic venous disease or post-thrombotic syndrome. *Eur. J. Vasc. Endovasc.* 55, 406–416. doi:10.1016/j.ejvs.2017.11.025

Kankariya, N., Laing R, M., and Wilson, C. (2021). Textile-based compression therapy in managing chronic oedema: complex interactions. *Phlebology* 36, 100–113. doi:10.1177/0268355520947291

Kankariya, N. J. (2022). Material, structure, and design of textile-based compression devices for managing chronic edema. *J. Ind. Text.* 52, 152808372211188. doi:10.1177/15280837221118844

Khot, S., and Borah, U. (2015). Finite element analysis of pin-on-disc tribology test. *Int. J. Sci. Res.* 4, 1475–1480.

Kim, Y., Png, C. M., Sumpio, B. J., DeCarlo, C. S., and Dua, A. (2021). Defining the human and health care costs of chronic venous insufficiency. *Seminars Vasc. Surg.* 34, 59–64. doi:10.1053/j.semvascsurg.2021.02.007

Korff, T., Horne, S. L., Cullen, S., and Blazevich, A. (2009). Development of lower limb stiffness and its contribution to maximum vertical jumping power during adolescence. *J. Exp. Biol.* 212, 3737–3742. doi:10.1242/jeb.033191

Le, S. G., Nordez, A., Andrade, R., Hug, F., Freitas, S., and Gross, R. J. (2017). Stiffness mapping of lower leg muscles during passive dorsiflexion. *J. Anat.* 230, 639–650. doi:10.1111/joa.12589

Li, Q., Sun, G., Chen, Y., Chen, X., Shen, Y., Xie, H., et al. (2020). Fabricated leg mannequin for the pressure measurement of compression stockings. *Text. Res. J.* 92, 3500–3510. doi:10.1177/00405175221083216

Lin, C. W., Tsui, P. H., Lu, C. H., Hung, Y. H., Tsai, M. R., Shieh, J., et al. (2021). Quantifying lower limb muscle stiffness as ambulation function declines in duchenne muscular dystrophy with acoustic radiation force impulse shear wave elastography. *Ultrasound. Med. Biol.* 47, 2880–2889. doi:10.1016/j.ultrasmedbio.2021.06.008

Liu, R., Guo, X., Lao, T. T., and Little, T. (2017). A critical review on compression textiles for compression therapy: textile-based compression interventions for chronic venous insufficiency. *Text. Res. J.* 87, 1121–1141. doi:10.1177/0040517516646041

Liu, R., Guo, X., Peng, Q., Zhang, L., Lao, T. T., Little, T., et al. (2018b). Stratified body shape-driven sizing system via three-dimensional digital anthropometry for compression textiles of lower extremities. *Text. Res. J.* 88, 2055–2075. doi:10.1177/0040517517715094

Liu, R., Lao, T. T., Little, T. J., Wu, X., and Ke, X. (2018a). Can heterogeneous compression textile design reshape skin pressures? A fundamental study. *Text. Res. J.* 88, 1915–1930. doi:10.1177/0040517518779254

Liu, R., Lao, T. T., and Wang, S. (2013). Technical knitting and ergonomical design of 3D seamless compression hosiery and pressure performances *in vivo* and *in vitro*. *Fiber. Polym.* 14, 1391–1399. doi:10.1007/s12221-013-1391-x

Liu, R., Xu, B., and Ye, C. (2019). "Biodigital design and functional visualization of multi-class personalized compression textiles for ergonomic fit," in International Conference on Applied Human Factors and Ergonomics, USA, July 24-27, 2024, 488–499. doi:10.1007/978-3-030-20444-0_51

Liu, Y. (2008). ANSYS and LS-DYNA used for structural analysis. *Int. J. Comput. Aided Eng. Technol.* 1, 31–44. doi:10.1504/IJCAET.2008.021254

Lu, Y., Zhang, D., Cheng, L., Yang, Z., and Li, J. (2021). Evaluating the biomechanical interaction between the medical compression stocking and human calf using a highly anatomical fidelity three-dimensional finite element model. *Text. Res. J.* 91, 1326–1340. doi:10.1177/0040517520979743

Marinopoulos, T., Zani, L., Li, S., and Silberschmidt, V. V. (2020). Modelling indentation of human lower-limb soft tissue: simulation parameters and their effects. *Contin. Mech. Therm.* 35, 939–955. doi:10.1007/s00161-020-00933-w

Mo, F., Li, Y., Li, J., Zhou, S., and Yang, Z. J. (2022). A three-dimensional finite element foot-ankle model and its personalisation methods analysis. *Int. J. Mech. Sci.* 219, 107108. doi:10.1016/j.ijmecsci.2022.107108

Morse, C. I. (2011). Gender differences in the passive stiffness of the human gastrocnemius muscle during stretch. *Eur. J. Appl. Physiol.* 111, 2149–2154. doi:10.1007/s00421-011-1845-z

Nemati, S., and Shojaei, S. J. (2019). Investigating effect of compression stocks on tissues of legs. *J. Tissues Mater.* 2, 14–20. doi:10.22034/JTM.2019.183444.1016

Ochi, M., Kohara, K., Tabara, Y., Kido, T., Uetani, E., Ochi, N., et al. (2010). Arterial stiffness is associated with low thigh muscle mass in middle-aged to elderly men. *Atherosclerosis* 212, 327–332. doi:10.1016/j.atherosclerosis.2010.05.026

Parker, M. (2016). *Identification of the mechanical properties of living skin: an instrumentation and modelling study*.

Plesec, V., Humar, J., Dobnik, D. P., and Harih, G. J. M. (2023). Numerical analysis of a transtibial prosthesis socket using 3D-printed bio-based PLA. *Materials* 16, 1985. doi:10.3390/ma16051985

Rackauskaite, E., Kotsovinos, P., and Rein, G. J. (2017). Model parameter sensitivity and benchmarking of the explicit dynamic solver of LS-DYNA for structural analysis in case of fire. *Fire Saf. J.* 90, 123–138. doi:10.1016/j.firesaf.2017.03.002

Ranger, B. J., Moerman, K. M., Anthony, B. W., and Herr, H. M. J. (2023). Constitutive parameter identification of transtibial residual limb soft tissue using ultrasound indentation and shear wave elastography. *J. Mech. Behav. Biomed.* 137, 105541. doi:10.1016/j.jmbbm.2022.105541

Razali, N. M., and Wah, Y. B. (2011). Power comparisons of shapiro-wilk, Kolmogorov-smirnov, lilliefors and anderson-darling tests. *J. Stat. Model. Anal.* 2, 21–33.

Reich, S., Surhoff, S., and Stücker, M. (2016). Pressure profiles of sport compression stockings. *J. Dtsch. Dermatol. Ges.* 14, 495–506. doi:10.1111/ddg.12779

Rohan, P. Y., Badel, P., Lun, B., Rastel, D., and Avril, S. J. (2015). Prediction of the biomechanical effects of compression therapy on deep veins using finite element modelling. *Ann. Biomed. Eng.* 43, 314–324. doi:10.1007/s10439-014-1121-6

Sangpradit, K., Liu, H., Dasgupta, P., Althoefer, K., and Seneviratne, L. (2011). Finite-element modeling of soft tissue rolling indentation. *IEEE Trans. Biomed. Eng.* 58, 3319–3327. doi:10.1109/TBME.2011.2106783

Shahzad, M., Kamran, A., Siddiqui, M. Z., and Farhan, M. (2015). Mechanical characterization and FE modelling of a hyperelastic material. *Mat. Res.* 18, 918–924. doi:10.1590/1516-1439.320414

Shi, Y., Liu, R., and Lv, J. (2023). Effects of knitting variables for pressure controlling of tubular compression fabrics. *Int. J. Mater. Text. Eng.* 17, 90–94.

Shi, Y., Liu, R., Wong, C., Ye, C., and Lv, J. (2024). Prediction of tensile behavior of compression therapeutic biomedical materials by mesoscale laid-in loop model. *Polymer* 302, 127094. doi:10.1016/j.polymer.2024.127094

Shi, Y., Ye, C. Y., and Liu, R. (2023). A novel optimization approach for bio-design of therapeutic compression stockings with pressure fit. *Comput. Biol. Med.* 168, 107768. doi:10.1016/j.compbiomed.2023.107768

Shuxian, Z., Wanhua, Z., and Bingheng, L. J. (2005). 3D reconstruction of the structure of a residual limb for customising the design of a prosthetic socket. *Med. Eng. Phys.* 27, 67–74. doi:10.1016/j.medengphy.2004.08.015

Tang, K., Fan, J., Zhang, J., Sarkar, M., and Kan, C. (2013). Effect of softeners and crosslinking conditions on the performance of easy-care cotton fabrics with different weave constructions. *Fiber. Polym.* 14, 822–831. doi:10.1007/s12221-013-0822-z

Ternifi, R., Kammoun, M., Pouletaut, P., Subramaniam, M., Hawse, J. R., and Bensamoun, S. (2020). Ultrasound image processing to estimate the structural and functional properties of mouse skeletal muscle. *Biomed. Signal Process. Control* 56, 101735. doi:10.1016/j.bspc.2019.101735

Tümer, E. H., and Erbil, H. (2021). Extrusion-based 3D printing applications of PLA composites: a review. *Coatings* 11, 390. doi:10.3390/coatings11040390

Wang, T., Liang, F., Liu, R., Simakov, S., Zhang, X., and Liu, H. (2018). "Model-based study on the hemodynamic effects of graduated compression stockings in supine and standing positions," in *2018 IEEE-EMBS conference on biomedical engineering and Sciences* (USA: IECBES), 27–31. doi:10.1109/IECBES.2018.8626656

Ye, C., and Liu, R. (2020). Biomechanical prediction of veins and soft tissues beneath compression stockings using fluid-solid interaction model. *Int. J. Biomed. Biol. Eng.* 14, 285–290.

Ye, C., Liu, R., Ying, M. T., Liang, F., and Shi, Y. (2023). Characterizing the biomechanical transmission effects of elastic compression stockings on lower limb tissues by using 3D finite element modelling. *Mat. Des.* 232, 112182. doi:10.1016/j.matdes.2023.112182

Yu, W., Fan, J., and Qian, X. M. (2004). A soft mannequin for the evaluation of pressure garments on human body. *Sen'i. Gakkaishi.* 60, 57–64. doi:10.2115/fiber.60.57

Zhan, X. H., Li, X. D., and Liu, Y. (2011). Research on reconstruction 3d cad data of automotive panel based on reverse engineering. *Adv. Mater. Res.* 328, 159–162. doi:10.4028/scientific.net/AMR.328-330.159

Zhang, Z., Yangyang, D., and Yanwei, H. J. M. (2019). Analytical nonlinear response for a rotor with the Hertz Contact and clearance. *Mechanics* 25, 473–479. doi:10.5755/j01.mech.25.6.24790

Ziaja, D., Kocełak, P., Chudek, J., and Ziaja, K. J. P. (2011). Compliance with compression stockings in patients with chronic venous disorders. *Phlebology* 26, 353–360. doi:10.1258/phleb.2010.010086

frontiers | Frontiers in Bioengineering and Biotechnology

TYPE Brief Research Report
PUBLISHED 16 July 2024
DOI 10.3389/fbioe.2024.1404508

OPEN ACCESS

EDITED BY
Ge He,
University of Wisconsin–Milwaukee,
United States

REVIEWED BY
Yuan Feng,
Shanghai Jiao Tong University, China
Longwei Liu,
University of Southern California, United States
Seungman Park,
University of Nevada, United States

*CORRESPONDENCE
Jiu-Tao Hang,
hangjt@xjtu.edu.cn
Hui Yang,
kittyyh@nwpu.edu.cn
Guang-Kui Xu,
guangkuixu@xjtu.edu.cn

RECEIVED 21 March 2024
ACCEPTED 28 June 2024
PUBLISHED 16 July 2024

CITATION
Zhang H, Hang J-T, Chang Z, Yu S, Yang H and Xu G-K (2024), Scaling-law mechanical marker for liver fibrosis diagnosis and drug screening through machine learning.
Front. Bioeng. Biotechnol. 12:1404508.
doi: 10.3389/fbioe.2024.1404508

Scaling-law mechanical marker for liver fibrosis diagnosis and drug screening through machine learning

Honghao Zhang[1], Jiu-Tao Hang[2]*, Zhuo Chang[2], Suihuai Yu[1], Hui Yang[3]* and Guang-Kui Xu[2]*

[1]School of Mechanical Engineering, Northwestern Polytechnical University, Xi'an, China, [2]Department of Engineering Mechanics, SVL, School of Aerospace Engineering, Xi'an Jiaotong University, Xi'an, China, [3]School of Life Sciences, Northwestern Polytechnical University, Xi'an, China

Studies of cell and tissue mechanics have shown that significant changes in cell and tissue mechanics during lesions and cancers are observed, which provides new mechanical markers for disease diagnosis based on machine learning. However, due to the lack of effective mechanic markers, only elastic modulus and iconographic features are currently used as markers, which greatly limits the application of cell and tissue mechanics in disease diagnosis. Here, we develop a liver pathological state classifier through a support vector machine method, based on high dimensional viscoelastic mechanical data. Accurate diagnosis and grading of hepatic fibrosis facilitates early detection and treatment and may provide an assessment tool for drug development. To this end, we used the viscoelastic parameters obtained from the analysis of creep responses of liver tissues by a self-similar hierarchical model and built a liver state classifier based on machine learning. Using this classifier, we implemented a fast classification of healthy, diseased, and mesenchymal stem cells (MSCs)-treated fibrotic live tissues, and our results showed that the classification accuracy of healthy and diseased livers can reach 0.99, and the classification accuracy of the three liver tissues mixed also reached 0.82. Finally, we provide screening methods for markers in the context of massive data as well as high-dimensional viscoelastic variables based on feature ablation for drug development and accurate grading of liver fibrosis. We propose a novel classifier that uses the dynamical mechanical variables as input markers, which can identify healthy, diseased, and post-treatment liver tissues.

KEYWORDS

cell mechanics, viscoelastic, machine learning, rheology, liver diagnosis

Introduction

Liver cirrhosis and cancer are serious liver diseases with high mortality rates due to their irreversibility (Tapper and Loomba, 2018; Agarwal et al., 2019), whereas liver fibrosis is the early stage of them (Friedman, 2010; Seitz et al., 2018; Stefan et al., 2019) and could be reversed by rational medication (Li et al., 2018; Salarian et al., 2019). To date, early diagnosis and quantification of the extent of liver fibrosis are of great clinical value for timely intervention and reversing the development of liver fibrosis (Friedman, 2010; Zhao et al., 2017; Tapper and Loomba, 2018; Balachandran et al., 2022). The current gold standard for

diagnosing liver disease is liver biopsy, which relies on the pathological examination of tissue samples obtained through invasive puncture. However, the invasive nature of biopsies significantly diminishes the patient experience and can potentially lead to complications (Eskew et al., 1997; Yasufuku and Fujisawa, 2007; Veronesi et al., 2010). In contrast, ultrasound has gained widespread applications as the preferred method for clinically screening liver diseases due to its radiation-free nature, cost-effectiveness, convenience, and invaluable real-time imaging capabilities (Bamber et al., 2013; Tapper and Loomba, 2018).

Currently, the primary diagnostic methods for the degree of liver fibrosis are semi-quantitative methods (Sun et al., 2017; Xu et al., 2021), such as liver examinations based on clinical, biochemical, and imaging methods. Therefore, there is a lack of a satisfactory method to accurately determine the degree of hepatic fibrosis. Liver pathology is a complex process characterized by various features at different stages. Utilizing a combination of diagnostic methods is advantageous compared to relying on a single biomarker, as it offers supplementary insights into the condition of the liver. It is well known that the mechanical properties of cells and tissues are closely related to their pathological states (Suresh, 2007; Grant and Twigg, 2013; Rigato et al., 2017; Mandal et al., 2019; Staunton et al., 2019; Guimarães et al., 2020). Utilizing elastography, it is possible to derive the modulus of elasticity of liver tissue and assess the grading of lesions based on their mechanical properties. Many experiments showed that the elastic stiffness is positively correlated with the degree of liver fibrosis (Ziol et al., 2005; Yin et al., 2007). Recent studies (Lei et al., 2017; Lewindon et al., 2019; Xue et al., 2020) have demonstrated that the combination of biochemical and mechanical parameters, along with imaging and ultrasound techniques, exhibits a markedly enhanced diagnostic efficacy for liver lesions compared to individual parameters alone. In addition, SVM has been successfully applied to classify cancerous and normal cells, yielding promising results (Wang et al., 2021). Linking mechanical properties to pathological states provides a novel precise and robust diagnostic marker for diagnosis (Staunton et al., 2019; Wang et al., 2021). However, soft biological tissues are not elastic materials, yet similar to living cells (Fabry et al., 2001; Dimitrije et al., 2004; Smith et al., 2005; Hoffman et al., 2006; Koenderink et al., 2009; Rigato et al., 2017; Hu et al., 2019), they are a viscoelastic material that exhibits a fascinating scaling-law creep response (Liu and Bilston, 2000; Chaudhuri et al., 2016; Chaudhuri et al., 2020). For liver tissues, scaling-law response is also observed in experiments (Chang et al., 2023). It puts doubts as to whether a single value of elastic modulus sufficiently discriminates the pathological stage of liver fibrosis. The correlation between the viscoelastic mechanical properties of liver tissue and liver lesions is currently unexplored. Therefore, quantifying the viscoelastic mechanical properties during liver fibrosis development can provide additional mechanical markers to grade the degree of liver fibrosis and to evaluate the effect of drug treatment, which further improves the precision of diagnosis. However, the high-dimensional mechanical data generated by viscoelastic characterization poses new challenges for evaluating the mechanics of liver fibrosis. The application of machine learning for medical diagnosis in imaging (Kononenko, 2001; Komura and Ishikawa, 2019; Soelistyo et al., 2022) provides us with a viable means to deal with such high-dimensional data.

In this study, we obtained the creep responses of mouse liver tissue sections by atomic force microscopy (AFM). Then, we characterized their creep responses using the self-similar hierarchical model and then acquired high-dimensional viscoelastic mechanical data of healthy, diseased, and MSCs-treated fibrotic liver tissues. Based on a supervised machine learning algorithm, the support vector machine (SVM) method is applied to discover useful mechanical markers, exploiting the hidden associations between viscoelastic parameters with liver pathological states. The combination of high-dimensional viscoelastic mechanical data and machine learning algorithm trained a liver pathological states classifier and the rest of the untrained data was used to test this classifier. We showed that the classifier could achieve 99% accuracy for healthy and diseased livers, 86% accuracy for healthy and MSCs-treated fibrotic livers, and 82% accuracy for a mixture of the three livers together using the viscoelastic mechanical parameters as the input markers.

Methods

Sections of the liver tissues of the mouse were used as the experimental object to acquire a more accurate viscoelastic mechanical response. The mouse liver tissues in the test were divided into three groups: healthy, diseased, and MSCs-treated fibrotic livers. The staging of liver biopsies through the fibrosis scoring systems, such as Batts and Ludwig or Metavir, is deemed most appropriate. Currently, achieving precise modulation for accurate staging of liver lesions during mouse culture remains challenging. Thus, we categorized the mice into three groups: healthy, diseased, and MSCs-treated fibrotic livers. During the mouse culture process, we implemented a relatively prolonged culture period to induce the development of noticeable lesions, with therapeutic drug injection serving as an intermediary state between the healthy and diseased states. C57BL/6 Mice were randomly assigned to three groups. The control group consisted of healthy, wildtype mice that did not receive any injections of MSCs therapy. Liver fibrosis was induced in the other two groups (diseased and MSCs-treated fibrotic groups, $n = 2$) by intraperitoneal injections of therapeutic drug (1 μL/g) for 7 weeks. At the end of the sixth week, half of the mice received a single intravenous infusion of 2 x105 MSCs. These mice constituted the MSCs-treated fibrotic groups. In the initial step, mouse liver extraction was performed, with particular attention given to isolating the tissues surrounding the portal veins, which connect the left lobe to the rest of the liver tissue. Subsequently, the liver tissues were immediately frozen at -80°C and cryo-sectioned to a nominal thickness of 15 μm using a Leica CM1850 cryostat (Leica Microsystems (United Kingdom) Ltd., Milton Keynes) and adhered to glass coverslips for future research. Afterward, the dynamical creep indentation test was performed on cells after conducting Masson's trichrome staining, Sirius Red staining, and aspartate aminotransferase (AST) assay. To mitigate the effects of local remodeling events on the tissue structure under investigation, measurements were carried out at multiple locations separated by a significant distance (i.e., > 50 μm). To reduce the influence of stiff collagen on tissue during characterization, dynamical and static indentation experiments were intentionally conducted away from the portal zones.

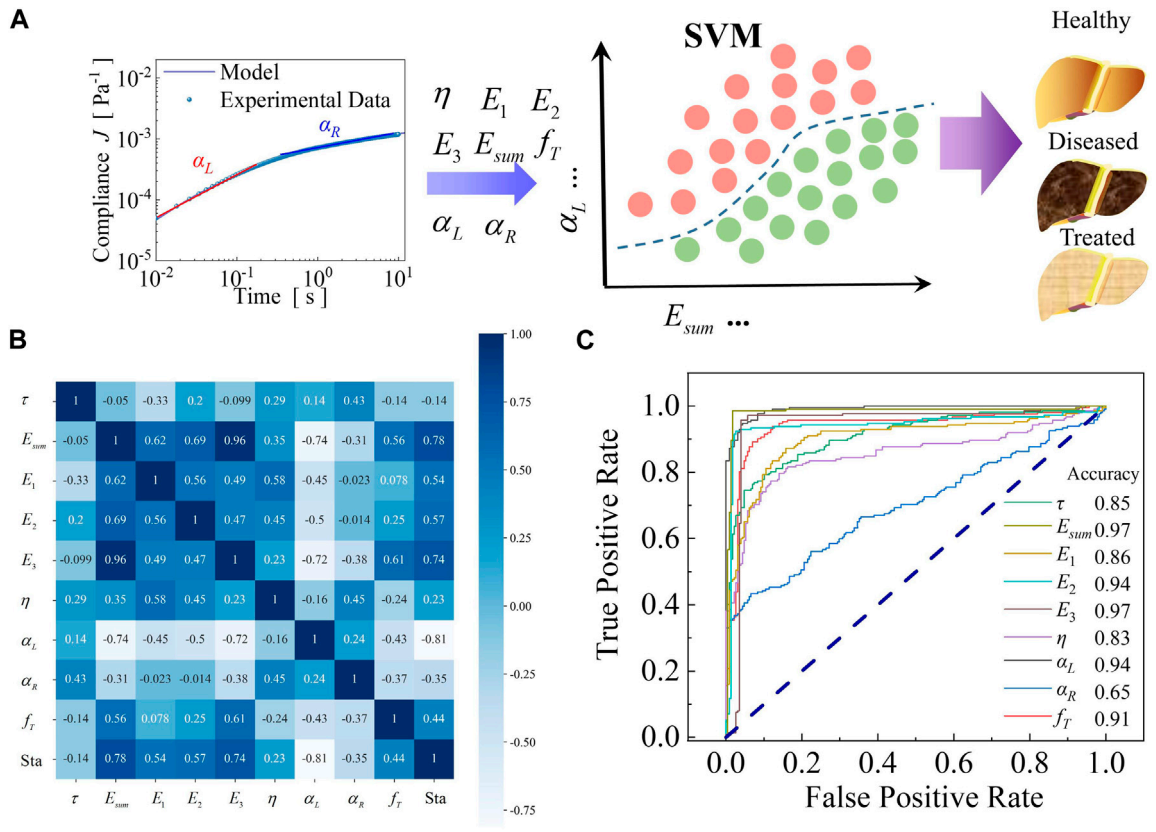

FIGURE 1
Performance assessment of single viscoelastic marker in the test data group of healthy and diseased livers. **(A)** Overview of machine learning-based liver states classification and diagnosis using viscoelastic mechanical parameters. E_1, E_2, E_3 and η can be obtained by performing creep testing through AFM and then characterizing them using the self-similar hierarchical model, while E_{sum} and f_T can be obtained by model parameter operations. The double power-law exponents (α_L and α_R) at different time scales can be obtained by the double power-law characterization of the creep compliance. The viscoelastic mechanical data set from the characterization of liver tissues is used to train the machine learning models for the classification of liver states. **(B)** The heat map of the Pearson correlation coefficient of viscoelastic variables between tissue status and viscoelastic variables of healthy and diseased livers. **(C)** Receiver operating characteristics (ROCs) of the classifier with each viscoelastic variable as a single mechanical marker input.

To obtain the viscoelastic mechanical properties of liver samples, the creep responses of the liver tissues were obtained by applying step stress to the samples by AFM with a customized spherical probe (diameter = 20 μm) and holding for 10 s. Each creep compliance indentation test was performed randomly on tissue sections with 100 μm spacing between two locations. Due to the relatively large sample area (~1 cm^2), each test performed by the micron-size spherical probe is regarded as a single mechanical measurement on 1 mouse. Each group received 800 measurements. Then, the viscosity (η) of cytoplasm, the elastic moduli of cytoplasm (E_1), cytoskeleton fiber (E_2), and whole cell structural network (E_3), and the transition frequency (f_T) can be acquired by characterizing the creep responses of liver tissues (Figure 1A) based on our previous self-similar hierarchical model (Hang et al., 2021; Hang et al., 2022), which provides a richer and physically meaningful description of the rheological behavior of biological tissues. The model can well fit the creep responses of cells and tissues, and more details about the model fitting can be found in our previous work (Hang et al., 2021; Hang et al., 2022). The R^2 values of creep compliance for the three liver tissues fitted using the self-similar hierarchical model are all above 0.9. The spherical indenter was used to apply step stress to the liver tissue sections, and the creep compliance expression can be obtained by the Hertz model (Lin and Horkay, 2008):

$$J = \frac{4\sqrt{R}\delta^{\frac{3}{2}}}{3F(1-\nu^2)}, \quad (1)$$

where R and δ are the radius and indentation depth of the spherical indenter, F is the step force, and ν is the Poisson's ratio with a value of 0.5 (i.e., incompressible). Experiments showed that the creep compliances (Eq. 1) of all three groups exhibit a universal two-stage scaling-law viscoelastic rheology (Chang et al., 2023). Typical creep curves of liver tissue showed that the power-law exponent of creep compliance is not constant with increasing loading time, reaching between 0.5 and 1.0 at small time scales (α_L) and stabilizing around 0.2 at larger timescales (α_R), which corresponds to the double power-law viscoelastic behavior of the complex modulus in the frequency domain (Rigato et al., 2017; Hurst et al., 2021). The double power-law viscoelastic model provides novel viscoelastic parameters as mechanical markers for liver fibrosis. SVM is well-suited for the analysis of high-dimensional data sets comprising numerous features, due to its ability to map data into a high-dimensional space. In such

scenarios, alternative classification algorithms often encounter dimensionality catastrophes, whereas SVMs efficiently handle the complexities of high-dimensional data (Dumais et al., 1998; Cristianini and Shawe-Taylor, 1999; Evgeniou et al., 2015). Since the individual viscoelastic parameters are not stand-alone and the training data are linearly inseparable, a nonlinear SVM classifier is developed by kernel method and soft interval maximization. The objective function for classification optimization is

$$\min\left(\frac{1}{2}\|\boldsymbol{w}\|^2\right) + C\sum_{i=1}^{n}\xi_i, \tag{2}$$

where the second is the regular term, $\boldsymbol{w}$ is the normal vector of the classified hyperplane (Eq. 2), C is a constant, and ξ_i is the relaxation factor. Here, we introduce the kernel function that can map the sample from the original space to a higher dimensional idiosyncratic space, making the sample linearly differentiable in the new space. The best classification in this study is the Gaussian kernel function with the expression of

$$\kappa\left(x_i, x_j\right) = \exp\left(-\frac{\left\|x_i - x_j\right\|^2}{2\sigma^2}\right), \tag{3}$$

where x_i and x_j denote the input categorical feature variables and σ is the width (Eq. 3) of the Gaussian kernel. In this way, a classifier (Figure 1A) for liver pathological states was built based on the SVM method and Python programming language. In each liver tissue sample, 70% of the data is allocated to the training group, while the remaining 30% is assigned to the testing group.

Ethical approval

It has been confirmed that the experimental data collection complied with relevant institutional, national, and international guidelines and legislation with permission from the administration committee of experimental animals of The Second Affiliated Hospital of Xi'an Jiaotong University, China. All methods reported follow ARRIVE guidelines.

Results and discussion

Assessment of classification accuracy for viscoelastic variables

The classification of healthy and diseased liver tissues with a single mechanical marker

After building the prediction classifier to output liver pathological states, we evaluated the accuracy of each viscoelastic variable based on the classifier for healthy and diseased livers. In the assessment of the viscoelastic variable of healthy and diseased livers, 70% of the data were treated as the training group and 30% of the data as the test group. The status variables for healthy and diseased liver tissues have been set as 0 and 2, respectively. We first analyze the correlation between the parameters through Pearson's correlation coefficient. Pearson's correlation coefficient was calculated by the following formula:

$$r = \frac{\sum(x-\bar{x})(y-\bar{y})}{\sqrt{\sum(x-\bar{x})^2\sum(y-\bar{y})^2}} \tag{4}$$

The Pearson correlation coefficient (Eq. 4) of each variable with others is shown in Figure 1B. It indicates that the status of the liver tissue exhibits the highest correlation with the power-law exponent at small time scales α_L, followed by the elastic modulus (E_{sum}, E_3, E_2, E_1) and transition frequency (f_T), while the viscosity and power-law exponent at large time scales α_R exhibit a minimal correlation with liver status. Moreover, it is noteworthy that the correlation between the elastic moduli is extremely high, suggesting that the increase in elastic moduli during liver lesions is all-encompassing and not limited to the cytoplasm or cytoskeleton. There was a significant positive correlation between the liver tissue lesion and the stiffness, which was consistent with many experiments (Yin et al., 2007; Patel et al., 2015). Different from previous experiments (Wang et al., 2021), we introduced several viscoelastic mechanical variables as classification features and obtained precise correlations between them and liver status. Overall, there is a clear perception that a higher value of α_L and a lower value of E_{sum} indicate a lower incidence of liver lesions. In addition, other variables, such as viscosity (η), relaxation time (τ), and transition frequency (f_T), showed a relatively low correlation with the status of liver tissue, however, they still have an appreciable degree of accuracy (85%). As shown in Figure 1C, the elastic modulus E_{sum} and E_1 have the highest accuracy, followed by α_L, and meanwhile, the accuracy of the transition frequency reaches more than 0.9. In contrast, the accuracy of α_R is extremely low, which is inextricably intertwined with the self-similar hierarchical properties of liver tissues due to its power-law exponent being concentrated around 0.2 at longer time scales. In the third-level hierarchical model, the power-law exponent tends to be constant as the stiffness increases, and thus, the increase in elastic modulus has minimal effect on α_R in this case.

The classification of healthy and diseased liver tissues with multiple mechanical markers

As the viscoelastic properties of liver tissues differ substantially between healthy and diseased states, high classification accuracy can be obtained using a single viscoelastic variable (such as E_{sum} and α_L). However, for the early stage of liver fibrosis, the single mechanical property does not change significantly compared to healthy tissues, and at this point, adding variables as classification features contribute greatly to the classification accuracy. Using a combination of viscoelastic mechanical variables without high accuracy as the input marker of the classifier, the classification accuracy could reach a higher level. As shown in Figure 2A, the classification accuracy of the classifier with double variables as classification input markers all reached over 0.93. Based on machine learning, the implied relationships between certain viscoelastic variables could be exploited to improve the accuracy of liver status classification. When two mechanical variables were used to classify healthy and diseased livers, they showed distinct areas of aggregation (Figure 2B). When the number of variables was increased to three, the accuracy of liver classification was further improved (Figure 2C), which benefited from the more pronounced aggregation characteristics of liver status (Figure 2D) at multivariate. Here, the combination of three variables without high accuracy as a

10.3389/fbioe.2024.1404508

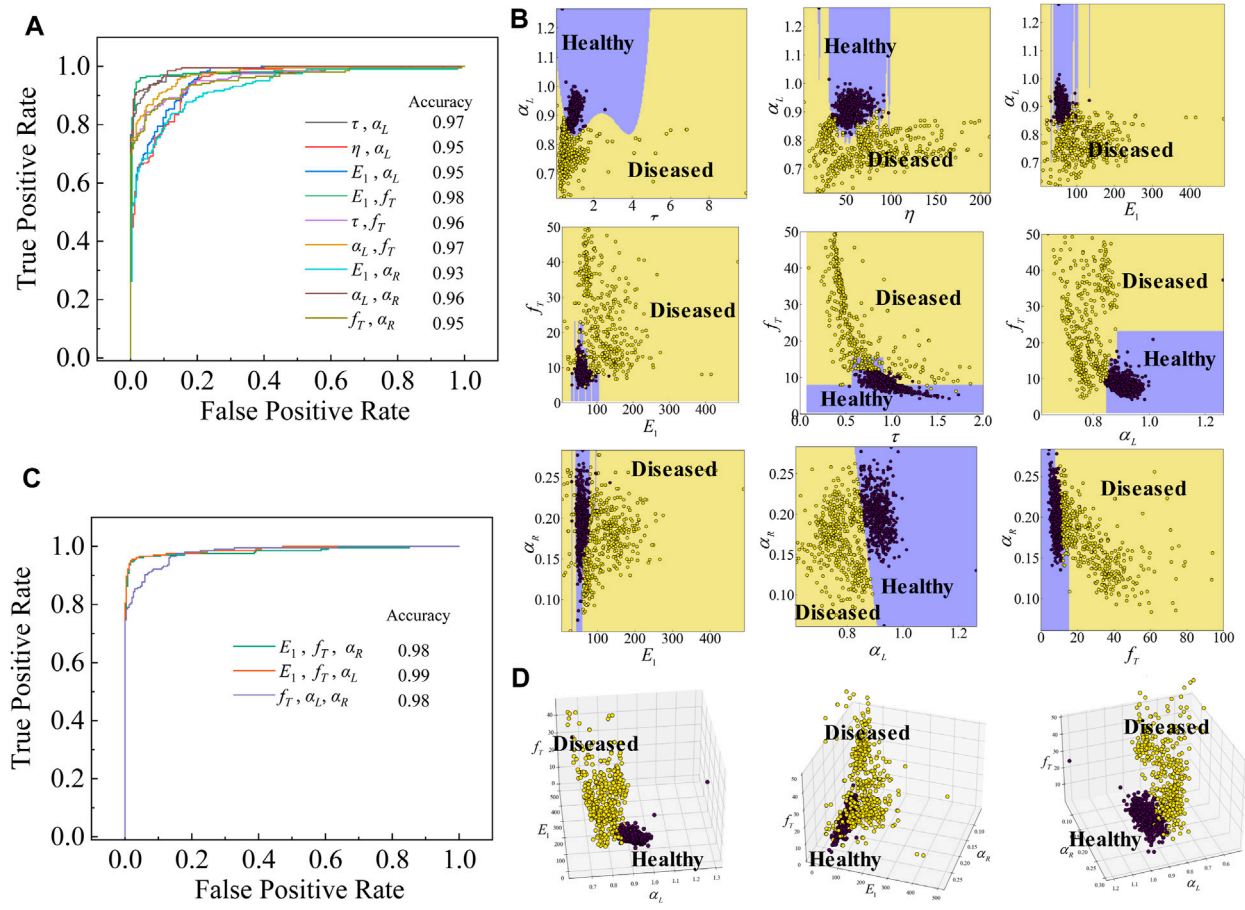

FIGURE 2
Multiple dynamical mechanical markers performance assessment on the test data group of healthy and diseased livers. **(A)** ROCs of the classifier with two viscoelastic variables as marker input. **(B)** Data points for healthy and diseased livers have their regions when double viscoelastic variables are used as marker input. **(C)** ROCs of the classifier with three viscoelastic variables as marker input. **(D)** When the three viscoelastic variables were used as classification marker input, the data point aggregation feature was more pronounced for healthy and diseased livers compared to that of the two variables used.

single marker input brings the classification accuracy to a higher level, even exceeding 0.98, which is a great improvement compared to that of a single input variable (Figure 1C). We tested nine different combinations of two variables and three different combinations of three variables as input markers of the classifier. Overall, the classification accuracy has reached the best performance when using three viscoelastic variables as marker input, and its classification accuracy even reaches 0.98. This demonstrates that the combination of viscoelastic mechanical variables can capture more salient liver states, enabling a more accurate pathological state prediction of liver tissues, by learning them directly from the implicit connections of the viscoelastic mechanical variables.

An interpretable predictive model for the liver pathological states

Adding diseased tissues after drug treatment to the classifier

Having enabled the classification of healthy and diseased livers, we next expanded the machine learning framework to investigate liver tissues after drug treatment (with the status variable of 1). We trained the prediction classifier and measured the accuracy by combining four different combinations of two viscoelastic variables as input markers to the prediction classifier. For each dataset, we split the data by liver status (healthy, diseased, and MSCs-treated fibrotic) and computed separate confusion matrices to ensure that there is no systematic bias in the predictions. Overall, the best-performing combination is the one combing the elastic modulus E_{sum} and the power-law exponent α_L, followed by the power-law exponent α_L and transition frequency f_T, which had relatively few data points in the junction regions of three liver tissues (Figure 3A). The increase in the number of viscoelastic mechanical variables to the classifier led to an increase in the classification accuracy (Figure 3B). With the introduction of the dataset of diseased livers after drug treatment, there were essentially no apparent changes in the Pearson correlation coefficient (Figure 3C) between the liver status and the individual viscoelastic variables, compared with the dataset of healthy and diseased livers (Figure 1B).

As shown in Refs. (Ziol et al., 2005; Yin et al., 2007), the elastic stiffness of healthy and diseased livers show significant differences.

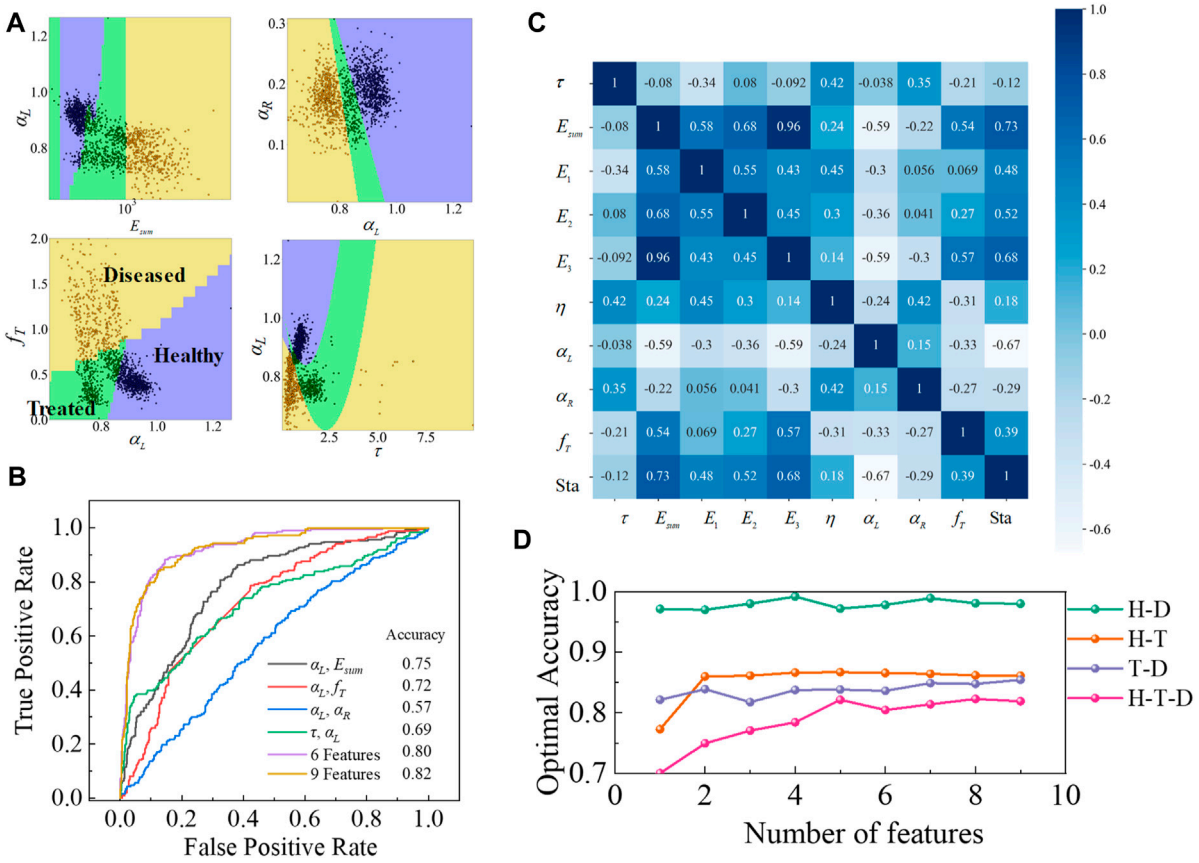

FIGURE 3
Multiple mechanical markers performance assessment on the test data group of healthy, diseased, and MSCs-treated fibrotic livers. **(A)** Data points for healthy, diseased, and MSCs-treated fibrotic livers have their regions when the two variables are used as classification marker inputs. **(B)** ROCs of the classifier with 2, 6, and 9 viscoelastic variables as marker input. **(C)** The heat map of the Pearson correlation coefficient of viscoelastic variables of healthy, diseased, and MSCs-treated fibrotic liver tissues. **(D)** Optimal accuracy was obtained when different numbers of variables were used for different liver classifications. Here, H, D, and T represent healthy, diseased, and MSCs-treated fibrotic liver tissues, respectively.

Since many viscoelastic parameters exhibit a strong correlation with the elastic stiffness of tissues, a single viscoelastic variable could achieve a sufficiently high classification accuracy. Consequently, when classifying healthy and diseased livers, we mainly investigated the cases of 2 and 3 variables as the marker input. With the introduction of MSCs-treated fibrotic livers, we used cross-validation to obtain optimal classification accuracy by feature elimination for different numbers of mechanical variables. We implemented a k-fold cross validation with k = 10, where the training set was divided into 10 subsamples and one subsample was reserved for model validation, while the remaining nine subsamples were utilized for training. During cross-validation, each subset is iteratively utilized as a test set once, while the remaining k-1 folds are employed as a training set to train the model and assess its performance on each fold. Subsequently, the results from all k evaluations are averaged to derive the final evaluation of the model's performance. As illustrated in Figure 3D, for the classification of healthy and diseased livers, the optimal classification accuracy is almost independent of the number of input markers, since E_{sum} achieves an accuracy of 0.97 by itself as the single input marker. The introduction of liver tissue data after drug treatment led to a significant trend of increasing the optimal accuracy with the number of input mechanical markers, especially when three liver tissues were mixed for classification accuracy exploration. A comparison of the classification accuracy data of several groups shows that the classification accuracy has reached the optimal value, when the maker number is around 5, after which the increase of markers has little effect on the improvement of accuracy. The viscoelastic variables corresponding to the optimal accuracy of five markers are E_{sum}, E_2, E_3, α_L, and f_T, which were also the top five viscoelastic variables in terms of accuracy of classification of healthy and diseased livers as a single marker input in the classifier. Compared to the case when only the elastic modulus E_{sum} was used as a marker, the addition of viscoelastic properties such as the power-law exponent α_L and transition frequency f_T remarkably improved the classification accuracy of the three liver tissues from 0.7 to 0.82, which is far more significant than the improvement in accuracy in the classification of the two liver tissues. The mean values of elastic modulus (E_{sum}) of MSCs-treated fibrotic liver tissues (681.4 MPa) were not significantly different from that of healthy liver tissues (456.1 MPa). The relatively small differences between the elastic moduli of healthy liver tissues and MSCs-treated fibrotic lives suggests the therapeutic efficacy of MSCs in ameliorating liver

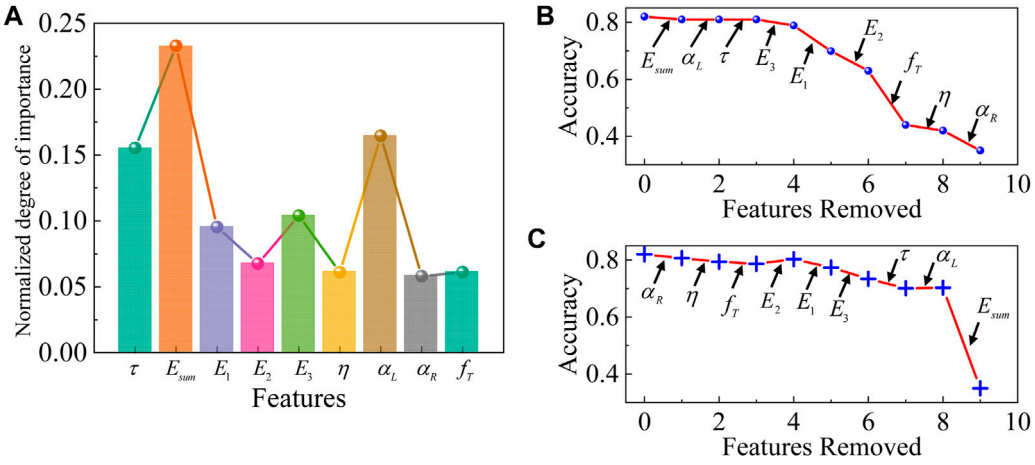

FIGURE 4
Feature ablation studies of the classifier with healthy, diseased, and MSCs-treated fibrotic liver tissues together. **(A)** The normalized importance of each feature. Feature ablation **(B)** from high to low importance and **(C)** from low to high importance. Feature ablation demonstrates the role of each principal viscoelastic variable in the prediction of the classifier. Each arrow indicates the cumulative replacement of a given principal viscoelastic variable with Gaussian noise.

fibrosis. For diseased liver tissue, the elastic modulus is approximately five times or more than that of healthy tissue (Ziol et al., 2005), which indicates that the elastic modulus may serve as a biomechanical marker for assessing liver fibrosis. When multiple variables were used as input markers, the classification accuracy reached 0.87, indicating that using multiple makers can classify liver tissues in different states by the implied relationships between viscoelastic variables. Therefore, the effect of using all viscoelastic variables as input markers for liver tissue classification will gradually show up with the increasing number of liver tissue statuses such as the grading of liver fibrosis, and eliminates the process of mechanical marker screening.

Feature ablation studies

In this study, we used nine viscoelastic mechanical variables as input markers in the classification of liver pathological states, but in fact, not only do the viscoelastic properties of liver tissues change when lesions occur, but also other properties such as plasticity, component protein characteristics, and image characteristics. Combining viscoelastic properties with these characteristics will greatly improve the quality of liver lesion diagnosis, but will also result in a considerable computational requirement, therefore, a reasonable selection of markers is crucial to improve the efficiency of liver diagnosis. To determine the minimal information required for liver state prediction, we first determined the importance (Figure 4A) ranking of the viscoelastic features of the tissue using Support Vector Machine Recursive Feature Elimination (SVM-RFE). Subsequently, recursive feature ablation is conducted via cross-validation to determine the optimal number of features. Then, we systematically removed individual principal viscoelastic variables (replacing them with Gaussian noise) and calculated the performance of the classifier after the removal of each viscoelastic variable. Through multiple iterations, we found that a single mechanical marker (α_R) could be used to predict liver tissues with 42% accuracy—apparently higher than random chance assuming the same probability of selecting a liver status (33.33%, Figure 4B). The elimination of E_{sum} in the positive-order feature ablation (Figure 4C) does not generate a significant decrease in accuracy, but the elimination of E_1 and E_2 has a significant effect on accuracy, which results from the high correlation between the elastic moduli, and a precipitous drop in accuracy when E_{sum} is finally eliminated in the inverted-order feature ablation. Feature ablation studies demonstrated that E_{sum} was the viscoelastic variable that contributed most to prediction accuracy. Feature ablation studies can determine the importance of input biomarkers and filter out invalid feature variables, thus improving classifier efficiency in high-dimensional data classification and liver diagnosis.

A method for evaluating drug treatment effects

Having established the SVM-based classifier that can classify livers in an interpretable manner, we sought to define a new approach to drug-based screening using a predictive classifier. To this end, we tested the classification accuracy of liver tissues after drug treatment against healthy and diseased livers to determine the effect of the indicated drug on liver states. The accuracy of classification of treated livers with healthy and diseased livers reached 0.86 and 0.85 (Figure 3D), respectively. The MSCs-treated fibrotic liver tissue was clearly classified from diseased liver tissues and there is a tendency for the elastic modulus to be greatly reduced, which indicates that the drug treatment has freed them from the diseased state. The accurate classification of healthy liver tissues also indicates that the drug treatment has not completely restored them to a healthy state. Overall, drug treatment allows the liver tissue to recover from the disease to healthy state. The accuracy of the classification of liver tissue after drug treatment compared to healthy and diseased liver tissues allows a clear determination of the effect of drug treatment and the need for continued drug use. When the classification accuracy of the MSCs-treated fibrotic liver tissues with healthy liver tissues is reduced to 0.33 and the classification accuracy with diseased tissue reaches a high level, we can assume that the liver tissue has recovered to its original state under drug treatment, which is, of course, the ideal situation. As an example, our method can be used to determine the effect of a drug by screening the recovery of viscoelastic properties induced by the drug. We

can further analyze the changes in the main viscoelastic biomarkers to determine the target of the action of the drug. In addition, in the process of liver fibrosis, there exists a grading of its lesion degree. At this time, our three-class classifier can be further extended to achieve accurate grading of liver fibrosis and provide the basis for subsequent treatment.

Discussions

Machine learning is now a powerful tool for medical diagnosis. Although many machine learning diagnostic models are mainly based on the recognition of image technology, they lack suitable mechanical markers, which makes them rarely used to identify tissue lesions in similar states or less severe lesions. Here, we analyzed the creep responses of liver tissues by a self-similar hierarchical model and obtained the viscoelastic properties of liver tissues in different states. Then, we built an SVM-based machine learning classifier with viscoelastic properties as input mechanical markers. Remarkably, our SVM classifier successfully identifies elastic modulus E_{sum} and power-law exponent α_L as the strongest predictors of liver tissue status. Furthermore, the addition of many viscoelastic variables makes the accuracy of this classifier greatly improved compared to the case where only a single variable is used. An extension of this work would be the use of this classifier for the quantitative assessment of drug treatment effects. The classification accuracy of liver tissue after drug treatment with healthy and diseased liver tissues can be obtained towards the classifier, and a lower classification accuracy with healthy tissue and a higher classification accuracy with diseased tissue indicated a better recovery effect of the drug. Furthermore, it is also feasible to combine multiple different states of liver tissue for classification, which provides a new strategy for grading liver fibrosis. For such cases, we also give screening methods based on feature ablation for inputting biomarkers at high dimensional data. We have shown that a novel classifier, based on the learned model, can predict the pathological states of liver tissue based on the implicit relationship of viscoelastic biomarkers. Once trained, this fully automated classifier can distinguish between normal, diseased, and MSCs-treated fibrotic liver tissue without any further human intervention, paving the way for drug screening and development. Currently, creep testing relies on liver tissue sections, which, despite their clinical utility, pose significant limitations. Biopsy-based procurement of liver tissue sections for clinical purposes is invasive, causing damage and discomfort. AFM measurements also fall slightly short in facilitating large-scale lesion diagnosis. However, this study presents a novel approach for characterizing liver tissue lesion progression. There are two main advantages of our proposed method in relation to existing methodologies. One is the richness of viscoelastic mechanical markers, which is conducive to improving the reliability of diagnosis. The second is the quantization of viscoelastic mechanical markers, which is conducive to improving the accuracy of diagnosis compared with the qualitative judgment of imaging. In future work, improving the culture conditions to achieve precise staging of liver lesions in mice will be the focus. Subsequently, further validation of the method proposed in this study will then be carried out, based on the improved staging of liver biopsies using fibrosis scoring systems. With the advancement of non-invasive detection techniques for liver tissues, our proposed viscoelastic mechanics markers and machine learning-based diagnostic method offer valuable insights for diagnosing liver tissue lesion progression.

Data availability statement

The original contributions presented in the study are included in the article/Supplementary Material, further inquiries can be directed to the corresponding authors.

Ethics statement

The animal study was approved by the administration committee of experimental animals of The Second Affiliated Hospital of Xi'an Jiaotong University, China. The study was conducted in accordance with the local legislation and institutional requirements.

Author contributions

HZ: Data curation, Formal Analysis, Investigation, Methodology, Software, Validation, Visualization, Writing–original draft. J-TH: Data curation, Formal Analysis, Investigation, Methodology, Project administration, Resources, Software, Supervision, Validation, Visualization, Writing–original draft, Writing–review and editing. ZC: Data curation, Formal Analysis, Investigation, Methodology, Software, Validation, Writing–original draft. SY: Formal Analysis, Investigation, Methodology, Software, Writing–original draft. HY: Data curation, Formal Analysis, Funding acquisition, Investigation, Methodology, Project administration, Resources, Software, Validation, Visualization, Writing–original draft, Writing–review and editing. G-KX: Conceptualization, Data curation, Formal Analysis, Funding acquisition, Investigation, Methodology, Project administration, Resources, Software, Supervision, Validation, Visualization, Writing–original draft, Writing–review and editing.

Funding

The author(s) declare that financial support was received for the research, authorship, and/or publication of this article. Financial supports from the National Natural Science Foundation of China (Grant No. 12302221), the Natural Science Basic Research Plan in Shaanxi Province of China (Grant No. 2019JC-02), and the Fundamental Research Funds for the Central Universities of China are acknowledged.

Conflict of interest

J-TH, ZC, and G-KX were employed by the SVL.

The remaining authors declare that the research was conducted in the absence of any commercial or financial relationships that could be construed as a potential conflict of interest.

Publisher's note

References

Agarwal, T., Subramanian, B., and Maiti, T. K. (2019). Liver tissue engineering: challenges and opportunities. *ACS Biomaterials Sci. Eng.* 5, 4167–4182. doi:10.1021/acsbiomaterials.9b00745

Balachandran, Y. L., Wang, W., Yang, H., Tong, H., Wang, L., Liu, F., et al. (2022). Heterogeneous iron oxide/dysprosium oxide nanoparticles target liver for precise magnetic resonance imaging of liver fibrosis. *ACS Nano* 16, 5647–5659. doi:10.1021/acsnano.1c10618

Bamber, J., Cosgrove, D., Dietrich, C., Fromageau, J., Bojunga, J., Calliada, F., et al. (2013). EFSUMB guidelines and recommendations on the clinical use of ultrasound elastography. Part 1: basic principles and technology. *Ultraschall Med.* 34, 169–184. doi:10.1055/s-0033-1335205

Chang, Z., Zhang, L., Hang, J.-T., Liu, W., and Xu, G.-K. (2023). Viscoelastic multiscale mechanical indexes for assessing liver fibrosis and treatment outcomes. *Nano Lett.* 23, 9618–9625. doi:10.1021/acs.nanolett.3c03341

Chaudhuri, O., Cooper-White, J., Janmey, P. A., Mooney, D. J., and Shenoy, V. B. (2020). Effects of extracellular matrix viscoelasticity on cellular behaviour. *Nature* 584, 535–546. doi:10.1038/s41586-020-2612-2

Chaudhuri, O., Klumpers, D., Darnell, M., Bencherif, S. A., Weaver, J. C., et al. (2016). Hydrogels with tunable stress relaxation regulate stem cell fate and activity. *Nat. Mater.* 15, 326–334. doi:10.1038/nmat4489

Cristianini, N., and Shawe-Taylor, J. (1999). *An introduction to support Vector Machines: and other kernel-based learning methods*. Cambridge University Press.

Dimitrije, S., Béla, S., Ben, F., Ning, W., Fredberg, J. J., and Buy, J. E. (2004). Rheology of airway smooth muscle cells is associated with cytoskeletal contractile stress. *J. Appl. Physiology* 96, 1600–1605. doi:10.1152/japplphysiol.00595.2003

Dumais, S., Platt, J., Heckerman, D., and Sahami, M. (1998). *Inductive learning algorithms and representations for text categorization.*

Eskew, L. A., Bare, R. L., and McCullough, D. L. (1997). Systematic 5 region prostate biopsy is superior to sextant method for diagnosing carcinoma of the prostate. *J. Urology* 157, 199–203. doi:10.1016/S0022-5347(01)65322-9

Evgeniou, T., and Pontil, M. (2015). in *Algorithmic learning theory*. Editors O. Watanabe and T. Yokomori (Springer Berlin Heidelberg), 106–117.

Fabry, B., Maksym, G. N., Butler, J. P., Glogauer, M., Navajas, D., and Fredberg, J. J. (2001). Scaling the microrheology of living cells. *Phys. Rev. Lett.* 87, 148102. doi:10.1103/physrevlett.87.148102

Friedman, S. L. (2010). Evolving challenges in hepatic fibrosis. *Nat. Rev. Gastroenterology Hepatology* 7, 425–436. doi:10.1038/nrgastro.2010.97

Grant, C. A., and Twigg, P. C. (2013). Pseudostatic and dynamic nanomechanics of the tunica adventitia in elastic arteries using atomic force microscopy. *ACS Nano* 7, 456–464. doi:10.1021/nn304508x

Guimarães, C. F., Gasperini, L., Marques, A. P., and Reis, R. L. (2020). The stiffness of living tissues and its implications for tissue engineering. *Nat. Rev. Mater.* 5, 351–370. doi:10.1038/s41578-019-0169-1

Hang, J.-T., Kang, Y., Xu, G.-K., and Gao, H. (2021). A hierarchical cellular structural model to unravel the universal power-law rheological behavior of living cells. *Nat. Commun.* 12, 6067. doi:10.1038/s41467-021-26283-y

Hang, J.-T., Xu, G.-K., and Gao, H. Frequency-dependent transition in power-law rheological behavior of living cells. *Sci. Adv.* 8, eabn6093. doi:10.1126/sciadv.abn60932022).

Hoffman, B. D., Gladys, M., Citters, K. M., and Van and Crocker, J. C. (2006). The consensus mechanics of cultured mammalian cells. *Proc. Natl. Acad. Sci. U. S. A.* 103, 10259–10264. doi:10.1073/pnas.0510348103

Hu, J., Li, Y., Hao, Y., Zheng, T., Gupta, S. K., Parada, G. A., et al. (2019). High stretchability, strength, and toughness of living cells enabled by hyperelastic vimentin intermediate filaments. *Proc. Natl. Acad. Sci.* 116, 17175–17180. doi:10.1073/pnas.1903890116

Hurst, S., Vos, B. E., Brandt, M., and Betz, T. (2021). Intracellular softening and increased viscoelastic fluidity during division. *Nat. Phys.* 17, 1270–1276. doi:10.1038/s41567-021-01368-z

Koenderink, G. H., Dogic, Z., Nakamura, F., Bendix, P. M., MacKintosh, F. C., Hartwig, J. H., et al. (2009). An active biopolymer network controlled by molecular motors. *Proc. Natl. Acad. Sci. U. S. A.* 106, 15192–15197. doi:10.1073/pnas.0903974106

Komura, D., and Ishikawa, S. (2019). Machine learning approaches for pathologic diagnosis. *Virchows Arch.* 475, 131–138. doi:10.1007/s00428-019-02594-w

Kononenko, I. (2001). Machine learning for medical diagnosis: history, state of the art and perspective. *Artif. Intell. Med.* 23, 89–109. doi:10.1016/S0933-3657(01)00077-X

Lei, B., Liu, Y., Dong, C., Chen, X., Zhang, X., Diao, X., et al. (2017). Assessment of liver fibrosis in chronic hepatitis B via multimodal data. *Neurocomputing* 253, 169–176. doi:10.1016/j.neucom.2016.09.128

Lewindon, P. J., Puertolas-Lopez, M. V., Ramm, L. E., Noble, C., Pereira, T. N., Wixey, J. A., et al. (2019). Accuracy of transient elastography data combined with APRI in detection and staging of liver disease in pediatric patients with cystic fibrosis. *Clin. Gastroenterology Hepatology* 17, 2561–2569.e5. doi:10.1016/j.cgh.2019.03.015

Li, C., Li, R., and Zhang, W. (2018). Progress in non-invasive detection of liver fibrosis. *Cancer Biol. Med.* 15, 124. doi:10.20892/j.issn.2095-3941.2018.0018

Lin, D. C., and Horkay, F. (2008). Nanomechanics of polymer gels and biological tissues: a critical review of analytical approaches in the Hertzian regime and beyond. *Soft Matter* 4, 669–682. doi:10.1039/B714637J

Liu, Z., and Bilston, L. (2000). On the viscoelastic character of liver tissue: experiments and modelling of the linear behaviour. *Biorheology* 37, 191–201. doi:10.1016/S1083-8791(00)70031-0

Mandal, K., Pogoda, K., Nandi, S., Mathieu, S., Kasri, A., Klein, E., et al. (2019). Role of a kinesin motor in cancer cell mechanics. *Nano Lett.* 19, 7691–7702. doi:10.1021/acs.nanolett.9b02592

Patel, K., Bedossa, P., and Castera, L. (2015). Diagnosis of liver fibrosis: present and future. *Seminars liver Dis.* 35, 166–183. doi:10.1055/s-0035-1550059

Rigato, A., Miyagi, A., Scheuring, S., and Rico, F. (2017). High-frequency microrheology reveals cytoskeleton dynamics in living cells. *Nat. Phys.* 13, 771–775. doi:10.1038/nphys4104

Salarian, M., Turaga, R. C., Xue, S., Nezafati, M., Hekmatyar, K., Qiao, J., et al. (2019). Early detection and staging of chronic liver diseases with a protein MRI contrast agent. *Nat. Commun.* 10, 4777. doi:10.1038/s41467-019-11984-2

Seitz, H. K., Bataller, R., Cortez-Pinto, H., Gao, B., Gual, A., Lackner, C., et al. (2018). Publisher correction: alcoholic liver disease. *Nat. Rev. Dis. Prim.* 4, 18. doi:10.1038/s41572-018-0021-8

Smith, B. A., Barbara, T., Martin, J. G., and Peter, G. (2005). Probing the viscoelastic behavior of cultured airway smooth muscle cells with atomic force microscopy: stiffening induced by contractile agonist. *Biophysical J.* 88, 2994–3007. doi:10.1529/biophysj.104.046649

Soelistyo, C. J., Vallardi, G., Charras, G., and Lowe, A. R. (2022). Learning biophysical determinants of cell fate with deep neural networks. *Nat. Mach. Intell.* 4, 636–644. doi:10.1038/s42256-022-00503-6

Staunton, J. R., So, W. Y., Paul, C. D., and Tanner, K. (2019). High-frequency microrheology in 3D reveals mismatch between cytoskeletal and extracellular matrix mechanics. *Proc. Natl. Acad. Sci.* 116, 14448–14455. doi:10.1073/pnas.1814271116

Stefan, N., Häring, H.-U., and Cusi, K. (2019). Non-alcoholic fatty liver disease: causes, diagnosis, cardiometabolic consequences, and treatment strategies. *Lancet Diabetes and Endocrinol.* 7, 313–324. doi:10.1016/S2213-8587(18)30154-2

Sun, Y., Zhou, J., Wang, L., Wu, X., Chen, Y., Piao, H., et al. (2017). New classification of liver biopsy assessment for fibrosis in chronic hepatitis B patients before and after treatment. *Hepatology* 65, 1438–1450. doi:10.1002/hep.29009

Suresh, S. (2007). Biomechanics and biophysics of cancer cells. *Acta Biomater.* 3, 413–438. doi:10.1016/j.actbio.2007.04.002

Tapper, E. B., and Loomba, R. (2018). Noninvasive imaging biomarker assessment of liver fibrosis by elastography in NAFLD. *Nat. Rev. Gastroenterology Hepatology* 15, 274–282. doi:10.1038/nrgastro.2018.10

Veronesi, U., Viale, G., Paganelli, G., Zurrida, S., Luini, A., Galimberti, V., et al. (2010). Sentinel lymph node biopsy in breast cancer: ten-year results of a randomized controlled study. *Ann. Surg.* 251, 595–600. doi:10.1097/sla.0b013e3181c0e92a

Wang, H., Zhang, H., Da, B., Tamura, R., Goto, K., et al. (2021). Mechanomics biomarker for cancer cells unidentifiable through morphology and elastic modulus. *Nano Lett.* 21, 1538–1545. doi:10.1021/acs.nanolett.1c00003

Xu, X., Zhou, X., Xiao, B., Xu, H., Hu, D., Qian, Y., et al. (2021). Glutathione-responsive magnetic nanoparticles for highly sensitive diagnosis of liver metastases. *Nano Lett.* 21, 2199–2206. doi:10.1021/acs.nanolett.0c04967

Xue, L.-Y., Jiang, Z. Y., Fu, T. T., Wang, Q. M., Zhu, Y. L., Dai, M., et al. (2020). Transfer learning radiomics based on multimodal ultrasound imaging for staging liver fibrosis. *Eur. Radiol.* 30, 2973–2983. doi:10.1007/s00330-019-06595-w

Yasufuku, K., and Fujisawa, T. (2007). Staging and diagnosis of non-small cell lung cancer: invasive modalities. *Respirology* 12, 173–183. doi:10.1111/j.1440-1843.2007.01035.x

Yin, M., Talwalkar, J. A., Glaser, K. J., Manduca, A., Grimm, R. C., Rossman, P. J., et al. (2007). Assessment of hepatic fibrosis with magnetic resonance elastography. *Clin. Gastroenterology Hepatology* 5, 1207–1213.e2. doi:10.1016/j.cgh.2007.06.012

Zhao, J., Zhai, F., Cheng, J., He, Q., Luo, J., Yang, X., et al. (2017). Evaluating the significance of viscoelasticity in diagnosing early-stage liver fibrosis with transient elastography. *PLoS ONE* 12, e0170073. doi:10.1371/journal.pone.0170073

Ziol, M., Handra-Luca, A., Kettaneh, A., Christidis, C., Mal, F., Kazemi, F., et al. (2005). Noninvasive assessment of liver fibrosis by measurement of stiffness in patients with chronic hepatitis C. *Hepatology* 41, 48–54. doi:10.1002/hep.20506

frontiers | Frontiers in Bioengineering and Biotechnology

TYPE Brief Research Report
PUBLISHED 18 July 2024
DOI 10.3389/fbioe.2024.1399611

OPEN ACCESS

EDITED BY
Ge He,
University of Wisconsin–Milwaukee,
United States

REVIEWED BY
Malek Adouni,
Abdullah Al Salem University, biomedical and instrumentation engineering, Kuwait
Uriel Zapata,
EAFIT University, Colombia

*CORRESPONDENCE
Ine Mylle,
ine.mylle@kuleuven.be

RECEIVED 12 March 2024
ACCEPTED 28 June 2024
PUBLISHED 18 July 2024

CITATION
Mylle I, Funaro A, Crouzier M, Bogaerts S and Vanwanseele B (2024), Achilles tendon compliance influences tendon loading more than Achilles tendon twist in Achilles tendinopathy: a musculoskeletal modeling approach.
Front. Bioeng. Biotechnol. 12:1399611.
doi: 10.3389/fbioe.2024.1399611

Achilles tendon compliance influences tendon loading more than Achilles tendon twist in Achilles tendinopathy: a musculoskeletal modeling approach

Ine Mylle[1]*, Alessia Funaro[1], Marion Crouzier[2], Stijn Bogaerts[3,4] and Benedicte Vanwanseele[1]

[1]Human Movement Biomechanics Research Group, Department of Movement Science, KU Leuven, Leuven, Belgium, [2]Movement Interactions Performance, MIP, UR 4334, Nantes University, Nantes, France, [3]Locomotor and Neurological Disorders Research Group, Department of Development and Regeneration, KU Leuven, Leuven, Belgium, [4]Department of Physical and Rehabilitation Medicine, University Hospitals Leuven, Leuven, Belgium

The Achilles tendon exhibits anatomical variations in subtendon twist among individuals, and its compliance can change due to conditions like Achilles tendinopathy. However, current musculoskeletal models overlook these material and morphological variations. This study aimed to investigate the impact of altering Achilles subtendon insertion points and compliance on the triceps surae muscle forces, and therefore tendon loading, during dynamic exercises in one Achilles tendinopathy patient. First, subtendon insertion points were altered in the musculoskeletal model based on a subject-specific 3D freehand ultrasound model and for three types of subtendon twists: low, medium, and high. Second, tendon compliance was modeled based on experimental values, creating three musculoskeletal models: compliant, mean, and stiff. Results indicated that tendon compliance had a larger effect than tendon twist on triceps surae muscle forces. Altering subtendon insertion points to the three types of twist showed a maximal change of 2.3% in muscle force contribution compared to the no-twist model. During the eccentric rehabilitation exercise—a common exercise choice during rehabilitation—the compliant tendon model showed substantial differences compared to the generic (control) musculoskeletal model, resulting in decreased gastrocnemius medialis (–3.5%) and gastrocnemius lateralis (–3.2%) contributions and increased soleus contribution (+ 6.6%). Our study results highlight the necessity of incorporating tendon compliance in musculoskeletal models to accurately predict triceps surae muscle forces, especially in individuals with increased tendon compliance, such as patients with Achilles tendinopathy. Such findings contribute to more accurate predictions of muscle forces and hence, personalized rehabilitation strategies.

KEYWORDS

Achilles tendinopathy, musculoskeletal modeling, twist, compliance, triceps surae

1 Introduction

The Achilles tendon is mechanically loaded through the triceps surae muscle forces—soleus (SOL), the gastrocnemius medialis (GM), and the gastrocnemius lateralis (GL) (Kharazi et al., 2021). As the Achilles tendon is mechanosensitive and adapts to mechanical loading (Magnusson et al., 2010; Joseph et al., 2014), the quantification of the triceps surae muscle forces is crucial to better understand (mal) the adaptation of the tendon. Currently, these muscle forces cannot be directly measured non-invasively. Different methods are used to estimate Achilles tendon load, such as an inverse dynamics approach; for a complete overview of different methods, see Finni and Vanwanseele (2023); however, they only provided a global estimate of the total Achilles tendon load. As the Achilles tendon is composed of three subtendons, each originating from its respective triceps surae muscle, the load on the tendon is not uniform (Mylle et al., 2023). Hence, a good estimation of the individual muscle forces when loading the Achilles tendon is crucial. Musculoskeletal modeling has emerged as a useful tool in biomechanics research, providing and enabling a deeper understanding of human movement and, hence, gaining insights into the loading of musculoskeletal tissues (De Groote and Falisse, 2021). For example, with the use of musculoskeletal modeling simulations, the muscle forces can be measured through a dynamic optimization approach (De Groote et al., 2016). However, these models still remain a simplification of the human body as the insertion of the muscle–tendon actuators and tendon compliance are generic and do not consider differences in morphological and/or material properties.

The three subtendons exhibit some degrees of twist from proximal to distal, caused by the collagen fiber arrangement (Pękala et al., 2017). This twist leads to a helical structure, which might enhance force transmission along the tendon during movement due to its effective design for energy storage and release (Bojsen-Møller and Magnusson, 2019) and affect the strain distribution within the tendon (Shim et al., 2018). In healthy tendons, the twist contributes to the ability to withstand tensile loads; hence, it has been hypothesized that tendon twist is linked to the development or progression of Achilles tendinopathy, as it might impact the mechanical behavior of Achilles tendon (Edama et al., 2016; 2019). This tendon twist not only redistributes the load and strain within the tendon but also influences the contribution of forces of each of the triceps surae muscle to the plantar flexor torque due to the altered insertion point on the calcaneus and hence displays differences in the individual moment arm of each triceps surae muscle (Rasske et al., 2017). By changing the insertion points of the muscle–tendon actuators, musculoskeletal models can help understand how tendon twist would influence the contribution of triceps surae muscle forces.

In the case of Achilles tendinopathy patients, the compliance of the Achilles tendon is increased when compared to asymptomatic participants (Arya and Kulig, 2010). Compliant tendons are known to reduce muscle fiber contraction velocities (Lichtwark and Barclay, 2010) or increase change in length (Cox et al., 2019). As the capacity for generating muscle force is affected by both muscle lengths and velocities (Arnold et al., 2013), these changes will influence the muscle force generation and therefore the load on the tendon. It is therefore possible that in the case of tendinopathy, muscle contractile behavior is altered and impacts the load borne by the tendon. Again, the use of musculoskeletal models could provide insights into how changes in tendon compliance may influence the muscle distribution.

Tendon twist and compliance are two important factors that could lead to variations in the distribution of force between the gastrocnemius and soleus muscles, leading to difference in load on the Achilles tendon. Understanding the role of tendon twist and compliance on the triceps surae muscle force distribution can provide crucial insights into the loading of the Achilles tendon in Achilles tendinopathy. To our knowledge, no previous study has yet investigated the influence of the different insertion points of the subtendon or different degrees of tendon compliance on the triceps surae muscle forces in patients with Achilles tendinopathy using musculoskeletal modeling. This study investigates how subtendon insertion points and compliance influence triceps surae muscle forces of individuals with Achilles tendinopathy, by employing a musculoskeletal modeling approach. Specifically, it compares models with varying degrees of tendon twist and compliance and assesses their deviations based on the standard generic model.

2 Materials and methods

2.1 Participant

One participant (male, 47 y, 184 cm, 85 kg) with clinically diagnosed Achilles tendinopathy (VISA-A: 65), selected from a larger cohort, volunteered to participate in this study and gave written informed consent. This study was approved by the local Ethical Committee KU/UZ Leuven (S63532). The participant was screened by a medical doctor in order to verify the following inclusion and exclusion criteria: i) having a documented history of recurring pain in the Achilles tendon lasting for over 6 consecutive weeks, along with episodes of worsening and improvement within the last 5 years, ii) experiencing pain upon palpation originating from the mid-portion of the Achilles tendon, iii) confirmation of Achilles tendinopathy by imaging, i.e., the presence of focal thickening and hypoechoic areas, and iv) no (previous) injuries to the ankle/foot complex or the Achilles tendon and/or a systemic disease affecting the collagenous tissue.

2.2 Experimental design

Upon arrival in the laboratory, the participant was given the Victorian Institute of Sport Assessment—Achilles questionnaire (VISA-A)—to quantify pathology severity and the International Physical Activity Questionnaire (IPAQ) to assess physical activity. Upon completion of a standardized warm-up, three-dimensional freehand ultrasonography (3DfUS) was conducted to measure the morphological and mechanical properties of the Achilles tendon during rest. Thereafter, the participant was prepared to perform three different exercises barefoot in a randomized order: a walk, an eccentric bilateral heel drop, and a concentric bilateral heel rise in the movement laboratory. These exercises were chosen based on the Alfredson eccentric protocol (Alfredson et al., 1998). For each exercise, three trials were recorded

upon visual and verbal guidance by the researcher prior to and during the exercise performance, following the familiarization trial. The bilateral heel-rise and heel-drop exercises were performed in a standardized way on a 15-cm box placed on the force plate for a total duration of 3 s and controlled with a metronome set at 1 Hz. Movement was instructed to reach complete plantar and dorsiflexion within their capabilities. Additionally, the patient's foot progression angle was controlled by a tape line on the box to ensure a neutral (0°) angle. Walking was instructed to be done at a self-selected and comfortable pace on the straight walkway, without specifying the location of the embedded force plate, so that gait kinematics were not altered. The tendinopathy leg was placed onto the (box placed on top) embedded force plate for all three exercises.

2.3 3D freehand ultrasonography (3DfUS)

3DfUS is a previously validated technique (Obst et al., 2014) used to capture and create 3D reconstructions of the Achilles tendon *in vivo* by combining 2D B-mode ultrasonography (ArtUS, UAB Telemed, Vilnius, Lithuania) with the 3D motion capture system (OptiTrack, NaturalPoint Inc., Corvallis, OR, United States) in the 3D slicer software (open source: www.slicer.org, version 4.11; (Fedorov et al., 2012). The Achilles tendon was imaged from the calcaneal insertion to the GM muscle–tendon junction in the transverse plane at rest and during submaximal plantarflexion contractions. Participants were lying prone—extended hip and knee joint—on an isokinetic dynamometer (Biodex system 4 MVP, Biodex Medical Systems, New York, United States). The participant's most affected ankle was fixated and strapped against a footplate in a neutral ankle angle—foot perpendicular to the shank—with the lateral malleolus carefully aligned with the ankle axis of rotation. The free Achilles tendon length—from calcaneal insertion to the SOL muscle–tendon junction—and 3D volume were segmented and calculated during rest and each submaximal contraction (Funaro et al., 2022).

2.4 Musculoskeletal modeling

2.4.1 Generic model

The generic gait2392 musculoskeletal model (Delp et al., 1990) was modified by removing the degrees of freedom in the lumbar joint and adding a degree of freedom in the knee joint (varus–valgus). The model finally consisted of 43 lower limb Hill-type muscles and 22 degrees of freedom. This generic model will be considered the healthy control subject.

2.4.2 Tendon twist model

To add subtendon insertion points into the musculoskeletal model, adjustments to the generic musculoskeletal model were made in OpenSim 3.3 (OpenSim, Stanford, United States) to account for the differences in subtendon insertion points of the individual muscle–tendon actuators. Based on the patient's 3D free Achilles tendon reconstruction, a free Achilles tendon finite element mesh was constructed using Materialise 3-matic (Materialise NV, Leuven, Belgium) (Funaro et al., 2022). The tendon model was divided into three subtendons based on the geometrical description, while also applying twist angles to produce three twisted structures, with both features corresponding to the AT twist classification described by Pękala et al. (2017). As such, three different tendon twist musculoskeletal models were created (Figure 1). The midpoint of each subtendon at the calcaneal insertion was retrieved from the finite element model, as well as the Achilles tendon midpoint, to align its coordinate system to the coordinate system of the musculoskeletal modeling. Insertion points of the three triceps surae muscle–tendon actuators were then adjusted from the generic musculoskeletal model based on the anatomical location of each subtendon's midpoint to create the three different types of tendon twists. Additionally, since tendon shapes are very subject-specific (Szaro et al., 2009; Edama et al., 2015; Pękala et al., 2017; Yin et al., 2021), insertion points of each muscle–tendon actuator were moved by factors of 50% and 100% of its original distance from the Achilles tendon midpoint to represent larger tendons. Final locations of the insertion points for all different tendon twist models compared to the generic model can be found in Supplementary Figure S1.

2.4.3 Tendon compliance model

Achilles tendon compliance values were experimentally measured (Arya and Kulig, 2010) and were converted to the normalized tendon stiffness. The generic musculoskeletal model assumes a normalized tendon stiffness value of 35 for all Hill-type muscles (Zajac, 1989). Therefore, we considered a normalized tendon stiffness value of 35 for our generic model so that it is equal to the mean experimental value measured (Arya and Kulig, 2010). In their study, considering that the AT group had a mean stiffness value that was 20% lower, a normalized value of 28 for the mean (AT) model was observed. This normalized value for the mean model was then used to calculate the value of the most compliant model based on mean and 2 standard deviations to acquire a value of 21. While for the stiffest model, the mean and 2 standard deviations of the control group obtained a value of 47.

2.5 Data analysis

An extended Plug-In Gait marker set, composed of 34 retroreflective markers, was placed on the participant's lower body while capturing 3D marker trajectories through 10 infrared motion capturing cameras (Vicon, Oxford Metrics, Oxford, United Kingdom) with a sampling rate of 100 Hz and ground reaction forces embedded in the walkway (AMTI Inc., MA, United States) and sampled at 1,000 Hz. Upon scaling the musculoskeletal model according to the subject's characteristics obtained during a static trial, joint angles were calculated through a Kalman smoothing algorithm (De Groote et al., 2008), while joint moments were calculated through an inverse dynamic approach based on the joint angle and ground reaction force data in OpenSim 3.3 (OpenSim, Stanford, United States). The data were low-pass filtered with a 6 Hz cutoff frequency. Through a dynamic optimization method (De Groote et al., 2016), in which the muscle redundancy problem was solved through the minimization of the sum of squared muscle activation, triceps surae muscle (GM, GL, and SOL) forces were calculated. A schematic overview of the modeling workflow can be found in

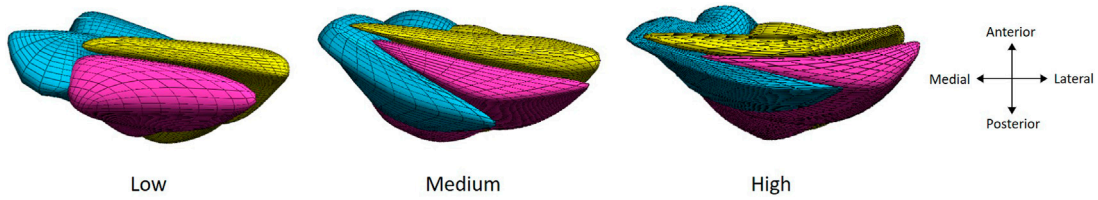

FIGURE 1
Three models of increasing tendon twisting (from left to right) based on a finite element modeling approach with the three subtendons: soleus (bleu), gastrocnemius medialis (pink), and gastrocnemius lateralis (yellow), displayed from the calcaneal insertion for a right leg.

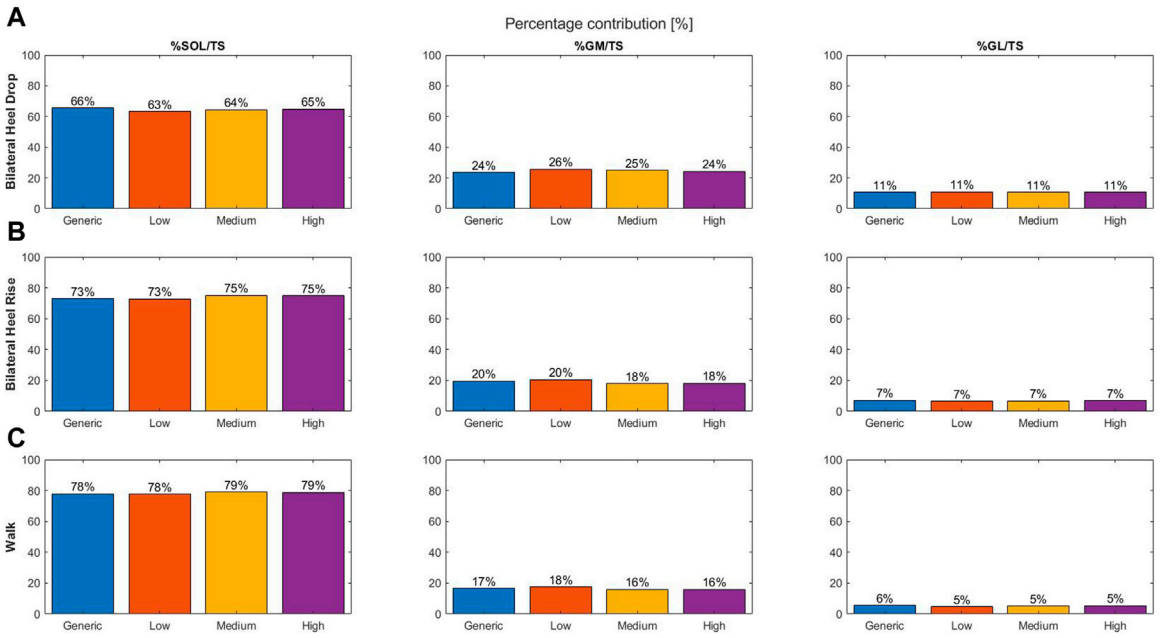

FIGURE 2
Percentage contribution of the individual muscle force to the total triceps surae muscle force at the moment of peak triceps surae force for different types of tendon twist models: generic (no twist; blue), low twist (orange), medium twist (yellow), and high twist (purple), and for the three different dynamic exercises: bilateral heel drop **(A)**, bilateral heel rise **(B)**, and walk **(C)**.

Supplementary Figure S2. Muscle force-sharing strategies were calculated for each exercise by dividing the individual muscle force by the sum of the three muscle forces at the moment of peak triceps surae force. All variables were normalized to the duration of the exercise. For the walking exercise, ground contact times for initial contact (0%) and toe-off (100%) were determined based on the ground reaction force data. The lowest and highest heel marker positions were used to determine the start (0%) and end (100%) of the bilateral heel-rise and heel-drop exercises.

3 Results

3.1 Tendon twist

Tendon twist had a minimal influence on the triceps surae muscle forces at peak triceps surae force, as the greatest difference in muscle contribution was a 2.3% change, compared to the generic model, for all exercises performed.

3.1.1 Bilateral heel drop

The SOL muscle force and its contribution to the total triceps surae muscle force increased with increase in degrees of twisting, while the opposite was true for the GM muscle force and contribution (Figure 2A). The generic model, with no tendon twist, displayed the lowest contribution for the GM and GL and the largest contribution for SOL.

3.1.2 Bilateral heel rise

Increasing twist resulted in a tendency toward increased SOL and GL and decreased GM muscle force and contribution (Figure 2B). The generic model showed the largest GL and GM and lowest SOL contribution compared to the three different models of tendon twist.

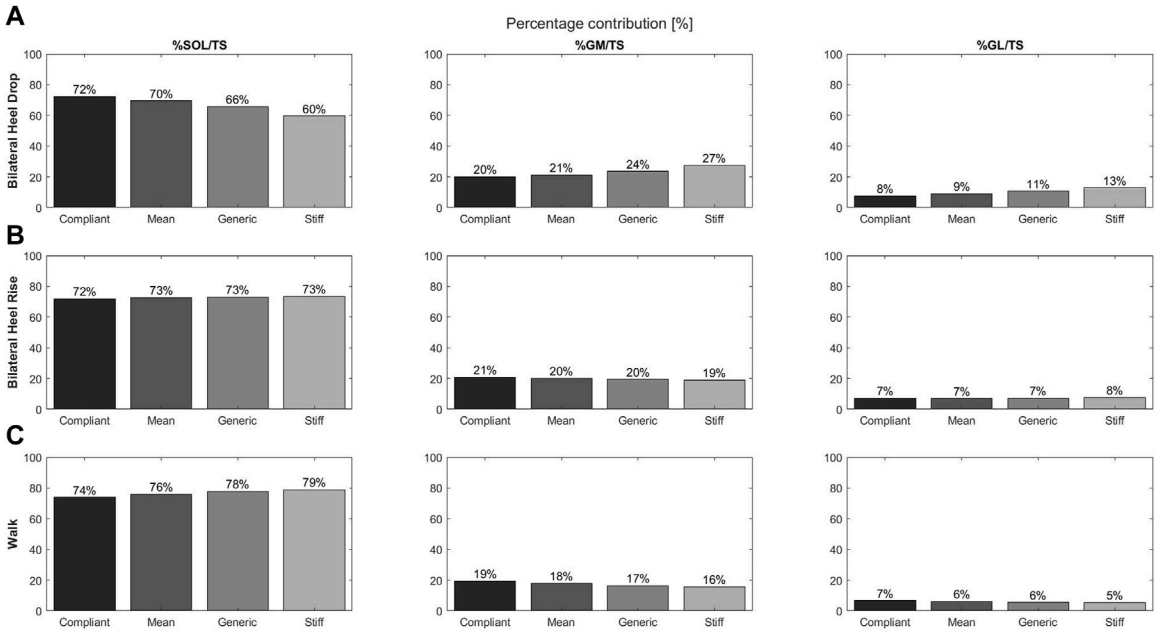

FIGURE 3
Contributions of individual muscle force to the total triceps surae muscle force for the soleus, gastrocnemius medialis, and gastrocnemius lateralis and during the bilateral heel drop **(A)**, bilateral heel rise **(B)**, and walk **(C)** at the moment of peak triceps surae force for the four tendon compliance models: compliant (21; black), mean (28; dark gray), generic (35; concrete), and stiff (47; light gray).

3.1.3 Walking

A tendency toward increased GL muscle force and contribution was observed with increasing twist (Figure 2C). Medium- and high-twist models do not display differences for the GM and SOL contributions; however, low twist models show a decrease in SOL and increase in GM contribution. The generic model's muscle contribution fits well between low twist and medium/high twist for the SOL and GM, but is the largest for the GL.

3.1.4 Effect on the moment arm

In addition, in larger tendons, where insertion points of the muscle–tendon actuator were further away from the origin (50% or 100% increase), the difference in triceps surae muscle force-sharing remained small. Even with changes of up to 2 mm (SOL), 1 mm (GM), and 2 mm (GL) in the moment arm of the muscle–tendon actuator compared to the generic model, the largest differences were observed for the GM compared to the generic model, with differences up to 3.5%, 6.4%, and 5.5% for the bilateral heel drop, bilateral heel rise, and walk, respectively (Supplementary Figure S1).

3.2 Tendon compliance

Increasing tendon compliance had an influence on the triceps surae muscle forces at peak triceps surae forces and generated differences in muscle contribution of up to 6.6% compared to the generic model.

3.2.1 Bilateral heel drop

With increasing compliance, SOL muscle force increased, while GM and GL muscle forces decreased (Figure 3A). Differences of + 12.6%, −7.3%, and −5.4% were found for the SOL, GM, and GL contributions, respectively, when comparing the compliant model to the stiff model, while differences of + 6.6%, −3.5%, and −3.1% were found in comparison to the generic model, respectively.

3.2.2 Bilateral heel rise

Differences in muscle contribution with increasing tendon compliance were less obvious; however, the compliant model displayed the largest differences with the SOL showing decreased contributions (−1.2%), while GM contribution increased by 1.2% compared to the generic model (Figure 3B).

3.2.3 Walking

SOL muscle force and contributions to the total triceps surae muscle force decreased with increasing compliance, while GM and GL forces and contributions had the opposite effect (Figure 3C). In comparison to the generic model, the differences were larger for the compliant model than for the stiffest model.

3.3 Tendon twist x compliance

A cross-analysis of both tendon twisting and tendon compliance revealed similar results, with tendon compliance having the largest effect on the triceps surae muscle force-sharing behavior, independent of the type of tendon twisting. For the bilateral heel-drop exercise, SOL showed an increased contribution and GM and GL showed a decreased contribution with increasing compliance and increasing twist (Table 1). Similarly, during both the bilateral heel-rise and walking exercises, all compliance models displayed a tendency toward increased SOL and GL contributions

10.3389/fbioe.2024.1399611

TABLE 1 Contributions of the individual triceps surae muscle force to the total triceps surae force at the moment of peak triceps surae muscle force: a cross-sectional analysis of tendon twist types and tendon compliance models compared to the generic model with no twist induced.

Cross-sectional analysis twist/compliance		% SOL/TS			% GM/TS			% GL/TS		
		Low	Medium	High	Low	Medium	High	Low	Medium	High
Bilateral heel drop	Generic_no twist	65, 63			23, 65			10, 72		
	Compliant	70, 74	71, 73	71, 51	21, 62	20, 73	20, 93	7, 64	7, 53	7, 56
	Mean	67, 44	68, 57	68, 95	23, 23	22, 24	21, 87	9, 33	9, 19	9, 17
	Generic	63, 32	64, 29	64, 90	25, 79	24, 95	24, 35	10, 89	10 ,76	10, 74
	Stiff	57, 14	57, 78	58, 49	29, 80	29, 22	28, 44	13, 07	13 ,00	13, 01
Bilateral heel rise	Generic_no twist	73, 14			19, 63			7, 23		
	Compliant	71, 97	73, 14	72, 56	21, 55	20, 12	20, 42	6, 48	6, 74	7, 02
	Mean	72, 55	74, 49	73, 99	21, 04	18, 87	19, 15	6, 41	6, 64	6, 86
	Generic	72, 90	75, 21	74, 80	20, 49	18, 01	18, 24	6, 60	6, 78	6, 96
	Stiff	72, 89	75, 32	75, 09	20, 05	17, 52	17, 62	7, 06	7, 16	7, 29
Walk	Generic_no twist	77, 81			16, 54			5, 65		
	Compliant	74, 32	74, 61	74, 11	19, 73	19, 14	19, 37	5, 95	6, 25	6, 52
	Mean	75, 92	76, 96	76, 42	18, 88	17, 54	17, 83	5, 20	5, 49	5, 76
	Generic	77, 67	79, 08	78, 72	17, 59	15, 83	15, 97	4, 74	5, 09	5, 31
	Stiff	78, 96	80, 36	80, 04	16, 33	14, 75	14, 93	4, 71	4, 89	5, 03

but decreased GM with increasing twist—medium and high twist are fairly similar for the SOL and GM. However, with increasing compliance, SOL contribution decreased, while the GM contribution increased.

4 Discussion

This simulation study provides insights into the influence of altering subtendon insertion points associated with tendon twist and altering tendon compliance on the muscle forces during different dynamic exercises. Findings suggest that tendon compliance has a larger influence on the triceps surae muscle forces than the degree of tendon twist. Specifically, during the commonly performed eccentric rehabilitation exercises, large differences were observed between the compliant tendon and the generic model.

Our results revealed that modeling a more compliant tendon leads to different triceps surae forces and contributions compared to modeling stiffer tendons. GM and GL contributions decreased, while the SOL contribution to total triceps surae force increased during the eccentric bilateral heel-drop exercise with a compliant tendon. In other words, a more compliant tendon might require an increased involvement of the SOL during eccentric contractions, yet the reverse effect where increased contribution leads to greater compliance might exist, but is not yet understood. Indeed, differential muscle forces within the different triceps surae muscles were found during different dynamic exercises (Mylle et al., 2023). This was also demonstrated with the use of finite element modeling, where individual muscle contributions of 63% for SOL, 23% for GM, and 14% for GL were found during eccentric contractions in healthy participants (Handsfield et al., 2017), which aligns well with our results for the generic model (66% SOL, 24% GM, and 11% GL). Additionally, Arnold et al. (2013) found that differences in muscle dynamics occur in different triceps surae muscles due to changes in fiber length and contraction velocities. Furthermore, force generation is dependent on tendon compliance as normal fiber length will be affected (Zajac, 1989). Hence, it was expected that differences exist for the different muscles and compliance models. In case of a compliant tendon, the muscle will function at shorter lengths and reduced fiber contraction velocities during a cyclic contraction (Lichtwark and Barclay, 2010). With increasing compliance models, a shift on the force–length curve toward shorter fascicle lengths was observed for all muscles and in all exercises (Supplementary Figure S3). During the eccentric bilateral heel-drop exercise, fascicle lengths operate on the descending limb of the curve, and hence, more optimal lengths for force production are achieved in the compliant model. Passive forces in the GM and GL may play a role in stiffer models to compensate for its decreased force–length potential. The opposite trend was observed during the concentric movements: the bilateral heel rise and the walk, where less optimal fascicle lengths and a lower contribution in the SOL were achieved. GM and GL operate on the plateau region, and as a result, smaller differences in force contribution were found compared to stiffer models. Increased compliance also resulted in reduced contraction velocities (Supplementary Figure S4); however, near isometric contractions were performed, and muscle force generating capacity was not impacted, in comparison to stiffer models.

Considering that Achilles tendinopathy patients have a more compliant tendon, it is worthwhile to model the tendon compliance

when investigating the triceps surae muscle force-sharing strategies. When compared to healthy participants, patients with Achilles tendinopathy demonstrated an altered triceps surae force-sharing behavior, with a significantly increased SOL and a trend toward decreased GM and GL force during the bilateral heel-drop exercise (Mylle et al., 2023). Our current study results confirmed this finding; for this same exercise, the compliant (tendinopathy) model showed a decrease in GM (−3.48%) and GL contribution (−3.15%) and an increase in SOL contribution (+ 6.63%) compared to the generic (healthy) model. Additionally, during isometric contractions, a reduced GL contribution and activation (Crouzier et al., 2020), a reduced GL motor unit neural discharge rate (Fernandes et al., 2023), and a tendency toward reduced non-uniform intratendinous sliding in patients with Achilles tendinopathy (Couppé et al., 2020) were reported. These observations all highlight the importance of GM and GL contributions in the rehabilitation of Achilles tendinopathy patients. Therefore, future studies should include tendon compliance in simulations in which musculoskeletal modeling is used to investigate contributions of triceps surae forces.

In this musculoskeletal modeling study, increasing the tendon twist—by adjusting the location of the subtendon's insertion point—did not have an impact on the triceps surae forces. Even when increasing the subtendon's insertion point by a factor of 100% to represent larger tendons, muscle force contributions did not change much compared to the those of the generic model. However, it is important to note that across different models and exercises, the maximum difference in the moment arm of the individual muscle–tendon actuator was 2 mm. Even though the moment arm has a considerable influence on the magnitude of the muscle forces to achieve the experimentally observed joint torques (Rasske et al., 2017; Holzer et al., 2020), tendon twist is responsible only for changes in the subtendon moment arm, and not for the Achilles tendon moment arm. Hence, in the current musculoskeletal modeling framework, incorporating tendon twisting did not significantly affect total triceps surae force-sharing. Nevertheless, the biomechanical significance of tendon twisting cannot be neglected since tendon twisting promotes strain distributions and, hence, force production (Dean et al., 2007).

Some limitations need to be discussed. First, the data presented above are based on observations from a single subject. Achilles (sub) tendon properties are highly individualized (Edama et al., 2015; Pękala et al., 2017), leading to different responses to loading (Shim et al., 2019) across the entire AT population. In this simulation study, kinematic and kinetic data from one patient were used as input for the musculoskeletal model. To represent morphological and altered material properties known to occur in AT patients, we simulated the effect of tendon twist, larger cross-sectional areas, and tendon compliance on the muscle force-sharing behavior. Our study demonstrates the importance of including tendon compliance when investigating muscle-force sharing behavior in this specific population. Using non-invasive imaging methods to assess tendon properties, such as tendon compliance, the diagnosis of tendon injuries could be enhanced and rehabilitation can be improved (Fouré, 2016). Therefore, measurement of tendon compliance could be incorporated into standard operating procedures during clinical assessments at the time of diagnosis as a determination of impairment. This measurement could then be easily integrated into data processing related to various exercises to assess weaknesses in SOL/GM, facilitating individualized and targeted training. If this complete workflow is not feasible, measuring tendon compliance during clinical assessments can still provide valuable reference guidelines for health professionals. These guidelines can help adapt patient care strategies, such as focusing more on strengthening the GM or GL muscles during eccentric exercises by adjusting foot positioning. In addition, the effect of tendon compliance (+ 6.6%) might not be significantly different compared to the effect of tendon twist (+ 2.3%) when compared to the generic model; hence, future studies are needed to confirm the clinical relevance of these differences in a broader AT population. Second, a simple generic musculoskeletal model with individual and independent muscle–tendon actuators was used. As a result, no sliding between different actuators, and thus subtendons, was incorporated, even though sliding between Achilles subtendons is known to occur (Bogaerts et al., 2017; Clark and Franz, 2018; Couppé et al., 2020). Third, Achilles tendon twisting was induced in this model by moving the calcaneal insertion point of each muscle–tendon actuator based on the experimentally retrieved 3D model implemented in the FE model consisting of subtendons (Funaro et al., 2022). However, future modeling investigations could implement insertion points in the muscle–tendon actuator at the location of each muscle–tendon unit to represent the tendon twisting better physiologically in the musculoskeletal model at the level of the tendon. Additionally, accurate muscle force estimations are important to be used as boundary conditions in FE models (Yamamura et al., 2014; Funaro et al., 2022). Finally, estimations of triceps surae forces are based on a dynamic optimization method, which is a simulation study. Thus far, it remains unknown how individual muscle forces can be estimated non-invasively *in vivo*.

In summary, the results of this simulation study highlight the significant influence of Achilles tendon compliance on triceps surae forces and their behavior during rehabilitation exercises and walking. This developed musculoskeletal modeling workflow is important, specifically to accurately predict muscle forces in the triceps surae muscles based on individualized material properties of the tendon. Understanding these effects can guide the development of more effective and personalized rehabilitation strategies for individuals with varying tendon compliance, such as during rehabilitation from Achilles tendinopathy. Further research in this area may help refine rehabilitation protocols and improve patient outcomes.

Data availability statement

The raw data supporting the conclusions of this article will be made available by the author, without undue reservation.

Ethics statement

The studies involving humans were approved by local ethical committee KU/UZ Leuven. The studies were conducted in accordance with the local legislation and institutional requirements. The participants provided their written informed consent to participate in this study.

Author contributions

IM: conceptualization, data curation, formal analysis, investigation, methodology, project administration, software, validation, visualization, writing–original draft, and writing–review and editing. AF: methodology, software, validation, visualization, and writing–review and editing. MC: supervision and writing–review and editing. SB: supervision and writing–review and editing. BV: conceptualization, funding acquisition, methodology, resources, supervision, and writing–review and editing.

Funding

The authors declare that financial support was received for the research, authorship, and/or publication of this article. Support was received from the Research Council KU Leuven (C24M/20/053).

Acknowledgments

The authors would like to thank the Research Council KU Leuven for providing financial support.

Conflict of interest

The authors declare that the research was conducted in the absence of any commercial or financial relationships that could be construed as a potential conflict of interest.

Publisher's note

All claims expressed in this article are solely those of the authors and do not necessarily represent those of their affiliated organizations, or those of the publisher, the editors, and the reviewers. Any product that may be evaluated in this article, or claim that may be made by its manufacturer, is not guaranteed or endorsed by the publisher.

Supplementary material

The Supplementary Material for this article can be found online at: https://www.frontiersin.org/articles/10.3389/fbioe.2024.1399611/full#supplementary-material

References

Alfredson, H., Pietilä, T., Jonsson, P., and Lorentzon, R. (1998). Heavy-load eccentric calf muscle training for the treatment of chronic achilles tendinosis. *Am. J. Sports Med.* 26, 360–366. doi:10.1177/03635465980260030301

Arnold, E. M., Hamner, S. R., Seth, A., Millard, M., and Delp, S. L. (2013). How muscle fiber lengths and velocities affect muscle force generation as humans walk and run at different speeds. *J. Exp. Biol.* 216, 2150–2160. doi:10.1242/jeb.075697

Arya, S., and Kulig, K. (2010). Tendinopathy alters mechanical and material properties of the Achilles tendon. *J. Appl. Physiol.* 108, 670–675. doi:10.1152/japplphysiol.00259.2009

Bogaerts, S., De Brito Carvalho, C., Scheys, L., Desloovere, K., D'hooge, J., Maes, F., et al. (2017). Evaluation of tissue displacement and regional strain in the Achilles tendon using quantitative high-frequency ultrasound. *PLoS One* 12, 01813644–e181416. doi:10.1371/journal.pone.0181364

Bojsen-Møller, J., and Magnusson, S. P. (2019). Mechanical properties, physiological behavior, and function of aponeurosis and tendon. *J. Appl. Physiol.* 126, 1800–1807. doi:10.1152/japplphysiol.00671.2018

Clark, W. H., and Franz, J. R. (2018). Do triceps surae muscle dynamics govern non-uniform Achilles tendon deformations? *PeerJ* 6, e5182. doi:10.7717/peerj.5182

Couppé, C., Svensson, R. B., Josefsen, C. O., Kjeldgaard, E., and Magnusson, S. P. (2020). Ultrasound speckle tracking of Achilles tendon in individuals with unilateral tendinopathy: a pilot study. *Eur. J. Appl. Physiol.* 120, 579–589. doi:10.1007/s00421-020-04317-5

Cox, S. M., Easton, K. L., Lear, M. C., Marsh, R. L., Delp, S. L., and Rubenson, J. (2019). The interaction of compliance and activation on the force-length operating range and force generating capacity of skeletal muscle: a computational study using a Guinea fowl musculoskeletal model. *Integr. Org. Biol.* 1, obz022. doi:10.1093/iob/obz022

Crouzier, M., Tucker, K., Lacourpaille, L., Doguet, V., Fayet, G., Dauty, M., et al. (2020). Force-sharing within the triceps surae: an achilles heel in achilles tendinopathy. *Med. Sci. Sports Exerc.* 52, 1076–1087. doi:10.1249/MSS.0000000000002229

Dean, M. N., Azizi, E., and Summers, A. P. (2007). Uniform strain in broad muscles: active and passive effects of the twisted tendon of the spotted ratfish *Hydrolagus colliei*. *J. Exp. Biol.* 210, 3395–3406. doi:10.1242/jeb.007062

De Groote, F., De Laet, T., Jonkers, I., and De Schutter, J. (2008). Kalman smoothing improves the estimation of joint kinematics and kinetics in marker-based human gait analysis. *J. Biomech.* 41, 3390–3398. doi:10.1016/j.jbiomech.2008.09.035

De Groote, F., and Falisse, A. (2021). Perspective on musculoskeletal modelling and predictive simulations of human movement to assess the neuromechanics of gait. *Proc. R. Soc. B Biol. Sci.* 288, 20202432. doi:10.1098/rspb.2020.2432

De Groote, F., Kinney, A. L., Rao, A. V., and Fregly, B. J. (2016). Evaluation of direct collocation optimal control problem formulations for solving the muscle redundancy problem. *Ann. Biomed. Eng.* 44, 2922–2936. doi:10.1007/s10439-016-1591-9

Delp, S. L., Loan, J. P., Hoy, M. G., Zajac, F. E., Topp, E. L., and Rosen, J. M. (1990). An interactive graphics-based model of the lower extremity to study orthopaedic surgical procedures. *IEEE Trans. Biomed. Eng.* 37, 757–767. doi:10.1109/10.102791

Edama, M., Kubo, M., Onishi, H., Takabayashi, T., Inai, T., Yokoyama, E., et al. (2015). The twisted structure of the human Achilles tendon. *Scand. J. Med. Sci. Sport.* 25, e497–e503. doi:10.1111/sms.12342

Edama, M., Kubo, M., Onishi, H., Takabayashi, T., Yokoyama, E., Inai, T., et al. (2016). Structure of the Achilles tendon at the insertion on the calcaneal tuberosity. *J. Anat.* 229, 610–614. doi:10.1111/joa.12514

Edama, M., Takabayashi, T., Inai, T., Kikumoto, T., Ito, W., Nakamura, E., et al. (2019). Differences in the strain applied to Achilles tendon fibers when the subtalar joint is overpronated: a simulation study. *Surg. Radiol. Anat.* 41, 595–599. doi:10.1007/s00276-019-02181-3

Fedorov, A., Beichel, R., Kalpathy-Cramer, J., Finet, J., Fillion-Robin, J., Pujol, S., et al. (2012). 3D slicer as an image computing platform for the quantitative imaging network. *Magn. Reson Imaging* 30, 1323–1341. doi:10.1016/j.mri.2012.05.001

Fernandes, G. L., Orssatto, L. B. R., Sakugawa, R. L., and Trajano, G. S. (2023). Lower motor unit discharge rates in gastrocnemius lateralis, but not in gastrocnemius medialis or soleus, in runners with Achilles tendinopathy: a pilot study. *Eur. J. Appl. Physiol.* 123, 633–643. doi:10.1007/s00421-022-05089-w

Finni, T., and Vanwanseele, B. (2023). Towards modern understanding of the Achilles tendon properties in human movement research. *J. Biomech.* 152, 111583. doi:10.1016/j.jbiomech.2023.111583

Fouré, A. (2016). New imaging methods for non-invasive assessment of mechanical, structural, and biochemical properties of human Achilles tendon: a mini review. *Front. Physiol.* 7, 324–329. doi:10.3389/fphys.2016.00324

Funaro, A., Shim, V., Crouzier, M., Mylle, I., and Vanwanseele, B. (2022). Subject-specific 3D models to investigate the influence of rehabilitation exercises and the twisted structure on achilles tendon strains. *Front. Bioeng. Biotechnol.* 10, 914137–914139. doi:10.3389/fbioe.2022.914137

Handsfield, G. G., Inouye, J. M., Slane, L. C., Thelen, D. G., Miller, G. W., and Blemker, S. S. (2017). A 3D model of the Achilles tendon to determine the mechanisms underlying nonuniform tendon displacements. *J. Biomech.* 51, 17–25. doi:10.1016/j.jbiomech.2016.11.062

Holzer, D., Paternoster, F. K., Hahn, D., Siebert, T., and Seiberl, W. (2020). Considerations on the human Achilles tendon moment arm for *in vivo* triceps surae muscle–tendon unit force estimates. *Sci. Rep.* 10, 19559–19611. doi:10.1038/s41598-020-76625-x

Joseph, M., Lillie, K., Bergeron, D., Cota, K., Yoon, J., Kraemer, W., et al. (2014). Achilles tendon biomechanics in response to acute intense exercise. *J. Strenght Cond. Res.* 28, 1181–1186. doi:10.1519/JSC.0000000000000361

Kharazi, M., Bohm, S., Theodorakis, C., Mersmann, F., and Arampatzis, A. (2021). Quantifying mechanical loading and elastic strain energy of the human Achilles tendon during walking and running. *Sci. Rep.* 11, 5830–5914. doi:10.1038/s41598-021-84847-w

Lichtwark, G. A., and Barclay, C. J. (2010). The influence of tendon compliance on muscle power output and efficiency during cyclic contractions. *J. Exp. Biol.* 213, 707–714. doi:10.1242/jeb.038026

Magnusson, S. P., Langberg, H., and Kjaer, M. (2010). The pathogenesis of tendinopathy: balancing the response to loading. *Nat. Rev. Rheumatol.* 6, 262–268. doi:10.1038/nrrheum.2010.43

Mylle, I., Crouzier, M., Hollville, E., Bogaerts, S., and Vanwanseele, B. (2023). Triceps surae muscle forces during dynamic exercises in patients with Achilles tendinopathy: a cross-sectional study. *Scand. J. Med. Sci. Sports* 33, 2219–2229. doi:10.1111/sms.14444

Obst, S. J., Newsham-West, R., and Barrett, R. S. (2014). InVivo measurement of human achilles tendon morphology using freehand 3-D ultrasound. *Ultrasound Med. Biol.* 40, 62–70. doi:10.1016/j.ultrasmedbio.2013.08.009

Pękala, P. A., Henry, B. M., Ochała, A., Kopacz, P., Tatoń, G., Młyniec, A., et al. (2017). The twisted structure of the Achilles tendon unraveled: a detailed quantitative and qualitative anatomical investigation. *Scand. J. Med. Sci. Sport.* 27, 1705–1715. doi:10.1111/sms.12835

Rasske, K., Thelen, D. G., and Franz, J. R. (2017). Variation in the human Achilles tendon moment arm during walking. *Comput. Methods Biomech. Biomed. Engin.* 20, 201–205. doi:10.1080/10255842.2016.1213818

Shim, V. B., Handsfield, G. G., Fernandez, J. W., Lloyd, D. G., and Besier, T. F. (2018). Combining *in silico* and *in vitro* experiments to characterize the role of fascicle twist in the Achilles tendon. *Sci. Rep.* 8, 13856–13912. doi:10.1038/s41598-018-31587-z

Shim, V. B., Hansen, W., Newsham-West, R., Nuri, L., Obst, S., Pizzolato, C., et al. (2019). Influence of altered geometry and material properties on tissue stress distribution under load in tendinopathic Achilles tendons – a subject-specific finite element analysis. *J. Biomech.* 82, 142–148. doi:10.1016/j.jbiomech.2018.10.027

Szaro, P., Witkowski, G., Śmigielski, R., Krajewski, P., and Ciszek, B. (2009). Fascicles of the adult human Achilles tendon - an anatomical study. *Ann. Anat.* 191, 586–593. doi:10.1016/j.aanat.2009.07.006

Yamamura, N., Alves, J. L., Oda, T., Kinugasa, R., and Takagi, S. (2014). Effect of tendon stiffness on the generated force at the Achilles tendon - 3D finite element simulation of a human triceps surae muscle during isometric contraction. *J. Biomech. Sci. Eng.* 9, 13–11. doi:10.1299/jbse.13-00294

Yin, N. H., Fromme, P., McCarthy, I., and Birch, H. L. (2021). Individual variation in achilles tendon morphology and geometry changes susceptibility to injury. *Elife* 10, e63204–e63215. doi:10.7554/eLife.63204

Zajac, F. E. (1989). Muscle and tendon: properties, models, scaling, and application to biomechanics and motor control. *Crit. Rev. Biomed. Eng.* 17, 359–411.

frontiers | Frontiers in Bioengineering and Biotechnology

TYPE Original Research
PUBLISHED 06 August 2024
DOI 10.3389/fbioe.2024.1437684

OPEN ACCESS

EDITED BY
Yih-Kuen Jan,
University of Illinois at Urbana-Champaign, United States

REVIEWED BY
Xianyue Shen,
Anhui Provincial Hospital, China
Zhenxian Chen,
Chang'an University, China

*CORRESPONDENCE
Zimin Wang,
drwangzimin@126.com
Cheng-Kung Cheng,
ckcheng2020@sjtu.edu.cn

†These authors have contributed equally to this work and share first authorship

RECEIVED 24 May 2024
ACCEPTED 12 July 2024
PUBLISHED 06 August 2024

CITATION
Wang H, Yao G, He K, Wang Z and Cheng C-K (2024), ACL reconstruction combined with anterolateral structures reconstruction for treating ACL rupture and knee injuries: a finite element analysis.
Front. Bioeng. Biotechnol. 12:1437684.
doi: 10.3389/fbioe.2024.1437684

ACL reconstruction combined with anterolateral structures reconstruction for treating ACL rupture and knee injuries: a finite element analysis

Huizhi Wang[1,2†], Gai Yao[3†], Kaixin He[1], Zimin Wang[4*] and Cheng-Kung Cheng[1*]

[1]School of Biomedical Engineering and Engineering Research Center for Digital Medicine of the Ministry of Education, Shanghai Jiao Tong University, Shanghai, China, [2]Center for Intelligent Medical Equipment and Devices (iMED), University of Science and Technology of China, Suzhou, Jiangsu, China, [3]The Fifth Medial Center of Chinese PLA General Hospital, Beijing, China, [4]Department of Orthopedic Surgery, Shanghai Ninth People's Hospital, Shanghai Jiao Tong University School of Medicine, Shanghai, China

Introduction: The biomechanical indication for combining anterolateral structures reconstruction (ASLR) with ACL reconstruction (ACLR) to reduce pivot shift in the knee remains unclear. This study aims to investigate knee functionality after ACL rupture with different combinations of injuries, and to compare the effectiveness of ALSR with ACLR for treating these injuries.

Methods: A validated finite element model of a human cadaveric knee was used to simulate pivot shift tests on the joint in different states, including 1) an intact knee; 2) after isolated ACL rupture; 3) after ACL rupture combined with different knee injuries or defect, including a posterior tibial slope (PTS) of 20°, an injury to the anterolateral structures (ALS) and an injury to the posterior meniscotibial ligament of the lateral meniscus (LP); 4) after treating the different injuries using isolated ACLR; v. after treating the different injuries using ACLR with ALSR. The knee kinematics, maximum von Mises stress (Max.S) on the tibial articular cartilage (TC) and force in the ACL graft were compared among the different simulation groups.

Results and discussion: Comparing with isolated ACL rupture, combined injury to the ALS caused the largest knee laxity, when a combined PTS of 20° induced the largest Max.S on the TC. The joint stability and Max.S on the TC in the knee with an isolated ACL rupture or a combined rupture of ACL and LP were restored to the intact level after being treated with isolated ACLR. The knee biomechanics after a combined rupture of ACL and ALS were restored to the intact level only when being treated with a combination of ACLR and ALSR using a large graft diameter (6 mm) for ALSR. However, for the knee after ACL rupture combined with a PTS of 20°, the ATT and Max.S on the TC were still greater than the intact knee even after being treated with a combination of ACLR and ALSR. The finite

Abbreviations: ACL, anterior cruciate ligament; ACLR, anterior cruciate ligament reconstruction; ALS, anterolateral structure; ALL, anterolateral ligament; ALC, anterolateral capsule; LP, posterior meniscotibial ligament of the lateral meniscus; PTS, posterior tibial slope; ALSR, anterolateral structures reconstruction; Max.S, maximum von Mises stress; TC tibial cartilage; ATT, anterior tibial translation; VTR, valgus tibial rotation; ITR, internal tibial rotation; Rup, rupture.

element analysis showed that ACLR should include ALSR when treating ACL ruptures accompanied by ALS rupture. However, pivot shift in knees with a PTS of 20° was not eliminated even after a combined ACLR and ALSR.

KEYWORDS

anterior cruciate ligament reconstruction, anterolateral structures reconstruction, pivot shift, articular stress, combined injury

1 Introduction

Rupture of the anterior cruciate ligament (ACL) can lead to knee laxity and often requires reconstruction surgery to stabilize the joint (Musahl et al., 2022). However, a positive pivot shift (excessive tibial translations and rotations) has been commonly reported after ACL reconstruction (ACLR) (Guenther et al., 2015), with an incidence rate of up to 25% (Sonnery-Cottet et al., 2017). The positive pivot shift indicates that the ACL graft is not bearing the expected load, which could lead to abnormal loads on other joint tissues (Du et al., 2016; Wang et al., 2020b), such as abnormal stress on the cartilage that may gradually develop into long-term osteoarthritis (Barenius et al., 2014; Shen et al., 2021).

Studies have found that people with concomitant knee injuries or anatomical defects experience greater pivot shifts. These concomitant injuries include ruptures of the anterolateral structures (ALSs), including the anterolateral ligament (ALL) and anterolateral capsule (ALC) (Song et al., 2017), rupture of the posterior meniscotibial ligament of the lateral meniscus (LP) (Tang et al., 2019; Ni et al., 2022), or instances of greater posterior tibial slope (PTS) (Ansari et al., 2017). However, few studies have explored the differences in the severity of pivot shifts among patients with various injuries and defects, and the surgical strategies that should be used to treat patients with such injury patterns remain unclear.

Anterolateral structures reconstruction (ALSR) (Chen et al., 2021), also termed as anterolateral ligament reconstruction (ALLR), has been reported as an efficient method of reducing pivot shift of the knee after ACLR (Nitri et al., 2016; Sonnery-Cottet et al., 2017; Wood et al., 2018; Ueki et al., 2019). Through a cadaveric study, Nitri et al. (2016) found that anatomical ACLR combined with ALSR significantly improved the rotatory stability of the knee compared to isolated ACLR in the presence of concurrent ALL deficiency with ACL rupture. Ueki et al. (2019) found that using additional ALS augmentation in patients with high preoperative pivot shift reduced the pivot-shift acceleration when compared to isolated ACLR. To provide a comprehensive reference for the anatomical and biomechanical basis of ALSR, an expert group consensus was published in 2017, containing a summary of the current scientific evidence and recommendations for improving surgical techniques (Sonnery-Cottet et al., 2017). The consensus document identified the importance of ALSR for people at high risk of pivot shifts, but the exact surgical indications remain unclear.

In the above context, the present study aimed to 1) explore differences in pivot shift (anterior and rotational displacements of the knee) and maximum stress (Max.S) values on the tibial cartilage (TC) when the knee was subjected to different combinations of injuries or defects accompanied by a ruptured ACL; further, the study 2) compares the effectiveness of using ALSR with ACLR for treating different combinations of injuries. Finite element analysis was used in this study, through which the variate was strictly controlled to one factor while maintaining the other factors constant. This permits the basic biomechanics of the joint to be examined clearly (Wang et al., 2022a). It was hypothesized that there would be considerable differences in the pivot shifts and articular stresses among knees with different injuries; further, by combining ACLR and ALSR, postoperative joint biomechanics can be restored in patients with certain injury patterns, while other injury patterns cannot achieve joint function restoration through ACLR and ALSR.

2 Materials and methods

A validated finite element model of a male human cadaveric knee joint (Wang et al., 2020b) was used in the current study to simulate pivot shift tests for different states of injury and repair: intact knee; isolated ACL rupture; ACL rupture with different combinations of knee injuries or defects, including rupture of the LP, ALS, and a PTS of 20°; ACLR using anatomical single-bundle grafts of various diameters; combined ALSR with ACLR. The knee kinematics, Max.S on the TC, and force in the ACL graft were compared among the different simulation groups to explore the differences in pivot shifts after different knee injuries as well as the effectiveness of ALSR combined with ACLR for restoring knee biomechanics when used to treat different knee injuries.

2.1 Development and validation of the finite element model of an intact cadaveric knee

The finite element model was built from a cadaveric human (45 years, male, 70 kg) knee joint (right side) (Figure 1) with prior approval from the Committee for Oversight of Research and Clinical Training Involving Decedents (Guenther et al., 2015). The knee was examined by an experienced orthopedic surgeon and determined to have normal tissue morphology with no observable injury or history of operation. The geometries of the knee structures were segmented using Mimics (Materialise N.V., Leuven, Belgium) from magnetic resonance images acquired with a slice thickness of 0.2 mm and scan resolution of 0.2 mm × 0.2 mm (field of view: 8 cm × 10 cm × 12 cm, TR = 53 ms, TE = 26.3 ms, field strength: 3.0 T). The model included bones (tibia, femur, and fibula), articular cartilage, meniscus, four major ligaments (posterior cruciate ligament, ACL, lateral collateral ligament, and medial collateral ligament), meniscal ligaments (anterior and posterior meniscotibial ligaments and meniscofemoral ligaments), capsule deep medial collateral ligament for medial stability, popliteofibular ligament with ALL and ALC for lateral stability, and four structures for maintaining posterior stability (lateral posterior capsule, medial posterior capsule, arcuate popliteal ligament, and oblique popliteal ligament).

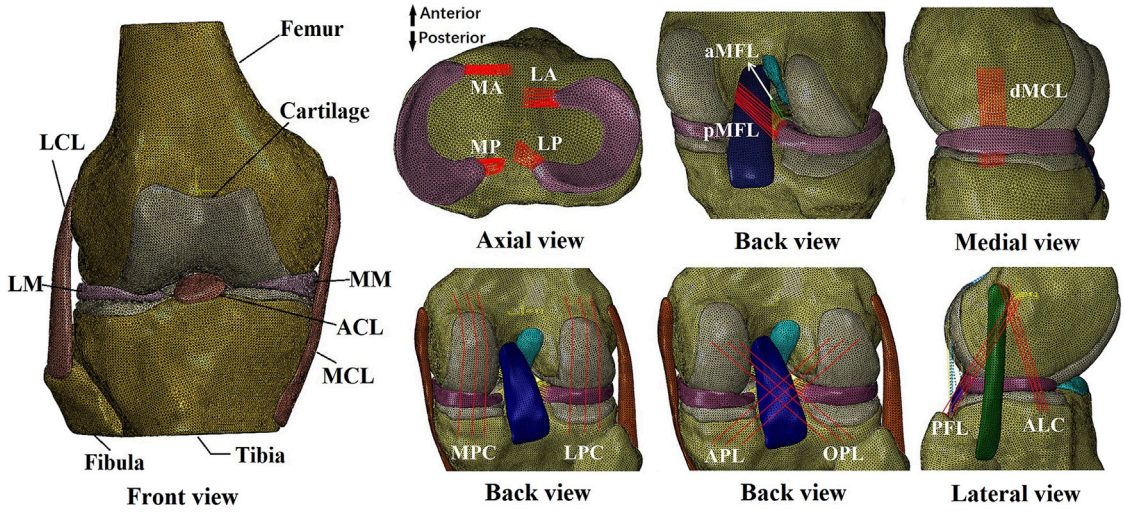

FIGURE 1
Finite element model of a human cadaveric right knee. LM, lateral meniscus; LCL, lateral collateral ligament; MM, medial meniscus; ACL, anterior cruciate ligament; MCL, medial collateral ligament; MA, anterior medial meniscotibial ligament; MP, posterior meniscotibial ligament; LA, anterior lateral meniscotibial ligament; LP, posterior lateral meniscotibial ligament; aMFL, anterior meniscofemoral ligament; pMFL, posterior meniscofemoral ligament; dMCL, deep medial collateral ligament; MPC, medial posterior capsule; LPC, lateral posterior capsule; APL, arcuate popliteal ligament; OPL, oblique popliteal ligament; PFL, popliteofibular ligament; ALC, anterolateral capsule.

TABLE 1 Material coefficients for the ligaments and joint capsules obtained from literature (Gupte et al., 2002; Song et al., 2004; Robinson et al., 2005; Hauch et al., 2010; Baldwin et al., 2012; Beidokhti et al., 2018; Wang et al., 2022a).

Tissue	Stiffness (N/mm)	Young's modulus (MPa)	Poisson's ratio
ACL	--	168	0.4
PCL	258	--	--
MCL	--	179	0.4
LCL	--	224	0.4
MA	169	--	--
LA	216	--	--
MP	207	--	--
LP	130	--	--
aMFL	200	--	--
pMFL	206	--	--
dMCL	42	--	--
ALL	16	--	--
ALC	25	--	--
PFL	38	--	--
MPC	15	--	--

ACL, anterior cruciate ligament; PCL, posterior cruciate ligament; MCL, medial collateral ligament; LCL, lateral collateral ligament; MA, anterior meniscotibial ligament of the medial meniscus; LA, anterior meniscotibial ligament of the lateral meniscus; MP, posterior meniscotibial ligament of the medial meniscus; LP, posterior meniscotibial ligament of the lateral meniscus; aMFL, anterior meniscofemoral ligament; pMFL, posterior meniscofemoral ligament; dMCL, deep medial collateral ligament; ALL, anterolateral ligament; ALC, anterolateral capsule; PFL, popliteofibular ligament; MPC, medial posterior capsule; LPC, lateral posterior capsule; APL, arcuate popliteal ligament; OPL, oblique popliteal ligament.

The 3D model was meshed using 4-node tetrahedral elements in HyperMesh (Altair Engineering, Japan). Convergence tests were conducted to obtain optimized element sizes (loading condition: 2.5 mm tibial load with the femur totally fixed at full knee extension; output: force in the ACL). The optimized element had a side length of 1 mm, resulting in a total of 659,251 elements in the final intact knee model.

TABLE 2 Anterior tibial translation, internal tibial rotation, and *in situ* force in the ACL obtained from previous literature (Kanamori et al., 2000; Wang et al., 2019) and the current finite element model calculation under the following loading conditions applied at a joint flexion angle of 30°: (a) 134 N anterior tibial load, (b) 10 Nm internal tibial moment, and (c) 10 Nm internal tibial moment with 10 Nm valgus tibial moment.

	134 N anterior tibial load		10 Nm internal tibial moment		10 Nm valgus tibial moment + 10 Nm internal tibial moment	
	Anterior tibial translation (mm)	*In situ* force in the ACL (N)	Internal tibial rotation (°)	*In situ* force in the ACL (N)	Internal tibial rotation (°)	*In situ* force in the ACL (N)
Experimental [18, 41]	5.1	124	20.5 ± 3.5	42 ± 22	22.3 ± 3.5	69 ± 32
Computational (current study)	5.2	126	17.6	37	19.1	56

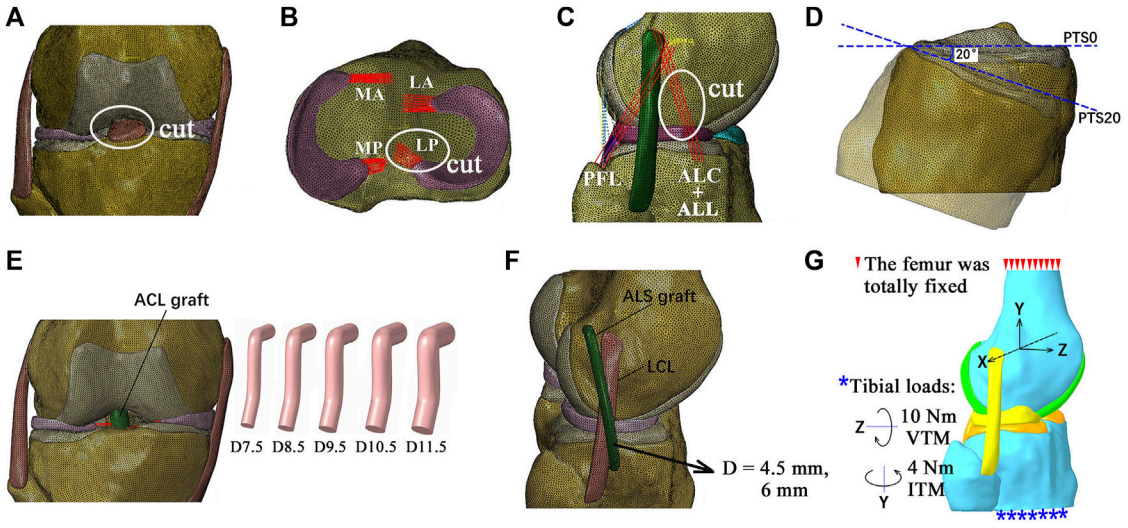

FIGURE 2
Diagrams of the finite element models simulating different combinations of knee injuries. **(A)** Simulation of an isolated ACL rupture by cutting the ACL. **(B)** Simulation of ACL rupture combined with rupture of the posterior lateral meniscotibial ligament (LP). **(C)** Simulation of ACL rupture combined with rupture of the anterolateral structures (ALSs), including the anterolateral ligament (ALL) and anterolateral capsule (ALC). **(D)** Simulation of a posterior tibial slope (PTS) of 20°. **(E)** Simulation of anatomical single-bundle (SB) ACL reconstructions (ACLRs) with different graft diameters. **(F)** ACLR combined with ALS reconstruction (ALSR) with ALS graft diameters of 4.5 mm and 6 mm. **(G)** Boundary and loading conditions for simulating pivot shifts. MA, anterior medial meniscotibial ligament; MP, posterior meniscotibial ligament; LA, anterior lateral meniscotibial ligament; PFL, popliteofibular ligament; D7.5, graft diameter of 7.5 mm; ITM, internal tibial moment; VTM, valgus tibial moment.

The material properties of the joint tissues were defined according to previous literature (Gupte et al., 2002; Song et al., 2004; Robinson et al., 2005; Hauch et al., 2010; Baldwin et al., 2012; Beidokhti et al., 2018; Wang et al., 2019) using Abaqus/CAE 2019 (Simulia, Inc., United States). The bones and cartilage were assumed to be linear isotropic elastic tissues (Young's modulus = 0.4 GPa and 5 MPa; Poisson's ratio = 0.33 and 0.46, respectively). The meniscus was assumed to be orthotropic elastic (E_θ = 125 MPa, $E_Z = E_R$ = 27.5 MPa, $G_{\theta R} = G_{\theta Z}$ = 2 MPa, G_{RZ} = 10.34, V_{RZ} = 0.33, and $V_{\theta R} = V_{\theta Z}$ = 0.1). The ligaments and knee capsules were defined as isotropic linear elastic tissues. The material coefficients for these tissues are shown in Table 1. Frictionless sliding was defined at the contact interfaces between the cartilages and menisci to permit sliding of the contact surfaces without penetration. Tie contacts were used to connect the ligaments/capsules to their bone interfaces and between the articular cartilage and corresponding bone surface so that there was no relative movements between the connected surfaces.

The model was validated by comparing the calculated data with experimental data from previous studies (Kanamori et al., 2000; Wang et al., 2020c). The compared data included knee kinematics and force in the ACL under the following three loading conditions at a knee flexion angle of 30°, with the femur completely fixed and having six degrees of freedom and the tibia subjected to (a) an anterior load of 134 N, (b) an internal moment of 10 Nm, and (c) an internal moment of 10 Nm and a valgus moment of 10 Nm. The results in Table 2 show that the model calculations were all within the range of values reported in cadaveric experiments.

2.2 Simulation of isolated ACL rupture and ACL ruptures with various injuries or knee defects

To simulate ruptured ACLs in intact and injured knees, the related tissues were removed from the model (Figure 2). To simulate

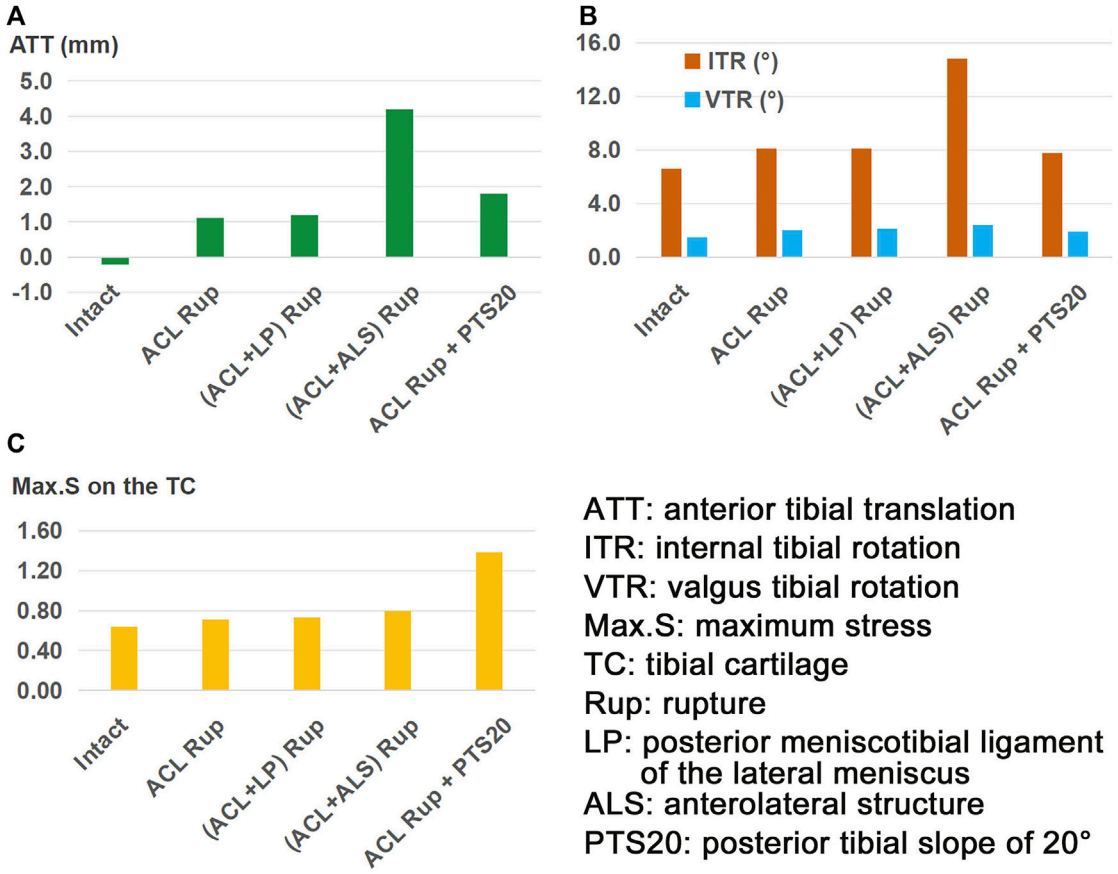

FIGURE 3
(A) Anterior tibial translation (ATT), **(B)** valgus tibial rotation (VTR) and internal tibial rotation (ITR), and **(C)** maximum von Mises stress (Max.S) on the tibial articular cartilage (TC) in response to a pivot shift loading condition in a knee with ACL rupture and different combinations of knee injuries or defects.

a PTS, the tibial plateau was rotated around the medial–lateral axis of the joint in the sagittal plane while all other degrees of freedom were unconstrained, as depicted in a previous study (Voos et al., 2012) (Figure 2D). Akoto et al. (2020) showed that patients with ACLR failure and high-grade anterior knee laxity had PTSs ranging from 13° to 20°. In this study, a PTS of 20° was simulated to represent a severe case. The following injury/defect modes were simulated: isolated ACL rupture (Figure 2A); combined ruptures of the ACL and LP (Figure 2B); combined ruptures of the ACL and ALS (Figure 2C); ACL rupture with a PTS of 20° (Figure 2D).

2.3 Simulation of anatomical single-bundle ACLR with varying graft diameters

The anatomical single-bundle ACLR for treating the abovementioned combinations of knee injuries and defects was simulated (Figure 2E). The entrances for the bone tunnels were placed at the centers of the anatomical insertion sites. The angles of the femoral tunnel with the sagittal and axial planes were 25° and 45°, and those of the tibial tunnel were 25° and 65°, respectively (Wang et al., 2022b). The ACL graft was simulated as a cylindrical structure using Creo Parametric 8.0 (PTC, MA, United States), with its Young's modulus set as 168 MPa (Wilson et al., 1999). The graft was simulated to be fixed to the bone tunnels by an endoscrew, which was also modeled as a cylinder (length of 10 mm and same diameter as the graft) (Wang et al., 2020a). The endoscrew was affixed to the graft at one end and in contact with the tunnel wall at its exterior surface so that there were no relative motions between these contact surfaces. The Young's modulus and Poisson's ratio of the endoscrew were respectively set to 110 GPa and 0.35 to simulate titanium material. The ACLR was simulated with different graft diameters (7.5, 8.5, 9.5, 10.5, and 11.5 mm) to determine the dimensions that were best able to restore knee functionality. The simulated bone tunnel diameters were similar to those of the graft.

2.4 Simulation of combined ALSR with ACLR

To evaluate the effectiveness of ALSR in restoring knee kinematics after injury to the ACL, the knee model was simulated with an isolated ACL rupture and treated using ALSR combined with ACLR (Figure 2F) and compared with the outcome after treatment through isolated ACLR (graft diameters: 8.5 mm and 10.5 mm). The diameter of the ALS graft was increased from 4.5 mm to 6 mm to explore the effect of the ALS graft diameter on the surgical outcome. Then, the effectiveness of combined ACLR and

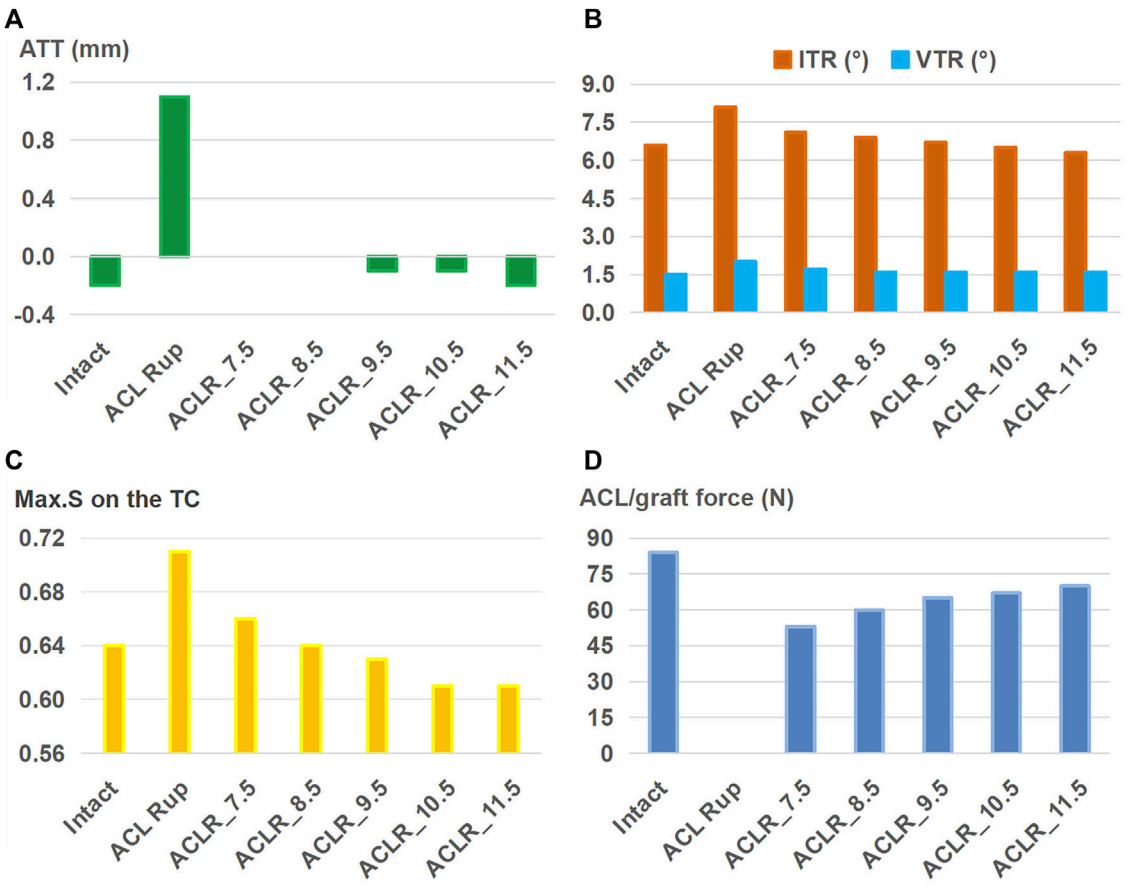

FIGURE 4
(A) Anterior tibial translation (ATT), **(B)** valgus tibial rotation (VTR) and internal tibial rotation (ITR), **(C)** maximum von Mises stress (Max.S) on the tibial articular cartilage (TC), and **(D)** graft forces in response to a pivot shift loading condition in a knee following ACL reconstructions (ACLRs) with varying graft diameters for treating isolated ACL rupture. Rup: rupture; ACLR_7.5: ACLR with a graft diameter of 7.5 mm.

ALSR was evaluated for treating different combinations of knee injuries.

The surgical techniques recommended by the 2017 expert group consensus (Sonnery-Cottet et al., 2017) were used to simulate the ALSR in this study. Specifically, the femoral tunnel was placed 8 mm proximal and 4 mm posterior to the lateral epicondyle, and the tibial tunnel was placed 10 mm below the joint line at the halfway point between the center of the fibula head and Gerdy's tubercle. A graft diameter of 4.5 mm was used, as suggested by the consensus, and the Young's modulus was set as 618.4 MPa (Hamner et al., 1999). The Poisson's ratio was the same as that of the other ligaments (0.4) in the model. The tunnel axes both lay in the sagittal plane. The angle of the femoral tunnel with respect to the transverse plane was 20°, and the angle of the tibial tunnel with respect to the transverse plane was 30°. The graft fixation method previously detailed for the ACLR model was also used for the ALSR models.

2.5 Loading conditions and outputs

To simulate pivot shifts, all models were loaded with an internal tibial moment of 4 Nm and a valgus tibial moment of 10 Nm at full knee extension (Wan et al., 2017; McLeod and Barber, 2023) (Figure 2G). The anterior tibial translation (ATT), valgus tibial rotation (VTR), internal tibial rotation (ITR), Max.S on the TC, and ACL/graft forces were compared among the different simulation groups.

3 Results

3.1 Outcomes for intact knee, isolated ACL rupture, and ACL rupture with various additional injuries or knee defects

The knee displacements and articular stresses in the models at different knee states are shown in Figure 3. Compared to the intact state, the knee displacements and articular stresses increased after ACL rupture (−0.2 mm vs. 1.1 mm for ATT (Figure 3A), 6.7° vs. 8.1° for ITR, 1.5° vs. 2.0° for VTR (Figure 3B), 0.65 MPa vs. 0.71 MPa for Max.S on the TC). Compared with the isolated ACL rupture, all other injury models showed greater knee displacements and articular stresses. Damage to the ALS destabilized the knee more than a combined PTS of 20° or LP rupture (4.2 mm vs. 1.8 mm vs. 1.2 mm for ATT, 14.8° vs. 7.8° vs. 8.1° for ITR, and 2.4° vs. 1.9° vs. 2.1° for VTR, respectively). The knee with an ACL + LP rupture

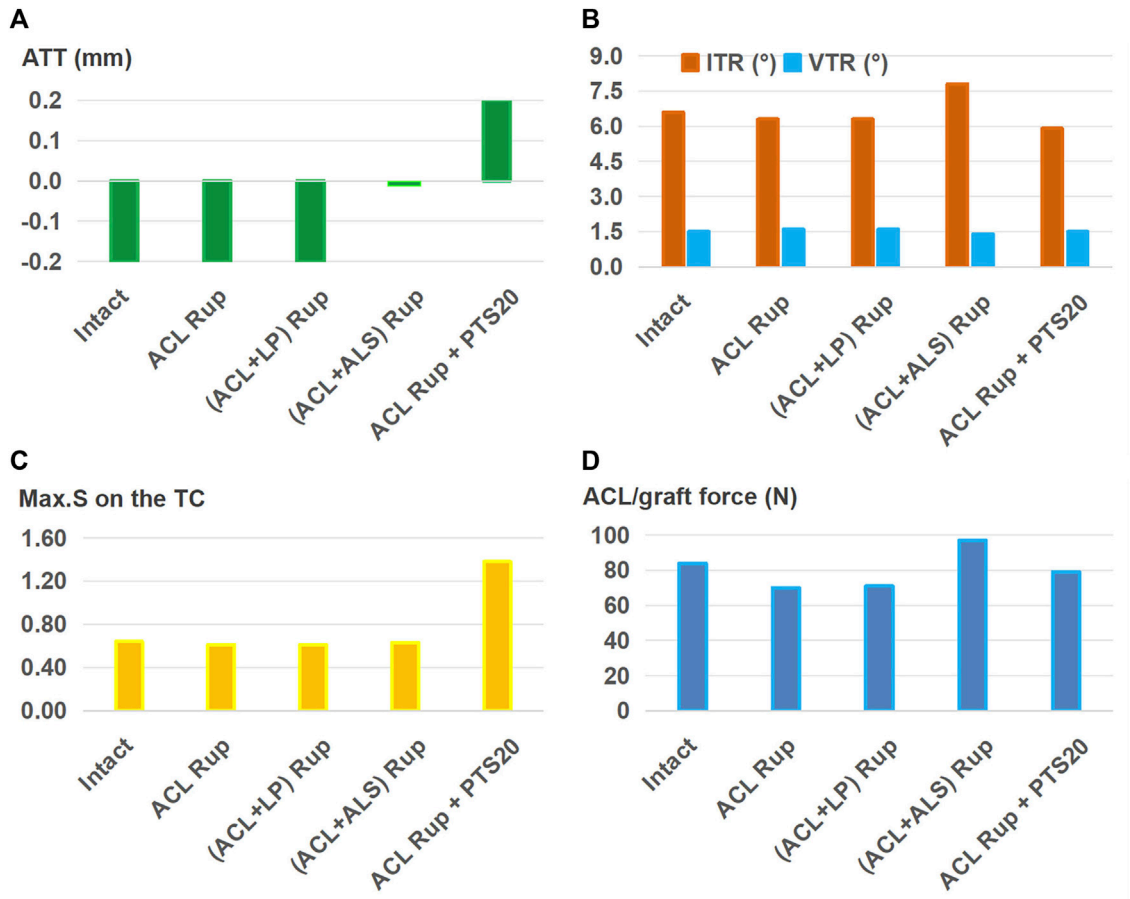

FIGURE 5
(A) Anterior tibial translation (ATT), **(B)** valgus tibial rotation (VTR) and internal tibial rotation (ITR), **(C)** maximum von Mises stress (Max.S) on the tibial articular cartilage (TC), and **(D)** graft forces in response to a pivot shift loading condition in a knee after ACL reconstruction (ACLR) with a graft of diameter 11.5 mm for treating different combinations of knee injuries. Rup, rupture; LP, posterior meniscotibial ligament of the lateral meniscus; ALS, anterolateral structure; PTS20, posterior tibial slope of 20°.

produced the most stable joint out of all combined injury models. In terms of the articular stress (Figure 3C), a PTS of 20° caused the highest Max.S on the TC, reaching over twice that of the intact knee (1.38 MPa vs. 0.64 MPa). The Max.S on the TC was higher after the ACL + ALS rupture than after ACL + LP rupture (0.80 MPa vs. 0.73 MPa).

3.2 Outcomes for ACLR with different combinations of knee injuries/defects

The outcomes of the ACLR model with varying graft diameters (7.5–11.5 mm) for treating an isolated ACL rupture are shown in Figure 4. Compared to the ACL rupture model (ACL Rup), ACLR reduced ATT (Figure 4A), ITR, VTR (Figure 4B), and Max.S on the TC (Figure 4C) to restore the ligament force (Figure 4D) closer to the intact state. Compared to the intact group, a 7.5-mm-diameter ACL graft produced larger anterior (ATT) and rotational (ITR, VTR) tibial displacements (0 mm vs. −0.2 mm, 7.1° vs. 6.6°, 1.7° vs. 1.5°) as well as resulted in higher stresses on the tibial articular cartilages (0.66 MPa vs. 0.64 MPa for LTC, 0.38 MPa vs. 0.34 MPa), but the force in the graft was lower (53 N vs. 84 N). Each successive increase in graft diameter resulted in values closer to those of the intact model. The ATT and VTR were restored to the intact levels with a graft of diameter 11.5 mm, but the ITR and Max.S on the TC were restored close to the intact levels with 10.5 mm and 8.5 mm diameter grafts, respectively. Although increasing the graft diameter resulted in graft forces closer to the intact levels, there were noticeable differences even when using the largest graft. Specifically, the force was 70 N for ACLR with a graft of diameter 11.5 mm compared to 84 N in the intact state. Overall, ACLR with a graft of diameter 11.5 mm could restore the anterior and rotational knee stabilities as well as Max.S on the TC to within the intact level after isolated ACL rupture. However, the graft force was lower than that in the intact ACL.

Based on the 11.5-mm graft, Figure 5 shows the results for ACLR after treatment with different combinations of knee injuries; it is seen that ACLR restored the anterior (Figure 5A) and rotational (Figure 5B) stabilities of the knee and articular stresses (Figure 5C) close to the intact levels when treating isolated ACL and ACL + LP ruptures. The graft forces (Figure 5D) in the groups simulating ACL and ACL + LP ruptures were also lower than that of the intact ACL after treatment by ACLR. The knee with an injury to the ALS still had greater anterior and internal rotational laxity as well as

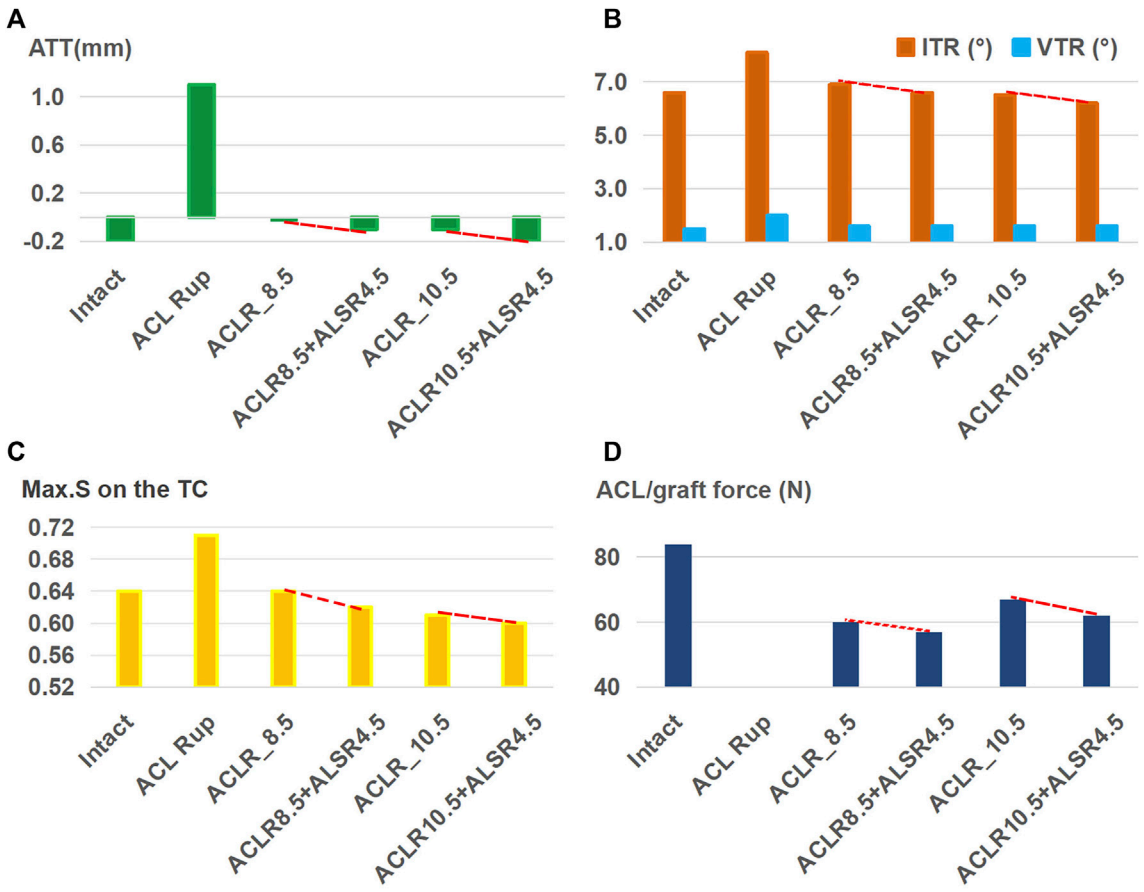

FIGURE 6
(A) Anterior tibial translation (ATT), **(B)** valgus tibial rotation (VTR) and internal tibial rotation (ITR), **(C)** maximum von Mises stress (Max.S) on the tibial articular cartilage (TC), and **(D)** graft forces in response to a pivot shift loading condition in a knee following I) ACL reconstructions (ACLRs) with graft diameters of 8.5 mm and 10.5 mm; II) anterolateral structures reconstruction (ALSR) with a graft of diameter 4.5 mm combined with ACLR with graft diameters of 8.5 mm and 10.5 mm. Both reconstruction techniques were used to treat an isolated ACL rupture. Rup, rupture; ACLR_8.5, ACLR with a graft of diameter 8.5 mm.

abnormally high graft force after treatment by ACLR when compared with the intact knee (0 mm vs. −0.2 mm for ATT, 7.8° vs. 6.6° for ITR, 97 N vs. 84 N for graft force). The knee with a PTS of 20° had a larger ATT (0.2 mm vs. −0.2 mm), and the Max.S on the TC was greater than that for the intact case (1.38 vs. 0.64 MPa).

3.3 Outcomes for ALSR with different combinations of knee injuries/defects

Figure 6 shows that when treating an isolated ACL rupture, ALSR (graft diameter: 4.5 mm) combined with ACLR (graft diameter: 8.5 mm) resulted in lower anterior (Figure 6A) and internal rotational (Figure 6B) displacements, articular stresses (Figure 6C), and graft forces (Figure 6D) than ACLR alone (−0.1 mm vs. 0 mm for ATT, 6.6° vs. 6.9° for ITR, 0.62 MPa vs. 0.64 MPa for Max.S on the TC, 57 N vs. 60 N for graft force). This trend was consistent between the two groups when using 8.5-mm and 10.5-mm diameter ACL grafts.

As shown in Figure 7, ALSR combined with ACLR restored the ATT (Figure 7A), VTR (Figure 7B), and Max.S on the TC (Figure 7C) to normal levels for ACL rupture treatment accompanied by injury to the ALS. However, the ITR was still greater (6.9° vs. 6.6°) and graft force was higher (98 N vs. 84 N) than those for the intact case (Figure 7B). For the ACL rupture with a PTS of 20°, the ATT and Max.S on the TC were still greater than those of the intact knee (0.1 mm vs. −0.2 mm for ATT, 1.38 MPa vs. 0.64 MPa), and the graft force was higher than that of the intact ACL (87 N vs. 84 N, Figure 7D).

Figure 8 shows that after using a larger graft diameter (6 mm) for ALSR, the knee displacement (Figures 8A, B), Max.S on the TC (Figure 8C), and graft force (Figure 8D) after ACL rupture accompanied by injury to the ALS were all restored to within the intact levels. However, for the ACL rupture with a PTS of 20°, the ATT and Max.S on the TC were still greater than those of the intact knee (0.1 mm vs. −0.2 mm for ATT, 1.38 MPa vs. 0.64 MPa for Max.S).

4 Discussion

It was found that compared to the isolated ACL rupture, combined injury to the LP, ALS, or increased PTS caused greater anterior and rotational knee laxity and articular stresses. Injury to

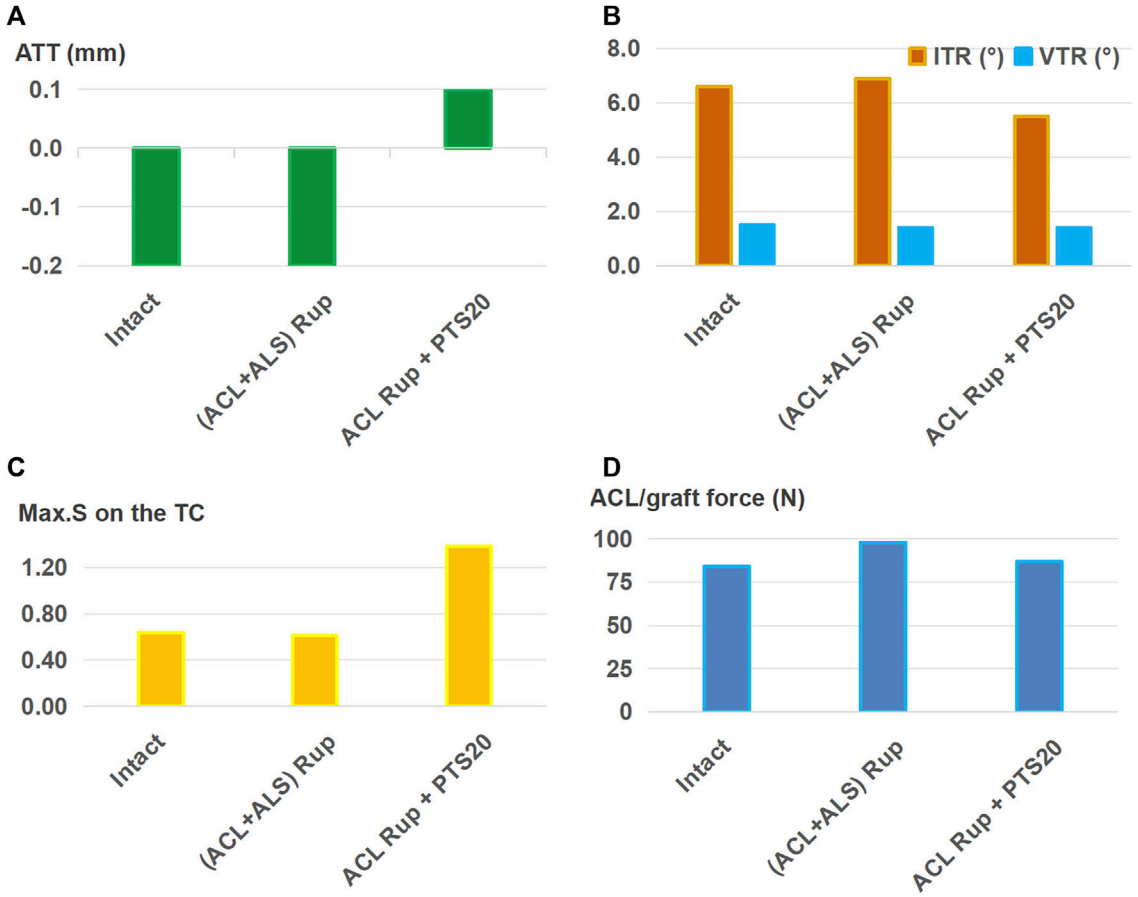

FIGURE 7
(A) Anterior tibial translation (ATT), **(B)** valgus tibial rotation (VTR) and internal tibial rotation (ITR), **(C)** maximum von Mises stress (Max.S) on the tibial articular cartilage (TC), and **(D)** graft forces in response to a pivot shift loading condition in a knee following anterolateral structures reconstruction (ALSR) (graft diameter: 4.5 mm) combined with ACLR (graft diameter: 11.5 mm). The procedure was used to treat different combined knee injuries. Rup, rupture; ALS, anterolateral structure; PTS20, posterior tibial slope of 20°.

the ALS caused the greatest knee laxity among all simulated conditions, and incorporating a PTS of 20° produced the largest Max.S on the TC. The joint stability and articular stress in the knee with isolated ACL rupture or ACL + LP rupture were restored close to those of the intact knee after treatment by isolated ACLR. An additional ALSR produced a lower pivot shift, articular stress, and force in the ACL graft than isolated ACLR, allowing better treatment of the ACL rupture with combined injuries to the ALS. ACLR combined with ALSR using a larger diameter of the ALSR graft (6 mm) than that suggested by the 2017 expert group consensus was shown to restore normal knee stability, articular stress, and graft force after injury to the ALS. However, even after treatment by ACLR combined with ALSR (graft diameter: 6 mm), incorporating a PTS of 20° resulted in greater ATT and Max.S on the TC than those for the intact knee. These findings may provide a scientific basis to further determine the surgical indications for ACLR combined with ALSR.

Compared to the intact state, both knee displacement and articular stress increased after isolated ACL rupture (Figure 3), indicating that the ACL is important for maintaining knee stability and normal articular stress. This is consistent with the findings of biomechanical and clinical follow-up studies that reported greater knee laxity and higher articular stress along with a high rate of long-term knee osteoarthritis after ACL injury (Arokoski et al., 2000; Barenius et al., 2014; Wang et al., 2020b). Injury to the ALS caused a larger knee displacement and maximum stress on the TC than injury to the LP likely because of the lateral location of the ALS on the knee joint, which plays a more important role in restraining the movement of the femoral condyle toward the tibial plateau than the more centrally located LP. The results of this study also show that compared with isolated ACL rupture, the ATT increases when combined with increased PTS, which is consistent with the findings of a previous study (Bauer et al., 2022). However, the ITR reduced slightly with the higher PTS, which could be caused by lifting of the anterior region of the tibial plateau as it rotates posteriorly. This might restrain the joint in the anterior space and produce less tibial rotation. Similarly, a PTS of 20° resulted in higher Max.S on the TC than injury to the LP or ALS, which could be attributed to the restrained motion from lifting of the anterior tibial plateau. In this study, the lowest values of knee laxity and articular stress were obtained after ACL rupture with an associated injury to the LP (Figure 3). Similarly, Tang et al. (2019) reported that the ATT in a knee placed under a simulated pivot-shift load increased only slightly after tearing of the posterior meniscal root.

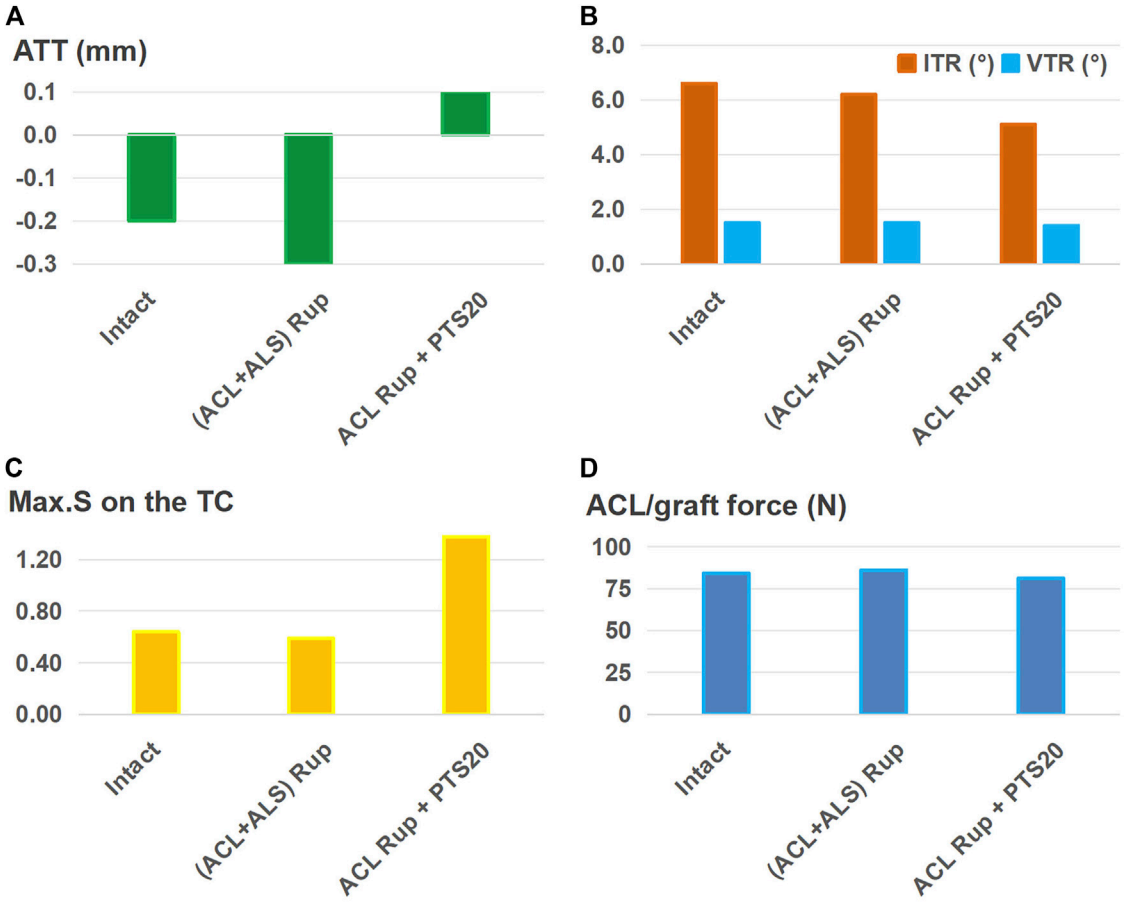

FIGURE 8
(A) Anterior tibial translation (ATT), **(B)** valgus tibial rotation (VTR) and internal tibial rotation (ITR), **(C)** maximum von Mises stress (Max.S) on the tibial articular cartilage (TC), and **(D)** graft forces in response to a pivot shift loading condition in a knee following anterolateral structures reconstruction (ALSR) (using a larger graft diameter of 6 mm) combined with ACLR (graft diameter: 11.5 mm). The procedure was used to treat different combined knee injuries. Rup, rupture; ALS, anterolateral structure; PTS20, posterior tibial slope of 20°.

ACLR was shown to reduce knee laxity and lower the Max.S on the tibial articular cartilage after isolated ACL rupture; it was also more effective as the diameter of the graft increased (Figure 4), which was consistent with literature (Wang et al., 2020b). Knee stability and articular stress were completely restored to normal levels when using a relatively large graft diameter (11.5 mm) to treat isolated ACL and ACL + LP ruptures (Figure 5). However, a large graft diameter may cause graft impingement on the femoral notch and increase the risk of early graft rupture after surgery (Dayan et al., 2015). Considering the large individual variations in the Young's modulus of the ACL grafts reported in previous studies (5–1500 MPa) (Smeets et al., 2017; Jacquet et al., 2020), grafts with larger values than those used in the present study may require smaller graft diameters for restoring the knee stability and articular stress to normal levels (Wang et al., 2022b).

This study also showed that ALSR further reduced the anterior and rotational knee displacements, articular stress, and ACL graft force compared to those of isolated ACLR (Figure 6). These outcomes are consistent with reports by Nitri et al. (2016) and Ueki et al. (2019). It is also postulated that ALSR may allow the use of a smaller graft diameter in ACLR and hence lower the risk of graft impingement on the femoral notch. This study identifies that injury to the ALS cannot be satisfactorily treated with the isolated ACLR or combination of ACLR and ALSR when using a graft of diameter 4.5 mm for the ALSR (Figure 7); however, successful treatment may be achieved with a combination of ACLR and ALSR when using a larger graft diameter (6 mm) for the ALSR (Figure 8). Moreover, a PTS of 20° still resulted in larger ATT and Max.S on the TC than those of the intact knee, even after treatment by a combination of ALSR (graft diameter: 6 mm) and ACLR (graft diameter: 11.5 mm). In this condition, an osteotomy may be needed to achieve better knee functionality and stress distribution on the articular cartilage.

The present study has some notable limitations. 1) The surgical technique for ALSR was according to the recommendations of the 2017 expert consensus (Sonnery-Cottet et al., 2017). Different surgical techniques, such as varying tunnel positions, were not explored in this study, which could affect the outcomes of ALSR. However, these factors were maintained constant across different simulation groups to exclude their impacts on the comparison outcomes. 2) The finite element model was adopted from a single subject, which may not represent the conditions of other subjects. Additionally, the Young's modulus of the ACL graft was obtained from literature, but it could vary with individual differences. However, the single finite element model allows the variate to be

controlled to one factor, which can be modified infinitely without causing damage to the sample. This permits the basic biomechanics to be revealed more clearly. Future research efforts could therefore include both cadaveric and *in vivo* studies to further validate the findings of this study. *In vivo* studies are particularly advantageous for examining the effects of individual differences and incorporating the effects of joint muscles. 3) Only a static loading condition was considered in this study, and complex loading environments representing different daily activities were not simulated. 4) Viscoelasticity and initial tension values of the ligaments were not considered in this study. In reality, stress relaxation occurs when the joint is subjected to external loading, and the initial tension of the ligaments can enhance their ability to better resist these loads. Therefore, the translations and rotations of the knee joint calculated in this study may have some systematic errors.

5 Conclusion

This study showed that combined injury to the LP and ALS with higher PTS angles led to higher degrees of anterior and rotational knee laxity and higher articular stresses in the ACL-deficient knee models. Injury to the ALS caused the greatest knee laxity among all conditions simulated, and incorporating a PTS of 20° produced the largest Max.S on the TC. Correspondingly, these combined injuries need to be treated with different surgical strategies to prevent postoperative pivot shifts and restore the articular stresses and graft forces to those similar to the intact knee. Using a human cadaver knee model, this study showed completely restored knee stability and articular stress after isolated ACL rupture or ACL rupture with combined LP injury when treated by isolated ACLR. Knee biomechanics after combined rupture of the ACL and ALS were only restored to those similar to the intact knee when treated by ACLR combined with ALSR using a large ALSR graft diameter (6 mm). However, ACL rupture combined with a PTS of 20° may need an additional strategy, such as osteotomy, to prevent pivot shift and reduce the risk of articular cartilage degeneration after ACLR.

Data availability statement

The original contributions presented in the study are included in the article/Supplementary Material, and any further inquiries may be directed to the corresponding authors.

Ethics statement

The studies involving humans were approved by the Committee for Oversight of Research and Clinical Training Involving Decedents. The studies were conducted in accordance with the local legislation and institutional requirements. The human samples used in this study were acquired from primarily isolated cases as part of a previous study, for which ethical approval was obtained. Written informed consent for participation was not required from the participants or their legal guardians/next of kin in accordance with the national legislation and institutional requirements.

Author contributions

HW: Conceptualization, Data curation, Formal analysis, Funding acquisition, Investigation, Methodology, Writing–original draft, Writing–review and editing. GY: Data curation, Formal analysis, Investigation, Writing–original draft, Writing–review and editing. KH: Formal analysis, Writing–original draft, Writing–review and editing. ZW: Conceptualization, Formal analysis, Investigation, Supervision, Writing–original draft, Writing–review and editing. C-KC: Conceptualization, Funding acquisition, Investigation, Supervision, Writing–original draft, Writing–review and editing.

Funding

The authors declare that financial support was received for the research, authorship, and/or publication of this article. This work was supported by the National Natural Science Foundation of China (grant number: 32101050) and Fundamental Research Funds for the Central Universities (project number: AF0820060).

Acknowledgments

The authors would like to thank Mr. Colin McClean for his assistance with editing this manuscript.

Conflict of interest

The authors declare that the research was conducted in the absence of any commercial or financial relationships that could be construed as a potential conflict of interest.

The author(s) declare that they were an editorial board member of Frontiers at the time of submission. This had no impact on the peer review process and the final decision.

Publisher's note

References

Akoto, R., Alm, L., Drenck, T. C., Frings, J., Krause, M., and Frosch, K. H. (2020). Slope-correction osteotomy with lateral extra-articular tenodesis and revision anterior cruciate ligament reconstruction is highly effective in treating high-grade anterior knee laxity. *Am. J. Sports Med.* 48 (14), 3478–3485. doi:10.1177/0363546520966327

Ansari, M. H., Claes, S., Wascher, D. C., Neyret, P., Stuart, M. J., and Krych, A. J. (2017). International perspective on revision anterior cruciate ligament reconstruction: what have we been missing? *Instr. Course Lect.* 66, 543–556.

Arokoski, J. P. A., Jurvelin, J. S., Väätäinen, U., and Helminen, H. J. (2000). Normal and pathological adaptations of articular cartilage to joint loading. *Scand. J. Med. Sci. Sports* 10 (4), 186–198. doi:10.1034/j.1600-0838.2000.010004186.x

Baldwin, M. A., Clary, C. W., Fitzpatrick, C. K., Deacy, J. S., Maletsky, L. P., and Rullkoetter, P. J. (2012). Dynamic finite element knee simulation for evaluation of knee replacement mechanics. *J. Biomech.* 45 (3), 474–483. doi:10.1016/j.jbiomech.2011.11.052

Barenius, B., Ponzer, S., Shalabi, A., Bujak, R., Norlén, L., and Eriksson, K. (2014). Increased risk of osteoarthritis after anterior cruciate ligament reconstruction A 14-year follow-up study of a randomized controlled trial. *Am. J. Sports Med.* 42 (5), 1049–1057. doi:10.1177/0363546514526139

Bauer, L., Thorwächter, C., Steinbrück, A., Jansson, V., Traxler, H., Alic, Z., et al. (2022). Does posterior tibial slope influence knee kinematics in medial stabilized TKA? *J. Clin. Med.* 11 (22), 6875. doi:10.3390/jcm11226875

Beidokhti, H. N., Janssen, D., van de Groes, S., and Verdonschot, N. (2018). The peripheral soft tissues should not be ignored in the finite element models of the human knee joint. *Med. Biol. Eng. Comput.* 56 (7), 1189–1199. doi:10.1007/s11517-017-1757-0

Chen, J. B., Wang, C., Xu, C. Q., Qiu, J. Y., Xu, J. J., Tsai, T. Y., et al. (2021). Effects of anterolateral structure augmentation on the *in vivo* kinematics of ACL-reconstructed knees: response. *Am. Am J Sports Med* 49 (9), NP43–NP44. doi:10.1177/03635465211023749

Dayan, E., Maderazo, A., and Fitzpatrick, D. (2015). Magnetic resonance imaging of complications of anterior cruciate ligament reconstruction. *Am. J. Orthop.* 44 (12), 569–571.

Du, G. Q., Zhan, H. S., Ding, D. F., Wang, S. W., Wei, X. C., Wei, F. Y., et al. (2016). Abnormal mechanical loading induces cartilage degeneration by accelerating meniscus hypertrophy and mineralization after ACL injuries *in vivo*. *Am. J. Sports Med.* 44 (3), 652–663. doi:10.1177/0363546515621285

Guenther, D., Griffith, C., Lesniak, B., Lopomo, N., Grassi, A., Zaffagnini, S., et al. (2015). Anterolateral rotatory instability of the knee. *Knee Surg. Sports Traumatol. Arthrosc.* 23 (10), 2909–2917. doi:10.1007/s00167-015-3616-6

Gupte, C. M., Smith, A., Jamieson, N., Bull, A. M. J., Thomas, R. D., and Amis, A. A. (2002). Meniscofemoral ligaments-structural and material properties. *J. Biomech.* 35 (12), 1623–1629. doi:10.1016/s0021-9290(02)00238-5

Hamner, D. L., Brown, C. H., Steiner, M. E., Hecker, A. T., and Hayes, W. C. (1999). Hamstring tendon grafts for reconstruction of the anterior cruciate ligament: biomechanical evaluation of the use of multiple strands and tensioning techniques. *J. Bone Jt. Surg. Am.* 81A (4), 549–557. doi:10.2106/00004623-199904000-00013

Hauch, K. N., Villegas, D. F., and Donahue, T. L. H. (2010). Geometry, time-dependent and failure properties of human meniscal attachments. *J. Biomech.* 43 (3), 463–468. doi:10.1016/j.jbiomech.2009.09.043

Jacquet, C., Jaubert, M., Pioger, C., Sbihi, A., Pithioux, M., Le Baron, M., et al. (2020). Presoaking of semitendinosus graft with vancomycin does not alter its biomechanical properties: a biomechanical *in vitro*-Controlled study using graft from living donors. *Arthroscopy* 36 (8), 2231–2236. doi:10.1016/j.arthro.2020.03.037

Kanamori, A., Woo, S. L. Y., Ma, C. B., Zeminski, J., Rudy, T. W., Li, G. A., et al. (2000). The forces in the anterior cruciate ligament and knee kinematics during a simulated pivot shift test: a human cadaveric study using robotic technology. *Arthroscopy* 16 (6), 633–639. doi:10.1053/jars.2000.7682

McLeod, K. C., and Barber, F. A. (2023). Pivot shift syndrome of the knee. *Sports Med. Arthrosc.* 31 (2), 34–40. doi:10.1097/jsa.0000000000000365

Musahl, V., Engler, I. D., Nazzal, E. M., Dalton, J. F., Lucidi, G. A., Hughes, J. D., et al. (2022). Current trends in the anterior cruciate ligament part II: evaluation, surgical technique, prevention, and rehabilitation. *Knee Surg. Sports Traumatol. Arthrosc.* 30 (1), 34–51. doi:10.1007/s00167-021-06825-z

Ni, Q. K., Wang, X. P., Guo, Q., Li, M., Liu, N., and Zhang, H. (2022). High-grade pivot-shift phenomenon after anterior cruciate ligament injury is associated with asymmetry of lateral and medial compartment anterior tibial translation and lateral meniscus posterior horn tears. *Knee Surg. Sports Traumatol. Arthrosc.* 30 (11), 3700–3707. doi:10.1007/s00167-022-06972-x

Nitri, M., Rasmussen, M. T., Williams, B. T., Moulton, S. G., Cruz, R. S., Dornan, G. J., et al. (2016). An *in vitro* robotic assessment of the anterolateral ligament, Part 2 anterolateral ligament reconstruction combined with anterior cruciate ligament reconstruction. *Am. J. Sports Med.* 44 (3), 593–601. doi:10.1177/0363546515620183

Robinson, J. R., Bull, A. M. J., and Amis, A. A. (2005). Structural properties of the medial collateral ligament complex of the human knee. *J. Biomech.* 38 (5), 1067–1074. doi:10.1016/j.jbiomech.2004.05.034

Shen, X. Y., Qin, Y. G., Zuo, J. L., Liu, T., and Xiao, J. L. (2021). A systematic review of risk factors for anterior cruciate ligament reconstruction failure. *Int. J. Sports Med.* 42 (08), 682–693. doi:10.1055/a-1393-6282

Smeets, K., Bellemans, J., Scheys, L., Eijnde, B. O., Slane, J., and Claes, S. (2017). Mechanical Analysis of Extra-Articular Knee Ligaments. Part two: tendon grafts used for knee ligament reconstruction. *Knee* 24 (5), 957–964. doi:10.1016/j.knee.2017.07.011

Song, G. Y., Zhang, H., Wu, G., Zhang, J., Liu, X., Xue, Z., et al. (2017). Patients with high-grade pivot-shift phenomenon are associated with higher prevalence of anterolateral ligament injury after acute anterior cruciate ligament injuries. *Knee Surg. Sports Traumatol. Arthrosc.* 25 (4), 1111–1116. doi:10.1007/s00167-017-4492-z

Song, Y. H., Debski, R. E., Musahl, V., Thomas, M., and Woo, S. L. Y. (2004). A three-dimensional finite element model of the human anterior cruciate ligament: a computational analysis with experimental validation. *J. Biomech.* 37 (3), 383–390. doi:10.1016/s0021-9290(03)00261-6

Sonnery-Cottet, B., Daggett, M., Fayard, J. M., Ferretti, A., Helito, C. P., Lind, M., et al. (2017). Anterolateral Ligament Expert Group consensus paper on the management of internal rotation and instability of the anterior cruciate ligament - deficient knee. *J. Orthop. Traumatol.* 18 (2), 91–106. doi:10.1007/s10195-017-0449-8

Tang, X., Marshall, B., Wang, J. H., Zhu, J. J., Li, J., Smolinski, P., et al. (2019). Lateral meniscal posterior root repair with anterior cruciate ligament reconstruction better restores knee stability. *Am. J. Sports Med.* 47 (1), 59–65. doi:10.1177/0363546518808004

Ueki, H., Katagiri, H., Otabe, K., Nakagawa, Y., Ohara, T., Shioda, M., et al. (2019). Contribution of additional anterolateral structure augmentation to controlling pivot shift in anterior cruciate ligament reconstruction. *Am. J. Sports Med.* 47 (9), 2093–2101. doi:10.1177/0363546519854101

Voos, J. E., Suero, E. M., Citak, M., Petrigliano, F. P., Bosscher, M. R. F., Citak, M., et al. (2012). Effect of tibial slope on the stability of the anterior cruciate ligament-deficient knee. *Knee Surg. Sports Traumatol. Arthrosc.* 20 (8), 1626–1631. doi:10.1007/s00167-011-1823-3

Wan, C., Hao, Z. X., Li, Z. C., and Lin, J. H. (2017). Finite element simulations of different hamstring tendon graft lengths and related fixations in anterior cruciate ligament reconstruction. *Med. Biol. Eng. Comput.* 55 (12), 2097–2106. doi:10.1007/s11517-017-1637-7

Wang, H. Z., Fang, C. H., Tao, M. Z., Shi, Q. Y., He, K. X., and Cheng, C. K. (2022b). Hourglass-shaped grafts are superior to conventional grafts for restoring knee stability and graft force at knee flexion angle of 30° following anterior cruciate ligament reconstruction: a finite element analysis. *Front. Bioeng. Biotechnol.* 10, 967411. doi:10.3389/fbioe.2022.967411

Wang, H. Z., Kang, H. J., Yao, J., Cheng, C. K., and Woo, S. L. Y. (2019). Evaluation of a magnesium ring device for mechanical augmentation of a ruptured ACL: finite element analysis. *Clin. Biomech.* 68, 122–127. doi:10.1016/j.clinbiomech.2019.06.002

Wang, H. Z., Tao, M. Z., Shi, Q. Y., He, K. X., and Cheng, C. K. (2022a). Graft diameter should reflect the size of the native anterior cruciate ligament (ACL) to improve the outcome of ACL reconstruction: a finite element analysis. *Bioeng. (Basel)* 9 (10), 507. doi:10.3390/bioengineering9100507

Wang, H. Z., Zhang, B., and Cheng, C. K. (2020a). Stiffness and shape of the ACL graft affects tunnel enlargement and graft wear. *Knee Surg. Sports Traumatol. Arthrosc.* 28 (7), 2184–2193. doi:10.1007/s00167-019-05772-0

Wang, H. Z., Zhang, M., and Cheng, C. K. (2020b). Changing the diameter of the bone tunnel is more effective than changing the tunnel shape for restoring joint functionality after ACL reconstruction. *Front. Bioeng. Biotechnol.* 8 (1), 173. doi:10.3389/fbioe.2020.00173

Wang, H. Z., Zhang, M., and Cheng, C. K. (2020c). A novel protection liner to improve graft-tunnel interaction following anterior cruciate ligament reconstruction: a finite element analysis. *J. Orthop. Surg. Res.* 15 (1), 232. doi:10.1186/s13018-020-01755-x

Wilson, T. W., Zafuta, M. P., and Zobitz, M. (1999). A biomechanical analysis of matched bone-patellar tendon-bone and double-looped semitendinosus and gracilis tendon grafts. *Am. J. Sports Med.* 27 (2), 202–207. doi:10.1177/03635465990270021501

Wood, R., Marsh, J., and Getgood, A. (2018). Anterolateral complex reconstruction: another fad or method to improve ACL outcomes? *Tech. Orthop.* 33 (4), 239–245. doi:10.1097/bto.0000000000000310

frontiers | Frontiers in Bioengineering and Biotechnology

TYPE Original Research
PUBLISHED 30 August 2024
DOI 10.3389/fbioe.2024.1471692

OPEN ACCESS

EDITED BY
Yih-Kuen Jan,
University of Illinois at Urbana-Champaign, United States

REVIEWED BY
Michail Klontzas,
University Hospital of Heraklion, Greece
Zekun Jiang,
Sichuan University, China

*CORRESPONDENCE
Wei Wang,
dr.wangwei@xjtu.edu.cn

RECEIVED 28 July 2024
ACCEPTED 22 August 2024
PUBLISHED 30 August 2024

CITATION
Alkhatatbeh T, Alkhatatbeh A, Li X and Wang W (2024) A single sequence MRI-based deep learning radiomics model in the diagnosis of early osteonecrosis of femoral head.
Front. Bioeng. Biotechnol. 12:1471692.
doi: 10.3389/fbioe.2024.1471692

A single sequence MRI-based deep learning radiomics model in the diagnosis of early osteonecrosis of femoral head

Tariq Alkhatatbeh[1], Ahmad Alkhatatbeh[2], Xiaohui Li[3] and Wei Wang[1]*

[1]Comprehensive Orthopedic Surgery Department, The Second Affiliated Hospital of Xi'an Jiaotong University, Xi'an, China, [2]Department of Orthopedics, The First Affiliated Hospital of Shantou University Medical College, Shantou, China, [3]Department of Radiology, The Second Affiliated Hospital of Xi'an Jiaotong University, Xi'an, China

Purpose: The objective of this study was to create and assess a Deep Learning-Based Radiomics model using a single sequence MRI that could accurately predict early Femoral Head Osteonecrosis (ONFH). This is the first time such a model was used for the diagnosis of early ONFH. Its simpler than the previously published multi-sequence MRI radiomics based method, and it implements Deep learning to improve on radiomics. It has the potential to be highly beneficial in the early stages of diagnosis and treatment planning.

Methods: MRI scans from 150 patients in total (80 healthy, 70 necrotic) were used, and split into training and testing sets in a 7:3 ratio. Handcrafted as well as deep learning features were retrieved from Tesla 2 weighted (T2W1) MRI slices. After a rigorous selection process, these features were used to construct three models: a Radiomics-based (Rad-model), a Deep Learning-based (DL-model), and a Deep Learning-based Radiomics (DLR-model). The performance of these models in predicting early ONFH was evaluated by comparing them using the receiver operating characteristic (ROC) and decision curve analysis (DCA).

Results: 1,197 handcrafted radiomics and 512 DL features were extracted then processed; after the final selection: 15 features were used for the Rad-model, 12 features for the DL-model, and only 9 features were selected for the DLR-model. The most effective algorithm that was used in all of the models was Logistic regression (LR). The Rad-model depicted good results outperforming the DL-model; AUC = 0.944 (95%CI, 0.862–1.000) and AUC = 0.930 (95%CI, 0.838–1.000) respectively. The DLR-model showed superior results to both Rad-model and the DL-model; AUC = 0.968 (95%CI, 0.909–1.000); and a sensitivity of 0.95 and specificity of 0.920. The DCA showed that DLR had a greater net clinical benefit in detecting early ONFH.

Conclusion: Using a single sequence MRI scan, our work constructed and verified a Deep Learning-Based Radiomics Model for early ONFH diagnosis. This strategy outperformed a Deep learning technique based on Resnet18 and a model based on Radiomics. This straightforward method can offer essential diagnostic data promptly and enhance early therapy strategizing for individuals with ONFH, all while utilizing just one MRI sequence and a more standardized and objective interpretation of MRI images.

KEYWORDS

radiomics, deep learning, osteonecrosis, femoral head, magnetic resonance image

1 Introduction

Osteonecrosis of the femoral head (ONFH) is a very common pathology of the hip that can lead to activity restrictions and catastrophic lifestyle changes. As demonstrated in our previous publication (Hu et al., 2024), the prevalence and the incidence of ONFH have significantly increased and may continue to increase, at least in China, for the next 2 decades. Therefore, early diagnosis and treatment planning of ONFH is crucial to preserve the femoral head and improve the prognosis. In 2019, The Association Research Circulation Osseous Staging System (ARCO) published a revised classification version for ONFH. They classified ONFH into Stage I: X-ray results are within normal range, but either magnetic resonance imaging (MRI) or scans of bones show positive findings. Stage II: The X-ray shows aberrant findings such as minor signals of increased bone density, localized bone loss, or cystic changes in the femoral head. However, there is no evidence of a fracture in the underlying bone, fracture in the necrotic area, or flattening of the femoral head. Stage III refers to a fracture that occurs in the subchondral or necrotic zone, which can be observed on X-ray or computed tomography (CT) scans. The third stage was subdivided into two categories: stage IIIA, which refers to early femoral head depression of 2 mm or less, and stage IIIB, which refers to late femoral head depression of more than 2 mm. Additionally, stage IV indicates the presence of osteoarthritis as evidenced by X-ray findings such as joint space narrowing, acetabular alterations, and/or joint destruction (Yoon et al., 2020). Our study and, according to the revised ARCO classification, classified only Stage I and II as early ONFH; afterwards we made use of their MRI scans for this investigation.

Traditional imaging modalities such as X-ray and CT (computed tomography) have restrictions when it comes to identifying early stages of osteonecrosis of the femoral head (ONFH), as there are no visible bone changes at this stage using these techniques. Therefore, the widely accepted gold standard for diagnosing early ONFH is MRI (Hu et al., 2015). However, it is user-dependent, which makes the interpretation of MRI vary between different radiologists. Thus, this necessitates the need for a robust and standard, reliable way to detect early ONFH using MRI.

Deep learning showed some promising results and an outstanding performance in detecting and classifying ONFH (Shen et al., 2023; Wang et al., 2021; Shen et al., 2024). But it comes at the cost of heavy data labeling time and preparations to train a successful model. Hence, making us look for another way that could achieve similar or better results with less work load.

Radiomics is a developing technique that entails converting regular radiological pictures into radiomics features. (Gillies et al., 2016), then recognizing important characteristics to create a distinctive framework for predicting clinical labels or outcomes. It is been widely used for the detection of various oncological changes by many researchers (Ding et al., 2021). In musculoskeletal disorders, Klontzas demonstrated that radiomics is capable of differentiating between Osteoporosis and Avascular necrosis (Klontzas et al., 2021). Wang introduced a radiomics method that utilizes MRI scans to diagnose early ONFH. His method specifically makes use of Multi-sequence MRI. In his investigation, he utilized T1 weighted with fat suppression and T2 weighted radiographs, along with coronal short time of inversion recovery pictures (Cor STIR) (Wang et al., 2024). Cheng reported that using a combined model of both Deep Learning and Radiomics; displayed an outstanding ability in diagnosing osteoporosis (Cheng et al., 2023). Liu also reported similar findings when combining radiomics with deep learning, he utilized Boruta selection to find the key features; and was able to distinguish between glioblastoma and brain metastasis (Liu et al., 2021). Another paper applied both deep learning and radiomics to differentiate between brain abscess and cystic glioma (Bo et al., 2021); they analyzed the features by spearman rank correlation test. Our aim is to be able to precisely diagnose early ONFH using a single-sequence MRI while reducing the up-front workload and the complexity of using different MRI sequences. Therefore, and for the first time; we are utilizing a Deep Learning-based Radiomics model for this purpose.

2 Materials and methods

2.1 Study participants

A total of 150 patients were included in this retrospective research: 80 healthy patients MRIs were acquired from those who came for routine checkups without any clinical or radiologic signs and symptoms of ONFH. In addition, 70 patients' radiographs were diagnosed by the radiology department of Xi'an Jiaotong University Second Hospital with early ONFH between FEB 2016 and APR 2024. The eligibility criteria for the patients were: 1) exhibited clinical symptoms such as hip pain or activity restriction. 2) only stage 1 and 2 ONFH patients were included based on ARCO classification. 3) Positive, clear MRI without artifacts. 4) No evidence of femoral head depression or fracture on normal radiograph, as that indicates a later stage of the disease. The data was acquired from the digital health record system of our hospital. The study design pipeline is illustrated in Figure 1. This retrospective investigation obtained permission from the ethics oversight Board of our hospital, with no requirement of informed consent from patients.

2.2 Region of interest segmentation

The MRI images were taken using a (Avanto, Siemens Healthineers; Erlangen, Germany) 1.5 T (tesla) scanner with the following values: Sequence type turbo spin echo (TSE); T2-weighted with fat suppressed (FS); slice thickness 4.5 mm, FOV 640*640 mm, acquisition matrix 0\320\240\, echo time 67 ms, repetition time 3000 ms, in the coronal plane; (Headfirst- Supine) position.

One skilled orthopedic surgeon (5 years of experience) manually segmented the region of interest (ROI) on each MRI slice; using ITK-SNAP 4.2.0 (https://www.itksnap.org/). Subsequently, an imaging specialist with 6 years of expertise in interpreting musculoskeletal MRI scans carefully examined all the segmented pictures to confirm their accuracy. Any disagreements were discussed or fixed till a satisfactory result was obtained. The ROI for healthy patients consisted of the femoral head and the closer part of the femoral neck. However, for patients with ONFH, the ROI was limited to the necrotic area only.

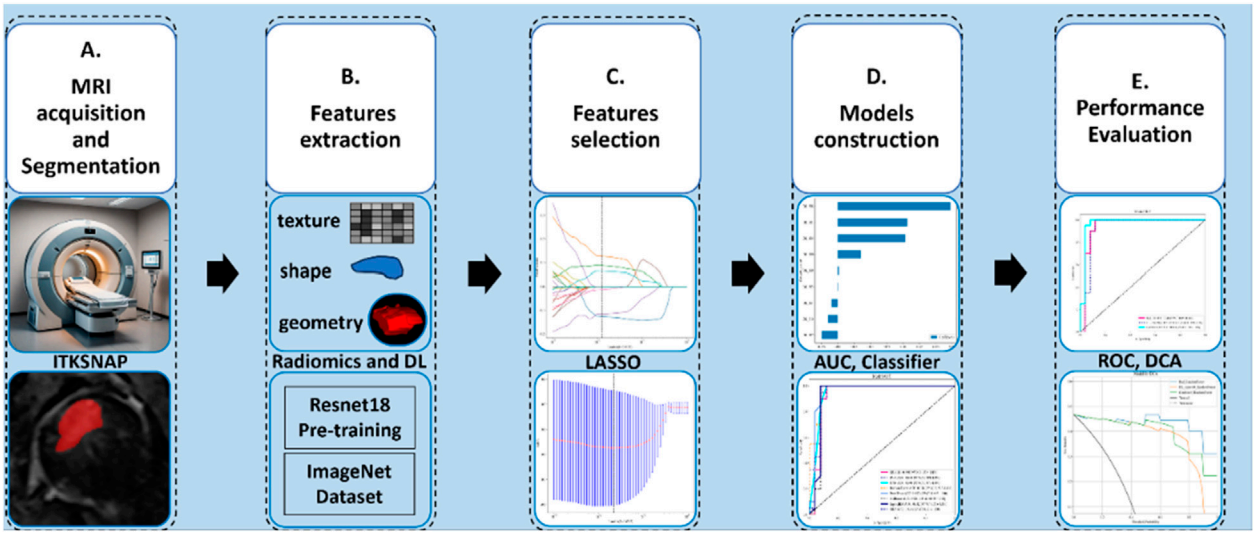

FIGURE 1
This study's design and work pipeline.

2.3 Image preprocessing

The cases were split into training and testing groups using a random distribution, with a ratio of 7:3. The entire training dataset was utilized to train the predictive model, whereas instances in the testing dataset were employed for the internal evaluation of the models' performance. In this experiment, we employed the fixed-resolution resampling method to address any variations in voxel spacing. The voxel spacing of all pictures was standardized by resampling them to a size of 1*1*1 mm. Ultimately, the data underwent z-score standardization, also known as zero-mean normalization.

2.4 Features extraction

The feature extraction in this work included conventional handcrafted radiomic features derived from the original radiographs, such as geometry, intensity, and texture. In addition to the deep learning features derived automatically from a Convolutional Neural Network (CNN) utilizing training data.

PyRadiomics was utilized to extract radiomic features. The manually generated radiomic features can be classified into three distinct categories: (a) geometric, (b) intensity, and (c) textural. The shape in three dimensions of the necrotic cells is referred to by the geometry features. The intensity features analyze the statistical spread of voxel intensities within the femoral head using first-order statistics. The texture features indicate the features that describe the patterns or the spatial distributions of intensities beyond the first order. Different approaches, including the gray-level run length matrix (GLRLM), neighborhood gray-tone difference matrix (NGTDM), gray-level size zone matrix (GLSZM), and the gray-level co-occurrence matrix (GLCM) are employed to retrieve texture features. Furthermore, to achieve high-throughput features, the nonlinear intensity of image voxels is converted using various transformations such as Square, Square Root, Logarithm, Gradient, LBP3D, and Exponential. The high Laplace filter utilizes sigma values of 1, 2, and 3. Additionally, the process of extracting first-order statistics and texture features involved the use of eight wavelet transform algorithms: HLL, HLH, HHL, HHH, LHH, LLL, LLH, and LHL. For a comprehensive explanation of all image features, please refer to the online resource at https://pyradiomics.readthedocs.io/en/latest/features.html.

The Resnet18 model was used as the convolutional neural network (CNN) architecture in this investigation to obtain deep learning features. The MRI slice with the largest necrotic area was cropped and chosen for each patient. Hence, the network was optimized by applying the stochastic gradient descent method. The Resnet18 model underwent pre-training using the ImageNet dataset (http://www.image-net.org/). Subsequently, the pre-trained model was utilized to initialize feature extraction. The model selected an average pooling layer to extract deep features and then used a principal component analysis to compress and obtain the finalized deep features. The CNN training parameters were as follows: batch size = 96, epochs = 30, and unit learning rate = 0.001.

2.5 Feature selection

Before feature selection, all the features were normalized by applying the z-score standardization method approach. Both the Radiomics and Deep Learning features underwent filtration through a series of four phases. 1) The Mann–Whitney U test was performed on all features, and only the features with a *P*-value less than 0.05 were retained. The Pearson test was employed to assess the relation between features and categories. Features having a *P*-value less than 0.05 were deemed possibly predictive. The Max-Relevance and Min-Redundancy (mRMR) technique was employed in our study, and it is been widely used in different radiomics methods before (Xie et al., 2024) to enhance the visualization of features by

TABLE 1 Basic characteristics of a total of 150 patients.

Characteristic	Healthy patients (*n* = 80)	Early ONFH patients (*n* = 70)
Age (years) Mean ± SD	40.1 ± 14.04	47.21 ± 14.91
Gender, No. (%)		
Male	30 (37.5%)	34 (48.58%)
Female	50 (62.5%)	36 (51.42%)

maximizing relevance and minimizing redundancy. Ultimately, the crucial features were evaluated by the utilization of the least absolute shrinkage and selection operators (LASSO).

2.6 Radiomics and deep learning (DL) models construction

Once the features were selected using LASSO, we utilized these features in a range of machine learning classifiers such as Random Forests (RF), K-Nearest Neighbors (KNN), Logistic Regression (LR), Support Vector Machines (SVM), XGBoost, and others. After comparing all the parameters, we chose the highest performance to build the prediction models. Here, we utilized 5-fold cross-validation to build the final Rad and DL models. To evaluate whether a combination of the features mentioned above could produce superior outcomes. Using the previously described approach, a Deep Learning-Based Radiomics (DLR) model was built by combining features from both Deep Learning and Radiomics.

2.7 Statistical analysis

The evaluation of data was conducted using the Python Statsmodels package (0.13.2 version), and a *p*-value below 0.05 was considered to have statistical significance. The predictive models' clinical importance in diagnosing early ONFH was evaluated by plotting Receiver Operating Characteristic (ROC) curves and analyzing the corresponding Area Under the Curve (AUC), diagnostic accuracy, sensitivity, specificity, positive predictive value (PPV), and negative predictive value (NPV). In addition, the model's discriminative power was assessed using calibration curves and decision curve analysis (DCA). We also utilized Delong's test to compare the ROC curve AUCs.

3 Results

3.1 Patients' characteristics

The study comprised a total of 150 patients' MRI scans, consisting of 80 healthy individuals and 70 patients with early ONFH, based on the specified criteria for inclusion. The patients were categorized into a training group of 105 individuals and a testing group of 45 individuals. Table 1 demonstrates a summary of the patient's primary attributes.

3.2 Feature extraction and selection

By utilizing a special feature analysis software integrated into Pyradiomics (http://pyradiomics.readthedocs.io), a total of 1,197 Radiomics features have been retrieved. The features included: 234 First Order, 182 (GLDM), 208 (GLRLM), 208 (GLSZM), 65 (NGTDM), 286 (GLCM), and 14 Shape features. Furthermore, Resnet18, which was pre-trained using the slice with the most necrotic tissue in its cross-section, was used to extract a total of 512 DL features.

We conducted a Mann-Whitney U test and performed feature screening on all of the chosen features. Only features with a *P*-value less than 0.05 were retained, resulting in the following numbers: The Rad model consists of 983 features. The DL model consists of 487 characteristics. The DLR model consists of 1,534 features.

The second phase involved evaluating features with high repeatability by utilizing the Pearson correlation coefficient, which measures the correlation between features. If the correlation coefficient between any two features exceeded 0.9, only one of them was kept. The Rad-model had 195 features, the DL-model had 35 features, and the DLR-model had 244 features.

In the third step, to ensure maximum feature representation, Max-Relevance and Min-Redundancy (mRMR) were used for further feature filtering. Rad-model = 30, DL-model = 30, DLR-model = 30 features.

In addition, the logistic regression model (LASSO) was employed to minimize the number of features and identify the most significant features for constructing the model. LASSO applies a shrinkage technique to all regression coefficients, pushing them toward zero and specifically setting the coefficients of unimportant features to zero based on the regulation weight Lambda (λ). In order to determine the ideal value of λ, a 10-fold cross-validation was conducted using a minimal criteria approach. The value of λ that resulted in the lowest cross-validation error was selected as the final value. The kept features with non-zero coefficients were utilized to fit a regression model and then integrated to create a Radiomics model. Afterward, we calculated a radiomics score for each patient by multiplying the retained features with their respective model coefficients and summing them up. The LASSO regression modeling was performed using the Python scikit-learn package, identifying 12 radiomics features, 14 DL features, and 9 DLR features. The figures below display the mean square errors (MSE) obtained from 10-fold validation, as well as a coefficient profile plot of the LASSO models. Each curve in the plot depicts the changing trajectory of each independent predictor. Figures 2A, C, E Explains the process of feature selection using the least absolute shrinkage and

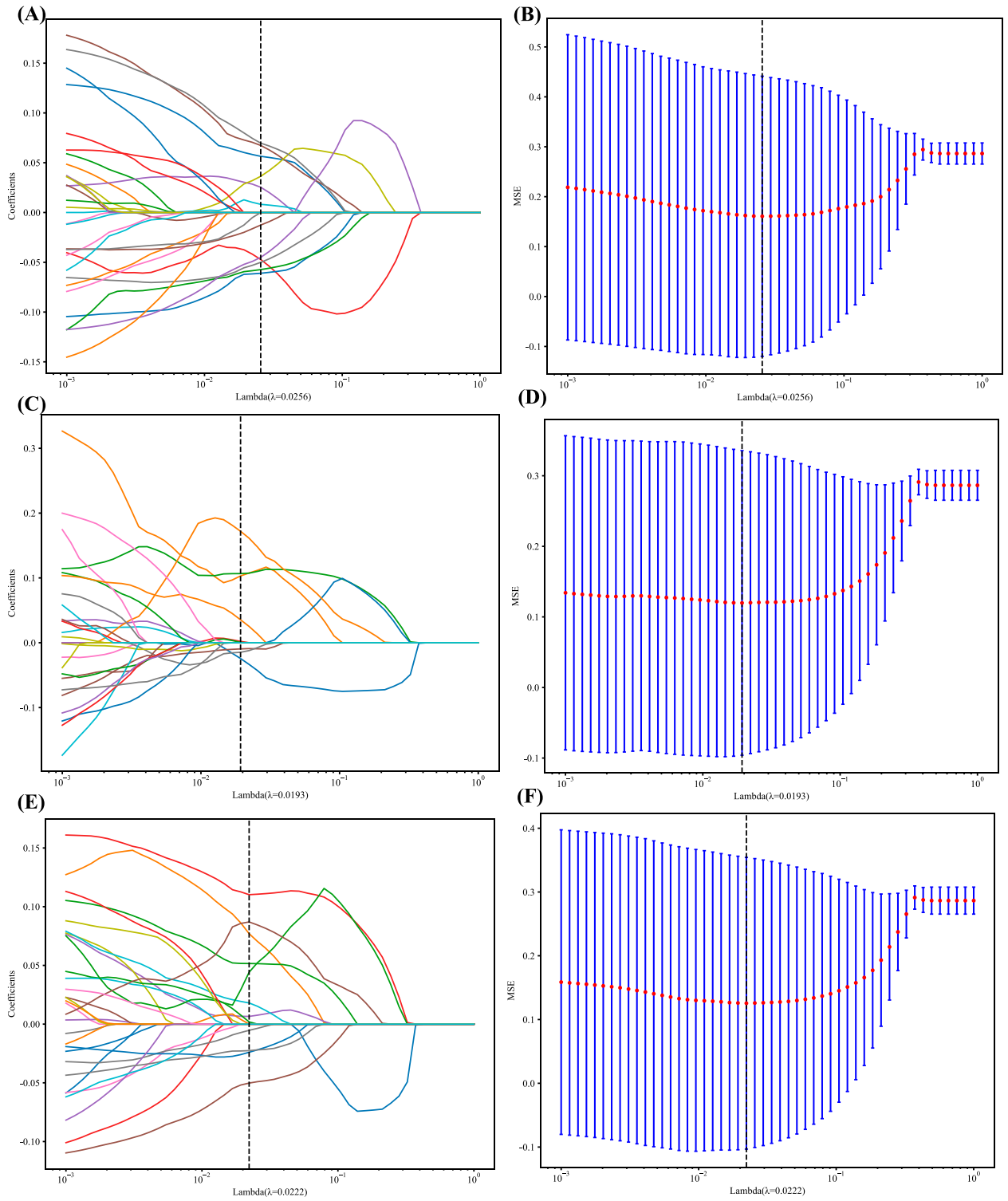

FIGURE 2
(A, C and E) LASSO Coefficients profile plot with various log(λ) is displayed; the vertical dashed line represents the selected features with nonzero coefficients chosen to the optimal lambda **(B, D and F)** MSE of 10-fold cross-validation for the most valuable features screened for the Rad, DL, and DLR models, respectively.

selection operator (LASSO) logistic regression in the Radiomics-model (A), DL-model (C), DLR-model (E). Figure 2 Shows the mean squared error (MSE) values obtained from doing 10-fold cross-validation for Radiomics-model (B), DL-model (D), DLR-model (F). The histogram of the selected features for the DLR-model is displayed in Figure 3.

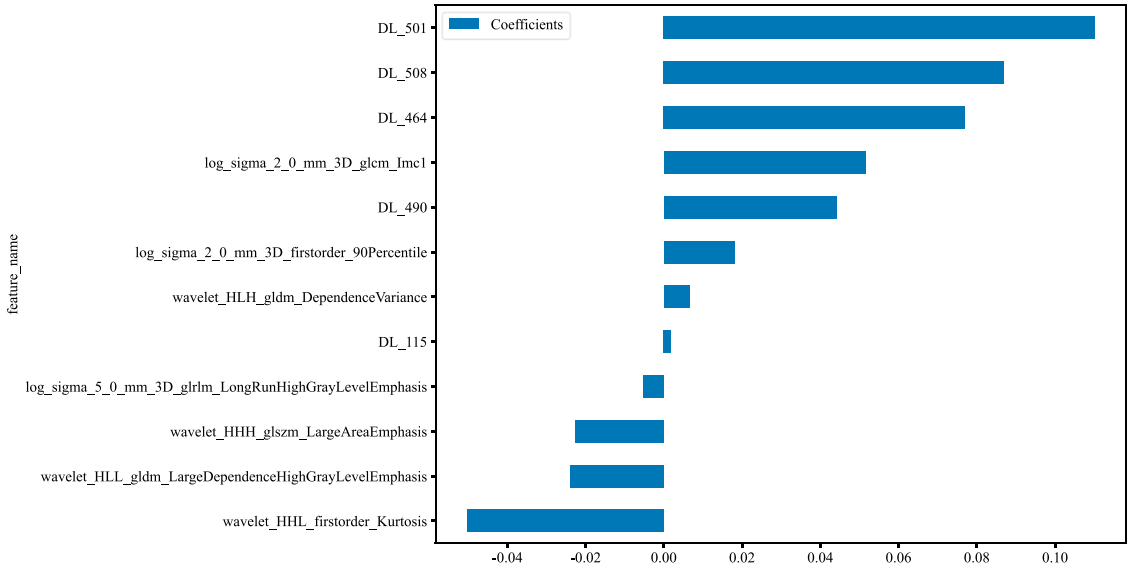

FIGURE 3
Histogram of the features selected for the DLR model, displaying each feature's contribution.

3.3 Predictive performance of radiomics, DL, and DLR models

As LR performed almost the best in each model, it was the classifier of choice for the construction of the Rad, DL, and DLR models. The Rad-model showed good results with an (AUC = 0.957) and (AUC = 0.944) in both the training and testing cohort, respectively, as shown in Figure 4 training (A), testing (B). Which outperformed the DL-model that showed (AUC = 0.935) and (AUC = 0.930) for the training and testing cohort correspondingly; illustrated in Figure 4 training (C), testing (D).

After the fusion of the selected Radiomics and DL features, the DLR-model was developed by integrating all (Kocak et al., 2024) features together in one model. The significant features selected for the DLR-model were as follows: DLR_LR_model = −0.2678082691039214 + +0.440703 * DL_464 + 0.444099 * log_sigma_2_0_mm_3D_glcm_Imc1 +0.576826 * DL_501−0.026022 * wavelet_HLH_gldm_DependenceVariance −0.590691 * wavelet_HHL_firstorder_Kurtosis +0.253499 * log_sigma_2_0_mm_3D_firstorder_90Percentile +0.377429 * DL_115−0.238724 * log_sigma_5_0_mm_3D_glrlm_LongRunHighGrayLevelEmphasis −0.656008 * wavelet_HLL_gldm_LargeDependenceHighGrayLevelEmphasis +0.089201 * DL_490 + 0.337023 * DL_508−0.160717 * wavelet_HHH_glszm_LargeAreaEmphasis. An improved performance over both the Rad-model and DL-model was found for the DLR-model; (AUC = 0.956) in the training dataset and (AUC = 0.968) in the testing dataset as displayed in Figure 4 training (E), testing (F). The diagnostic AUC, 95%CI, accuracy, sensitivity, specificity, PPV, NPV, precision, recall, and F1 of the three models are likewise demonstrated in Table 2. In addition, the calibration curves showed good agreement between all models, as shown in Figure 5. The *P*-values of the Hosmer-LemeShow test in Table 3 were 0.446, 0.051, and 0.234 for the Radiomics, DL, and DLR models, respectively. This indicates a good-fitting model, as all of the values were greater than 0.05. Delong's test has been used to compare the ROC curve AUCs of all models, as shown in Table 4. Both the CLEAR (Kocak et al., 2023) and METRICS (Kocak et al., 2024) checklists of this study were presented in Supplementary Figures S1, S2. Furthermore, the net benefit was plotted against threshold probability in Figure 6, which displays the Decision curve analysis (DCA); it indicates that the DLR-model has the highest net benefit in identifying ONFH, which means that the DLR-model was useful for predicting early ONFH from healthy patients.

4 Discussion

In this study, we presented how Radiomics and Deep learning features can be combined to make a Deep Learning-based Radiomics model that can predict early ONFH accurately; AUC = 0.968 (95%CI 0.909–1.000). This model has shown superior results to both the Rad-model (AUC = 0.944 (95%CI 0.862–1.000) and the DL-model (AUC = 0.930 (95%CI 0.838–1.000). The ROC for the three models is illustrated in Figure 7; it shows that the DLR-model has an improved and higher AUC = 0.968 than the other two models. Our study was based on a single sequence MRI (T2W1), that has been utilized to extract Radiomics and Deep learning features. Unlike Wang (Wang et al., 2024), which used a multi-sequence (T1W1, FS-T2W1, and Cor STIR) MRI-based method to predict early ONFH using Radiomics only. He claimed that in order to thoroughly diagnose early ONFH, it is imperative to take into account various MRI sequences. However, we have demonstrated that a single sequence MRI is sufficient and can achieve a high accuracy using a Deep Learning-based Radiomics method rather than multi-MRI sequences and Radiomics only. In his study, he also considered ONFH stage I, II and IIIA as early stages, which we disagree with. According to the revised ARCO classification (Yoon et al., 2020), only stage I and II are considered early stages. Stage IIIA

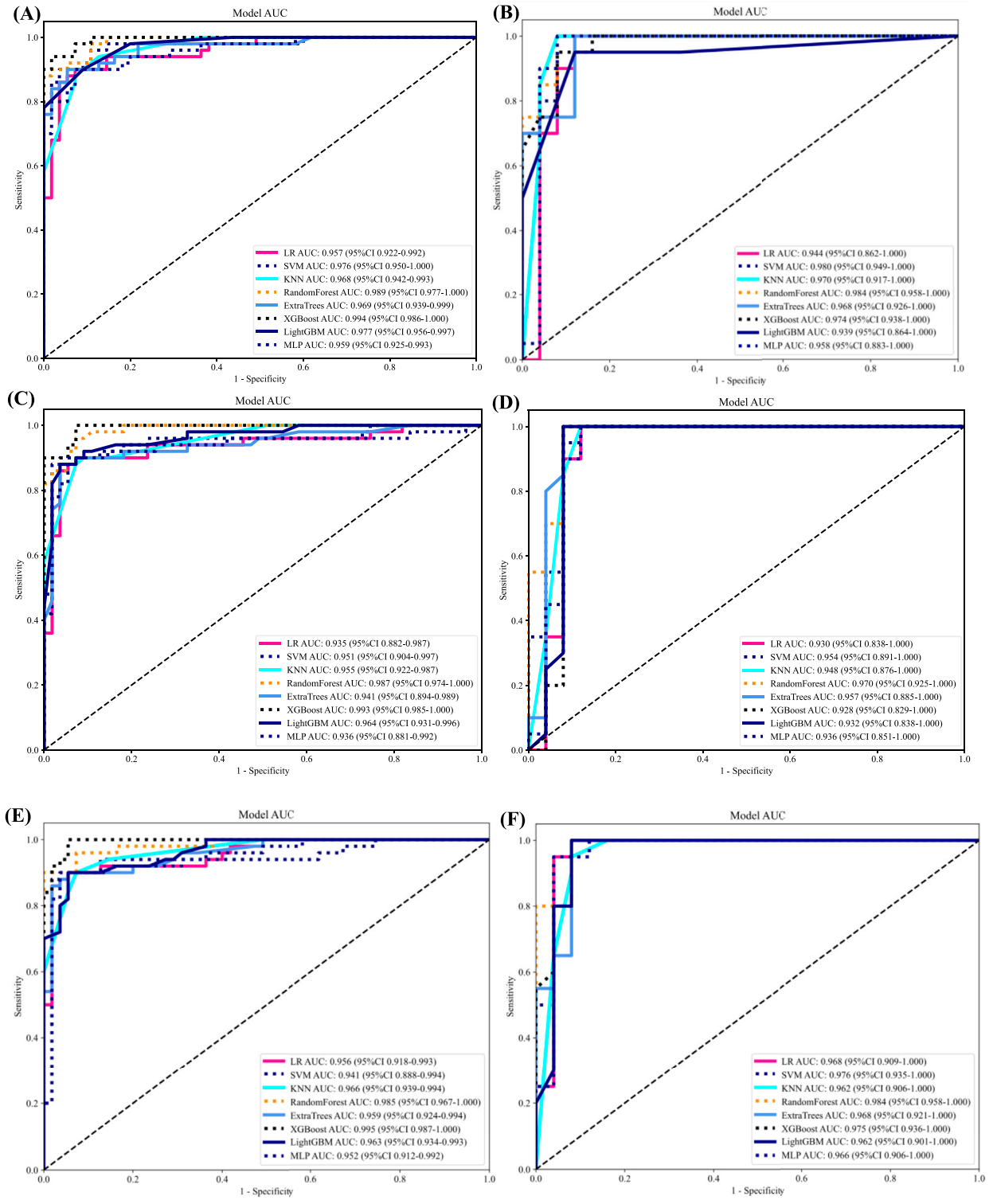

FIGURE 4
ROC curves for all models in both the training and testing groups. **(A)** ROC curves of different classifiers on Radiomic-model (training). **(B)** ROC curves of different classifiers on Radiomic-model (testing) **(C)** ROC curves of different classifiers on DL-model (training). **(D)** ROC curves of different classifiers on Radiomic-model (testing). **(E)** ROC curves of different classifiers on DLR-model (training). **(F)** ROC curves of different classifiers on DLR-model (testing).

shows microfractures or depression in the femoral head that could be visible on a more affordable CT scan and does not necessarily need an MRI that is more expensive and might not be available in many institutions. In addition, the whole purpose of using radiomics or deep learning in detecting early ONFH is accuracy and simplicity. Hence, achieving those results using a single widely used MRI

TABLE 2 All the metrics for the Radiomic, DL, and DLR models.

Model	Classifier	Acc	AUC	95% CI	Sen	Spec	PPV	NPV	PREC	Recall	F1	Cohort
Rad	LR	0.905	0.957	0.9217–0.9925	0.88	0.927	0.917	0.895	0.917	0.88	0.898	Train
Rad	LR	0.911	0.944	0.8622–1.0000	0.95	0.880	0.864	0.957	0.864	0.95	0.905	Test
DL	LR	0.905	0.935	0.8824–0.9874	0.88	0.927	0.917	0.895	0.917	0.88	0.898	Train
DL	LR	0.911	0.930	0.8377–1.0000	0.95	0.880	0.864	0.957	0.864	0.95	0.905	Test
DLR	LR	0.914	0.956	0.9183–0.9930	0.88	0.945	0.936	0.897	0.936	0.88	0.907	Train
DLR	LR	0.933	0.968	0.9085–1.0000	0.95	0.920	0.905	0.958	0.905	0.95	0.927	Test

ACC, Accuracy; AUC, area under curve; CI, confidence interval; SEN, Sensitivity; Spec, Specificity; PPV, positive predictive value; NPV, negative predictive value; PREC, Precision.

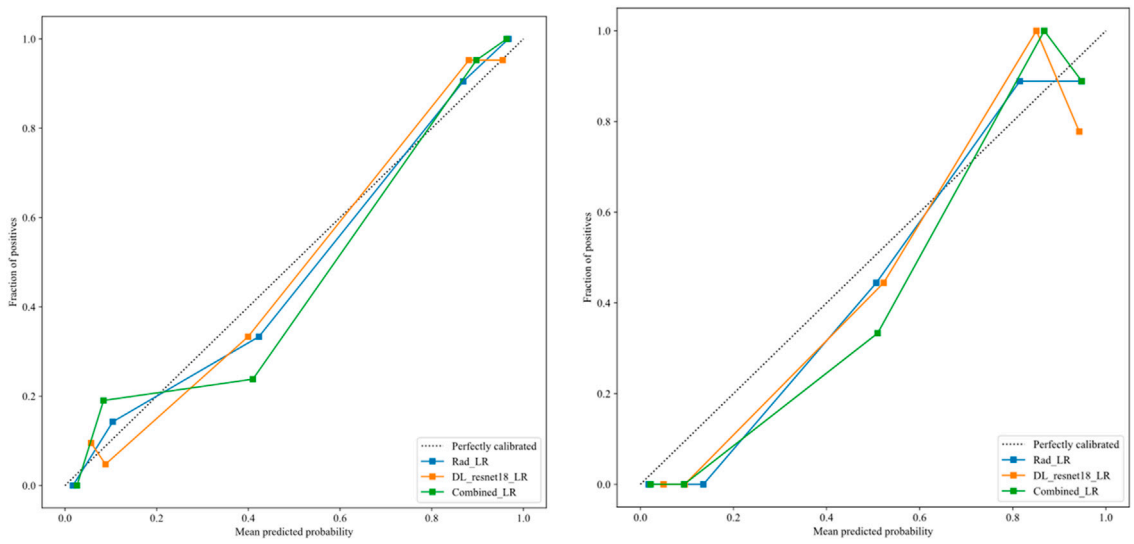

FIGURE 5
The calibration curves for DLR-model in the training group (left), and testing group (right), demonstrate a strong correlation between the average predicted probability (*x*-axis) and the proportion of positive outcomes (*y*-axis), indicating successful calibration with the perfect calibrated line.

TABLE 3 Illustrates the significance levels (*p* values) obtained by the Hosmer-Lemeshow test, which is used to assess the goodness-of-fit of models.

Model	Rad-model	DL-model	DLR-model	Cohort
P	0.952	0.549	0.380	Train
P	0.446	0.051	0.234	Test

TABLE 4 Delong test for each of the models.

Cohort	DLR Vs. Rad	DLR Vs. DL	DL Vs. Rad
Train	0.870	0.133	0.185
Test	0.594	0.145	0.800

sequence is a great advantage. Besides that, Klontazs applied radiomics and machine learning to differentiate between Osteoporosis and avascular necrosis of the hip (AVN). It was not mentioned what stages were included or excluded or following which grading system for AVN. Following feature extraction, he only used three machine learning classifiers (XGboost, CatBoost and SVM) to perform the experiment. Whereas we have used LR, SVM, KNN, RandomForest, ExtraTrees, XGBoost, LightGBM, and MLP and compared them all to obtain the best performing model. In his paper, XGboost displayed the best results achieving AUC of 93.7%. on the other hand, our top performer LR based on the combined model; showed superior results with an AUC of 0.9698. Other previous studies have used deep-learning methods to detect early ONFH (Shen et al., 2023; Wang et al., 2021; Klontzas et al., 2023; Li et al., 2023). Deep learning uses features from a single image with the largest necrotic area, whereas radiomics obtains quantitative features from multiple MRI slices at once. It can detect more features, as we proved in our study; we could extract 1,197 radiomic features, whereas deep learning features were 512 only. In addition, deep learning requires an extensive amount of labeled data for the training. Nonetheless, radiomics has an advantage over DL as it is effective even when using smaller

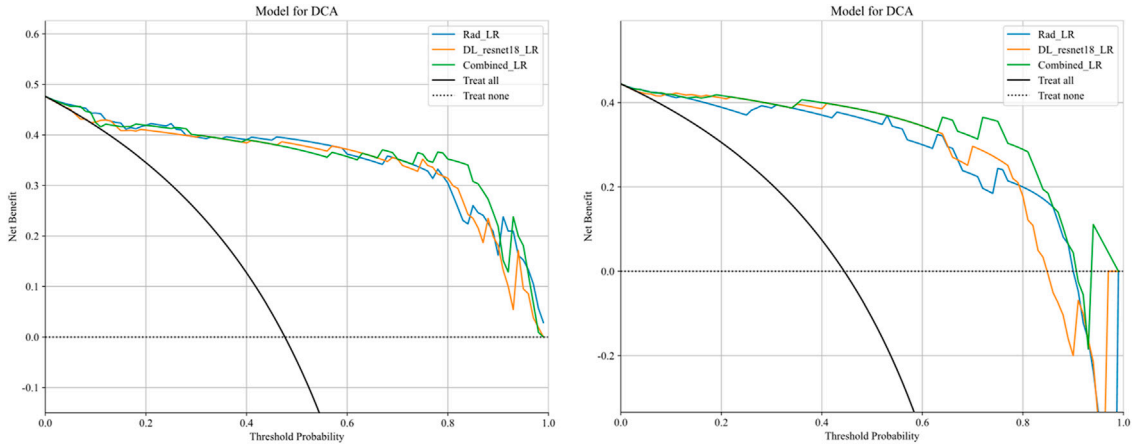

FIGURE 6
Decision curve analysis was performed on the DLR-model across the training group (left) and the testing group (right). The *y*-axis represents the net benefit, while the *x*-axis represents the threshold probability. The DLR model demonstrates a superior total beneficial effect in predicting early ONFH in healthy patients.

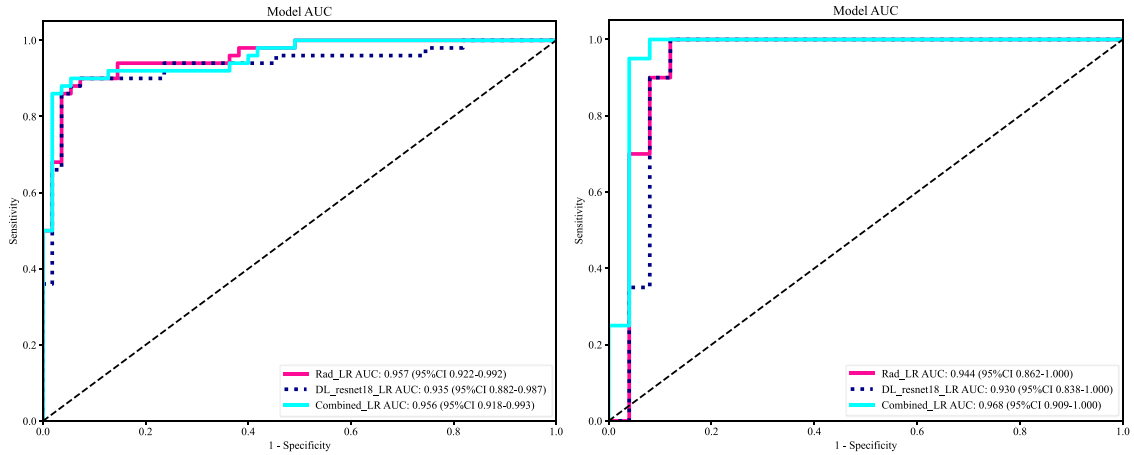

FIGURE 7
ROC of the radiomic-model, DL-model, and DLR-model, training set (left), testing set (right). That shows an improvement of AUC = 0.968 using the fused features.

datasets. We have not compared our results to a radiologist, which is a disadvantage of our study. Still, other studies did compare them, and radiomics always had either similar results to an experienced radiologist or even better ones (Klontzas et al., 2021; Wang et al., 2024). We think by using a combined Deep Learning-Based Radiomics method and a single sequence MRI only; we provided a great diagnostic method for the early detection of ONFH and a significant contribution to the research. As far as we know, we are the first to combine deep learning and radiomics for this specific task. Our study has some limitations, including 1) moderate sample size for both the training and testing. 2) We have made our study only using a single center, a multi-center study in the future could further display better analysis for using Radiomics to detect early ONFH. In conclusion, using a single sequence MRI scan, our work constructed and verified a Deep Learning-Based Radiomics Model for early ONFH diagnosis. This strategy outperformed a Deep learning technique based on Resnet18 and a model based on Radiomics. This straightforward method can offer essential diagnostic data promptly and enhance early therapy strategizing for individuals with ONFH, all while utilizing just one MRI sequence and a more standardized and objective interpretation of MRI images.

5 Conclusion

In conclusion, using a single sequence MRI scan, our work constructed and verified a Deep Learning-Based Radiomics Model for early ONFH diagnosis. This strategy outperformed a Deep learning technique based on Resnet18 and a model based on Radiomics. This straightforward method can offer essential diagnostic data promptly and enhance early therapy strategizing

for individuals with ONFH, all while utilizing just one MRI sequence and a more standardized and objective interpretation of MRI images.

Data availability statement

The original contributions presented in the study are included in the article/Supplementary Material, further inquiries can be directed to the corresponding author.

Ethics statement

The studies involving humans were approved by Ethics Committee of the Second Affiliated Hospital of Xi'an Jiaotong University, 157 Xi Wu Road, Xi'an, Shaanxi Province, 710004, P.R. China. The studies were conducted in accordance with the local legislation and institutional requirements. The ethics committee/institutional review board waived the requirement of written informed consent for participation from the participants or the participants' legal guardians/next of kin because This study is retrospective; thus, the ethics committee has exempted the patients' informed consent.

Author contributions

TA: Conceptualization, Data curation, Formal Analysis, Investigation, Methodology, Validation, Writing–original draft. AA: Data curation, Formal Analysis, Methodology, Software, Writing–review and editing. XL: Data curation, Resources, Supervision, Writing–review and editing. WW: Funding acquisition, Project administration, Supervision, Validation, Writing–review and editing.

Funding

The author(s) declare that financial support was received for the research, authorship, and/or publication of this article. 1- National Natural Science Foundation of China—General Program: Micro/nano structural biomimetic material implanted via all-range core decompression to promote *in situ* bone repair of osteonecrosis of the femoral head Project Number: 82072522 2- Shaanxi Provincial Universities Joint Medical and Engineering Cross Project: Research and Application of "Digital-Magnetic-Network" Intelligent Diagnosis and Treatment Technology for Osteoarthritis Knee Joint Replacement Surgery. Project Number: 2020GXLH.Y_001 (500,000 yuan) 3- National Administration of Traditional Chinese Medicine Clinical Cooperation and Innovation Project: Research on the Clinical Collaborative Diagnosis and Treatment Plan for Osteoarthritis of the Elderly Using a Step-by-Step Combination of Traditional Chinese and Western Medicine. Project Number: GZY-KJS2021-002 4- Shaanxi Provincial Administration of Traditional Chinese Medicine Clinical Cooperation and Innovation Project: Research on the Clinical Collaborative Diagnosis and Treatment Plan for Osteoarthritis of the Elderly Using a Step-by-Step Combination of Traditional Chinese and Western Medicine. Project Number: 2020-ZXY-003.

Conflict of interest

The authors declare that the research was conducted in the absence of any commercial or financial relationships that could be construed as a potential conflict of interest.

Publisher's note

Supplementary material

The Supplementary Material for this article can be found online at: https://www.frontiersin.org/articles/10.3389/fbioe.2024.1471692/full#supplementary-material

References

Bo, L., Zhang, Z., Jiang, Z., Yang, C., Huang, P., Chen, T., et al. (2021). Differentiation of brain abscess from cystic glioma using conventional MRI based on deep transfer learning features and hand-crafted radiomics features. *Front. Med.* 8, 748144. doi:10.3389/fmed.2021.748144

Cheng, L., Cai, F., Xu, M., Liu, P., Liao, J., and Zong, S. (2023). A diagnostic approach integrated multimodal radiomics with machine learning models based on lumbar spine CT and X-ray for osteoporosis. *J. Bone Min. Metab.* 41 (6), 877–889. doi:10.1007/s00774-023-01469-0

Ding, H., Wu, C., Liao, N., Zhan, Q., Sun, W., Huang, Y., et al. (2021). Radiomics in oncology: a 10-year bibliometric analysis. *Front. Oncol.* 11, 689802. doi:10.3389/fonc.2021.689802

Gillies, R. J., Kinahan, P. E., and Hricak, H. (2016). Radiomics: images are more than pictures, they are data. *Radiology* 278 (2), 563–577. doi:10.1148/radiol.2015151169

Hu, L. B., Huang, Z. G., Wei, H. Y., Wang, W., Ren, A., and Xu, Y. Y. (2015). Osteonecrosis of the femoral head: using CT, MRI and gross specimen to characterize the location, shape and size of the lesion. *Br. J. Radiol.* 88 (1046), 20140508. doi:10.1259/bjr.20140508

Hu, S., Li, Y., Zhang, X., Alkhatatbeh, T., and Wang, W. (2024). Increasing burden of osteoarthritis in China: trends and projections from the global burden of disease study 2019. *Med. Sci. Monit.* Available at: https://www.medscimonit.com/abstract/index/idArt/942626 (cited July 23, 2024)

Klontzas, M. E., Manikis, G. C., Nikiforaki, K., Vassalou, E. E., Spanakis, K., Stathis, I., et al. (2021). Radiomics and machine learning can differentiate transient osteoporosis from avascular necrosis of the hip. *Diagn Basel Switz.* 11 (9), 1686. doi:10.3390/diagnostics11091686

Klontzas, M. E., Vassalou, E. E., Spanakis, K., Meurer, F., Woertler, K., Zibis, A., et al. (2023). Deep learning enables the differentiation between early and late stages of hip avascular necrosis. *Eur. Radiol.* 34 (2), 1179–1186. doi:10.1007/s00330-023-10104-5

Kocak, B., Akinci D'Antonoli, T., Mercaldo, N., Alberich-Bayarri, A., Baessler, B., Ambrosini, I., et al. (2024). METhodological RadiomICs Score (METRICS): a quality scoring tool for radiomics research endorsed by EuSoMII. *Insights Imaging* 15 (1), 8. doi:10.1186/s13244-023-01572-w

Kocak, B., Baessler, B., Bakas, S., Cuocolo, R., Fedorov, A., Maier-Hein, L., et al. (2023). CheckList for EvaluAtion of Radiomics research (CLEAR): a step-by-step

reporting guideline for authors and reviewers endorsed by ESR and EuSoMII. *Insights Imaging* 14 (1), 75. doi:10.1186/s13244-023-01415-8

Li, X., Lv, S., Tong, C., Qin, Y., Liang, C., Ma, Y., et al. (2023). MsgeCNN: multiscale geometric embedded convolutional neural network for ONFH segmentation and grading. *Med. Phys.* 50 (6), 3788–3800. doi:10.1002/mp.16302

Liu, Z., Jiang, Z., Meng, L., Yang, J., Liu, Y., Zhang, Y., et al. (2021). "Handcrafted and deep learning-based radiomic models can distinguish GBM from brain metastasis,". Editor J. C. Lou, 2021, 1–10. doi:10.1155/2021/5518717*J. Oncol.*

Shen, X., He, Z., Shi, Y., Liu, T., Yang, Y., Luo, J., et al. (2024). Development and validation of an automated classification system for osteonecrosis of the femoral head using deep learning approach: a multicenter study. *J. Arthroplasty* 39 (2), 379–386.e2. doi:10.1016/j.arth.2023.08.018

Shen, X., Luo, J., Tang, X., Chen, B., Qin, Y., Zhou, Y., et al. (2023). Deep learning approach for diagnosing early osteonecrosis of the femoral head based on magnetic resonance imaging. *J. Arthroplasty* 38 (10), 2044–2050. doi:10.1016/j.arth.2022.10.003

Wang, P., Liu, X., Xu, J., Li, T., Sun, W., Li, Z., et al. (2021). Deep learning for diagnosing osteonecrosis of the femoral head based on magnetic resonance imaging. *Comput. Methods Programs Biomed.* 208, 106229. doi:10.1016/j.cmpb.2021.106229

Wang, Y., Sun, D., Zhang, J., Kong, Y., Morelli, J. N., Wen, D., et al. (2024). Multi-sequence MRI-based radiomics: an objective method to diagnose early-stage osteonecrosis of the femoral head. *Eur. J. Radiol.* 177, 111563. doi:10.1016/j.ejrad.2024.111563

Xie, J., Yang, Y., Jiang, Z., Zhang, K., Zhang, X., Lin, Y., et al. (2024). MRI radiomics-based decision support tool for a personalized classification of cervical disc degeneration: a two-center study. *Front. Physiol.* 14, 1281506. doi:10.3389/fphys.2023.1281506

Yoon, B. H., Mont, M. A., Koo, K. H., Chen, C. H., Cheng, E. Y., Cui, Q., et al. (2020). The 2019 revised version of association research circulation osseous staging system of osteonecrosis of the femoral head. *J. Arthroplasty* 35 (4), 933–940. doi:10.1016/j.arth.2019.11.029

frontiers | Frontiers in Bioengineering and Biotechnology

TYPE Original Research
PUBLISHED 25 September 2024
DOI 10.3389/fbioe.2024.1463047

OPEN ACCESS

EDITED BY
Lei Fan,
Marquette University, United States

REVIEWED BY
Xiaogang Wu,
Taiyuan University of Technology, China
Shaobai Wang,
Shanghai University of Sport, China

*CORRESPONDENCE
Jialei Chen,
jialeichen2016@163.com

†These authors have contributed equally to this work and share first authorship

RECEIVED 11 July 2024
ACCEPTED 10 September 2024
PUBLISHED 25 September 2024

CITATION
Xiao G, Zhang X, Duan A, Li J and Chen J (2024) Impact of augmentation strategy variations on the mechanical characteristics of patients with osteoporotic proximal humerus fractures with medial column instability.
Front. Bioeng. Biotechnol. 12:1463047.
doi: 10.3389/fbioe.2024.1463047

Impact of augmentation strategy variations on the mechanical characteristics of patients with osteoporotic proximal humerus fractures with medial column instability

Guoqing Xiao[1,2†], Xiang Zhang[3†], Alin Duan[3], Jian Li[1] and Jialei Chen[3*]

[1]Sports Medicine Center, Department of Orthopedic Surgery, West China Hospital, Sichuan University, Chengdu, Sichuan, China, [2]Department of Orthopedic Surgery, The Second Affiliated Hospital of Chengdu Medical College, China National Nuclear Corporation 416 Hospital, Chengdu, Sichuan, China, [3]Department of Orthopedic Surgery, West China Hospital, Sichuan University, Chengdu, Sichuan, China

Introduction: Low bone density and lack of medial support are the two most important factors affecting the stability of locking plate fixation for osteoporotic proximal humeral fractures (PHFs). This study aimed to compare the biomechanical characteristics of PHILOS locking plates combined with calcar screws, bone cement, fibular allografts, and medial locking plate support strategies for treating osteoporotic PHFs with medial column instability.

Methods: A three-part osteoporotic PHF (AO 11-B3.2) model with metaphyseal loss was generated using 40 synthetic humeri and fixed via four distinct medial support strategies. All models were mechanically tested to quantify the mechanical characteristics. Subsequently, finite element models were created for each biomechanical test case. The stress distribution and displacement of the four different fixation structures were analyzed using finite element analysis.

Results: The results demonstrated that the PHILOS locking plate combined with the medial locking plate, exhibited the greatest stability when subjected to axial, shear, and torsional loading. Furthermore, the PHILOS locking plate combined with bone cement showed structural stability similar to that of the PHILOS locking plate combined with fibular allograft but with lower stress levels on the fracture surface.

Discussion: In conclusion, the PLP-MLP fixation structure showed superior biomechanical properties under axial, shear, and torsional loading compared

Abbreviations: PHFs, proximal humeral fractures; FEA, finite element analysis; PLP-CS, PHILOS locking plate combined with medial support of calcar screws; PLP-BC, PHILOS locking plate combined with bone cement augmentation; PLP-FA, PHILOS locking plate combined with the medial support of a fibular allograft; PLP-MLP, PHILOS locking plate combined with a medial locking plate; HSRD, humeral head-shaft relative displacement; TA, torsional angle; IVMS, implant Von Misses stress; HGFVMS, humeral head-greater tuberosity fracture surface Von Misses stress; HGFS, humeral head-greater tuberosity fracture surface strain.

to other medial support methods. Repairing the medial support when treating osteoporotic PHFs with medial column instability can enhance the mechanical stability of the fracture end in both the short and long term.

KEYWORDS

proximal humeral fractures, medial support, osteoporosis, biomechanics, finite element analysis

1 Introduction

As the second most common upper limb fracture, proximal humerus fractures (PHFs) are commonly found in individuals over the age of 65 years who have osteoporosis and are associated with a high mortality rate (Koeppe et al., 2023; Sumrein et al., 2023). Severe fractures in patients are caused by a combination of advanced age, osteoporosis, and poor initial displacement (Foruria et al., 2011). There is clear evidence that restoring the anatomy of the proximal humerus and maintaining the stability of the fracture ends are particularly crucial for improving the long-term prognosis of the shoulder joint in such patients (Miltenberg et al., 2022). Compared with standard nonlocking plates, locking plates are the preferred therapy for osteoporotic and comminuted PHFs due to the advantages of higher failure loads, less damage to soft tissues, and the ability to provide multidirectional fixation (Röderer et al., 2011). Subsequent studies conducted over a long period have demonstrated that most patients with displaced and unstable PHFs who undergo treatment with locking plates experience positive results (Ockert et al., 2014). Nevertheless, despite the biomechanical benefits, the occurrence of screw penetration and varus deformity after using locking plate fixation for PHF is as high as 44%. This complication is more prevalent in patients with osteoporotic PHF who also have medial column loss or epiphyseal comminution (Kralinger et al., 2014; Barlow et al., 2020). Osteoporotic PHFs are characterized by a cancellous bone deficiency in the central part of the humeral head (Carbone et al., 2018). The screws need to be long enough to reach the subchondral bone, increasing the risk of screw penetration (Erhardt et al., 2012). Furthermore, comminution of the medial column of the humeral neck due to reduced bone mass further reduces the mechanical stability of implant fixation.

The metaphyseal bone defect caused by fracture comminution is the underlying cause of the elevated risk of postoperative complications in patients with osteoporotic PHFs (Zeng et al., 2018). Both clinical practice and biomechanical studies have demonstrated that medial support can be augmented by using a combination of calcar screws, autogenous bone grafts, allograft bone grafts, bone cement, and dual-plate fixation methods to enhance the stability of the fracture ends (Sun et al., 2020). However, no study has comprehensively analyzed the biomechanical characteristics of these different medial support methods (Zhang et al., 2014; Yang et al., 2015). This study aimed to compare the biomechanical stability of different medial support augmentation strategies for treating osteoporotic PHFs with medial column instability through biomechanical tests and finite element analysis (FEA), providing a biomechanical basis for selecting suitable medial support augmentation methods in clinical practice.

2 Materials and methods

2.1 Fracture model preparation

Forty synthetic humeri (LSH5350, Synbone, Sweden) of the same size and density were used for biomechanical studies. The distal section of all humerus models was partially resected, and the proximal 20 cm length was retained. A 5 cm section of the distal humerus was then encapsulated by embedding it in a square of polymethylmethacrylate to provide a secure fixation of the distal humerus (Cristofolini et al., 2021). Previous studies have shown that synthetic bone can represent the anatomical morphology of the humerus in most individuals and is a suitable alternative to using cadaveric bone for biomechanical studies (Lescheid et al., 2010; Grover et al., 2011). A three-part osteoporotic PHF with a metaphyseal loss model (AO 11-B3.2) was simulated using osteotomy techniques based on the osteotomy protocol developed by Tilton et al. (2020).

First, an osteotomy was performed below the humeral diaphysis, parallel to the surgical neck. Then, a second osteotomy was performed 10 mm below the first osteotomy to mimic a comminuted metaphysis fracture. The third cut was a vertical osteotomy along the greater tuberosity-intertrochanteric groove to detach the greater tuberosity from the humeral head and shaft (Supplementary Figure 1). Furthermore, to simulate the loss of medial support under severe osteoporotic conditions [21], a ø30 mm drill bit was employed to extract the internal cancellous bone of the humeral head in each synthetic specimen while retaining 40% of the cancellous bone volume to imitate an "eggshell defect" in the humeral head (Feerick et al., 2013). This fracture type represents a severe injury lacking medial cortical support and is predominant in elderly osteoporotic patients (Handoll et al., 2022).

2.2 Surgical techniques and grouping

An experienced orthopedic surgeon reconstructed all of the PHF models. Identical PHILOS locking plates (JIASKANG, China) were used in all fracture models. The plates were placed 1 cm below the greater tuberosity following the recommended guidelines (Omid et al., 2021; Zhelev et al., 2023). Locking screws of appropriate lengths (6 proximal and 3 distal) were chosen based on the measurement of the probing depth. All fracture models were randomly divided into 4 groups of 10 specimens each: 1. PHILOS locking plate combined with medial support of calcar screws (PLP-CS, Figure 1A). The PHF was stabilized using a PHILOS locking plate, and 6 locking screws were placed into the humeral head fragment, with all of the proximal screws at a distance of more than 5–8 mm from the subchondral bone to avoid screw

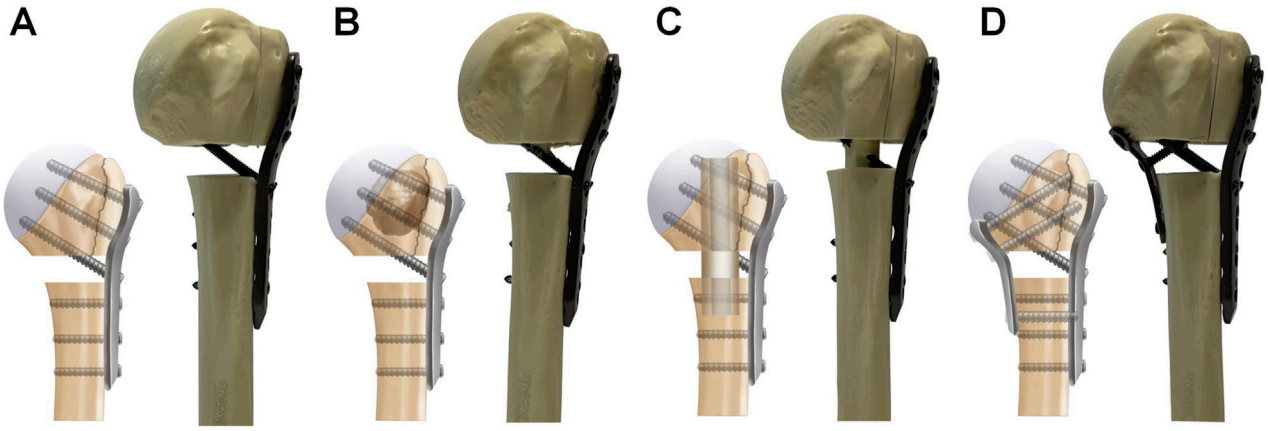

FIGURE 1
Schematic representation of the four medial support methods for fixation. **(A)** PLP-CS, PHILOS locking plate combined with the medial support of calcar screws; **(B)** PLP-BC, PHILOS locking plate combined with bone cement augmentation; **(C)** PLP-FA, PHILOS locking plate combined with the medial support of a fibular allograft; **(D)** PLP-MLP, PHILOS locking plate combined with a medial locking plate.

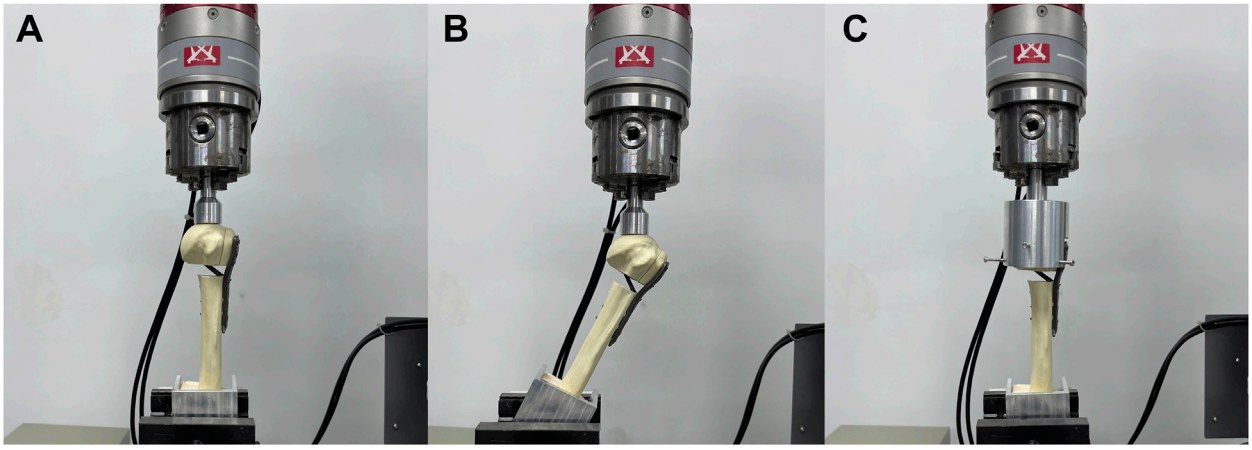

FIGURE 2
Three types of loading performed in biomechanical tests. The distal fragment of the humeral shaft was embedded in square polymethylmethacrylate for encapsulation. **(A)** Axial force, **(B)** shear force and **(C)** torsional forces were applied to the models.

penetration [24]. Three locking screws were used to fix the humeral shaft fragment. 2. PHILOS locking plate combined with bone cement augmentation (PLP-BC, Figure 1B). Based on the PLP-CS fixation construct, 8 mL of medium-viscosity bone cement (PALACOS®, Germany) was manually placed through the lateral window of the fracture into the humeral head fracture fragment to fill the humeral head (Zhelev et al., 2023). 3. PHILOS locking plate combined with the medial support of a fibular allograft (PLP-FA, Figure 1C). Based on the PLP-CS fixation structure, a 60 mm allograft fibula was implanted into the fracture model and secured using locking screws, with the upper part of the fibula fixed below the cortical apex of the humeral head. The allograft fibula was positioned close to the medial cortical bone to improve the medial support (Cui et al., 2019). 4. PHILOS locking plate combined with a medial locking plate (PLP-MLP, Figure 1D). Based on the PLP-CS fixation structure, the medial side was fixed with a three-hole locking plate (JIASKANG, China) to provide medial support.

2.3 Biomechanical tests

The fracture models were fixed using a customized XY table and subjected to biomechanical tests on an INSTRON E3000 series universal mechanical testing machine (INSTRON Corporation, United States). Axial, shear, and torsional loads were applied to each group of fixed models to test their structural stiffness (Figure 2) (Zhang et al., 2014). For axial stiffness, a vertical load (preload = 50 N) was applied to the tip of the humeral head at a rate of 5 mm/min until the humeral head fragment was displaced vertically up to 0.5 mm. In the shear loading test, the model's angle was adjusted by 20° following the axial condition to simulate the shear force on the

TABLE 1 Element information consisting of finite element models.

Finite element models	PLP-CS	PLP-BC	PLP-FA	PLP-MLP
Number of nodes	390,793	406,581	396,361	396,964
Number of elements	254,486	264,987	257,087	256,337
Size of element, mm				
Mean	0.79	0.78	0.79	0.78
Maximum	1.00	1.00	1.00	0.99
Minimum	1.55×10^{-2}	1.54×10^{-2}	1.54×10^{-2}	0.92×10^{-2}

fractured end when the patient was standing with abductor weight, except that the maximum displacement was set at 1 mm. To test the torsional stiffness, a displacement controller was used to apply torque at a rate of 12°/min (maximum angle = 5°, pretorque = 0 N m) to simulate the rotating movement of the humeral head in the glenoid. The maximum load and the torque were recorded for each group, and the structural stiffness was determined by fitting the slope. All fracture fixation model deformations were within the elastic range of the line to prevent bone and fixation structure damage.

All models that underwent stiffness tests were subjected to cyclic shear loading tests to assess the long-term stability of the fracture ends fixed with different medial support methods during postoperative shoulder functional exercises. According to previous studies, a set of 1,000 cycles was programmed into the software Instron Wave Matrix2 (INSTRON Corporation, United States), and cyclic shear loads varying from 50 N to 623 N were applied to the humeral head at 1 Hz (Burke et al., 2014). Cycle–displacement curves were recorded. At the end of the cyclic shear test, a shear load (preload = 50 N) was applied to each fracture model at a rate of 5 mm/min for the destructive experiment until fixation failure occurred. Fixation failure was defined as plate or screw bending, screw cutting, the appearance of new fracture lines, a relative displacement of the fracture end greater than 5 mm (Neer et al., 1970) considered ≥5 mm displacement to be an indication for surgical treatment of PHFs, and a sudden change in the load-displacement curve.

2.4 Finite element modelling

The overall FEA workflow is illustrated in Supplementary Figure 2. CT images of the synthetic humerus (LSH5350, Synbone, Sweden) were imported into Mimics 21.0 (The Materialise Group, Belgium) for 3D modelling of the proximal humerus. The 3D model of the proximal humerus in the STL format was imported into Geomagic Wrap 2021 (Geomagic, United States) for further surface processing. Subsequently, Boolean operations were employed in SolidWorks 2021 (SolidWorks, United States) to segment the proximal humerus cortical and cancellous bone models. A three-part osteoporotic PHF with medial column deficiency (AO 11-B3.2) was constructed according to the osteotomy protocol used in the biomechanical experiments. Three-dimensional models of the PHILOS locking plate, locking screws, bone cement, fibular allograft, and three-hole locking plate were constructed in SolidWorks 2021 software according to the dimensional information provided by the manufacturer. The internal fixation models were assembled and grouped with the fracture models based on the biomechanical experimental fixation scheme.

Meshing was performed using a tetrahedral ten-node cell (C3D10) with a size of 1 mm based on the mesh planning element size in previous study (Yang et al., 2015). The numbers of nodes and elements for each group of models are shown in Table 1. Subsequently, four distinct medial support augmentation models were imported into ANSYS Workbench 2020 R2 (Ansys, Canonsburg, PA) for FEA. All models were assumed to be homogeneous, isotropic linear elastic materials. Young's modulus and Poisson's ratio of each model are shown in Table 2 (Kennedy et al., 2013a; Yang et al., 2015; Chen et al., 2020). Friction contact was defined as friction between the fracture ends and the plate-bone interface, with friction coefficients of 0.46 and 0.3, respectively. The interfaces between the screw-plate, screw-bone, and screw-cement interfaces were defined as bounded contacts.

2.5 Boundary conditions and load settings

The freedom of the distal humerus was restricted to 0. Axial, shear, and rotational load applications were applied according to the biomechanical experimental protocol (Figure 3). To simulate axial loads, a load of 500 N was applied vertically in the coronal and sagittal planes (He et al., 2017). The model was made to abduct by 20° to simulate the shear force on the proximal humerus when the patient was standing up from a chair or weight-bearing on crutches. A torque of 3.5 N m was applied around the humeral shaft to simulate torsional loading (Chen et al., 2020). We recorded and analyzed the maximum humeral head-shaft relative displacement (HSRD), maximum torsional angle (TA) (Figure 4), maximum implant Von Misses stress (IVMS), maximum humeral head-greater tuberosity fracture surface Von Misses stress (HGFVMS), maximum head-greater tuberosity fracture surface strain (HGFS), and internal fixation stiffness [stiffness (N/mm) = load (N)/displacement (mm)] under different loading conditions to assess the biomechanical stability of PHF fixation augmented by different medial support methods.

2.6 Statistical analysis

Statistical analysis was performed with GraphPad Prism 9. The Shapiro-Wilk test was used to test the normality of the experimental data. If the data of each group conformed to a normal distribution,

10.3389/fbioe.2024.1463047

TABLE 2 Material properties of models in finite element analysis.

Material types	Young's modulus, MPa	Poisson's ratio
Osteoporotic cortical bone	8,844	0.3
Osteoporotic cancellous bone	660	0.3
Titanium alloy (Ti-6AL-7Nb)	13,400	0.3
Fibular allograft	1,520	0.3
Bone cement	110,000	0.3

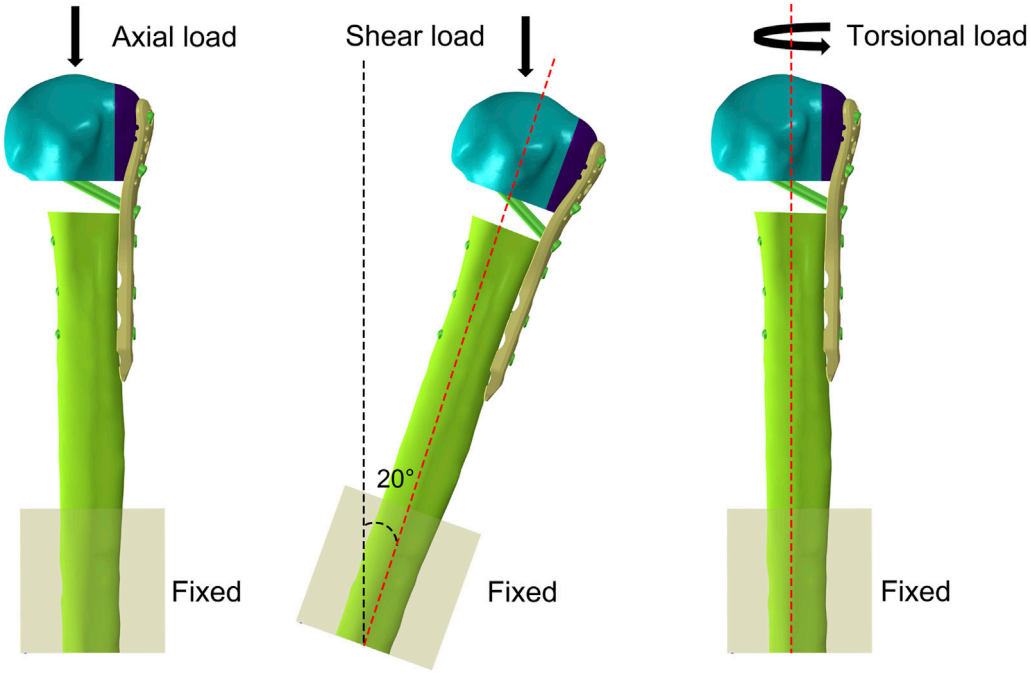

FIGURE 3
Boundary condition settings in FEA. The freedom of the distal humerus was restricted to 0. Axial, shear, and torsional load were applied to the models.

the ANOVA was used to compare the groups, and the LSD-test was used for two-way comparisons between groups; if not, the Kruskal-wallis test was used to compare the groups, and Bonferroni's correction was used for two-way comparisons between groups. The level of significance was set to 0.05.

3 Results

3.1 Stiffness

The stiffness values obtained from the biomechanical tests and FEA were within ±1 standard deviation, validating the reliability of the finite element modelling and demonstrating that the modelling approach is suitable for further research. Biomechanical experiments (Figures 5A1–C1; Supplementary Table 1). The axial, shear, and torsional stiffnesses of the PLP-CS group were the smallest among all of the groups, at 295 N/mm ± 41 N/mm, 198 N/mm ± 15 N/mm, and 0.68 N m/° ± 0.03 N m/°, respectively, while those of the PLP-MLP group were the largest, which were 2.7, 2.3 and 1.4 times greater than those of the PLP-CS group ($p < 0.05$). The axial stiffness of the PLP-BC group was greater than that of the PLP-FA group ($p < 0.05$), while the shear stiffness results were the opposite ($p < 0.05$), and the torsional stiffness was close to that of both groups ($p > 0.05$). The FEA results showed the same trend (Figures 5A2–C2; Supplementary Table 1). The axial, shear, and torsional stiffnesses of the PLP-CS group were the smallest among all of the groups, with values of 334 N/mm, 200 N/mm, and 0.54 N m/°, respectively. In contrast, the PLP-MLP group had the highest stiffness. The axial stiffness of the PLP-BC group (562 N/mm) was greater than that of the PLP-FA group (505 N/mm), with opposite results for shear and torsional stiffness.

3.2 Cyclic loading test

After 1,000 cycles of cyclic shear loading, the HSRD in the PLP-CS group (1.49 ± 0.17 mm) was approximately twice as high as that in the PLP-MLP group; the HSRD in the PLP-FA group (1.16 ± 0.19 mm) was greater than that in the PLP-BC group (1.03 ± 0.07). Interestingly, the HSRD was lower in the PLP-FA group than in the PLP-BC group before the 400th loading cycle, whereas the opposite

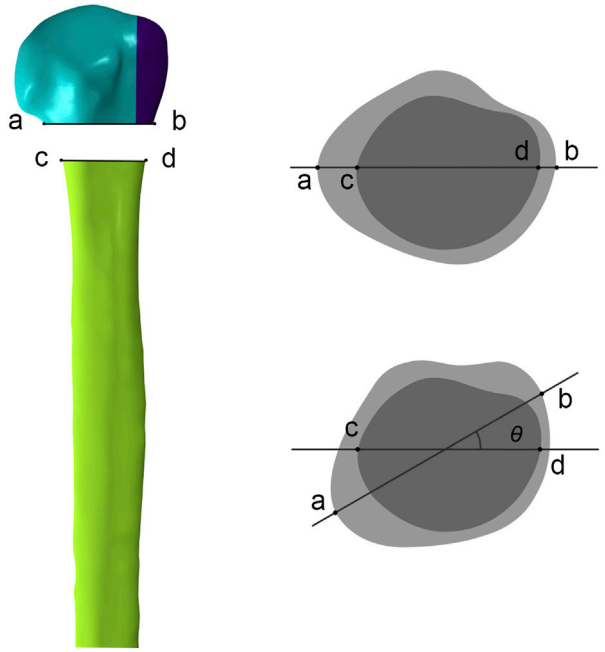

FIGURE 4
Measurement of the torsional angle (θ) of the humeral head relative to the humeral shaft after torsional loading tests. In anterior-posterior view, **ab** represents the line connecting the fractured ends of the humeral head on the front view, and **cd** represents the line connecting the fractured ends of the humeral shaft. In top view, the torsional angle (θ) is obtained by measuring the angle between **ab** and **cd** after applying the torsional load.

result was shown after the 400th cycle (Figure 6; Supplementary Table 2).

3.3 Destructive test

The results of the destructive test (Figure 7; Supplementary Table 3) showed that the PLP-MLP fixation structure exhibited the highest failure load (2.43 kN ± 0.14 kN), approximately twice as high as that of the PLP-CS fixation structure. The PLP-BC fixation structure (2.04 kN ± 0.11 kN) had a greater failure load than did the PLP-FA (1.57 kN ± 0.07 kN).

3.4 FEA

Under axial and shear loading, the HSRD was significantly greater for the PLP-CS group (2.19 mm, 1.06 mm) than for the PLP-MLP group (0.27 mm, 0.42 mm). Although the HSRD of the PLP-FA group was greater than that of the PLP-BC group under axial loading, the opposite results were obtained under shear loading (Figures 8A1, A2; Supplementary Table 4). Under a torque of 3.5 Nm, the torsion angle of the PLP-CS group was the largest at 6.68°, and the TAs of the PLP-BC, PLP-FA, and PLP-MLP fixed structures were similar (Figure 8A3; Supplementary Table 4).

The nephograms and IVMS results are shown in (Figures 8B1–B3, Figures 9A1–D1, Supplementary Figures 3, 4). The IVMS of the PLP-CS group under axial, shear, and torsional loads was the largest among all of the groups, at 994 MPa, 881 MPa, and 521 MPa, respectively; that of the PLP-MLP group was the smallest; and that of the PLP-BC group was larger than that of the PLP-FA group. According to the VMS distribution nephograms, the maximum VMS in the PLP-CS and PLP-BC groups was mainly concentrated at the locking plate in the bone defect region, suggesting a greater risk of failure. In contrast, the stress distribution in the PLP-FA group tended to be relatively dispersed, with the fibular allografts sharing part of the stress. The IVMS of the PHILOS locking plate in the PLP-MLP group was significantly lower than that in the other groups, with the medial locking plate accepting most of the stress. The HGFVMS results showed a similar trend (Figures 8C1–C3; Figures 9A2–D2). The HGFVMS under axial, shear, and torsional loads were the largest in the PLP-CS group and the smallest in the PLP-MLP group. In addition, the HGFVMS in the PLP-BC group was lower than that in the PLP-FA group. The PLP-BC group exhibited the smallest HGFS under different loads, and the rest of the groups had increased HGFS, which was mainly concentrated at the bone-screw interface (Figures 8D1–D3; Figures 9A3–D3).

4 Discussion

Fractures in elderly osteoporotic patients are usually comminuted, and the medial column fragments of the proximal humerus are prone to be missed after fracture reduction is achieved (Klahs et al., 2024). Due to the lack of medial support, the postoperative complication rates of fixation failure, bone nonunion, malunion, and humeral head necrosis remain high in these patients (Laux et al., 2017). Choosing an appropriate medial support method to reconstruct the medial column can effectively reduce the risk of postoperative complications and improve the long-term prognosis of these patients. This study systematically investigated the biomechanical characteristics of PLP-CS, PLP-BC, PLP-FA, and PLP-MLP fixation structures in treating osteoporotic PHFs with medial column instability. We found that although the PLP-CS fixation structure stabilized and fixed the PHF under axial, shear, and torsional loading, the stability of fracture end fixation was significantly enhanced with the introduction of bone cement, fibular allografts, and medial locking plates, reducing the risk of fixation failure.

The biomechanical stability of the fracture end is a crucial determinant of the healing process for PHF, and deterioration of the biomechanical environment will lead to malunion of the proximal humerus or even nonunion of the fracture (Wright et al., 2021). Although the use of inferomedial calcar screws increases the axial and shear stiffness of PHF fixation, the overall biomechanical stability is not improved (Bai et al., 2014). Therefore, direct medial support may be a more effective strategy. The medial locking plate in the PLP-MLP fixation structure provides direct medial support, and its axial, shear, and torsional stiffnesses are the highest among all of the fixation structures, which agrees with the results of a previous study (Chen et al., 2020). In a retrospective study, Seok and Park (2023) reported that dual-plate fixation for osteoporotic PHF patients with medial column instability and varus deformity had superior imaging and clinical outcomes to single plate

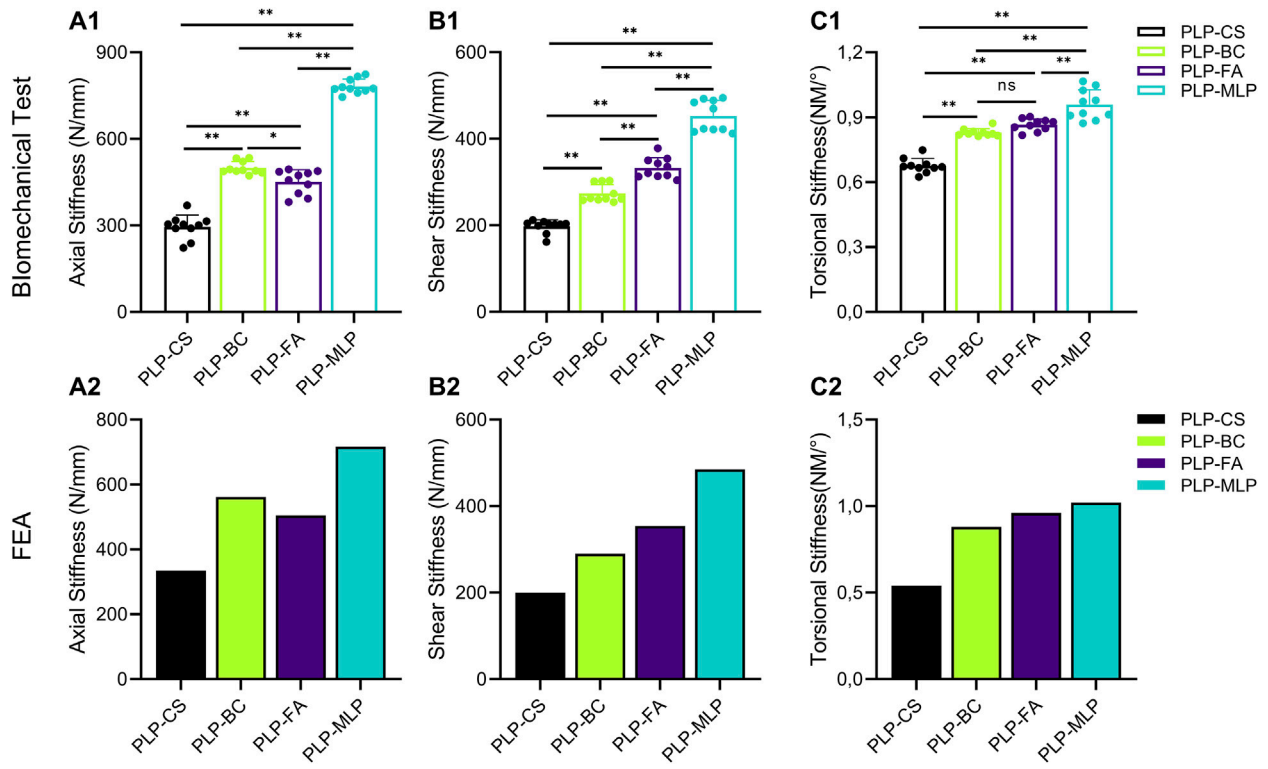

FIGURE 5
The Structural stiffness of different medial supporting methods measured by biomechanical tests and FEA. **(A1,A2)** axial stiffness; **(B1,B2)** shear stiffness; **(C1,C2)** torsional stiffness (*$p < 0.05$).

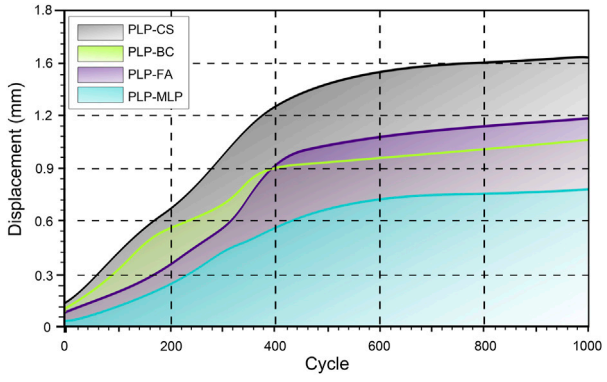

FIGURE 6
Humeral head and shaft relative displacement analysis of the humeral head and shaft during cyclic tests. The shaded region indicates the range of the displacement for each group. The X-axis starts from 20 cycles.

fixation. However, introducing medial locking plates in clinical practice may increase the risk of iatrogenic neurovascular injury and subsequent humeral head necrosis. In addition, the PLP-BC fixation structure had greater axial stiffness than the PLP-FA, while the shear stiffness showed the opposite result. In osteoporotic patients, the screw-bone interface is prone to loosening and failure due to reduced bone mineral density (Choma et al., 2011). Bone cement augmentation increased the screw–bone contact area in the area of the bone defect, resulting in a more uniform screw stress distribution and greater resistance to extraction. Furthermore, the bone cement contributed to the bonding of the humeral head-greater tuberosity fracture surface, hence improving its axial rigidity. In contrast, the PLP-FA fixation structure provided direct support and increased the screw-bone contact area in the humeral head fragment. The shear stiffness of the PLP-FA was greater than that of the PLP-BC fixation structure.

Reinforcing the medial support of the proximal humerus can effectively increase the mechanical properties of locking plate fixation for PHFs (Jabran et al., 2018). The cyclic shear loading test results showed that the HSRD significantly decreased after the introduction of different medial support methods, and this change became more pronounced with increasing loading cycles. The medial support structure can share a portion of the load transmitted through the upper and lower sections of the fracture for the PHILOS locking plate, thus reducing the stress concentration in the locking plate and reducing the risk of fixation failure. He et al. (2017) compared the biomechanical properties of four different fixation modalities for the treatment of PHF with medial column instability using FEA and revealed that direct medial support is an effective method for the treatment of PHF with medial column instability. In addition, this study revealed that the use of bone cement increased the overall stiffness of PHF fixation for medial column instability to achieve damage resistance comparable to that of fibular allograft implantation. Interestingly, this study also revealed that PLP-BC fixation was structurally less stable than PLP-FA before 400 loading cycles. However, during the

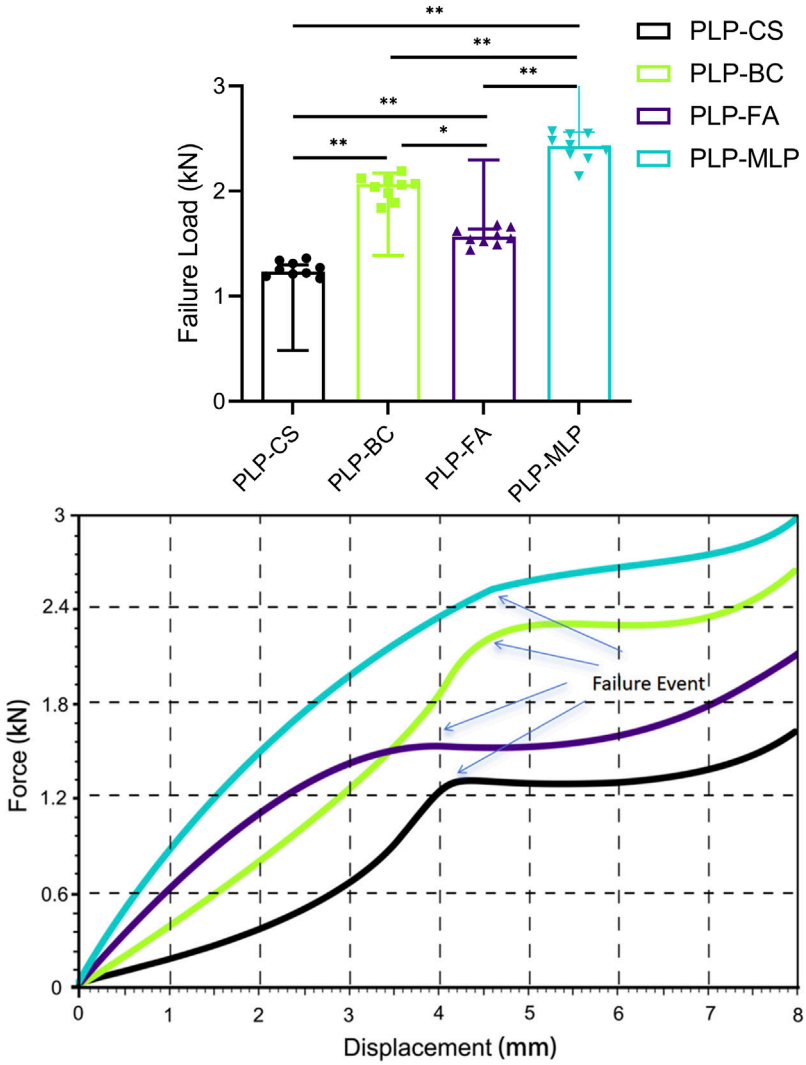

FIGURE 7
Typical displacement-force diagrams for each group throughout the mechanical destructive test. Although the failure criterion was a migration of 5 mm, the test was extended as far as 8 mm to ensure that failure became evident in all specimens (*$p < 0.05$).

subsequent cyclic cycles, the results were reversed. We hypothesized that during the start of loading period, PLP-FA exhibited greater shear stability than did PLP-BC because of the direct support provided by the fibular allograft. With cyclic loading, the stability of the screw support on the humeral head-greater tuberosity fracture surface decreased in the PLP-FA fixation structure. However, the PLP-BC structure significantly improved the durability of the fixation structure due to a more even distribution of the load per locking screw by the bone cement, which was more pronounced in conditions of osteoporosis-induced bone loss (Kuang et al., 2018). Nevertheless, the risk of cement leakage and the thermal apoptotic necrosis of chondrocytes caused by the exothermic reaction should also be considered when using bone cement (Blazejak et al., 2013).

Destruction experiments effectively measure the secondary stability of different medial bracing schemes (Brunner et al., 2012). The results of the destruction experiment showed that the PLP-MLP fixation structure increased the stability of the head–neck fracture ends due to the support of the medial locking plate, and the humeral head-greater tuberosity fracture surfaces were relatively displaced due to the reduction in the screw–bone contact area and stability, leading to fixation failure. In osteoporotic patients, the central cavity of the humerus lacks cancellous bone, and bone cement matches the mechanical properties of cancellous bone and is an effective filling material (Kennedy et al., 2013b). These findings suggest that from a biomechanical point of view, the PLP-BC fixation structure enhances medial column stability and reduces the risk of fracture end displacement, contributing to improved functional outcomes and a reduced risk of reoperation when treating PHFs with medial column instability. In addition, compared with those of the PLP-BC fixation structure, the FE and biomechanical models of PLP-FA and PLP-MLP are more difficult to construct, implying that these two fixation structures may be more challenging in clinical practice. The FEA stress results further explain the mechanical mechanisms of the biomechanical tests. The stress distribution in the nephograms showed that the stresses in the PLP-MLP and PLP-BC fixation structures were mainly concentrated

10.3389/fbioe.2024.1463047

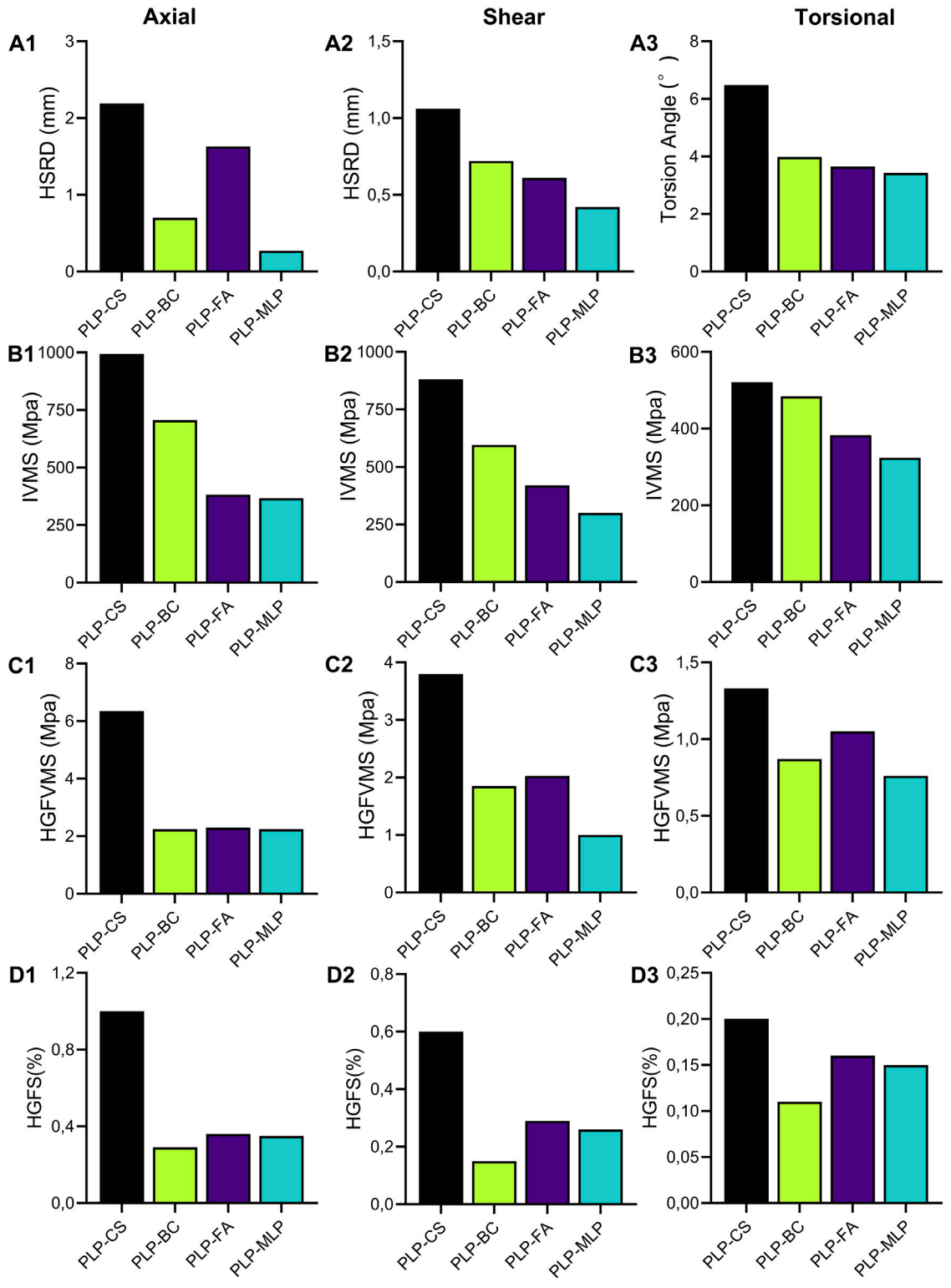

FIGURE 8
The maximum humeral head-shaft relative displacement (HSRD) **(A1,A2)**, maximum torsional angle **(A3)**, maximum implant Von Misses stress (IVMS) **(B1–B3)**, maximum humeral head-greater tuberosity fracture surface Von Misses stress (HGFVMS) **(C1–C3)**, and maximum head-greater tuberosity fracture surface strain (HGFS) **(D1–D3)** for each group under axial, shear, and torsional loading.

on the locking plate at the bone defect, which was the main site of fixation failure in the destructive tests. In the PLP-FA fixation structure, the fibular allograft shares part of the stresses of the PHILOS locking plate. However, in the PLP-MLP fixation structure, the medial locking plate shares some of the stress, reducing the risk of fixation failure. With the introduction of enhanced medial

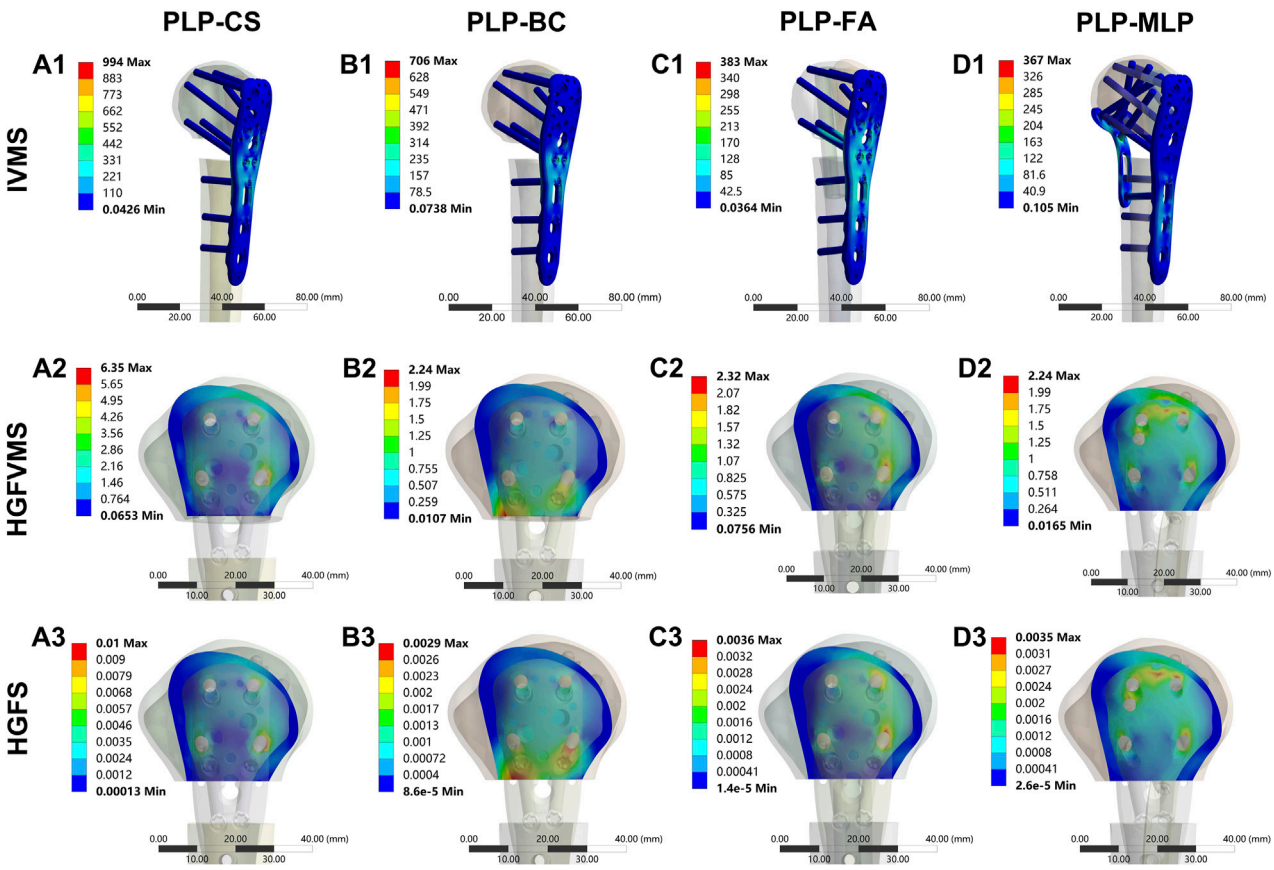

FIGURE 9
Distribution of IVMS **(A1–D1)**, HGFVMS **(A2–D2)**, and HGFS **(A3–D3)** for PHFs fixed by different medial support methods under axial loading.

support methods, adequate short-term fixation stability is given to the fracture end, contributing to the early healing of the fracture (Jang and Kim, 2021). The HGFVMS of the PLP-BC fixation structure is concentrated on the bone surface close to the defective area of the proximal humerus. In contrast, the HGFVMS of the PLP-CS, PLP-FA, and PLP-MLP fixation structures are mainly concentrated at the bone–screw interface, and the humeral head-greater tuberosity fracture surface tended toward greater separation motion. Although moderate compressive stress on the fracture surface contributes to fracture healing, shear and separation motion at the fracture site is detrimental to scab formation and even increases the risk of postoperative complications (Claes and Meyers, 2020). The HGFS results provide further evidence that the bonding effect of bone cement is effective in decreasing the fracture surface strain and decreasing the risk of trabecular disruption due to bone-screw interface displacements.

There are several limitations in this study. First, the model used in the biomechanical test and FEA was a synthetic humerus, which is somewhat different from cadaveric bone in terms of material properties and anatomical structure. Overall, synthetic bone models could substantially reduce costs and improve the accuracy of simulation results. Second, it is important to note that the complexity of PHF is related not only to the fracture itself but also to the influence of soft tissues such as muscles and ligaments. Despite these limitations, the present study on the biomechanical characterization of different medial support methods to enhance the stability of PHFs can provide a mechanistic reference for clinical decision-making.

5 Conclusion

In conclusion, when treating osteoporotic PHFs with medial column instability, restoring the medial support helps to increase the short- and long-term stability of the fracture end. The PLP-MLP fixation structure showed superior biomechanical properties under axial, shear, and torsional loading compared to other medial support methods. In addition, the PLP-BC fixation structure provided adequate stability for PHFs with less damage and easier implementation than PLP-FA, which could be an option for trauma surgeons to treat osteoporotic PHFs with medial column instability.

Data availability statement

The original contributions presented in the study are included in the article/Supplementary Material, further inquiries can be directed to the corresponding author.

Author contributions

GX: Conceptualization, Investigation, Methodology, Software, Writing–original draft, Writing–review and editing. XZ: Data curation, Formal Analysis, Methodology, Writing–original draft, Writing–review and editing. AD: Conceptualization, Methodology, Validation, Writing–original draft. JL: Data curation, Formal Analysis, Methodology, Project administration, Writing–original draft, Writing–review and editing. JC: Conceptualization, Methodology, Project administration, Supervision, Validation, Visualization, Writing–original draft.

Funding

The author(s) declare that no financial support was received for the research, authorship, and/or publication of this article.

Acknowledgments

We would like to thank Mr. Tao Zhu for his assistance in drawing the diagram.

Conflict of interest

The authors declare that the research was conducted in the absence of any commercial or financial relationships that could be construed as a potential conflict of interest.

Publisher's note

Supplementary material

The Supplementary Material for this article can be found online at: https://www.frontiersin.org/articles/10.3389/fbioe.2024.1463047/full#supplementary-material

References

Bai, L., Fu, Z., An, S., Zhang, P., Zhang, D., and Jiang, B. (2014). Effect of calcar screw use in surgical neck fractures of the proximal humerus with unstable medial support: a biomechanical study. *J. Orthop. Trauma* 28 (8), 452–457. doi:10.1097/bot.0000000000000057

Barlow, J. D., Logli, A. L., Steinmann, S. P., Sems, S. A., Cross, W. W., Yuan, B. J., et al. (2020). Locking plate fixation of proximal humerus fractures in patients older than 60 years continues to be associated with a high complication rate. *J. Shoulder Elb. Surg.* 29 (8), 1689–1694. doi:10.1016/j.jse.2019.11.026

Blazejak, M., Hofmann-Fliri, L., Büchler, L., Gueorguiev, B., and Windolf, M. (2013). *In vitro* temperature evaluation during cement augmentation of proximal humerus plate screw tips. *Injury* 44 (10), 1321–1326. doi:10.1016/j.injury.2013.04.028

Brunner, A., Resch, H., Babst, R., Kathrein, S., Fierlbeck, J., Niederberger, A., et al. (2012). The Humerusblock NG: a new concept for stabilization of proximal humeral fractures and its biomechanical evaluation. *Arch. Orthop. Trauma Surg.* 132 (7), 985–992. doi:10.1007/s00402-012-1503-x

Burke, N. G., Kennedy, J., Cousins, G., Fitzpatrick, D., and Mullett, H. (2014). Locking plate fixation with and without inferomedial screws for proximal humeral fractures: a biomechanical study. *J. Orthop. Surg* 22 (2), 190–194. doi:10.1177/230949901402200215

Carbone, S., Mezzoprete, R., Papalia, M., Arceri, V., Carbone, A., and Gumina, S. (2018). Radiographic patterns of osteoporotic proximal humerus fractures. *Eur. J. Radiol.* 100, 43–48. doi:10.1016/j.ejrad.2017.12.025

Chen, H., Zhu, Z. G., Li, J. T., Chang, Z. H., and Tang, P. F. (2020). Finite element analysis of an intramedulary anatomical strut for proximal humeral fractures with disrupted medial column instability: a cohort study. *Int. J. Surg.* 73, 50–56. doi:10.1016/j.ijsu.2019.11.026

Choma, T. J., Frevert, W. F., Carson, W. L., Waters, N. P., and Pfeiffer, F. M. (2011). Biomechanical analysis of pedicle screws in osteoporotic bone with bioactive cement augmentation using simulated *in vivo* multicomponent loading. *Spine (Phila Pa 1976)* 36 (6), 454–462. doi:10.1097/brs.0b013e3181d449ec

Claes, L. E., and Meyers, N. (2020). The direction of tissue strain affects the neovascularization in the fracture-healing zone. *Med. Hypotheses* 137, 109537. doi:10.1016/j.mehy.2019.109537

Cristofolini, L., Ruspi, M. L., Marras, D., Cavallo, M., and Guerra, E. (2021). Reconstruction of proximal humeral fractures without screws using a reinforced bone substitute. *J. Biomech.* 115, 110138. doi:10.1016/j.jbiomech.2020.110138

Cui, X., Chen, H., Ma, B., Fan, W., and Li, H. (2019). Fibular strut allograft influences reduction and outcomes after locking plate fixation of comminuted proximal humeral fractures in elderly patients: a retrospective study. *BMC Musculoskelet. Disord.* 20 (1), 511. doi:10.1186/s12891-019-2907-3

Erhardt, J. B., Stoffel, K., Kampshoff, J., Badur, N., Yates, P., and Kuster, M. S. (2012). The position and number of screws influence screw perforation of the humeral head in modern locking plates: a cadaver study. *J. Orthop. Trauma* 26 (10), e188–e192. doi:10.1097/bot.0b013e31823db922

Feerick, E. M., Kennedy, J., Mullett, H., Fitzpatrick, D., and Mcgarry, P. (2013). Investigation of metallic and carbon fibre PEEK fracture fixation devices for three-part proximal humeral fractures. *Med. Eng. Phys.* 35 (6), 712–722. doi:10.1016/j.medengphy.2012.07.016

Foruria, A. M., De Gracia, M. M., Larson, D. R., Munuera, L., and Sanchez-Sotelo, J. (2011). The pattern of the fracture and displacement of the fragments predict the outcome in proximal humeral fractures. *J. Bone Jt. Surg. Br.* 93 (3), 378–386. doi:10.1302/0301-620x.93b3.25083

Grover, P., Albert, C., Wang, M., and Harris, G. F. (2011). Mechanical characterization of fourth generation composite humerus. *Proc. Inst. Mech. Eng. H.* 225 (12), 1169–1176. doi:10.1177/0954411911423346

Handoll, H. H., Elliott, J., Thillemann, T. M., Aluko, P., and Brorson, S. (2022). Interventions for treating proximal humeral fractures in adults. *Cochrane Database Syst. Rev.* 6 (6), Cd000434. doi:10.1002/14651858.cd000434.pub5

He, Y., Zhang, Y., Wang, Y., Zhou, D., and Wang, F. (2017). Biomechanical evaluation of a novel dualplate fixation method for proximal humeral fractures without medial support. *J. Orthop. Surg. Res.* 12 (1), 72. doi:10.1186/s13018-017-0573-4

Jabran, A., Peach, C., and Ren, L. (2018). Biomechanical analysis of plate systems for proximal humerus fractures: a systematic literature review. *Biomed. Eng. Online* 17 (1), 47. doi:10.1186/s12938-018-0479-3

Jang, Y., and Kim, D. (2021). Biomechanical study of Proximal humeral fracture fixation: locking plate with medial support screw vs. locking plate with intramedullary fibular graft. *Clin. Biomech. (Bristol, Avon)* 90, 105510. doi:10.1016/j.clinbiomech.2021.105510

Kennedy, J., Feerick, E., Mcgarry, P., Fitzpatrick, D., and Mullett, H. (2013a). Effect of calcium triphosphate cement on proximal humeral fracture osteosynthesis: a finite element analysis. *J. Orthop. Surg* 21 (2), 167–172. doi:10.1177/230949901302100210

Kennedy, J., Molony, D., Burke, N. G., Fitzpatrick, D., and Mullett, H. (2013b). Effect of calcium triphosphate cement on proximal humeral fracture osteosynthesis: a cadaveric biomechanical study. *J. Orthop. Surg* 21 (2), 173–177. doi:10.1177/230949901302100211

Klahs, K. J., Hagen, M., Scanaliato, J., Hettrich, C., Fitzpatrick, K. V., and Parnes, N. (2024). Geriatric proximal humerus fracture operative management: a Truven Health Analytics database study (2015-2020). *J. Shoulder Elb. Surg.* 33 (3), 715–721. doi:10.1016/j.jse.2023.07.012

Koeppe, J., Stolberg-Stolberg, J., Fischhuber, K., Iking, J., Marschall, U., Raschke, M. J., et al. (2023). The incidence of proximal humerus fracture-an analysis of insurance data. *Dtsch. Arztebl Int.* 120 (33-34), 555–556. doi:10.3238/arztebl.m2023.0132

Kralinger, F., Blauth, M., Goldhahn, J., Käch, K., Voigt, C., Platz, A., et al. (2014). The influence of local bone density on the outcome of one hundred and fifty proximal humeral fractures treated with a locking plate. *J. Bone Jt. Surg. Am.* 96 (12), 1026–1032. doi:10.2106/jbjs.m.00028

Kuang, G. M., Wong, T. M., Wu, J., Ouyang, J., Guo, H., Zhou, Y., et al. (2018). Augmentation of a locking plate system using bioactive bone cement-experiment in a proximal humeral fracture model. *Geriatr. Orthop. Surg. Rehabil.* 9, 215145931879531. doi:10.1177/2151459318795312

Laux, C. J., Grubhofer, F., Werner, C. M. L., Simmen, H. P., and Osterhoff, G. (2017). Current concepts in locking plate fixation of proximal humerus fractures. *J. Orthop. Surg. Res.* 12 (1), 137. doi:10.1186/s13018-017-0639-3

Lescheid, J., Zdero, R., Shah, S., Kuzyk, P. R., and Schemitsch, E. H. (2010). The biomechanics of locked plating for repairing proximal humerus fractures with or without medial cortical support. *J. Trauma* 69 (5), 1235–1242. doi:10.1097/ta.0b013e3181beed96

Neer, C. S. (1970). Displaced proximal humeral fractures. II. treatment of three-part and four-part displacement. *J. Bone. Joint. Surg. Am.* 52 (6), 1090–1103.

Miltenberg, B., Masood, R., Katsiaunis, A., Moverman, M. A., Puzzitiello, R. N., Pagani, N. R., et al. (2022). Fracture dislocations of the proximal humerus treated with open reduction and internal fixation: a systematic review. *J. Shoulder Elb. Surg.* 31 (10), e480–e489. doi:10.1016/j.jse.2022.04.018

Ockert, B., Siebenbürger, G., Kettler, M., Braunstein, V., and Mutschler, W. (2014). Long-term functional outcomes (median 10 years) after locked plating for displaced fractures of the proximal humerus. *J. Shoulder Elb. Surg.* 23 (8), 1223–1231. doi:10.1016/j.jse.2013.11.009

Omid, R., Trasolini, N. A., Stone, M. A., and Namdari, S. (2021). Principles of locking plate fixation of proximal humerus fractures. *J. Am. Acad. Orthop. Surg.* 29 (11), e523–e535. doi:10.5435/jaaos-d-20-00558

Röderer, G., Erhardt, J., Kuster, M., Vegt, P., Bahrs, C., Kinzl, L., et al. (2011). Second generation locked plating of proximal humerus fractures--a prospective multicentre observational study. *Int. Orthop.* 35 (3), 425–432. doi:10.1007/s00264-010-1015-7

Seok, H. G., and Park, S. G. (2023). Dual-Plate fixation for proximal humerus fractures with unstable medial column in patients with osteoporosis. *J. Orthop. Trauma* 37 (10), e387–e393. doi:10.1097/bot.0000000000002645

Sumrein, B. O., Berg, H. E., Launonen, A. P., Landell, P., Laitinen, M. K., Felländer-Tsai, L., et al. (2023). Mortality following proximal humerus fracture-a nationwide register study of 147,692 fracture patients in Sweden. *Osteoporos. Int.* 34 (2), 349–356. doi:10.1007/s00198-022-06612-7

Sun, Q., Wu, X., Wang, L., and Cai, M. (2020). The plate fixation strategy of complex proximal humeral fractures. *Int. Orthop.* 44 (9), 1785–1795. doi:10.1007/s00264-020-04544-7

Tilton, M., Armstrong, A., Sanville, J., Chin, M., Hast, M. W., Lewis, G. S., et al. (2020). Biomechanical testing of additive manufactured proximal humerus fracture fixation plates. *Ann. Biomed. Eng.* 48 (1), 463–476. doi:10.1007/s10439-019-02365-3

Wright, M. A., Lobao, M. H., Abbasi, P., Parks, B. G., Mistretta, K. L., and Murthi, A. M. (2021). Altered glenohumeral biomechanics in proximal humeral fracture malunion. *J. Am. Acad. Orthop. Surg.* 29 (23), e1167–e1175. doi:10.5435/jaaos-d-20-00555

Yang, P., Zhang, Y., Liu, J., Xiao, J., Ma, L. M., and Zhu, C. R. (2015). Biomechanical effect of medial cortical support and medial screw support on locking plate fixation in proximal humeral fractures with a medial gap: a finite element analysis. *Acta Orthop. Traumatol. Turc* 49 (2), 203–209. doi:10.3944/AOTT.2015.14.0204

Zeng, L. Q., Zeng, L. L., Jiang, Y. W., Wei, H. F., Zhang, W., and Chen, Y. F. (2018). Influence of medial support screws on the maintenance of fracture reduction after locked plating of proximal humerus fractures. *Chin. Med. J. Engl.* 131 (15), 1827–1833. doi:10.4103/0366-6999.237396

Zhang, W., Zeng, L., Liu, Y., Pan, Y., Zhang, W., Zhang, C., et al. (2014). The mechanical benefit of medial support screws in locking plating of proximal humerus fractures. *PLoS One* 9 (8), e103297. doi:10.1371/journal.pone.0103297

Zhelev, D., Hristov, S., Zderic, I., Ivanov, S., Visscher, L., Baltov, A., et al. (2023). Treatment of metaphyseal defects in plated proximal humerus fractures with a new augmentation technique-A biomechanical cadaveric study. *Med. Kaunas.* 59 (9), 1604. doi:10.3390/medicina59091604

frontiers | Frontiers in Bioengineering and Biotechnology

TYPE Review
PUBLISHED 27 September 2024
DOI 10.3389/fbioe.2024.1472509

OPEN ACCESS

EDITED BY
Yih-Kuen Jan,
University of Illinois at Urbana-Champaign, United States

REVIEWED BY
Jorge Grasa,
University of Zaragoza, Spain
Alessio Gizzi,
Campus Bio-Medico University, Italy

*CORRESPONDENCE
Silvia Todros,
silvia.todros@unipd.it

RECEIVED 29 July 2024
ACCEPTED 17 September 2024
PUBLISHED 27 September 2024

CITATION
Spadoni S, Todros S and Pavan PG (2024) Numerical modeling of the abdominal wall biomechanics and experimental analysis for model validation.
Front. Bioeng. Biotechnol. 12:1472509.
doi: 10.3389/fbioe.2024.1472509

Numerical modeling of the abdominal wall biomechanics and experimental analysis for model validation

Silvia Spadoni[1], Silvia Todros[1]* and Piero G. Pavan[1,2]

[1]Department of Industrial Engineering, University of Padova, Padova, Italy, [2]Fondazione Istituto di Ricerca Pediatrica Città della Speranza, Padova, Italy

The evaluation of the biomechanics of the abdominal wall is particularly important to understand the onset of pathological conditions related to weakening and injury of the abdominal muscles. A better understanding of the biomechanics of the abdominal wall could be a breakthrough in the development of new therapeutic approaches. For this purpose, several studies in the literature propose finite element models of the human abdomen, based on the geometry of the abdominal wall from medical images and on constitutive formulations describing the mechanical behavior of fascial and muscular tissues. The biomechanics of the abdominal wall depends on the passive mechanical properties of fascial and muscle tissue, on the activation of abdominal muscles, and on the variable intra-abdominal pressure. To assess the quantitative contribution of these features to the development and validation of reliable numerical models, experimental data are fundamental. This work presents a review of the state of the art of numerical models developed to investigate abdominal wall biomechanics. Different experimental techniques, which can provide data for model validation, are also presented. These include electromyography, ultrasound imaging, intraabdominal pressure measurements, abdominal surface deformation, and stiffness/compliance measurements.

KEYWORDS

abdominal wall, numerical modeling, muscle contraction, intra-abdominal pressure, *in vivo* experiments

1 Introduction

Understanding the mechanical behavior of the abdominal wall can help in the investigation of its healthy and pathological conditions. Despite many efforts made over the years, the biomechanics of the abdominal wall is still not fully understood from a quantitative point of view, due to the complex geometry and mechanics of the anatomical region, the lack of extensive experimental datasets, the high costs of clinical trials, and related ethical aspects. Increasing knowledge on the biomechanics of the abdomen can be useful, in particular, to address rational design and use of surgical meshes for hernia repair (Deeken and Lake, 2017).

In silico analysis through the Finite Element Method (FEM) has shown the ability to provide a deeper understanding of the mechanical properties of biological tissues, lowering costs and time with respect to an experimental or clinical approach. FEM-based models can consider the geometric and material properties of the anatomical structures and simulate

the interactions between muscle fibers, fascial tissue, and other involved tissues. By applying external loads or constraints to the model, it is possible to simulate a wide range of scenarios and analyze the resulting deformations, stresses, and strains within each tissue.

A mandatory aspect of this process is the validation of FEM models, which consists in verifying that the obtained numerical results are feasible. Generally, this can be achieved by replicating specific experimental conditions by means of numerical analysis, and comparing numerical outcomes and experimental data. Alternatively, or in combination, the results can be compared to the outcomes from similar–but already validated–models. Once validated, the models can be adopted to enlarge the numerical analysis to a broader range of conditions. To assess the required accuracy of FEM models, it should be necessary to first evaluate the variability of biological data, including anthropometric characteristics of the anatomical regions and mechanical properties of the constituent tissues, due to age, sex, BMI or presence of pathologies. Some considerations about the importance of the validation process are proposed in the Discussion section.

FEM models can be also personalized to individual anatomical variations, allowing patient-specific simulations. This capability is particularly relevant in clinical applications, such as in the surgical planning or in the design of patient-specific prosthetics. By incorporating medical imaging data, such as Computed Tomography (CT) or Magnetic Resonance Imaging (MRI), FEM models can potentially be tailored to accurately represent the unique anatomy of an individual patient.

Advances in imaging technology, computational power, and material modeling techniques have significantly improved the precision and predictive capabilities of numerical models. Therefore, computational methods have the potential to provide information on the mechanical behavior of abdominal muscles under different loading conditions, contributing to a better understanding of their function, the development of improved rehabilitation strategies, and the design of innovative medical devices.

Investigating the biomechanics of the abdomen is particularly important in the case of pathologies. Among all pathologies, those that affect the abdominal wall, such as hernia, show a prevalence of 1.7% for all ages and 4% for people over 45 years (Jenkins and O'Dwyer, 2008). The most common surgical technique for hernia repair is the laparoscopic approach with a surgical mesh (Heniford et al., 2003; Colavita et al., 2013), where the selection of the most appropriate prosthesis is mainly based on the surgeon's experience (Mudge and Hughes, 1985). As shown in several follow-ups, an improper solution can cause discomfort and postoperative pain for the patient; therefore, choosing the most suitable mesh is crucial. This selection may be supported by FEM analysis, which could provide information on the effects of different mesh configurations and sizes, considering the complexity of the surrounding anatomical region.

To study the biomechanics of the abdominal wall, it is fundamental to account for the activation of the abdominal muscles and to understand its correlation with intra-abdominal pressure (IAP) during different physiological functions and motor tasks (Bjerkefors et al., 2010). In this context, the introduction of minimally invasive instruments and imaging methods has revolutionized clinical practice (Meier et al., 2001); in particular, electromyography (EMG), ultrasound (US) imaging, IAP measurements, and the evaluation of abdominal deformation and compliance represent fundamental tools to evaluate abdominal behavior *in vivo*. Integration of EMG, US imaging, deformation, and IAP measurements has significantly improved our understanding of abdominal muscle function and its role in various contexts, such as sports performance, injury prevention, and rehabilitation. These technologies allow researchers and clinicians to assess muscle activation patterns, visualize muscle structure, and measure muscle deformation and mechanical properties during different tasks. This knowledge is essential to design effective numerical models, identify muscle imbalances or dysfunctions, and develop targeted rehabilitation strategies. Continuous progress in these technologies will undoubtedly contribute to further advances in understanding the function of abdominal muscles and their influence on human performance and health.

The aim of this work is to review the different FEM models developed in the literature, as well as several measurement techniques used to develop and validate these models. For this purpose, the anatomy of the human abdominal wall is described first, as a basis for defining the geometry of FEM models. The mechanical properties of abdominal tissues are presented, according to experimental tests available in the literature, on the abdominal wall of human subjects. These data are useful for the development of constitutive models capable of describing the behavior of abdominal tissue in FEM models. Then, computational models of the abdominal wall are presented, including mostly passive models and also considering a few cases with active muscular behavior. Lastly, *in vivo* measurements in human subjects, such as EMG, US imaging, IAP measurements, abdominal surface deformation, and stiffness measurements, are collected. This overview allows evaluating the limited availability of *in vivo* data for the validation of FEM models and highlighting possible gaps to be filled for a deeper understanding of abdominal biomechanics.

2 Abdominal wall anatomy

The abdominal wall includes seven layers: skin, subcutaneous tissue, superficial fascia, deep fascia, muscle, extraperitoneal fascia, and peritoneum.

According to Lancerotto et al. (2011), there are three layers under the dermis in the subcutaneous tissue of the anterior abdominal region: a superficial adipose layer, a membranous layer and a deep adipose layer. These layers cover the deep fascia that encloses the muscles of the abdominal wall.

The abdominal muscles include the External Oblique (EO), Internal Oblique (IO), Transversus Abdominis (TA), and Rectus Abdominis (RA), which are interdigitated with each other and ensure core strength (Flynn and Vickerton, 2022). In the anterior part of the abdominal wall, each flat muscle forms an aponeurosis (AP) that covers the RA muscle. The APs of all flat muscles are linked in the midline, forming Linea Alba (LA), a fibrous structure that extends from the xiphoid process of the sternum to the pubic symphysis. The RA runs vertically down the front of the abdomen

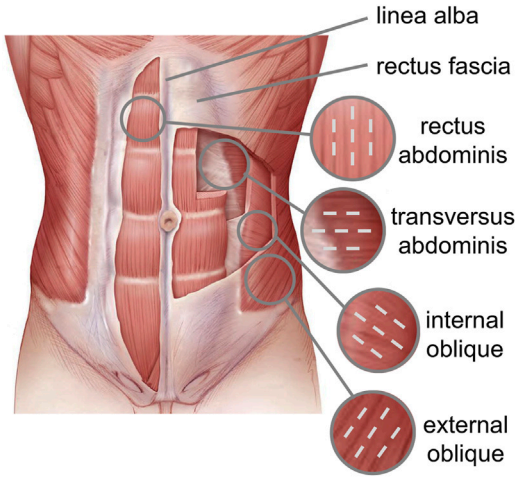

FIGURE 1
Abdominal wall anatomy with different fiber orientations highlighted with dotted lines.

and is responsible for flexing the spine and creating spinal stability. The IO and EO are located on the sides of the abdomen and help in rotating and bending the trunk. The role of the abdominal wall is essential not only in protecting the visceral structures, but also in stabilizing the trunk and distributing loads (Grevious et al., 2006).

The spatial orientation of the muscle fibers is different for each abdominal muscle (Figure 1). The EO fibers diffuse caudally to the iliac crest and inguinal ligament and medially to the LA, the IO fibers emerge from the inguinal ligament and iliac crest and are inserted into the anterolateral surface of the cartilages of the last three ribs and into the LA perpendicular to the EO fibers. The TA fibers extend circumferentially in a downward direction, while the RA muscle fibers are parallel to the LA.

An interesting analysis of the architecture of the abdominal wall muscles can be found in Brown et al. (2011), where a correlation between the length of the sarcomere and the biomechanical functions of each muscle is proposed. Based on cadaveric data, RA shows the lowest Physiological Cross Area (PCA), associated with the highest sarcomere length (3.29 ± 0.07 μm) among all abdominal muscles; this can be correlated with the generation of the smallest isometric force. Differently, IO is characterized by the largest PCA and the smallest sarcomere length (2.61 ± 0.06 μm), thus being able to generate the highest contraction force among all abdominal muscles, but with a small range of motion.

Abdominal muscles are enveloped by a thin epimysial fascia, allowing the various muscular layers to glide. In particular, the fascial layers surrounding the RA are divided into Anterior and Posterior Rectus Sheath (ARS and PRS, respectively). In the ARS, oblique bundles of collagen fibril are interlaced with each other, whereas the PRS consists predominantly of transverse fibril bundles (Axer et al., 2001). This structural conformation is considered responsible for the mechanical anisotropy of both ARS and PRS (Astruc et al., 2018). Proximally, the transversalis fascia (TF) separates the anterior abdominal wall from the extraperitoneal fat, while posteriorly, it is continuous with the thoracolumbar fascia. Understanding the structure and biomechanical role of abdominal fasciae is relevant from a surgical point of view, for example, in the evaluation of the choice of direction of laparotomy incision, and in the analysis of the overall biomechanics of the abdominal wall.

3 Review methodology

The literature research was conducted using the English-language databases PubMed, Web of Science and Elsevier ScienceDirect. Keywords and inclusion criteria adopted were different for each of the topics described and are therefore specified in the following.

The review of the numerical models of abdominal wall biomechanics is systematic and covers–to the best of the knowledge of the authors–the relevant works published on the topic. The sections dedicated to the experimental testing on abdominal wall are focused on collecting those elements that can be relevant for the development and validation of numerical models of the abdominal wall. Search was not restricted to specific geographic regions and also references present in the articles were included.

3.1 Mechanical characterization of abdominal wall tissues

The following combination of keywords was considered: (“tensile test” OR “mechanical test”) AND (“human abdominal wall” OR “human abdominal muscle” OR “human linea alba” OR “human abdominal fascia”). The study inclusion criteria were as follows: experimental test need to be on human abdominal tissues, experimental protocols needed to be described, quantitative results about the stress-strain behavior had to be reported. Eight articles were selected.

3.2 Numerical modeling of the human abdominal wall

The following combination of keywords was considered: (“finite element model” OR “finite element method” OR “FEM”) AND (“human abdominal wall” OR “human abdomen” OR “abdominal wall contraction” OR “abdominal muscles” OR “abdominal hernia”). The study inclusion criteria were as follows: the FEM models needed to include the human abdominal wall, detailed methodology for the development of the abdomen FEM models needed to be described, the different abdominal tissues needed to be presented (studies with rough monolayer models were discarded), FEM models needed to describe the mechanical behavior of the human abdominal wall in passive and/or active condition of the muscles. Thirteen articles were selected.

3.3 Electromyography

The following combination of keywords was considered: (“electromyography” OR “EMG”) AND (“human abdominal

wall" OR "human abdominal tissue" OR "human abdominal muscle" OR "abdominal exercise"). The study inclusion criteria were as follows: experimental protocols needed to be described, results about one or more human abdominal muscle had to be presented, results had to include quantitative description of muscle response, results had to describe muscle activation during different motor tasks. Twenty-seven articles were selected. Among these, seven articles in which the experimental testing included also simultaneous ultrasound imaging were presented in a separate section (Paragraph 6.3).

3.4 Ultrasound imaging

The following combination of keywords was considered: "ultrasound imaging" AND ("human abdominal wall" OR "human abdominal muscle" OR "abdominal contraction"). The study inclusion criteria were as follows: experimental protocols had to be described, results about one or more human abdominal tissues had to be presented, results had to include quantitative description of muscle behavior, results needed to describe muscle activation during different motor tasks and/or change in muscle thickness. Thirty-one articles were selected. Among these, seven articles in which the experimental testing included also simultaneous electromyography were presented in a separate section (Paragraph 6.3).

3.5 Intra-abdominal pressure measurement

The following combination of keywords was considered: ("intraabdominal pressure" OR "intra-abdominal pressure" OR "IAP") AND ("human abdominal wall" OR "motor task"). The study inclusion criteria were as follows: experimental protocols needed to be described, results needed to include measurements of the intraabdominal pressure variation related to specific activities or motor tasks in human subjects. Fourteen articles were selected.

3.6 Stiffness measurements

The following combination of keywords was considered: ("stiffness" OR "compliance") AND "human abdominal wall". The study inclusion criteria were as follows: experimental protocols needed to be described, results needed to include measurements of the human abdominal stiffness, experimental tests needed to include *in vivo* studies. Five articles were selected.

3.7 Surface deformation measurements

The following combination of keywords was considered: ("surface" OR "deformation" OR "optical measurement") AND "human abdominal wall". The study inclusion criteria were as follows: experimental protocols needed to be described, results needed to include measurements of deformation on human living subjects. Six articles were selected.

4 Mechanical characterization of abdominal wall tissues

A limited number of studies in the literature investigate the mechanical properties of the human abdominal wall, mainly due to the limited availability of human samples and to the concurrent issues in tissue preservation. Furthermore, this approach can consider only the passive behavior of the tissues and cannot include the evaluation of the active behavior of abdominal muscles.

In general, most of the experimental studies in the literature focus on specific layers of the abdominal wall, which are dissected and isolated from other abdominal structures.

Several works investigate the mechanical behavior of LA. Gräβel et al. (2005) evaluate the compliance of human LA in longitudinal and transverse directions to assess anisotropy in a high number of subjects (15 female and 16 male). They find that LA compliance is about two times higher in the longitudinal than in the transverse direction; moreover, some comparisons between the mechanical properties of LA in men and women are proposed. Hollinsky and Sandberg, (2007) measure the ultimate tensile stress for human LA of 66 cadaveric subjects with mean age of 77 (range: 17–94 years) in the transverse and longitudinal direction. In the epigastric region, they find mean values of 4.5 ± 1.0 MPa and 10.0 ± 3.4 MPa in the longitudinal and transverse direction, respectively; in the hypogastric region, they estimate mean values of 4.1 ± 2.5 MPa and 8.4 ± 3.1 MPa in the longitudinal and transverse direction, respectively. Förstemann et al. (2011) carry out uniaxial tensile tests up to failure on samples obtained from 6 donors to measure the ultimate membrane force in the transversal and longitudinal directions. The mean values reported for the ultimate membrane force are 7.5 N/mm and 1.1 N/mm in the transverse and longitudinal directions, respectively, showing a high strength ratio. Levillain et al. (2016) perform uniaxial tensile tests, comparing human and porcine LA, and evaluating the correlation of mechanical properties with the distribution of elastin and collagen fibers. According to their results, human and porcine LA show similar microstructure and nonlinear anisotropic mechanical behavior; however, porcine LA was approximately 1.5 times stiffer than human LA.

Therefore, according to these works, LA is characterized by anisotropic mechanical behavior, showing higher stiffness and strength in the transverse direction compared to those in the longitudinal direction. A direct comparison among the proposed data is complicated by differences in mechanical test protocols and measurements.

Other studies are dedicated to the analysis of the mechanical behavior of human ARS up to failure under uniaxial loading conditions. Hollinsky and Sandberg, (2007) present experimental data from 66 cadaveric subjects with a mean age of 77 (range: 17–94 years) showing an ultimate tensile stress equal to 8.1 ± 2.1 MPa and 3.4 ± 1.6 MPa for the ARS in the epigastric region in the transverse and longitudinal directions, respectively, and equal to 8.5 ± 2.5 MPa and 3.4 ± 2.0 MPa for the ARS in the hypogastric region in the transverse and longitudinal directions, respectively.

Martins et al. (2012) perform uniaxial tensile tests on samples from 12 female donors, finding a Young's modulus of 30.3 ± 10.5 MPa and 10.1 ± 5.3 MPa in the longitudinal and transverse directions, respectively. Ben Abdelounis et al. (2013) evaluate the

TABLE 1 Mean parameters obtained by Cardoso, 2012 from uniaxial experimental tests: secant modulus E_s, tangent modulus E_t, maximum tensile stress σ_{max}, and corresponding ultimate stretch λ_U.

	E_s (MPa)	E_t (MPa)	σ_{max} (MPa)	λ_U
FT	3.54	9.06	2.86	1.56
EO	0.33	1.00	0.57	1.98
IO	0.26	0.65	0.39	1.94
RA	0.33	0.52	0.23	1.60
TA	0.31	1.03	0.73	2.19

TABLE 2 Tangent elastic modulus E (median and interquartile range) of abdominal wall tissues from FNF and FF samples (Kriener et al., 2023).

	E (MPa)	
	FNF	FF
ARS	6.02 (10.14)	8.29 (15.76)
PRS	14.32 (57.62)	7.31 (67.69)
LA	2.67 (6.87)	3.92 (3.80)
peritoneum	6.79 (6.09)	4.42 (14.15)
RA	0.19[a]	0.30 (0.88)
EO	0.24 (0.37)	0.57 (1.27)
IO	0.42 (0.068)	0.58 (1.11)
TA	2.75 (5.42)	0.81 (2.44)

[a]Sample size is three.

mechanical response of three human ARS using two loading rates, corresponding to quasi-static (0.01 s^{-1}) and almost-instantaneous (50 s^{-1}) strain rates. The mean values of the Young's modulus, equal to 5.6 MPa and 14 MPa, are found for the quasi-static and almost-instantaneous test, respectively.

As mentioned above, only a few contributions give an overall view of the mechanical properties of the human abdominal wall including the different muscles. Cardoso, (2012) evaluates 119 samples of FT, RA, TA, EO, and IO from 12 cadavers. All muscles are tested in uniaxial tensile mode in the direction of the fibers; characteristic parameters are obtained, among which the secant modulus E_s, the tangent modulus E_t, the maximum tensile stress σ_{max}, and the corresponding ultimate stretch λ_U. This study also explores the influence of age, sex and body mass index (BMI) on the mechanical properties of the abdominal tissues. The parameters obtained in the study are reported in Table 1.

In a more recent contribution Kriener et al. (2023) characterize the tensile properties of each layer of the human abdominal wall from 15 cadaveric subjects, comparing samples from fresh-never-frozen (FNF) and fresh-frozen (FF) cadavers. They collect a total of 232 samples in longitudinal and transverse directions for ARS and PRS, peritoneum, LA, RA, EO, IO, and TA. Samples are tested at a strain rate varying between 0.01 s^{-1} and 0.006 s^{-1} and the tangent elastic modulus E of each tissue layer is evaluated in the almost-linear portion of the stress-strain curve, following the toe region. The values obtained are reported in Table 2. According to these data, FF tissues are generally stiffer than FNF tissues, except in the case of PRS, peritoneum, and TA.

As reported above, the experimental data coming from uniaxial tensile tests of human abdominal tissues are consistent, even if with high variability. However, there is a lack of data in the biaxial tensile mode, which would be useful to better understand the biomechanics of the abdominal wall under physiological loading conditions. In fact, the abdominal wall experiences multidirectional loads and deformations during daily activities, such as bending, twisting, and stretching.

Another lack in the literature is the study of the active behavior of single muscle fibers or bundles derived from human abdominal wall muscles. These studies would allow us to obtain information on the maximum isometric tension, which is a necessary parameter to assess the contractile capability of muscular tissue.

5 Numerical modeling of the human abdominal wall

Numerical modeling, generally based on the FEM approach, can be useful for obtaining quantitative information on the biomechanics of the abdominal wall and to assess different healthy and pathological conditions. In fact, a simple approach based on experimental analyses does not allow the understanding of a complex biomechanical scenario that involves muscle contraction, IAP variation, non-linear mechanical response of the tissues, and a complex anatomy.

A large part of the literature in this field is focused on the passive mechanical response of the human abdominal wall. Hernández-Gascón et al. (2014) develop a FEM model of the abdominal wall with a simplified geometry, aiming at evaluating the performance of hernia meshes in their interaction with the surrounding tissues. In particular, the focus is on numerical aspects concerning the constitutive modeling of surgical meshes, by using refined or more simple approaches. The abdomen is modeled as an extruded ellipse with a size compatible with a male abdomen, and the abdominal wall is considered as a single muscular layer with a thickness of 15 mm. This layer is described adopting a hyperelastic anisotropic constitutive model with parameters based on experimental data previously acquired from an animal model (Hernández et al., 2011). Numerical analyses simulate the effects of an intra-abdominal pressure (IAP) of 171 mmHg (corresponding to jumping) on a herniated wall repaired with a surgical mesh. The results of this work focus on the comparison of different surgical meshes and modeling methods, even though the geometry of the abdomen is simplified. In fact, the analysis of the biomechanics of the abdominal wall considering the effective geometry is beyond the scope of the work.

A more detailed FEM model of the human abdomen is proposed by Hernández-Gascón et al. (2013a) to study the passive mechanical response related to physiological tasks. The geometry of the model is extracted from MRI data from a healthy 38-year-old man. The LA, RA, AP and lateral muscles are identified by manual segmentation and the lateral muscles are described as single layer due to the difficulty in recognizing IO, EO, and TA from medical images. The model includes TF, ARS, PRS, diaphragm, and pelvis, while skin and fat are not included due to their negligible stiffness. Abdominal

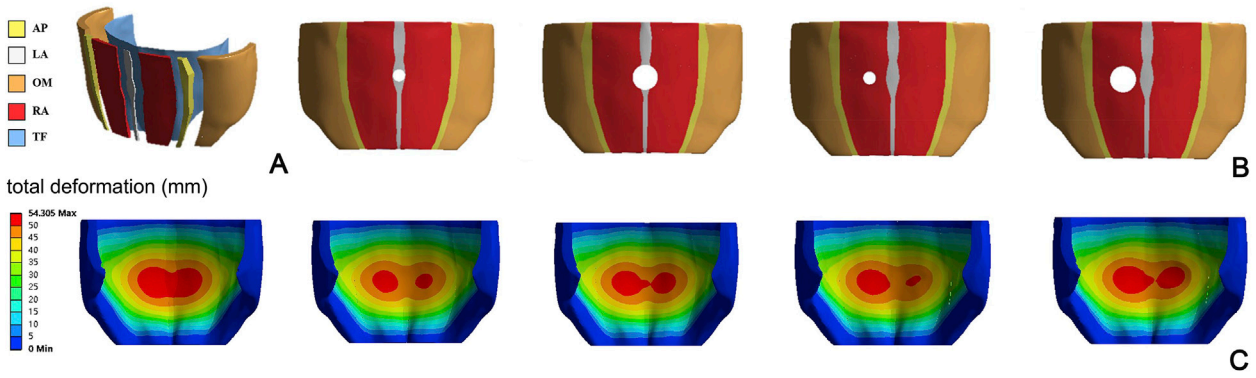

FIGURE 2
Representation of the FEM model proposed by He et al., 2020 **(A)**, with different locations and size of hernia **(B)**. Magnitude displacement field of the abdominal wall in deformed configuration for different hernia conditions **(C)** Reprinted from He et al. (2020), Copyright 2019, with permission from Elsevier.

muscles–in their passive behavior–and aponeuroses are modeled as fiber-reinforced hyperelastic materials, while the diaphragm and pelvis are described assuming a neo-Hookean hyperelastic formulation. The constitutive parameters are set on the basis of experimental data from both human subjects (when available) and animal models. The basal stress state of the abdominal muscles in the geometrical configuration corresponding to MRI data of the subject in supine position is obtained by an optimization procedure. This model is used to simulate the mechanical response of the abdominal wall to the IAP induced by physiological loads, assessing the deformation profile of the abdomen in the craniocaudal and mediolateral directions related to the level of IAP.

This model is used as a basis to simulate the occurrence of hernia and the interaction between the abdominal wall and different types of meshes after surgical repair (Hernández-Gascón et al., 2013b), applying an IAP corresponding to different motor tasks. Numerical results show that the overall mechanical response, as well as the stress acting on the prostheses, are significantly affected by the levels of surgical mesh anisotropy and stiffness.

A similar approach is used by Pachera et al. (2016) to develop a model describing the passive behavior of an abdominal wall in physiological conditions and the mechanical response under different IAP corresponding to daily life activities. The geometry of the model is reconstructed from MRI data of a healthy male subject and includes LA, RA, a single structure that resembles the lateral muscles (TA, IO, and EO), AP and all fascial tissues. The model is simplified by assuming a symmetry with respect to the sagittal plane. Based on data from tensile tests on human abdominal tissues (Förstemann et al., 2011; Cardoso, 2012; Ben Abdelounis et al., 2013), fiber-reinforced and almost-incompressible hyperelastic constitutive models are assumed to describe the mechanical response of the different tissues. Numerical results show the deformed configuration of the abdominal wall at different IAPs and are compared to experimental data acquired on human cadavers (Konerding et al., 2011) and living subjects (Song et al., 2006), confirming the reliability of the model. The previous model is then adopted to numerically simulate the occurrence of a hernia and surgical repair (Todros et al., 2018), focusing on the consequent changes in compliance of the abdominal wall in passive condition.

Even in the work of He et al. (2020), a numerical model of a human abdomen in passive condition is developed. CT images of a healthy male abdomen are used to reconstruct the geometry of all abdominal structures, including LA, RA, AP, lateral muscles, and TF (Figure 2A). A fiber-reinforced hyperelastic constitutive model is used to describe the mechanical behavior of connective and muscle tissues; constitutive parameters are evaluated based on previous studies (Hernández-Gascón et al., 2013a; Pachera et al., 2016). The focus of this work is to evaluate the effects of surgical repair with meshes of different stiffness on the compliance of the abdominal wall, depending on the position and size of hernia (Figures 2B, C).

Tuset et al. (2022) develop a FEM model to study the influence of stoma locations on the abdominal wall mechanics. The model is based on CT images taken from an anatomy database and includes LA, RA, TA, IO, and EO (Figure 3A). All tissues are described assuming an isotropic linear elastic behavior, with engineering constants based on previous experimental works (Cardoso, 2012; Cooney et al., 2016). Seventeen different locations of the stoma are taken into account to evaluate the effect of increasing the IAP to about 150 mmHg, in terms of deformation of the region of the abdominal wall next to the stoma. An example of a specific position of the stoma is shown in Figure 3B.

Karrech et al. (2023) develop a FEM model of the abdominal wall aimed at evaluating failure stress around different types of hernia, based on fracture mechanics. The geometry of the model, based on CT data from an anatomy repository, is symmetric with respect to the sagittal plane and encompasses LA, RA, AP, TA, IO, and EO. The hernia is simulated as a damage zone of the abdominal wall in the umbilical position in the LA and RA (incisional hernia). A surgical mesh is included to simulate repair in different surgical conditions (onlay, anterectus, retrorectus, and preperitoneal mesh positioning). The passive response of muscles is modeled assuming them as hyperelastic isotropic materials, with constitutive parameters based on human data (Cardoso, 2012). Surgical mesh is also described as an isotropic elastic material but with linear behavior. The internal surface of the abdominal wall is subjected to an IAP of 6 mmHg, representing the basal IAP in a human subject. The numerical results focus on the evaluation of severe hernia damages and the identification of the best surgical mesh positioning, based on the type and location of hernia.

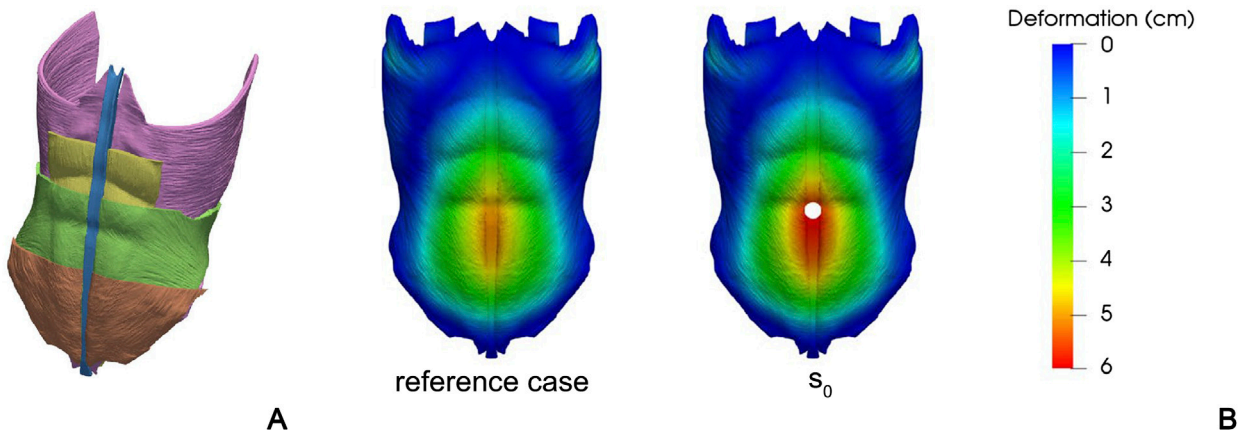

FIGURE 3
Different anatomical structures of the FEM model developed by Tuset et al., 2022: TA (purple), RA (yellow), IO (green), EO (brown), and LA (blue) **(A)**. Contour of magnitude displacement in a healthy reference case and in a specific stoma position **(B)** This file is licensed under the Creative Commons Attribution 4.0 International license. Figures come from Tuset et al. (2022).

Since the abdominal wall is largely composed of muscular structures, the effects of muscle contraction on the overall biomechanical behavior must be assessed. In particular, several studies described above take into account high IAP values applied to the abdominal wall in a passive state, while this condition is not true to the physiology of the abdomen.

In this context, the first model capable of describing the active behavior of the abdominal wall is attributed to Grasa et al. (2016), who develop *in vitro* experimental tests and the corresponding FEM models, even tough on a rabbit. The aim of this study is the analysis of the active mechanical response of small rectangular samples taken from the abdominal wall. The numerical models are developed with a geometry resembling the samples and include different layers corresponding to the single abdominal muscles. Constitutive models account for the anisotropic response given by the specific spatial orientation of both collagen and muscle fibers. According to the authors, this constitutive model can be adopted to simulate abdominal biomechanics, extending it to the overall geometry of the wall.

The biomechanical response of the entire abdominal wall of a human subject under muscle contraction is simulated by Pavan et al. (2019). All muscles and fascial tissues are included in the FEM model, considering the specific spatial orientation of the fibers in each muscular layer. Connective tissues are described as fiber-reinforced and almost-incompressible hyperelastic materials, while muscle tissues are modeled with a Hill type three-element formulation (Marcucci et al., 2017). This model can accurately mimic abdominal contraction and assess its deformed shape in relation to IAP corresponding to different daily tasks. The numerical results show a relevant difference in abdominal compliance between passive and active conditions with the same value of IAP.

A refinement of this model is proposed by Todros et al. (2020), adding a structure with a suitable volumetric stiffness, resembling the abdominal cavity. By using this model, it is possible to generate IAP as a direct effect of muscular contraction. This model is partially validated on the basis of experimental data from *in vivo* tests on human subjects.

A similar FEM model is developed by Karami et al. (2023), who refine the constitutive formulation of the muscular tissue considering a chemomechanical approach. In this way, the biomechanical response of the abdominal wall can be related to *in vivo* electromyographic data.

In view of forthcoming patient-specific approaches, Jourdan et al. (2024) develop a FEM model of the abdomen based on a simplified geometry, which is built on seven ellipses placed at different levels along the cranio-caudal axis and scaled to fit the abdomen size of three subject types with different BMI (corresponding to normal, overweight, and obese subjects) (Figure 4). The model includes abdominal muscles (RA, EO, IO, TA and dorsal muscles), bones (ribcage, pelvis, spine), and connective tissue (LA, ARS, PRS, and aponeuroses). As in other previous studies, the connective tissues are modeled as fiber-reinforced almost-incompressible hyperelastic materials and the active behavior of muscles is simulated by means of a Hill type three-element model. This approach aims to analyze the effects of inter-individual variability on the abdominal wall biomechanics in different loading conditions, including both passive (e.g., pre-surgical inflation) and active (i.e., daily motor tasks) behavior.

Technical details regarding all the numerical models previously presented are reported in Table 3. For all the considered articles FEM software is indicated, while other details such as the type of the analyses and the number of degrees of freedom of the models are reported, when available. Table 3 also indicates whether standard constitutive models (at disposal in the software) are adopted for the abdominal wall tissues, or if *ad hoc* constitutive formulations are developed and implemented through specific user subroutines. In spite of the fact that few data about the size of the FEM models are reported in the different studies, it can be assumed that a detailed model of the abdominal wall can be obtained with a number of degrees of freedom in the order of 300,00 ÷ 900,000, largely depending on the extension of the modelled anatomical part. This information can help in estimating the computational complexity associated to a

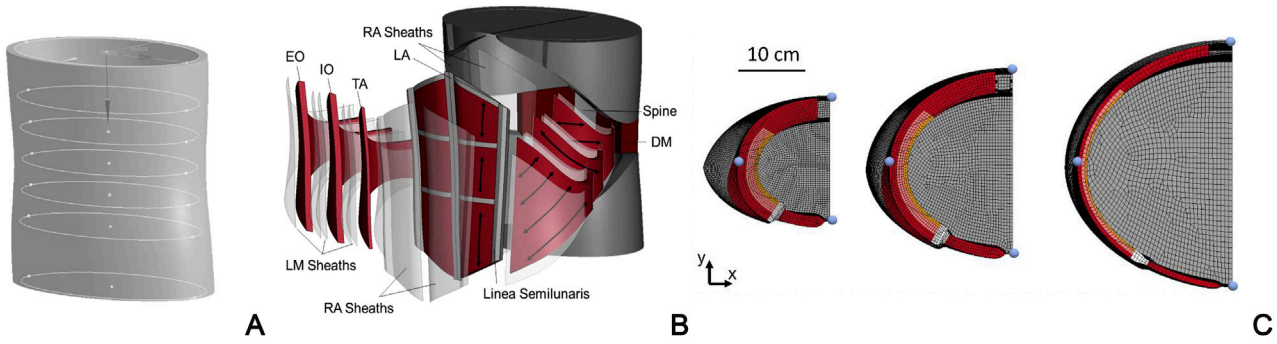

FIGURE 4
FEM model of the abdominal wall developed by Jourdan et al., 2024: development of the 3D model geometry based on elliptical sections **(A)**; exploded view including all connective and muscular tissues **(B)**; examples of three subject types with different BMI and tissue conformation: normal BMI and high muscular thickness, overweight BMI and medium muscular thickness, obese subjects and low muscular thickness **(C)** Reprinted from Jourdan et al., 2024, Copyright 2023, with permission from Elsevier.

TABLE 3 Basic data of the abdominal wall FEM models.

Reference	Software	Type of analysis	Degrees of freedom	Constitutive modeling
Hernández-Gascón et al. (2014)	Abaqus	N/A	885,738[a]	standard
Hernández-Gascón et al. (2013a)	Abaqus	static implicit	N/A	standard and user subroutine
Hernández-Gascón et al. (2013b)	Abaqus	static implicit	N/A	standard and user subroutine
Pachera et al. (2016)	Abaqus	N/A	N/A	standard
Todros et al. (2018)	Abaqus	N/A	N/A	standard
He et al. (2020)	Ansys	N/A	N/A	standard
Tuset et al. (2022)	Code_aster	N/A	N/A	standard
Karrech et al. (2023)	Abaqus	N/A	N/A	standard
Grasa et al. (2016)	Abaqus	N/A	N/A	user subroutine
Pavan et al. (2019)	Abaqus	quasi-static implicit	N/A	standard and user subroutine
Todros et al. (2020)	Abaqus	N/A	N/A	standard and user subroutine
Karami et al. (2023)	Abaqus	N/A	N/A	user subroutine
Jourdan et al. (2024)	Ansys	N/A	N/A	standard

[a]Estimated on the basis of the number of nodes and type of elements.

model and in the choice of a computational framework suitable to run these type analyses. Moreover, the non-linearity of the problems related to abdominal wall biomechanics (material non-linearity, large strains, contact conditions) must be considered, since it represents an additional cause of the computational complexity.

The literature described above shows that the general trend in this research field is characterized by an increasing refinement of the constitutive models of the abdominal muscles and the addition of the abdominal cavity, which allow for a more realistic description of the abdominal biomechanics. However, the increased model complexity and the multiple interactions among muscular activation, IAP variation, and abdominal wall deformation in different motor tasks require extensive *in vivo* data for model validation.

6 *In vivo* characterization of abdominal muscle activation

6.1 Electromyography

EMG is a technique commonly used to assess muscle recruitment, measuring myoelectric activity in response to nerve stimulation. The ability of a muscle to respond to this stimulation is evaluated in terms of an action potential signal, whose intensity and shape depend on the number of motor units involved in the task. Applied to the abdominal region, EMG measurements provide data on the excitation pattern of the abdominal muscles during various activities. These data could be an important part of the validation process of numerical models that include the active behavior of the abdominal muscles. A relevant review on studies in the literature investigating EMG measurements during

abdominal exercises is proposed by Monfort-Pañego et al. (2009). While reporting more than 80 studies mainly on healthy subjects, the authors highlight that EMG signals are not always normalized to the maximum voluntary contraction, thus limiting the possible comparison between different conditions.

Specific studies take into account different abdominal strengthening exercises that elicit varying levels of RA, IO, and EO excitation (Drysdale et al., 2004; Urquhart et al., 2005; Moraes et al., 2009; Bjerkefors et al., 2010; Escamilla et al., 2010; Okubo et al., 2010; Crommert et al., 2011; García-Vaquero et al., 2012; Czaprowski et al., 2014; Kim S. Y. et al., 2016; Kim et al., 2016 C. R.; Min-Kyu et al., 2016; Southwell et al., 2016; Anders and Steiniger, 2018; Vaičienė et al., 2018; Mandroukas et al., 2022).

Despite the large availability of experimental data, myoelectric activity patterns are rarely used for the development and validation of models of the active muscular behavior. Some studies (Biewener et al., 2014; Knodel et al., 2022; Schwaner et al., 2024) propose different approaches to correlate *in vivo* muscle dynamics based on EMG signals to *in situ* force length and force-velocity functions, aiming at the development of Hill type constitutive models. However, this approach, which could provide an advancement in muscle constitutive modeling, is not applied to the muscles of the human abdominal wall.

6.2 Ultrasound imaging

Another non-invasive technique used to quantitatively assess abdominal muscle contraction is US imaging. By providing visual feedback, US images offer valuable information on muscle activation, coordination, and function (ShahAli et al., 2019). The US images are obtained by means of a transducer-equipped ultrasound machine: a high-frequency sound wave emitted by the transducer is used to create a real-time image of the muscles, which is analyzed to evaluate the variation of muscle architecture and thickness during contraction and relaxation (Leighton, 2007).

Different authors evaluate the thickness of abdominal muscles at rest and during contraction in different positions (Hodges et al., 2003; Ainscough-Potts et al., 2006; Norasteh et al., 2007; Brown and McGill, 2008; Mew, 2009; Arab et al., 2013; Nabavi et al., 2014; ShahAli et al., 2015; Tran et al., 2016; Pirri et al., 2019; Johnson et al., 2021; Lin et al., 2021) or during expiratory loading (Kaneko et al., 2006).

Others focus on the difference in myogenic activation between healthy and pathological patients with chronic lower back pain (Vasseljen and Fladmark, 2010; Rasouli et al., 2011; Pulkovski et al., 2012), or on the effectiveness of rehabilitation in strengthening deep abdominal muscles, particularly the TA (McGalliard et al., 2010; Ishida and Watanabe, 2013; Sugimoto et al., 2018; Park et al., 2022). Further studies investigate possible differences in the size and conformation of the abdominal wall due to sex (Rho et al., 2013) or postpartum conditions (Coldron et al., 2008).

6.3 Combined EMG and ultrasound measurements

Although EMG and US imaging are effective tools to evaluate different features related to abdominal muscle contraction, each measurement alone is not sufficient to develop and validate FEM models of the abdominal wall. The increase in muscle thickness measured by US imaging during different motor tasks is generally interpreted as an indicator of muscle force generation. However, US measurements should be correlated with EMG data acquired simultaneously on the same subject, to associate muscle thickness increase with a specific myogenic activation.

Few studies consider the coupling of EMG and US to evaluate abdominal muscle contraction, since the correlation between increased muscle thickness and myogenic activation is still controversial. Although some authors try to find a positive correlation between muscle thickness in US images and EMG activity of the abdominal muscles, inconsistent relationships are generally identified during different motor tasks (Hodges et al., 2003; McMeeken et al., 2004; John and Beith, 2007; Brown and McGill, 2010). In addition, some studies (John and Beith, 2007; Coghlan et al., 2008) highlight a decrease in the thickness of lateral abdominal muscles during specific tasks.

Other approaches are proposed to evaluate the anatomical and mechanical properties of muscular motor units through the integration of high-density surface EMG and ultrafast US imaging in other skeletal muscles (Waasdorp et al., 2021; Carbonaro et al., 2023), identifying the regions where single motor unit fibers are located within the muscle cross-section *in vivo*. However, this approach is not directly applicable for the development and validation of FEM models at a larger scale.

6.4 Intra-abdominal pressure measurement

The IAP is defined as the pressure within the abdominal cavity that results from the interaction between the abdominal wall and the viscera. The physiological value of IAP oscillates due to the respiratory phases and to the activation of abdominal muscles (Milanesi and Caregnato, 2016).

The value of IAP can be measured directly or indirectly. Direct measurements are obtained by means of a needle or catheter in the peritoneal space, and IAP is measured using a fluid column or pressure transducer system (Risin et al., 2006). This method is generally considered the most accurate, even if it could be associated with side effects such as intestinal perforation and peritonitis. Indirect methods involve the measurement of the pressure transmitted to the lumen of an intra-abdominal structure or organ, including intragastric, intrarectal, intrauterine, intravesical, and vena cava access (Davis et al., 2005). Due to the common practice of intravesical catheterization, IAP is more frequently measured indirectly from intra-bladder pressure (IBP), since Kron et al. (1984) first proposed instrumental measurements with fluid-filled catheters. The reliability of this method is not fully established, and human studies correlating IAP with IBP are limited to few subjects and not entirely reproducible (Malbrain, 2004; Al-Abassi et al., 2018). Nonetheless, this indirect measurement is widely adopted in clinical practice and the IAP value is generally assumed to be equal to the IBP value. A comprehensive review of the different types of IAP sensors and their features, in terms of miniaturization, remote monitoring, and multiplexing is provided by Liao et al. (2021).

Basal IAP is usually less than 7 mmHg in healthy adults, while higher physiological baseline levels (9 to 14 mmHg) are found in

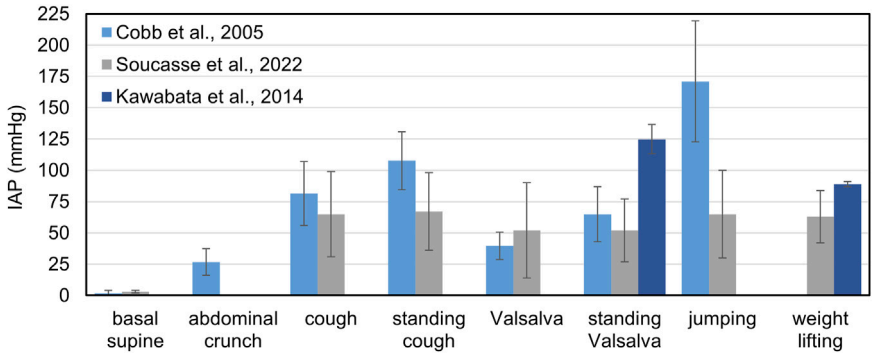

FIGURE 5
Mean values of IAP measured during several motor tasks by different authors.

morbidly obese patients (De Keulenaer et al., 2009). One of the first comprehensive studies assessing the value of IAP during different motor tasks is carried out by Cobb et al. (2005), who examine a group of 20 subjects (10 male and 10 female) with a mean age of 22.7 years and an average BMI of 24.6. No differences are recorded between men and women; however, the results exhibit high variability between subjects.

Chionh et al. (2006) consider 58 patients (40 men and 18 women) with an age range between 31 and 92 years and measure IAP in supine position and at different degrees of back rising. An increase in the mean IAP value is found as patient position becomes more upright: the mean values of IAP in the supine, 30° and 45° positions are 7.7 mmHg, 9.6 mmHg and 11.0 mmHg for men, and 5.1 mmHg, 7.0 mmHg and 9.6 mmHg, for women. Blazek et al. (2019) review the IAP measurements acquired in several studies during the Valsalva maneuver and different resistance exercises, reaching extremely high values of IAP over 200 mmHg in specific exercises such as squats and deadlift (Kawabata et al., 2010; 2014). Soucasse et al. (2022) propose an extensive analysis of IAP through an intragastric wireless sensor in 20 healthy subjects, both during supervised exercises and during their daily activities. Interestingly, this study highlights that during daily life the IAP values exceeding 50 mmHg, 100 mmHg, and 150 mmHg can be detected on average five times, twice, and once per hour, respectively. Kawabata and Shima, (2023) couple the measurements of IAP, by means of a pressure transducer placed intra-rectally, and EMG on fourteen healthy subjects, to evaluate the combined effect of different breathing patterns and postures on the activation abdominal muscle and the consequent IAP increase. Combining different methods for assessing muscular activity and IAP *in vivo* could be very useful for the development of FEM models of the abdominal wall.

A summary of the IAP values measured in different studies for specific motor tasks is reported in Figure 5.

6.5 Stiffness measurements

In daily clinical practice, abdominal stiffness is commonly assessed by palpation (Mota et al., 2013), which means that gentle pressure is applied manually to the abdomen and the wall compliance is evaluated qualitatively.

However, more accurate quantitative measurements are needed for the development of FEM models of the abdominal wall. To this purpose, several evaluations are made in the literature to assess the stiffness of the abdominal wall using different techniques, mainly in passive conditions. Some authors measure abdominal wall stiffness during inflation of the abdominal cavity with air. Van Ramshorst et al. (2011) perform a coupled *in vitro-in vivo* study: the abdomen of fourteen cadaveric subjects is insufflated in the *in vitro* study, whereas forty-two healthy subjects are enrolled to perform different motor tasks in the *in vivo* study. Using a custom-made indentation device, the stiffness of the abdominal wall is estimated in different regions (i.e., LA, RA, and lateral muscles), while recording the IAP values corresponding to the increase in the volume of inflation. This study demonstrates a correlation between IAP and the increase in abdominal stiffness, both in passive and active conditions. Tran et al. (2016) evaluate the local stiffness of the abdominal wall in eleven healthy subjects during different motor tasks, using ultrasound shear wave elastography. They show a significant increase of abdominal wall stiffness during muscle activation in the Valsalva maneuver and find that the values of local stiffness are more homogenous on the overall antero-lateral wall during muscular contraction than in passive conditions. Although shear wave elastography is a well-established technique (Dubois et al., 2015), its reliability may be affected by the difficulties in replicating and maintaining voluntary contraction during acquisition.

Remus et al. (2024) analyze the mechanical response of the antero-lateral abdominal wall of ten healthy subjects in different lying positions applying local indentation with a hemispherical probe and monitoring the displacement of the abdominal wall surface through 3D optical measurements. The acquisition is performed during both muscle contraction and relaxation, continuously monitoring myogenic activation with EMG. The force-displacement data obtained are used to estimate the stiffness of the abdominal tissue. Even in this study, an increase in the mean stiffness of the abdominal wall is found during muscle activation, with no significant differences between the regions considered for measurement acquisition. Moreover, inverse FEM modeling is used to estimate the constitutive parameters that allow to simulate the experimental behavior of the abdominal wall tissues. This study shows that local stiffness measurement, coupled with

other experimental data such as 3D geometric reconstruction and continuous EMG acquisition on the same subject can be adopted for the development and refinement of FEM models of the abdominal wall.

6.6 Surface deformation measurements

Another relevant aspect in the analysis of the abdomen biomechanics is related to the variation in the shape of the abdominal wall due to muscle activation in different motor tasks. While the passive abdomen is uniformly bulging under increasing IAP during inflation, the activation of the abdominal muscles induces specific deformed shapes of the antero-lateral wall depending on the different activation level of each muscle and related trunk motion. Quantitate data on 3D abdomen surface geometry are critically important for the validation of FEM models.

Szymczak et al. (2012) evaluate the abdominal wall deformation of eight healthy subjects during different standing movements, such as bending, stretching, and expiration, through.

The acquisition of markers position on the abdomen surface with two cameras placed in front of the subject. This method allows creating a surface that resembles the subject-specific abdomen in a relaxed standing position and during movements.

Differently, Todros et al. (2019) use laser scanning technique to acquire the surface of the abdominal wall of ten healthy subjects in a relaxed supine condition and during abdominal crunch. Their results show that muscular contraction induces an elevation of the abdominal wall in the region adjacent to LA in the posterior-anterior direction and a concurrent lowering of the lateral muscles in the mediolateral direction. Statistical analyses show a significant difference between the surfaces of the relaxed and contracted abdominal wall for each involved subject. The laser scanning technique adopted in this work is an accurate and reliable method of evaluating surface changes in the abdominal wall during muscular contraction. Nonetheless, as other optical methods of surface analysis, the presence of skin and subcutaneous fat tissue limit the reliability of the investigation to very thin subjects.

Lubowiecka et al. (2022) acquire *in vivo* optical measurements to determine the geometry of the abdominal wall while increasing the IAP, and build subject-specific 3D surface geometry of the anterior abdominal wall before and after the increase of IAP. This work provides information on the strain range of the living human abdominal wall in passive condition, showing strain up to 17% at maximum IAP of 13.6 mmHg. However, the investigation is limited to passive behavior and cannot be adopted to validate FEM models that simulate the active behavior. Similarly, Szepietowska et al. (2023) use digital image correlation to evaluate the deformation of the abdominal wall of twelve healthy subjects at different IAP levels (Figure 6). They highlight that the specific abdomen deformations found in each subject are difficult to correlate with IAP, due to a high variability among the mechanical properties of the abdominal tissues of the subjects.

A more accurate way to evaluate the deformation of the abdominal wall is dynamic MRI, which allows for repeated imaging of the trunk region and monitoring of both the superficial and deep components of the abdomen. Jourdan et al. (2021) develop a semi-automatic method for post-processing of dynamic MRI images to quantify the deformations of the abdominal wall muscles in ten healthy subjects during controlled breathing. This approach is then used (Jourdan et al., 2022) to compare the effect of different motor tasks, such as forced breathing, coughing, and Valsalva maneuver, on the abdominal wall geometry of twenty healthy subjects. The results show that in all the exercises lateral muscles shortening, thickening and inward displacement is observed. On the other hand, inhalation is correlated with a large outward displacement of RA muscles.

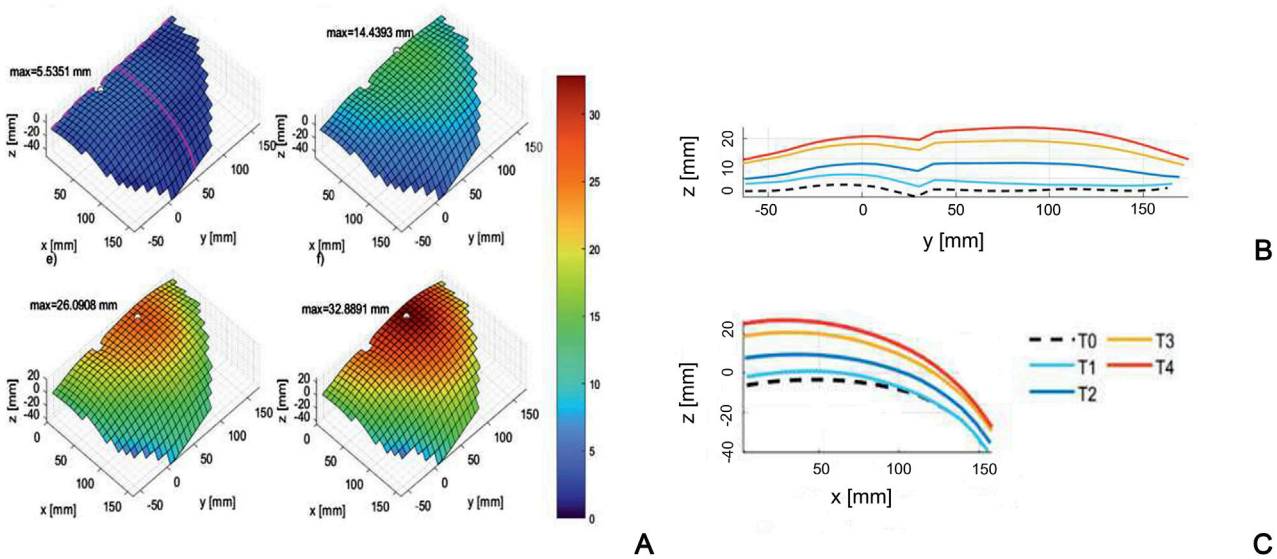

FIGURE 6
Surface of the abdominal wall of a subject **(A)** at different levels of the inflation process (T0÷T4), with corresponding profiles in craniocaudal **(B)** and mediolateral **(C)** sections. Reprinted from Szepietowska et al. (2023), Copyright 2023, with permission from Elsevier

In general, the combination of different techniques, including surface imaging associated with IAP measurement, or dynamic MRI with related image analysis and post-processing, represent useful tools to evaluate abdominal wall deformation during abdominal contraction and, therefore, to validate FEM models.

7 Discussion

As highlighted in the studies presented in this review, FEM-based numerical modeling can potentially be a valuable tool to improve our understanding of abdominal biomechanics in both healthy and pathological states. Computational approach may allow assessing the response of the abdominal wall under different loading conditions, such as under persistently elevated IAP induced in the abdominal compartment syndrome, or post-operative configuration, such as in hernia repair with surgical meshes.

The key aspect in the development and use of numerical models in the biomechanical field, and therefore also in the field of abdominal biomechanics, probably lies in their validation. This is a process which is implemented on experimental data obtained with various techniques. These techniques are used to assess a range of factors, including muscle contraction, muscle thickness, IAP variation, and abdominal surface deformation *in vivo* in human subjects. This is done with the aim of obtaining a comprehensive dataset that can be used to validate these models. Given the considerable complexity and variability of the anatomical site, the validation of a model seems to be intrinsically related to the need to be patient-specific, to consider multiple factors, such as anthropometric dimensions, muscular architecture, biomechanical characteristics of the various tissues, and the stiffness of the abdominal cavity, among others. Although this is undoubtedly the ideal approach, it is important to recognize that many of the techniques used to evaluate the necessary experimental data are, to some extent, invasive. Furthermore, it is understandable that such an approach may not be feasible as a routine one, particularly in view of the associated costs and time constraints. For instance, one might consider the evaluation of intra-abdominal pressure in various subjects as a function of the level of muscle activation or the intrinsic characteristics of muscle fibers, the latter of which can only be obtained through biopsies. It seems that these reasons may be the basis for the fact that the models proposed in the literature thus far have only been partially validated. This is not intended as a criticism of the various approaches, all of which are very rigorous from a scientific standpoint. Rather, it is simply a reflection on the inherent complexity of the problem. For this reason, the scientific community should be encouraged to build a public database containing all the necessary details of experimental protocols and corresponding results.

In the literature, there are both models that focus only on the passive behavior of the abdomen, and models that consider the phenomena of muscle contraction, typical of various motor tasks. Intuitively, models that consider the active behavior of the abdominal muscles appear potentially more effective for describing the behavior both in healthy conditions and in other conditions, for example, after post-surgical repair of abdominal hernias. Models that consider the active behavior of muscles are obviously more complex in their construction, but also require additional efforts for their validation. Integrating measurement of muscle thickness, activation, deformation, and variation in IAP is essential to improve the understanding of abdominal muscle function and its role in various contexts, such as injury prevention and rehabilitation. It should be noted, however, that each different measurement technique alone cannot fully describe the behavior of the abdominal wall structure. To properly assess active muscle behavior, all the available information from different test methods should be combined to better understanding of abdominal biomechanics and improve the accuracy of numerical models.

It seems reasonable to assume that in the future there will be a growing number of patient-specific models of the abdomen, at least in terms of anatomical data. It is already possible to reconstruct anatomical details, such as the thickness of muscles or fascial systems, using highly versatile software. This would require the experimental basis available with MRI, CT, or ultrasound methods. It is also worth noting that there is still room for improvement in terms of the constitutive modeling of the mechanical characteristics of the tissues, whether they are connective or muscular. Obviously, these characteristics cannot be obtained from the subject/patient on which to define the model. It seems reasonable to suggest making every effort to broaden as much as possible the mechanical data on the various tissues from *in vitro* or *ex vitro* tests. This would allow to build a data set that would enable us to define confidence intervals for the various tissues (for example, stiffness for fascial tissues, force-length curves and maximum isometric tension for muscle tissues). These confidence intervals could then be used in the numerical models to obtain the corresponding response intervals from the models.

Author contributions

SS: Formal Analysis, Writing–original draft. ST: Conceptualization, Writing–review and editing. PP: Conceptualization, Writing–review and editing.

Funding

The author(s) declare financial support was received for the research, authorship, and/or publication of this article. Open Access funding provided by Università degli Studi di Padova | University of Padua, Open Science Committee.

Conflict of interest

The authors declare that the research was conducted in the absence of any commercial or financial relationships that could be construed as a potential conflict of interest.

The author(s) declared that they were an editorial board member of Frontiers, at the time of submission. This had no impact on the peer review process and the final decision.

Publisher's note

References

Ainscough-Potts, A. M., Morrissey, M. C., and Critchley, D. (2006). The response of the transverse abdominis and internal oblique muscles to different postures. *Man. Ther.* 11, 54–60. doi:10.1016/j.math.2005.03.007

Al-Abassi, A. A., Al Saadi, A. S., and Ahmed, F. (2018). Is intra-bladder pressure measurement a reliable indicator for raised intra-abdominal pressure? A prospective comparative study. *BMC Anesthesiol.* 18, 69. doi:10.1186/s12871-018-0539-z

Anders, C., and Steiniger, B. (2018). Main force directions of trunk muscles: a pilot study in healthy male subjects. *Hum. Mov. Sci.* 60, 214–224. doi:10.1016/j.humov.2018.06.012

Arab, A. M., Rasouli, O., Amiri, M., and Tahan, N. (2013). Reliability of ultrasound measurement of automatic activity of the abdominal muscle in participants with and without chronic low back pain. *Chiropr. Man. Ther.* 21, 37. doi:10.1186/2045-709X-21-37

Astruc, L., De Meulaere, M., Witz, J.-F., Nováček, V., Turquier, F., Hoc, T., et al. (2018). Characterization of the anisotropic mechanical behavior of human abdominal wall connective tissues. *J. Mech. Behav. Biomed. Mater* 82, 45–50. doi:10.1016/j.jmbbm.2018.03.012

Axer, H., Keyserlingk, D. G. v., and Prescher, A. (2001). Collagen fibers in linea alba and rectus sheaths. *J. Surg. Res.* 96, 239–245. doi:10.1006/jsre.2000.6071

Ben Abdelounis, H., Nicolle, S., Otténio, M., Beillas, P., and Mitton, D. (2013). Effect of two loading rates on the elasticity of the human anterior rectus sheath. *J. Mech. Behav. Biomed. Mater* 20, 1–5. doi:10.1016/j.jmbbm.2012.12.002

Biewener, A. A., Wakeling, J. M., Lee, S. S., and Arnold, A. S. (2014). Validation of hill-type muscle models in relation to neuromuscular recruitment and force-velocity properties: predicting patterns of *in vivo* muscle force. *Integr. Comp. Biol.* 54, 1072–1083. doi:10.1093/icb/icu070

Bjerkefors, A., Ekblom, M. M., Josefsson, K., and Thorstensson, A. (2010). Deep and superficial abdominal muscle activation during trunk stabilization exercises with and without instruction to hollow. *Man. Ther.* 15, 502–507. doi:10.1016/j.math.2010.05.006

Blazek, D., Stastny, P., Maszczyk, A., Krawczyk, M., Matykiewicz, P., and Petr, M. (2019). Systematic review of intra-abdominal and intrathoracic pressures initiated by the Valsalva manoeuvre during high-intensity resistance exercises. *Biol. Sport* 36, 373–386. doi:10.5114/biolsport.2019.88759

Brown, S. H. M., and McGill, S. M. (2008). An ultrasound investigation into the morphology of the human abdominal wall uncovers complex deformation patterns during contraction. *Eur. J. Appl. Physiol.* 104, 1021–1030. doi:10.1007/s00421-008-0858-8

Brown, S. H. M., and McGill, S. M. (2010). A comparison of ultrasound and electromyography measures of force and activation to examine the mechanics of abdominal wall contraction. *Clin. Biomech.* 25, 115–123. doi:10.1016/j.clinbiomech.2009.10.001

Brown, S. H. M., Ward, S. R., Cook, M. S., and Lieber, R. L. (2011). Architectural analysis of human abdominal wall muscles: implications for mechanical function. *Spine (Phila Pa 1976)* 36, 355–362. doi:10.1097/BRS.0b013e3181d12ed7

Carbonaro, M., Rohlén, R., Seoni, S., Meiburger, K. M., Vieira, T., Grönlund, C., et al. (2023). Combining high-density electromyography and ultrafast ultrasound to assess individual motor unit properties *in vivo*. *bioRxiv* 2023. doi:10.1101/2023.07.03.547503

Cardoso, M. (2012). Experimental study of the human anterolateral abdominal wall: biomechanical properties of fascia and muscles. Available at: https://repositorio-aberto.up.pt/bitstream/10216/65576/1/000154315.pdf.

Chionh, J. J. L., Wei, B. P. C., Martin, J. A., and Opdam, H. I. (2006). Determining normal values for intra-abdominal pressure. *ANZ J. Surg.* 76, 1106–1109. doi:10.1111/j.1445-2197.2006.03849.x

Cobb, W. S., Burns, J. M., Kercher, K. W., Matthews, B. D., James Norton, H., and Todd Heniford, B. (2005). Normal intraabdominal pressure in healthy adults. *J. Surg. Res.* 129, 231–235. doi:10.1016/j.jss.2005.06.015

Coghlan, S., Crowe, L., McCarthyPersson, U., Minogue, C., and Caulfield, B. (2008). "Electrical muscle stimulation for deep stabilizing muscles in abdominal wall," in 2008 30th annual international conference (IEEE Engineering in Medicine and Biology Society), 2756–2759. doi:10.1109/IEMBS.2008.4649773

Colavita, P. D., Tsirline, V. B., Walters, A. L., Lincourt, A. E., Belyansky, I., and Heniford, B. T. (2013). Laparoscopic versus open hernia repair: outcomes and sociodemographic utilization results from the nationwide inpatient sample. *Surg. Endosc.* 27, 109–117. doi:10.1007/s00464-012-2432-z

Coldron, Y., Stokes, M. J., Newham, D. J., and Cook, K. (2008). Postpartum characteristics of rectus abdominis on ultrasound imaging. *Man. Ther.* 13, 112–121. doi:10.1016/j.math.2006.10.001

Cooney, G. M., Lake, S. P., Thompson, D. M., Castile, R. M., Winter, D. C., and Simms, C. K. (2016). Uniaxial and biaxial tensile stress-stretch response of human linea alba. *J. Mech. Behav. Biomed. Mater* 63, 134–140. doi:10.1016/j.jmbbm.2016.06.015

Crommert, M. E., Ekblom, M. M., and Thorstensson, A. (2011). Activation of transversus abdominis varies with postural demand in standing. *Gait Posture* 33, 473–477. doi:10.1016/j.gaitpost.2010.12.028

Czaprowski, D., Afeltowicz, A., Gebicka, A., Pawłowska, P., Kedra, A., Barrios, C., et al. (2014). Abdominal muscle EMG-activity during bridge exercises on stable and unstable surfaces. *Phys. Ther. Sport* 15, 162–168. doi:10.1016/j.ptsp.2013.09.003

Davis, P. J., Koottayi, S., Taylor, A., and Butt, W. W. (2005). Comparison of indirect methods of measuring intra-abdominal pressure in children. *Intensive Care Med.* 31, 471–475. doi:10.1007/s00134-004-2539-3

Deeken, C. R., and Lake, S. P. (2017). Mechanical properties of the abdominal wall and biomaterials utilized for hernia repair. *J. Mech. Behav. Biomed. Mater* 74, 411–427. doi:10.1016/j.jmbbm.2017.05.008

De Keulenaer, B. L., De Waele, J. J., Powell, B., and Malbrain, M. L. N. G. (2009). What is normal intra-abdominal pressure and how is it affected by positioning, body mass and positive end-expiratory pressure? *Intensive Care Med.* 35, 969–976. doi:10.1007/s00134-009-1445-0

Drysdale, C. L., Earl, J. E., and Hertel, J. (2004). Surface electromyographic activity of the abdominal muscles during pelvic-tilt and abdominal-hollowing exercises. *J. Athl. Train.* 39, 32–36.

Dubois, G., Kheireddine, W., Vergari, C., Bonneau, D., Thoreux, P., Rouch, P., et al. (2015). Reliable protocol for shear wave elastography of lower limb muscles at rest and during passive stretching. *Ultrasound Med. Biol.* 41, 2284–2291. doi:10.1016/j.ultrasmedbio.2015.04.020

Escamilla, R. F., Lewis, C., Bell, D., Bramblet, G., Daffron, J., Lambert, S., et al. (2010). Core muscle activation during Swiss ball and traditional abdominal exercises. *J. Orthop. Sports Phys. Ther.* 40, 265–276. doi:10.2519/jospt.2010.3073

Flynn, W., and Vickerton, P. (2022). *Anatomy, abdomen and pelvis, abdominal wall.* Treasure Island (FL): StatPearls Publishing. Available at: http://europepmc.org/books/NBK551649.

Förstemann, T., Trzewik, J., Holste, J., Batke, B., Konerding, M. A., Wolloscheck, T., et al. (2011). Forces and deformations of the abdominal wall-A mechanical and geometrical approach to the linea alba. *J. Biomech.* 44, 600–606. doi:10.1016/j.jbiomech.2010.11.021

García-Vaquero, M. P., Moreside, J. M., Brontons-Gil, E., Peco-González, N., and Vera-Garcia, F. J. (2012). Trunk muscle activation during stabilization exercises with single and double leg support. *J. Electromyogr. Kinesiol.* 22, 398–406. doi:10.1016/j.jelekin.2012.02.017

Grasa, J., Sierra, M., Lauzeral, N., Muñoz, M. J., Miana-Mena, F. J., and Calvo, B. (2016). Active behavior of abdominal wall muscles: experimental results and numerical model formulation. *J. Mech. Behav. Biomed. Mater* 61, 444–454. doi:10.1016/j.jmbbm.2016.04.013

Gräβel, D., Prescher, A., Fitzek, S., Keyserlingk, D. G. v., and Axer, H. (2005). Anisotropy of human linea alba: a biomechanical study. *J. Surg. Res.* 124, 118–125. doi:10.1016/j.jss.2004.10.010

Grevious, M. A., Cohen, M., Shah, S. R., and Rodriguez, P. (2006). Structural and functional anatomy of the abdominal wall. *Clin. Plast. Surg.* 33, 169–179. doi:10.1016/j.cps.2005.12.005

He, W., Liu, X., Wu, S., Liao, J., Cao, G., Fan, Y., et al. (2020). A numerical method for guiding the design of surgical meshes with suitable mechanical properties for specific abdominal hernias. *Comput. Biol. Med.* 116, 103531. doi:10.1016/j.compbiomed.2019.103531

Heniford, B. T., Park, A., Ramshaw, B. J., and Voeller, G. (2003). Laparoscopic repair of ventral hernias. *Ann. Surg.* 238, 391–400. doi:10.1097/01.sla.0000086662.49499.ab

Hernández, B., Peña, E., Pascual, G., Rodríguez, M., Calvo, B., Doblaré, M., et al. (2011). Mechanical and histological characterization of the abdominal muscle. A previous step to modelling hernia surgery. *J. Mech. Behav. Biomed. Mater* 4, 392–404. doi:10.1016/j.jmbbm.2010.11.012

Hernández-Gascón, B., Espés, N., Peña, E., Pascual, G., Bellón, J. M., and Calvo, B. (2014). Computational framework to model and design surgical meshes for hernia repair. *Comput. Methods Biomech. Biomed. Engin* 17, 1071–1085. doi:10.1080/10255842.2012.736967

Hernández-Gascón, B., Mena, A., Peña, E., Pascual, G., Bellón, J. M., and Calvo, B. (2013a). Understanding the passive mechanical behavior of the human abdominal wall. *Ann. Biomed. Eng.* 41, 433–444. doi:10.1007/s10439-012-0672-7

Hernández-Gascón, B., Peña, E., Grasa, J., Pascual, G., Bellón, J. M., and Calvo, B. (2013b). Mechanical response of the herniated human abdomen to the placement of different prostheses. *J. Biomech. Eng.* 135, 51004–51008. doi:10.1115/1.4023703

Hodges, P. W., Pengel, L. H. M., Herbert, R. D., and Gandevia, S. C. (2003). Measurement of muscle contraction with ultrasound imaging. *Muscle Nerve* 27, 682–692. doi:10.1002/mus.10375

Hollinsky, C., and Sandberg, S. (2007). Measurement of the tensile strength of the ventral abdominal wall in comparison with scar tissue. *Clin. Biomech.* 22, 88–92. doi:10.1016/j.clinbiomech.2006.06.002

Ishida, H., and Watanabe, S. (2013). Changes in lateral abdominal muscles' thickness immediately after the abdominal drawing-in maneuver and maximum expiration. *J. Bodyw. Mov. Ther.* 17, 254–258. doi:10.1016/j.jbmt.2012.12.002

Jenkins, J. T., and O'Dwyer, P. J. (2008). Inguinal hernias. *Bmj* 336, 269–272. AD. doi:10.1136/bmj.39450.428275.ad

John, E. K., and Beith, I. D. (2007). Can activity within the external abdominal oblique be measured using real-time ultrasound imaging? *Clin. Biomech.* 22, 972–979. doi:10.1016/j.clinbiomech.2007.07.005

Johnson, A. W., Adams, L., Kho, J. B., Green, D. M., Pace, N. B., and Mitchell, U. H. (2021). Extended field-of-view ultrasound imaging is reliable for measuring Transversus Abdominis muscle size at rest and during contraction. *BMC Musculoskelet. Disord.* 22, 282–310. doi:10.1186/s12891-021-04157-0

Jourdan, A., Dhume, R., Guérin, E., Siegel, A., Le Ruyet, A., and Palmer, M. (2024). Numerical investigation of a finite element abdominal wall model during breathing and muscular contraction. *Comput. Methods Programs Biomed.* 244, 107985. doi:10.1016/j.cmpb.2023.107985

Jourdan, A., Le Troter, A., Daude, P., Rapacchi, S., Masson, C., Bège, T., et al. (2021). Semiautomatic quantification of abdominal wall muscles deformations based on dynamic MRI image registration. *NMR Biomed.* 34, e4470. doi:10.1002/nbm.4470

Jourdan, A., Rapacchi, S., Guye, M., Bendahan, D., Masson, C., and Bège, T. (2022). Dynamic-MRI quantification of abdominal wall motion and deformation during breathing and muscular contraction. *Comput. Methods Programs Biomed.* 217, 106667. doi:10.1016/j.cmpb.2022.106667

Kaneko, H., Sato, H., and Maruyama, H. (2006). Evaluation of lateral abdominal muscle activity during expiratory threshold loading by ultrasonography. *J. Phys. Ther. Sci.* 18, 187–191. doi:10.1589/jpts.18.187

Karami, M., Zohoor, H., Calvo, B., and Grasa, J. (2023). A 3D multi-scale skeletal muscle model to predict active and passive responses. Application to intra-abdominal pressure prediction. *Comput. Methods Appl. Mech. Eng.* 415, 116222. doi:10.1016/j.cma.2023.116222

Karrech, A., Ahmad, H., and Hamdorf, J. M. (2023). Biomechanical stability of hernia-damaged abdominal walls. *Sci. Rep.* 13, 4936. doi:10.1038/s41598-023-31674-w

Kawabata, M., and Shima, N. (2023). Interaction of breathing pattern and posture on abdominal muscle activation and intra-abdominal pressure in healthy individuals: a comparative cross-sectional study. *Sci. Rep.* 13, 11338. doi:10.1038/s41598-023-37629-5

Kawabata, M., Shima, N., Hamada, H., Nakamura, I., and Nishizono, H. (2010). Changes in intra-abdominal pressure and spontaneous breath volume by magnitude of lifting effort: highly trained athletes versus healthy men. *Eur. J. Appl. Physiol.* 109, 279–286. doi:10.1007/s00421-009-1344-7

Kawabata, M., Shima, N., and Nishizono, H. (2014). Regular change in spontaneous preparative behaviour on intra-abdominal pressure and breathing during dynamic lifting. *Eur. J. Appl. Physiol.* 114, 2233–2239. doi:10.1007/s00421-014-2944-4

Kim, C. R., Park, D. K., Lee, S. T., and Ryu, J. S. (2016a). Electromyographic changes in trunk muscles during graded lumbar stabilization exercises. *PM R* 8, 979–989. doi:10.1016/j.pmrj.2016.05.017

Kim, S. Y., Kang, M. H., Kim, E. R., Jung, I. G., Seo, E. Y., and Oh, J. seop (2016b). Comparison of EMG activity on abdominal muscles during plank exercise with unilateral and bilateral additional isometric hip adduction. *J. Electromyogr. Kinesiol.* 30, 9–14. doi:10.1016/j.jelekin.2016.05.003

Knodel, N. B., Calvert, L. B., Bywater, E. A., Lamia, J. P., Patel, S. N., and Nauman, E. A. (2022). An electromyography-based constitutive law for force generation in skeletal muscle—Part II: model validation on the ankle joint complex. *J. Biomech. Eng.* 144, 101006. doi:10.1115/1.4054275

Konerding, M. A., Bohn, M., Wolloscheck, T., Batke, B., Holste, J.-L., Wohlert, S., et al. (2011). Maximum forces acting on the abdominal wall: experimental validation of a theoretical modeling in a human cadaver study. *Med. Eng. Phys.* 33, 789–792. doi:10.1016/j.medengphy.2011.01.010

Kriener, K., Lala, R., Anthony, R., Homes, P., Williams, M. K., Midwinter, M. J., et al. (2023). Mechanical characterization of the human abdominal wall using uniaxial tensile testing. *Bioeng. (Basel).* 10, 1213. doi:10.3390/bioengineering10101213

Kron, I. L., Harman, P. K., and Nolan, S. P. (1984). The measurement of intra-abdominal pressure as a criterion for abdominal Re-exploration. *Ann. Surg.* 199, 28–30. doi:10.1097/00000658-198401000-00005

Lancerotto, L., Stecco, C., Macchi, V., Porzionato, A., Stecco, A., and De Caro, R. (2011). Layers of the abdominal wall: anatomical investigation of subcutaneous tissue and superficial fascia. *Surg. Radiologic Anat.* 33, 835–842. doi:10.1007/s00276-010-0772-8

Lee, D. H., Hong, S. K., Lee, Y.-S., Kim, C.-H., Hwang, J. M., Lee, Z., et al. (2018). Is abdominal hollowing exercise using real-time ultrasound imaging feedback helpful for selective strengthening of the transversus abdominis muscle? *Medicine* 97, e11369. doi:10.1097/MD.0000000000011369

Leighton, T. G. (2007). What is ultrasound? *Prog. Biophys. Mol. Biol.* 93, 3–83. doi:10.1016/J.PBIOMOLBIO.2006.07.026

Levillain, A., Orhant, M., Turquier, F., and Hoc, T. (2016). Contribution of collagen and elastin fibers to the mechanical behavior of an abdominal connective tissue. *J. Mech. Behav. Biomed. Mater* 61, 308–317. doi:10.1016/j.jmbbm.2016.04.006

Liao, C.-H., Cheng, C.-T., Chen, C.-C., Wang, Y.-H., Chiu, H.-T., Peng, C.-C., et al. (2021). Systematic review of diagnostic sensors for intra-abdominal pressure monitoring. *Sensors* 21, 4824. doi:10.3390/s21144824

Lin, S., Zhu, B., Zheng, Y., Huang, G., Zeng, Q., and Wang, C. (2021). Effect of real-time ultrasound imaging for biofeedback on trunk muscle contraction in healthy subjects: a preliminary study. *BMC Musculoskelet. Disord.* 22, 1–8. doi:10.1186/s12891-021-04429-9

Lubowiecka, I., Szepietowska, K., Tomaszewska, A., Bielski, P. M., Chmielewski, M., Lichodziejewska-Niemierko, M., et al. (2022). A novel *in vivo* approach to assess strains of the human abdominal wall under known intraabdominal pressure. *J. Mech. Behav. Biomed. Mater* 125, 104902. doi:10.1016/j.jmbbm.2021.104902

Malbrain, M. L. N. G. (2004). Different techniques to measure intra-abdominal pressure (IAP): time for a critical re-appraisal. *Intensive Care Med.* 30, 357–371. doi:10.1007/s00134-003-2107-2

Mandroukas, A., Michailidis, Y., Kyranoudis, A. E., Christoulas, K., and Metaxas, T. (2022). Surface electromyographic activity of the rectus abdominis and external oblique during isometric and dynamic exercises. *J. Funct. Morphol. Kinesiol* 7, 67. doi:10.3390/jfmk7030067

Marcucci, L., Reggiani, C., Natali, A. N., and Pavan, P. G. (2017). From single muscle fiber to whole muscle mechanics: a finite element model of a muscle bundle with fast and slow fibers. *Biomech. Model Mechanobiol.* 16, 1833–1843. doi:10.1007/s10237-017-0922-6

Martins, P., Peña, E., Jorge, N. R. M., Santos, A., Santos, L., Mascarenhas, T., et al. (2012). Mechanical characterization and constitutive modelling of the damage process in rectus sheath. *J. Mech. Behav. Biomed. Mater* 8, 111–122. doi:10.1016/j.jmbbm.2011.12.005

McGalliard, M. K., Dedrick, G. S., Brismée, J. M., Cook, C. E., Apte, G. G., and Sizer, P. S. (2010). Changes in transversus abdominis thickness with use of the abdominal drawing-in maneuver during a functional task. *PM R* 2, 187–194. doi:10.1016/j.pmrj.2010.01.015

McMeeken, J. M., Beith, I. D., Newham, D. J., Milligan, P., and Critchley, D. J. (2004). The relationship between EMG and change in thickness of transversus abdominis. *Clin. Biomech.* 19, 337–342. doi:10.1016/j.clinbiomech.2004.01.007

Meier, A. H., Rawn, C. L., and Krummel, T. M. (2001). Virtual reality: surgical application - challenge for the new millennium. *J. Am. Coll. Surg.* 192, 372–384. doi:10.1016/S1072-7515(01)00769-4

Mew, R. (2009). Comparison of changes in abdominal muscle thickness between standing and crook lying during active abdominal hollowing using ultrasound imaging. *Man. Ther.* 14, 690–695. doi:10.1016/j.math.2009.05.003

Milanesi, R., and Caregnato, R. C. A. (2016). Intra-abdominal pressure: an integrative review. *Einstein (Sao Paulo)* 14, 423–430. doi:10.1590/S1679-45082016RW3088

Min-Kyu, K., Cho, Y.-H., Park, J.-W., Choi, J.-H., and Ko, Y.-M. (2016). The effects of the contraction degree of hip joint adductor on abdominal muscle activity during bilateral lower extremity raising. *J. Korean Phys. Ther.* 28, 217–220. doi:10.18857/jkpt.2016.28.3.217

Monfort-Pañego, M., Vera-García, F. J., Sánchez-Zuriaga, D., and Sarti-Martínez, M. Á. (2009). Electromyographic studies in abdominal exercises: a literature synthesis. *J. Manip. Physiol. Ther.* 32, 232–244. doi:10.1016/j.jmpt.2009.02.007

Moraes, A. C., Pinto, R. S., Valamatos, M. J., Valamatos, M. J., Pezarat-Correia, P. L., Okano, A. H., et al. (2009). EMG activation of abdominal muscles in the crunch exercise performed with different external loads. *Phys. Ther. Sport* 10, 57–62. doi:10.1016/j.ptsp.2009.01.001

Mota, P., Pascoal, A. G., Sancho, F., Carita, A. I., and Bø, K. (2013). Reliability of the inter-rectus distance measured by palpation. Comparison of palpation and ultrasound measurements. *Man. Ther.* 18, 294–298. doi:10.1016/J.MATH.2012.10.013

Mudge, M., and Hughes, L. E. (1985). Incisional hernia: a 10 year prospective study of incidence and attitudes. *Br. J. Surg.* 72, 70–71. doi:10.1002/bjs.1800720127

Nabavi, N., Mosallanezhad, Z., Haghighatkhah, H. R., and Ali Mohseni Bandpeid, M. (2014). Reliability of rehabilitative Ultrasonography to measure transverse abdominis and multifidus muscle dimensions. *Iran. J. Radiology* 11, e21008–e21013. doi:10.5812/iranjradiol.21008

Norasteh, A., Ebrahimi, E., Salavati, M., Rafiei, J., and Abbasnejad, E. (2007). Reliability of B-mode ultrasonography for abdominal muscles in asymptomatic and patients with acute low back pain. *J. Bodyw. Mov. Ther.* 11, 17–20. doi:10.1016/j.jbmt.2005.11.002

Okubo, Y., Kaneoka, K., Mai, A., Shiina, I., Tatsumura, M., Izumi, S., et al. (2010). Electromyographic analysis of transversus abdominis and lumbar multifidus using wire electrodes during lumbar stabilization exercises. *J. Orthop. Sports Phys. Ther.* 40, 743–750. doi:10.2519/jospt.2010.3192

Pachera, P., Pavan, P. G., Todros, S., Cavinato, C., Fontanella, C. G., and Natali, A. N. (2016). A numerical investigation of the healthy abdominal wall structures. *J. Biomech.* 49, 1818–1823. doi:10.1016/j.jbiomech.2016.04.019

Park, S. Y., Oh, S., Baek, K. H., Bae, S. S., and Kwon, J. W. (2022). Comparison of abdominal muscle thickness between the abdominal draw-in maneuver and maximum abdominal contraction maneuver. *Healthc. Switz.* 10, 251. doi:10.3390/healthcare10020251

Pavan, P. G., Todros, S., Pachera, P., Pianigiani, S., and Natali, A. N. (2019). The effects of the muscular contraction on the abdominal biomechanics: a numerical investigation. *Comput. Methods Biomech. Biomed. Engin* 22, 139–148. doi:10.1080/10255842.2018.1540695

Pirri, C., Todros, S., Fede, C., Pianigiani, S., Fan, C., Foti, C., et al. (2019). Inter-rater reliability and variability of ultrasound measurements of abdominal muscles and fasciae thickness. *Clin. Anat.* 32, 948–960. doi:10.1002/ca.23435

Pulkovski, N., Mannion, A. F., Caporaso, F., Toma, V., Gubler, D., Helbling, D., et al. (2012). Ultrasound assessment of transversus abdominis muscle contraction ratio during abdominal hollowing: a useful tool to distinguish between patients with chronic low back pain and healthy controls? *Eur. Spine J.* 21, 750–759. doi:10.1007/s00586-011-1707-8

Rasouli, O., Arab, A. M., Amiri, M., and Jaberzadeh, S. (2011). Ultrasound measurement of deep abdominal muscle activity in sitting positions with different stability levels in subjects with and without chronic low back pain. *Man. Ther.* 16, 388–393. doi:10.1016/j.math.2011.01.009

Remus, R., Sure, C., Selkmann, S., Uttich, E., and Bender, B. (2024). Soft tissue material properties based on human abdominal *in vivo* macro-indenter measurements. *Front. Bioeng. Biotechnol.* 12, 1384062. doi:10.3389/fbioe.2024.1384062

Rho, M., Spitznagle, T., Van Dillen, L., Maheswari, V., Oza, S., and Prather, H. (2013). Gender differences on ultrasound imaging of lateral abdominal muscle thickness in asymptomatic adults: a pilot study. *PM R* 5, 374–380. doi:10.1016/j.pmrj.2013.03.003

Risin, E., Kessel, B., Ashkenazi, I., Lieberman, N., and Alfici, R. (2006). A new technique of direct intra-abdominal pressure measurement: a preliminary study. *Am. J. Surg.* 191, 235–237. doi:10.1016/j.amjsurg.2005.07.038

Schwaner, M. J., Mayfield, D. L., Azizi, E., and Daley, M. A. (2024). Linking *in vivo* muscle dynamics to *in situ* force-length and force-velocity reveals that Guinea fowl lateral gastrocnemius operates at shorter than optimal lengths. *J. Exp. Biol.* doi:10.1242/jeb.246879

ShahAli, S., Arab, A. M., Talebian, S., Ebrahimi, E., Bahmani, A., Karimi, N., et al. (2015). Reliability of ultrasound thickness measurement of the abdominal muscles during clinical isometric endurance tests. *J. Bodyw. Mov. Ther.* 19, 396–403. doi:10.1016/j.jbmt.2014.05.009

ShahAli, S., Shanbehzadeh, S., ShahAli, S., and Ebrahimi Takamjani, I. (2019). Application of ultrasonography in the assessment of abdominal and lumbar trunk muscle activity in participants with and without low back pain: a systematic review. *J. Manip. Physiol. Ther.* 42, 541–550. doi:10.1016/j.jmpt.2019.05.003

Song, C., Alijani, A., Frank, T., Hanna, G. B., and Cuschieri, A. (2006). Mechanical properties of the human abdominal wall measured *in vivo* during insufflation for laparoscopic surgery. *Surg. Endosc.* 20, 987–990. doi:10.1007/s00464-005-0676-6

Soucasse, A., Jourdan, A., Edin, L., Gillion, J.-F., Masson, C., and Bege, T. (2022). A better understanding of daily life abdominal wall mechanical solicitation: investigation of intra-abdominal pressure variations by intragastric wireless sensor in humans. *Med. Eng. Phys.* 104, 103813. doi:10.1016/j.medengphy.2022.103813

Southwell, D. J., Hills, N. F., McLean, L., and Graham, R. B. (2016). The acute effects of targeted abdominal muscle activation training on spine stability and neuromuscular control. *J. Neuroeng Rehabil.* 13, 19–28. doi:10.1186/s12984-016-0126-9

Sugimoto, T., Yokogawa, M., Miaki, H., Madokoro, S., and Nakagawa, T. (2018). Changes in thickness of the transversus abdominis during the abdominal drawing-in manoeuvre and expiratory muscle training in elderly people. *J. Phys. Ther. Sci.* 30, 119–123. doi:10.1589/jpts.30.119

Szepietowska, K., Troka, M., Lichodziejewska-Niemierko, M., Chmielewski, M., and Lubowiecka, I. (2023). Full-field *in vivo* experimental study of the strains of a breathing human abdominal wall with intra-abdominal pressure variation. *J. Mech. Behav. Biomed. Mater* 147, 106148. doi:10.1016/j.jmbbm.2023.106148

Szymczak, C., Lubowiecka, I., Tomaszewska, A., and Śmietański, M. (2012). Investigation of abdomen surface deformation due to life excitation: implications for implant selection and orientation in laparoscopic ventral hernia repair. *Clin. Biomech.* 27, 105–110. doi:10.1016/j.clinbiomech.2011.08.008

Todros, S., de Cesare, N., Concheri, G., Natali, A. N., and Pavan, P. G. (2020). Numerical modelling of abdominal wall mechanics: the role of muscular contraction and intra-abdominal pressure. *J. Mech. Behav. Biomed. Mater* 103, 103578. doi:10.1016/j.jmbbm.2019.103578

Todros, S., de Cesare, N., Pianigiani, S., Concheri, G., Savio, G., Natali, A. N., et al. (2019). 3D surface imaging of abdominal wall muscular contraction. *Comput. Methods Programs Biomed.* 175, 103–109. doi:10.1016/j.cmpb.2019.04.013

Todros, S., Pachera, P., Baldan, N., Pavan, P. G., Pianigiani, S., Merigliano, S., et al. (2018). Computational modeling of abdominal hernia laparoscopic repair with a surgical mesh. *Int. J. Comput. Assist. Radiol. Surg.* 13, 73–81. doi:10.1007/s11548-017-1681-7

Tran, D., Podwojewski, F., Beillas, P., Ottenio, M., Voirin, D., Turquier, F., et al. (2016). Abdominal wall muscle elasticity and abdomen local stiffness on healthy volunteers during various physiological activities. *J. Mech. Behav. Biomed. Mater* 60, 451–459. doi:10.1016/j.jmbbm.2016.03.001

Tuset, L., López-Cano, M., Fortuny, G., López, J. M., Herrero, J., and Puigjaner, D. (2022). Virtual simulation of the biomechanics of the abdominal wall with different stoma locations. *Sci. Rep.* 12, 3545–3549. doi:10.1038/s41598-022-07555-z

Urquhart, D. M., Hodges, P. W., Allen, T. J., and Story, I. H. (2005). Abdominal muscle recruitment during a range of voluntary exercises. *Man. Ther.* 10, 144–153. doi:10.1016/j.math.2004.08.011

Vaičienė, G., Berškienė, K., Slapsinskaite, A., Mauricienė, V., and Razon, S. (2018). Not only static: stabilization manoeuvres in dynamic exercises – a pilot study. *PLoS One* 13, 02010177. doi:10.1371/journal.pone.0201017

Van Ramshorst, G. H., Salih, M., Hop, W. C. J., Waes, O. J. F. V., Kleinrensink, G. J., Goossens, R. H. M., et al. (2011). Noninvasive assessment of intra-abdominal pressure by measurement of abdominal wall tension. *J. Surg. Res.* 171, 240–244. doi:10.1016/j.jss.2010.02.007

Vasseljen, O., and Fladmark, A. M. (2010). Abdominal muscle contraction thickness and function after specific and general exercises: a randomized controlled trial in chronic low back pain patients. *Man. Ther.* 15, 482–489. doi:10.1016/j.math.2010.04.004

Waasdorp, R., Mugge, W., Vos, H. J., de Groot, J. H., Verweij, M. D., de Jong, N., et al. (2021). Combining ultrafast ultrasound and high-density EMG to assess local electromechanical muscle dynamics: a feasibility study. *IEEE Access* 9, 45277–45288. doi:10.1109/ACCESS.2021.3067162

frontiers | Frontiers in Bioengineering and Biotechnology

TYPE Original Research
PUBLISHED 01 October 2024
DOI 10.3389/fbioe.2024.1436235

OPEN ACCESS

EDITED BY
Yih-Kuen Jan,
University of Illinois at Urbana-Champaign, United States

REVIEWED BY
Ioannis Manousakas,
I-Shou University, Taiwan
Ben-Yi Liau,
Feng Chia University, Taiwan

*CORRESPONDENCE
Xiao Hou,
houxiao0327@bsu.edu.cn
Tingting Sun,
bsustt@163.com

†These authors have contributed equally to this work and share first authorship

RECEIVED 21 May 2024
ACCEPTED 28 June 2024
PUBLISHED 01 October 2024

CITATION
Jia Y, Liu Y, Lei J, Wang H, Wang R, Zhao P, Sun T and Hou X (2024), Using nonlinear dynamics analysis to evaluate time response of cupping therapy with different intervention timings on reducing muscle fatigue.
Front. Bioeng. Biotechnol. 12:1436235.
doi: 10.3389/fbioe.2024.1436235

Using nonlinear dynamics analysis to evaluate time response of cupping therapy with different intervention timings on reducing muscle fatigue

Yuanyuan Jia[1,2†], Yining Liu[3†], Juntian Lei[4], Huihui Wang[1,2], Rong Wang[1,2], Pengrui Zhao[4], Tingting Sun[1*] and Xiao Hou[1,2*]

[1]Key Laboratory of Exercise and Physical Fitness, Beijing Sport University, Ministry of Education, Beijing, China, [2]School of Sport Science, Beijing Sport University, Beijing, China, [3]Harrison International Peace Hospital, Hengshui, China, [4]School of Sports Medicine and Rehabilitation, Beijing Sport University, Beijing, China

Background: Cupping therapy has been indicated effective in reducing muscle fatigue after 24 h based on the spectral analyses of surface electromyography (sEMG). However, there is no sufficient evidence showing changes of sEMG nonlinear indexes at more time points after cupping therapy. Furthermore, it is unclear whether the intervention timings of cupping therapy affect the recovery from muscle fatigue. The purpose of this study was to use the sEMG nonlinear analysis to assess the difference of time response of cupping therapy between different intervention timings after muscle fatigue.

Materials and methods: This randomized controlled trial recruited 26 healthy volunteers. Cupping therapy (−300 mmHg pressure for 5 min by the 45 mm-diameter cup) was applied before (i.e., pre-condition) or after (i.e., post-condition) muscle fatigue induced by performing repeated biceps curls at 75% of the 10 repetitions of maximum (RM) on the non-dominant upper extremity. Subjects were randomly allocated to the pre-condition group or the post-condition group. The sEMG signals during the maximal voluntary isometric contractions (MVC) of the biceps were recorded at four time points (i.e., baseline; post 1: immediate after cupping-fatigue/fatigue-cupping interventions; post 2: 3 h after cupping-fatigue/fatigue-cupping interventions; post 3: 6 h after cupping-fatigue/fatigue-cupping interventions). Two nonlinear sEMG indexes (sample entropy, SampEn; and percent determinism based on recurrence quantification analysis, %DET) were used to evaluate the recovery from exercise-introduced muscle fatigue. The Friedman test followed by the Nemenyi test and the Mann-Whitney U test were applied in statistics.

Results: The SampEn and %DET change rate did not show any significant differences at four time points in the pre-condition group. However, there were significant delayed effects instead of immediate effects on improving muscle fatigue in the post-condition group (SampEn change rate: baseline 0.0000 ± 0.0000 vs. post 2 0.1105 ± 0.2253, $p < 0.05$; baseline 0.0000 ± 0.0000 vs. post 3 0.0627 ± 0.4665, $p < 0.05$; post 1−0.0321 ± 0.2668 vs. post 3 0.0627 ± 0.4665, $p < 0.05$; and %DET change rate: baseline 0.0000 ± 0.0000 vs. post 2−0.1240 ± 0.1357, $p < 0.01$; baseline 0.0000 ± 0.0000 vs. post 3 0.0704 ± 0.6495, $p < 0.05$; post 1 0.0700 ± 0.3819 vs. post 3 0.0704 ±

0.6495, $p < 0.05$). Moreover, the SampEn change rate of the post-condition group (0.1105 $\pm$ 0.2253) was significantly higher than that of the pre-condition group (0.0006 $\pm$ 0.0634, $p < 0.05$) at the post 2 time point. No more significant between-groups difference was found in this study.

Conclusion: This is the first study demonstrating that both the pre-condition and post-condition of cupping therapy are useful for reducing muscle fatigue. The post-condition cupping therapy can e ffectively alleviate exercise-induced muscle fatigue and there is a significant delayed effect, especially 3 h after the interventions. Although the pre-condition cupping therapy can not significantly enhance muscle manifestations, it can recover muscles into a non-fatigued state.

KEYWORDS

cupping therapy, pre-condition, post-condition, nonlinear dynamics analysis, muscle fatigue

Introduction

Muscle fatigue, defined as the inability to generate a constant force after sustained or intense muscle contractions (Barry and Enoka, 2007), is traditionally categorized into central fatigue (central origin, the involved mechanism relates to the spinal and supra-spinal tract) and peripheral fatigue (peripheral origin, the involved mechanism relates to the structures distal of the neuromuscular junction) (Rampichini et al., 2020). Muscle fatigue can have detrimental effects. For athletes, muscle fatigue may impact physical and tactical performance (Coutinho et al., 2018), increasing risks of tissue injuries (i.e., tear, rupture, and fracture) (Edwards, 2018; Silva et al., 2018), which may lead to poor grades. For the general population, long-term muscle fatigue from the long-term stable motions in daily work results in a high susceptibility to musculoskeletal diseases (Punnett and Wegman, 2004). Consequently, identifying effective therapies for mitigating muscle fatigue is paramount.

Cupping therapy, a form of complementary and alternative medicine (CAM) utilizing negative pressure, has been employed to ameliorate exercise-induced muscle status. There are evidences that cupping therapy is useful for the increase of local blood flow (Hou et al., 2020), the reduction of muscle pain (Lauche et al., 2012), and the release of muscle stiffness (Jan et al., 2021). And all of these therapeutic effects may contribute to alleviate exercise-induced muscle fatigue. For example, one repeated-measures study investigated the effectiveness of a single cupping therapy compared to a sham-cupping therapy in twelve healthy untrained participants following a muscle fatigue protocol. Significant differences in surface electromyography (sEMG) linear indexes (mean frequency, MNF; median frequency, MDF; and spectral moments ratio, SMR) were described after 24 h rather than immediately after fatigue and cupping/sham-cupping interventions, which showed that cupping therapy reduced muscle fatigue significantly with a delayed effect (Hou et al., 2021). Based on these, further research is needed to delineate the conditions under which cupping therapy achieves optimal efficacy.

Intervention timings could influence the therapeutic effects of CAM. They can be divided into pre-condition (i.e., CAM therapies are applied before the exercise training) and post-condition (i.e., CAM therapies are applied after the exercise training). Different intervention timings of CAM therapy may yield distinct effects. For instance, Tuina is a Chinese therapeutic massage with CAM. Wei et al. has demonstrated that the Tuina after exercise (post-Tuina) was better to enhance the Ca^{2+} and Ca^{2+}-adenosine triphosphatase (ATPase) concentration than the Tuina before exercise (pre-Tuina) 24 h after Tuina-exercise/exercise-Tuina interventions (Wei et al., 2022). It implied that post-Tuina could be the optimal strategy for promoting the skeletal muscle mitochondrial Ca^{2+}-ATPase activity and the ability of mitochondria to transport Ca^{2+} to protect muscle tissue (Cully et al., 2017). Similarly, cupping therapy exerts its healing effects through mechanical shear strain on the soft tissue (Tham et al., 2006; Jan et al., 2021), which is analogous to the mechanical shear stress applied during massage (Smith et al., 1994). Therefore, significant differences may exist between pre-condition and post-condition cupping therapy. However, evidence regarding the effects of different intervention timings on cupping therapy remains insufficient. Moreover, current evidence indicates that the delayed effects of post-condition cupping therapy only manifested 24 h after muscle fatigue (Hou et al., 2021; Liao et al., 2021). Little is known about the more detailed time response for pre-condition and post-condition cupping therapy. Therefore, it is necessary to delve into additional time points for both pre-condition and post-condition to elucidate the time response of cupping therapy in alleviating muscle fatigue.

The sEMG can record the continuous myoelectric activity by the non-invasive electrodes placed on the local skin (González-Izal et al., 2012). It has been used to detect the effects of cupping therapy after exercise-induced muscle fatigue. The researchers validated the recovery effects of cupping therapy on fatigued muscles through sEMG linear analyses (such as MDF, MNF, SMR) (Chen et al., 2018; Hou et al., 2021). However, the aforementioned analytical methods originated from traditional linear dynamics, which were the most common analytical tools for describing two-body problems (linear systems) before the maturity of nonlinear dynamics theory. On the other hand, researchers have demonstrated that sEMG signals exhibited with nonlinear chaotic characteristics (Erfanian et al., 1996; Meng and Liu, 2006), which was conducted by the complex nonlinear neuromuscular system (Röhrle et al., 2019). So the nonlinear analysis (e.g., entropy, recurrence quantification analysis, and so on) seems better to assess information on fatigue-induced changes of neuromuscular processes that could be ignored by the linear analysis approaches (Merletti and Parker, 2004).

Subsequent research should employ nonlinear analyses to elucidate the underlying mechanisms of sEMG signal changes following cupping therapy.

In a word, it remains unclear whether the intervention timings of cupping therapy affect the recovery from muscle fatigue. And there is insufficient evidence demonstrating changes in sEMG nonlinear indices at multiple time points after cupping therapy. This study aims to employ the sEMG nonlinear methods to detect the difference in time response of cupping therapy between various intervention timings following muscle fatigue. Specifically, our hypothesis is that post-condition cupping therapy yields superior results compared to pre-condition cupping therapy, with a delayed effect on reducing exercise-induced muscle fatigue.

Methods

Study design

A parallel-group randomized controlled trial (RCT) was conducted in this study. According to different intervention timings, participants were randomly assigned to a group of either: 1) pre-condition group: cupping therapy conducted before biceps brachii fatigue protocol (i.e., cupping-fatigue), or 2) post-condition group: cupping therapy conducted after biceps brachii fatigue protocol (i.e., fatigue-cupping). Assessments were conducted at baseline (before cupping therapy and fatigue protocol), post 1 (immediately after cupping-fatigue/fatigue-cupping interventions), post 2 (3 h after cupping-fatigue/fatigue-cupping interventions) and post 3 (6 h after cupping-fatigue/fatigue-cupping interventions) by sEMG during the maximum voluntary contraction (MVC) of biceps brachii.

Participants

The recruitment process for this study was conducted at Beijing Sport University (BSU) through advertisements and word-of-mouth. Prospective participants underwent a rigorous prescreening procedure via an electronic questionnaire to ensure adherence to specific eligibility criteria (shown in Supplementary Appendix SA). Ethical approval for the study was obtained from the Sports Science Experiment Ethics Committee of BSU (Approval No. 2023022H), and informed consent was obtained from all participants. The sample size was calculated as 24 based on the power analysis with an assumption of a very large effect size (1.2), alpha level at 0.05, power at 0.95 and two groups for the independent samples t-test. This effect size choice was informed by previous literature demonstrating the impact of cupping therapy on sEMG linear indexes (Hou et al., 2021). Considering the drop-out, the sample size was determined as 26, 13 per group.

Participants were evenly allocated to two groups using a random number table method. We used Excel to generate the respective random numbers for each participant. Subsequently, participants were sorted in descending order based on their random numbers, with the top half allocated to the pre-condition group and the rest allocated to the post-condition group.

FIGURE 1
The photograph of the cupping device.

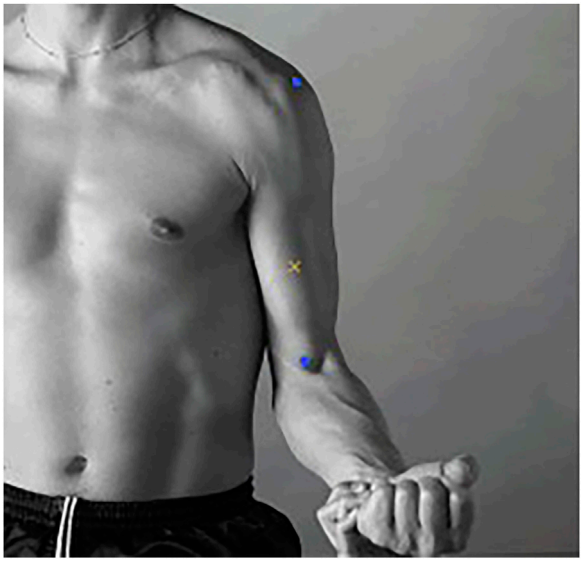

FIGURE 2
The abdominal center of the biceps brachii. (Notes: The two blue markers represent the medial acromion and the fossa cubit from top to bottom. The yellow cross represents the abdominal center of the biceps brachii).

Cupping therapy

Cupping therapy in this study utilized a cup of 45 mm inner diameter with the negative pressure of 300 mmHg for 5 min conducted by an electric negative pressure gauge (MF-H96,

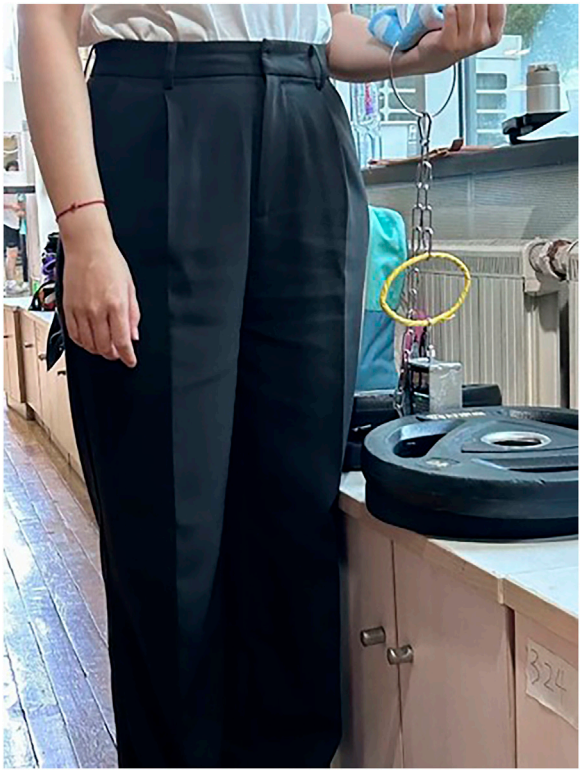

FIGURE 3
The photographs of the MVC test.

Baoyizhen, China; see in Figure 1). According to a previous study, the cupping therapy dose has been indicated the significant improvement on muscle fatigue. The treatment site was at the abdominal center of the biceps brachii (on the line between the medial acromion and the fossa cubit at 1/3 of the way from the fossa cubit; see the yellow cross in Figure 2) (Hou et al., 2021).

sEMG assessment

The sEMG assessment comprised three 5-s MVC tests of the biceps brachii, each separated by a 60-s interval. Signals were recorded using a wireless EMG system (Delsys, Inc., Natick, MA) with a 16-channel sensor setup, sampled at 1,000 Hz. Sensors were affixed with 3M tape and muscle patches for stability. Participants performed the MVC test by exerting maximal force on a force transducer (DY920, Freud, Daysensor, China) while maintaining a 90° angle at the elbow of their non-dominant arm (Hermens et al., 2000). The force transducer, inverted onto the platform and secured with a weight, was pulled perpendicular to it (see in Figure 3). Participants monitored sEMG tracings on a computer screen to stabilize force output. Sensor placement was standardized at the abdominal center of the biceps brachii, and an indelible marker was used to ensure consistent positioning for each intervention (Hermens et al., 2000).

Experimental procedures

The flowchart in Figure 4 shows the experimental procedures. Participants in both groups (pre-condition and post-condition) completed 4 visits to assess basic information (Visit 1), immediate effects (Visits 2) and delayed effects (Visits 3 and 4). Before the experiment, participants relaxed in a seated position for ≥ 5 min during each visit.

During the Visit 1, an online questionnaire was completed for basic information and inclusion/exclusion criteria. The Edinburgh Handedness Inventory was then administered to determine the non-dominant arm (Veale, 2014), minimizing daily-life-induced muscle fatigue. After signing of the "Participant Information and Informed Consent Form," participants engaged in a 5-min warm-up involving unloaded dynamic bicep curls on the non-dominant side. Subsequent tests determined the one-repetition maximum (1RM) for bicep curls using varying dumbbell weights, with a 3-min rest period between attempts. A formula was utilized to calculate the 10-repetition maximum (10 RM): $1RM = 8.841 + (1.1828 \times 7 - 10RM)$ (Abadie et al., 1999), with 75% of this weight applied for the second test to induce muscle fatigue.

During the Visit 2, participants were calibrated to the test position. Baseline sEMG assessments were conducted after skin preparation with 70% isopropyl alcohol. After a 3-min rest, participants underwent the first sEMG assessment. Referring to previous studies, the muscle fatigue protocol was isolated biceps curls with 75% of 10 repetition maximum (RM) until exhaustion of the non-dominant arm at the pace of 15 repetitions per min (Hou et al., 2021). The pre-condition group received "cupping-fatigue" interventions (cupping: cupping therapy; and fatigue: muscle fatigue protocol), while the post-condition group received "fatigue-cupping" interventions. Immediate post 1 sEMG assessments were conducted.

At 3 h (post 3) and 6 h (post 4) after Visit 2, participants performed three 5-s MVC tests with sEMG assessment twice (Visit 3 and 4), following the detailed process described above.

EMG analysis

The EMG signals were filtered of a zero-lag band pass filter and processed by absolute value using the EMGworks Analysis (Delsys, Inc., Natick, MA). Then, two nonlinear dynamic analysis methods were applied to evaluate the effect of cupping therapy on alleviating muscle fatigue using Python. Sample entropy (SampEn) quantifies time series entropy by assessing the likelihood that similar sequences remain similar within epochs (Richman and Moorman, 2000). It has been applied to detect muscle fatigue. The SampEn in this study was calculated as the following formula (Eq. 1):

$$SampEn(m, r, N) = -\log\left(\frac{\sum_{i=1}^{N-m} A_i}{\sum_{i=1}^{N-m} \mathrm{B}_i}\right) = -\log\left(\frac{A}{B}\right) \quad (1)$$

where N is the number of data points in the time series (a resample frequency of 250 Hz and a segment length of 5 s), m is the length of the template (taken as 2), r is the similar capacity of each signal segment, A_i is taken to be 1 in the similar case and 0 in the opposite

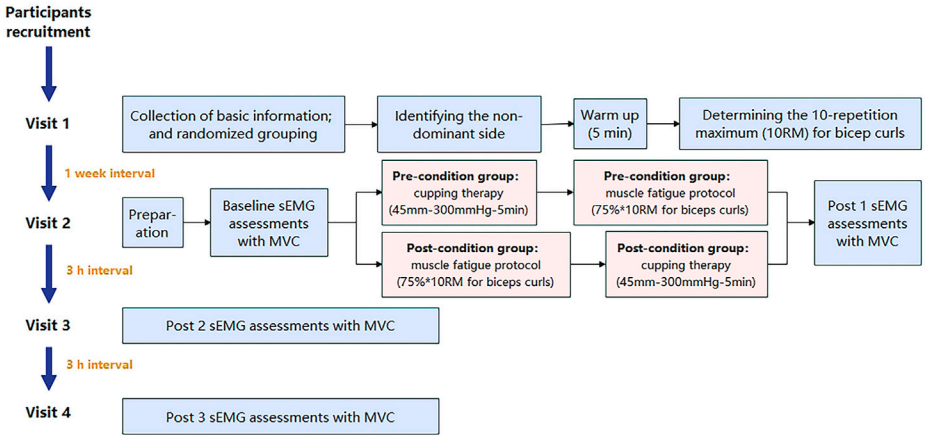

FIGURE 4
The flowchart of experimental procedures. (Note: sEMG: surface electromyography; MVC, maximum voluntary contraction).

case, A is the total number of matches of the ith template of length $m + 1$ data points, B_i and B are the number of matches of the ith template of length m data points (Richman and Moorman, 2000).

Another nonlinear dynamic method, the recurrence quantification analysis (RQA) identifies recurring patterns and non-stationarities (Caballero-Pintado et al., 2018). Percent determinism (%DET), a common RQA measure, calculates the ratio of connected diagonals to all ones in the matrix (Webber Jr and Zbilut, 2007). The %DET in this study was calculated as the following formula (Eq. 2):

$$\%DET = \frac{\sum_{l=l_{min}}^{N} lP(l)}{\sum_{i,j=1}^{N} R_{i,j}} \quad (2)$$

where l is the length of the line segment, l_{min} is the minimum length of the line segment (generally taken as 2), $P(l)$ is the number of line segments parallel to the main diagonal and of length l, and the $R_{i,j}$ represents the points on the recurrence plot.

The SampEn and the %DET were computed from the most forceful of three 5-s MVC tests. The SampEn and the %DET change rates were then utilized to evaluate cupping therapy's impact on fatigue reduction. These rates represent the difference between SampEn or %DET at various time points and their respective baseline values, divided by the baseline values. For instance, considering SampEn, the formula was as follows (Eq. 3):

$$SampEn\,chage\,rate = \frac{SampEn_{at\,a\,given\,time} - SampEn_{baseline}}{SampEn_{baseline}} \quad (3)$$

Statistical analysis

All statistical analyses were performed by the SPSS (Version 26, Chicago, IL, United States). Firstly, the normality of the results was checked using Shapiro–Wilk tests. The Friedman test, with Nemenyi post-hoc test was performed to examine the differences in the SampEn and the %DET change rate among different time points within both the pre-condition and the post-condition groups. The differences in the SampEn and the %DET change rate between pre-condition cupping therapy and post-condition cupping therapy at various time points were examined using Mann-Whitney U tests.

Results

In this study, 26 healthy, young participants (8 male and 18 female) were recruited for this study. No participants dropped out during the trail. The demographic data and basic characteristics were as follows: age (years) = 20.35 ± 1.32; height (m) = 1.69 ± 0.08; weight (kg) = 65.28 ± 13.76; body mass index (BMI, kg/m^2) = 22.74 ± 4.32; and the maximum force value output during MVC (Newton): baseline-value = 195.64 ± 93.76, post 1-value = 169.51 ± 90.62, post 2-value = 176.17 ± 93.30, post 3-value = 171.33 ± 106.76. Only two of the 26 participants were left-handed. The specifics of the pre-condition and post-condition cupping therapy group were presented in Table 1.

The SampEn change rate

Figure 5 showed the SampEn change rate of the sEMG signals during MVC tests at four time points (i.e., baseline, post 1, post 2, and post 3) in the pre-condition cupping therapy group and the post-condition cupping therapy group.

In case of the pre-condition group, the SampEn change rate did not show any significant differences at four time points. In case of the post-condition group, the SampEn change rate showed significant increases from baseline to post 2 (baseline 0.0000 ± 0.0000 vs. post 2 0.1105 ± 0.2253, $p < 0.05$), from baseline to post 3 (baseline 0.0000 ± 0.0000 vs. post 3 0.0627 ± 0.4665, $p < 0.05$), and from post 1 to post 3 (post 1–0.0321 ± 0.2668 vs. post 3 0.0627 ± 0.4665, $p < 0.05$). It meant that delayed effects of cupping therapy were found in the post-condition group rather than immediate effects. Moreover, the SampEn change rate of the post-condition group (0.1105 ± 0.2253) was significantly higher than that of the pre-condition group (0.0006 ± 0.0634, $p < 0.05$) at the post 2 time point. No more significant between-groups difference was found in this study. The specifics of two groups were presented in Supplementary

10.3389/fbioe.2024.1436235

TABLE 1 Demographic data and basic characteristics.

	Pre-condition group (N = 13)	Post-condition group (N = 13)
Age, mean (SD), yr	20.08 (1.44)	20.62 (1.19)
Female (%)	69.23%	69.23%
Height, mean (SD), m	1.69 (0.08)	1.69 (0.09)
Weight, mean (SD), kg	62.85 (12.39)	67.72 (15.11)
BMI, mean (SD), kg/m^2	21.88 (2.81)	23.59 (5.43)
Right-handed (%)	84.62%	100.00%
Maximum force value output during MVC, Newton		
Baseline	206.85 (109.96)	184.43 (77.16)
Post 1	179.32 (105.02)	159.71 (76.63)[a]
Post 2	183.13 (105.18)	169.21 (83.47)
Post 3	176.67 (115.46)[a]	165.98 (101.75)[a]

Note: BMI, body mass index; MVC, maximum voluntary contraction. The symbols [a] indicates $p < 0.05$ compared to baseline.

Appendix SB. The original results of SampEn are included in Supplementary Appendix SC.

The %DET change rate

Figure 6 visualized the results of the %DET change rate of the sEMG signals during MVC tests at four time points (i.e., baseline, post 1, post 2, and post 3) in the pre-condition cupping therapy group and the post-condition cupping therapy group.

When cupping therapy was performed before muscle fatigue (pre-condition), there was no significant differences of the %DET change rate at all time points. When cupping therapy was performed after muscle fatigue (post-condition), there were significant delayed effects instead of immediate effects on improving muscle fatigue in the post-condition group (baseline 0.0000 ± 0.0000 vs. post 2 −0.1240 ± 0.1357, $p < 0.01$; baseline 0.0000 ± 0.0000 vs. post 3 0.0704 ± 0.6495, $p < 0.05$; post 1 0.0700 ± 0.3819 vs. post 3 0.0704 ± 0.6495, $p < 0.05$). When comparing the %DET change rate between the pre-condition group and the post-condition group, the differences were not significant at all time points. The specifics of two groups were presented in Supplementary Appendix SB. The original results of %DET are included in Supplementary Appendix SC.

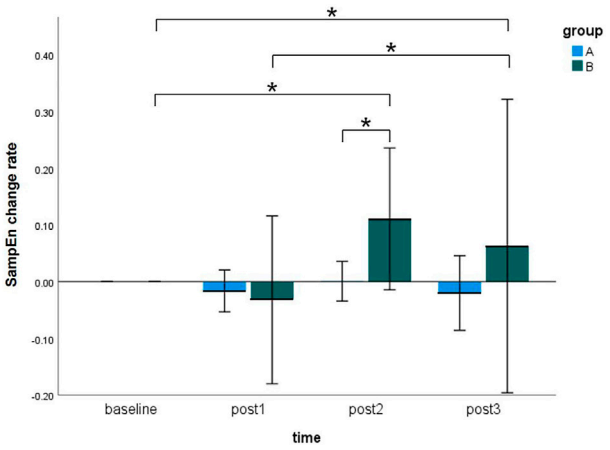

FIGURE 5
Comparison of the SampEn change rate within-groups and between-groups at all time points. (Notes: A: the pre-condition group; B: the post-condition group; post1: immediate after interventions; post 2: 3 h after interventions; post 3: 6 h after interventions. The symbols * indicates $p < 0.05$).

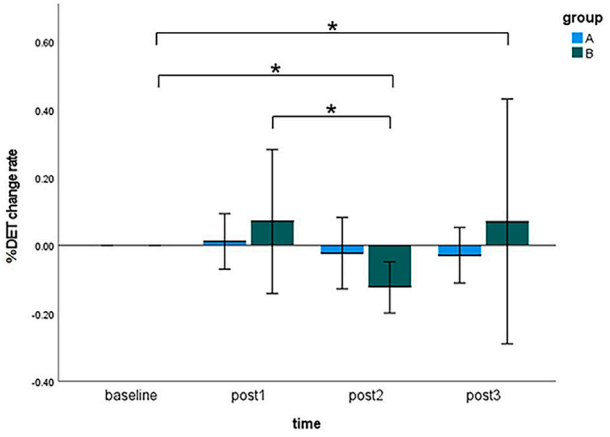

FIGURE 6
Comparison of the %DET change rate within-groups and between-groups at all time points. (Notes: A: the pre-condition group; B: the post-condition group; post1: immediate after interventions; post 2: 3 h after interventions; post 3: 6 h after interventions. The symbols * indicates $p < 0.05$).

Discussion

The study indicated the efficacy of both the pre-condition and the post-condition cupping therapy in mitigating muscle fatigue. Notably, significant delayed effects were observed in the post-condition group instead of immediate effects. The pre-condition cupping therapy demonstrated the ability to restore muscles to a non-fatigued state. Particularly, results indicated superiority of the post-condition group over the pre-condition group, evidenced by SampEn at post 2 time points, which corroborated our initial hypothesis. To the best of our knowledge, this study is the first to detect differences in the time response of cupping therapy between different intervention timings after muscle fatigue.

In this study, the methodological selection of nonlinear analysis was motivated by the following considerations. Nonlinear indices were preferred over traditional linear indices due to the limitations of linear analysis in capturing the complexity of the neuromuscular system. Linear methods attempt to isolate stable components but often oversimplify interactions among system elements. Nonlinear

analysis methods provide a more comprehensive approach, hence their exclusive use in this paper. Among them, entropy analysis serves as an effective tool for assessing system complexity, describing regularity and predictability in time series data. Lower entropy values indicate more regular systems, reflecting reduced complexity (Rampichini et al., 2020). In the neuromuscular system, muscle fatigue is regarded as an unhealthy pathological state with decreased signal complexity, evidenced by declining entropy values (Şaylı and Çotuk, 2015). As a form of entropy analysis, SampEn shares these characteristics. Pethick et al. found a decrease in SampEn with increasing muscle fatigue during 100% MVC tasks (Pethick et al., 2015). Considering the physiological significance of SampEn, our study utilized it to evaluate the efficacy of cupping therapy in alleviating muscle fatigue. Results revealed no significant reduction in SampEn change rates in either the pre-condition or the post-condition cupping therapy groups compared to their respective baseline values. It suggested that cupping therapy with different intervention timings effectively prevented declines in neuromuscular system complexity following muscle fatigue. This aligns with findings by Liao et al. (2021), who observed significantly smaller reductions in entropy values among cupping group participants compared to sham cupping group participants following muscle fatigue.

Another sEMG nonlinear analysis method, %DET was also employed in this study. Consistent with SampEn findings, both the pre-condition and the post-condition cupping therapy effectively modulated muscle performance decline following exercise-induced muscle fatigue. Specifically, %DET monitors activity at the micro-level of the neuromuscular system (i.e., motor unit behavior). Both types of changes in motor units following fatigue can lead to alterations in %DET. Specifically, an increase in motor unit synchronization (MUS) and a decrease in motor unit conduction velocity (MUCV) result in an elevated %DET (Şaylı and Çotuk, 2015). And the parameters MUS and MUCV are respectively associated with central and peripheral fatigue respectively, resulting in %DET reflecting both central and peripheral fatigue. For example, a previous research indicated that high-intensity isometric contractions led to increased MUS, which was considered as an effective strategy by the central nervous system to counteract cortical fatigue (Kleine et al., 2001). On the other hand, peripheral fatigue involved the decrease in MUCV due to changes in electrochemical factors such as phosphate accumulation and intracellular pH increase (Brody et al., 1991). In this study, %DET results indicated no significant increases in the pre-condition group at all post-intervention time points (post 1, post 2, post 3), and in the post-condition group at the first two post-intervention time points (post 1, post 2), compared to their respective baseline values. It showed that cupping therapy effectively prevents post-fatigue increases in MUS and decreases in MUCV at these time points. Conversely, a significant increase in %DET at the post 3 compared to baseline indicated an elevation in MUCV and a decrease in MUS, reflecting a deepening level of fatigue.

Our results showed differences between pre-condition and post-condition. At the post 2 time point, the SampEn change rate in the post-condition cupping therapy group significantly exceeded that of the pre-condition group. This meant that post-condition cupping therapy could enhance neuromuscular system complexity 3 h after fatigue. Furthermore, the post-condition cupping therapy exhibited significant delayed improvement effects on fatigue-induced SampEn increase and %DET decrease, even surpassing baseline levels (i.e., a non-fatigued state). In contrast, pre-condition cupping therapy only restored the aforementioned muscle fatigue-related characteristics to a non-fatigued state.

For the differences between pre-condition and post-condition, the underlying mechanism might be attributed to the hemodynamics. The blood circulation promotion theory suggested a potential physiological mechanism by which cupping therapy improves muscle condition, involving local hemodynamic changes regulated by positive pressure under the cup rims and negative pressure under the cup during cupping. For the effects of positive pressure, studies indicated that 200 mmHg intermittent pressure caused by a cuff could induce intermittent vascular occlusion and promote blood flow reperfusion post-cuff removal, which was aided in muscle stiffness and fatigue (Nakajima et al., 2022). Moreover, during cupping therapy, compression of tissues at the cup rim generates pressure approximately an order of magnitude greater than the negative pressure under the cup (Tham et al., 2006). For instance, assuming a negative pressure of 300 mmHg under the cup, the corresponding positive pressure at the cup rim is approximately 3,000 mmHg. Compared to the 200 mmHg intermittent pressure, maintaining this pressure intensity for 5 min during cupping is sufficient to induce local blood flow reperfusion. In addition, tensile stress of tissue under the cup increases shear stress between blood flow in capillaries and endothelial cells, which stimulates endothelial cells to release more nitric oxide (NO) and promotes vasodilation (Moncada, 1992). Collectively, these mechanisms lead to enhanced local blood flow and accelerated circulation following cupping therapy. And the negative pressure suction also causes capillary rupture, leading to the extravasation of red blood cells into tissue fluid, manifested as petechiae and ecchymosis on the skin (Kim and Lee, 2014; Lowe, 2017). On the other hand, exercise training accompanies increased blood flow and changes in hemodynamics (Clifford, 2007). However, the intramuscular pressure generated during muscle contraction ranges from 270 to 570 mmHg (Sejersted et al., 1984), which is lower than the high-intensity compression and suction exerted externally. Thus, when cupping therapy and skeletal muscle contraction jointly regulate hemodynamics, the intervention sequence may be a critical factor influencing efficacy. In the pre-condition group, the reperfusion and NO effects after cupping therapy resulted in rapid increases in muscle blood flow and capillary rupture. Subsequent muscle contractions exacerbated local blood flow, further perfusing already damaged capillaries and aggravating skeletal muscle damage (de Carvalho et al., 2023). The cupping therapy before exercise training accelerated the clearance of metabolic waste and transport of nutrients under non-fatigued conditions. So it enhanced tissue status before exercise and facilitated post-fatigue recovery to a non-fatigued state. However, the pre-condition cupping therapy failed to effectively clear metabolic waste caused by subsequent muscle contractions, ultimately leading to limited muscle fatigue recovery. In the post-

condition group, cupping therapy led to increased blood flow and accelerated blood circulation after exercise-induced muscle fatigue. It was most conducive to clearing metabolic waste, transporting nutrients and facilitating post-exercise muscle fatigue recovery. Based on these results, we suggested that post-condition cupping therapy had a greater advantage in improving exercise-induced muscle fatigue.

In addition to the different intervention timings, our study also indicated that post-condition cupping therapy exhibited significant delayed effects. The 3 h after intervention may be a critical time point for the effectiveness of cupping therapy on recovery muscle fatigue. One previous study has confirmed the delayed effect of the post-condition cupping therapy. Hou et al. (2021) found that cupping therapy effectively alleviated biceps brachii muscle fatigue at 24 h post-interventions based on sEMG linear indicators (i.e., MDF, MNF, and SMR). This seemingly contradicted our findings that cupping therapy significantly improved muscle fatigue at 3 h post-interventions. Although both studies employing sEMG as a measurement tool, their specific analytical methods and physiological implications differ, potentially contributing to inconsistent conclusions. Additionally, exercise-induced fatigue can be divided into peripheral and central fatigue. Peripheral fatigue phenomena involve changes in metabolic and structural components at the muscle level. Central nervous system regulates the peripheral system, and central fatigue affects peripheral fatigue. Hou et al. (2021) attributed changes in sEMG linear indicators to the effects of cupping therapy on peripheral fatigue phenomena such as post-exercise hydrogen ion (H^+) accumulation and immune response. In our study, we employed nonlinear indicators to explore the modulation mechanism of cupping therapy on "central-peripheral" fatigue. Previous studies have shown that SampEn and %DET are associated with β-band coherence activity between the brain and muscles, reflecting cortico-muscular coherence (i.e., the central nervous system's regulation of the peripheral system) (McManus et al., 2016). With the progression of muscle fatigue, the central nervous system's regulatory capacity over the peripheral system decreases, as evidenced by reduced β-band cortico-muscular coherence (Yang et al., 2009). Our study showed that the post-condition cupping therapy significantly increased SampEn and decreased %DET at 3 h post-interventions compared to baseline. It suggested that the post-condition cupping therapy might enhance the β-band coherence activity beyond baseline levels. Considering the physiological significance of SampEn and %DET, the increased complexity of the neuromuscular system, decreased MUS, and increased MUCV after the post-condition cupping therapy might suggest with the improvement in β-band cortico-muscular coherence. Additionally, this regulation pathway involves fast neural transmission pathways so that the post-condition cupping therapy showed optimal therapeutic effects on the central fatigue level appearing at an earlier time.

To the best of our knowledge, this is the first study to detect the difference of time response of cupping therapy between different intervention timings after muscle fatigue based on the sEMG nonlinear dynamic analysis. However, this study has several limitations: 1) The study only collected sEMG signals at four time points: baseline, immediate, 3 h and 6 h after "cupping-fatigue" or "fatigue-cupping" tasks, without exploring additional time points. Further investigation into the time response of cupping therapy requires monitoring more time points in the future; 2) Different sEMG signal nonlinear analysis methods may reveal different physiological meanings of the neuromuscular system. This study only investigated the effects of cupping therapy on muscle fatigue improvement using two analysis methods (SampEn and %DET). Future research could explore the potential mechanisms of cupping therapy in restoring exercise-induced muscle fatigue using other algorithms.

Conclution

This study is the first to demonstrate that both pre-condition and post-condition cupping therapy effectively reduce muscle fatigue. Cupping therapy conducted after muscle fatigue can effectively alleviate exercise-induced muscle fatigue and there is a significant delayed effect, especially 3 h after the intervention. Although conducting cupping therapy before exercise-induced muscle fatigue can not significantly enhance muscle manifestations, it can recover muscles into a non-fatigued state.

Data availability statement

The original contributions presented in the study are included in the article/Supplementary Material, further inquiries can be directed to the corresponding authors.

Ethics statement

The studies involving humans were approved by the Sports Science Experiment Ethics Committee of Beijing Sport University. The studies were conducted in accordance with the local legislation and institutional requirements. The participants provided their written informed consent to participate in this study.

Author contributions

YJ: Conceptualization, Data curation, Formal Analysis, Investigation, Methodology, Project administration, Resources, Validation, Visualization, Writing–original draft, Writing–review and editing. YL: Validation, Visualization, Writing–original draft. JL: Data curation, Formal Analysis, Writing–original draft. HW: Writing–original draft. RW: Writing–review and editing. PZ: Investigation, Resources, Writing–review and editing. TS: Conceptualization, Methodology, Project administration, Supervision, Writing–review and editing. XH: Conceptualization, Methodology, Project administration, Supervision, Writing–review and editing.

Funding

The author(s) declare that financial support was received for the research, authorship, and/or publication of this article. This study was funded by the Fundamental Research Funds for the Central Universities (grant number: 2024TZJK003).

Conflict of interest

The authors declare that the research was conducted in the absence of any commercial or financial relationships that could be construed as a potential conflict of interest.

Publisher's note

All claims expressed in this article are solely those of the authors and do not necessarily represent those of their affiliated organizations, or those of the publisher, the editors and the reviewers. Any product that may be evaluated in this article, or claim that may be made by its manufacturer, is not guaranteed or endorsed by the publisher.

Supplementary material

The Supplementary Material for this article can be found online at: https://www.frontiersin.org/articles/10.3389/fbioe.2024.1436235/full#supplementary-material

References

Abadie, B. R., Altorfer, G. L., and Schuler, P. B. (1999). Does a regression equation to predict maximal strength in untrained lifters remain valid when the subjects are technique trained? *J. Strength Cond. Res.* 13, 259–263. doi:10.1519/1533-4287(1999)013<0259:daretp>2.0.co;2

Barry, B. K., and Enoka, R. M. (2007). The neurobiology of muscle fatigue: 15 years later. *Integr. Comp. Biol.* 47, 465–473. doi:10.1093/icb/icm047

Brody, L. R., Pollock, M. T., Roy, S. H., De Luca, C. J., and Celli, B. (1991). pH-induced effects on median frequency and conduction velocity of the myoelectric signal. *J. Appl. Physiol.* 71, 1878–1885. doi:10.1152/jappl.1991.71.5.1878

Caballero-Pintado, M. V., Matilla-GarcíA, M., and Ruiz MaríN, M. (2018). Symbolic recurrence plots to analyze dynamical systems. *Chaos* 28, 063112. doi:10.1063/1.5026743

Chen, C.-L., Lung, C.-W., Jan, Y.-K., Liau, B.-Y., and Tang, J.-S. (2018). *The effects of cupping therapy on reducing fatigue of upper extremity muscles—a pilot study.*

Clifford, P. S. (2007). Skeletal muscle vasodilatation at the onset of exercise. *J. Physiol.* 583, 825–833. doi:10.1113/jphysiol.2007.135673

Coutinho, D., GonçALVES, B., Wong, D. P., Travassos, B., Coutts, A. J., and Sampaio, J. (2018). Exploring the effects of mental and muscular fatigue in soccer players' performance. *Hum. Mov. Sci.* 58, 287–296. doi:10.1016/j.humov.2018.03.004

Cully, T. R., Murphy, R. M., Roberts, L., Raastad, T., Fassett, R. G., Coombes, J. S., et al. (2017). Human skeletal muscle plasmalemma alters its structure to change its Ca(2+)-handling following heavy-load resistance exercise. *Nat. Commun.* 8, 14266. doi:10.1038/ncomms14266

De Carvalho, E. G., Corsini, W., and Hermes, T. A. (2023). Severe muscle damage after a short period of ischemia and reperfusion in an animal model. *Surgery* 174, 363–368. doi:10.1016/j.surg.2023.04.033

Edwards, W. B. (2018). Modeling overuse injuries in Sport as a mechanical fatigue phenomenon. *Exerc. Sport Sci. Rev.* 46, 224–231. doi:10.1249/jes.0000000000000163

Erfanian, A., Chizeck, H., and Hashemi, R. (1996) "Chaotic activity during electrical stimulation of paralyzed muscle," in Proceedings of 18th annual international conference of the IEEE engineering in medicine and biology society, 1996, Amsterdam, NL, 31 October 1996–03 November 1996 (IEEE), 1756–1757.

González-Izal, M., Malanda, A., Gorostiaga, E., and Izquierdo, M. (2012). Electromyographic models to assess muscle fatigue. *J. Electromyogr. Kinesiol.* 22, 501–512. doi:10.1016/j.jelekin.2012.02.019

Hermens, H. J., Freriks, B., Disselhorst-Klug, C., and Rau, G. (2000). Development of recommendations for SEMG sensors and sensor placement procedures. *J. Electromyogr. Kinesiol* 10, 361–374. doi:10.1016/s1050-6411(00)00027-4

Hou, X., He, X., Zhang, X., Liao, F., Hung, Y. J., and Jan, Y. K. (2020). Using laser Doppler flowmetry with wavelet analysis to study skin blood flow regulations after cupping therapy. *Skin Res. Technol.* 27, 393–399. doi:10.1111/srt.12970

Hou, X., Wang, X., Griffin, L., Liao, F., Peters, J., and Jan, Y.-K. (2021). Immediate and delayed effects of cupping therapy on reducing neuromuscular fatigue. *Front. Bioeng. Biotechnol.* 9, 678153. doi:10.3389/fbioe.2021.678153

Jan, Y.-K., Hou, X., He, X., Guo, C., Jain, S., and Bleakney, A. (2021). Using elastographic ultrasound to assess the effect of cupping size of cupping therapy on stiffness of triceps muscle. *Am. J. Phys. Med. Rehabilitation* 100, 694–699. doi:10.1097/phm.0000000000001625

Kim, S. B., and Lee, Y. H. (2014). Numerical analysis of the change in skin color due to ecchymosis and petechiae generated by cupping: a pilot study. *J. Acupunct. Meridian Stud.* 7, 306–317. doi:10.1016/j.jams.2013.09.004

Kleine, B. U., Stegeman, D. F., Mund, D., and Anders, C. (2001). Influence of motoneuron firing synchronization on SEMG characteristics in dependence of electrode position. *J. Appl. Physiol.* 91, 1588–1599. doi:10.1152/jappl.2001.91.4.1588

Lauche, R., Cramer, H., Hohmann, C., Choi, K.-E., Rampp, T., Saha, F. J., et al. (2012). The effect of traditional cupping on pain and mechanical thresholds in patients with chronic nonspecific neck pain: a randomised controlled pilot study. *Evidence-Based Complementary Altern. Med.* 2012, 1–10. doi:10.1155/2012/429718

Liao, F., Zhang, X., Cao, C., Hung, I. Y., Chen, Y., and Jan, Y. K. (2021). Effects of muscle fatigue and recovery on complexity of surface electromyography of biceps brachii. *Entropy (Basel)* 23, 1036. doi:10.3390/e23081036

Lowe, D. T. (2017). Cupping therapy: an analysis of the effects of suction on skin and the possible influence on human health. *Complement. Ther. Clin. Pract.* 29, 162–168. doi:10.1016/j.ctcp.2017.09.008

Mcmanus, L., Hu, X., Rymer, W. Z., Suresh, N. L., and Lowery, M. M. (2016). Muscle fatigue increases beta-band coherence between the firing times of simultaneously active motor units in the first dorsal interosseous muscle. *J. Neurophysiol.* 115, 2830–2839. doi:10.1152/jn.00097.2016

Meng, Y., and Liu, B. (2005) "Test nonlinear determinacy of electromyogram," in IEEE engineering in medicine and biology 27th annual conference, 2006, Shanghai, China, January 17-18, 2006 (IEEE), 4592–4595.

Merletti, R., and Parker, P. J. (2004). *Electromyography: physiology, engineering, and non-invasive applications*. John Wiley and Sons.

Moncada, S. (1992). Nitric oxide: physiology, pathophysiology and pharmacology. *J. Clin. Investig.* 89, 747–752.

Nakajima, M., Tsuro, T., and Endo, A. (2022). Sustained compression with a pneumatic cuff on skeletal muscles promotes muscle blood flow and relieves muscle stiffness. *Int. J. Environ. Res. Public Health* 19, 1692. doi:10.3390/ijerph19031692

Pethick, J., Winter, S. L., and Burnley, M. (2015). Fatigue reduces the complexity of knee extensor torque fluctuations during maximal and submaximal intermittent isometric contractions in man. *J. Physiology* 593, 2085–2096. doi:10.1113/jphysiol.2015.284380

Punnett, L., and Wegman, D. H. (2004). Work-related musculoskeletal disorders: the epidemiologic evidence and the debate. *J. Electromyogr. Kinesiol.* 14, 13–23. doi:10.1016/j.jelekin.2003.09.015

Rampichini, S., Vieira, T. M., Castiglioni, P., and Merati, G. (2020). Complexity analysis of surface electromyography for assessing the myoelectric manifestation of muscle fatigue: a review. *Entropy* 22, 529. doi:10.3390/e22050529

Richman, J. S., and Moorman, J. R. (2000). Physiological time-series analysis using approximate entropy and sample entropy. *Am. J. Physiol. Heart Circ. Physiol.* 278, H2039–H2049. doi:10.1152/ajpheart.2000.278.6.H2039

RöHRLE, O., Yavuz, U., Klotz, T., Negro, F., and Heidlauf, T. (2019). Multiscale modeling of the neuromuscular system: coupling neurophysiology and skeletal muscle mechanics. *Wiley Interdiscip. Rev. Syst. Biol. Med.* 11, e1457. doi:10.1002/wsbm.1457

Şaylı, Ö., and Çotuk, H. B. (2015) "Use of entropy, spectral parameters and recurrence quantification analysis for the evaluation of muscle fatigue from surface electromyography," in 2015 19th national biomedical engineering meeting (BIYOMUT), November 5–6, 2015 (Istanbul, Turkey: IEEE), 1–3. doi:10.1109/BIYOMUT.2015.736945

Sejersted, O. M., Hargens, A. R., Kardel, K. R., Blom, P., Jensen, O., and Hermansen, L. (1984). Intramuscular fluid pressure during isometric contraction of human skeletal muscle. *J. Appl. Physiol. Respir. Environ. Exerc Physiol.* 56, 287–295. doi:10.1152/jappl.1984.56.2.287

Silva, J. R., Rumpf, M. C., Hertzog, M., Castagna, C., Farooq, A., Girard, O., et al. (2018). Acute and residual soccer match-related fatigue: a systematic review and meta-analysis. *Sports Med.* 48, 539–583. doi:10.1007/s40279-017-0798-8

Smith, L. L., Keating, M. N., Holbert, D., Spratt, D. J., Mccammon, M. R., Smith, S. S., et al. (1994). The effects of athletic massage on delayed onset muscle soreness, creatine kinase, and neutrophil count: a preliminary report. *J. Orthop. Sports Phys. Ther.* 19, 93–99. doi:10.2519/jospt.1994.19.2.93

Tham, L. M., Lee, H. P., and Lu, C. (2006). Cupping: from a biomechanical perspective. *J. Biomech*. 39, 2183–2193. doi:10.1016/j.jbiomech.2005.06.027

Veale, J. F. (2014). Edinburgh Handedness Inventory - short Form: a revised version based on confirmatory factor analysis. *Laterality* 19, 164–177. doi:10.1080/1357650x.2013.783045

Webber, C. L., and Zbilut, J. P. (2007). Recurrence quantifications: feature extractions from recurrence plots. *Int. J. Bifurcation Chaos* 17, 3467–3475. doi:10.1142/s0218127407019226

Wei, Q., Zhao, Q., Gu, J., Lin, J., Zhu, Y., Song, Z., et al. (2022). Effects of Tuina on serum creatine kinase and skeletal muscle mitochondria in delayed onset muscle soreness model rats. *J. Acupunct. Tuina Sci.* 20, 446–452. doi:10.1007/s11726-022-1344-2

Yang, Q., Fang, Y., Sun, C. K., Siemionow, V., Ranganathan, V. K., Khoshknabi, D., et al. (2009). Weakening of functional corticomuscular coupling during muscle fatigue. *Brain Res.* 1250, 101–112. doi:10.1016/j.brainres.2008.10.074

frontiers | Frontiers in Bioengineering and Biotechnology

TYPE Original Research
PUBLISHED 18 October 2024
DOI 10.3389/fbioe.2024.1477405

OPEN ACCESS

EDITED BY
Yih-Kuen Jan,
University of Illinois at Urbana-Champaign, United States

REVIEWED BY
Sofia Panteliou,
University of Patras, Greece
Huizhi Wang,
University of Science and Technology of China, China

*CORRESPONDENCE
Spyros D. Masouros,
s.masouros04@imperial.ac.uk

RECEIVED 07 August 2024
ACCEPTED 09 October 2024
PUBLISHED 18 October 2024

CITATION
Morgan GT, Low L, Ramasamy A and Masouros SD (2024) A novel strain-based bone-fracture healing algorithm is able to predict a range of healing outcomes.
Front. Bioeng. Biotechnol. 12:1477405.
doi: 10.3389/fbioe.2024.1477405

A novel strain-based bone-fracture healing algorithm is able to predict a range of healing outcomes

George T. Morgan[1], Lucas Low[1], Arul Ramasamy[1,2,3] and Spyros D. Masouros[1]*

[1]Department of Bioengineering, Imperial College London, London, United Kingdom, [2]Academic Department of Military Trauma and Orthopaedics, Royal Centre for Defence Medicine, ICT Centre, Birmingham, United Kingdom, [3]Trauma and Orthopaedics, Milton Keynes Hospital NHS Foundation Trust, Milton Keynes, United Kingdom

Fracture healing is a complex process which sometimes results in non-unions, leading to prolonged disability and high morbidity. Traditional methods of optimising fracture treatments, such as *in vitro* benchtop testing and *in vivo* randomised controlled trials, face limitations, particularly in evaluating the entire healing process. This study introduces a novel, strain-based fracture-healing algorithm designed to predict a wide range of healing outcomes, including both successful unions and non-unions. The algorithm uses principal strains as mechanical stimuli to simulate fracture healing in response to local mechanical environments within the callus region. The model demonstrates good agreement with experimental data from ovine metatarsal osteotomies across six fracture cases with varying gap widths and inter-fragmentary strains, replicates physiological bony growth patterns, and is independent of the initial callus geometry. This computational approach provides a framework for developing new fracture-fixation devices, aid in pre-surgical planning, and optimise rehabilitation strategies.

KEYWORDS

fracture healing algorithm, bone, principal strains, fracture fixation, *in silico* trial, healing assessment, non-union

1 Introduction

Fracture healing is a complex process influenced by several mechanobiological parameters. In order to optimise fracture healing whilst taking into account these parameters, best treatment practices are determined typically by comparing treatments through *in vitro* benchtop testing and *in vivo* randomised controlled trials (RCTs). However, the debate over optimal surgical treatments for certain fractures, such as distal femoral fractures, persists due to limitations of *in vitro* testing and *in vivo* RCTs (Megafu et al., 2022; Wadhwa et al., 2022). *In vitro* testing of fracture fixation is constrained by the scope of bioreactor ossification, which is limited to early stages of callus formation (Hoffmann et al., 2015) or bony ingrowth and remodelling of *ex vivo* bone (Kohli et al., 2023). *In vitro* assessments are therefore limited to the initial fixation stiffness and preclude evaluation of the effects of loading on the healing process itself. *In vivo* testing through RCTs can be limited by challenges in patient and surgeon recruitment, especially in less common fractures, as demonstrated by a feasibility study which concluded that an adequately

powered RCT for distal femoral fracture fixation would not be viable due to limited patient and surgeon recruitment (Griffin et al., 2019). Similar medical questions which have been left unanswered by traditional testing have recently been addressed effectively by *in silico* trials (Pappalardo et al., 2022; Pappalardo et al., 2019; Sarrami-Foroushani et al., 2021; Viceconti et al., 2021). Currently, there is no such *in silico* trial for fracture treatment as computational tools for fracture healing are under-developed.

Fracture-healing numerical algorithms have been developed that simulate fracture-healing progression in response to local mechanical environments in the callus region. These algorithms have previously been applied to the optimisation of fracture-fixator stiffness to improve healing outcomes (Nayak et al., 2024; Quinn et al., 2022; Steiner et al., 2014). Further potential applications of this technology include novel fracture-fixation device development, pre-surgical planning, and rehabilitation-regime optimisation. Previous fracture healing algorithms, however, have limited abilities to explore such applications adequately. While some algorithms have been compared against *in vivo* experimental data, they have generally only been shown to replicate successful healing cases; they have not been shown to predict cases resulting in non-union. This limits these algorithms from being used as predictive tools for non-union risk assessment and therefore pre-clinical decision making and improvement of fracture treatment.

The ability of existing algorithms to demonstrate a physiological healing sequence is dependent upon, and highly sensitive to, the diffusion-rate parameter, which represents either a process of cellular diffusion (Ghiasi et al., 2019; Isaksson et al., 2008; Lacroix and Prendergast, 2002; Quinn et al., 2022) or angiogenesis (Shefelbine et al., 2005; Simon et al., 2011). These processes require the presence of mesenchymal stem cells or vascularisation, respectively, in a specific region of the callus to allow ossification to occur. Diffusion is initialised from the external callus boundary, which prevents spurious bony union in the inter-cortical gap. This means that, in addition to these algorithms being highly sensitive to the diffusion rate parameter, they are also highly sensitive to the initial callus region geometry. As callus geometry is highly variable between fracture types and the callus shape is unknown at the point of pre-surgical planning, this limitation further precludes these algorithms from several possible applications. To address this limitation, a recent algorithm did not include a diffusion process and instead used a spatial proximity function which specifically prevented early ossification in the inter-cortical gap (Schwarzenberg et al., 2021b). This attempt, however, had the same effect in prescribing the callus ossification pathway as the algorithms which used a diffusion process.

All fracture healing algorithms which include strains as mechanical stimuli use the strain thresholds identified by Claes and Heigele (Claes and Heigele, 1999) for distortional and dilatational strain. Distortional strain has been identified as the more important strain input of the two in fracture-healing algorithms (Isaksson et al., 2006). While distortional strain is highly correlated to both minimum and maximum principal strains based on its mathematical formulation, it is not possible to determine the greater of the magnitudes of minimum and maximum principal strain based on the value of distortional strain. Therefore, distortional strain is an insufficient description of the strain state of the callus in fracture-healing modelling. During secondary fracture healing, intramembranous ossification occurs on the growing bony bulges on the periosteum where shear dominates, however, the material directly external to the bulges experiences tension, which can be represented with maximum principal strain (Figure 1). Chondrogenesis and endochondral ossification occur in the region between the bulges where compression dominates, and this can be represented by the magnitude of minimum principal strain. Therefore, the main processes of secondary fracture-healing can be predicted by the local minimum and maximum principal strains in the callus region. In this study, a novel fracture-healing algorithm, which is the first to use minimum and maximum principal strains as the mechanical stimuli, is presented and tested for validation against *in vivo* experimental data of cases which resulted in both successful unions and non-union.

2 Materials and methods

2.1 Fracture healing algorithm

The fracture-healing algorithm developed and used in the present study is described by the flowchart in Figure 2, where each of the boxes "FE Model", "Biological Controller", and "Healing Assessment" are described in more detail below. A finite-element (FE) model was developed of the fracture site, the initial callus domain, and the fixator. Each callus finite-element was represented as a mixture of 3 tissue types: woven bone, cartilage, and soft tissue. Axial loading was applied and the resultant callus element strains were used as inputs to the biological controller, which determined updated tissue-type proportions, and in turn updated the callus element material properties in the FE model. This process was performed iteratively 150 times. The final FE model was then adapted to simulate a bending test to assess the bending stiffness of the final callus.

Six different fracture cases were modelled with initial gap widths of 1 mm, 2 mm, and 6 mm, and initial allowed inter-fragmentary strains (IFS) of 7% and 31%. Gap width is the distance between the two bone segments in the compressed state (Claes et al., 1997). IFS is the amount of axial displacement of the bone segments relative to each other divided by the initial gap width. The combination of gap widths and initial IFS for each case is given in Table 1. These 6 models correspond to the groups used in an *in vivo* experimental study on ovine metatarsal osteotomies stabilised with a custom external fixator (Claes et al., 1997), therefore allowing comparison between simulation results and experimental observations. The experimental groups included groups which resulted in successful unions and groups which resulted in non-unions.

2.2 FE model

An axisymmetric non-linear FE model was developed in MSC.Marc (v2021, MSC Software) of a simple transverse mid-diaphyseal metatarsal ovine osteotomy secured with an external fixator. The callus was modelled explicitly (Figure 3A). An 80 mm

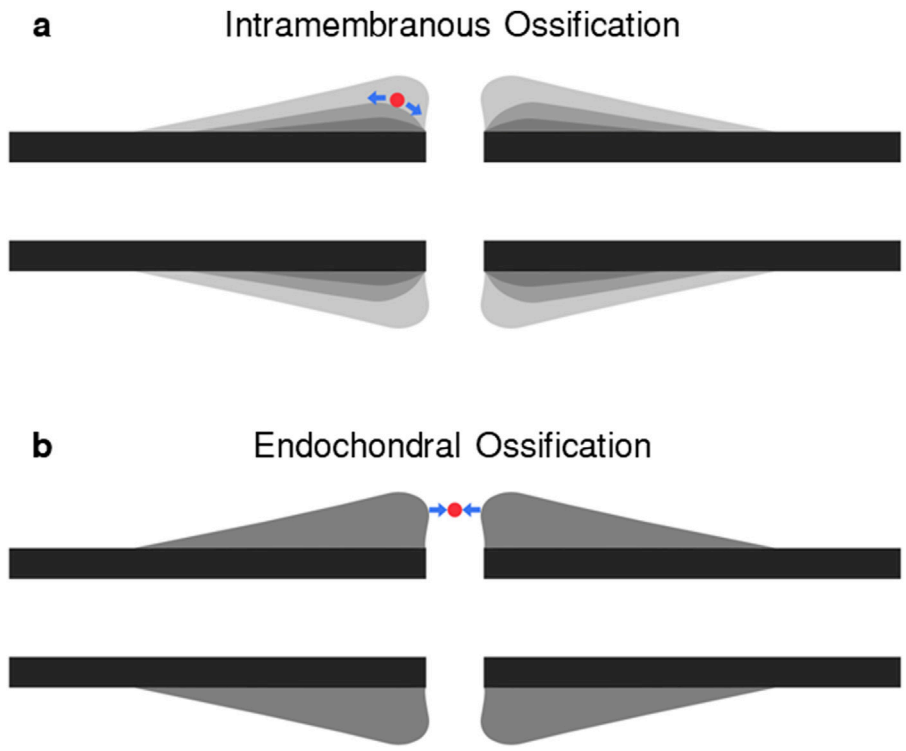

FIGURE 1
Diagram of **(A)** intramembranous ossification and **(B)** endochondral ossification pathways. In each panel, a representative "cell" laying on the ossification pathway is shown in red. During axial compression, the "cell" in panel **(A)** will experience shear, resulting in tensile strains, or high maximum principal strains, and in panel **(B)** will experience compressive strains, or high minimum principal strains.

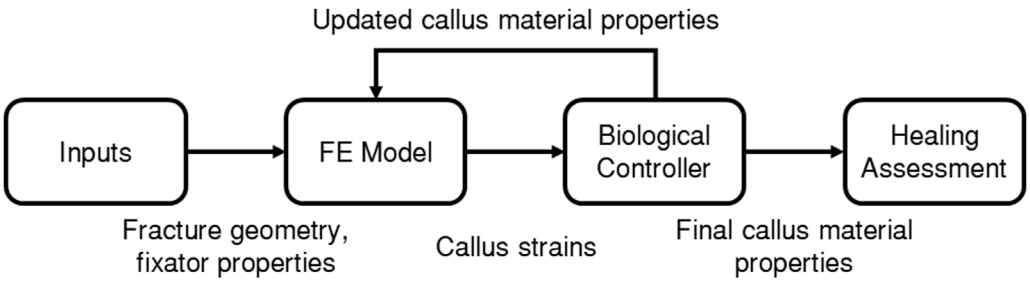

FIGURE 2
Flowchart of the fracture healing algorithm.

TABLE 1 Fracture gap width and initial inter-fragmentary strain (IFS) in each of the simulated groups, corresponding to the groups used in an experimental study by Claes et al.

Group	A	B	C	D	E	F
Gap Width (mm)	1	1	2	2	6	6
IFS (%)	7	31	7	31	7	31

long section of the fracture region was modelled with the metatarsus represented as a hollow cylinder, with outer diameter and thickness of 16 mm and 2 mm, respectively. The callus domain was initialised with a diameter of 48 mm and a length of 52 mm, and shaped according to a standardised callus domain geometry in fracture healing algorithms (Claes and Heigele, 1999; Shefelbine et al., 2005; Simon et al., 2011). The gap width of 1 mm, 2 mm, or 6 mm, references the gap width in the loaded state, as described in the experimental study by Claes et al. (1997). The geometry was meshed using linear triangular elements with an average element edge-length of 0.35 mm.

The tissue types modelled were soft tissue, cartilage, woven bone, and lamellar bone. These were assigned Young's moduli of 3, 200, 4,000, and 10,000 MPa, respectively, and Poisson's ratios of 0.30, 0.45, 0.36, and 0.36, respectively (Ren and Dailey, 2020; Simon et al., 2011). All materials were modelled as linearly elastic and isotropic (Ren and Dailey, 2020; Simon et al., 2011). All callus elements were

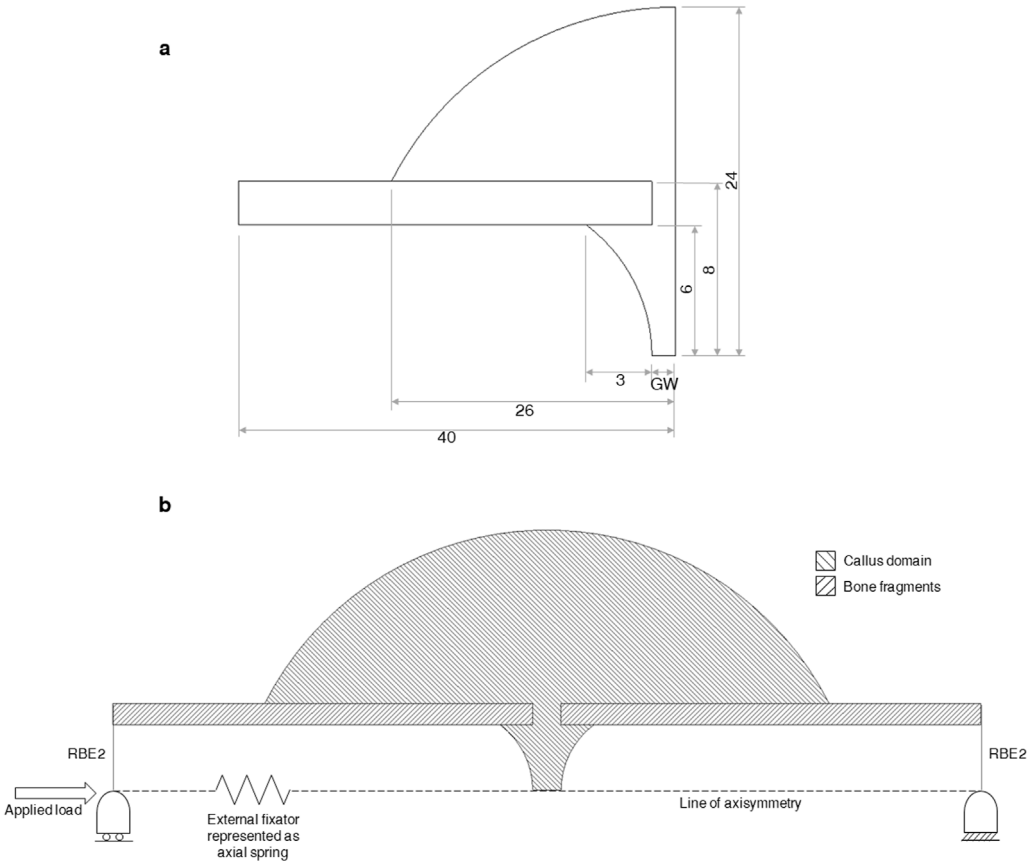

FIGURE 3
(A) Dimensions (in mm) of the bone fragments and callus region. GW denotes "gap width" in the uncompressed state and equals 1.07, 1.31, 2.14, 2.62, 6.42, and 7.86 mm for groups A-F, respectively. The gap widths of 1, 2, and 6 mm reported by Claes et al. were measured in the compressed state and must be scaled by the allowed initial interfragmentary strain of 7% or 31% to determine the gap width in the uncompressed state. **(B)** Diagram of the axisymmetric FE model of a fracture, callus domain, and fixator. The external fixator is represented as a non-linear axial spring running from the far ends of both bone fragments. The securement of the fixator to each bone section is represented with rigid-body-elements (RBE2's) connecting the far end of each bone fragment to a node located on the line of axisymmetry. Boundary and loading conditions are shown. The callus domain is initialised with soft tissue material properties and the bone fragments are modelled as lamellar bone.

assigned soft tissue material properties at the first iteration. After each iteration, the Young's modulus and Poisson's ratio of each callus element were calculated from the updated proportion of each tissue type within the element according to a cubic, and linear rule of mixture, respectively (Simon et al., 2011), as shown in Equations 1, 2, where E_{element} and ν_{element} are the Young's modulus and Poisson's ratio of the element, E_{tissue} and ν_{tissue} are the Young's modulus and Poisson's ratio of a tissue type, and $c_{element,tissue}$ is the concentration of the tissue in the element, where the expressions $E_{tissue}c^3_{element,tissue}$ and $\nu_{tissue}c_{element,tissue}$ are summed over all 3 tissue types allowed in the callus region: soft tissue, cartilage, and woven bone.

$$E_{element} = \sum_{tissue} E_{tissue}c^3_{element,tissue} \quad (1)$$

$$\nu_{element} = \sum_{tissue} \nu_{tissue}c_{element,tissue} \quad (2)$$

The external fixator used in Claes et al. was designed to allow for a pre-determined amount of axial motion (Claes et al., 1995). The amount of free axial movement allowed was set to the desired distance while the fixated limb was in the loaded state (Claes et al., 1997). In the present study, the fixator was modelled as a non-linear axial spring, with an initial stiffness of 4600 N mm^{-1} up to a force of 100 N, then a stiffness of 10 N mm^{-1} up to the desired free movement distance, and a stiffness of 4600 N mm^{-1} beyond (Claes et al., 1997; Simon et al., 2011).

Boundary conditions were applied at both ends of the bone construct (Figure 3). Nodes on the distal cut-face were held in three translational directions and nodes on the proximal cut-face were held in two translational directions, allowing for relative axial movement. These conditions were applied in FE by using rigid-body-elements (RBE2s) with a control node for each face placed on the line of axisymmetry. Ovine metatarsals experience predominantly axial loading (Duda et al., 1997) and the shear and torsional rigidities of the fixator are reported to be high, allowing for only axial movement (Claes et al., 1995; Claes et al., 1997; Claes and Heigele, 1999), therefore only axial loading was modelled, allowing the use of an axisymmetric modelling approach. The spring representing the external fixator connected the two retained nodes of the RBE2s at the bone ends. An axial load of 500 N was applied to the proximal retained node (Claes and Heigele, 1999; Simon et al., 2011).

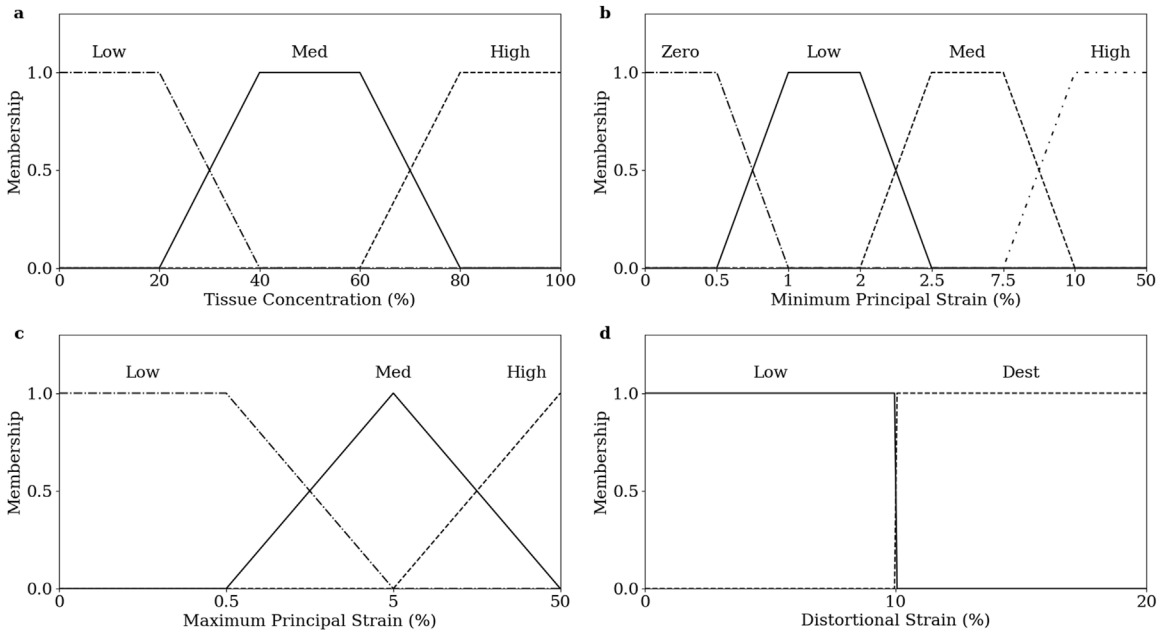

FIGURE 4
Fuzzy membership functions of inputs, **(A)** tissue prop, **(B)** minimum principal strain, **(C)** maximum principal strain, and **(D)** distortional strain.

2.3 Biological controller

A fuzzy logics approach was used to simulate some of the biological processes involved in secondary fracture healing based on previous fracture-healing algorithms (Ament and Hofer, 2000; Schwarzenberg et al., 2021b; Shefelbine et al., 2005; Simon et al., 2011), but using minimum and maximum principal strains as mechanical inputs for the first time. The biological fuzzy logic controller was developed using the Scikit-Fuzzy (v0.4.2) fuzzy logic toolbox (Warner et al., 2019) in Python (v3.6, Python Software Foundation). The fuzzy logic controller determines the proportion of soft tissue, cartilage, and woven bone in each finite-element at the next iteration. The inputs to the fuzzy controller are the minimum principal, maximum principal, and distortional strains in each element in the current iteration, as well as the proportion of cartilage and woven bone in each element (c_{cart} and c_{bone}) and the maximum proportion of cartilage and bone of all neighbouring elements (c_{nCart} and c_{nBone}). Neighbouring elements are defined as elements which share at least 1 node. The proportion of soft tissue in each element (c_{soft}) is determined from the relation given in Equation 3.

$$c_{soft} = 1 - c_{cart} - c_{bone} \quad (3)$$

Inputs are "fuzzified" by determining their membership of linguistic categorisations in their corresponding membership functions. The degree of membership is calculated on a 0 to 1 scale. Fuzzy membership functions were defined for tissue proportions (Figure 4A), minimum principal strain (Figure 4B), maximum principal strain (Figure 4C), and distortional strain (Figure 4D).

Four of the biological processes involved in the fracture healing process were implemented: chondrogenesis, cartilage calcification, intramembranous ossification, and endochondral ossification. Chondrogenesis was disabled for the first 7 iterations to prevent non-physiological periosteal cartilage formation. Each biological process was modelled as a fuzzy logic rule; the set of rules is given in Table 2.

The degree of activation of each rule was determined by interpreting the linguistic rule numerically. The membership of each individual statement was a value between 0 and 1, as determined by their input value and corresponding membership function. Each rule yields a single value between 0 and 1 which represents the degree of activation of that rule for the element. The effects on bone and cartilage concentration of all rules were summed for each element to determine the overall change in composition for the element. A temporal smoothing function was applied in which the bone and cartilage concentrations in the current iteration were calculated as the mean un-smoothed concentrations calculated by the algorithm on the previous N iterations (Lacroix and Prendergast, 2002). A parameter coefficient was used to scale the changes in bone and cartilage concentrations according to the element size. This parameter and the temporal smoothing parameter N were used to achieve mesh convergence. The results of a mesh convergence study are given in Supplementary Material.

2.4 Healing assessment

Bending stiffness of the fracture site was used as the healing assessment as IFM is a poor indicator of union (Ren and Dailey, 2020) and the corresponding experimental data includes a final bending stiffness assessment (Claes et al., 1997). Each axisymmetric FE model was converted to its corresponding 3D FE model to assess the bending stiffness of the final construct and resultant callus. The bone fragments were extended axially to create a 150 mm long fracture region, as was used in the experimental bending stiffness assessment by Claes et al. (1997). The bone fragments and callus were meshed with linear tetrahedral elements with element sizes of 1 mm and 0.5 mm, respectively. Material properties for the callus elements were mapped from the 2D callus by linearly interpolating

TABLE 2 The four fuzzy logics rules implemented in the fracture healing algorithm.

Rule	Bone	Cart	nBone	nCart	Minimum principal strain	Maximum principal strain	Distortional strain	ΔBone	ΔCart
Intramembranous Ossification		Low	Med or High			Med	Low	1	0
Chondrogenesis	Low		Med or High		Med	Low	Low	0	1
Chondrogenesis	Low			Med or High	Med	Low	Low	0	1
Cartilage Calcification	High	Low	High					1	−1
Endochondral Ossification		Med or High	Med or High		Low			1	−1

values of Young's modulus and Poisson's ratio from the centroids of the 2D callus elements, or by using a "nearest" extrapolation for 3D callus elements whose centroids fell outside of the interpolation window created by the 2D callus element centroids. The cylindrical coordinates of the 3D callus-element centroids were mapped to the 2D coordinate system for this interpolation. This process was automated. The spring representing the external fixator was removed, as the fixator was explanted prior to experimental bending stiffness assessment (Claes et al., 1997). A bending moment of 1500 N mm was applied through the retained node of the RBE2s at each bone fragment end. The distal retained node was fixed in all 5 other degrees of freedom, and the proximal retained node was fixed in 4 degrees of freedom, allowing for axial translation. Deflection was measured at the central-most node of the callus. Bending stiffness was calculated as the applied moment divided by the mid-span deflection.

2.5 Code availability

The code used to implement the fracture healing algorithm in this study is available at https://github.com/GeorgeTMorgan/fracture-healing-algorithm.

3 Results

3.1 Effect of initial callus domain size

No difference was observed on the qualitative progression on the simulated healing for Group B when increasing the initial region of the callus by 13% in radius and 20% in length, thereby demonstrating callus domain independence (Figure 5). The convergence of the healing simulation, defined by a change in IFM of less than 1% from the previous iteration, was delayed by 4 iterations in the simulation with a larger callus domain size.

3.2 Algorithm-predicted sequence of healing

Figure 6 illustrates the Young's modulus, bone concentration, cartilage concentration, and intramembranous ossification activation level at each callus finite-element during iterations 28, 56, 84, 112, and 140 of the simulation of group D. Notably, the healing algorithm demonstrates physiological bony growth on the periosteum via intramembranous ossification, with bridging occurring at the outer callus, rather than in the direct inter-cortical gap. The bridging process involves cartilage formation via chondrogenesis, and subsequent ossification through endochondral ossification, rather than intramembranous ossification.

3.3 Algorithm convergence

Simulations of groups A-E converged at iterations 55, 102, 73, 136, and 120, respectively. The simulation of group F failed to converge within 150 iterations. The IFM progressions of each group are visually represented in Figure 7A, while the mean IFM progressions for each corresponding experimental group are displayed in Figure 7B (Claes et al., 1997). Notably, the IFM progressions in the simulated groups closely mirror those observed in the experimental groups, and indicate that one healing day in the experimental data corresponds approximately to three simulation iterations.

3.4 Virtual mechanical testing

Virtual mechanical testing, conducted at the conclusion of the 150 iterations on the corresponding 3D FE model, measured bending stiffnesses of 6.9, 7.3, 7.2, 8.4, 7.8, and 1.8 N m mm^{-1} for groups A through F, respectively. The corresponding experimental bending stiffnesses were 24.3 ± 7.6, 35.6 ± 23.1, 26.6 ± 18.6, 15.8 ± 14.6, 8.9 ± 7.0, and 1.6 ± 0.9 N m mm^{-1}, respectively (Claes et al., 1997).

3.5 Healing sequence across groups

Figure 8 shows the Young's modulus at each callus finite-element during iterations 14, 28, 42, 56, 84, and 112 for groups A-F. The higher strain groups B, D, and F exhibited more extensive bony callus development compared to the lower strain groups A, C, and E. However, bony bridging in the higher strain groups was delayed compared to their lower strain counterparts.

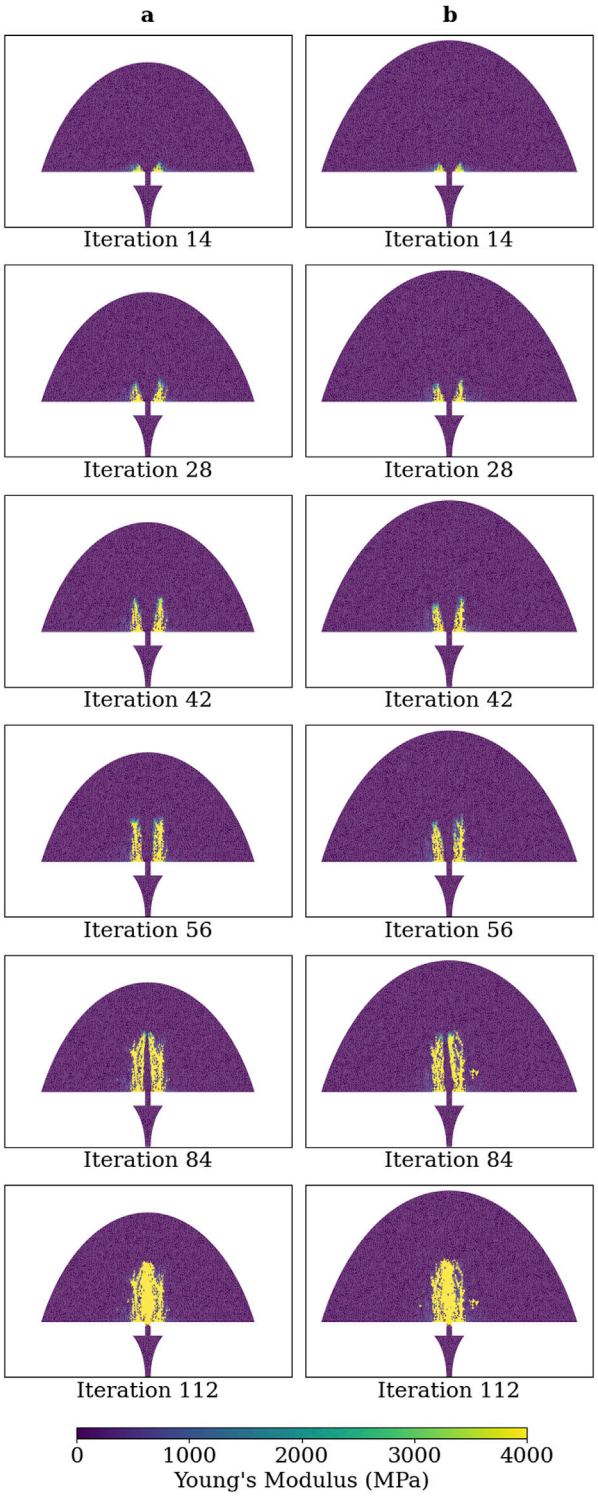

FIGURE 5
Young's modulus of each callus finite-element in simulations of group B at iterations: 14, 28, 42, 56, 84, and 112. **(A)** Callus domain geometry initialised as described in Figure 3A and **(B)** callus domain initialised with radius and length increased by 13% and 20%, respectively.

4 Discussion

This study introduced a novel fracture-healing algorithm based on principal strains as the primary mechanical stimuli. The algorithm was able to match closely experimental observations across different fixation stabilities and initial fracture-gap widths. Notably, this algorithm is the first of its kind capable of predicting cases not only of fracture union, but also non-union. There is no clear definition of non-union in the literature; non-union is characterised by a failure to restore the physiological function of the bone, such as weight-bearing in lower-limb long bones. Non-unions are diagnosed radiographically by observing a lack of bony bridging (Litrenta et al., 2015; Whelan et al., 2010); they are quantified *in vitro* using mechanical testing (Claes et al., 1997), and *in silico* using virtual mechanical testing (Ren et al., 2024; Schwarzenberg et al., 2021a). This study used virtual mechanical testing of bending stiffness to quantify bony union and non-union. The ability to distinguish between scenarios which are likely to result in union *versus* non-union is a primary clinical application of fracture-healing algorithms as early predictors of non-union.

Intramembranous ossification is stimulated by shearing between the periosteum of the bone fragments and the soft callus region, with areas closer to the fracture experiencing higher shear forces and greater bony outgrowth. These characteristics of intramembranous ossification are effectively captured by maximum principal strain, as used in this fracture-healing algorithm. Chondrogenesis and endochondral ossification occur between the bony protrusions where compression, represented by minimum principal strain, dominates. Previous fracture-healing algorithms utilised porous flow (Ghiasi et al., 2019; Isaksson et al., 2008), dilatational strain, and distortional strain (Isaksson et al., 2006; Shefelbine et al., 2005; Simon et al., 2011), with distortional strain identified as the dominant mechanical stimulus (Isaksson et al., 2006). Although distortional strain is closely correlated with both minimum and maximum principal strains, it cannot distinguish between the two. The use of principal strains as mechanical stimuli in this healing algorithm enabled a physiological fracture-healing process.

The patterns of IFM progression across the six groups align well with the corresponding experimental data (Figure 7). The healing algorithm was not temporally calibrated prior to the analyses conducted in this study, but the IFM progression patterns in Figure 7 suggest that three simulated healing iterations correspond approximately to 1 day of healing. While the ability of the healing algorithm to predict similar IFM progression patterns as experimental data is encouraging, the IFM itself is not an accurate measure of fracture healing. This inaccuracy is exemplified by Group F in both the simulated and experimental results of Claes et al. (1997), where IFM decreases significantly over the course of healing, yet union is not achieved. Instead, more informative measures of successful fracture union should be used, such as bending stiffness or torsional rigidity (Ren and Dailey, 2020).

The bending stiffness assessments of simulated healing cases using this healing algorithm revealed that the healing algorithm could distinguish between groups that clearly healed (groups A-D)

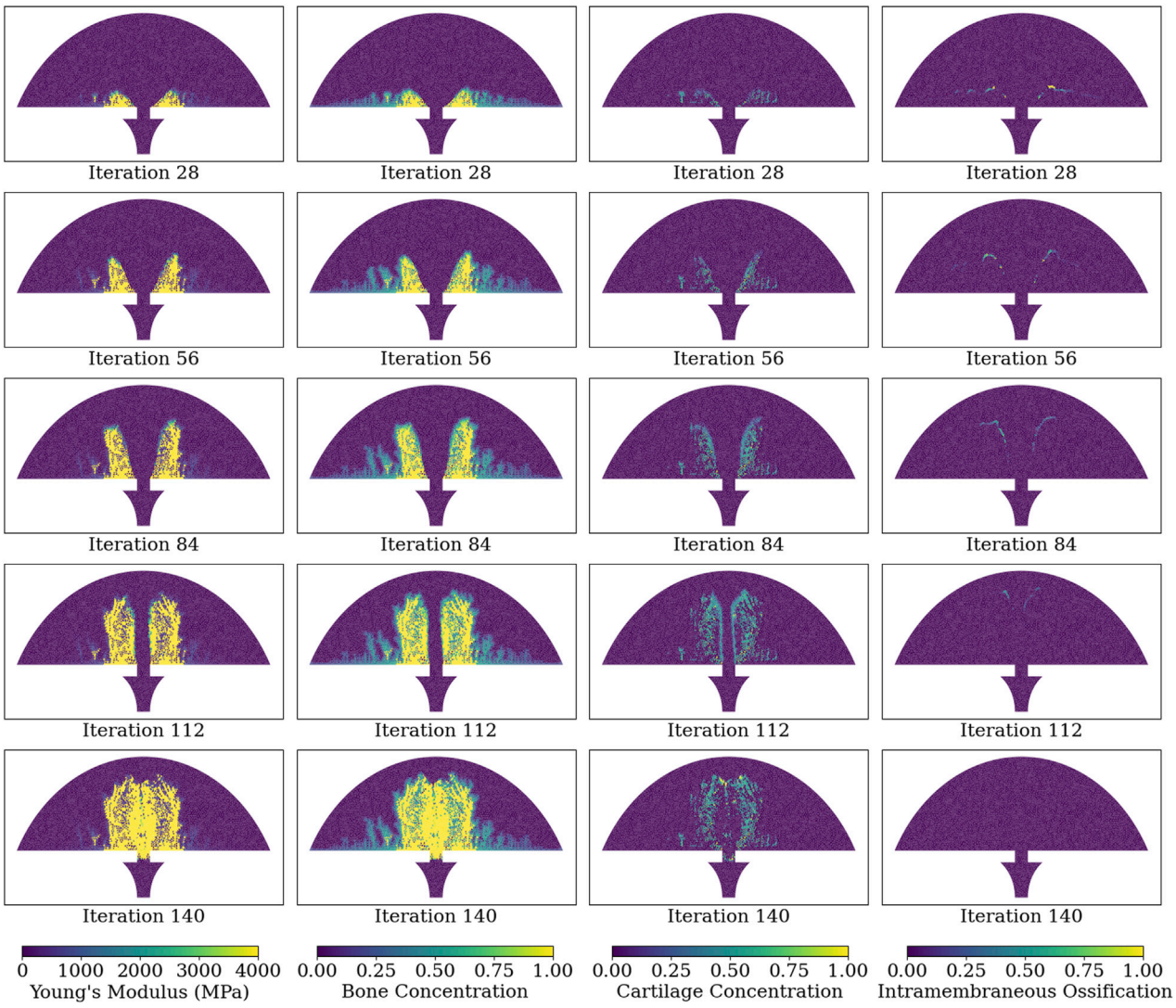

FIGURE 6
Simulated healing dynamics of Group D at iterations: 28, 56, 84, 112, and 140. The plotted variables for each callus finite-element span from the leftmost to the rightmost column: Young's modulus, bone concentration, cartilage concentration, and intramembranous ossification activation. Bone and cartilage concentrations are depicted as tissue proportions within the finite-element, with a bone concentration of 1.0 indicating full ossification. Intramembranous ossification is quantified as an activation proportion, with a value of 1.0 denoting complete biological rule activation.

and those that did not (group F), mirroring the trends in bending stiffness among the corresponding groups in experimental data (Claes et al., 1997). Although the trend in bending stiffness between the different groups was similar in the healing algorithm and the experimental data, a limitation of the current study is the discrepancy in the magnitudes of bending stiffness. For instance, the bending stiffness of group A was greater than that of group F in both the healing algorithm and experimental results, but the magnitudes of bending stiffness for group A were 6.9 and 24.3 N m mm^{-1} for simulation and experiment, respectively. This discrepancy is likely due to the absence of bone remodelling in the healing algorithm; woven bone does not get replaced with stiffer lamellar bone, in a process that physiologically occurs from early-on in the secondary fracture-healing process (Ren and Dailey, 2020). Incorporating a remodelling process into the fracture-healing algorithm would likely further ossify the periosteally formed bone, which is further from the fracture, and in the current model does not achieve a bone concentration greater than approximately 30% (Figure 6). Another limitation of the current healing algorithm is its deterministic nature in simulating of "borderline" healing cases; the algorithm predicted successful fracture union in group E, whereas experimental data showed group E to have a mean bending stiffness between those of successful healing groups A-D and the unsuccessful healing group F. The large variance in the experimental bending stiffnesses, with a standard deviation of 7.0 N m mm^{-1} and a mean of 8.9 N m mm^{-1} in group E, suggests that rather than all of the sheep healing partially, likely some of the sheep in the group healed successfully while others experienced non-unions. This group represents an ambiguous healing case in which the specifics of loading, fracture geometry, and fixator stiffness are likely required to predict accurately the healing outcome, rather than the idealised parameters which were used in this study.

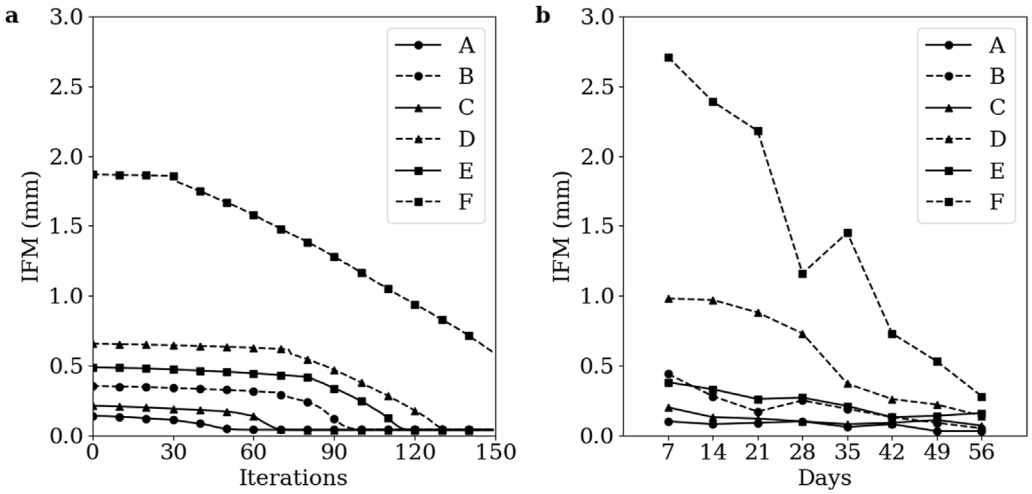

FIGURE 7
Temporal evolution of IFM across the healing process for groups A-F **(A)** Simulation data. **(B)** Corresponding experimental data. Groups A-F are as defined by Claes et al. The low strain groups A, C, and E are denoted with solid lines and the high strain groups B, D, and F are denoted with dashed lines. The 1 mm, 2 mm, and 6 mm initial gap size groups are denoted with circle, triangle, and square markers, respectively. Markers in the simulation data are denoted every 10 iterations.

A significant advantage of the fracture-healing algorithm presented in this study is its independence from the initial callus domain and the absence of a pre-defined hard callus geometry, while exhibiting physiologically accurate stages of secondary fracture healing. The simulations for all successful healing groups began with periosteal bony outgrowth followed by cartilaginous, and later bony, initial bridging of the fracture gap at the external callus, and importantly, not in the intercortical gap. These qualitative stages of secondary fracture healing are in agreement with established literature (Claes et al., 2012; Iwaki et al., 1997; Vetter et al., 2010). Previous fracture-healing algorithms have either shown inter-cortical bridging (Ament and Hofer, 2000; Ren and Dailey, 2020) or enforced external callus bridging using a pre-defined spatial proximity function which inhibits bone formation in the intercortical gap (Schwarzenberg et al., 2021b). Other algorithms prevent inter-cortical bridging through a "cellular diffusion" (Isaksson et al., 2006; Lacroix and Prendergast, 2002) or "vascular perfusion" (Shefelbine et al., 2005; Simon et al., 2011) parameter, which begins at the outer surface of the callus and diffuses inwards, only allowing bone formation where this parameter is active. Algorithms which use this diffusion parameter are therefore highly sensitive to the initial callus domain and diffusion rate (Isaksson et al., 2009). Given that callus geometry is highly variable between fracture types, and that the callus does not form until after surgical intervention, a fracture-healing algorithm that relies on accurate prescribed callus geometry may be useful for post-surgical rehabilitation management and early diagnosis of non-union, but is less suited for pre-operative planning, novel device development, or *in silico* clinical trials. The fracture healing algorithm presented in this study, demonstrating callus domain independence, is better suited for these applications.

Although the fracture-healing algorithm in this study aligns qualitatively with established literature and quantitatively with corresponding experimental data, the fracture scenario modelled is quite basic: it simulates an ovine metatarsal, which predominantly experiences axial loading (Duda et al., 1997), and the high reported bending and torsional stiffness of the external fixator (Claes et al., 1995) allows for an axisymmetric approximation to reduce computational expense. Realistic clinical fracture scenarios and fixators will require the ability to model non-axisymmetric loading. Therefore, this fracture-healing algorithm should be expanded into a 3D representation to accommodate these expected loads. Modelling in 3D would also enable patient-specific simulations, where bone fragment geometries are identified using CT imaging, and loads are derived from gait analysis and musculoskeletal modelling (Orth et al., 2023). For computational simplicity this first version of the algorithm utilises a static loading case, accepting that this is a slight deviation from the dynamic loading expected in reality.

The tissues modelled in this study are physiologically anisotropic, but were assumed isotropic for simplification, similarly to previous fracture-healing algorithms. The incorporation of anisotropic material models may allow the algorithm to capture more accurately the physiological deformations throughout the healing process. As the present version of the algorithm was able to capture the overall healing progressions and outcomes of the cases simulated nevertheless, modelling anisotropy was deemed unnecessary at this stage. Additionally, the values of material properties used in this study are an uncertainty, reflecting the wide range of values reported from experimental studies and used in numerical simulations. A parametric analysis of the algorithm to material models and material properties used should be considered in future, to understand the sensitivity of the algorithm's predicted healing outcome to input material properties. A future version of the healing algorithm should consider the results for the sensitivity study and amend the material models of the tissues involved appropriately to reflect reality more accurately.

The significance of principal strains in the fracture-healing process has not been investigated experimentally. Such investigation may help validate the use of minimum and

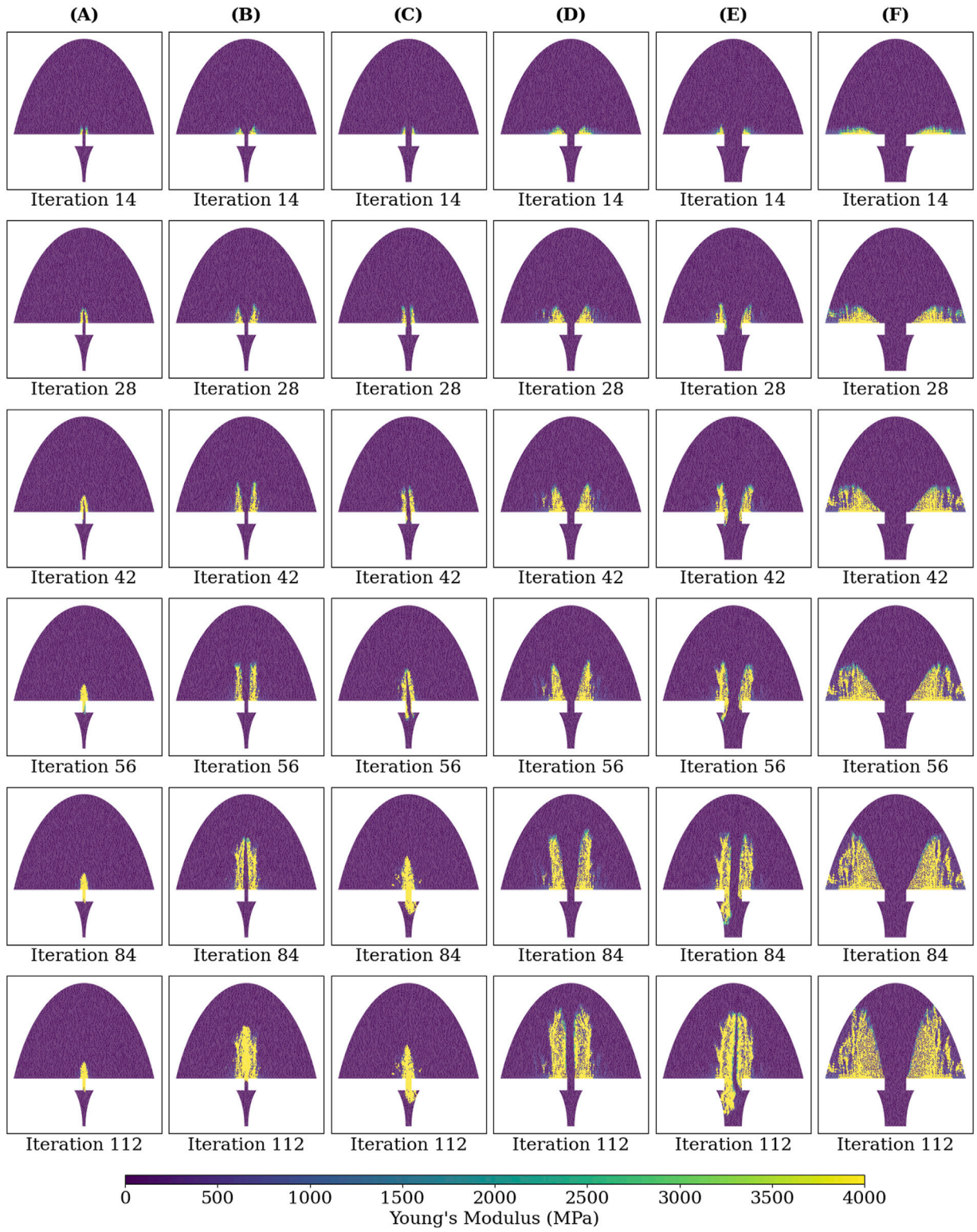

FIGURE 8
Young's modulus of each callus finite-element at iterations: 14, 28, 42, 56, 84, and 112 of the simulated healing process for groups **(A-F)**.

maximum principal strains as mechanical stimuli for the biological fracture-repair process in the fracture-healing algorithm presented here. A previous *in vivo* study on rats has explored various strain measures, including maximum principal strain, in different tissue types during secondary fracture healing, but unfortunately did not report minimum and maximum principal strains to investigate their individual effects on separate ossification processes (Morgan et al., 2010).

5 Conclusion

This study presents a novel fracture-healing algorithm which uses minimum and maximum principal strains as the mechanical inputs. The use of these strains allowed for the callus domain independence of the algorithm, without the need to prescribe the temporal-spatial ossification pathway of the callus. Validation was performed against published data from experimental animal studies for cases resulting in both union and, importantly, non-union. The capabilities demonstrated by this algorithm allow for its practical application to pre-surgical planning, novel fracture-fixation device development, rehabilitation-regime management, and non-union risk assessment. Future steps in the development of this algorithm will focus on its expansion to 3D simulation to capture a wider variety of fracture geometries and fixator types. This will allow the comparison between treatments for fracture types which have been insufficiently addressed by traditional clinical trials.

Data availability statement

The original contributions presented in the study are included in the article/Supplementary Material, further inquiries can be directed to the corresponding author.

Author contributions

GM: Methodology, Software, Validation, Visualization, Writing–original draft, Writing–review and editing. LL: Software, Writing–review and editing. AR: Conceptualization, Writing–review and editing. SM: Conceptualization, Methodology, Supervision, Writing–review and editing.

Funding

The author(s) declare that financial support was received for the research, authorship, and/or publication of this article. GM was supported by a DTP studentship from the Engineering and Physical Sciences Research Council (grant number EP/T51780X/1). For the purpose of open access, the authors have applied a Creative Commons Attribution (CC BY) license to any Author Accepted Manuscript version arising.

Conflict of interest

The authors declare that the research was conducted in the absence of any commercial or financial relationships that could be construed as a potential conflict of interest.

Publisher's note

Supplementary material

The Supplementary Material for this article can be found online at: https://www.frontiersin.org/articles/10.3389/fbioe.2024.1477405/full#supplementary-material

References

Ament, C., and Hofer, E. P. (2000). A fuzzy logic model of fracture healing. *J. Biomech.* 33, 961–968. doi:10.1016/s0021-9290(00)00049-x

Claes, L., Augat, P., Suger, G., and Wilke, H. (1997). Influence of size and stability of the osteotomy gap on the success of fracture healing. *J. Orthop. Res.* 15, 577–584. doi:10.1002/jor.1100150414

Claes, L., Recknagel, S., and Ignatius, A. (2012). Fracture healing under healthy and inflammatory conditions. *Nat. Rev. Rheumatol.* 8, 133–143. doi:10.1038/nrrheum.2012.1

Claes, L., Wilke, H.-J., Augat, P., Rübenacker, S., and Margevicius, K. (1995). Effect of dynamization on gap healing of diaphyseal fractures under external fixation. *Clin. Biomech.* 10, 227–234. doi:10.1016/0268-0033(95)99799-8

Claes, L. E., and Heigele, C. A. (1999). Magnitudes of local stress and strain along bony surfaces predict the course and type of fracture healing. *J. Biomech.* 31, 51. doi:10.1016/s0021-9290(98)80105-x

Duda, G. N., Eckert-Hübner, K., Sokiranski, R., Kreutner, A., Miller, R., and Claes, L. (1997). Analysis of inter-fragmentary movement as a function of musculoskeletal loading conditions in sheep. *J. Biomech.* 31, 201–210. doi:10.1016/S0021-9290(97)00127-9

Ghiasi, M. S., Chen, J. E., Rodriguez, E. K., Vaziri, A., and Nazarian, A. (2019). Computational modeling of human bone fracture healing affected by different conditions of initial healing stage. *BMC Musculoskelet. Disord.* 20, 562. doi:10.1186/s12891-019-2854-z

Griffin, X. L., Costa, M. L., Phelps, E., Parsons, N., Dritsaki, M., Png, M. E., et al. (2019). Retrograde intramedullary nail fixation compared with fixed-angle plate fixation for fracture of the distal femur: the TrAFFix feasibility RCT. *Health Technol. Assess.* 23, 1–132. doi:10.3310/hta23510

Hoffmann, W., Feliciano, S., Martin, I., de Wild, M., and Wendt, D. (2015). Novel perfused compression bioreactor system as an *in vitro* model to investigate fracture healing. *Front. Bioeng. Biotechnol.* 3, 10. doi:10.3389/fbioe.2015.00010

Isaksson, H., Van Donkelaar, C. C., Huiskes, R., and Ito, K. (2008). A mechano-regulatory bone-healing model incorporating cell-phenotype specific activity. *J. Theor. Biol.* 252, 230–246. doi:10.1016/j.jtbi.2008.01.030

Isaksson, H., Van Donkelaar, C. C., and Ito, K. (2009). Sensitivity of tissue differentiation and bone healing predictions to tissue properties. *J. Biomech.* 42, 555–564. doi:10.1016/j.jbiomech.2009.01.001

Isaksson, H., Wilson, W., Van Donkelaar, C. C., Huiskes, R., and Ito, K. (2006). Comparison of biophysical stimuli for mechano-regulation of tissue differentiation during fracture healing. *J. Biomech.* 39, 1507–1516. doi:10.1016/j.jbiomech.2005.01.037

Iwaki, A., Jingushi, S., Oda, Y., Izumi, T., Shida, J.-I., Tsuneyoshi, M., et al. (1997). Localization and quantification of proliferating cells during rat fracture repair: detection of proliferating cell nuclear antigen by immunohistochemistry. *J. Bone Min. Res.* 12, 96–102. doi:10.1359/jbmr.1997.12.1.96

Kohli, N., Theodoridis, K., Hall, T. A. G., Sanz-Pena, I., Gaboriau, D. C. A., and Van Arkel, R. J. (2023). Bioreactor analyses of tissue ingrowth, ongrowth and remodelling around implants: an alternative to live animal testing. *Front. Bioeng. Biotechnol.* 11, 1054391. doi:10.3389/fbioe.2023.1054391

Lacroix, D., and Prendergast, P. J. (2002). A mechano-regulation model for tissue differentiation during fracture healing: analysis of gap size and loading. *J. Biomech.* 35, 1163–1171. doi:10.1016/S0021-9290(02)00086-6

Litrenta, J., Iii, P. T., Mehta, S., Jones, C., O'Toole, R. V., Bhandari, M., et al. (2015). Determination of radiographic healing: an assessment of consistency using RUST and modified RUST in metadiaphyseal fractures. *J. Orthop. Trauma* 29, 516–520. doi:10.1097/bot.0000000000000390

Megafu, M., Mian, H., Megafu, E., Singhal, S., Lee, A., Cassie, R., et al. (2022). The fragility of statistical significance in distal femur fractures: systematic review of randomized controlled trials. *Eur. J. Orthop. Surg. Traumatol.* 33, 2411–2418. doi:10.1007/s00590-022-03452-3

Morgan, E. F., Salisbury Palomares, K. T., Gleason, R. E., Bellin, D. L., Chien, K. B., Unnikrishnan, G. U., et al. (2010). Correlations between local strains and tissue phenotypes in an experimental model of skeletal healing. *J. Biomech.* 43, 2418–2424. doi:10.1016/j.jbiomech.2010.04.019

Nayak, G. S., Roland, M., Wiese, B., Hort, N., and Diebels, S. (2024). Influence of implant base material on secondary bone healing: an *in silico* study. *Comput. Methods Biomech. Biomed. Engin.*, 1–9. doi:10.1080/10255842.2024.2338121

Orth, M., Ganse, B., Andres, A., Wickert, K., Warmerdam, E., Müller, M., et al. (2023). Simulation-based prediction of bone healing and treatment recommendations for lower leg fractures: effects of motion, weight-bearing and fibular mechanics. *Front. Bioeng. Biotechnol.* 11, 1067845. doi:10.3389/fbioe.2023.1067845

Pappalardo, F., Russo, G., Tshinanu, F. M., and Viceconti, M. (2019). *In silico* clinical trials: concepts and early adoptions. *Brief. Bioinform.* 20, 1699–1708. doi:10.1093/bib/bby043

Pappalardo, F., Wilkinson, J., Busquet, F., Bril, A., Palmer, M., Walker, B., et al. (2022). Toward A regulatory pathway for the use of *in silico* trials in the ce marking of medical devices. *IEEE J. Biomed. Health Inf.* 26, 5282–5286. doi:10.1109/JBHI.2022.3198145

Quinn, C., Kopp, A., and Vaughan, T. J. (2022). A coupled computational framework for bone fracture healing and long-term remodelling: investigating the role of internal fixation on bone fractures. *Int. J. Numer. Methods Biomed. Eng.* 38, e3609. doi:10.1002/cnm.3609

Ren, T., and Dailey, H. L. (2020). Mechanoregulation modeling of bone healing in realistic fracture geometries. *Biomech. Model. Mechanobiol.* 19, 2307–2322. doi:10.1007/s10237-020-01340-5

Ren, T., Inglis, B., Darwiche, S., and Dailey, H. L. (2024). Torsion constants and virtual mechanical tests are valid image-based surrogate measures of ovine fracture healing. *J. Orthop. Res.* 42, 1810–1819. doi:10.1002/jor.25836

Sarrami-Foroushani, A., Lassila, T., MacRaild, M., Asquith, J., Roes, K. C. B., Byrne, J. V., et al. (2021). In-silico trial of intracranial flow diverters replicates and expands insights from conventional clinical trials. *Nat. Commun.* 12, 3861. doi:10.1038/s41467-021-23998-w

Schwarzenberg, P., Klein, K., Ferguson, S. J., Von Rechenberg, B., Darwiche, S., and Dailey, H. L. (2021a). Virtual mechanical tests out-perform morphometric measures for assessment of mechanical stability of fracture healing *in vivo*. *J. Orthop. Res.* 39, 727–738. doi:10.1002/jor.24866

Schwarzenberg, P., Ren, T., Klein, K., Von Rechenberg, B., Darwiche, S., and Dailey, H. L. (2021b). Domain-independent simulation of physiologically relevant callus shape in mechanoregulated models of fracture healing. *J. Biomech.* 118, 110300. doi:10.1016/j.jbiomech.2021.110300

Shefelbine, S. J., Augat, P., Claes, L., and Simon, U. (2005). Trabecular bone fracture healing simulation with finite element analysis and fuzzy logic. *J. Biomech.* 38, 2440–2450. doi:10.1016/j.jbiomech.2004.10.019

Simon, U., Augat, P., Utz, M., and Claes, L. (2011). A numerical model of the fracture healing process that describes tissue development and revascularisation. *Comput. Methods Biomech. Biomed. Engin.* 14, 79–93. doi:10.1080/10255842.2010.499865

Steiner, M., Claes, L., Ignatius, A., Simon, U., and Wehner, T. (2014). Numerical simulation of callus healing for optimization of fracture fixation stiffness. *PLoS ONE* 9, e101370. doi:10.1371/journal.pone.0101370

Vetter, A., Epari, D. R., Seidel, R., Schell, H., Fratzl, P., Duda, G. N., et al. (2010). Temporal tissue patterns in bone healing of sheep. *J. Orthop. Res.* 28, 1440–1447. doi:10.1002/jor.21175

Viceconti, M., Emili, L., Afshari, P., Courcelles, E., Curreli, C., Famaey, N., et al. (2021). Possible contexts of use for *in silico* trials methodologies: a consensus-based review. *IEEE J. Biomed. Health Inf.* 25, 3977–3982. doi:10.1109/JBHI.2021.3090469

Wadhwa, H., Salazar, B. P., Goodnough, L. H., Van Rysselberghe, N. L., DeBaun, M. R., Wong, H.-N., et al. (2022). Distal femur replacement versus open reduction and internal fixation for treatment of periprosthetic distal femur fractures: a systematic review and meta-analysis. *J. Orthop. Trauma* 36, 1–6. doi:10.1097/BOT.0000000000002141

Warner, J., Sexauer, J., Scikit-Fuzzy, Twmeggs, A., Aishwarya, U., Castelão, G., et al. (2019). JDWarner/scikit-fuzzy: Scikit-Fuzzy version 0.4.2. doi:10.5281/ZENODO.3541386

Whelan, D. B., Bhandari, M., Stephen, D., Kreder, H., McKee, M. D., Zdero, R., et al. (2010). Development of the radiographic union score for tibial fractures for the assessment of tibial fracture healing after intramedullary fixation. *J. Trauma Inj. Infect. Crit. Care* 68, 629–632. doi:10.1097/TA.0b013e3181a7c16d

frontiers | Frontiers in Bioengineering and Biotechnology

TYPE Original Research
PUBLISHED 23 December 2024
DOI 10.3389/fbioe.2024.1459056

OPEN ACCESS

EDITED BY
Lei Fan,
Marquette University, United States

REVIEWED BY
Simone Ranaldi,
Roma Tre University, Italy
Andrea Tigrini,
Marche Polytechnic University, Italy

*CORRESPONDENCE
Saeed Mollaee,
smol775@aucklanduni.ac.nz

RECEIVED 03 July 2024
ACCEPTED 25 November 2024
PUBLISHED 23 December 2024

CITATION
Mollaee S, HajiRassouliha A, Budgett DM, Taberner AJ and Nielsen PMF (2024) Model-based design of a pneumatic actuator for a dynamically reconfigurable socket for transtibial amputees.
Front. Bioeng. Biotechnol. 12:1459056.
doi: 10.3389/fbioe.2024.1459056

Model-based design of a pneumatic actuator for a dynamically reconfigurable socket for transtibial amputees

Saeed Mollaee[1]*, Amir HajiRassouliha[1], David M. Budgett[1], Andrew J. Taberner[1,2] and Poul M. F. Nielsen[1,2]

[1]Auckland Bioengineering Institute, The University of Auckland, Auckland, New Zealand, [2]Department of Engineering Science and Biomedical Engineering, The University of Auckland, Auckland, New Zealand

In this work, a cost-effective, scalable pneumatic silicone actuator array is introduced, designed to dynamically conform to the user's skin and thereby alleviate localised pressure within a prosthetic socket. The appropriate constitutive models for developing a finite element representation of these actuators are systematically identified, parametrised, and validated. Employing this computational framework, the surface deformation fields induced by 270 variations in soft actuator array design parameters under realistic load conditions are examined, achieving predictive accuracies within 70 µm. The results elucidate how individual design factors influence surface deformation and, consequently, pressure distribution. A novel speckle imaging technique is employed to address the complex non-linear deformations, enabling surface displacement measurements with an accuracy of approximately 40 µm. These measurements confirm that the Ogden N3 model can predict actuator deformation with an accuracy of 16%. These findings elucidate the relationships among actuator geometry, material behaviour, and surface deformation. Although demonstrated in a dynamically reconfigurable socket for transtibial amputees, these insights are readily transferable to other robotics applications that require soft, deformable, load-bearing interfaces. This validated modelling strategy and imaging technique provide a foundation for optimising soft actuator arrays, ultimately improving user comfort and enhancing the functionality of future prosthetic and robotic devices.

KEYWORDS

finite element method, pneumatic soft actuator array, adjustable prosthetic socket, image registration algorithm, hyperelastic modelling, computer vision, reconfigurable socket

Introduction

The global incidence of lower limb amputation is escalating, primarily from diabetes and its consequent 8- to 24-fold increase in rates of amputation (Fosse et al., 2009). The World Health Organisation reported 415 million diabetes cases in 2015, with predicted growth to 642 million in 2040 and a corresponding increase in amputations (W. H. Organization and USAID). In 2005 it was estimated that in United States alone about 1.6 million people suffered lower limb amputation, projected to increase to 3.6 million by 2050 (Ziegler-Graham et al., 2008).

Limb amputations cause severe physical disabilities which affect the amputee's quality of life. One of the most common treatments to restore lost functionality following lower-limb amputation is to use a prosthetic leg that attaches to the residual limb *via* a socket

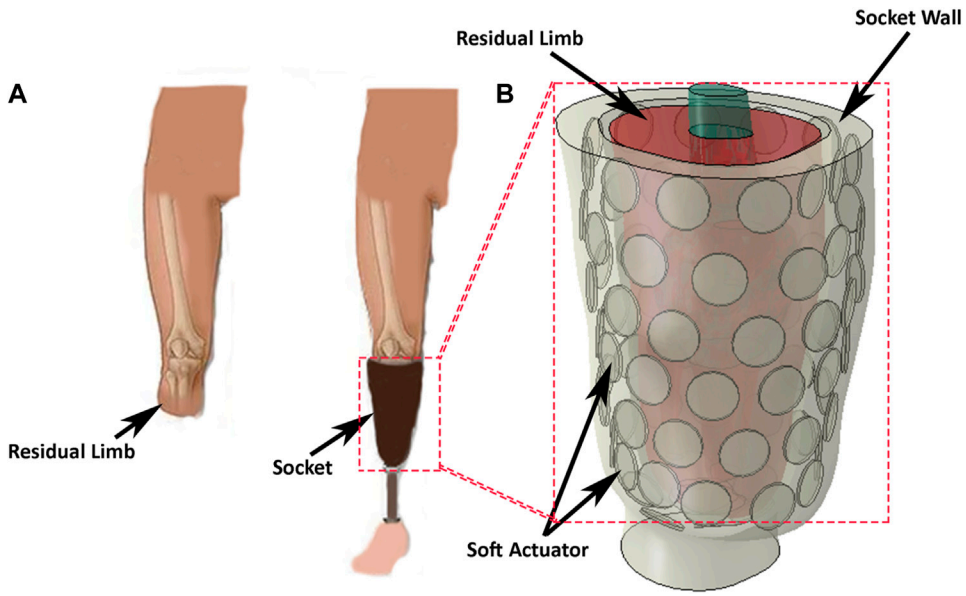

FIGURE 1
(A) A transtibial left-amputee, wearing a socket and prosthesis, and with the prosthesis removed. **(B)** Concept of a reconfigurable socket incorporating a soft-actuator array to manage the interface between the prosthesis and the skin surface of the stump.

(Figure 1A). In transtibial amputees, the body load must be supported by the surface of the residual limb (stump), resulting in high stresses in the residual limb soft tissues (Sanders and Daly, 1993). But soft tissues are typically not well-suited for carrying such high stresses.

Two socket designs are commonly used to minimise tissue damage and alleviate pain. The first of these is the patella tendon bearing (PTB) socket design, which applies loads to regions of the residual limb known as "pressure tolerant" areas. The second is the total surface bearing (TSB) socket design which distributes the load almost uniformly over the residual limb surface. Both designs have shortcomings, the most common being fit and comfort (Baars et al., 2018), (Sherman, 1999), (Pezzin et al., 2004).

Socket comfort depends principally on the pressure distribution at the interface between the socket and the residual limb (Mollaee et al., 2024). In one study of approximately 600 amputees, more than 60% were dissatisfied with their prostheses (Sinha et al., 2011) mainly because of discomfort resulting from poor socket fit. Often poor fit arises due to residual limb volume fluctuation (Gailey et al., 2010), (Paternò et al., 2018), which can result in pressure concentrations at the socket/stump interface. Regions of the stump that are overloaded for long durations can experience poor blood circulation and severe damage, such as vascular occlusions (Meulenbelt et al., 2009), skin irritation, pressure ulcers, and other dermatological problems (Lyon et al., 2000). Thus, controlling the pressure distribution at the socket/stump interface may reduce discomfort and skin-related problems (Mirjavadi et al., 2021).

Over the past few decades, work on transtibial socket design has concentrated on enhancing the socket fit and controlling the pressure distribution. Previously, sockets had a generic residual limb shape, with a tight corset to partially off-load the stump, or used a hydrostatic technique to provide uniform pressure distribution over the stump (Sewell et al., 2000). Some sockets used a combination of these techniques to improve socket fit (Pirouzi et al., 2014), (Stevens et al., 2019), adjusting stiffness at particular regions (Sengeh and Herr, 2013a) to control the pressure distribution or including movable sections to adjust the socket size and compensate for stump volume fluctuation (Weathersby et al., 2022).

Kahle et al. (2020) stated that socket design significantly impacts both gait stability and comfort in prosthetic users, with discomfort frequently reported in commonly used designs, such as the ischial ramus containment socket. Their study observed no significant differences in comfort or skeletal motion among ischial ramus containment, dynamic, and sub-ischial sockets, suggesting that alternative designs could provide comparable support without compromising comfort. Åström and Stenström (2004) mentioned that the polyurethane socket concept significantly enhanced comfort and physical capacity in transtibial amputees compared to conventional suspension systems. Despite these improvements in comfort, gait registration did not provide useful insights into amputees' satisfaction or socket comfort. Hsu et al. (2018) illustrated that the design of the prosthetic socket is a key factor influencing the comfort of amputees, as improper fitting can lead to localized pressure points and discomfort. They further emphasized that advancements in socket design, such as improved pressure relief and better interface stress distribution, can significantly enhance comfort and overall user satisfaction.

In recent years, the development of 'soft robotics' (El-Atab et al., 2020) has found many applications from manufacturing to healthcare (Rosso et al., 2005; Morales et al., 2014). In prosthetic design, soft pneumatic sensorised liners have been used inside transtibial sockets to accommodate volume change in residual limbs and allow pressure control on the residual limb (Carrigan et al., 2016) which are mainly made of hyperelastic materials, especially elastomers like rubber, silicone, and some types of polyurethane, are widely studied for their behavior under different loading conditions (Mollaee et al., 2023). Hyperelastic

modeling of the skin, using a three-parameter hyperelastic model, is crucial for optimizing prosthetic socket designs by accurately simulating the skin's nonlinear deformation and ensuring a better fit to reduce discomfort and pressure points. Recently, several researchers have focused on modeling hyperelastic structures for use in biomedical applications, including prosthetic socket design (Afshari et al., 2022; Mirjavadi et al., 2020; Forsat, 2020). Others Paterno et al. (2022) have added an actuator between two fibre layers to create an inner flexible socket for transfemoral amputees.

High costs and limited functionality in existing lower-limb prosthetic solutions have created a need for advanced, multifunctional devices. To address this, new prosthetic socket designs should integrate soft actuators that facilitate real-time pressure sensing, enhancing user comfort and fit. Additionally, incorporating myoelectric sensors, as demonstrated in recent gait phase recognition studies, could significantly improve the controllability and adaptability of these devices, enabling smoother, more natural movements for users (Tigrini et al., 2024).

Despite these advances there remain several shortcomings with prosthetic sockets (Paternò et al., 2018), (Mak et al., 2001). Principal among these is poor control of the displacement of soft actuators in prosthetic sockets, and designs that are complicated to manufacture (Weathersby et al., 2022; Carrigan et al., 2016; Paterno et al., 2022). Furthermore, no study has thoroughly characterised the behaviour of a soft actuator array under realistic loading conditions and provided an easily-manufactured, cost-efficient, and simple design for a soft actuator array (Mollaee et al., 2023). Consequently, no device has yet been constructed that enables the user to redistribute the pressure over the whole residual limb, nor control socket volume fluctuation over stump.

Here, we present the design of a pneumatic actuator array suitable for use in a dynamically reconfigurable socket (Figure 1B). The array comprises multiple independent pneumatic actuators that can be reconfigured to control the internal shape of the socket and/or the pressure distribution at the socket/stump interface. This approach provides control over the pressure distribution and volume adjustment over the stump and may alleviate discomfort by temporarily or permanently removing the load from sensitive areas.

We first detail the design and construction of a soft actuator array constructed from a silicone elastomer. Next, we model the array with a suite of finite element (FE) models, using a variety of constitutive relations for the elastomeric material. The predictions of the models are validated by using a force/torque transducer to indent the surface of a prototype soft actuator, while the shape and deformation of the soft actuator array surface is profiled at high-resolution. We thus identify the constitutive relation and material parameters that best predict actuator deformation. Next, we use the model to study the effect of design parameters on the surface deformation and surface pressure distribution of an array of actuators. Finally, we discuss how each design parameter affects the soft actuator surface pattern and surface displacement.

Methods

Design requirements

During normal activity, the load experienced by the stump greatly exceeds the static load imposed by the user's weight. Several studies have investigated the pressure at different regions of the residual limb during various activities, reporting the shear and normal stress, or simply the pressure (Ko et al., 2018; Sanders et al., 1998; Dou et al., 2006; Rajtukova et al., 2014; Sengeh and Herr, 2013b; Swanson et al., 2018). Based on these data, it is, reasonable to assume that the maximum normal stress and maximum shear stress developed at the stump-socket interface is limited to approximately 200 kPa and 10 kPa, respectively.

We propose that the inner surface of a socket be assembled from an array of soft actuators to allow control over the surface shape and/or the pressure distribution applied to the stump (Figure 1A). To explore the feasibility of this proposition, we constructed a linear array of four pneumatically driven disc-shaped 'voids' embedded in a silicone elastomer. Platinum-catalysed silicones were selected for the actuators because they are flexible and are able to be subjected to repeatable strains of over 150% without damage (Smooth On Ecoflex 00-50).

A proof-of-concept array comprised four independently controlled actuators spaced along the length of a rectangular block of silicone (Figure 2). Each actuator was operated by inflating the void with air at controlled pressure, thereby extending the silicone, predominantly in the axial direction of the void. The bottom surface of the actuator was fixed to a stiff base layer of acrylic (not shown). The soft actuator array was 90 mm long, 25 mm wide, and 16 mm thick, dimensions suitable for embedding in the proposed socket. The void diameter was set to 16 mm, with voids spaced 18 mm apart, resulting in an equal distance between the void centres.

Soft actuator construction

The soft actuator array was cast in an acrylic mould which comprised a shell producing the desired thickness for the soft actuator, four discs to form voids inside the soft actuator base, and four screws for holding the voids at the desired distance from the base. Two-part silicone (Ecoflex 00-50) was mixed and degassed in a vacuum chamber to eliminate entrapped air and poured into the mould. Following curing at room temperature for 12 h, the discs forming the voids were removed through the screw holes, which were later used for inflation. Silicone tubes were adhered to the holes on the base and used to pressurise each void individually. A black speckle pattern was airbrushed on the actuator surface to generate a wide-spatial-density random pattern for optical tracking using a stereo image reconstruction algorithm (Figure 3).

Measuring soft-actuator array performance

Actuators were driven by applying, independently, an air pressure to each void, using four electronic pressure regulators (ITV1000, SMC Corporation, Japan). Each regulator was controlled through an analogue input/output device (National Instruments myRIO-1900) from LabVIEW 2019 (NI). The regulators were connected to the actuators using silicone tubes with internal and external diameters of 2 mm and 4 mm respectively. The actuators were pre-inflated to a pressure of 60 kPa.

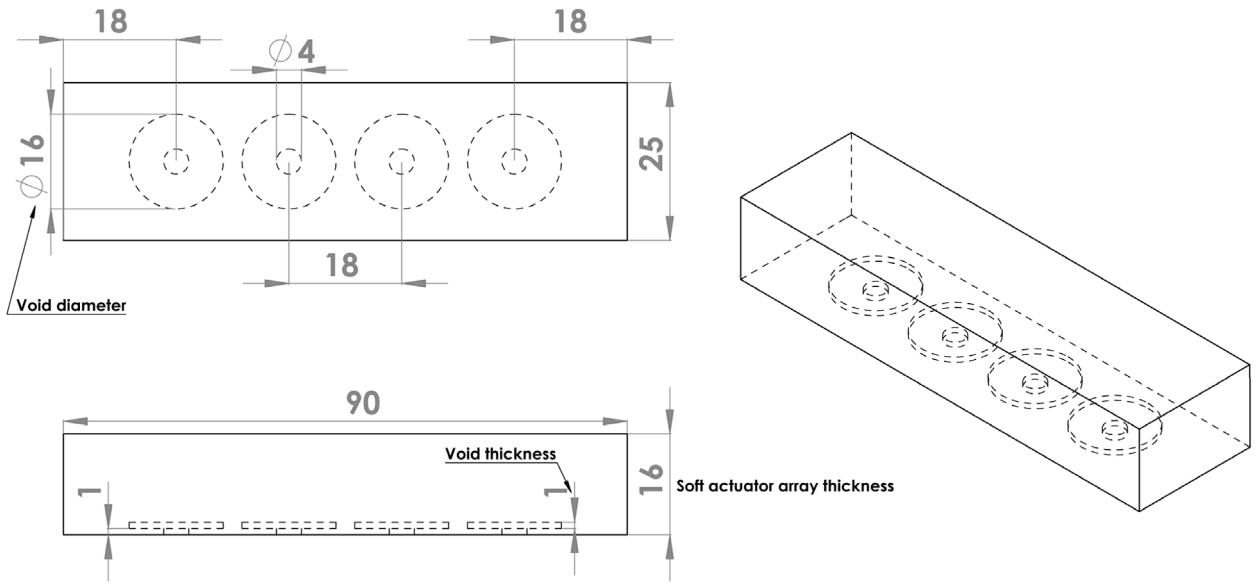

FIGURE 2
Soft actuator array design. All dimensions are in mm.

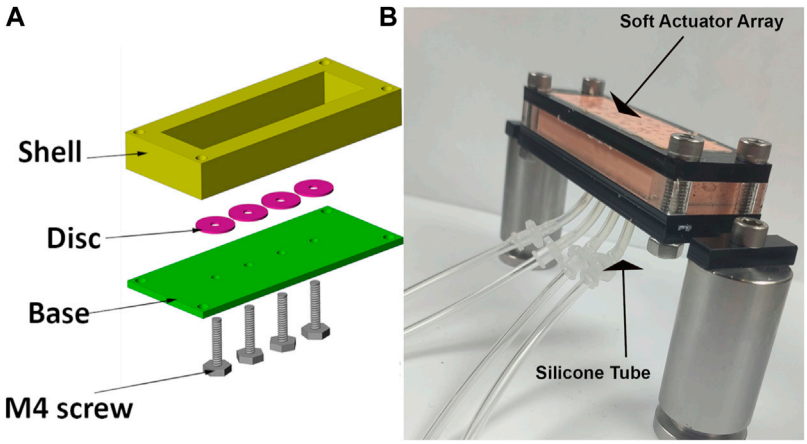

FIGURE 3
(A) mould components to construct the soft actuator arrays. Disc used to form the void and held in location during curing with M4 screw. **(B)** Photograph of assembled soft actuator arrays and silicone tubes connected to each void.

Actuator force/torque production and deformation was measured using a mechanical testing apparatus. A six-axis force-torque transducer (nano 17, ATI Industrial Automation) with an attached cylindrical tip (2.66 mm diameter) was manually advanced against the actuator array surface by a micrometer. The 3D reaction force vector was measured while the micrometer was advanced by a displacement measured to 10 µm resolution (Figure 4). The deformation of the actuator surface was measured across a rectangular area of 15 mm × 25 mm centred on the location of the indenter tip, using a custom stereoscopic imaging system. The indentation started at 0 mm and ended at 2.5 mm, after 25 increments of 100 µm.

Surface deformation was measured using a stereoscopic system consisting of four machine-vision cameras (Flea3 FL3-U3-13Y3M, Teledyne FLIR LCC, United States), each equipped with 6 mm lenses (Fujinon Lens DF6HA-1B, Fujifilm Corporation, Japan). To reduce specular reflections, circular polarisers (PL-CIR S 27 mm/0.75, Hoya Corporation, Japan) were attached to each lens. Cameras were mounted at 45° on acrylic blocks at the four corners of a rectangular aluminium optical breadboard, with sides approximately 225 mm and 150 mm (Figure 4). Software-triggered image acquisition was performed in at a rate of one capture per indentation increment. Surface illumination was provided by four green (560 nm) light-emitting diodes (LEDs), mounted between the cameras. Identification of the cameras' intrinsic and extrinsic parameters was achieved using a multi-camera calibration technique, which automatically calculated parameters from sets of calibration images of a checkerboard pattern (Haji Rassouliha, 2017).

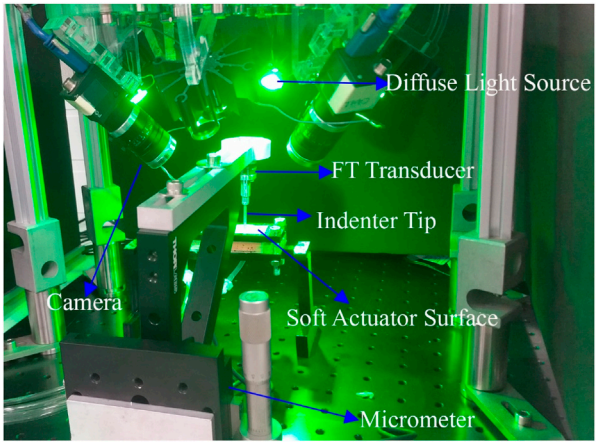

FIGURE 4
The indentation experiment setup. Micrometre and four camera stereoscope performing indentation experiment on an Ecoflex 0050 soft actuator. Force-torque transducer records the force data during the indentation, and cameras take a picture from four different views at each step.

Surface profiling

The calibrated stereoscope system was used to reconstruct the 3D geometry by integrating the overlapping views of at least two cameras using the method of HajiRassouliha et al. (2019) for surface profiling. We applied biquadratic polynomial transforms into three views to align with the view from a fourth camera, known as the reference camera.

At each pair view (the overlapping view of two cameras), approximately 90 distinct points were matched as an initial guess to estimate the surface shape and deformation. To generate the new position of the features at each indentation step, we used the subpixel image registration algorithm of HajiRassouliha et al. (2017) with a 64 pixel × 64 pixel window. This algorithm generated a point cloud corresponding to the surface shape at each indentation step, including the new coordinates of the tracked points in 3D (HajiRassouliha et al., 2019; HajiRassouliha et al., 2013) When imaging the soft actuator under the indentation, some areas of the surface were obscured due to occlusion by the indenter tip. To address this issue, the coordinates from non-obscured cameras were used to reconstruct the surface and compensate for the missing data in the reference camera view (Figure 5).

Finite element models

The behaviour of the soft actuators can be predicted by the FE method after identifying a hyperelastic constitutive relation suitable for describing silicone rubber. Previous studies have typically a variety pf constitutive relations to characterise the mechanical

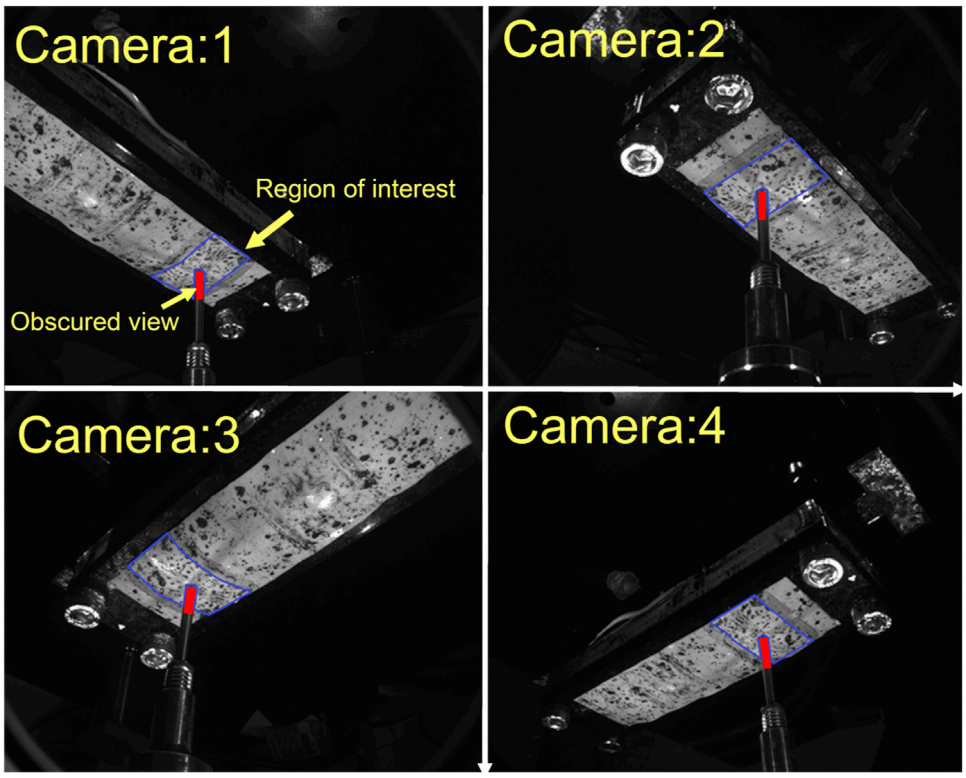

FIGURE 5
View from four different cameras. Region of interest for 3D reconstruction coloured by blue-bordered area. View obscured by indenter tip is coloured by red.

TABLE 1 Constitutive relation coefficients, fitted by ABAQUS to uniaxial experimental measurement.

Model	Model Equation	Coefficient	Model	Model Equation	Coefficient
Neo-Hookean	He et al. (2021) $W = C_{10}(I_1 - 3)$	C_{10} = 22.4 kPa	**Yeoh**	$W = \sum_{i=1}^{N=3} C_{i0}(I_1 - 3)^i$ (He et al., 2021)	C_{10} = 21.9 kPa C_{20} = 0.0690 kPa C_{30} = 0.0167 kPa
Reduced Polynomial N2	Dias et al. (2014) $W = \sum_{i=1}^{N=2} C_{i0}(I_1 - 3)^i$	C_{10} = 20.2 kPa C_{20} = 0.0575 kPa	Ogden N1	$W = \sum_{i=1}^{N=1} \frac{2\mu_i}{\alpha_i^2}(\lambda_1^{-\alpha_i} + \lambda_2^{-\alpha_i} + \lambda_3^{-\alpha_i})$ (He et al., 2021)	μ = 39.5 MPa α = 2.41
Arruda-Boyce	Arruda and Boyce (1993) $W = \mu \sum_{i=1}^{N} \frac{C_i}{\lambda_m^{2i-1}}(\bar{I}_1^i - 3^i)$ $C_1 = \frac{1}{2}$, $C_2 = \frac{1}{20}$, $C_3 = \frac{11}{1050}$ $C_4 = \frac{19}{7000}$, $C_5 = \frac{519}{673750}$	λ_m = 2.42 μ = 36.1 kPa	Ogden N3	$W = \sum_{i=1}^{N=3} \frac{2\mu_i}{\alpha_i^2}(\lambda_1^{-\alpha_i} + \lambda_2^{-\alpha_i} + \lambda_3^{-\alpha_i})$ (He et al., 2021)	μ_1 = −37.1 kPa μ_2 = 23.1 kPa μ_3 = 70.2 kPa α_1 = 1.63 α_2 = 3.36 α_3 = −2.92

behaviour of silicone materials. Researchers have previously used Ogden N3 (Elsayed et al., 2014; Choi et al., 2017), Yeoh (Sarkar et al., 2019), and Arruda-Boyce (Shivapooja et al., 2015) hyperelastic relations to model the behaviour of Ecoflex 0050. The lack of consensus in the above literature led us to perform our own analysis to identify an appropriate hyperelastic relation for Ecoflex 0050.

We employed commercially-available FE analysis software (ABAQUS Inc., Dassault Systems Corp) to perform finite element simulations. We developed and evaluated finite element models using six different hyperelastic constitutive relations to find a suitable model for Ecoflex 0050.

- Reduced Polynomial Order 1 (Neo-Hookean)
- Reduced Polynomial Order 2 (Reduced Polynomial N2)
- Reduced Polynomial Order 3 (Yeoh)
- Arruda-Boyce
- Ogden Order 1 (Ogden N1)
- Ogden Order 3 (Ogden N3)

Uniaxial stress-strain data were acquired from dogbone-shaped samples of Ecoflex 0050 (as recommended in ASTM standard D412) using an electro-mechanical universal testing machine (Instron 5567). ABAQUS's inbuilt optimisation package was then used to estimate the best-fit coefficients for each hyperelastic constitutive model ("Fitting of hyperelastic and hyperfoam), assuming the material to be isotropic and incompressible (Martins et al., 2006; Asadi Khanouki et al., 2019). (Table 1) shows the best-fit coefficients optimised by ABAQUS for each constitutive relation.

Having identified the optimised coefficients for constitutive models for Ecoflex 0050, we then validated a FE model of our actuators. Model results were compared to data recorded during an indentation test conducted on our prototype actuators. Literature on the normal and shear stress on the stump indicate maximum normal and shear stresses of 200 kPa and 10 kPa, respectively. We thus applied these stresses in our FEM studies of soft actuator arrays. The array was constrained in all directions except the surface to which the external load was applied (Figure 3).

During indentation, we controlled the indentation depth and recorded the force produced at each step. The experimentally recorded forces were used as 3D boundary forces to indent the soft actuator surface in the FE model. The displacement of the indented area was exported from the FE model at each indentation step for each hyperelastic model and compared with the experimental data. We also compared the measured displacement of points neighbouring the indenter tip with those predicted by the FE model.

Design parameter study

In the second part of the study, we investigated the behaviour of the soft actuator array under various loading conditions, as design parameters (e.g., thickness, void size, input pressure) were varied. We investigated different ranges of design parameters to evaluate their effect.

- Input Pressure (*P*) above atmosphere: 150 kPa, 175 kPa, 200 kPa, 225 kPa, 250 kPa
- Void Diameter (*VD*): 8 mm, 12 mm, 16 mm
- Void Thickness (*VT*): 1 mm, 2 mm
- Soft Actuator Thickness (*T*): 8 mm, 12 mm, 16 mm

To investigate the consequences of different combinations of the design parameters, the input pressures were varied up to the maximum reported pressure (i.e. 200 kPa). Other geometric properties were selected such that the soft actuator surface reached about 5 mm, which is a comfortable range adjustment for amputees (McLean et al., 2019) and also enables the dynamically reconfigurable socket to accommodate −11%–7% of residual limb volume fluctuation (Board et al., 2001). Combinations of the design parameters were studied under normal stress, shear stress, and a combination of both, yielding a total of 270 models. All models used the Ogden N3 hyperelastic constitutive relation.

The range of selected design parameters also enable us to investigate each parameter's effect on the surface deformation, and demonstrate the combination that can produce concave and convex surface shapes, and uneven and smooth surface shapes. Based on the stresses reported in the literature (summarised in Table 2), the normal external stress and shear stress applied on the surface of the soft actuator array were set at 200 kPa and 10 kPa, respectively.

TABLE 2 Maximum stump-socket interface stresses and pressures for lower limb amputees.

Study	Normal stress (kPa)	Shear stress (kPa)	Pressure (kPa)
Ko et al. (2018)	159.3	4.2	—
Sanders et al. (1998)	78.8	10.1	—
Dou et al. (2006)	—	—	215.8
Rajtukova et al. (2014)	—	—	81
Sengeh and Herr (2013b)	—	—	58
Swanson et al. (2018)	—	—	60

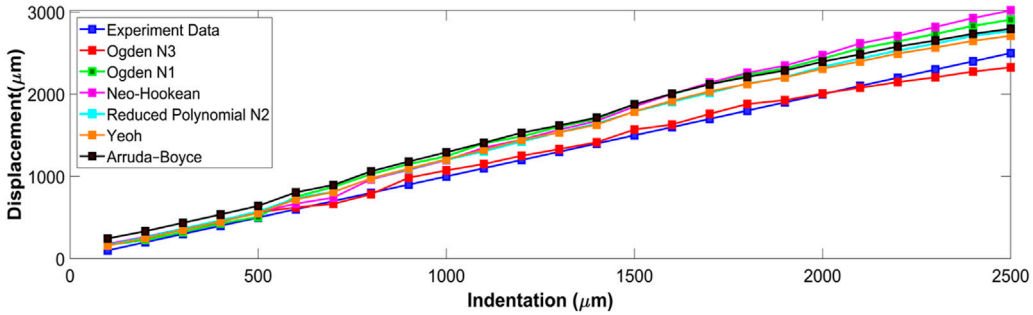

FIGURE 6
Predicted indentation for all constitutive relations compared to experimental data.

Results and discussion

Constitutive relation evaluation

Six hyperelastic constitutive relations were investigated by comparing FE model predictions with experimental measurements at each indentation step (Figure 6). displays the mean displacement of the indentation area, and compares the experiment tip indentation depth to that predicted by the FE model using each constitutive relation. The predictions of Ogden N3 were closest to the experimentally measured displacements with a maximum error of 173 μm at full indentation. Neo-Hookean had the largest discrepancy with indentation depth, with a maximum discrepancy of 527 μm at full indentation (Figure 6).

The RMS error for each constitutive relation is listed in Table 3. Ogden N3 displayed the best performance with 68 μm RMS error, with the next best constitutive relations being Yeoh and Reduced Polynomial N2 with 223 μm and 241 μm RMS error, respectively.

Fitting the surface of the dense point cloud, corresponding to the soft actuator surface, generated an RMS error of 42 μm. The location of the indenter tip in the stereoscopic images caused an approximately 3 mm × 3 mm area of missing points surrounding and beneath the indenter tip. FE models were fitted to the point clouds to quantify the discrepancy between the predictions and experimental displacement.

The absolute displacement difference between the FE models and point cloud measured at each step, and the average of the discrepancy for all steps, were calculated and are depicted in (Figure 7). The error was highest (~400 μm) close to the point of indentation, but gradually decreased towards the edges (<150 μm). Of the constitutive relations considered, the Ogden N3 yielded the closest predictions to measured deformations, while the Neo-Hookean relation had the highest error. The Ogden N3 constitutive relation was thus selected for all subsequent model analyses.

TABLE 3 The table shows the RMS error of the indentation region for all constitutive relations. The Ogden N3 relation had the lowest RMS error.

Constitutive relation	RMS error (μm)
Ogden N3	68
Ogden N1	320
Neo-Hookean	338
Reduced Polynomial N2	241
Yeoh	230
Arruda–Boyce	310

Design parameter study

Next, we used the model to investigate the effect on surface shape of four main design parameters: void diameter (*VD*); void thickness (*VT*); soft actuator thickness (*T*); and input pressure (*P*) (Figure 2). The resulting shape of the soft actuators for the various combinations of design parameters belong to two main groups. The

10.3389/fbioe.2024.1459056

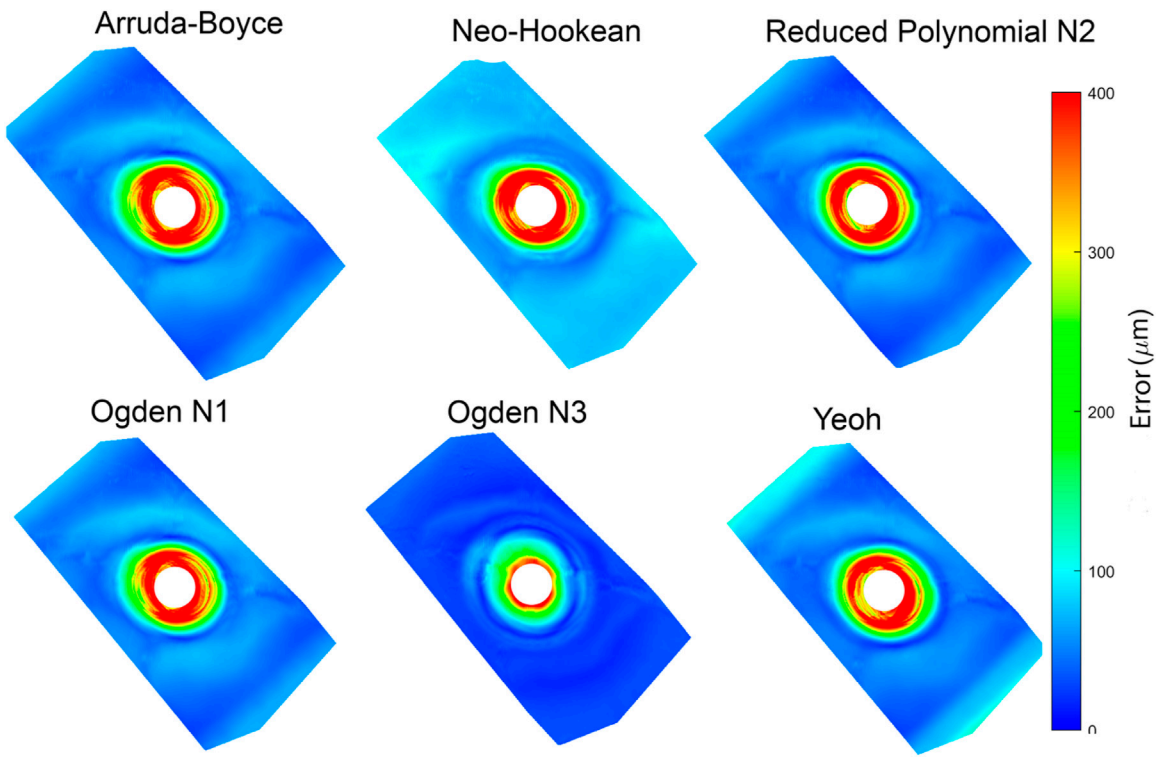

FIGURE 7
The average error between the stereo reconstruction and six different FEM predictions.

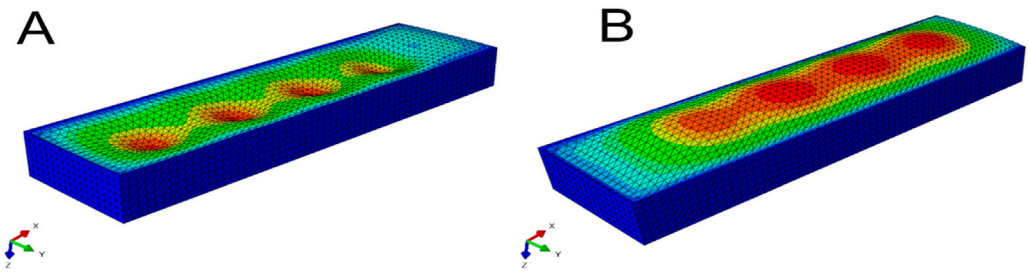

FIGURE 8
Picture **(A)** shows the soft actuator in the negative-deformation condition, and picture **(B)** displays the soft actuator in the positive-deformation condition.

first group is a *negative-deformation* surface shape (Figure 8A) in which the external loading overcame the load applied from the soft actuator, and resulted in surface concavity. The second group is exhibited *positive-deformation* (Figure 8B) where the soft actuator surface generated sufficient force to overcome the external stresses applied to the surface, and producing a convex shape.

To evaluate the effect of each design parameter on the soft actuator surface shape under loading, it is helpful to visualise and compare the surface data. Due to the complexity of visualising 270 full 3D surface profiles, data were extracted along the *y*-centre line ($x = 0$) of the soft actuator (Figure 9).

By extracting these data, we can plot the various types of soft actuator array surface deformation that can be achieved by manipulating the design parameters (Figure 10). Each panel in Figure 10 shows the vertical displacement for the soft actuator array with a specific void thickness, void diameter, and actuator thickness, at five pressure differences between the void pressure and the external stress.

In each panel, the pressure difference can change the surface deformation from negative to positive. For positive ΔP, the surface displacement magnitude is approximately proportional to ΔP regardless of other design parameters. In some cases (Panels A, H, where $VD = T$) the deformation in response to $-\Delta P$ is approximately the inverse of that to ΔP. However, in other cases (Panels C, E, G) negative pressure difference leads to 'collapse' of the actuator void towards its minimum possible thickness as the top surface of the void contacts the bottom surface.

The soft actuator array thickness T (left column vs. right column) has an inverse effect on the magnitude of the surface

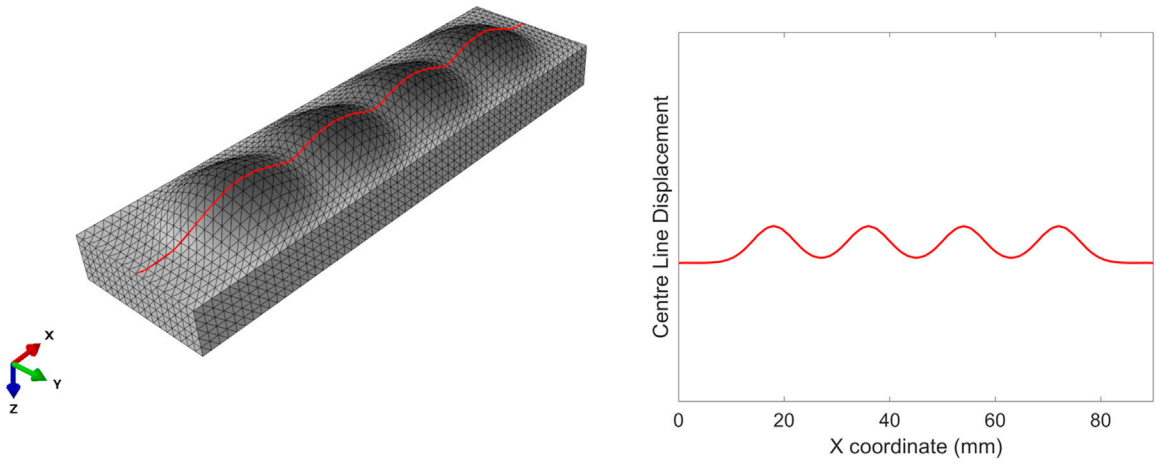

FIGURE 9
Centre line on the left (in red) along which the surface deformation of the soft actuators is extracted (right).

displacement, and results in a smoother surface. On the other hand, larger T reduces local control over surface deformation with pressure. The overall surface displacement increases with increasing void diameter (e.g., Figure 10, A cf C, E cf G). Smaller void diameters cause the mid points between actuators to remain constrained to near-zero displacement; larger void diameters VD allow the entire actuator surface to offset in the positive direction.

Increasing the soft actuator array thickness and increasing the void diameter simultaneously (Figure 10A, and D) gradually increases the surface displacement magnitude and provides a more uniform surface deformation. Increasing the void thickness (VT) allowed slightly larger deformation (Figure 10, A cf E, C cf G).

These data can be further analysed by quantifying the *shape* of the surface (Figure 11). Here, we define the 'shape waviness' as the average of peak-trough amplitude for each model divided by the average of the peaks' magnitude across all models; positive shape waviness indicates convex surface deformation (Figure 8B) and negative shape waviness indicates concave surface deformation (Figure 8A):

$$\Delta AveragePeak = \left(\frac{\sum_{1}^{4} PeakValue}{4}\right) - \left(\frac{\sum_{1}^{3} TroughValue}{3}\right)$$

$$Average_{AllPeaks} = \left(\frac{\sum_{1}^{i} PeakValue}{i}\right)$$

$$Shape\ waviness = \frac{\Delta AveragePeak}{Average_{AllPeaks}}$$

Shape waviness increases with void thickness VT (Figure 11A CF Figure 11B), and decreases with array thickness T. Under a negative pressure difference, any increase in the pressure difference (i.e., towards zero) reduces waviness and the soft actuator surface becomes smoother. With positive pressure difference, a further increase in the pressure difference leads to additional shape waviness. There is no direct relation between the void diameter and the shape waviness.

An important consideration is the performance of the actuator to shear loading. Figure 12 shows the result for the models when shear stress alone is applied to the surface of the soft actuators. The graphs in (Figure 12) depict the tangential displacement of each node along the x-axis (shear stress direction). The results show that Increasing the void diameter VD and/or void pressure VP results in increased shear displacement. However, increasing the soft actuator array thickness reduces the shear displacement magnitude. In some cases (Figures 12C, D, G, H) shear displacement is negative for some of the surface. By increasing the void thickness to 2 mm (Figures 12E, F, G, H), the general trend remains the same as the void thickness of 1 mm (Figures 12A–D). Nevertheless, the magnitude of shear displacement increased.

The maximum shear displacement for the soft actuator array with a void diameter of 8 mm of a thickness of 8 mm is about 2,500 μm (Figure 12E), but reaches about 6,000 μm when the void diameter becomes 16 mm (Figure 12G). For the void diameter of 8 mm (Figures 12E, F) the shear displacement at the centre of each void coordinate (i.e., x = 18 mm, x = 36 mm, x = 54 mm, and x = 72 mm) is almost the same. However, by increasing the void diameter more difference in the shear displacement at the void centres appears. For example (Figure 12G), shows that the magnitude maximum shear displacement for the last void centre is about 6,000 μm, while the magnitude of maximum shear displacement of the first void centre is about 1,200 μm. Increasing the soft actuator array thickness reduces the shear displacement difference between the centre of the first void and the last void.

Often, external shear stress and normal stress will be applied simultaneously (Figure 13); depicts two examples of surface profile of the soft actuator array under a combination of shear and normal stress. The existence of shear stress shifts the surface profile to the right. The surface displacement for the void pressure of 200 kPa (gray line) is almost the same across all models. The main effect of increasing the void diameter is on the magnitude of surface displacement. For example, Figure 13 shows the surface displacement magnitude for soft actuator array with void thickness 1 mm (Figure 13A) and void thickness 2 mm

10.3389/fbioe.2024.1459056

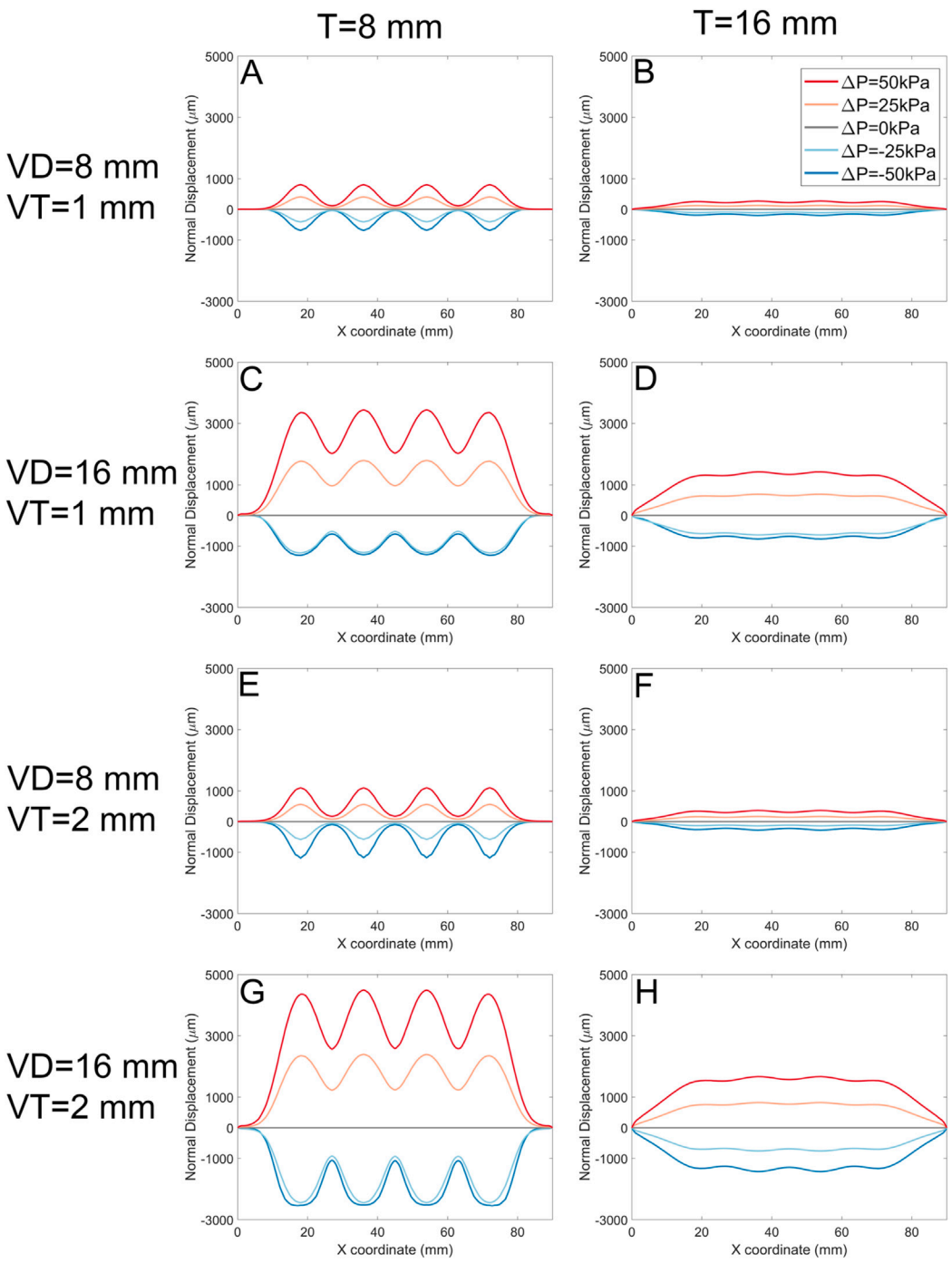

FIGURE 10
The normal displacement for models with 1 mm, and 2 mm void thickness (VT). Each panel represents data for a specific soft actuator thickness (T), void diameters (VD), and VT. Across panels, lines with the same colour represent the same soft actuator pressure. The first row of the panels **(A, B)** belongs to the data with the VD 8 mm, VT 1 mm, and T 8 mm, and 16 mm, respectively. The second row **(C, D)** demonstrates the results for the VD 16 mm, VT 1 mm, and T 8 mm, and 16 mm, respectively. The third row **(E, F)** demonstrates results for analysis with the VD 8 mm, VT 2 mm, and T 8 mm, and 16 mm, respectively. The fourth row **(G, H)** demonstrates FE results for the VD 16 mm, VT 2 mm, and T 8 mm, and 16 mm, respectively.

(Figure 13B). The graph shows no evident difference in the surface shape, but the surface displacement increases by increasing the void thickness from 1 mm to 2 mm. For instance, for the void pressure of 250 kPa, the maximum surface displacement reached about 4,800 μm (Figure 13B) from about 3,200 μm (Figure 13A). The effect of void diameter and soft actuator thickness remained the same as discussed before on the surface shape of soft actuator array under combination of normal and shear stress.

Figure 14 presents experimental data that characterises the pressure distribution across four critical regions of the residual limb: the distal end, popliteal muscle, fibular head, and distal tibia. It illustrates the recorded pressure profiles over a 600-s interval

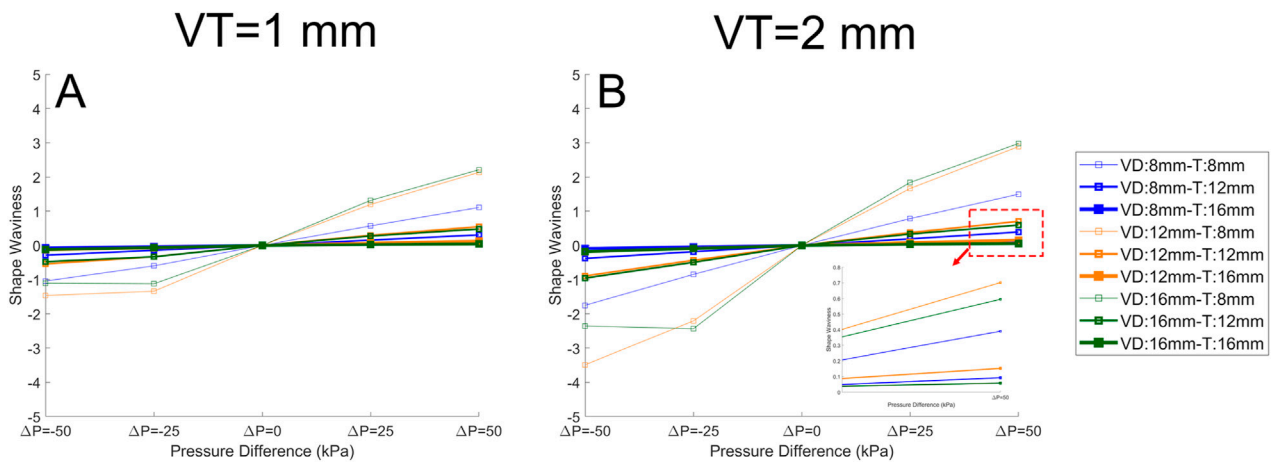

FIGURE 11
The quantified surface shape for the soft actuator arrays when the VT (void thickness) is 1 mm **(A)**, and the VT is 2 mm **(B)**. The pressure difference is plotted against the average peak-trough percentage for each model divided by the average peak in all models (shape waviness). It is clear that pressure difference has a significant effect on the shape waviness, and on the other hand, increasing thickness reduces the shape waviness. In the legend the "VD" stands for void diameter and "T" stands for soft actuator array thickness. The lines with the same color have the same "VD", and the lines with the same thickness have the same "T".

following the establishment of steady-state conditions, alongside the corresponding displacement of the voice coil actuator. The experiment details is discussed in (Mollaee et al., 2024).

The findings reveal that the distal end of the residual limb consistently experiences the highest pressure, particularly under a 15 N load applied vertically to the prosthetic socket. This elevated pressure concentration at the distal end indicates an imbalance in load distribution, which has significant implications for user comfort and may lead to tissue strain or injury with prolonged use. Such insights underscore the impact of socket design and load application on the comfort and functional mobility of amputees.

The results highlight the necessity for a pressure-optimised prosthetic socket design that minimises concentrated load, particularly in sensitive regions of the residual limb. Future iterations of socket design must prioritise the careful selection of materials and the optimisation of socket topology, particularly in the region of the distal end, to ensure a more uniform pressure distribution. This approach aims to enhance overall comfort, mitigate risks of pressure-induced tissue damage, and improve the quality of life for amputees by reducing discomfort during extended periods of use.

This study reports on a cost-efficient, easy manufacturing methodology for designing a dynamically reconfigurable socket, toward improving the socket's comfort and fit for transtibial amputees by controlling the pressure distribution over the stump and compensating for residual limb volume fluctuation. Here, we predict the performance of an array of soft actuators, which can be used as a building block for creating a dynamically reconfigurable socket, or a similar deformable load-bearing surface. We have identified an appropriate hyperelastic constitutive model describing the soft actuator array and then explored the effect of different design parameters on the deformation of the array under realistic loading conditions.

In this study, we used a microrobot and 3D surface profiling to identify the Ogden N3 constitutive relation as the most accurate for predicting deformation of our pneumatic actuators (Table 3). We used the Ogden N3 hyperelastic constitutive model for our finite element models to investigate the effect of soft actuator array design parameters under loading conditions by simulating the actuator with loads developed at the prosthetic socket and residual limb interface. Maximum boundary normal and shear stress were applied to the surface of the soft actuator array based on values reported in the literature. Shear stress caused asymmetry in the surface shape. This was also observed in the FE model where the surface was squeezed and packed tightly at the end of the soft actuator surface where located at the endpoint of shear stress distribution (x = 90 mm), and manifested itself in the graphs steep negative slope (Figure 13).

Throughout the FE models, it could be seen that the soft actuator thickness had a significant effect on the surface shape and surface displacement under pressure. Increasing the soft actuator thickness resulted in a smoother surface (smaller shape waviness). Increasing the soft actuator thickness would also increase the soft actuator array bending stiffness (since it increases the second moment of inertia) and naturally requires greater pressure to deform, supporting the observation of an inverse relation between thickness and surface displacement.

The next design parameter studied was the void diameter. Increasing the void diameter increased the surface displacement magnitude (Figure 10). By increasing the void diameter, the same pressure would be applied to a bigger area, generating additional force and greater surface displacement. Despite this, increasing the void diameter does not essentially mean reducing the surface smoothness or shape waviness (Figure 11). Shape waviness change due to altering the void diameter significantly depend on the soft actuator thickness. Inflating the void would require the void to expand the layer on the top of it and lift the layer at the gap between the edge of the voids (Figure 2). Thus, there is a trade-off between the void diameter and soft actuator array thickness to change the shape waviness.

10.3389/fbioe.2024.1459056

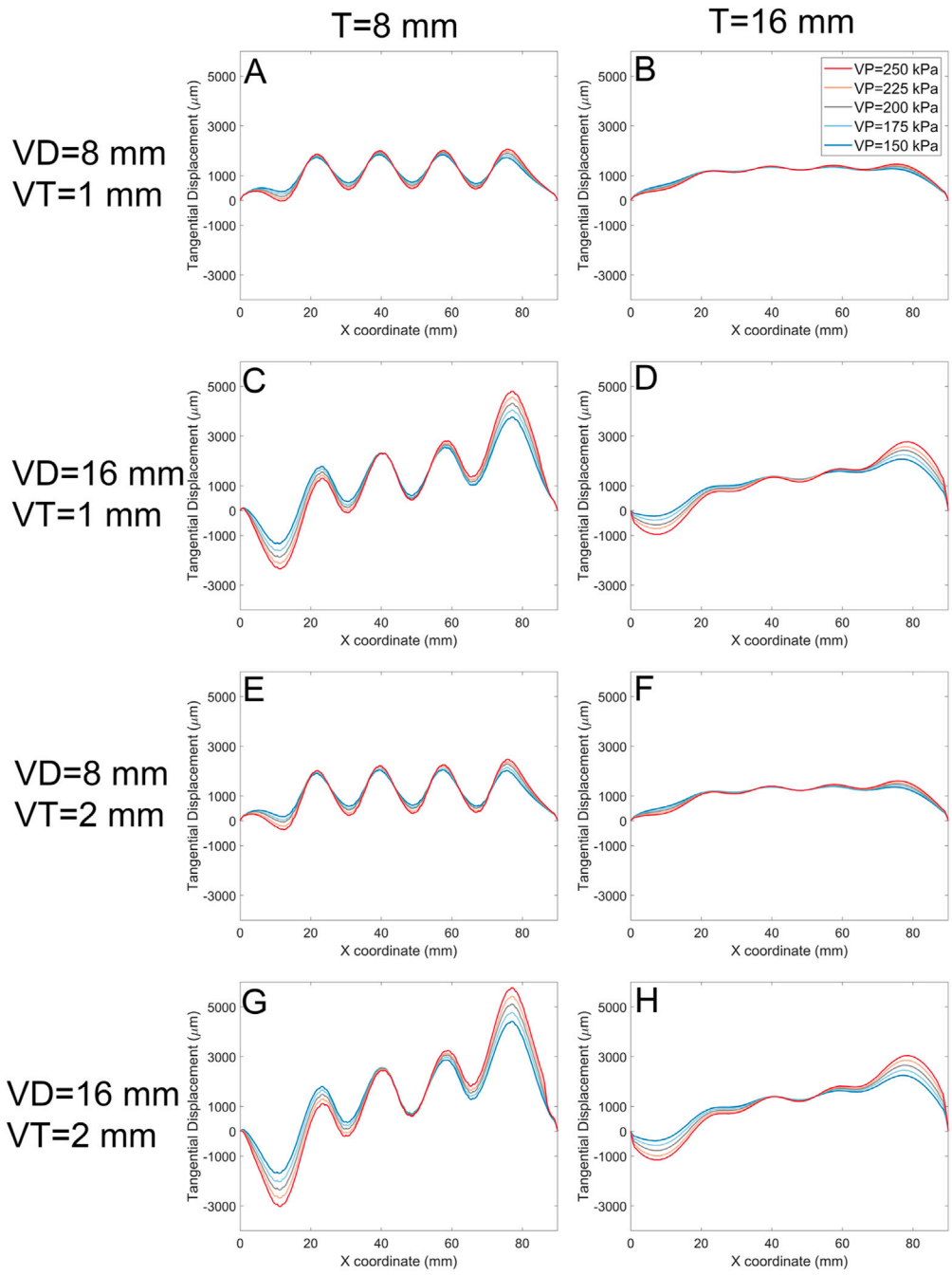

FIGURE 12
The tangential displacement (every node displacement along the shear stress direction) for models with 1 mm, and 2 mm void thickness (VT). Each panel represents data for a specific soft actuator thickness (T), void diameters (VD), and VT. Across panels, lines with the same colour represent the same soft actuator pressure. The first row of the panels **(A, B)** belongs to the data with the VD 8 mm, VT 1 mm, and T 8 mm, and 16 mm, respectively. The second row **(C, D)** demonstrates the results for the VD 16 mm, VT 1 mm, and T 8 mm, and 16 mm, respectively. The third row **(E, F)** demonstrates results for analysis with the VD 8 mm, VT 2 mm, and T 8 mm, and 16 mm, respectively. The fourth row **(G, H)** demonstrates FE results for the VD 16 mm, VT 2 mm, and T 8 mm, and 16 mm, respectively.

The input pressure for the soft actuator array has a strong influence on surface shape, and can be changed dynamically as a load on a socket varies. Increasing the pressure resulted in increased surface displacement and shape waviness. Due to the incompressibility assumption of the material, when the external normal stress was equal to the void pressure, the surface displacement was zero, and the soft actuator array was flat regardless of other design parameters. The surface deformation was positively correlated with pressure difference.

For the combination of design parameters that produced high shape waviness, the shear displacement has higher magnitudes. For example (Figure 12A), has a shape waviness of about 1 and displacement magnitude about 2000 μm. However, by decreasing the shape waviness to about 0.12 (Figure 12C), the displacement

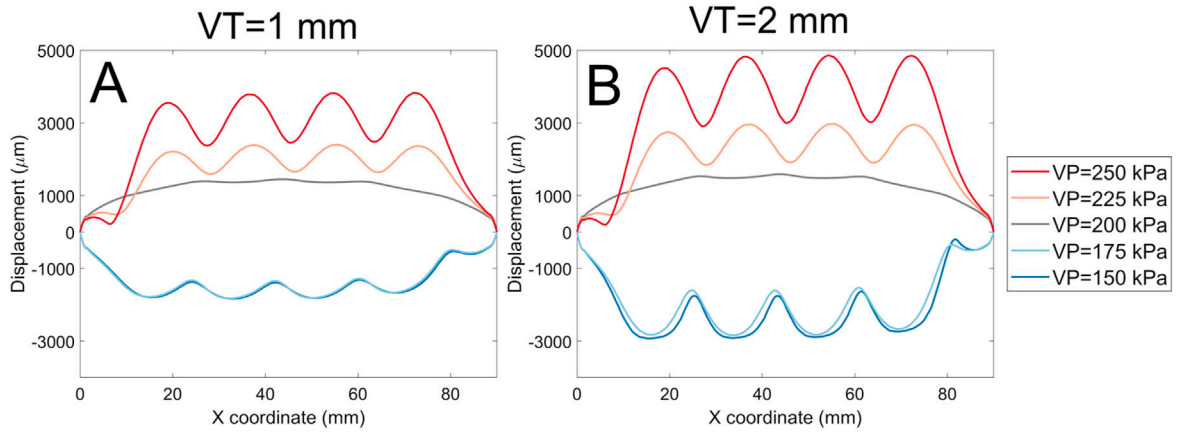

FIGURE 13
A comparison of surface displacement magnitude for the void thickness of 1 mm **(A)**, and void thickness of 2 mm **(B)** for the soft actuator array with the void diameter of 8 mm and thickness of 16 mm.

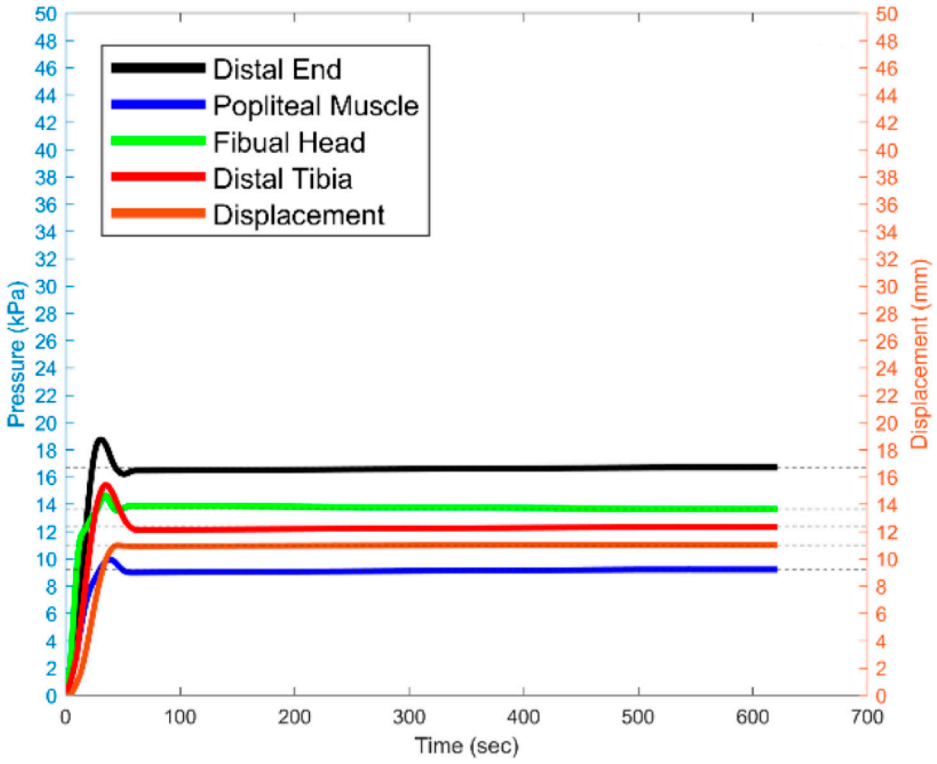

FIGURE 14
The recorded pressure for the sensitive areas, and voice coil actuator displacement for 600 s since the steady state moment the 15 N is being applied.

magnitude reduced to around 1,000 μm. The negative shear displacement shows that the tangential displacement as the result of the inflation was more than the displacement due to the shear stress, and always happens near the shear stress start point (x = 0 mm). The displacement magnitude for the $\Delta P = 0$ kPa was almost the same since the shape waviness was approximately zero, and the only reason the surface was deformed was due to the existence of shear stress.

The shape waviness factor determines the resolution of the contact surface between the stump and the soft actuator array. By increasing the shape waviness, the resolution of the contact surface increases, which means that in case we need to locally add more pressure, for instance, redistribute the larger portion of the weight load to more tolerant stump areas, we can use the setting with higher shape waviness. The design setting resulting in smaller shape waviness (smoother surface) would enable the user to

distribute the pressure over various regions of the stump uniformly.

It is desirable to minimise the socket's weight and size and, to achieve this, it is preferable that the actuators would be thin. A very thin membrane thickness will also minimise the overall size. However, if the membrane is very thin, there will be very little resistance to forces tangential to the soft actuator and the socket may slip and increase the chance for skin irritation. Furthermore, if the void diameter is too small, it requires more input pressure to reach a certain displacement, and if it is too large, the resolution of pressure distribution at the socket/stump interface reduces. There is thus a tradeoff between the design parameters setting to achieve a certain soft actuator array surface deformation and shape. The dynamically reconfigurable socket includes several soft actuator arrays that, according to the amputee requirements, make it feasible to embed soft actuator arrays with different settings against different areas of the stump.

Our results show that a dynamically reconfigurable socket design can be optimised by using a combination of arrays of actuators. For the pressure tolerable areas of a residual limb, a soft actuator array with low thickness, such as 8 mm should be used to apply the load to pressure tolerable areas, such as the patellar tendon area. To provide sufficient control over applied load, the size of the void diameter should be big enough to cover the pressure tolerable area. A uniform pressure distribution may provide comfort and avoid tissue damage for the sensitive areas of the residual limb, such as the distal end of the tibia.

Conclusion

This study demonstrated a practical design methodology investigation for a cost-efficient and easy manufacturing pneumatic soft actuator array, a building block for manufacturing a dynamically reconfigurable transtibial socket for controlling stump pressure distribution, and compensating for stump volume fluctuation, which are essential for improving the amputee's quality of life. A mechanism for determining the hyperelastic properties of Ecoflex 0050 silicone was presented. This is a potential candidate for a soft actuator material given its reversible large strain capacity and softness. Deformation testing was performed with indentation and deformation caused by pressurising an internal pocket of air. To deal with the highly non-linear surface deformation, a new speckle imaging technique was used which was able to quantify the accuracy of the surface displacement to 40 μm. These measurements enable the Ogden N3 model to be identified as being able to predict actuator deformation to an accuracy of within 16%. This part of the study aimed to identify a suitable constitutive model to conduct FE analysis to identify appropriate soft actuator array configurations for use in a dynamically reconfigurable socket for lower limb amputees. This application determined some boundaries for interface stresses and pressures.

The FE model analysis showed that soft actuator array thickness would significantly affect the surface displacement magnitude and the surface shape. Void diameter and void thickness also play important roles in determining the surface displacement magnitude. However, their effect on the soft actuator array surface shape depends on its thickness. Input pressure was critical in determining the surface displacement and surface shape. It was observed that surface deformations are positively correlated with the pressure difference. Positive surface deformation enables us to control the surface profile and the pressure distribution over the stump by tuning it and reconfiguring the soft actuators' surface shape. Soft actuators offer the prospect of a reconfigurable interface between a prosthetic socket and a limb stump of an amputee. This has the potential to improve prosthetic performance by improving comfort. However, the very nature of a soft actuator means that the interface will be flexible and to some extent compliant. This means that the deformation characteristics of the soft actuator will need to be determined accurately to provide the necessary support during active use. This paper presents the tools required to evaluate the properties of the soft actuators to allow their performance in this application to be evaluated with numerical models.

Data availability statement

The raw data supporting the conclusions of this article will be made available by the authors, without undue reservation.

Author contributions

SM: Writing–review and editing, Writing–original draft, Validation, Software, Methodology, Investigation, Formal Analysis, Data curation, Conceptualization. AH: Writing–review and editing, Validation, Supervision. DB: Writing–review and editing, Visualization, Supervision. AT: Writing–review and editing, Supervision, Resources. PN: Writing–review and editing, Supervision, Resources, Funding acquisition.

Funding

The author(s) declare that financial support was received for the research, authorship, and/or publication of this article. The authors thank the support provided by Auckland Bioengineering Institute (ABI) and New Zealand Artificial Limb Service (NZALS) for this study. AT is supported by a James Cook Research Fellowship provided by the Royal Society of New Zealand.

Conflict of interest

The authors declare that the research was conducted in the absence of any commercial or financial relationships that could be construed as a potential conflict of interest.

Publisher's note

References

Afshari, B. M., Mirjavadi, S. S., and Barati, M. R. (2022). Investigating nonlinear static behavior of hyperelastic plates using three-parameter hyperelastic model. *Adv. Concr. Constr.* 13 (5), 377–384. doi:10.12989/ACC.2022.13.5.377

Arruda, E. M., and Boyce, M. C. (1993). A three-dimensional constitutive model for the large stretch behavior of rubber elastic materials. *J. Mech. Phys. Solids* 41 (2), 389–412. doi:10.1016/0022-5096(93)90013-6

Asadi Khanouki, M., Sedaghati, R., and Hemmatian, M. (2019). Experimental characterization and microscale modeling of isotropic and anisotropic magnetorheological elastomers. *Compos. Part B Eng.* 176, 107311. doi:10.1016/j.compositesb.2019.107311

Åström, I., and Stenström, A. (2004). Effect on gait and socket comfort in unilateral trans-tibial amputees after exchange to a polyurethane concept. *Prosthetics Orthot. Int.* 28 (1), 28–36. doi:10.3109/03093640409167922

Baars, E. C., Schrier, E., Dijkstra, P. U., and Geertzen, J. H. B. (2018). Prosthesis satisfaction in lower limb amputees. *Med. Baltim.* 97 (39), e12296. doi:10.1097/MD.0000000000012296

Board, W. J., Street, G. M., and Caspers, C. (2001). A comparison of trans-tibial amputee suction and vacuum socket conditions. *Prosthetics Orthot. Int.* 25 (3), 202–209. doi:10.1080/03093640108726603

Carrigan, W., Nothnagle, C., Savant, P., Gao, F., and Wijesundara, M. B. J. (2016). "Pneumatic actuator inserts for interface pressure mapping and fit improvement in lower extremity prosthetics," in *Proceedings of the IEEE RAS and EMBS international conference on biomedical robotics and biomechatronics* (IEEE Computer Society), 574–579. doi:10.1109/BIOROB.2016.7523687

Choi, D. Y., Kim, M. H., Oh, Y. S., Jung, S. H., Jung, J. H., Sung, H. J., et al. (2017). Highly stretchable, hysteresis-free ionic liquid-based strain sensor for precise human motion monitoring. *ACS Appl. Mater. Interfaces* 9 (2), 1770–1780. doi:10.1021/acsami.6b12415

Dias, V., Odenbreit, C., Hechler, O., Scholzen, F., and Ben Zineb, T. (2014). Development of a constitutive hyperelastic material law for numerical simulations of adhesive steel–glass connections using structural silicone. *Int. J. Adhes. Adhes.* 48, 194–209. doi:10.1016/J.IJADHADH.2013.09.043

Dou, P., Jia, X., Suo, S., Wang, R., and Zhang, M. (2006). Pressure distribution at the stump/socket interface in transtibial amputees during walking on stairs, slope and non-flat road. *Clin. Biomech.* 21 (10), 1067–1073. doi:10.1016/j.clinbiomech.2006.06.004

El-Atab, N., Mishra, R. B., Al-Modaf, F., Joharji, L., Alsharif, A. A., Alamoudi, H., et al. (2020). Soft actuators for soft robotic applications: a review. *Adv. Intell. Syst.* 2 (10), 2000128. doi:10.1002/aisy.202000128

Elsayed, Y., Vincensi, A., Lekakou, C., Geng, T., Saaj, C. M., Ranzani, T., et al. (2014). Finite element analysis and design optimization of a pneumatically actuating silicone module for robotic surgery applications. *Soft Robot.* 1 (4), 255–262. doi:10.1089/soro.2014.0016

Fitting of hyperelastic and hyperfoam constants. Accessed: December 29, 2020 Available at: https://abaqus-docs.mit.edu/2017/English/SIMACAETHERefMap/simathe-c-fithyperconst.htm

Forsat, M. (2020). Investigating nonlinear vibrations of higher-order hyper-elastic beams using the Hamiltonian method. *Acta Mech.* 231 (1), 125–138. doi:10.1007/s00707-019-02533-5

Fosse, S., Hartemann-Heurtier, A., Jacqueminet, S., Ha Van, G., Grimaldi, A., and Fagot-Campagna, A. (2009). Incidence and characteristics of lower limb amputations in people with diabetes. *Diabet. Med.* 26 (4), 391–396. doi:10.1111/j.1464-5491.2009.02698.x

Gailey, R., McFarland, L. V., Cooper, R. A., Czerniecki, J., Gambel, J. M., Hubbard, S., et al. (2010). Unilateral lower-limb loss: prosthetic device use and functional outcomes in servicemembers from Vietnam war and OIF/OEF conflicts. *J. Rehabil. Res. Dev.* 47 (4), 317. doi:10.1682/JRRD.2009.04.0039

Haji Rassouliha, A. (2017). *A toolbox for precise and robust deformation measurement - the university of Auckland*. University of Auckland. Available at: https://catalogue.library.auckland.ac.nz/primo-explore/fulldisplay?docid=uoa_alma21284845390002091&amp=&amp=&amp=&amp=&amp=&amp=&amp=&amp=&amp=&amp=&amp=&amp=&context=L&vid=NEWUI&lang=en_US&search_scope=Combined_Local&adaptor=LocalSearchEngine&tab=combi (Accessed January 09, 2021).

HajiRassouliha, A., Gamage, T. P. B., Parker, M. D., Nash, M. P., Taberner, A. J., and Nielsen, P. M. F., "2013, 3D surface profiling using arbitrarily positioned cameras," 358–363. doi:10.1109/IVCNZ.2013.6727068

HajiRassouliha, A., Taberner, A. J., Nash, M. P., and Nielsen, P. M. F. (2017). Subpixel measurement of living skin deformation using intrinsic features. *Comput. Biomech. Med. (2017).*, 91–99. doi:10.1007/978-3-319-54481-6_8

HajiRassouliha, A., Tang, E. J. L. P., Taberner, A. J., Nash, M. P., and Nielsen, P. M. F., "2019, A method for three-dimensional measurements using widely angled stereoscopic cameras," , 1–5. doi:10.1109/I2MTC.2019.8827086

He, H., Zhang, Q., Zhang, Y., Chen, J., Zhang, L., and Li, F. (2021). A comparative study of 85 hyperelastic constitutive models for both unfilled rubber and highly filled rubber nanocomposite material. *Nano Mater. Sci.* 4, 64–82. doi:10.1016/J.NANOMS.2021.07.003

Hsu, C.-H., Ou, C.-H., Hong, W.-L., and Gao, Y.-H. (2018). Comfort level discussion for prosthetic sockets with different fabricating processing conditions. *Biomed. Eng. Online* 17 (S2), 145. doi:10.1186/s12938-018-0577-2

Kahle, J., Miro, R. M., Ho, L. T., Porter, M., Lura, D. J., Carey, S. L., et al. (2020). The effect of the transfemoral prosthetic socket interface designs on skeletal motion and socket comfort. *Prosthetics Orthot. Int.* 44 (3), 145–154. doi:10.1177/0309364620913459

Ko, C. Y., Kim, S. G., Cho, Y. K., Lee, D., Kim, D. H., Ryu, J., et al. (2018). Development of a sensor to measure stump/socket interfacial shear stresses in a lower-extremity amputee. *Int. J. Precis. Eng. Manuf.* 19 (6), 899–905. doi:10.1007/s12541-018-0106-z

Lyon, C. C., Kulkarni, J., Zimerson, E., Van Ross, E., and Beck, M. H. (2000). Skin disorders in amputees. *J. Am. Acad. Dermatol.* 42 (3), 501–507. doi:10.1016/S0190-9622(00)90227-5

Mak, A. F. T., Zhang, M., and Boone, D. A. (2001). State-of-the-art research in lower-limb prosthetic biomechanics-socket interface: a review. *J. Rehabil. Res. Dev.* 38 (2), 161–174.

Martins, P. A. L. S., Natal Jorge, R. M., and Ferreira, A. J. M. (2006). A comparative study of several material models for prediction of hyperelastic properties: application to silicone-rubber and soft tissues. *Strain* 42 (3), 135–147. doi:10.1111/j.1475-1305.2006.00257.x

McLean, J. B., Redd, C. B., Larsen, B. G., Garbini, J. L., Brzostowski, J. T., Hafner, B. J., et al. (2019). Socket size adjustments in people with transtibial amputation: effects on residual limb fluid volume and limb-socket distance. *Clin. Biomech.* 63, 161–171. doi:10.1016/j.clinbiomech.2019.02.022

Meulenbelt, H. E., Geertzen, J. H., Jonkman, M. F., and Dijkstra, P. U. (2009). Determinants of skin problems of the stump in lower-limb amputees. *Arch. Phys. Med. Rehabil.* 90 (1), 74–81. doi:10.1016/j.apmr.2008.07.015

Mirjavadi, S. S., Forsat, M., and Badnava, S. (2020). Nonlinear modeling and dynamic analysis of bioengineering hyper-elastic tubes based on different material models. *Biomech. Model. Mechanobiol.* 19 (3), 971–983. doi:10.1007/s10237-019-01265-8

Mirjavadi, S. S., Taberner, A. J., Nash, M. P., and Nielsen, P. M. F. (2021). "Characterising the soft tissue mechanical properties of the lower limb of a below-knee amputee: a review," in *Computational biomechanics for medicine* (Cham: Springer International Publishing), 99–111. doi:10.1007/978-3-030-70123-9_8

Mollaee, S., Budgett, D. M., Taberner, A. J., and Nielsen, P. M. F. (2023). Hyperelastic constitutive model parameters identification using optical-based techniques and hybrid optimisation. *Int. J. Mech. Mater. Des.* 20, 233–249. doi:10.1007/s10999-023-09673-6

Mollaee, S., Fuentes-Aguilar, R. Q., Huegel, J. C., Budgett, D. M., Taberner, A. J., and Nielsen, P. M. F. (2024). A pneumatic reconfigurable socket for transtibial amputees. *Int. J. Numer. method. Biomed. Eng.* 40 (2), e3801. doi:10.1002/cnm.3801

Morales, D., Palleau, E., Dickey, M. D., and Velev, O. D. (2014). Electro-actuated hydrogel walkers with dual responsive legs. *Soft Matter* 10 (9), 1337–1348. doi:10.1039/c3sm51921j

Paterno, L., Ibrahimi, M., Gruppioni, E., and Menciassi, A. (2022). "Variable stiffness and shape prosthetic socket based on layer jamming technology," in *2022 IEEE 5th international conference on soft robotics (RoboSoft)* (IEEE), 729–734. doi:10.1109/RoboSoft54090.2022.9762224

Paternò, L., Ibrahimi, M., Gruppioni, E., Menciassi, A., and Ricotti, L. (2018). Sockets for limb prostheses: a review of existing technologies and open challenges. *IEEE Trans. Biomed. Eng.* 65 (9), 1996–2010. doi:10.1109/TBME.2017.2775100

Pezzin, L. E., Dillingham, T. R., MacKenzie, E. J., Ephraim, P., and Rossbach, P. (2004). Use and satisfaction with prosthetic limb devices and related services 11No commercial party having a direct financial interest in the results of the research supporting this article has or will confer a benefit on the author(s) or on any organization with which the author(s) is/are associated. *Arch. Phys. Med. Rehabil.* 85 (5), 723–729. doi:10.1016/J.APMR.2003.06.002

Pirouzi, G., Abu Osman, N. A., Eshraghi, A., Ali, S., Gholizadeh, H., and Wan Abas, W. A. B. (2014). Review of the socket design and interface pressure measurement for transtibial prosthesis. *ScientificWorldJournal.* 2014, 1–9. doi:10.1155/2014/849073

Rajtukova, V., Hudak, R., Zivcak, J., Halfarova, P., and Kudrikova, R. (2014). Pressure distribution in transtibial prostheses socket and the stump interface. *Procedia Eng.* 96, 374–381. doi:10.1016/J.PROENG.2014.12.106

Rosso, F., Marino, G., Giordano, A., Barbarisi, M., Parmeggiani, D., and Barbarisi, A. (2005). Smart materials as scaffolds for tissue engineering. *J. Cell. Physiol.* 203 (3), 465–470. doi:10.1002/jcp.20270

Sanders, J. E., Bell, D. M., Okumura, R. M., and Dralle, A. J. (1998). Effects of alignment changes on stance phase pressures and shear stresses on transtibial amputees: measurements from 13 transducer sites. *IEEE Trans. Rehabil. Eng.* 6 (1), 21–31. doi:10.1109/86.662617

Sanders, J. E., and Daly, C. H. (1993). Normal and shear stresses on a residual limb in a prosthetic socket during ambulation: comparison of finite element results with

experimental measurements. *J. Rehabil. Res. Dev.* 30 (2), 191–204. Available at: https://pdfs.semanticscholar.org/bb0b/773849e1c4af0a9efab9bff7017b85aeb4ff.pdf (Accessed: June 08, 2018).

Sarkar, D., Dasgupta, S., Reddy, S. N., Arora, A., and Sen, S. (2019). "A soft bending-type actuator using hyper-elastic materials: development, analysis and characterization," in *ACM international conference proceeding series* (New York, NY, USA: Association for Computing Machinery), 1–7. doi:10.1145/3352593.3352668

Sengeh, D. M., and Herr, H. (2013a). A variable-impedance prosthetic socket for a transtibial amputee designed from magnetic resonance imaging data. *JPO J. Prosthetics Orthot.* 25 (3), 129–137. doi:10.1097/JPO.0b013e31829be19c

Sengeh, D. M., and Herr, H. (2013b). A variable-impedance prosthetic socket for a transtibial amputee designed from magnetic resonance imaging data. *JPO J. Prosthetics Orthot.* 25 (3), 129–137. doi:10.1097/JPO.0b013e31829be19c

Sewell, P., Noroozi, S., Vinney, J., and Andrews, S. (2000). Developments in the transtibial prosthetic socket fitting process: a review of past and present research. *Prosthet. Orthot. Int.* 24 (2), 97–107. doi:10.1080/03093640008726532

Sherman, R. A. (1999). Utilization of prostheses among US veterans with traumatic amputation: a pilot survey. *J. Rehabil. Res. Dev.* 36 (2), 100–108. Available at: http://www.ncbi.nlm.nih.gov/pubmed/10661526 (Accessed: August 05, 2018).

Shivapooja, P., Wang, Q., Szott, L. M., Orihuela, B., Rittschof, D., Zhao, X., et al. (2015). Dynamic surface deformation of silicone elastomers for management of marine biofouling: laboratory and field studies using pneumatic actuation. *Biofouling* 31 (3), 265–274. doi:10.1080/08927014.2015.1035651

Sinha, R., van den Heuvel, W. J., and Arokiasamy, P. (2011). Factors affecting quality of life in lower limb amputees. *Prosthet. Orthot. Int.* 35 (1), 90–96. doi:10.1177/0309364610397087

Smooth On Ecoflex 00-50. Available at: https://www.smooth-on.com/products/ecoflex-00-50/.

Stevens, P. M., DePalma, R. R., and Wurdeman, S. R. (2019). Transtibial socket design, interface, and suspension: a clinical practice guideline. *JPO J. Prosthetics Orthot.* 31 (3), 172–178. doi:10.1097/JPO.0000000000000219

Swanson, E. C., McLean, J. B., Allyn, K. J., Redd, C. B., and Sanders, J. E. (2018). Instrumented socket inserts for sensing interaction at the limb-socket interface. *Med. Eng. Phys.* 51, 111–118. doi:10.1016/j.medengphy.2017.11.006

Tigrini, A., Mobarak, R., Mengarelli, A., Khushaba, R. N., Al-Timemy, A. H., Verdini, F., et al. (2024). Phasor-based myoelectric synergy features: a fast hand-crafted feature extraction scheme for boosting performance in gait phase recognition. *Sensors* 24 (17), 5828. doi:10.3390/s24175828

Weathersby, E. J., Vamos, A. C., Larsen, B. G., McLean, J. B., Carter, R. V., Allyn, K. J., et al. (2022). Performance of an auto-adjusting prosthetic socket during walking with intermittent socket release. *J. Rehabil. Assist. Technol. Eng.* 9, 20556683221093271. doi:10.1177/20556683221093271

W. H. Organization and USAID. *WHO standards for prosthetics and orthotics*. Geneva: World Health Organization. Available at: https://apps.who.int/iris/handle/10665/259209.

Ziegler-Graham, K., MacKenzie, E. J., Ephraim, P. L., Travison, T. G., and Brookmeyer, R. (2008). Estimating the prevalence of limb loss in the United States: 2005 to 2050. *Arch. Phys. Med. Rehabil.* 89 (3), 422–429. doi:10.1016/j.apmr.2007.11.005

frontiers | Frontiers in Bioengineering and Biotechnology

TYPE Original Research
PUBLISHED 11 March 2025
DOI 10.3389/fbioe.2025.1493476

OPEN ACCESS

EDITED BY
Lei Wang,
Capital Normal University, China

REVIEWED BY
Jiaqiu Wang,
London South Bank University, United Kingdom
Arsalan Marghoub,
University College London, United Kingdom

*CORRESPONDENCE
Dingkun Lin,
lindingkun@126.com
Ji Qi,
haoruiml@163.com

RECEIVED 09 September 2024
ACCEPTED 24 February 2025
PUBLISHED 11 March 2025

CITATION
Lin F, Cai Y, Li J, Zhan J, Gao Z, Zeng X, Feng M, Li Y, Lin D and Qi J (2025) Noncontact optical 3D strain measurements in cervical soft tissues biomechanics by digital image correlation under tensile test: an experimental approach. *Front. Bioeng. Biotechnol.* 13:1493476. doi: 10.3389/fbioe.2025.1493476

Noncontact optical 3D strain measurements in cervical soft tissues biomechanics by digital image correlation under tensile test: an experimental approach

Fangzheng Lin[1,2], Yaoqian Cai[3], Jing Li[1,2], Jiheng Zhan[4,5,6], Zibo Gao[3], Xiaolong Zeng[4,5,6], Minshan Feng[1,2], Yongjin Li[4,5,6,7], Dingkun Lin[4,5,6,7]* and Ji Qi[4,5,6,7]*

[1]Wangjing Hospital of China Academy of Chinese Medical Sciences, Beijing, China, [2]Key Laboratory of Beijing of TCM Bone Setting, Beijing, China, [3]The Second Clinical Medical College, Guangzhou University of Traditional Chinese Medicine, Guangzhou, China, [4]The Second Affiliated Hospital, Guangzhou University of Traditional Chinese Medicine, Guangzhou, China, [5]Department of Orthopedics, Guangdong Provincial Hospital of Traditional Chinese Medicine, Guangzhou, China, [6]Guangzhou Key Laboratory of Cervical Mechanobiology, Guangzhou, China, [7]Chinese Medicine Guangdong Laboratory, Zhuhai, China

Background: Digital image correlation (DIC) is widely used to measure surface strain in loaded objects. When studying the deformation of the cervical spine, the complexity and non-planarity of the structure complicate the speckle pattern required for applying DIC. While this non-invasive technique has shown promise in biomechanical testing, its application to cervical spine analysis presents unique challenges, particularly in achieving dynamic full-scale multi-aspect strain measurements. The aim of this paper is to introduce a method for exploring the stress-strain relationship on cervical cadaveric specimen by optical non-contact measurement system.

Method: Cervical cadaveric specimens were selected as subjects. Before testing, anatomical exposure, embedding, and spraying were performed sequentially. Specimen preparation was optimized through transverse process removal to enhance visualization of key anatomical structures. The surface strain under tensile testing was analyzed by the Aramis non-contact measurement system.

Result: High-quality three-dimensional strain images were obtained with improved inspection points across all aspects, particularly in the lateral aspect (5397.25 ± 723.76 vs. 3268.25 ± 573.17, $P < 0.05$). Under 60N tensile loading, strain distribution revealed concentration in soft tissue regions while preserving clear visualization of vertebral bodies, intervertebral discs, and foramina. Quantitative analysis shown consistent deformation patterns across cervical segments (C4-C7), with no significant differences in segmental parameters ($P > 0.05$).

Conclusion: The application of an optical non-contact measurement system in this study of cervical spine biomechanics has been proven effective. This method potentially mitigates some of the limitations associated with previous DIC

techniques when applied to cervical cadaveric specimens. As a result, it enables more available measurements of multidimensional strain, which may enhance our understanding of the mechanics of the cervical spine.

KEYWORDS

digital correlation imaging, cervical spine, *in vitro*, tensile test, biomechanics

1 Introduction

In recent decades, collaboration between orthopedics and biomechanics has grown significantly. Within this progress, *in vitro* mechanical testing on cadaveric specimens has become a critical component of orthopedic research. It could provide helpful experimental evidence for clinical practice, such as the way of internal fixation, the effects of mechanical environment on bone healing, the safety of non-surgical treatment, and so on (Le et al., 2015; Ettinger et al., 2018). Regardless of the type of test—compression, torsion, traction, or specific load—each requires the materials to undergo observed strain and deformation. Generally, strain is used to estimate by the extent of deformation in materials. Conventional approaches include strain gauge, linear variable differential transformers, fiber bragg grating (Grassi and Isaksson, 2015). However, these measurement methods present several disadvantages. First, they are costly and cumbersome to operate, with their accuracy significantly influenced by external environmental conditions such as temperature and moisture. Second, methods like linear variable differential transformers, strain gauges involve manual sensor attachment and or only provide localized response values, which hinders the evaluation of global mechanical behaviors. While finite element analysis can provide overall strain distribution predictions, it relies on idealized models and assumptions that may not fully capture the complex behaviors of actual biological tissues, thus cannot serve as a complete substitute for *in vitro* biomechanical testing. Third, the invasive nature of inserting sensors to measure internal strain can alter mechanical behaviors (Brandolini et al., 2014; Danesi et al., 2016). Consequently, there is a demand for non-contact strain measurement techniques in biomechanical applications.

Digital image correlation (DIC) is an optical method that utilizes one or multiple cameras to quantify surface strains on an object subjected to loading. In the early 1990s, the integration of DIC with stereovision led to the development of three-dimensional (3D)-DIC, a non-contact strain measurement technique using multiple cameras to capture the 3D positions on objects. The basic principle of the method is to find the image correlation between a reference image and a deformation image under different load levels (Lucas, 1981). By storing digital images, it is possible to measure the displacement and strain fields in the region of interest based on greyscale similarity (Schreier et al., 2009). This advanced technique has been applied in fields ranging from aerospace (Sutton and Michael, 2003), micro-scale measurements (Schreier et al., 2004; Sutton et al., 2008) to biomechanics of spine and joints (Dickinson et al., 2011; Cano-Luis et al., 2012; Holsgrove et al., 2015). However, its application in cervical spine biomechanics has revealed several challenges.

These challenges can be categorized into two main aspects: technical limitations and specimen-related factors. While technical limitations such as camera resolution, shooting speed, noise, calibration errors, and software algorithms remain largely fixed constraints (Pan, 2018), specimen-related factors present variable challenges that warrant particular attention. The cervical spine's complex anatomical structure introduces unique difficulties in DIC application. The primary challenge lies in the cervical spine's complex and non-planar nature. Its multiple overlapping structures, including transverse processes, vertebrae, and ligaments, create optical path obstructions that affect measurement quality.

Previous studies have attempted to address these challenges with varying approaches. Liu (Liu et al., 2014) demonstrated the effectiveness of DIC in measuring strain distribution in porcine IVD under unconfined compression and tension loads. Yang (Yang et al., 2022) found that the 3D-DIC system can accurately assess the radial bulging and axial strains of porcine IVD during creep. However, most studies have predominantly focused on animal specimens or short-segment human specimens (Causa et al., 2002; Spera et al., 2011; Holsgrove et al., 2015), with observations primarily confined to single-segment analysis and single-aspect imaging, limiting our understanding of the cervical spine's integrated biomechanical behavior. And so on, the complex structures complicate the application of speckle patterns necessary for DIC and impacts image quality, which can lead to inaccuracies in strain measurements, and it is a critical concern in biomechanical studies (Cristofolini, 2017). Therein, cervical soft tissues such as intervertebral disc (IVD) and ligamentum flavum (LF) are affected by these structural complexities, which also extend to other crucial structures like the intervertebral foramen (IVF). These structures are essential for understanding the mechanical mechanisms underlying various spinal diseases and corresponding interventions (Anderst et al., 2016; Wong et al., 2022). Furthermore, intricacy affects the application of DIC in the dynamic loading of cervical cadaveric specimens (such as flexion, extension, torsion, and traction), potentially limiting its utility in certain *in vitro* biomechanical experiments.

These technical challenges in measuring soft tissue response become particularly relevant in the context of cervical traction therapy, a well-established conservative treatment for chronic cervical disorders (Blanpied et al., 2017; Graham et al., 2008). While this non-invasive method has demonstrated significant clinical efficacy in symptom management through controlled tensile forces that increase intervertebral space and neural foraminal area (Côté et al., 2016; Zhu et al., 2016), the underlying biomechanical mechanisms, particularly regarding soft tissue response during traction, remain inadequately understood.

Therefore, this paper aims to address these challenges by presenting an experimental approach for preparing cervical cadaveric specimens and applying DIC to measure strain and deformation during *in vitro* tensile testing.

2 Materials and methods

2.1 Ethics

All procedures performed in this study involving human participants followed the Declaration of Helsinki (as revised in 2013). The procedures were approved by the Ethics Committee of Guangdong Provincial Hospital of Chinese Medicine. The donors have dedicated their bodies for educational and research purposes to the local Institute of Anatomy prior to death, in compliance with local institutional and legislative requirements.

2.2 Materials

A total of four resh frozen cervical cadaveric specimens (C0-T1) were visually selected and examined by X-ray to rule out bone abnormalities such as tumor, fracture, dislocation, deformity, and severe osteoporosis. These specimens, ranging in age from 38 to 52 years, were preserved from the occipital bone to the T1 vertebra. All specimens were donated voluntarily, and approved and kept by the Department of Anatomy, Southern Medical University.

2.3 Specimens preparation

The cervical cadaveric specimens were carefully dissected, removing all soft tissues (skin, muscles, nerves, and blood vessels) while preserving the bony structures, ligaments, and joint capsules. The transverse processes were removed to clearly expose the intervertebral foramen (IVF), facilitating anatomical visualization and experimental measurements. After the dissection, specimens were wrapped in paper towel, sprayed with 0.9% saline solution, triple sealed in plastic bags, and then stored at −24°C.

On the morning of testing, each specimen was left to thaw for 6 h at room temperature (20°C ± 2°C). Four screws (2 mm diameter) were inserted into specific locations: the cerebellar fossae of the occipital bone, T1 vertebra, and T1 spinous process. Additional screws were added when necessary to enhance the specimen-potting block interface. To stabilize the highly mobile atlantoaxial joint, 1.2 mm Kirschner wires were bilaterally inserted from C1 to C2 transverse processes. Then, the specimens were potted in an embedding mold using a denture base resin mixture (powder: solvent = 1:1 ratio, total 200 mL), solidified naturally to hold the specimen securely during the process. Special attention was given to keep the cranial and caudal ends aligned, ensuring accurate mechanical testing.

2.4 Application of speckle pattern

For Digital Image Correlation (DIC) measurements, specimens were first dried and then painted with a white base coat. The black speckle pattern was then applied separately to each surface (anterior, left lateral, right lateral, left posterior arch, and right posterior arch) using an airbrush technique. During the application process, adjacent surfaces were masked to ensure the randomness of the speckle pattern and maintain high black-white contrast on each surface (Figure 1). This systematic method to speckle pattern application ensures optimal conditions for DIC tracking of surface displacements and strains.

2.5 DIC system setup and tensile test

The cervical specimens were mounted on the servo-hydraulic material testing system (Bose Electro Force 3520-AT; Bose, MN, United States). A non-contact optical 3D strain measuring system (Aramis 3D camera 6M, GOM, Braunschweig, Germany) was used to record specimen deformation and strain during testing (Figure 2A).

The dual-camera system was calibrated by adjusting camera heights and distances until optimal image clarity was achieved. For anterior view measurements of C4-C7, cameras were centered on the C5 vertebral body, ensuring coverage from C4 lower endplate to C7 upper endplate. Similar setups were applied for lateral and posterior views. This configuration enabled full-scale imaging of the IVD, IVF, and lamina range C4-C7. Images were captured at 4 frames/second with a resolution of 2,448 × 2,050 pixels and a displacement precision of 0.001 mm.

Biomechanical testing was conducted using Win Test Digital software. Laboratory temperature was maintained at (20°C ± 2°C) throughout the testing process. Prior to the tensile test, 4-5 static images were captured by the Aramis system to verify focus quality and speckle pattern integrity. The measurement module was opened to select 3-5 initial inspection points on each target area such as C4/5 IVD, C5/6 IVD, C6/7 IVD. A minimum of 4,000 3D inspection points were required across anterior, lateral, and posterior aspects of C4-C7. Remarkably, the removal of the TP eliminated previous challenges related to focus interference and overlapping of the IVF, which allowed for clear contour imaging and precise measurement of the IVF structure (Figures 2C, D, E).

Between each test, specimens remained mounted but completely unloaded, with 2-min intervals between tests. Specimens were kept moistened throughout testing. If surface fluid seepage or paint deterioration was observed, the affected areas were promptly dried and repainted. Testing commenced with the activation of the Aramis strain measurement system. Each specimen was subjected to a 60N axial tensile force (Jellad et al., 2009) followed by immediate release (Figure 2B).

2.6 Measurements

2.6.1 3D inspection points

The number of 3D inspection points was calculated by the measurement module of Aramis system.

2.6.2 3D Surface strain

3D Surface Strain (SS) characterizes the mechanical response of specimens under tensile testing by measuring the relative displacement between tracked points on the specimen surface. In this study, major strain was defined as longitudinal strain. All 3D SS values represent maximum measurements obtained at a 60N tensile load, comprising both global SS and local SS.

Global SS values were calculated by the Aramis system and presented in 3D visualization. Local SS values were specifically

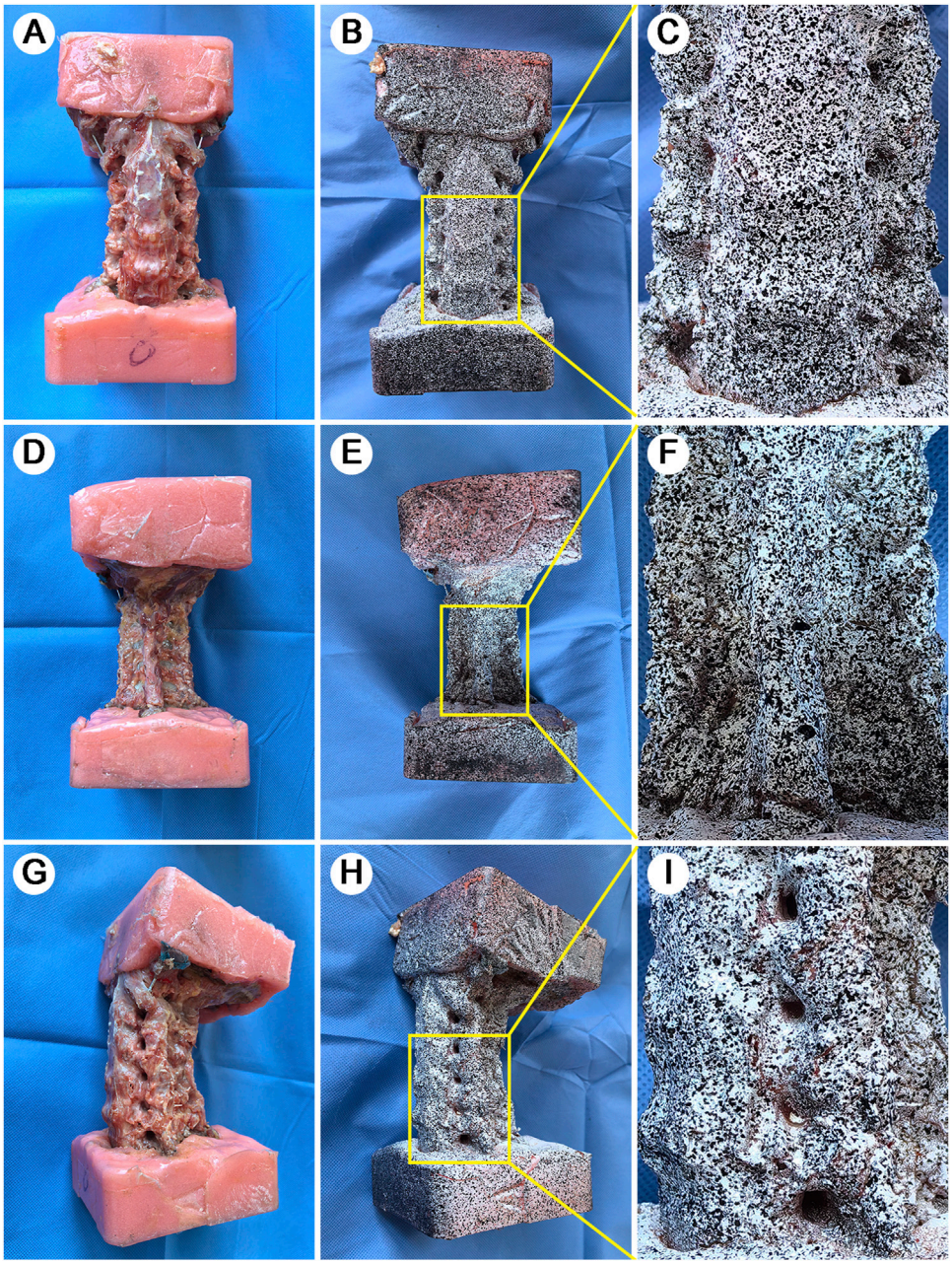

FIGURE 1
Specimen preparation and speckle pattern application. A full-scale view of specimen preparation across multiple anatomical aspects. **(A)**: Anterior view of the potted specimen showing standardized embedding technique. **(B)**: Anterior aspect after white base coat and black speckle pattern application. **(C)**: Magnified view of vertebral-disc interface highlighting pattern detail and anatomical definition. **(D)**: Posterior view after soft tissue removal showing vertebral plate. **(E)**: Posterior speckle pattern application. **(F)**: Magnified view of spinous process and lamina complex with applied pattern. **(G)**: Lateral view following TP removal for enhanced DIC 3D visualization. **(H)**: Lateral speckle pattern showing clear delineation of IVF. **(I)**: Magnified view of vertebra-disc-articular process complex demonstrating pattern integrity across different tissue types.

focused on the central region of the anterior IVD surface for analysis (Figure 3A).

2.6.3 Intervertebral disc height

IDH is measured as the distance between the midpoint of the upper endplate of the target segment and the midpoint of the lower endplate of the adjacent segment, using a lateral cervical radiograph (Jin et al., 2021). The change in IDH (ΔIDH) is then calculated to quantify the disc height alteration before and after axial tensile test (Figure 3C).

2.6.4 Height of intervertebral foramen and width of intervertebral foramen

The hIVF is determined by the distance between the superior medial point and the inferior medial point of the foramen. The wIVF was measured by calculating the distance from the anterior medial

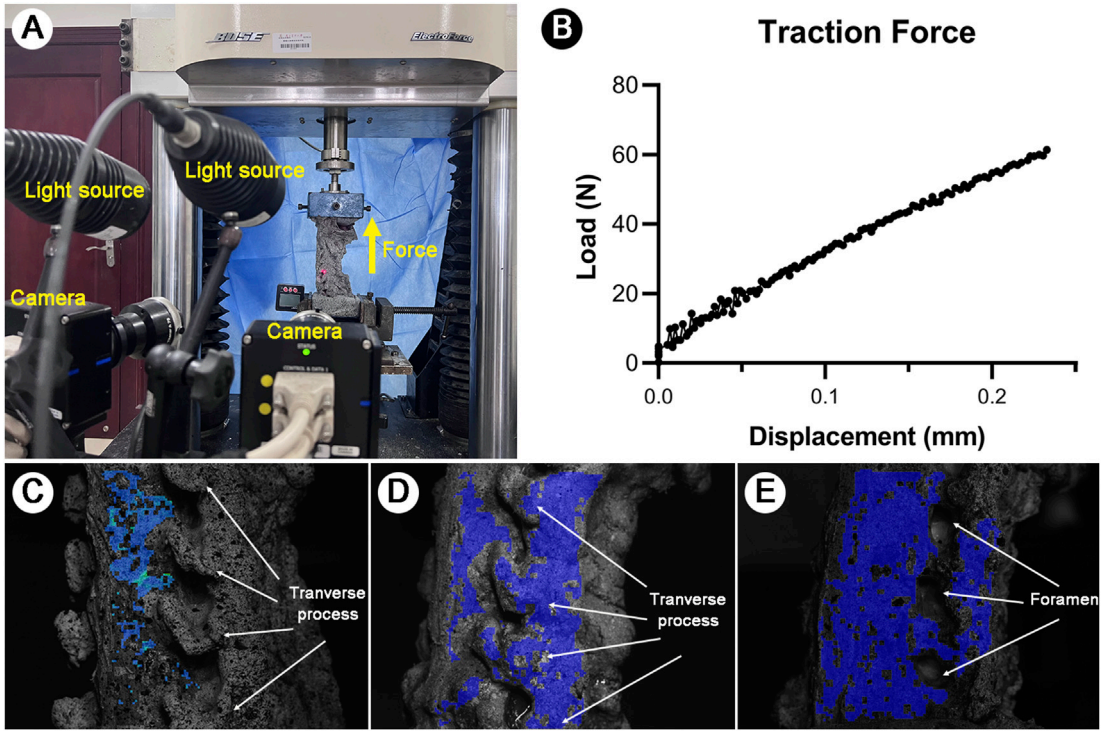

FIGURE 2
Experimental setup and methodological optimization. **(A)**: Integrated testing configuration showing servo-hydraulic system and dual-camera DIC setup. **(B)**: Loading protocol diagram illustrating the 60N progressive axial tensile force application. **(C)**: Focus interference caused by the overlapped TP and inadequate 3D inspection points. **(D)**: The overlapping of the TP caused 3D inspection points were identified only on the TP and articular facets, but it was failure to measure the IVF. **(E)**: Optimized lateral view following transverse process removal. Clear visualization of vertebral bodies, IVF and sufficient 3D inspection points for 3D SS modeling during tensile testing.

point to the posterior medial point of the foramen (Sun et al., 2021). The change in height (ΔhIVF) and width (ΔwIVF) captures alterations pre- and post-axial traction (Figure 3B).

2.6.5 Height of and lamina height

Measurement of LH at the posterior side of cervical cadaveric specimen. The hLH was defined by selecting the lower edge of the upper lamina and the upper edge of the lower lamina, measured at the midpoint of each segment's lamina (Park et al., 2022). △hLH determined the change in pre- and post-test in axial (Figure 3D).

2.7 Statistical analysis

The sample size was calculated using the number of 3D inspection point at lateral side as the primary efficacy parameter. Based on the result of preliminary experiment and related literature, a sample size of 3 specimens per group was estimated to provide 90% power to detect a paired between-group difference of 2000, assuming a standard deviation of 5000, and two-sided significance level of 5%. To compensate for a 25% failure to biomechanical tests, the sample size was increased to 4 specimens in each group. Variables such as the number of 3D inspection point, maximum SS (%), SS of the IVD (%), △IDH (mm), △hIVF (mm), and △hLH (mm) were expressed as mean ± standard deviation. To compare the differences in inspection point between approaches, paired t-test was analyzed. Difference in SS under tensile test among the anterior, lateral and posterior sides, and differences in SS of the IVD (%), △IDH (mm), △hIVF (mm), and △hLH (mm) between segments, were performed by analysis of variance of randomized complete block design. All statistical analysis was conducted using SPSS software (version 20, IBM Corp). All statistical tests were two-sided, and the threshold for statistical significance was set at $P < 0.05$.

3 Results

3.1 3D inspection points distribution

In the lateral side, the number of 3D inspection points under the modified method, increased significantly, compared to the origin method ($P < 0.05$) (Table 1). Meanwhile, no significant difference was found in the anterior and posterior side ($P > 0.05$) (Figure 4A).

3.2 3D surface strain

Following the described preparation method for cervical cadaveric specimen, successful generation of 3D SS models of the anterior, lateral, and posterior aspects was achieved. The inspection points are densely distributed and uniform, clearly delineating the

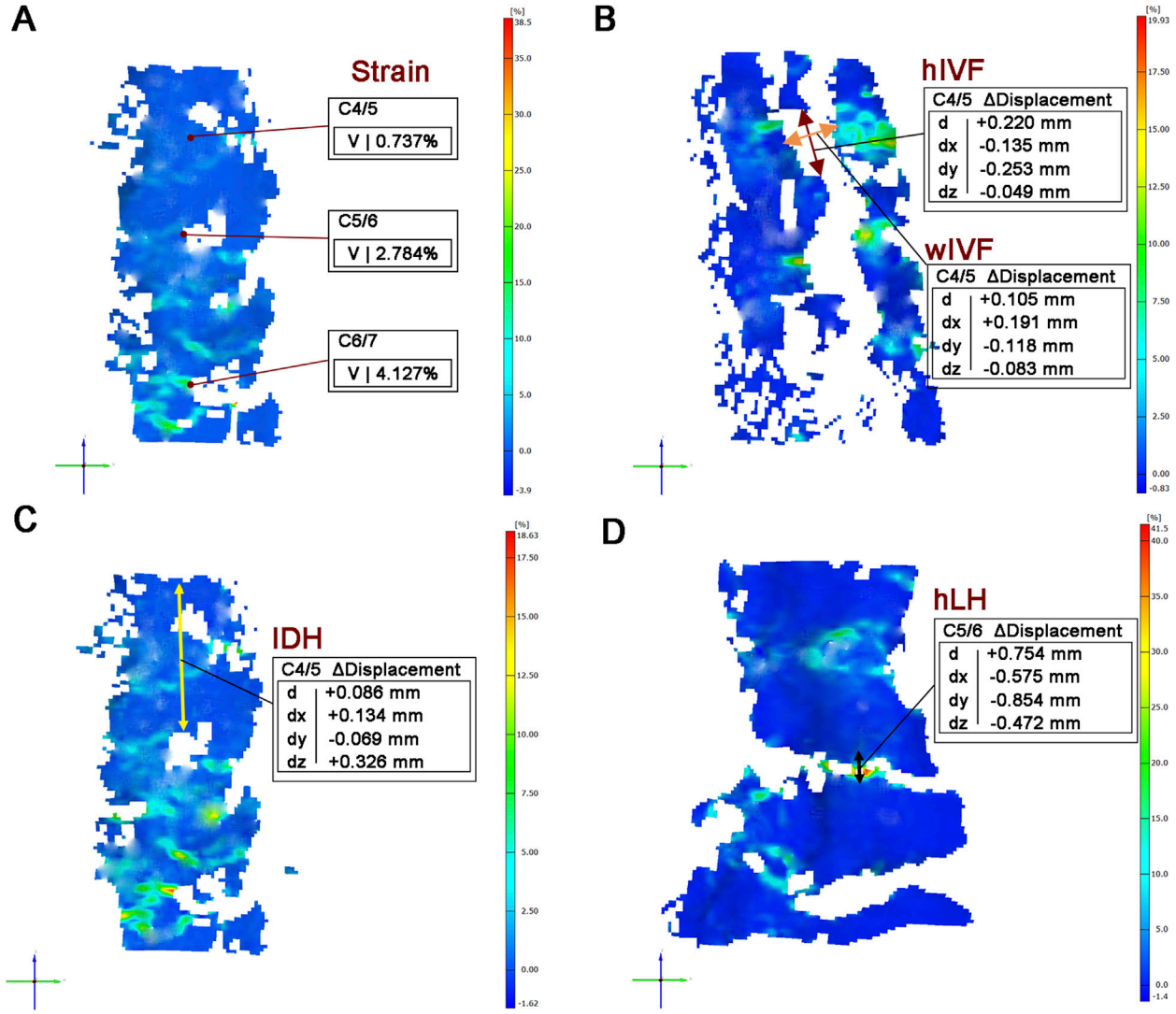

FIGURE 3
Quantitative measurement parameters for biomechanical analysis. **(A)**: The local SS values of IVD. **(B)**: Measurement of hIVF and wIVF at C4/5 level. **(C)**: Measurement of IDH at C4/5 level. **(D)** Measurement of LH at C5/6 level. Note: V: values; d: displacement XYZ; dx: displacement X; dy: displacement Y; dz: displacement Z.

3D contours of the cervical cadaveric specimens. The imaging distinctly displays the structural hierarchy of the vertebral bodies, IVD, IVF, articular processes, and lamina (Figures 5B, D, F) under maximum loading (60N), in comparison with the baseline (0N) (Figures 5A, C, E).

During the tensile test, the maximum global SS values were around 30%, without significant difference found among the anterior, posterior and lateral side ($P > 0.05$) (Figure 4B). The SS of IVD (%) showed an increasing trend from C4-C5, C5-C6 to C6-C7, indicating higher SS of IVD in lower segments, but there were no significant differences in the SS of IVD ($P > 0.05$) (Figure 4C).

3.3 Deformation of IDH, IVF and LH

The results of deformation of △IDH, △IVF and △LH showed increasing trends from C4-C5, C5-C6 to C6-C7, suggesting greater deformation in lower cervical segments under tensile load, but there were no significant differences in the increase of deformation ($P > 0.05$) (Figure 4D).

4 Discussion

The present study investigated the application of DIC technology for examining cervical soft tissue biomechanics through non-contact optical strain measurements under tensile loading conditions. This investigation focused on developing and validating an experimental approach for cervical cadaveric specimen preparation and testing methodology that would enable reliable 3D SS analysis across multiple anatomical aspects of the cervical spine. The experimental method integrated traditional biomechanical testing methods with optical measurement techniques, allowing for simultaneous assessment of various structural parameters

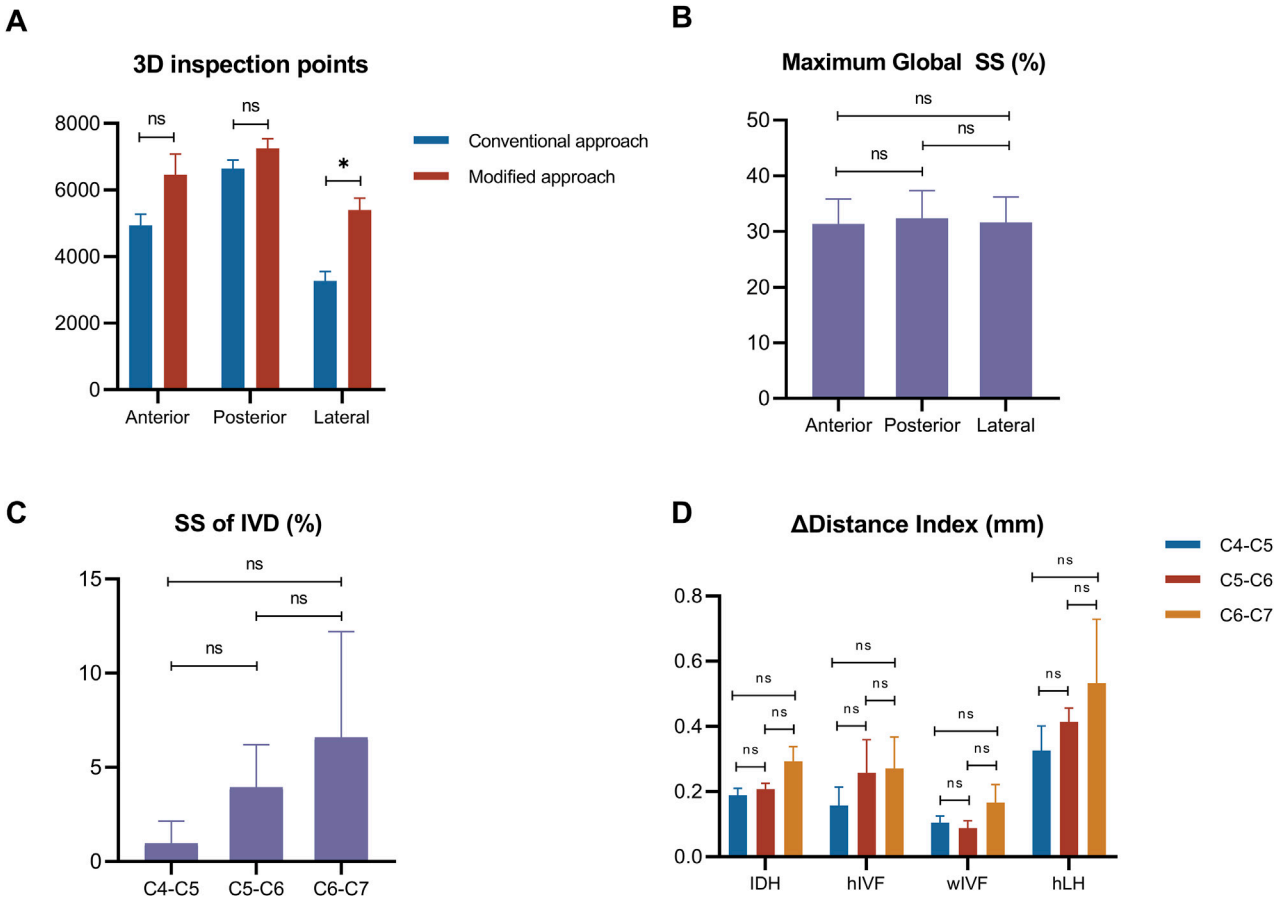

FIGURE 4
Distribution of 3D inspection points and parameter changes across segments. **(A)**: Comparison of 3D inspection point numbers between conventional and modified methods across different aspects. **(B)**: Maximum global SS comparison between aspects. **(C)**: Segmental analysis of local SS of IVD. **(D)**: Combined analysis of dimensional changes. Notes: *P < 0.05; ns = none significant difference.

during tensile loading. This technical framework may contribute to our understanding of cervical spine biomechanics through non-contact measurement methods.

4.1 DIC technology

DIC is a non-contact experimental method for storing images of material surfaces in digital form (Yoon et al., 2021). The system captures images at predetermined intervals, which are analyzed to determine displacement and strain distribution across the disc surface. This capability is particularly valuable in the context of cervical spine biomechanics, where understanding the strain distribution during dynamic loading conditions can inform surgical interventions and rehabilitation protocols.

Initially, the technique was only capable of measuring a single plane. With the development of imaging technology, the application of 2 or more high-speed camera imaging enables the detection of 3D disembodied space (Grassi and Isaksson, 2015; Yoon et al., 2021). DIC technology was first applied to the testing of engineering materials and is now used more in biomechanical testing in dentistry and orthopedics (Bay, 1995; Lu and Cary, 2000; Poissant and Barthelat, 2010).

The technology has the following advantages (Grassi and Isaksson, 2015): (1) Sensor technology alters the displacement or deformation information of an object, DIC is a non-contact method and provides a richer set of discrete data points compared to sensing technology; (2) DIC technology is faster to analyze, cheaper and easy to integrate and consolidate with a few other technologies. However, the accuracy of DIC technology is based on high-quality imaging, which is affected by hardware, software, and the material itself.

4.2 Specimen preparation

Given these technical characteristics of DIC, careful attention must be paid to specimen preparation to ensure measurement accuracy, particularly when applying this technology to complex anatomical structures like the cervical spine. On irregular anatomical structures such as spine and joints, which do not have a flat surface like materials such as teeth and endothelial plants, preparation of specimen and speckles spraying becomes more difficult and inefficient. Xu (Xu et al., 2018)successfully detected the strain field of the inferior tibiofibular coalition ligament using the DIC technique, which was also used in the

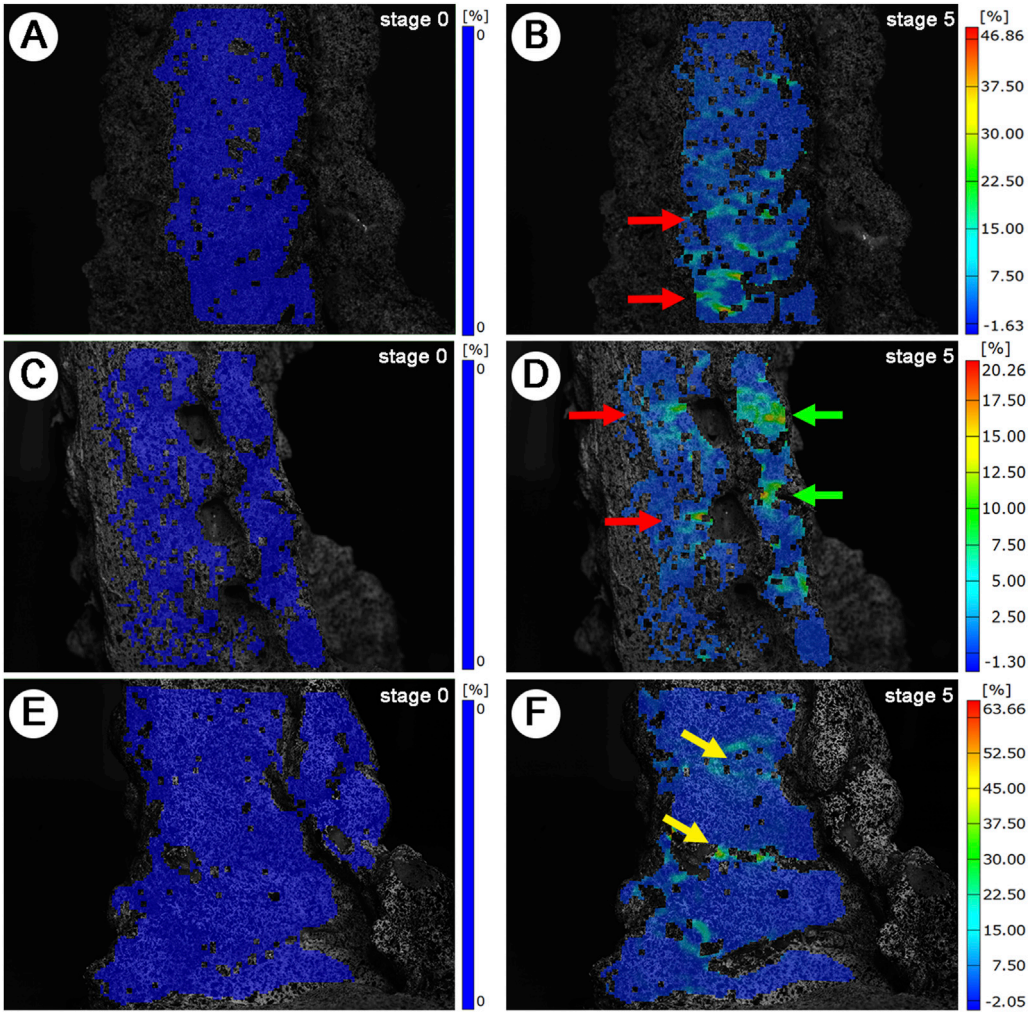

FIGURE 5
3D Strain Distribution Under Tensile Loading. **(A, C, E)**: Baseline (0N) strain distribution. **(A)**: Anterior view. **(C)**: Lateral view. **(E)**: Posterior view. **(B, D, F)**: Maximum load (60N) strain distribution. Red arrows: IVD SS concentrations. Green arrows: Lateral IVD SS and articular process SS concentrations. Yellow arrows: Laminar space SS concentrations.

author's team's previous study to achieve imaging and detection of the sacroiliac joint (Li et al., 2022).

The complexity of cervical spine presented significant challenges for DIC visualization. It was imperative to ensure that specific areas like IVD, IVF and LF were sufficiently flat to maximize 3D inspection points. A particular challenge emerged in the lateral aspect observation, where protruding TP affected speckle pattern application and obstructed camera focus, hindering strain detection of the IVD and IVF. Our solution involved careful excision of the cervical TP, which preserved bony structure stability while significantly improving visualization of key anatomical structures. This modification enabled precise measurements of IVF and enhanced strain detection across IVD, LF, and articular processes.

Tissue hydration management emerged as another critical consideration due to the high-water content of cervical soft tissues, particularly the IVD. To maintain normal physiological properties and mechanical performance (Causa et al., 2002), specimens were wrapped in wet towels and sealed in plastic bags before speckle pattern application. During testing, when surface fluid seepage occurred, affected areas were carefully dried and speckle patterns reapplied to ensure measurement accuracy. Through this optimized preparation protocol, we successfully monitored strains and deformations across multiple anatomical planes of C4-C7 during dynamic tensile testing. The instantaneous loading protocol (0–60N) employed in this study significantly minimized the risk of tissue dehydration during testing. Furthermore, while tissue hydration is crucial for maintaining physiological properties, it is noteworthy that previous biomechanical studies have rarely provided detailed documentation of environmental conditions and specimen humidity control (as shown in Table 2).

4.3 Application of speckle pattern

The effectiveness of DIC technology heavily relies on the uniform application and quality of speckle patterns across the

TABLE 1 The number of 3D inspection points by different approaches.

Aspect	Conventional approach	Modified approach	*t*	*P*
Anterior	4,936.25 ± 666.77	6,460.00 ± 1241.16	2.947	0.060
Posterior	6,647.00 ± 502.16	7,247.00 ± 597.73	2.211	0.114
Lateral	3,268.25 ± 573.17	5,397.25 ± 723.76	5.709	0.011*

*$P < 0.05$.

TABLE 2 Comparison of DIC applications in spinal biomechanical studies.

Specimen	Number of specimens	Type of mechanical test	Aspect of observation	Type of speckle pattern	Strain ponits	DIC system	Reported quantities	References
Human lumbar (L3/4)	14	3 directions of motion	Lateral of IVD	N.A	N.A	N.A	Strain	Wangsawatwong et al. (2023)
Porcine cervical (C2-C7)	10	Compression	Anterior of IVD	N.A	N.A	VIC-3D	Deformation and strain	Yang et al. (2022)
Human pelvic	6	compression, tensile, rotation	Lateral	Airbrush	N.A	Aramis 6M	N.A	Li et al. (2022)
Porcine cervical (C2-C6)	8	Compression	Anterior of cervical (C2-C6)	N.A	Each specimen equating to approximately 3,000 inspection points in the entire anterior aspect	Vic-3D	Deformation and strain	Holsgrove et al. (2015)
Human lumbar (L5)	1	N.A	Anterior of vertebra	Airbrush	N.A	Dantec Dynamics	Strain	Palanca et al. (2015)
Porcine lumbar (Single segment)	1	Compression	Anterior, posterior, lateral of IVD	Powder	N.A	Dalsa falcon	Deformation and strain	Spera et al. (2011)
Human cervical	4	Tensile	Anterior, posterior, lateral of cervical (C4-C7)	Air brush	Each specimen had an average of 6460, 5397, and 7247 inspection points on the anterior, posterior and lateral, aspects	Aramis 6M	Deformation and strain	Our study

Notes: References are listed in chronological order within each subsection.
N.A = information not available.

entire area of interest. While existing literature provides general guidance on speckle pattern optimization, there remains no standardized protocol for speckle application on cervical cadaveric specimens. According to Quino's study (Quino et al., 2021), the optimal speckle size is typically determined based on the resolution of the imaging system and the expected deformation of the material being tested. Larger speckles may be appropriate for materials undergoing significant deformation, while smaller speckles are more suitable for materials with minimal movement (Cariero et al., 2014).

In our study, we first validated the collection of sufficient 3D inspection points through static image capture before proceeding with tensile testing. The results demonstrated remarkable improvements in data collection density, with the anterior aspect detecting (6460.00 ± 1241.16) inspection points, the posterior aspect (7247.00 ± 597.73) points, and the lateral aspect (5397.25 ± 723.76) points. These results significantly exceed and more comprehensive than the previously reported threshold of approximately 3,000 points from the anterior aspect by Holsgrove (Holsgrove et al., 2015), indicating a substantial enhancement in measurement resolution. This higher density of inspection points carries several critical implications for biomechanical analysis. First, it enables the construction of multi-aspect and accurate 3D SS model. Second, it allows for precise measurement of strain values at each inspection point, particularly crucial for analyzing complex anatomical interfaces such as IVD and IVF. Furthermore, this enhanced resolution facilitates more accurate measurements of 3D vertebral angles and strain directions, providing a more complete understanding of cervical spine biomechanics.

Our review of existing literature reveals that DIC applications in spinal biomechanics have been relatively limited, particularly regarding multi-aspect and multi-segment strain analysis (Table 2). Most previous studies focused on single aspects (anterior or lateral) or individual segments of the spine, primarily

using porcine models. Our study extends this scope by simultaneously analyzing anterior, posterior, and lateral aspects across multiple cervical segments (C4-C7) in human specimens, potentially providing a more comprehensive understanding of cervical spine biomechanics under tensile loading conditions.

Additionally, regarding speckle application methods, several techniques such as airbrushing, spin coating and powder, have been developed for DIC analysis, as documented by Dong (Dong and Pan, 2017). Maintaining consistent gray intensity distribution before and after deformation is crucial for accurate image correlation (Yoon et al., 2021). While powder-based methods offer precise control over speckle dimensions, they often struggle with pattern adhesion during mechanical testing, particularly problematic for hydrated tissues (Dong et al., 2015; Jonnalagadda et al., 2010). The airbrush method, in contrast, demonstrates superior control over pattern characteristics and has been extensively validated in biomechanical studies (Ottenio et al., 2015; Palanca et al., 2015; Zhang and Arola, 2004). This technique allows for better management of pattern density and distribution, providing more uniform coverage and enhanced pattern stability during deformation (Lionello and Cristofolini, 2014). Its versatility in accommodating different specimen sizes has made it a preferred choice in numerous soft tissue studies (Lauret et al., 2009; Yamaguchi et al., 2011; Zhang and Arola, 2004).

4.4 Dynamic test

Few studies have mentioned DIC technology may not be suitable for dynamic testing conditions where rapid loading or unloading occurs (Lisický et al., 2022). It is because the DIC technology can be limited by the need for high-resolution imaging and sophisticated software for data analysis. However, Timothy (Holsgrove et al., 2015) has demonstrated the viability of using DIC for capturing structural damage in cervical cadaveric specimen within 10 ms after impact. The damage from impacts was localized at C5/6, though it was a high-speed impact. In our opinion, the quality of DIC technology it is also related to the range of motion designed for the specimens and the condition of mechanical loading.

In this study, we employed axial tensile testing, a widely recognized method for investigating cervical spine biomechanics (Zhao et al., 2020). By comparing variables such as SS, ΔIVD, ΔhIVF, ΔwIVF, and ΔLH across different segments, we observed that the DIC system could accurately measure evenly distributed changes in segment parameters. Our observation that neutral position traction resulted in more evenly distributed stress patterns in the lower cervical spine corroborates previous findings by Lin (Lin et al., 2023), thereby lending additional credence to the accuracy of this study. Another notable observation was the differential strain distribution pattern between soft tissues and bony structures. As shown in Figure 5, strain predominantly manifested in the interstitial spaces, specifically the IVD, LF, and articular processes, while bony structures exhibited minimal deformation. This pattern aligns with the therapeutic mechanisms of cervical traction, where controlled tensile forces are applied to decompress neural structures and increase intervertebral space. During mechanical loading, we observed strain concentration across multiple IVDs, articular process and laminar spaces, accompanied by increased height in these areas. These observations may provide insights into the mechanical properties of soft tissues through various measured parameters. As the IVDs undergo deformation under tensile testing, the strain experienced can lead to changes in their height, which is often measured using imaging techniques such as MRI or CT scans (Khuyagbaatar et al., 2017). Moreover, the observed elongation of the LF, indicated by changes in LH, reflects its crucial role in force distribution and neural structure protection (Dorsi et al., 2024).

These findings demonstrate DIC technology is a reliable tool for simultaneously monitoring multiple anatomical aspects and quantifying subtle deformations and provides a validated experimental framework that future researchers can build upon when studying cervical spine biomechanics and therapeutic mechanisms of cervical traction. This strain distribution pattern aligns with the therapeutic mechanisms of cervical traction, where controlled tensile forces are applied to decompress neural structures and increase intervertebral space.

To sum up, the experimental approach mentioned in this study has proven to be a reliable method for conducting biomechanical experiments on cervical cadaveric specimens *in vitro*. The DIC system effectively recorded and quantified changes in segment parameters, demonstrating its utility even under dynamic conditions. This methodology provides a validated experimental framework for future research in cervical spine biomechanics and therapeutic traction mechanisms.

4.5 Limitations

However, this study still has a certain limitation. In terms of specimen preparation, although fresh cadaveric specimens were used, the process of applying the speckle pattern may have induced tissue dehydration, potentially altering the viscoelastic properties of soft tissues during testing. As a surface measurement technique, DIC cannot provide direct insights into internal stress distributions or failure mechanisms occurring within the specimen under loading. The integration of DIC with finite element analysis may be able to measure the strain of overall IVD and the size of internal IVF. Furthermore, the current study was limited to tensile testing alone. The effectiveness of DIC technology in evaluating other mechanical stress modalities, such as compression and torsion, on large samples of cervical cadaveric specimens remains to be investigated. Future research should explore the applicability of DIC across various loading conditions to establish its broader utility in biomechanical testing.

5 Conclusion

In summary, this study applies DIC technology to explore biomechanical behaviors in cervical cadaveric specimens under dynamic conditions. The findings suggest the potential utility of DIC in cervical spine biomechanics research, offering a reliable and reproducible methodological foundation. This could significantly inform future studies aiming to broaden the application of DIC technology, potentially improving the diagnosis and treatment of cervical disorders.

Data availability statement

The raw data supporting the conclusions of this article will be made available by the authors, without undue reservation.

Ethics statement

Written informed consent was obtained from the individual(s) for the publication of any potentially identifiable images or data included in this article.

Author contributions

FL: Conceptualization, Data curation, Investigation, Methodology, Writing–original draft, Writing–review and editing. YC: Data curation, Formal Analysis, Investigation, Methodology, Software, Supervision, Validation, Visualization, Writing–review and editing. JL: Data curation, Formal Analysis, Investigation, Methodology, Writing–review and editing. JZ: Data curation, Methodology, Writing–original draft. ZG: Data curation, Investigation, Writing–review and editing. XZ: Methodology, Supervision, Writing–review and editing, Visualization. MF: Methodology, Supervision, Writing–review and editing. YL: Project administration, Resources, Writing - review and editing, Visualization. DL: Conceptualization, Funding acquisition, Project administration, Resources, Supervision, Writing–review and editing. JQ: Conceptualization, Funding acquisition, Supervision, Writing–review and editing, Data curation, Formal Analysis, Investigation, Methodology, Software, Validation, Visualization, Writing–original draft.

Funding

The author(s) declare that financial support was received for the research, authorship, and/or publication of this article. This work was supported by National Natural Science Fund Project (No. 82205150); Science and Technology Project of Chinese Medicine Guangdong Laboratory (No. HQL2024PZ007); Project of Clinical Key Laboratory ofTCMSyndrome of Guangdong Province (No.2023KT15480-YN2023ZH05); Research Fund for Qingmiao Talents of Guangdong Provincial Hospital of Chinese Medicine (SZ2024QN03); the Research Fund of Guangdong Provincial Hospital of Chinese Medicine (YN2023WSSQ08).

Conflict of interest

The authors declare that the research was conducted in the absence of any commercial or financial relationships that could be construed as a potential conflict of interest.

Publisher's note

All claims expressed in this article are solely those of the authors and do not necessarily represent those of their affiliated organizations, or those of the publisher, the editors and the reviewers. Any product that may be evaluated in this article, or claim that may be made by its manufacturer, is not guaranteed or endorsed by the publisher.

References

Anderst, W., Donaldson, W., Lee, J., and Kang, J. (2016). Cervical spine disc deformation during *in vivo* three-dimensional head movements. *Ann. Biomed. Eng.* 44 (5), 1598–1612. doi:10.1007/s10439-015-1424-2

Bay, B. K. (1995). Texture correlation: a method for the measurement of detailed strain distributions within trabecular bone. *J. Orthop. Res.* 13 (2), 258–267. doi:10.1002/jor.1100130214

Blanpied, P. R., Gross, A. R., Elliott, J. M., Devaney, L. L., Clewley, D., Walton, D. M., et al. (2017). Neck pain: revision 2017: clinical practice guidelines linked to the international classification of functioning, disability and health from the orthopaedic section of the American physical therapy association. *J. Orthop. and Sports Phys. Ther.* 47, A1–A83. doi:10.2519/jospt.2017.0302

Brandolini, N., Cristofolini, L., and Viceconti, M. (2014). Experimental methods for the biomechanical investigation of the human spine: a Review. *J. Mech. Med. and Biol.* 14 (01), 1430002–1430415. doi:10.1142/S0219519414300026

Cano-Luis, P., Giráldez-Sanchez, M. A., Martínez-Reina, J., Serrano-Escalante, F. J., Galleguillos-Rioboo, C., Lázaro-Gonzálvez, A., et al. (2012). Biomechanical analysis of a new minimally invasive system for osteosynthesis of pubis symphysis disruption. *Injury* 43 (Suppl. 2), S20–S27. doi:10.1016/s0020-1383(13)70175-x

Carriero, A., Abela, L., Pitsillides, A. A., and Shefelbine, S. J. (2014). *Ex vivo* determination of bone tissue strains for an *in vivo* mouse tibial loading model. *J. Biomechanics* 47, 2490–2497. doi:10.1016/j.jbiomech.2014.03.035

Causa, F., Manto, L., Borzacchiello, A., De Santis, R., Netti, P. A., Ambrosio, L., et al. (2002). Spatial and structural dependence of mechanical properties of porcine intervertebral disc. *J. Mater Sci. Mater Med.* 13 (12), 1277–1280. doi:10.1023/a:1021143516436

Côté, P., Wong, J. J., Sutton, D., Shearer, H. M., Mior, S., Randhawa, K., et al. (2016). Management of neck pain and associated disorders: a clinical practice guideline from the Ontario Protocol for Traffic Injury Management (OPTIMa) Collaboration. *Eur. Spine J.* 25, 2000–2022. doi:10.1007/s00586-016-4467-7

Cristofolini, L. (2017). Full-field *in vitro* investigation of hard and soft tissue strain in the spine by means of Digital Image Correlation. *Muscles Ligaments Tendons J.* 7 (4), 538–545. doi:10.11138/mltj/2017.7.4.538

Danesi, V., Erani, P., Brandolini, N., Juszczyk, M. M., and Cristofolini, L. (2016). Effect of the *in vitro* boundary conditions on the surface strain experienced by the vertebral body in the elastic regime. *J. Biomech. Eng.* 138 (10). doi:10.1115/1.4034383

Dickinson, A. S., Taylor, A. C., Ozturk, H., and Browne, M. (2011). Experimental validation of a finite element model of the proximal femur using digital image correlation and a composite bone model. *J. Biomech. Eng.* 133 (1), 014504. doi:10.1115/1.4003129

Dong, Y., Kakisawa, H., and Kagawa, Y. (2015). Development of microscale pattern for digital image correlation up to 1400°C. *Opt. Lasers Eng.* 68, 7–15. doi:10.1016/j.optlaseng.2014.12.003

Dong, Y. L., and Pan, B. (2017). A review of speckle pattern fabrication and assessment for digital image correlation. *Exp. Mech.* 57, 1161–1181. doi:10.1007/s11340-017-0283-1

Dorsi, M. J., Buchanan, P., Vu, C., Bhandal, H. S., Lee, D. W., Sheth, S., et al. (2024). Pacific spine and pain society (PSPS) evidence review of surgical treatments for lumbar degenerative spinal disease: a narrative review. *Pain Ther.* 13, 349–390. doi:10.1007/s40122-024-00588-4

Ettinger, M., Karkosch, R., Horstmann, H., Savov, P., Calliess, T., Smith, T., et al. (2018). Biomechanical properties of adjustable extracortical graft fixations in ACL reconstruction. *J. Exp. Orthop.* 5 (1), 41. doi:10.1186/s40634-018-0154-4

Graham, N., Gross, A., Goldsmith, C. H., Klaber Moffett, J., Haines, T., Burnie, S. J., et al. (2008). Mechanical traction for neck pain with or without radiculopathy. *Cochrane Database Syst. Rev.*, CD006408. doi:10.1002/14651858.CD006408.pub2

Grassi, L., and Isaksson, H. (2015). Extracting accurate strain measurements in bone mechanics: a critical review of current methods. *J. Mech. Behav. Biomed. Mater* 50, 43–54. doi:10.1016/j.jmbbm.2015.06.006

Holsgrove, T. P., Cazzola, D., Preatoni, E., Trewartha, G., Miles, A. W., Gill, H. S., et al. (2015). An investigation into axial impacts of the cervical spine using digital image correlation. *Spine J.* 15 (8), 1856–1863. doi:10.1016/j.spinee.2015.04.005

Jellad, A., Ben Salah, Z., Boudokhane, S., Migaou, H., Bahri, I., and Rejeb, N. (2009). The value of intermittent cervical traction in recent cervical radiculopathy. *Ann. Phys. Rehabilitation Med.* 52, 638–652. doi:10.1016/j.rehab.2009.07.035

Jin, Y. Z., Zhao, B., Lu, X. D., Zhao, Y. B., Zhao, X. F., Wang, X. N., et al. (2021). Mid- and long-term follow-up efficacy analysis of 3D-printed interbody fusion cages for anterior cervical discectomy and fusion. *Orthop. Surg.* 13 (7), 1969–1978. doi:10.1111/os.13005

Jonnalagadda, K. N., Chasiotis, I., Yagnamurthy, S., Lambros, J., Pulskamp, J., Polcawich, R., et al. (2010). Experimental investigation of strain rate dependence of nanocrystalline Pt films. *Exp. Mech.* 50, 25–35. doi:10.1007/s11340-008-9212-7

Khuyagbaatar, B., Kim, K., Park, W. M., Lee, S., and Kim, Y. H. (2017). Increased stress and strain on the spinal cord due to ossification of the posterior longitudinal ligament in the cervical spine under flexion after laminectomy. *Proc. Inst. Mech. Eng. H.* 231, 898–906. doi:10.1177/0954411917718222

Lauret, C., Hrapko, M., Van Dommelen, J. A. W., Peters, G. W. M., and Wismans, J. S. H. M. (2009). Optical characterization of acceleration-induced strain fields in inhomogeneous brain slices. *Med. Eng. and Phys.* 31, 392–399. doi:10.1016/j.medengphy.2008.05.004

Le, V. H., Heckmann, N., Jain, N., Wang, L., Turner, A. W., Lee, T. Q., et al. (2015). Biomechanical evaluation of supplemental percutaneous lumbo-sacro-iliac screws for spinopelvic fixation following total sacrectomy. *J. Spinal Disord. Tech.* 28 (4), E181–E185. doi:10.1097/bsd.0000000000000241

Li, J., Li, Y., Ping, R., Zhang, Q., Chen, H. Y., Lin, D., et al. (2022). Biomechanical analysis of sacroiliac joint motion following oblique-pulling manipulation with or without pubic symphysis injury. *Front. Bioeng. Biotechnol.* 10, 960090. doi:10.3389/fbioe.2022.960090

Lin, D., He, Z., Weng, R., Zhu, Y., Lin, Z., Deng, Y., et al. (2023). Comparison of biomechanical parameters of two Chinese cervical spine rotation manipulations based on motion capture and finite element analysis. *Front. Bioeng. Biotechnol.* 11, 1195583. doi:10.3389/fbioe.2023.1195583

Lionello, G., and Cristofolini, L. (2014). A practical approach to optimizing the preparation of speckle patterns for digital-image correlation. *Meas. Sci. Technol.* 25, 107001. doi:10.1088/0957-0233/25/10/107001

Lisický, O., Avril, S., Eydan, B., Pierrat, B., and Burša, J. (2022). Evaluation of image registration for measuring deformation fields in soft tissue mechanics. *Strain* 58, e12424. doi:10.1111/str.12424

Liu, Q., Wang, T. Y., Yang, X. P., Li, K., Gao, L. L., Zhang, C. Q., et al. (2014). Strain distribution in the intervertebral disc under unconfined compression and tension load by the optimized digital image correlation technique. *Proc. Inst. Mech. Eng. H.* 228 (5), 486–493. doi:10.1177/0954411914529756

Lu, H., and Cary, P. D. (2000). Deformation measurements by digital image correlation: implementation of a second-order displacement gradient. *Exp. Mech.* 40 (4), 393–400. doi:10.1007/BF02326485

Lucas, B. D. (1981). An iterative image registration technique with an application to stereo vision. *Proc. Ijcai* 81 (3), 674–679. doi:10.1042/cs0730285

Ottenio, M., Tran, D., Ní Annaidh, A., Gilchrist, M. D., and Bruyère, K. (2015). Strain rate and anisotropy effects on the tensile failure characteristics of human skin. *J. Mech. Behav. Biomed. Mater.* 41, 241–250. doi:10.1016/j.jmbbm.2014.10.006

Palanca, M., Brugo, T. M., and Cristofolini, L. (2015). Use of digital image correlation to investigate the biomechanics of the vertebra. *J. Mech. Med. Biol.* 15, 1540004. doi:10.1142/S0219519415400047

Pan, B. (2018). Digital image correlation for surface deformation measurement: historical developments, recent advances and future goals. *Meas. Sci. Technol.* 29, 082001. doi:10.1088/1361-6501/aac55b

Park, E. J., Min, W. K., and Sim, S. (2022). Bicortical laminar screws for posterior fixation of subaxial cervical spine: a radiologic analysis with computed tomography images. *Glob. Spine J.* 12 (1), 85–91. doi:10.1177/2192568220947054

Poissant, J., and Barthelat, F. (2010). A novel "subset splitting" procedure for digital image correlation on discontinuous displacement fields. *Exp. Mech.* 50 (3), 353–364. doi:10.1007/s11340-009-9220-2

Quino, G., Chen, Y., Ramakrishnan, K. R., Martínez-Hergueta, F., Zumpano, G., Pellegrino, A., et al. (2021). Speckle patterns for DIC in challenging scenarios: rapid application and impact endurance. *Meas. Sci. Technol.* 32 (1), 015203. doi:10.1088/1361-6501/abaae8

Schreier, H., Orteu, J.-J., and Sutton, M. A. (2009). *Image correlation for shape, motion and deformation measurements: basic Concepts,Theory and applications*. Boston, MA: Springer US. doi:10.1007/978-0-387-78747-3

Schreier, H. W., Garcia, D., and Sutton, M. A. (2004). Advances in light microscope stereo vision. *Exp. Mech.* 44, 278–288. doi:10.1007/BF02427894

Spera, D., Genovese, K., and Voloshin, A. (2011). Application of stereo-digital image correlation to full-field 3-D deformation measurement of intervertebral disc. *Strain* 47 (s1), e572–e587. doi:10.1111/j.1475-1305.2009.00658.x

Sun, B., Xu, C., Zhang, Y., Wu, S., Wu, H., Zhang, H., et al. (2021). Intervertebral foramen width is an important factor in deciding additional uncinate process resection in ACDF-a retrospective study. *Front. Surg.* 8, 626344. doi:10.3389/fsurg.2021.626344

Sutton, M. A., Ke, X., Lessner, S. M., Goldbach, M., Yost, M., Zhao, F., et al. (2008). Strain field measurements on mouse carotid arteries using microscopic three-dimensional digital image correlation. *J. Biomed. Mater. Res. Part A* 86a (2), 569. doi:10.1002/jbm.a.32102

Sutton, and Michael, A. (2003). Deformations in wide, center-notched, thin panels, part I: three-dimensional shape and deformation measurements by computer vision. *Opt. Eng.* 42 (5), 1293–1305. doi:10.1117/1.1566001

Wangsawatwong, P., de Andrada Pereira, B., Lehrman, J. N., Sawa, A. G. U., O'Neill, L. K., Turner, J. D., et al. (2023). Biomechanical effects of facet joint violation after single-level lumbar fusion with transpedicular screw and rod instrumentation. *Spine (Phila Pa 1976)* 48 (14), 1033–1040. doi:10.1097/brs.0000000000004698

Wong, C. E., Hu, H. T., Kao, L. H., Liu, C. J., Chen, K. C., and Huang, K. Y. (2022). Biomechanical feasibility of semi-rigid stabilization and semi-rigid lumbar interbody fusion: a finite element study. *BMC Musculoskelet. Disord.* 23 (1), 10. doi:10.1186/s12891-021-04958-3

Xu, D., Wang, Y., Jiang, C., Fu, M., Li, S., Qian, L., et al. (2018). Strain distribution in the anterior inferior tibiofibular ligament, posterior inferior tibiofibular ligament, and interosseous membrane using digital image correlation. *Foot Ankle Int.* 39 (5), 618–628. doi:10.1177/1071100717753160

Yamaguchi, H., Kikugawa, H., Asaka, T., Kasuya, H., and Kuninori, M. (2011). Measurement of cortical bone strain distribution by image correlation techniques and from fracture toughness. *Mater. Trans.* 52, 1026–1032. doi:10.2320/matertrans.M2010426

Yang, M., Xiang, D., Wang, S., and Liu, W. (2022). The radial bulging and axial strains of intervertebral discs during creep obtained with the 3D-DIC system. *Biomolecules* 12 (8), 1097. doi:10.3390/biom12081097

Yoon, S., Jung, H. J., Knowles, J. C., and Lee, H. H. (2021). Digital image correlation in dental materials and related research: a review. *Dent. Mater* 37 (5), 758–771. doi:10.1016/j.dental.2021.02.024

Zhang, D., and Arola, D. D. (2004). Applications of digital image correlation to biological tissues. *J. Biomed. Opt.* 9, 691. doi:10.1117/1.1753270

Zhao, X. F., Zhao, Y. B., Lu, X. D., Wang, W. X., Qi, D. T., Yang, X., et al. (2020). Development and biomechanical study of a new open dynamic anterior cervical nail plate system. *Orthop. Surg.* 12 (1), 254–261. doi:10.1111/os.12622

Zhu, L., Wei, X., and Wang, S. (2016). Does cervical spine manipulation reduce pain in people with degenerative cervical radiculopathy? A systematic review of the evidence, and a meta-analysis. *Clin. Rehabil.* 30, 145–155. doi:10.1177/0269215515570382

frontiers | Frontiers in Bioengineering and Biotechnology

TYPE Original Research
PUBLISHED 07 April 2025
DOI 10.3389/fbioe.2025.1494793

OPEN ACCESS

EDITED BY
Ge He,
Lawrence Technological University,
United States

REVIEWED BY
Gennaro Vitucci,
Politecnico di Bari, Italy
Mustapha Zidi,
Université Paris-Est Créteil Val de Marne, France
Giuseppe Saccomandi,
University of Perugia, Italy

*CORRESPONDENCE
Alejandro Aparici-Gil,
aparici@unizar.es

RECEIVED 11 September 2024
ACCEPTED 12 March 2025
PUBLISHED 07 April 2025

CITATION
Aparici-Gil A, Peña E and Pérez MM (2025) Uniaxial, biaxial, and planar tension properties of deep fascia and a constitutive model to simultaneously reproduce these strain states. *Front. Bioeng. Biotechnol.* 13:1494793. doi: 10.3389/fbioe.2025.1494793

Uniaxial, biaxial, and planar tension properties of deep fascia and a constitutive model to simultaneously reproduce these strain states

Alejandro Aparici-Gil[1]*, Estefanía Peña[1,2] and Marta M. Pérez[3]

[1]Aragón Institute for Engineering Research (I3A), University of Zaragoza, Zaragoza, Spain, [2]Biomedical Research Networking Center in Bioengineering, Biomaterials and Nanomedicine (CIBER-BBN), Zaragoza, Spain, [3]Department of Anatomy, Embryology and Genetics, Veterinary Faculty, University of Zaragoza, Zaragoza, Spain

This study aims to provide an in-depth analysis of the mechanical behavior of deep fascia through a comprehensive multidimensional characterization, including uniaxial, biaxial, and planar tension tests. To determine material parameters via test fitting, both a newly developed coupled exponential energy function and a previously proposed uncoupled exponential model—both considering two perpendicular fiber directions—are evaluated. For the uniaxial response, the mean stress measured was 3.96 MPa in the longitudinal direction and 0.6 MPa in the transverse direction at a stretch (λ) of 1.055. In planar tension tests, stress values of 0.43 MPa and 0.11 MPa were recorded for the longitudinal and transverse directions, respectively, at λ = 1.72. Under equibiaxial loading conditions, the mean stresses were 3.16 MPa and 1.2 MPa for the longitudinal and transverse directions when λ reached 1.037, respectively. The fitting results indicate that while the uncoupled exponential model effectively captures the uniaxial and equibiaxial experimental data, it fails to predict other mechanical responses accurately. In contrast, the coupled exponential strain energy function (SEF) demonstrates robust performance in both fitting and prediction. Additionally, an analysis was conducted to assess how the number and combination of tests influence the determination of material parameters. Findings suggest that a single biaxial test incorporating three loading ratios is sufficient to accurately capture and predict uniaxial, planar tension, and other biaxial strain states.

KEYWORDS

fascia lata, constitutive models, material characterization, optimization, mechanical tests

1 Introduction

The medical field is evolving due to computational technologies such as artificial intelligence, computational simulations, and extended reality. These technologies have the potential to guide processes and improve biomedical outcomes (Samant et al., 2023). Ramachandra et al. (2016) demonstrate how computational simulation can be used to study surgical procedures. It provides a powerful tool for simulating the hemodynamics and wall mechanics of grafts in patient-specific coronary artery bypass procedures. Additionally, it

enables the characterization of variations in mechanical stimulus indices between arterial and venous surgeries (Ramachandra et al., 2016). Pavan et al. (2015) focus their study on fascia simulation using finite element analysis, which facilitates the interpretation of the correlation between alterations in the volume and pressure of muscle compartments and the deformation of the crural fascia.

Fascia is a tissue of great importance, yet it remains largely unexplored. It consists of collagenous connective tissue that surrounds and interpenetrates skeletal muscles, joints, organs, nerves, and vascular structures. Fascial tissue forms a whole-body, three-dimensional viscoelastic matrix that provides structural support (Klingler et al., 2014). According to Langevin and Huijing (2009), it is composed of three main structures: the superficial fascia, located directly beneath the skin, consisting of dense and areolar connective tissue along with fat; the deep fascia, a continuous sheet primarily made of dense, irregularly arranged connective tissue that restricts changes in the shape of underlying tissues; and muscle-related layers, characterized by irregularly arranged collagen fiber sheets that envelop muscles and may include both dense and areolar connective tissue layers.

Fascia forms a continuous network throughout the body and plays a crucial role in transmitting mechanical forces between muscles (Findley et al., 2012). Under basal tension from muscle insertions, the fascia maintains an inherent state of tension. When muscles contract, their insertions transmit a portion of the traction to the fascia, activating nerve endings embedded within its structure (Stecco et al., 2007), which provide essential sensory feedback to the brain about the body's state. However, fascia is not merely a passive force transmitter. Schleip et al. (2019) found that fascial tissue exhibits a contractile response to different pharmacological agents, suggesting active behavior. Another key function of fascia is elastic energy storage, where energy accumulated during the stance phase is later released to propel the limb forward during the swing phase (Eng et al., 2014). Additionally, fascia helps regulate mechanical stress by absorbing, storing, and releasing kinetic energy (Zullo et al., 2017).

Concerning the mechanical behavior and biomechanics of fascia, it is known that fascia is an incompressible tissue; thus, the application of large displacement theory for incompressible, non-linear, and anisotropic materials should be employed (Findley et al., 2012). Its anisotropic behavior is attributed to the spatial orientation of collagen fibers, which vary along the sheet to ensure an appropriate response to mechanical demands. Like other soft tissues, fascia also exhibits viscoelastic properties, partly due to fluid movement within its solid matrix and the friction between its fluid and solid components (Peña et al., 2008).

To better understand fascia behavior under both normal and pathological conditions, as well as the relationship between structure and function, a numerical formulation capable of describing its mechanical properties is highly useful (Stecco et al., 2009). Several studies have been conducted to characterize these mechanical properties, including constitutive models that associate material properties with microstructure and parameters. Because different strain states exist, various testing protocols have been developed, such as uniaxial, biaxial, pure shear, and planar tension tests. Pavan et al. (2015) performed uniaxial tests and proposed a constitutive model for the crural fascia. Eng et al. (2014) and Pancheri et al. (2014) carried out biaxial and planar tests, respectively, proposing constitutive models based on the microstructure. However, these studies only considered a single strain state. Ruiz-Alejos et al. (2016) examined both uniaxial and pure shear properties, proposing a constitutive model that incorporates two strain states. However, this study did not include biaxial testing, and according to Sednieva et al. (2020), biaxial testing provides a more accurate representation of fascia loading than uniaxial or pure shear testing.

The present work aims to investigate in depth the mechanical behavior of the deep fascia through a multidimensional characterization, incorporating uniaxial (UT), biaxial (BxT), and planar tension (PT) tests. Although constitutive models for connective tissues, such as tendons and ligaments, already exist, the unique anatomical and histological characteristics of the fascia require adaptations to these models (Stecco et al., 2009). To determine material parameters through test fitting, we analyze a previously proposed uncoupled exponential-type strain energy function (SEF) (Pancheri et al., 2014) and introduce a newly proposed coupled SEF that accounts for two perpendicular fiber directions, following Stecco et al. (2009). Uncoupled structural models are unable to provide accurate fits when considering perpendicular anisotropic directions; therefore, a new coupled SEF is proposed based on Costa et al. (2001) and modified using invariants (Laita et al., 2024). In addition, we conducted a test combination study to identify the optimal set of experiments that yield parameters capable of both fitting and predicting different deformation states. The fitting process provides a parameter set that ensures that computational simulations can be performed with confidence, regardless of the deformation state being simulated.

2 Materials and methods

We propose three mechanical tests (UT, BxT, and PT) to reproduce the strain states in which the fascia primarily functions. Both selected constitutive models are structural models, which means that the model parameters are associated with the structural components of the tissue. Therefore, a relationship must exist between the parameter values and the physiological function of the corresponding tissue component. The two different SEFs are analyzed using the mean curves obtained from experimental tests. Finally, an analysis is performed to determine the number of tests needed for proper fitting and prediction.

2.1 Multidimensional characterization

The uniaxial tensile test is the most widely used method for material characterization (Calvo et al., 2010; Martins et al., 2010; Stecco et al., 2013). It provides stiffness measurements through Young's modulus, and if the sample undergoes loading and unloading cycles, it also offers insights into viscoelastic properties (Peña et al., 2010). Soft biological tissues such as the arteries, heart, and fascia contain fibers oriented in different directions, forming their internal structure. As a result, their mechanical response varies depending on the loading direction (Guo et al., 2023; Ren et al., 2022; Eng et al., 2014). Biaxial tensile tests are commonly used to evaluate the mechanical anisotropy of these tissues (Takada et al., 2023).

However, uniaxial or biaxial tests do not always fully characterize deformation states. In certain cases, tissue behavior cannot be solely described as uniaxial or biaxial, making it necessary to include planar tension tests. For example, Acosta Santamaría et al. (2015) investigated the mechanical behavior of the linea alba in the context of laparotomy closure using planar tension tests. For these reasons, in this work, a multidimensional characterization was conducted using UT, PT, and BxT to replicate the strain states in which the fascia primarily functions.

2.1.1 Sample preparation

The fascia tissues were obtained from male sheep aged 1 year and harvested by veterinarians at the University of Zaragoza. The animals were sacrificed in a slaughterhouse for another study, which does not affect the results or the purpose of this work. After euthanasia (pentobarbital sodium, 8 mL), the fascia lata, attached to the aponeurosis of the tensor fasciae latae muscle, was removed. Once the fascia sheets were dissected, they were frozen at −20°C until the testing day. Previous experience from various experimental tests in our laboratory indicates that cryopreservation helps maintain mechanical properties. Our findings are supported by Stemper et al. (2007), who demonstrated that specimens preserved for 3 months using standard freezing techniques retained their physiological, subfailure, and rupture mechanical properties. The fascia sheet is thawed on the same day it is tested. Once it reaches room temperature, muscle and connective tissue residues are removed using a blade, and samples are cut.

A specific punch was designed for each test: for UT, a dog-bone punch with a central region of interest measuring 25 mm × 5 mm (5:1 aspect ratio), with 25 mm between clamps, was used. For PT, a rectangular punch with a 5 mm × 35 mm region of interest (1:7 aspect ratio) and a distance of 5 mm between the clamps was used. Finally, for BxT, a cruciform punch was chosen, with a central region of interest measuring 15 mm × 15 mm.

After cutting the samples, a black paint spray was applied to create randomized markers for tracking points and measuring the strain map. To prevent slippage between the fascia and clamps, sandpaper was fixed to the ends of the samples using cyanoacrylate glue (Loctite 401), as shown in Figure 1.

To avoid dehydration effects, UT and BxT tests were conducted while submerged in PBS solution (sodium chloride physiological solution, BioUltra tablet, Sigma-Aldrich GmbH). For PT, pneumatic clamps were required, so a humidifier was used to maintain proper hydration conditions, as the sample size prevented using a submerged testing chamber.

Following Stecco et al. (2009), the collagen fibers in adjacent fascia layers are oriented in two preferred directions, forming an angle between 80° and 90°. For our model, we assume a 90° orientation between anisotropy directions, referring to them as the longitudinal and transverse directions. When collecting samples, the longitudinal direction corresponds to the primary fiber alignment within the tissue. To ensure proper orientation, the punch's longitudinal axis was aligned parallel to these macroscopically distinguishable fibers. We obtained samples in the transverse direction by rotating the punch 90° from this position.

2.1.2 Histological analysis

Histological sections were analyzed using Masson's trichrome (Figure 2A), where collagen appears in blue, and Picrosirius Red (Figures 2B, C), which, under polarized light, reveals collagen fibers in red-orange against a black background.

2.1.3 Mechanical testing and protocols

Fourteen uniaxial tests were considered, seven for each direction, from a total of 15 longitudinal and 13 transverse samples to obtain the mean curve. In addition, 20 biaxial tests and 17 planar tension tests were performed—nine in the longitudinal direction and eight in the transverse direction, with six tests used to determine the mean curves for each strain state.

UT and PT followed the same protocol: three strain levels (2.5%, 5%, and 7.5%) with a strain rate of 10%/min were applied, subjecting the sample to five cycles at each level. After the last cycle was completed, the sample was stretched to rupture. The sample was first placed on the upper clamp, and a load balance was performed to compensate for the weight effect. The other end of the sample was then attached to the bottom clamp and stretched to achieve a 0 N load. Once at 0 N, the chamber was filled with PBS, and a second load balance was conducted to compensate for the fluid effect before stretching the sample to the pre-load level.

UT tests were performed using the Instron MicroTester 5548, equipped with steel clamps and a 50 N load cell with a sensitivity of±0.025% of the measured load. The pre-load level was set at 0.08 N, following Pancheri et al. (2014). For PT, the Instron MicroTester 5848 was used, featuring pneumatic steel clamps and a 50 N load cell. A pre-load value of 1.5 N was chosen to ensure a proper initial state.

For the biaxial protocol, a strain level of 10% and a strain rate of 20%/min were applied, along with five loading ratios: 1:1, 0.5:1, 1:0.5, and 0.75:1, denoted as E1, E2, E3, E4, and E5, respectively. The first value of each ratio corresponds to the longitudinal direction. Ratios E1 to E3 were used to fit the material parameters, while E4 and E5 were employed to evaluate the predictive capability of the constitutive model. Each ratio was tested over five cycles. Biaxial tests were conducted using the Instron Planar Biaxial Soft Tissue Test System, equipped with four 50 N load cells. Steel clamps were used, with sandpaper glued to the sample using Loctite 401 and secured with screws to prevent slippage between the sample and the clamps. According to Vitucci (2024), the sample geometry can lead to errors. However, this phenomenon was studied by Cilla et al. (2019), suggesting that our geometry and clamped system leads to shear stresses in the central region close to zero. A pre-load value of 0.5 N was established.

UT and BxT tests were recorded at a frame rate of 3 Hz using the LaVision camera system. The acquired images were processed using the free version of GOM Correlate, a digital image correlation (DIC) software for tracking patterns and computing displacements and deformations. A virtual gauge was defined, as shown in Figure 3B, and strain values were obtained from this gauge. The initial position and length of the virtual gauge were kept consistent across all tests to minimize potential sources of error and variability. In soft tissues, the displacement between clamps is typically larger than in the central region. Because the formulation is valid only in the central region, DIC was necessary to accurately measure deformations in the region of interest. For PT, the DIC system was not used because the distance between clamps was small, making it reasonable to assume that clamp displacement corresponded to the displacement of the region of interest.

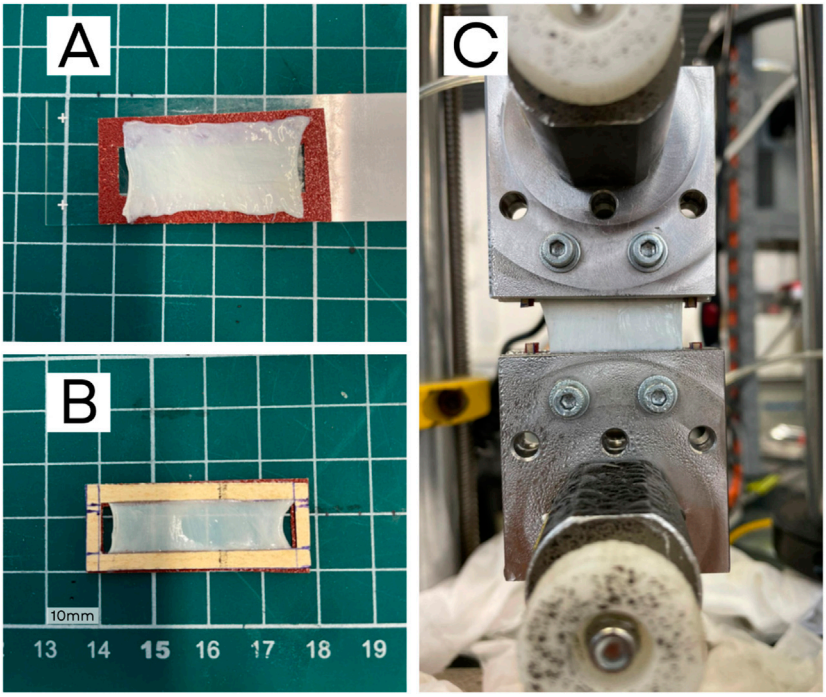

FIGURE 1
Preparation of a PT sample: **(A)** sample on a sandpaper frame, **(B)** sandpaper frame glued to the fascia, and **(C)** sample placed in the testing machine with pneumatic clamps and screws. The frame sides are cut prior to testing.

2.2 Constitutive models

Soft tissues are usually modeled as composite materials consisting of an isotropic base material reinforced by collagen fibers aligned in two different directions (Peña et al., 2010).

To ensure an accurate reproduction of the fascia's mechanical response, two material models have been considered (Laita et al., 2024). The first model, based on Holzapfel et al. (2000) and proposed by Pancheri et al. (2014), assumes exponential uncoupled volumetric-deviatoric responses and has been widely used to describe the mechanical behavior of fiber-reinforced soft tissues (Peña et al., 2010; Calvo et al., 2010; Eng et al., 2014). The second model, proposed herein, is a modified exponential invariant-based version of the Costa model (Costa et al., 2001), as introduced by Laita et al. (2024), which considers a coupled response. Within the framework of hyperelasticity, both models assume the tissue is incompressible, undergoes large displacements, and exhibits non-linear anisotropic behavior.

2.2.1 Fundamental equations

An arbitrary point identified by its position vector, $\mathbf{X}$, belonging to an undeformed configuration called reference configuration, $\mathcal{B}_r$, is chosen. The external mechanical forces deform $\mathcal{B}_r$, therefore, $\mathbf{X}$ has a new position $\mathbf{x} = \chi(\mathbf{X})$ belonging to the deformed configuration $\mathcal{B}$. The deformation of the body is described by the vector field χ, which assigns to points $\mathbf{X}$ a particular position $\mathbf{x}$ in $\mathcal{B}$ and attributes a particular reference position $\mathbf{X}$ in $\mathcal{B}_r$ to each point $\mathbf{x}$ (Holzapfel et al., 2000).

Following the standard notation, we call $\mathbf{F}$ the deformation gradient tensor relative to $\mathcal{B}_r$ and define it as $\mathbf{F} = \nabla\chi(\mathbf{X})$, with the Cartesian components $F_{iJ} = \partial x_i/\partial X_J$ with $i, J \in \{1, 2, 3\}$. J is the determinant of the deformation gradient tensor $\mathbf{F}$ representing the local volume ratio. The left and right Cauchy–Green deformation tensors are defined as $\mathbf{B} = \mathbf{F}\mathbf{F}^{\mathrm{T}}$ and $\mathbf{C} = \mathbf{F}^{\mathrm{T}}\mathbf{F}$, respectively.

The theory of hyperelasticity describes the elastic behavior of a body through a strain energy function, denoted as Ψ, which is defined per unit volume in the reference configuration $\mathcal{B}_r$. This work assumes an incompressible material, hence $J = \det \mathbf{F} \equiv 1$. The first Piola–Kirchhoff tensor $\mathbf{P}$ and the Cauchy stress tensor $\boldsymbol{\sigma}$ are given by Equation 1:

$$\mathbf{P} = \frac{\partial \Psi}{\partial \mathbf{F}} - p\mathbf{F}^{-1} \quad \boldsymbol{\sigma} = \mathbf{F}\frac{\partial \Psi}{\partial \mathbf{F}} - p\mathbf{I}, \tag{1}$$

where p is the hydrostatic pressure. The two directions of anisotropy are given by the unit vectors $\mathbf{M}$ and $\mathbf{N}$ in the undeformed configuration $\mathcal{B}_r$. Structural tensors are defined, following Spencer (1971) and Ogden (2001), as $\mathbf{M} \otimes \mathbf{M}$ and $\mathbf{N} \otimes \mathbf{N}$. Then, the form of Ψ is reduced to the dependence on the principal invariants I_1, I_2, I_3 of $\mathbf{C}$ and I_4, I_5, I_6, I_7, I_8 of $\mathbf{M}$ and $\mathbf{N}$. Based on the structure of fascia and following the simplification suggested by Holzapfel et al. (2000), we reduce the number of invariants to I_1, I_4, I_6. Therefore, the expression of the Cauchy stress tensor is reduced to Equation 2:

$$\boldsymbol{\sigma} = 2\Psi_1\mathbf{B} + 2\Psi_4\mathbf{m} \otimes \mathbf{m} + 2\Psi_6\mathbf{n} \otimes \mathbf{n} - p\mathbf{I}, \tag{2}$$

where $\Psi_i = \partial\Psi/\partial \mathrm{I}_i$ with $i \in \{1, 4, 6\}$, $\mathbf{m} = \mathbf{F}\mathbf{M}$, $\mathbf{n} = \mathbf{F}\mathbf{N}$, and invariants are defined as follows: $I_1 = \mathrm{tr}\mathbf{C}$, $I_4 = \mathbf{M} \cdot (\mathbf{C}\mathbf{M})$, and $I_6 = \mathbf{N} \cdot (\mathbf{C}\mathbf{N})$.

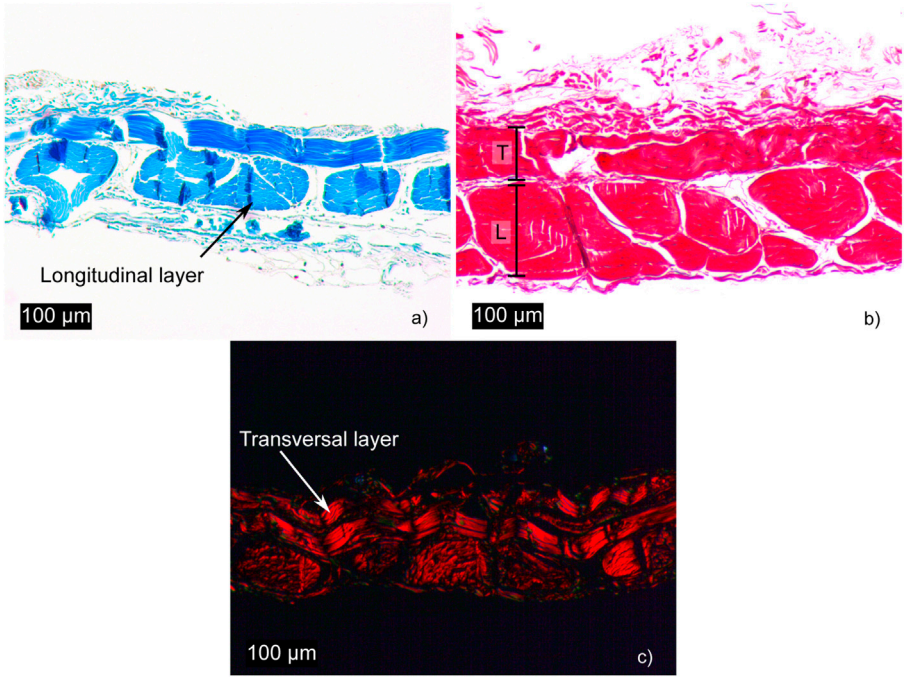

FIGURE 2
Histological sections of fascia: **(a, b)**, stained with Masson's trichrome and Picrosirius Red, respectively, show the different collagen fiber densities in the longitudinal (L) and transverse (T) layers. **(c)**, stained with Picrosirius Red, reveals collagen fibers under polarized light.

Following experimental observations in Section 2.1.1, this work considers a 90° angle between anisotropy directions; thus, unit vectors are defined as

$$\mathbf{M} = \{1, 0, 0\} \quad \mathbf{N} = \{0, 1, 0\}.$$

For planar tissue, components of the deformation gradient $\mathbf{F}$ can be expressed by Equation 3:

$$\mathbf{F} = \begin{bmatrix} F_{11} & F_{12} & 0 \\ F_{21} & F_{22} & 0 \\ 0 & 0 & F_{33} \end{bmatrix}. \tag{3}$$

Finally, for each deformation state, and assuming incompressibility ($\lambda_1\lambda_2\lambda_3 = 1$), the deformation gradient tensor is given by Equation 4:

$$\mathbf{F}_{\mathbf{UT}} = \begin{bmatrix} \lambda_i & 0 & 0 \\ 0 & 1/\sqrt{\lambda_i} & 0 \\ 0 & 0 & 1/\sqrt{\lambda_i} \end{bmatrix} \quad \mathbf{F}_{\mathbf{PT}} = \begin{bmatrix} \lambda_i & 0 & 0 \\ 0 & 1 & 0 \\ 0 & 0 & 1/\lambda_i \end{bmatrix}$$
$$\mathbf{F}_{\mathbf{BxT}} = \begin{bmatrix} \lambda_1 & 0 & 0 \\ 0 & \lambda_2 & 0 \\ 0 & 0 & 1/\lambda_1\lambda_2 \end{bmatrix}, \tag{4}$$

where $i = 1, 2$ 1 refers to the longitudinal direction, while 2 refers to the transversal direction.

2.2.2 Uncoupled strain energy function

The uncoupled SEF based on Pancheri et al. (2014) is expressed as a combination of two parts: one related to the homogeneous properties of the substrate material and the other to the anisotropy resulting from the included fibers. It follows Equation 5:

$$\Psi = \Psi_{iso} + \Psi_{aniso} = \Psi_{iso}(I_1) + \Psi_{fib_4}(I_4) + \Psi_{fib_6}(I_6). \tag{5}$$

The isotropic contribution of the matrix, Ψ_{iso}, is modeled following the Demiray exponential strain energy function (Demiray, 1972) expressed by Equation 6:

$$\Psi_{iso} = \frac{\mu_{iso}}{2\alpha}\{\exp[\alpha(I_1 - 3)] - 1\}, \tag{6}$$

where μ_{iso} is a positive stress-like parameter and α is a dimensionless material parameter.

The anisotropic part of the model, Ψ_{aniso}, also follows an exponential strain form; it has two uncoupled terms, one related to the longitudinal direction (l) and the other to the transverse direction (t) and is expressed by Equation 7:

$$\Psi_{fib} = \frac{\mu_l}{2k_l}\{\exp[k_l(I_4 - 1)^2] - 1\} + \frac{\mu_t}{2k_t}\{\exp[k_t(I_6 - 1)^2] - 1\}. \tag{7}$$

The parameters μ_{iso}, μ_l, and μ_t are positive stress-like parameters; α, k_l, and k_t are dimensionless parameters. μ_l and μ_t quantify the level of anisotropy, while k_l and k_t are associated with the respective directions.

According to Equation 2 and following the definition for Ψ_i, we obtain Equation 8:

$$\begin{aligned} \Psi_1 &= \frac{\mu_{iso}}{2}\exp[\alpha(I_1 - 3)] \\ \Psi_4 &= \mu_l \exp[k_l(I_4 - 1)^2](I_4 - 1) \\ \Psi_6 &= \mu_t \exp[k_t(I_6 - 1)^2](I_6 - 1). \end{aligned} \tag{8}$$

We denote this model as uncoupled because the derivatives of Ψ with respect to I_i, Ψ_i, depend only on I_i, Equation 8.

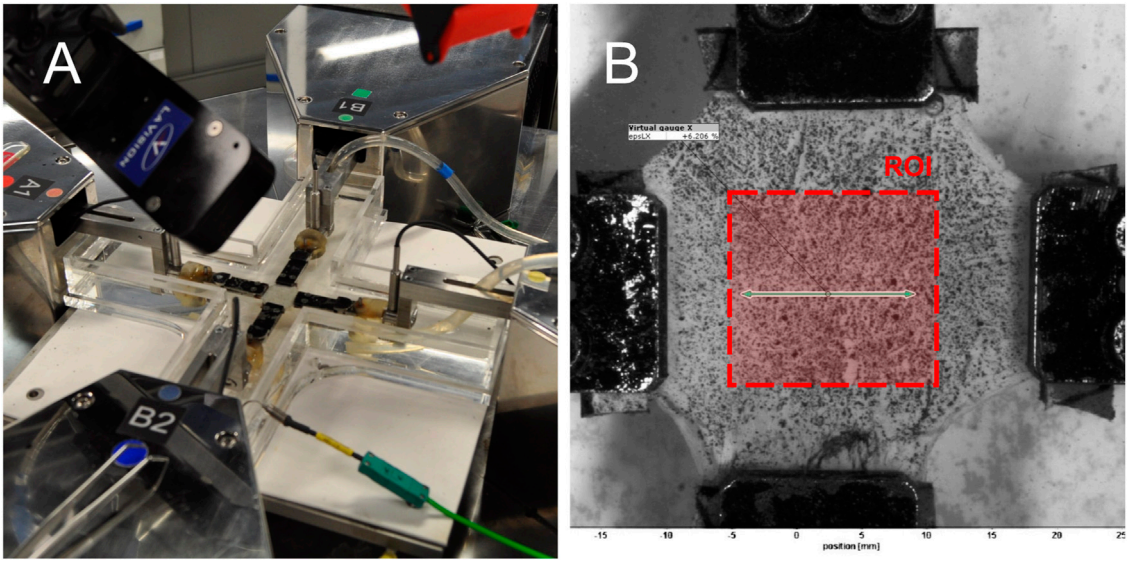

FIGURE 3
Biaxial testing setup: **(A)** Instron Planar Biaxial Soft Tissue Test System during a test and **(B)** image from DIC analysis. Note that the region of interest for strain calculation is defined by the area corresponding to the width of the clamps.

2.2.3 Coupled strain energy function

The proposed coupled SEF is based on the one proposed by Costa et al. (2001) and Laita et al. (2024) for myocardial tissue and is given by Equation 9:

$$\Psi = C_0\,(e^{Q} - 1), \tag{9}$$

where C_0 is a positive stress-like parameter, and Q is the exponent of the exponential function that includes the isotropic and anisotropic character. This work proposes Q as the sum of three terms: a linear term for the isotropic matrix contribution and two quadratic terms related to the anisotropy directions. Thus, Q is defined as Equation 10:

$$Q = C_1\,(I_1 - 3) + C_2\,(I_4 - 1)^2 + C_3\,(I_6 - 1)^2, \tag{10}$$

with C_1, C_2, C_3 being dimensionless parameters. The quadratic term dependent on I_4 represents the longitudinal fiber direction, while the term dependent on I_6 is associated to the transverse direction. Following Equation 2 shown before, the terms Ψ_1, Ψ_4, and Ψ_6 are given by Equation 11:

$$\begin{aligned} \Psi_1 &= C_0\,C_1\,e^{Q} \quad \Psi_4 = C_0\,C_2\,e^{Q}\,(2I_4 - 2) \\ \Psi_6 &= C_0\,C_3\,e^{Q}\,(2I_6 - 2). \end{aligned} \tag{11}$$

We denote our proposed SEF as coupled due to the terms Ψ_i depending on all invariants that are associated with the isotropic and anisotropic contributions through e^{Q}.

2.3 Fitting procedure, combination of tests, and model comparison

A MATLAB script was developed to analyze the optimal combination of tests and optimize the fitting process. Five types of tests were available for fitting (UT, PT, E1, E2, and E3). The number of tests to combine could be chosen while leaving the rest for prediction, in addition to E4 and E5 biaxial ratios. In this way, combinations of three tests were conducted for both uncoupled and coupled models to study the structural parameters obtained by fitting. The model that provides the best fitting and prediction was chosen to study the combinations with different numbers of tests involved.

Given $\mathbf{p}$, a vector of the q unknown parameters of the SEF, the referred minimization problem can be stated as Equation 12:

$$\min_{\mathbf{p}} \|\chi(\mathbf{p})\|_2^2 = \min_{\mathbf{p}} \left(\sum_{i=1}^{N} \left[(\sigma_i - \sigma_1^{\Psi})^2 \right] \right), \tag{12}$$

where N is the number of considered points, σ is the stress computed from the experimentally measured force, σ^{Ψ} is the analytical stress, q is the number of parameters of the SEF, and the overlined symbols refer to the mean.

For choosing the proper combination $\mathbf{p}^{\star}$, we analyze the R-square error, R^2, the root mean square error (RMSE), ε, and the relative error $err^{\star}$ (Destrade et al., 2017) of the fit and predictive processes for all possible combinations, as described in Equation 13:

$$\begin{aligned} R^2 &= 1 - \frac{\sum_{i=1}^{N} (\sigma_i - \sigma_i^{\Psi})^2}{\sum_{i=1}^{N} (\sigma_i^{\Psi} - \overline{\sigma^{\Psi}})^2} \quad \varepsilon = \frac{\sqrt{\sum_{i=1}^{N} (\sigma_i - \sigma_i^{\Psi})^2 / (N-q)}}{\bar{\sigma}} \\ err^{\star} &= \max_i \left| \left(\frac{\sigma_i - \sigma^{\Psi}(\mathbf{p}^{\star})}{\sigma_i} \right) \right|. \end{aligned} \tag{13}$$

Following the incompressibility hypothesis ($\lambda_1\lambda_2\lambda_3 = 1$), the analytical expressions for the non-null Cauchy stress terms obtained from our proposed coupled exponential SEF for the biaxial strain state are described by Equations 14, 15:

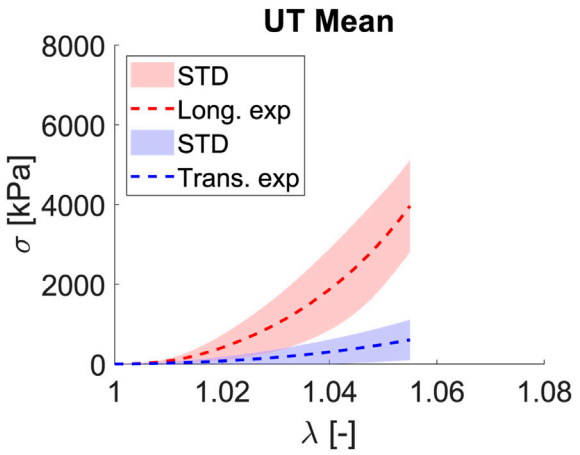

FIGURE 4
Mean and STD (shaded) for Cauchy stress σ [kPa] and stretch λ [–] curves for the longitudinal (red) and transverse (blue) fibers subjected to a uniaxial test.

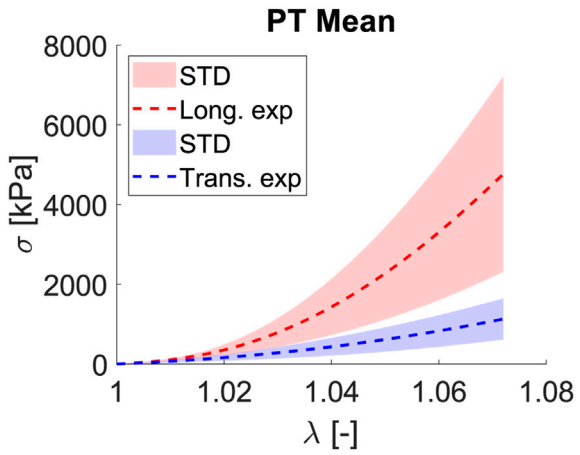

FIGURE 5
Mean and STD (shaded) for Cauchy stress σ [kPa] and stretch λ [–] curves for the longitudinal (red) and transverse (blue) fibers subjected to a planar tension test.

$$\sigma_l = -\frac{2\ C_0\ e^{C_1(I_1-3)+C_2(I_4-1)^2+C_3(I_6-1)^2}\left(C_1 - C_1\ \lambda_l^4\ \lambda_t^2 + 2\ C_2\ \lambda_l^4\ \lambda_t^2 - 2\ C_2\ I_4\ \lambda_l^4\ \lambda_t^2\right)}{\lambda_l^2\ \lambda_t^2}, \tag{14}$$

$$\sigma_t = -\frac{2\ C_0\ e^{C_1(I_1-3)+C_2(I_4-1)^2+C_3(I_6-1)^2}\left(C_1 - C_1\ \lambda_l^2\ \lambda_t^4 + 2\ C_3\ \lambda_l^2\ \lambda_t^4 - 2\ C_3\ I_6\ \lambda_l^2\ \lambda_t^4\right)}{\lambda_l^2\ \lambda_t^2}. \tag{15}$$

In the case of a uniaxial strain state, the analytical expressions are given by Equations 16, 17:

$$\sigma_l = -\frac{2\ C_0\ e^{C_1(I_1-3)+C_2(I_4-1)^2+C_3(I_6-1)^2}\left(C_1 - C_1\ \lambda_l^3 + 2\ C_2\ \lambda_l^3 - 2\ C_2\ I_4\ \lambda_l^3\right)}{\lambda_l}, \tag{16}$$

$$\sigma_t = -\frac{2\ C_0\ e^{C_1(I_1-3)+C_2(I_4-1)^2+C_3(I_6-1)^2}\left(C_1 - C_1\ \lambda_t^3 + 2\ C_3\ \lambda_t^3 - 2\ C_3\ I_6\ \lambda_t^3\right)}{\lambda_t}. \tag{17}$$

Finally, for the planar tension strain state, the expressions are given by Equations 18, 19:

$$\sigma_l = -\frac{2\ C_0\ e^{C_1(I_1-3)+C_2(I_4-1)^2+C_3(I_6-1)^2}\left(C_1 - C_1\ \lambda_l^4 + 2\ C_2\ \lambda_l^4 - 2\ C_2\ I_4\ \lambda_l^4\right)}{\lambda_l^2}, \tag{18}$$

$$\sigma_t = -\frac{2\ C_0\ e^{C_1(I_1-3)+C_2(I_4-1)^2+C_3(I_6-1)^2}\left(C_1 - C_1\ \lambda_t^4 + 2\ C_3\ \lambda_t^4 - 2\ C_3\ I_6\ \lambda_t^4\right)}{\lambda_t^2}. \tag{19}$$

3 Results

3.1 Histological results

The longitudinal layer is characterized by a high density of collagen fibers forming fascicles, whereas the transverse layer is thinner, as illustrated in Figure 2A. The results demonstrate that fascia is a highly organized tissue with a clearly defined bilayered structure, as shown in Figure 2B. These layers intersect at an angle of approximately 90°. It can be observed that the transverse layer contains only a single row of collagen fibers, a finding consistent with Pancheri et al. (2014). Figure 2C, stained with Picrosirius Red and observed under polarized light, highlights the nearly 90-degree angle between the layers.

3.2 Mechanical experiments

Fascia lata, which surrounds the principal muscles of limbs, works preferentially along one direction, with most of the collagen fibers following this preferred direction, which we denoted as longitudinal; hence, the matrix and fiber transversal direction will play a secondary role in the mechanics and functionality of the fascia. Proof of this is the curves for the uniaxial tests shown in Figure 4. For a stretch of $\lambda = 1.055$, the longitudinal behavior is totally different from transverse, while σ_1 has an average stress value of 3.96 ± 1.15 MPa (mean ± STD), σ_2 only achieves a value of 0.60 ± 0.50 MPa. Following the mechanical behavior that soft tissues usually exhibit, the test begins with an initial zone with no stress increment, and then a strain increment appears (toe region). This is because the unfolding fibers are being stretched; when a value of $\lambda = 1.020$ is reached, an exponential increase in stress values is experienced.

The planar tension test uses a large aspect ratio between width and length to measure shear properties. According to Moreira and Nunes (2013), for small deformations, the stress–stretch response for planar tension and simple shear is the same. Nevertheless, a divergence between planar tension and simple shear occurs for stretch values greater than 1.30. As we are far from λ values of 1.30, we consider planar tension valid for measuring simple shear properties. Curves for planar tension shown in Figure 5 describe a mechanical behavior with a longitudinal direction that exhibits greater stiffness in contrast to the transversal direction of fibers, as we observed in the uniaxial test. Longitudinal stress values are 4.77 ± 2.45 MPa (mean ± STD), whereas in the transversal direction, we observed 1.13 ± 0.51 MPa for a λ value of 1.072. A less pronounced non-linear behavior is observed compared to uniaxial curves. Regarding the deviation of the longitudinal curves from the mean, it has been noted that planar tension exhibits greater dispersion.

TABLE 1 Mean value for σ (mean ± STD) and η for equibiaxial, uniaxial, and planar tension strain states at a stretch value of 1.037.

Test	σ_1 [MPa]	σ_2 [MPa]	η [–]
Equibiaxial	2.92 ± 1.17	1.38 ± 0.49	2.12
Uniaxial	1.58 ± 0.92	0.26 ± 0.27	6.08
Planar tension	1.22 ± 0.59	0.38 ± 0.19	3.21

The mean curves depicted in Figure 6 correspond to the last load cycle at each ratio for biaxial tests. The equibiaxial ratio (1:1) exhibits greater stiffness in both the longitudinal and transverse directions than in uniaxial and planar tension tests. Stretching one fiber family implies an increase in the stiffness of the other. Evidence of this effect is clearly observed by comparing the E1 and E4 ratios: Using the equibiaxial as a reference and considering the described effect of the ratios, a greater stretch in one direction leads to a stiffer curve in the opposite direction than the equivalent curve in the equibiaxial ratio, ensuring the proper performance of the biaxial test. This can be observed in Figure 6F, where the mean curves for each direction and ratio are presented.

Table 1 compiles the mean maximum stress and strain values for each direction and ratio obtained. We include the anisotropy ratio ($\eta = \sigma_l/\sigma_t$), defined as the ratio between the longitudinal stress value and the transverse stress value for a specific λ value. In order to compare η across the equibiaxial, uniaxial, and planar strain states, a stretch value of 1.037 has been chosen as a reference.

The η for the uniaxial test exhibits the highest value, of 6.08, followed by the η of the planar tension test, which reaches 3.21 and finally, the equibiaxial, where we found a η value of 2.12. The obtained values for η are reasonable given the characteristics of the different strain states, as the equibiaxial test involves both directions. As observed in Figure 6, increased stretching in one direction results in a stiffer curve

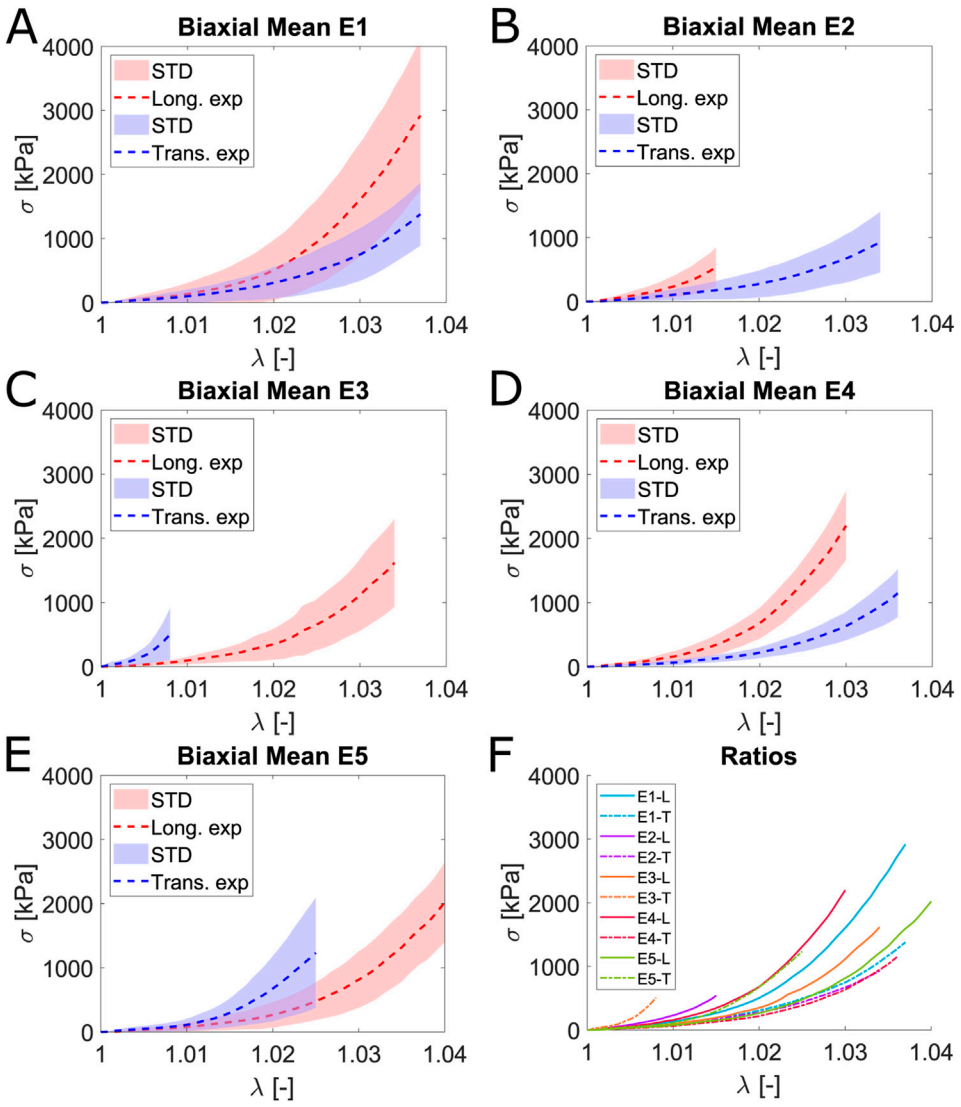

FIGURE 6
Mean and STD (shaded) Cauchy stress σ [kPa] and stretch λ [–] curves for the longitudinal (red) and transverse (blue) fibers subjected to different ratios in the biaxial test. **(A)** corresponds to the equibiaxial (1:1) ratio, while the curves in **(B)** show the ratio 0.5:1; **(C)**, **(D)**, and **(E)** correspond to the ratios 1:0.5, 0.75:1, and 1:0.75, respectively. **(F)** represents the mean Cauchy stress and stretch curves for both longitudinal and transverse fibers across all ratios.

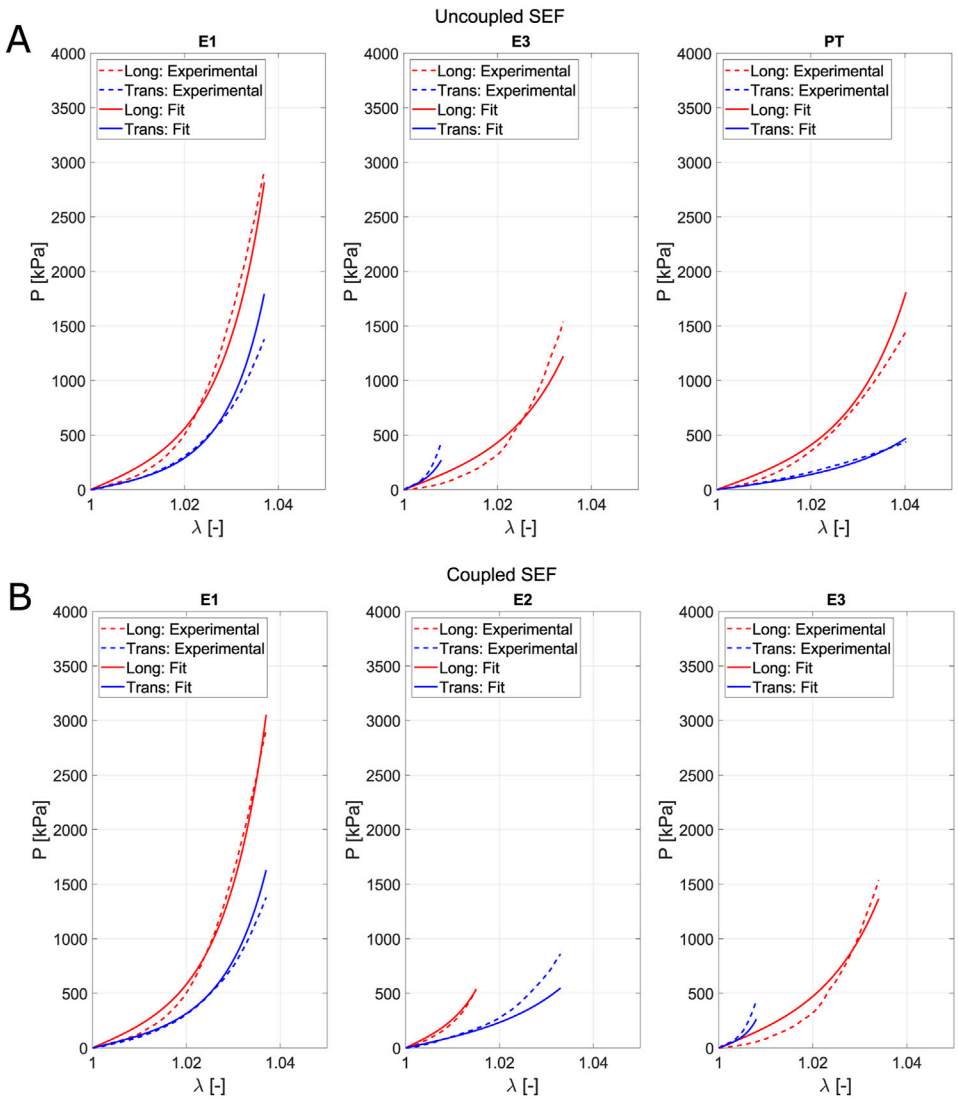

FIGURE 7
Fitting of the uncoupled model **(A)** and the coupled model **(B)** for the optimal combination of tests. Solid lines refer to the Cauchy stress from fitting, while the dash-dotted lines represent the mean Cauchy stress from experiments. Red lines indicate the longitudinal direction, and blue lines indicate the transversal.

in the opposite direction. Evidence of this is that the maximum transversal stress, σ_2, for λ equal to 1.037 is obtained with the equibiaxial test.

A common point observed in all tests is the significant deviation found in the experiments. Two factors contributing to this could be the extraction area, as regions closer to the tendon or bone may exhibit greater stiffness, and the local mechanical demands the tissue must withstand. If one area supports more stress than another, the fiber density must be higher.

3.3 Constitutive modeling

Fitting is used to determine the parameters that define the model. It is based on a minimization problem where successive iterations of the parameters are performed until reaching a minimum in Equation 12. The objective of this step is to compare whether the uncoupled or coupled model is more appropriate based on their fitting and prediction capabilities. Figure 7 represents the average experimental curve for the fifth loading cycle (dashed lines) for each direction and the curves obtained from the fitting (solid lines) through the minimization process. Fitting accounts for the entire range of deformation reached in the different biaxial tests. However, for both the uniaxial and planar tension tests, the maximum values ofλ only reach 1.04. Thus, all tests are fitted within the same range of deformation.

We derive the parameters for the fitting process by combining three tests. When the uncoupled model (based on Pancheri et al., 2014) was applied, the optimal combination of test with no constraints in the value of parameters was E1, E3 and PT (Figure 7A) with R^2_{fit} = 0.964 and R^2_{pred} = 0.879. Regarding the structural parameters, the following values were obtained: μ_{iso} = 1470 kPa, α = 113.47, μ_l = 2442 kPa, k_l = 167.19, μ_t = 0.00 kPa, k_t = 0.01. We observe that the parameters associated with the family of transverse fibers are equal to zero, which is not physiologically plausible. If we consider the model

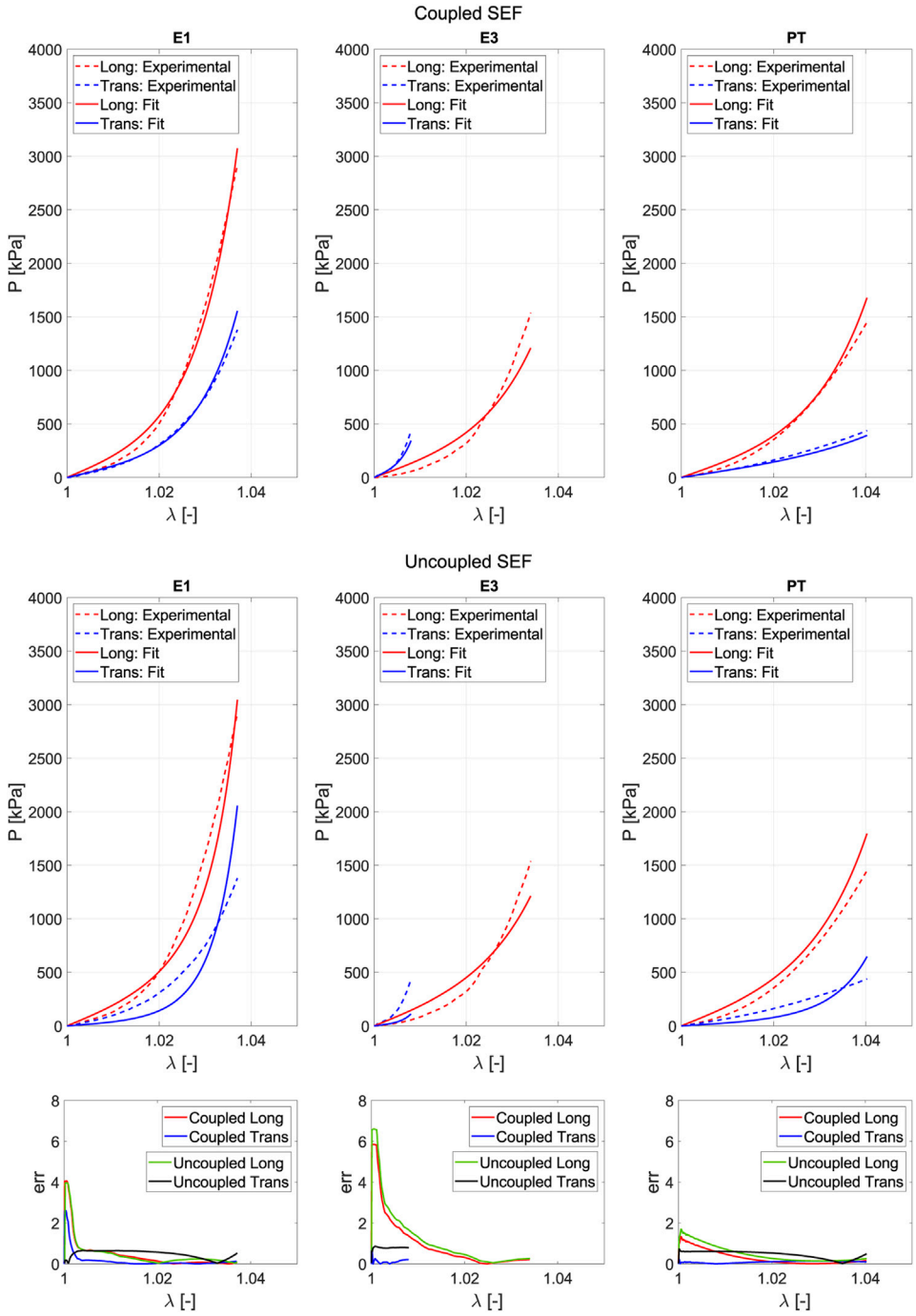

FIGURE 8
Comparison of the *err** for the coupled and uncoupled models for the test combination with the best R^2_{fit}. The uncoupled model fitting was performed with constraints to ensure the parameters have physical meaning.

as structural, there must be a relationship between the parameter and the tissue's physiology. On the other hand, for the coupled model proposed in this work, the optimal combination was the ratios E1, E2, and E3 (Figure 7b) with R^2_{fit} = 0.972 and R^2_{pred} = 0.878, the values of the structural parameters were C_0 = 13.88 kPa, C_1 = 28.78, C_2 = 124.62, C_3 = 49.07. Unlike the uncoupled model, the parameter values in this case align with the expected structural function. The parameter associated with the longitudinal direction is greater than that of the transverse direction, and the latter is greater than that of the matrix. Comparing *err** (see Equation 13) in both models for the maximum R^2_{fit} obtained with the uncoupled model (E1, E3, and PT), the coupled model exhibits lower relative errors, especially when the transversal direction is fitted, as shown in Figure 8. The longitudinal direction has a similar relative error in both models along λ, but it is slightly lower in the coupled model. The fitting for the uncoupled

10.3389/fbioe.2025.1494793

TABLE 2 Material structural parameters from fitting for the different combinations of tests using the proposed coupled strain energy function.

Combination	C_0 [kPa]	C_1 [–]	C_2 [–]	C_3 [–]	R^2_{fit}	ε_{fit}	R^2_{pred}	ε_{pred}
E1	**13.02**	**32.13**	**129.28**	**40.00**	**0.994**	**0.087**	**0.882**	**0,406**
E2	7.88	$1.13.10^{-5}$	230.96	155.52	0.999	0.032	0.719	0.686
E3	4.29	135.68	149.29	$1.17.10^{-5}$	0.995	0.089	0.620	1,084
UT	13.66	$1.00.10^{-5}$	147.36	36.72	0.990	0.128	0.499	0.951
PT	13.80	$1.26.10^{-5}$	129.99	61.49	0.995	0.071	0.442	0.843
E1, E2	16.42	$1.00.10^{-5}$	152.17	78.89	0.986	0.147	0.803	0.494
E1, E3	12.35	60.41	97.06	2.95	0.986	0.149	0.873	0.423
E1, UT	**12.57**	**40.87**	**124.76**	**24.09**	**0.989**	**0.126**	**0.854**	**0.471**
E1, PT	11.98	67.93	82.81	$1.00.10^{-5}$	0.992	0.106	0.846	0.452
E2, E3	4.89	67.96	203.04	120.29	0.988	0.125	0.576	0.971
E2, UT	9.03	86.77	124.90	11.69	0.945	0.270	0.740	0.688
E2, PT	9.36	90.82	78.25	12.47	0.958	0.199	0.856	0.472
E3, UT	7.74	73.24	148.30	11.56	0.978	0.191	0.830	0.590
E3, PT	9.41	94.38	81.30	$1.00.10^{-5}$	0.967	0.193	0.858	0.486
UT, PT	12.75	$1.00.10^{-5}$	144.51	52.57	0.968	0.206	0.364	0.994
E1, E2, E3	**13.88**	**28.78**	**124.62**	**49.07**	**0.972**	**0.211**	**0,878**	**0.371**
E1, E2, UT	14.08	37.39	116.67	29.28	0.973	0.202	0.870	0.412
E1, E2, PT	13.21	62.27	80.05	7.94	0.976	0.185	0.860	0.408
E1, E3, UT	11.59	62.27	129.16	24.98	0.983	0.166	0.844	0.492
E1, E3, PT	12.42	66.20	84.01	$1.00.10^{-5}$	0.983	0.157	0.846	0.454
E1, UT, PT	11.11	44.82	122.59	29.37	0.972	0.198	0.859	0.461
E2, E3, UT	7.00	90.18	142.75	26.59	0.953	0.258	0.710	0.739
E2, E3, PT	8.06	111.86	142.75	0.84	0.950	0.228	0.747	0.631
E2, UT, PT	13.25	30.94	116.83	39.75	0.917	0.317	0.894	0.369
E3, UT, PT	11.63	34.20	127.28	33.08	0.942	0.284	0.868	0.442
E1, E2, E3, UT	**13.02**	**39.60**	**120.63**	**30.52**	**0.969**	**0.222**	**0.861**	**0,417**
E1, E2, E3, PT	13.46	61.16	81.82	7.78	0.969	0.210	0.858	0.404
E1, E2, UT, PT	12.38	43.22	114.24	30.98	0.960	0.238	0.877	0.403
E1, E3, UT, PT	11.41	46.85	119.01	25.49	0.969	0.215	0.848	0.475
E2, E3, UT, PT	10.86	52.84	117.21	32.45	0.921	0.313	0.918	0.325
E1, E2, E3, UT, PT	**12.42**	**44.79**	**112.95**	**25.75**	**0.958**	**0.247**	**0.862**	**0,406**

Bold rows represent the best result of each combination.

model was performed while considering constraints to ensure the physical meaning of the parameters. The relative error indicates that the proposed model achieves better results when different strain states are evaluated for soft-fibered tissues with fiber orientations close to 90°. The graphs show that the model better fits stress values for $\lambda > 1.005$. Note that $err^* = 0$ means the model perfectly matches the experimental stress.

Observing the better fitting, improved prediction, and the physiological relevance of the parameters, the coupled model was chosen to study how the combination of tests affects the model's predictive capability, considering its structural nature.

3.4 Constitutive model predictions

In this section, the combination of one to five tests is analyzed. It is essential to strike a balance between fitting and prediction. When

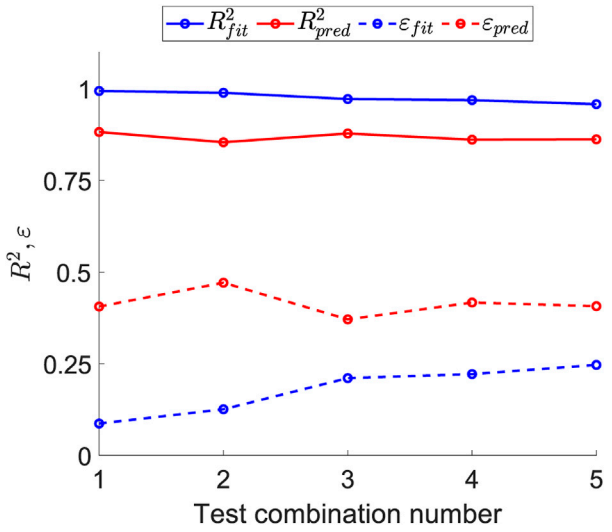

FIGURE 9
Sensitivity of the fitting and prediction errors as the number of tests used to obtain the structural parameters increases. R^2 and ε values correspond to the best result of each test combination.

parameters are obtained based on a single strain state, the fitting error is minimal, but the predictive capability is lost as the parameters become specific to that strain state.

Table 2 summarizes the material parameters and errors for each combination. Structural material parameters exhibit similar values, all within the same order of magnitude, except for the first fitting using only one test. As shown in Table 2, fitting becomes more challenging as the number of tests increases and the strain states become more diverse.

Fitting with two strain states ($R^2_{pred} = 0.854$; $\varepsilon = 0.471$) implies losing precision when predicting tissue behavior for other strain states compared to fitting with three strain states ($R^2_{pred} = 0.878$; $\varepsilon = 0.371$). It should be noted that an excessive increase in the number of tests used for fitting does not necessarily result in an improvement in prediction error. While increasing from a single strain state to the combination of two may enhance prediction, fitting with four tests ($R^2_{pred} = 0.861$; $\varepsilon = 0.417$) does not yield a better prediction than fitting with three. In this sense, fitting with one strain state and with five strain states simultaneously was tested to corroborate the previous idea. Using only a single test, the E1 ratio yielded the best results in terms of the physiological meaning of the parameters and the prediction error R^2_{pred} that was equal to 0.882 with a $\varepsilon = 0.406$; however, the adjustment error R^2_{fit} was 0.994 with $\varepsilon = 0.087$. Using five tests, the fitting error R^2_{fit} is 0.958 with $\varepsilon = 0.247$, and the prediction error worsens with respect to the combination of three tests ($R^2_{pred} = 0,878$; $\varepsilon = 0,371$) with $R^2_{pred} = 0.862$ and $\varepsilon = 0.406$.

Figure 9 illustrates the effect of the number of fitting tests on the errors in fitting and prediction. For each number of tests combined, the optimal prediction has been selected; that is, for the combination of three tests, the R^2 and ε values for the E1, E2, and E3 case are depicted.

Figure 10 depicts the prediction curve for the tests that are not included when fitting with the three strain states (E1, E2, and E3). For low strain values, the prediction curve more accurately follows the real behavior experienced in the test. However, it is also observed that the biaxial ratio E5 proves challenging to predict because it represents a strain state that forces greater stiffness in the softer direction of anisotropy, which contradicts the tests used for fitting.

4 Discussion

Computational simulation is a powerful tool for studying and analyzing pathologies, treatments, and surgeries in the context of biomechanics. To achieve accurate results, an exhaustive characterization and the use of an adequate constitutive model capable of predicting tissue behavior are necessary. The fascia forms a continuous structure that can store approximately 20% of the total force produced by muscles (Blottner et al., 2019). Its stiffness is associated with plantar fasciopathy (Barreto Rabelo et al., 2023) and biomechanical responses (Cheung et al., 2004), among other functions. Computational simulation could help improve the understanding of its behavior and related pathologies. Despite its importance, the fascia remains an understudied tissue. For this reason, we have chosen fascia as the focus of our study.

4.1 Experimental remarks

Throughout this work, a multidimensional characterization has been presented, including three different tests that reproduce a wide range of strain states. The results show that fascia is a highly stiff tissue due to its structure, which consists of layers of collagen fibers spatially oriented in two directions. The highest deformation observed in our tests occurs in the plane tension test, reaching a maximum value of 7.5%. In the other tests, the maximum deformation reached is 5%. These elongation values are consistent with those reported in previous studies (Eng et al., 2014; Pancheri et al., 2014; Ruiz-Alejos et al., 2016). Fascia's mechanical behavior is characterized by high stiffness, especially when compared to other soft tissues such as the myocardium and arteries. This stiffness allows the fascia to sustain high levels of stress with minimal strain, a characteristic typical of collagenous fibrous tissues like tendons. If tension increases by 8%–10%, it leads to visible tearing of tendon fibers, ultimately resulting in tendon rupture (Wang et al., 2012). The difference in stiffness between the longitudinal and transverse directions is related to the thickness and number of collagen fibers in each direction, which are greater in the longitudinal direction than in the transverse direction, as shown in the histological images in Figure 2A). Similar results were reported by Pancheri et al. (2014).

Eng et al. (2014) obtained 3.5 MPa in biaxial tests for a strain of 4%, while in our study, we measured 3 MPa for the same strain range. Pancheri et al. (2014) reported a maximum strain of 6% in biaxial tests and 8% in uniaxial tests. Regarding maximum stress values in uniaxial tests, they obtained 7 MPa for a strain level of 5.5%, whereas in our study, we reached 4 MPa at the same strain level. Comparing stress in biaxial tests, Pancheri et al. (2014) reported 3 MPa for a 4% strain, which matches our results. Additionally, Ruiz-Alejos et al. (2016) found that deep fascia exhibited a stress of 2.5 MPa at 5.5% elongation in uniaxial tests. Both results are within the same order of magnitude, with the

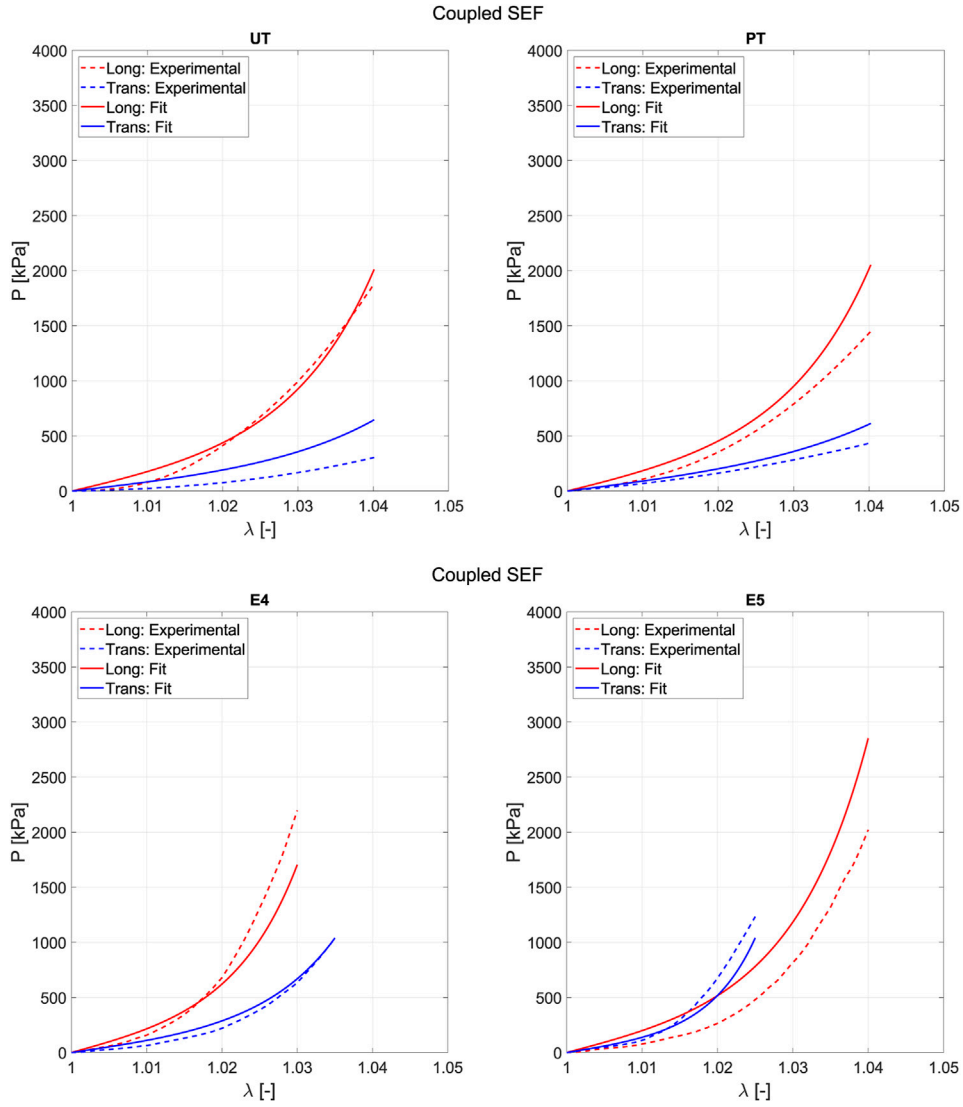

FIGURE 10
Prediction results when fitting is performed using three tests (E1, E2, and E3) with the proposed coupled SEF.

difference accounted for by deviation. As observed by Pancheri et al. (2014), the data illustrate that specimens stretched along the longitudinally oriented fibers exhibit higher stiffness than those stretched in the transverse direction. Despite the different origins of the fascia samples, we observed similar values in sheep fascia lata to those reported by Stecco et al. (2013) for human crural fascia under the same stretch range. As seen in the literature and confirmed by our experimental results across different strain states, fascia exhibits high variability. The stress–strain curves presented in this work show that this deviation is consistent with that reported in other experimental studies.

4.2 Constitutive model remarks

In this study, we evaluated the accuracy of the model proposed by Pancheri et al. (2014). As they described, a generic angle φ is used despite histological sections showing that collagen fibers form an angle between 80° and 90° (Stecco et al., 2009). We proposed a constitutive model based on a coupled strain energy function, assuming a 90° angle between the anisotropy directions representing the fiber orientations in the tissue. This assumption affects the choice of the constitutive model. Referring back to the formulation in Section 2.2, the unit vectors are defined as $\mathbf{M} = \{1, 0, 0\}$ and $\mathbf{N} = \{0, 1, 0\}$, which, in turn, impacts the expressions used for stress calculation. In the model by Pancheri et al. (2014), the stress value in one direction does not depend on the other, as seen in the expressions for Ψ_1, Ψ_4, and Ψ_6 (Equation 8). Although the model can fit the experimental data (Figure 11A), issues arise with the obtained parameters, as they lack structural meaning. Specifically, the parameters related to the transverse fiber direction are reduced to 0, effectively neglecting one fiber direction. When we impose constraints in the minimization problem to ensure that the transverse parameters remain nonzero and greater than those

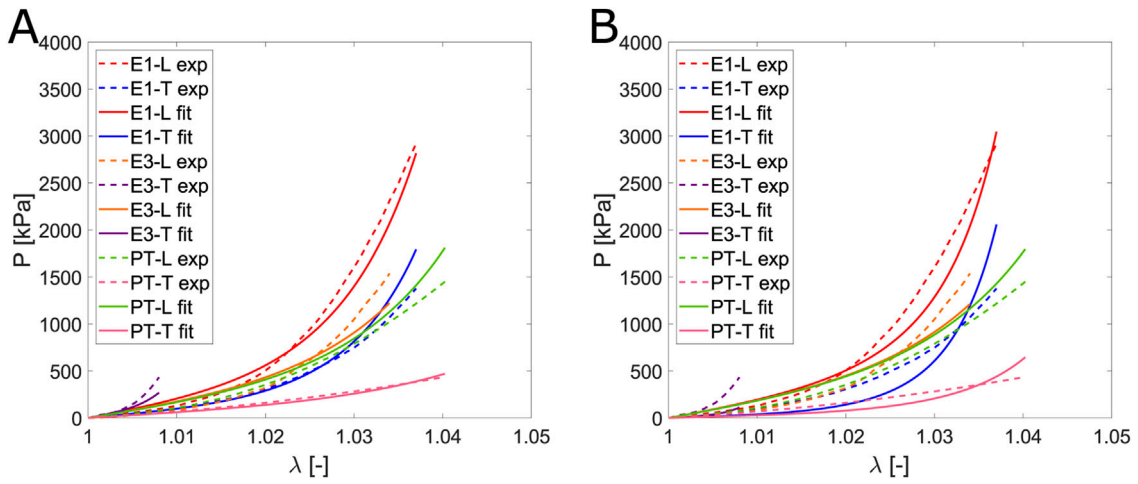

FIGURE 11
Comparison of the fit for the Pancheri et al. (2014) model: **(A)** without constraints and **(B)** with the constraint that the transverse parameters are greater than those associated with the matrix.

TABLE 3 Material parameters proposed for fascia characterization based on our SEF.

Combination	C_0	C_1	C_2	C_3
E1, E2, E3	13.88	28.78	124.62	49.07

associated with the matrix, the model is no longer able to fit the experimental data properly, as shown in Figure 11B.

To use an uncoupled constitutive model, it is necessary to not assume that the angle between the anisotropy directions is 90°. Instead, this angle becomes an additional parameter in the problem, defining the unit vectors as $\mathbf{M} = \{cos(\varphi), -sin(\varphi), 0\}$ and $\mathbf{N} = \{cos(\varphi'), sin(\varphi'), 0\}$, where φ represents the fiber angle relative to the 1-axis, and thus $\varphi' = 90°\text{-}\varphi$. As stated in Pancheri et al. (2014), φ is a phenomenological parameter that they compare to the angle formed by fascia collagen fibers, despite describing a structural strain energy function (SEF). With the unit vectors defined in terms of sine and cosine, the analytical expression for stress calculation in one direction depends on the other. The model we propose in this work effectively fits the experimental data while assuming that the fibers form a 90° angle between them. This is because it incorporates both longitudinal and transverse contributions within the same exponential term, allowing stress in one direction to depend on the other. Even if the angle were treated as a parameter, our model could still accommodate it by incorporating it into the vector definitions, providing flexibility in considering different anisotropy angles.

Considering these aspects, the parameter fitting process was optimized using the coupled model proposed in this work. The main objective is to determine the minimal set of deformation states required for fitting in order to obtain accurate parameters that enable reliable predictions of fascia behavior with the fewest possible experiments.

Regarding the optimal combination of tests among the options studied and listed in Table 2, greater emphasis was placed on minimizing prediction error and reducing the number of test types required, as this directly impacts the number of samples and overall testing effort. As shown in Figure 9, which illustrates the variation of fitting and prediction errors with an increasing number of tests, both R^2_{fit} and R^2_{pred} stabilize and remain constant beyond three tests. This indicates that including more than three tests in the fitting process does not enhance prediction accuracy. Additionally, the three necessary tests—biaxial ratios E1, E2, and E3—belong to the same test type, reducing the number of specimens required and the overall testing time by eliminating the need for multiple testing machines.

The aim of a computational model is to enable simulations, making predictability a crucial factor. Our proposed coupled SEF demonstrates excellent predictability with only four parameters, considering that it accounts for three strain states. The material parameters we propose for characterizing fascia and predicting various strain states are listed in Table 3.

Throughout this work, we have emphasized the importance of the obtained parameter values in relation to the structural nature of the model used for fitting. There must be coherence between these values and the structural components they represent. In this regard, it is possible to establish similarities with parameters from other studies. The parameters determined in this study represent a solution to a problem that does not have a unique solution. Therefore, direct comparisons of individual values to establish, for example, a stiffness criterion are not meaningful. Moreover, even if the two models are structural, their defining SEFs may differ. In fact, this work presents an SEF distinct from those proposed by Pancheri et al. (2014) and Ruiz-Alejos et al. (2016). Regardless of the absolute parameter values, a clear pattern emerges: parameters associated with the primary fiber direction are greater than those in the transverse direction. In turn, transverse parameters exceed those related to the isotropic component, which corresponds to the tissue matrix and lacks a mechanical function.

4.3 Limitations

This work has some limitations, one of which is that we tested samples from an animal model rather than human fascia. Although

our results are similar to those obtained by Stecco et al. (2013), they cannot be directly extrapolated to the human model. Therefore, the parameters we propose should be used with caution in simulations for human studies.

Regarding the coupled SEF proposed in this study, as discussed by Anssari-Benam et al. (2024), the selection of classical invariants for the isotropic component may be suboptimal if I_2 is excluded, and similarly for the anisotropic component if I_5 and I_7 are not considered. The goal of this study is to develop a model that not only achieves a good fit but also enhances predictive accuracy across different deformation states while maintaining a straightforward formulation. To this end, we have chosen to use models that incorporate a simple exponential function and standard invariants commonly referenced in the literature.

Additionally, our model does not account for viscoelastic properties, which play a significant role in the behavior of soft tissues. The viscoelastic properties of fascia are typically analyzed through stress relaxation and dynamic mechanical analysis (DMA), both of which are widely documented in the literature (Bonifasi-Lista et al., 2005; Prevost et al., 2011; García et al., 2012; Calvo et al., 2014). These properties will be the subject of future studies. The perpendicularity of the fibers is considered; however, soft tissues exhibit fiber dispersion relative to the main direction. The next step to enhance the proposed model would be to incorporate a new parameter for dispersion using techniques such as polarized microscopy (Sáez et al., 2016). The mechanical behavior of soft tissues is governed by their underlying microstructure, particularly the extracellular matrix with embedded collagen fibers. Therefore, studying the micromechanical behavior of individual fibers can provide valuable insights into the macroscopic mechanical response. This approach is commonly used in microstructural models, where the behavior of individual fibers is represented and then homogenized by integrating over the surface of a sphere (Alastrué et al., 2009; Gasser, 2011; Weisbecker et al., 2015; Sáez et al., 2016). This work focuses on the macroscopic response and does not account for the micromechanical behavior of collagen fibers.

5 Conclusion

Characterizing soft biological tissues is challenging due to the many factors influencing accurate results. Tissue-related characteristics, such as heterogeneity, harvesting area, and inter-individual differences within the same species, as well as handling and testing protocols, can lead to variations across studies. Despite these considerations, our multidimensional characterization has yielded stress values that closely match those reported in the literature for the same strain levels.

This study highlights the importance of considering tissue characteristics and modeling assumptions when selecting an appropriate constitutive model. We assumed that fiber directions form an approximately 90° angle, which necessitates the use of a coupled constitutive model. An uncoupled model fails to properly fit the parameters under the condition that transverse parameters are neither 0 nor lower than the isotropic ones, as we consider the model to be structural. Furthermore, the uncoupled model lacks predictability, making it unsuitable for future simulations. These limitations motivated the development of the coupled SEF proposed in this work. Using this coupled model, we can accurately predict uniaxial, biaxial, and planar tension strain states with a single set of parameters.

Beyond proposing a new SEF that addresses the challenge of modeling anisotropic directions at 90°, we also analyzed the impact of the number of tests on fitting and prediction. Our results demonstrate that increasing the number of fitting tests does not improve the prediction of other strain states. Specifically, the biaxial ratios E1, E2, and E3 are sufficient to predict uniaxial, planar tension, and biaxial strain states.

The diversity of tests, the well-defined testing protocols, the experimental stress-strain curves, and their comparison with literature values, combined with the proposal of a new SEF and material parameters capable of predicting different strain states, provide a comprehensive and accurate understanding of the mechanical behavior of fascia. In addition to introducing a study on test combinations, this work offers valuable insights that contribute to a deeper understanding of fascia mechanics.

6 Statement of significance

Fascia is a collagen-rich soft tissue that has recently gained increasing importance in human physiology. Understanding its mechanical behavior is essential for comprehending its functions. To achieve this, we conduct a multidimensional characterization that includes different strain states. Additionally, we analyze two constitutive models: one widely used and another proposed in this study. Our findings highlight the importance of tissue structure when selecting an appropriate constitutive model. The primary goal of a constitutive model is to accurately predict strain states, which depends on the material parameters obtained through fitting. Therefore, this study also explores the combination of mechanical tests to optimize the fitting process.

Data availability statement

The raw data supporting the conclusions of this article will be made available by the authors, without undue reservation.

Ethics statement

Ethical approval was not required for the study involving animals in accordance with the local legislation and institutional requirements because animals were sacrificed in the slaughterhouse for another study that does not affect the results or purposes of this work.

Author contributions

AA-G: investigation, methodology, writing – original draft, and writing – review and editing. EP: conceptualization, funding acquisition, supervision, and writing – review and editing. MP:

conceptualization, investigation, methodology, and writing – review and editing.

Funding

The author(s) declare that financial support was received for the research and/or publication of this article. This work was supported by the research project PID2022-140219OB-I00 and T24-20R funding.

Acknowledgments

The authors gratefully acknowledge research support from the ICTS "NANBIOSIS," specifically, from the Tissue & Scaffold Characterization Unit (U13) of the CIBER in Bioengineering, Biomaterials & Nanomedicne (CIBER BBN at the University of Zaragoza). Special thanks to laboratory technician C. Marzo for his valuable assistance and support during the experimental testing.

Conflict of interest

The authors declare that this research was conducted without any commercial or financial interests that could present a potential conflict of interest.

Publisher's note

All claims expressed in this article are solely those of the authors and do not necessarily represent those of their affiliated organizations, or those of the publisher, the editors and the reviewers. Any product that may be evaluated in this article, or claim that may be made by its manufacturer, is not guaranteed or endorsed by the publisher.

References

Acosta Santamaría, V., Siret, O., Badel, P., Guerin, G., Novacek, V., Turquier, F., et al. (2015). Material model calibration from planar tension tests on porcine linea alba. *J. Mech. Behav. Biomed. Mater.* 43, 26–34. doi:10.1016/j.jmbbm.2014.12.003

Alastrué, V., Martínez, M., Doblaré, M., and Menzel, A. (2009). Anisotropic micro-sphere-based finite elasticity applied to blood vessel modelling. *J. Mech. Phys. Solids* 57, 178–203. doi:10.1016/j.jmps.2008.09.005

Anssari-Benam, A., Goriely, A., and Saccomandi, G. (2024). Generalised invariants and pseudo-universal relationships for hyperelastic materials: a new approach to constitutive modelling. *J. Mech. Phys. Solids* 193, 105883. doi:10.1016/j.jmps.2024.105883

Barreto Rabelo, D., Coelho Figueira Freire, A. P., Colen Milagres Brandão, F., Oliveira Melo, S., Ocarino, J. M., Saldanha dos Anjos, M. T., et al. (2023). Myofascial stiffness of plantar fascia and achilles tendon in individuals with plantar fasciopathy: an observational cross-sectional study. *Musculoskelet. Sci. Pract.* 66, 102781. doi:10.1016/j.msksp.2023.102781

Blottner, D., Huang, Y., Trautmann, G., and Sun, L. (2019). The fascia: continuum linking bone and myofascial bag for global and local body movement control on Earth and in Space. A scoping review. *a scoping Rev. REACH* 14–15, 100030. doi:10.1016/j.reach.2019.100030

Bonifasi-Lista, C., Lakez, S. P., Small, M. S., and Weiss, J. A. (2005). Viscoelastic properties of the human medial collateral ligament under longitudinal, transverse and shear loading. *J. Orthop. Res.* 23, 67–76. doi:10.1016/j.orthres.2004.06.002

Calvo, B., Ramírez, A., Alonso, A., Grasa, J., Soteras, F., Osta, R., et al. (2010). Passive nonlinear elastic behaviour of skeletal muscle: experimental results and model formulation. *J. Biomechanics* 43, 318–325. doi:10.1016/j.jbiomech.2009.08.032

Calvo, B., Sierra, M., Grasa, J., Muñoz, M., and Peña, E. (2014). Determination of passive viscoelastic response of the abdominal muscle and related constitutive modeling: stress-relaxation behavior. *J. Mech. Behav. Biomed. Mater.* 36, 47–58. doi:10.1016/j.jmbbm.2014.04.006

Cheung, J. T.-M., Zhang, M., and An, K.-N. (2004). Effects of plantar fascia stiffness on the biomechanical responses of the ankle–foot complex. *Clin. Biomech.* 19, 839–846. doi:10.1016/j.clinbiomech.2004.06.002

Cilla, M., Corral, A. V., Peña, J. A., and Peña, E. (2019). Analysis of the accuracy on computing nominal stress in a biaxial test for arteries. *Strain* 56. doi:10.1111/str.12331

Costa, K. D., Holmes, J. W., and Mcculloch, A. D. (2001). Modelling cardiac mechanical properties in three dimensions. *Philosophical Trans. R. Soc. Lond. Ser. A Math. Phys. Eng. Sci.* 359, 1233–1250. doi:10.1098/rsta.2001.0828

Demiray, H. (1972). A note on the elasticity of soft biological tissues. *J. Biomechanics* 5, 309–311. doi:10.1016/0021-9290(72)90047-4

Destrade, M., Saccomandi, G., and Sgura, I. (2017). Methodical fitting for mathematical models of rubber-like materials. *Proc. R. Soc. A* 473, 20160811. doi:10.1098/rspa.2016.0811

Eng, C. M., Pancheri, F. Q., Lieberman, D. E., Biewener, A. A., and Dorfmann, L. (2014). Directional differences in the biaxial material properties of fascia lata and the implications for fascia function. *Ann. Biomed. Eng.* 42, 1224–1237. doi:10.1007/s10439-014-0999-3

Findley, T., Chaudhry, H., Stecco, A., and Roman, M. (2012). Fascia research – a narrative review. *J. Bodyw. Mov. Ther.* 16, 67–75. doi:10.1016/j.jbmt.2011.09.004

García, A., Martínez, M. A., and Peña, E. (2012). Viscoelastic properties of the passive mechanical behavior of the porcine carotid artery: influence of proximal and distal positions. *Biorheology* 49, 271–288. doi:10.3233/BIR-2012-0606

Gasser, T. C. (2011). An irreversible constitutive model for fibrous soft biological tissue: a 3-d microfiber approach with demonstrative application to abdominal aortic aneurysms. *Acta Biom* 7, 2457–2466. doi:10.1016/j.actbio.2011.02.015

Guo, X., Gong, C., Zhai, Y., Yu, H., Li, J., Sun, H., et al. (2023). Biomechanical characterization of normal and pathological human ascending aortic tissues via biaxial testing experiment, constitutive modeling and finite element analysis. *Comput. Biol. Med.* 166, 107561. doi:10.1016/j.compbiomed.2023.107561

Holzapfel, G. A., Gasser, T. C., and Ogden, R. W. (2000). A new constitutive framework for arterial wall mechanics and a comparative study of material models. *J. Elast.* 61, 1–48. doi:10.1023/a:1010835316564

Klingler, W., Velders, M., Hoppe, K., Pedro, M., and Schleip, R. (2014). Clinical relevance of fascial tissue and dysfunctions. *Curr. Pain Headache Rep.* 18, 439. doi:10.1007/s11916-014-0439-y

Laita, N., Rosales, R. M., Wu, M., Claus, P., Janssens, S., Martínez, M. n., et al. (2024). On modeling the *in vivo* ventricular passive mechanical behavior from *in vitro* experimental properties in porcine hearts. *Comput. Struct.* 292, 107241. doi:10.1016/j.compstruc.2023.107241

Langevin, H. M., and Huijing, P. A. (2009). Communicating about fascia: history, pitfalls, and recommendations. *Int. J. Ther. Massage Bodyw.* 2, 3–8. doi:10.3822/ijtmb.v2i4.63

Martins, P., Peña, E., Calvo, B., Doblaré, M., Mascarenhas, T., Natal Jorge, R., et al. (2010). Prediction of nonlinear elastic behaviour of vaginal tissue: experimental results and model formulation. *Comput. Methods Biomechanics Biomed. Eng.* 13, 327–337. doi:10.1080/10255840903208197

Moreira, D., and Nunes, L. (2013). Comparison of simple and pure shear for an incompressible isotropic hyperelastic material under large deformation. *Polym. Test.* 32, 240–248. doi:10.1016/j.polymertesting.2012.11.005

Ogden, R. W. (2001). *Elements of the theory of finite elasticity*. Cambridge University Press, 1–57. doi:10.1017/cbo9780511526466.002

Pancheri, F., Eng, C., Lieberman, D., Biewener, A., and Dorfmann, L. (2014). A constitutive description of the anisotropic response of the fascia lata. *J. Mech. Behav. Biomed. Mater.* 30, 306–323. doi:10.1016/j.jmbbm.2013.12.002

Pavan, P. G., Pachera, P., Stecco, C., and Natali, A. N. (2015). Biomechanical behavior of human crural fascia in anterior and posterior regions of the lower limb. *Med. Biol. Eng. Comput.* 53, 951–959. doi:10.1007/s11517-015-1308-5

Peña, E., Alastrué, V., Laborda, A., Martínez, M., and Doblaré, M. (2010). A constitutive formulation of vascular tissue mechanics including viscoelasticity and softening behaviour. *J. Biomechanics* 43, 984–989. doi:10.1016/j.jbiomech.2009.10.046

Peña, E., Peña, J. A., and Doblaré, M. (2008). On modelling nonlinear viscoelastic effects in ligaments. *J. Biomechanics* 41, 2659–2666. doi:10.1016/j.jbiomech.2008.06.019

Prevost, T. P., Balakrishnan, A., Suresh, S., and Socrate, S. (2011). Biomechanics of brain tissue. *Acta Biomater.* 7, 83–95. doi:10.1016/j.actbio.2010.06.035

Ramachandra, A. B., Kahn, A. M., and Marsden, A. L. (2016). Patient-specific simulations reveal significant differences in mechanical stimuli in venous and arterial coronary grafts. *J. Cardiovasc. Transl. Res.* 9, 279–290. doi:10.1007/s12265-016-9706-0

Ren, M., Ong, C. W., Buist, M. L., and Yap, C. H. (2022). Biventricular biaxial mechanical testing and constitutive modelling of fetal porcine myocardium passive stiffness. *J. Mech. Behav. Biomed. Mater.* 134, 105383. doi:10.1016/j.jmbbm.2022.105383

Ruiz-Alejos, D., Peña, J. A., Pérez, M. M., and Peña, E. (2016). Experiments and constitutive model for deep and superficial fascia: digital image correlation and finite element validation. *Strain* 52, 436–445. doi:10.1111/str.12198

Sáez, P., García, A., Peña, E., Gasser, T. C., and Martínez, M. A. (2016). Microstructural quantification of collagen fiber orientations and its integration in constitutive modeling of the porcine carotid artery. *Acta Biomat* 33, 183–193. doi:10.1016/j.actbio.2016.01.030

Samant, S., Bakhos, J. J., Wu, W., Zhao, S., Kassab, G. S., Khan, B., et al. (2023). Artificial intelligence, computational simulations, and extended reality in cardiovascular interventions. *JACC Cardiovasc. Interv.* 16, 2479–2497. doi:10.1016/j.jcin.2023.07.022

Schleip, R., Gabbiani, G., Wilke, J., Naylor, I., Hinz, B., Zorn, A., et al. (2019). Fascia is able to actively contract and may thereby influence musculoskeletal dynamics: a histochemical and mechanographic investigation. *Front. Physiology* 10, 336. doi:10.3389/fphys.2019.00336

Sednieva, Y., Viste, A., Naaim, A., Bruyère-Garnier, K., and Gras, L.-L. (2020). Strain assessment of deep fascia of the thigh during leg movement: an *in situ* study. *Front. Bioeng. Biotechnol.* 8, 750. doi:10.3389/fbioe.2020.00750

Spencer, A. (1971). *Theory of invariants*. Elsevier, 239–353. doi:10.1016/b978-0-12-240801-4.50008-x

Stecco, C., Gagey, O., Belloni, A., Pozzuoli, A., Porzionato, A., Macchi, V., et al. (2007). Anatomy of the deep fascia of the upper limb. second part: study of innervation. *Morphologie* 91, 38–43. doi:10.1016/j.morpho.2007.05.002

Stecco, C., Pavan, P., Pachera, P., De Caro, R., and Natali, A. (2013). Investigation of the mechanical properties of the human crural fascia and their possible clinical implications. *Surg. Radiologic Anat.* 36, 25–32. doi:10.1007/s00276-013-1152-y

Stecco, C., Pavan, P. G., Porzionato, A., Macchi, V., Lancerotto, L., Carniel, E. L., et al. (2009). Mechanics of crural fascia: from anatomy to constitutive modelling. *Surg. Radiologic Anat.* 31, 523–529. doi:10.1007/s00276-009-0474-2

Stemper, B. D., Yoganandan, N., Stineman, M. R., Gennarelli, T. A., Baisden, J. L., and Pintar, F. A. (2007). Mechanics of fresh, refrigerated, and frozen arterial tissue. *J. Surg. Res.* 139, 236–242. doi:10.1016/j.jss.2006.09.001

Takada, J., Hamada, K., Zhu, X., Tsuboko, Y., and Iwasaki, K. (2023). Biaxial tensile testing system for measuring mechanical properties of both sides of biological tissues. *J. Mech. Behav. Biomed. Mater.* 146, 106028. doi:10.1016/j.jmbbm.2023.106028

Vitucci, G. (2024). Biaxial extension of cruciform specimens: embedding equilibrium into design and constitutive characterization. *Exp. Mech.* 64, 539–550. doi:10.1007/s11340-024-01052-2

Wang, J. H.-C., Guo, Q., and Li, B. (2012). Tendon biomechanics and mechanobiology—a minireview of basic concepts and recent advancements. *J. Hand Ther.* 25, 133–141. doi:10.1016/j.jht.2011.07.004

Weisbecker, H., Unterberger, M. J., and Holzapfel, G. A. (2015). Constitutive modelling of arteries considering fibre recruitment and three-dimensional fibre distribution. *J. R. Soc. Interface* 12, 20150111. doi:10.1098/rsif.2015.0111

Zullo, A., Mancini, F., Schleip, R., Wearing, S., Yahia, L., and Klingler, W. (2017). The interplay between fascia, skeletal muscle, nerves, adipose tissue, inflammation and mechanical stress in musculo-fascial regeneration. *J. Gerontology Geriatrics* 65, 271–283.

Frontiers in
Bioengineering and Biotechnology

Accelerates the development of therapies, devices, and technologies to improve our lives

A multidisciplinary journal that accelerates the development of biological therapies, devices, processes and technologies to improve our lives by bridging the gap between discoveries and their application.

Discover the latest Research Topics

See more →

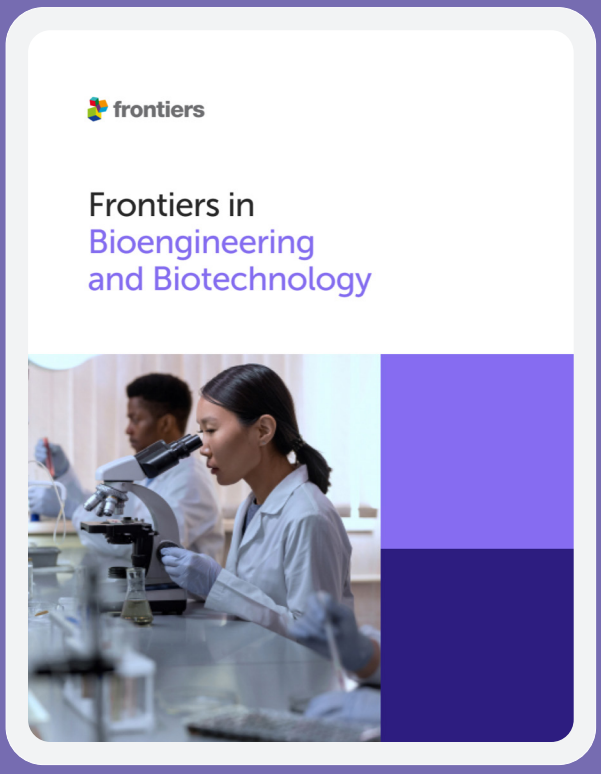

Frontiers

Avenue du Tribunal-Fédéral 34
1005 Lausanne, Switzerland
frontiersin.org

Contact us

+41 (0)21 510 17 00
frontiersin.org/about/contact